PETROLOGY AND F AND CL SYSTEMATICS OF RATTLESNAKE MOUNTAIN AND BONE SPRINGS SILLS, TRANS-PECOS MAGMATIC PROVINCE, TEXAS

by

CHRISTIAN M. SCHRADER

(Under the Direction of Alberto E. Patiño Douce)

ABSTRACT

This study investigates the petrogenesis and differentiation history of Rattlesnake Mountain Sill (RMS) and Bone Springs Sills (BSS) from the Trans-Pecos Magmatic Province (TPMP). Both are nepheline-normative shallow intrusions.

I conducted piston-cylinder experiments on a fine-grained sample of RMS, chosen to represent the benmoreitic composition of the intruding magma. Experimental conditions spanned 8 to 20 kb with 0, 2, 4, and 8% added H_2O. Garnet is common above 15 kb with <4% added H_2O. Apatite and ilmenite are nearly ubiquitous, and biotite, amphibole, and clinopyroxene are common. No run products contain olivine, indicating that the RM magma is not a primary mantle melt and that it last differentiated at pressures less than the experimental pressures. The melt (glass) compositions show that it is possible to reach silica saturation from undersaturated compositions with biotite rather than amphibole fractionation as the primary agent. Evidence is insufficient to claim that this occurred in the TPMP, but it warrants consideration for provinces that have both silica-saturated and –undersaturated rocks.

Bones Springs Sill differentiated from tephritic magma to a bimodal monzogabbro-monzosyenite suite. Monzosyenite liquid was generated by ~50% crystallization. Most of the

liquid crystallized in the interstices of the monzogabbro but some segregated into discrete monzosyenite bodies in the upper 1/3rd of the sill. The most felsic monzosyenites were generated by an additional ~8% crystallization. Apatite and biotite compositions record Cl loss concurrent with the separation and segregation of the differentiated monzosyenite liquid. This is probably related to the exsolution of a volatile phase during which volume expansion ruptured the crystalline framework and allowed migration of the interstitial liquid. Devolatilization caused an attendant loss of Cl by its partitioning into the vapor phase. Apatite and biotite in the monzosyenite-rich upper portion of BSS have the highest F/Cl in the sill as a result of F increase with differentiation and Cl loss to vapor exsolution. An apatite-biotite mineral pair included in Ti-magnetite from this section records a temperature of 1093° ± 103° C. These minerals have high F/Cl, suggesting that their inclusion postdates devolatilization and segregation of the residual liquid.

INDEX WORDS: Trans-Pecos Magmatic Province, Big Bend, alkaline igneous rocks, fractional crystallization, halogens

PETROLOGY AND F AND CL SYSTEMATICS OF RATTLESNAKE MOUNTAIN AND BONE SPRINGS SILLS, TRANS-PECOS MAGMATIC PROVINCE, TEXAS

by

CHRISTIAN M. SCHRADER

B.S., University of Alaska Fairbanks, 1998

M.S., University of Georgia, 2001

A Dissertation Submitted to the Graduate Faculty of The University of Georgia in Partial Fulfillment of the Requirements for the Degree

DOCTOR OF PHILOSOPHY

ATHENS, GEORGIA

2009

PETROLOGY AND F AND CL SYSTEMATICS OF RATTLESNAKE MOUNTAIN AND BONE SPRING SILLS, TRANS-PECOS MAGMATIC PROVINCE, TEXAS

by

CHRISTIAN M. SCHRADER

Major Professor: Alberto E. Patiño Douce

Committee: Michael F. Roden
Doug E. Crowe
Sam E. Swanson
John A. Wolff

Electronic Version Approved:

Maureen Grasso
Dean of the Graduate School
The University of Georgia
December 2009

DEDICATION

I dedicate this to my Mom, my Dad, and Sara: Thank you for always supporting me and for letting me find my own way.

ACKNOWLEDGEMENTS

I want to first acknowledge my advisor, Alberto, for all the help he's given me over the years and, especially, for his patience. Each member of my committee from UGA has been a source of great insight and knowledge to me in my roles as student, researcher, and teaching assistant. And special thanks to John Wolff, for providing geochemical analyses.

To my professors and colleagues at UAF: my deepest thanks go to Rainer Newberry, my first real mentor, whose brilliance, enthusiasm, and attention convinced me to start me on this path, and to Paul Layer and Jeff Drake. During my time spent in the field and core shed in southeast Alaska I learned much from John Proffett, Norm Duke, and Andy West.

Thanks to the Wheeler-Watts and Allard Fund committees at UGA and to the Geological Society of America and Sigma Xi for financial support. Thanks to Chris Fleisher for help on the microprobe, and to my fellow graduate students for camaraderie.

Thanks to Doug Rickman and Ernestine Cothran for allowing me the time to finish this work – it ended up taking much more than I thought and they were patient and understanding through it all.

And last, special thanks to Sarah for putting up with me and helping me during this seemingly interminable process.

TABLE OF CONTENTS

Page

LIST OF TABLES

Page

LIST OF FIGURES

Page

CHAPTER 1

INTRODUCTION

Description of study

This study investigates the nature of alkaline magmatism in the Big Bend region of southwest Texas. Big Bend is the southernmost portion of the Trans-Pecos Magmatic Province (TPMP). Specifically, this work focuses on two alkaline sills in Big Bend National Park: Bone Springs Sill (BSS) and Rattlesnake Mountain Sill (RMS). Bone Springs Sill is among the most mafic of the alkaline intrusions in the TPMP. It has a bulk composition of tephrite and it crystallized as a monzogabbroic body with internal segregations of monzosyenite. Rattlesnake Mountain Sill has a more differentiated bulk composition of mugearite/benmorite and it crystallized in a similar fashion to BSS as a monzonite intrusion with syenite segregations.

The post-intrusion history of RMS has been well-studied by Carman et al. (1975), who investigated the fractional crystallization and the formation of its monzonite-hosted syenite bodies. Chapter 2 of this document describes the piston-cylinder experimental investigation of phase relations of the RMS magma. The experimental conditions spanned 8 to 20 kb and 925-1165° C, with each run containing capsules of sample plus 0, 2, 4, and 8% added H_2O. I undertook this work to explore the petrogenesis of the RMS magma, and by association the petrogeneses of other TPMP intermediate alkaline magmas.

In a follow-up to the Carman et al. (1975) study on RMS, Carman (1994) expanded his work to apply to other internally differentiated alkaline igneous intrusions in the Big Bend area and elsewhere around the globe. Together, these studies (Carman et al., 1975, and Carman, 1994)

contain a reconnaissance survey of BSS, including a cursory description of the field relations and a few geochemical analyses of BSS margin rocks. Chapter 3 of this document describes my detailed examination of BSS, including a map of the sill and a petrographic and geochemical investigation. I interpret the crystallization history of BSS and the processes that lead to the differentiation and segregation of the monzosyenite liquids.

Chapter 4 of this study investigates the F and Cl compositions of biotite and apatite in BSS, which I use to deduce the history of volatile saturation and boiling in BSS. The devolatilization event in BSS is intimately tied to its differentiation and to the separation of residual liquid to form the monzosyenite bodies. Additionally, I compare my observations of BSS and RMS F and Cl systematics to other well-studied alkaline and subalkaline intrusions. This illuminates the contrasting halogen budgets and behavior between alkaline rocks around the world and how they differ from large subalkaline layered igneous intrusions. This work sets the stage for further investigation into the role of halogens in TPMP igneous processes.

Geologic setting of the Trans-Pecos Magmatic Province

The Trans-Pecos Magmatic Province (TPMP) is an alkaline volcanic and intrusive belt delineated to the south and west by the Rio Grande River, to the east by the Pecos River, and to the north by a line 12 km north of the Texas-New Mexico border (Barker, 1977). The borders of the TPMP are arbitrary to the south and southeast, as alkaline rocks continue into Mexico for at least 200 km (Barker, 1977). To the west, partially contemporaneous igneous rocks grade to a calc-alkaline composition, including the Sierra Madre Occidental continental arc and beyond to the western coast of Mexico (James and Henry, 1991). The eastern border of the TPMP at the Pecos River marks the easternmost extent of exposed igneous rocks. Barker (1977) recognized a belt of broadly contemporaneous alkaline rocks stretching along the eastern border of the

Cordillera from Canada into Mexico, of which the TPMP, at least spatially if not genetically, is a part. Figure 1-1 shows the location and igneous rocks of the TPMP and Big Bend National Park.

The timing of magmatism in the TPMP ranges from 48 to 17 Ma (Henry and McDowell, 1986). Despite its similarities to intraplate, rift-related magmatic provinces like that of Kenya, geophysical surveys have discerned no gravity or magnetic anomalies indicative of continental rifting (Barker, 1977 and 1987). Rather, studies such as Henry and others (1991) and James and Henry (1991) on the temporal relation of stress regimes to magma compositions indicate that magmatism in the TPMP spans three tectonic regimes. The first was a compressive regime, interpreted as related to eastward subduction of the Farallon plate below North America (48-32 Ma), during which alkaline magmatism in the TPMP was accompanied to the west by the metaluminous Sierra Madre Occidental continental arc. This was followed by an incipient extensional regime characterized by the absence of widespread normal faulting (31-27 Ma), and, after a hiatus, magmatism related to Basin and Range extension with accompanying normal faults (24-17 Ma). The focus of Chapter 2 of this study, Rattlesnake Mountain Sill (RMS), with an age of 28.6 ± 0.4 Ma (Henry et al., 1986) is the best exposed and studied of about ten syenodiorite to syenogabbro sills found in the Big Bend area (Carman, 1994) which are characteristic of the initial extensional regime. The subject of Chapters 3 and 4, Bone Springs Sill (BSS), is the most mafic of these early extensional sills. While BSS is grouped with these sills based on its intrusive and differentiation style (Carman, 1994) and fits the geochemical characteristics of magmas from the extensional period (James and Henry, 1991;Barker, 1987), it has not been dated.

The earlier igneous rocks of the TPMP (48-32 Ma) make up differentiation-related suites, with examples of quartz-saturated and nepheline-normative series, ranging from basaltic to

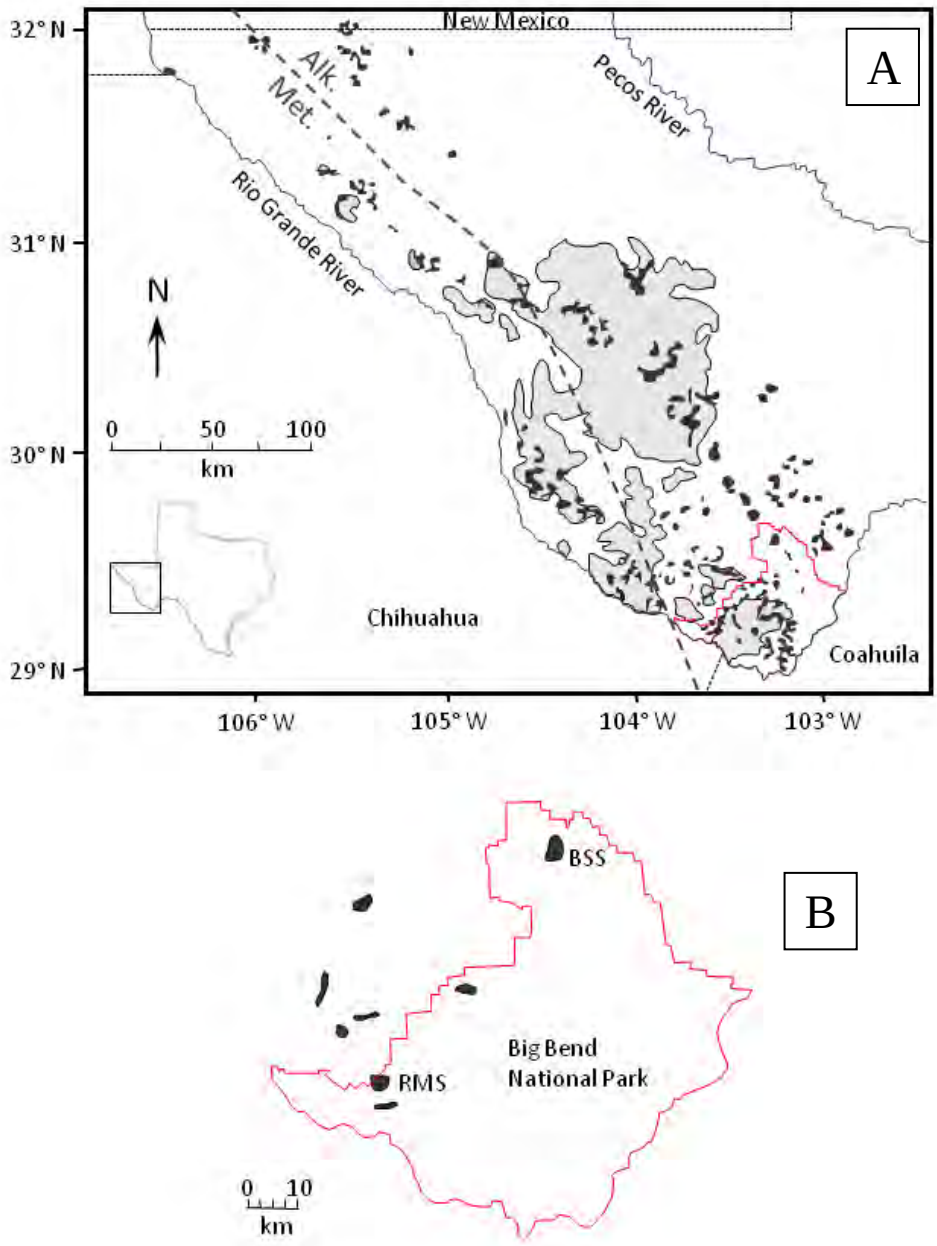

Figure 1-1. Tertiary igneous rocks of the Trans-Pecos Magmatic Province. (A): Distribution of Cenozoic volcanic (gray) and intrusive (black) rocks with locations adapted from Barker (1977) and White (2006); the green bold dashed line separates the western dominantly metaluminous subalkaline rocks from the Eastern Alkalic Belt (location after Barker, 1977); the boundary of Big Bend National Park is shown in red. **(B):** Inset of Big Bend National Park and selected early extensional internally differentiated sills, showing the locations of Bone Springs Sill (BSS) and Rattlesnake Mountain Sill (RMS) after Carman et al. (1975).

rhyolitic and trachytic compositions (James and Henry, 1991; Henry and McDowell, 1986). They occur within a compressional stress regime, as determined by structural measurements of folds, fractures and dike orientations (Henry et al., 1991; James and Henry, 1991). The TPMP rocks of this period are contemporaneous with arc-related rocks to the west, and share trace element signatures with them, such as relative depletion in Ta and Nb, and high Ba/Nb, Y/Nb and Zr/Nb, which are consistent with an origin in a continental arc (Barker, 1987; James and Henry, 1991). During this period, the gradation of metaluminous rocks in Mexico to predominantly alkaline rocks in Texas is attributed by James and Henry (1991) to increasing W-E distance from the subduction trench, and a likely corresponding reduction in partial melt fractions as the slab progressively dewaters. This period of magmatism is further divided into an early stage (48-38 Ma) and a main stage (38-32 Ma), characterized by a greater abundance of magmatism in the main stage rather than by compositional differences (Henry et al., 1991; James and Henry, 1991).

The period of magmatism associated with initial extension spans from 31 to 28 Ma (Henry et al., 1991), and is spatially limited to the southern TPMP, in and north of the Big Bend area. On the whole, igneous activity was less voluminous and more alkaline than the previous, compressive stage, and is dominantly bimodal: it is comprised of silicic alkaline caldera-related eruptions and shallow intrusions, and by mafic alkaline sills (Henry et al., 1986; James and Henry, 1991). There are approximately ten alkaline mafic sills emplaced in and around the Big Bend Area during this period, with bulk compositions ranging from tephrite to benmorite (syenogabbro to syenodiorite) (Carman, 1994). Rattlesnake Mountain Sill, on the western border of Big Bend National Park, is the best preserved, exposed, and studied of these occurrences (Carman et al., 1975; Carman, 1994). Trace element signatures of these magmas are distinct

from the earlier, compression-related phase, having lower Ba/Nb, Y/Nb and Zr/Nb; however, they partially overlap with later, Basin and Range magmas. This signature suggests a relation to oceanic island basalts (OIB) or continental rifting, rather than to arc magmatism (James and Henry, 1991).

There was little or no magmatism in the TPMP during the period 27-25 Ma (Henry et al., 1986). From 24-17 Ma, normal faulting began, marking the period of true Basin and Range extension (Henry et al., 1991). Magmatism during this period was dominated by alkali basalt with trace element signatures similar to early extension-related magmatism but with even lower Zr/Nb, suggestive of OIB or continental rift-related magmatism.

The TPMP is divided into the dominantly metaluminous western belt and the eastern alkalic belt (Barker, 1977). The eastern alkalic belt has rocks differentiated to phonolite and nepheline trachyte (Potter, 1996). The likely parental magma to this series is a tephrite of which Bone Springs Sill is probably the best-exposed intrusive example (Potter, 1996).

Fluorine and Cl in igneous rocks

Volatile budgets have important effects on magmatic and magmatic-hydrothermal processes. Water and F act as fluxes to lower liquidus and solidus temperatures and affect liquidus mineral assemblages (Wyllie and Tuttle, 1961). Chlorine is a primary complexing agent in transporting metals in aqueous phases (Williams et al., 1995; Yang and Scott, 2002) and F complexes can mobilize elements normally immobile under hydrothermal conditions (e.g., Zr) (Humphris and Thompson, 1978). Water and F alter the densities and viscosities of magmas (Lange, 1994). Because Cl preferentially partitions into vapor while F partitions into the melt (Carroll and Webster, 1994), careful documentation of their relative behavior can constrain magmatic-hydrothermal behavior (Zhu and Sverjensky, 1992).

Apatite is a ubiquitous mineral in igneous rocks on Earth and other planetary bodies. As the chief, and often the only, carrier of halogens in igneous and metamorphic rocks, its importance in aiding understanding of halogen behavior in these systems belies its occurrence as a trace mineral. Apatite has been investigated as a probe into F-Cl-OH systematics in terrestrial planetary systems (Patiño Douce and Roden, 2006), mantle xenoliths (Wass and Rogers, 1980; O'Reilly and Griffin, 2000), mid-ocean ridge cumulates (Meurer and Natland, 2001), layered mafic intrusions – specifically the Stillwater Complex (Boudreau and McCallum, 1989), the Great Dyke in Zimbabwe (Boudreau et al., 1995), and the Bushveld Complex (Willmore et al., 2000), to name a few – felsic igneous rocks (Piccoli and Candela, 1994), hydrothermal systems (Zhu and Sverjensky, 1991), and alkaline igneous rocks (Nash, 1972) and carbonatites (Seifert et al., 2000).

Biotite halogen contents have been investigated in magmatic-hydrothermal systems to unravel fluid compositions and temperatures (Munoz, 1984 and 1992; Zhu and Sverjensky, 1991; Ayati et al., 2008), in silica-saturated felsic igneous rocks (Sallet, 2000; Dooley and Patiño Douce, 1996), and in potassic and ultrapotassic rocks (Edgar and Arima, 1985; Foley, 1989).

The contents of octahedral sites in biotite exert a significant effect on halogen contents – the so-called "Mg-Cl" and "Fe-F avoidance effects" (Munoz, 1984; Volfinger et al., 1985), whereas apatite exhibits no such crystal chemical control on F-Cl-OH contents and the mixing of these elements can be treated as ideal at high temperatures (Tacker and Stormer, 1989). With appropriate mixing models, the halogen contents of coexisting biotite and apatite are used as a geothermometer (Stormer and Carmichael, 1971; Zhu and Sverjensky, 1992).

It is generally accepted that alkaline magmas are enriched in halogens, especially F, relative to sub- or nonalkaline magmas (Bailey, 1977; Carroll and Webster, 1994; Sallet, 2000).

This enrichment is owing to (1) the association of F and Cl with Na and K by magmatic and fluid complexing (Carroll and Webster, 1994); (2) the incompatible behavior of F and Cl coupled with the enrichment of alkaline rocks in incompatible elements (Edgar, 1987; Carroll and Webster, 1994); and possibly (3) the presence of halogens in mantle source regions in phases such as phlogopite (Edgar and Arima, 1985; Edgar, 1987), apatite, and/or amphibole (Wass and Rogers, 1980). The last argument is particularly compelling for potassic and ultrapotassic rocks.

CHAPTER 2

EXPERIMENTAL STUDY OF RATTLESNAKE MOUNTAIN SILL ANALCIME MONZONITE, 8-20 KILOBARS WITH ADDED H_2O

Abstract

I conducted piston-cylinder experiments on a sample of Rattlesnake Mountain Sill (RMS) from Big Bend National Park in the Trans-Pecos Magmatic Province. The sill has an outer analcime-monzonite border zone enclosing a slightly more mafic interior which contains segregations of analcime-syenite. I selected a sample of the RMS border monzonite to serve as an approximation of the bulk composition of the intrusion and thus of the intruding magma. The composition is benmoreitic and nepheline-normative (5% normative ne) and is similar to calculated bulk RMS composition previously published.

Experimental conditions span 8 to 20 kb, with each run containing capsules of sample plus 0, 2, 4, and 8% added H_2O. All run products contain melt. Garnet is common above 15 kb with <4% added H_2O. Apatite and ilmenite are nearly ubiquitous, and biotite, amphibole, and clinopyroxene are common. No run products contain free silica, olivine, or feldspathoid. The experiments yield super-liquidus run products with 2% and 4% H_2O at 12.5 kb, 1110° C. Ilmenite is on the liquidus at 12.5 kb, 1110°, 8% added H_2O. At 15 kb and 1125°, ilmenite is a liquidus phase with 4% H_2O and apatite is a liquidus phase, coexisting with a vapor phase, at 8% H_2O. At 18 kb, 1165° C, and 8% H_2O, clinopyroxene, orthopyroxene, and rutile coexist with

>95% melt. Pargasitic amphibole is a near liquidus phase at ~15 kb and occurs across a spectrum of pressures.

An interesting experimental result is that it is shown to be possible to reach silica-saturation from under-saturated compositions with biotite rather than amphibole fractionation as the primary agent. Evidence is insufficient to claim that it occurred in the Trans-Pecos region or elsewhere, but it is a possibility for provinces that bear silica-saturated and –undersaturated magmas and warrants further investigation.

Introduction

Depth of fractionation for alkaline intermediate magmas

Many alkali olivine basalts bear mantle xenoliths and have geochemical signatures that indicate they are near-primary mantle melts. A subset of more evolved alkaline igneous rocks, with compositions of hawaiite to phonolite, shows evidence of high pressure residence and fractionation. This evidence includes: (1) the presence of high-pressure minerals like kaersutite or titaniferous pargasite and spinel in xenoliths and megacrysts; (2) the lack of negative Eu anomalies that would indicate fractionation of plagioclase in the uppermost mantle or crust (Irving and Price, 1981; Irving and Green, 2008); (3) Ni contents and *Mg'* (molar 100*Mg/[Mg/Fe]) too low to represent primary mantle melts (Irving and Price, 1981). The presence of pargasite or kaersutite alone is not sufficient evidence of high pressure because pargasite is stable at pressures as low as 500 bars in some bulk compositions (Jenkins, 1983; Evans, 2007), but it is the pargasitic component, particularly Na, that allows for stability at mantle temperatures and pressures (Jenkins, 1983).

Xenolith-bearing mugearites and hawaiites from Australia have been well-studied (Knutson and Green, 1975; Wilkinson and Hensel, 1991; Irving and Green, 2008), and other

locales include southeastern Arizona, U.S.A. (Evans and Nash, 1979), Nigeria (Wright, 1969; Irving and Price, 1981), East Germany (Irving and Price, 1981), New Zealand (Wright, 1966; Price and Wallace, 1976), and Japan (Irving and Price, 1981). While most of the cited research invokes high-pressure fractionation for the Australian rocks, Wilkinson and Hensel (1991) argue that the Spring Mountain mugearite is a primary mantle melt.

Intermediate alkaline rocks that fractionate at high pressures probably do so over a range of depths (Irving and Green, 2008; Nekvasil et al., 204), but some fractionation pressures have been calculated that represent points in the magma histories: in the southwest U.S., 12-15 kb for fractionation to hawaiites and mugearites from alkali basalt (Evans and Nash, 1979) and, in New South Wales, Australia, 6.5-8 kb for hawaiite derivation by fractionation of orthopyroxene + olivine + clinopyroxene + ilmenite to alkali basalt (Knutson and Green, 1975). Irving and Green (2008) present a large experimental dataset on ne-basanites, ne-hawaiites, ne-mugearites, and, high pressure fractionation under hydrous conditions. They convincingly link a ne-mugearite to a primary ne-basanite from Victoria, Australia by a fractionation assemblage including amphibole and mica at ~14 kb. Their experimentally determined phase relations support the possible derivation of ne-hawaiites to phonolites from primary ne-basanites from 14 to 17 kb (Irving and Green, 2008).

The Trans-Pecos Magmatic Province (TPMP) was active from ~48-17 Ma (Henry and McDowell, 1986), during which there occurred thousands of volcanic eruptions and shallow intrusive events. The majority of this activity was of an alkaline character, though there was abundant subalkaline metaluminous magmatism as well, particularly in the western province (Barker, 1977). The alkaline mafic rocks are generally hawaiites and mugearites (Barker, 1977), though some tephrites and rare basanites can be found (Barker, 1987; Potter, 1996; this study).

The mafic rocks are not primary mantle melts – they have Ni <120 ppm and *Mg'* < 66 that indicates fractionation from their parental magmas (Barker, 1987), which were probably alkali olivine basalts or basanites. Additionally, the mafic alkaline rocks have either no negative Eu anomalies or have mildly positive Eu anaomalies (Cameron et al., 1986; Barker, 1987; this study); this is the case with some of both the ne-normative and the Q-normative felsic rocks (e.g., Cameron et al., 1986).

Barker (1987) proposed that olivine + augite + kaersutite + plagioclase could be a common, if not dominant, fractionating assemblage in TPMP magma evolution up to the composition of benmoreite from basaltic or basinitic parent magmas. Stratigraphic reconstructions and the presence of miarolitic cavities indicate that most Big Bend intrusive bodies crystallized at fairly shallow depths of <1 km (Barker, 1987; Barker, 2000) and very few bear xenoliths (Barker, 1987; Barker, 2000). However, some mafic, ne-normative members of TPMP magma series contain phenocrysts, megacrysts, and xenocrysts of kaersutite. These are found in the chilled zones of the least differentiated Diablo plateau rocks (nepheline-augite syenite) and as mantled xenocrysts and autoliths in more evolved rocks (Barker and Hodges, 1977) and in kaersutite gabbro of Slickrock mountain (Hill and Barnes, 1987). These grains are partially resorbed and have reaction textures indicating that they were stable at depth but not at the level of intrusion. The tephritic Bone Springs sill contains an unidentified resorbed mafic phase in the chill zones that could have been kaersutitic amphibole as well (this study). All of this makes a good case for some degree of deep differentiation of the mafic alkaline TPMP rocks.

Silica and alumina saturation of TPMP alkaline magmas

The alkaline magmatism in the TPMP is characterized by both quartz-normative and nepheline-normative compositions (Barker, 1977 and 1987), often occurring in close proximity or intimately related, such as in the Diablo Plateau (Barker et al., 1977), the Paisano volcanic complex (Parker, 1983), and Slickrock Mountain (Hill and Barnes, 1987). The presence of both q-normative basalts and ne-normative alkali basalts and basanite/tephrites in the TPMP has led many to invoke the derivation of the silica-saturated and silica-undersaturated magmas from two different parental magmas (Barker, 1977 and 1987). In some cases, silica-saturated felsic magmas have been tied to alkali basalt parents by wall-rock assimilation during fractional crystallization (e.g., White et al., 2006) or by magma-mixing with crustal melt followed by fractional crystallization (White and Urbanczyk, 2001). Different crustal sources for assimilation or magma mixing have been invoked to explain peralkaline felsic rocks (White et al., 2006) and peraluminous felsic rocks (White and Urbanczyk, 2001). The quartz-bearing rocks of the Diablo Plateau may be products of deuteric alteration of ne-normative rocks (Barker, 1987).

It has been demonstrated that the fractionation of silica-poor calcic amphibole can drive liquids across the thermal divide from silica-unsaturated to silica-saturated compositions (Giret et al., 1980; Martin, 2007). Amphiboles like kaersutite and pargasite have SiO_2 contents of ~38-43 wt.% and a proportion of silica to alkalis that is lower than all but the most primitive magmas; thus, their removal drives the melt to proportionately higher SiO_2 and lower alkalis that can result in silica-saturation. This requires efficient removal of the fractionating assemblage, and how often this actually happens is an open question. This mechanism has been proposed for locales with intimate associations of ne- and Q-normative rocks like the Red Hill complex in New Hampshire (Dorais and MacRae, 1994).

For Slickrock Mountain in the TPMP, Hill and Barnes (1987) were able to model the generation of quartz syenite from silica-undersaturated olivine gabbro by fractionation of kaersutite + plagioclase + olivine + clinopyroxene + Fe-Ti oxide + apatite (an assemblage comprising the adjacent kaersutite-gabbro) with satisfactory results ($\sum r^2 < 1$). However, they were unable to explain the Rb and Sr contents of the two rocks with these fractionation models or with assimilation or magma mixing, and so they propose different parental melts as the remaining option. The Slickrock Mountain kaersutite and olivine gabbros have cumulate textures (Hill and Barnes, 1987) and fractionation models utilizing major or trace elements are suspect in the absence of the liquid compositions. The possibility of a relationship by fractionation at high P_{total} or high P_{H2O} remains open.

Geologic background

The TPMP is an alkaline volcanic and intrusive belt delineated to the south and west by the Rio Grande river, to the east by the Pecos River, and to the north by the Organ Mountains 12 km north of the Texas-New Mexico border (Barker, 1977). (See Figure 2-1 for location map.) The borders of the TPMP are arbitrary to the south and southeast, as alkaline rocks continue into Mexico for at least 200 km (Barker, 1977). To the west, partially contemporaneous igneous rocks grade to calc-alkaline compositions, including the Sierra Madre Occidental continental arc and beyond to the western coast of Mexico (James and Henry, 1991), where there is an early Cenozoic paleotrench (Keith, 1978). The eastern border of the TPMP at the Pecos River marks the easternmost extent of exposed igneous rocks. The TPMP is divided between an eastern alkalic belt and a western metaluminous belt (Barker, 1977; Potter, 1996). Barker (1974) recognized a belt of broadly contemporaneous alkaline rocks stretching along the eastern border of the Cordillera from Canada into Mexico, which the TPMP, at least spatially if not genetically,

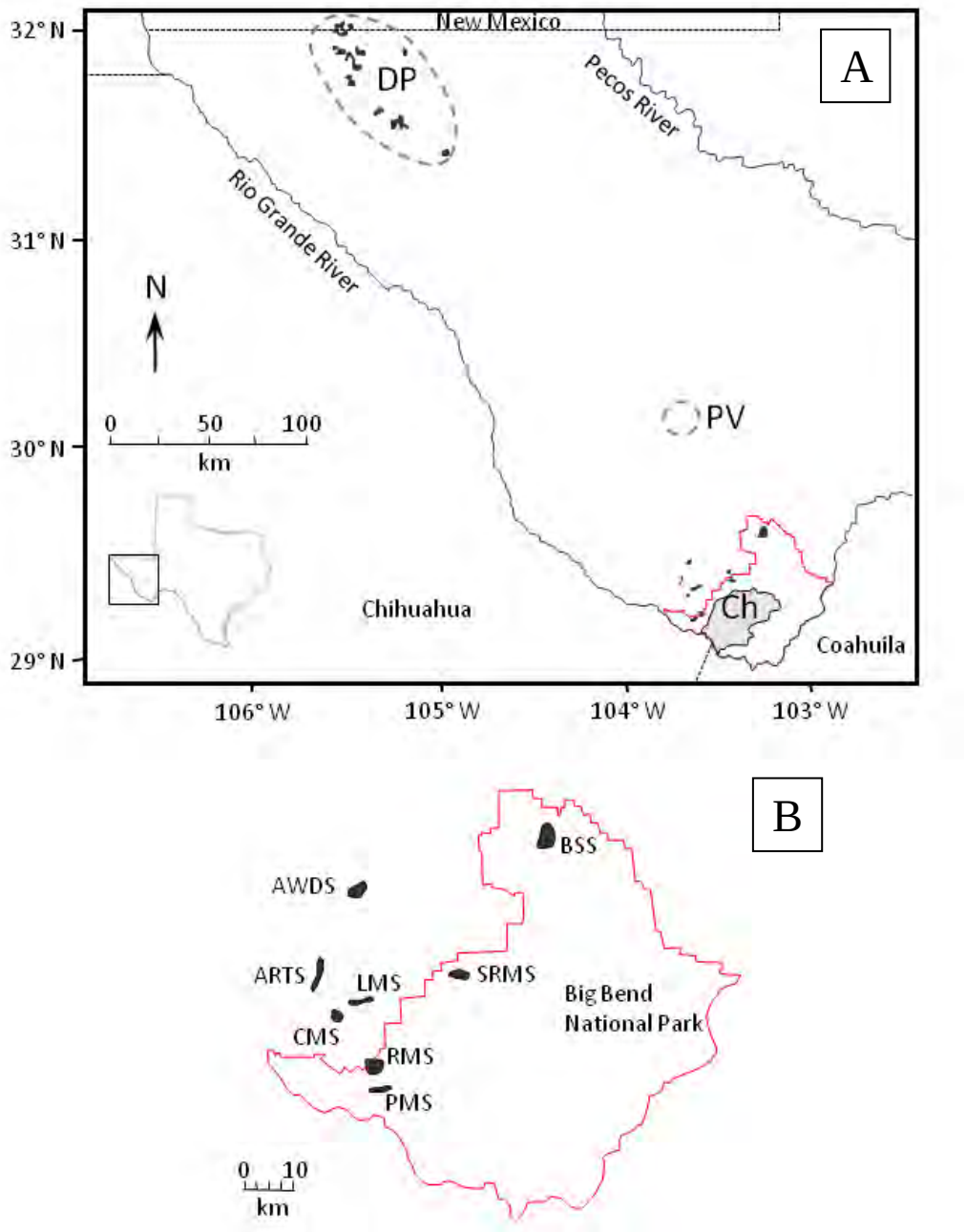

Figure 2-1. Selected Tertiary igneous rocks of the Trans-Pecos Magmatic Province. Distribution of Cenozoic volcanic (gray) and intrusive (black) rocks mentioned in the text, with locations adapted from Barker (1977) and White (2006). The boundary of Big Bend National Park is shown in red. **(A):** Ch = Chisos Mountains, DP = Diablo Plateau, and PV = Paisano Volcano. **(B):** Inset of Big Bend National Park and selected early extensional internally differentiated sills: ARTS = Al Reed Trail Sill, AWDS = Adobe Walls Draw Sill, BSS = Bone Springs Sill (BSS), CMS = Cigar Mountain Sill, LMS = Leon Mountain Sill, PMS = Peña Mountain Sill, RMS = Rattlesnake Mountain Sill, and SRMS = Slickrock Mountain Sill. Locations after Carman et al. (1975).

is a part. The timing of magmatism in the TPMP spans from 48 to 17 Ma (Henry and McDowell, 1986).

The temporal relation of stress regime to magma compositions indicate that magmatism in the TPMP persists through a change in stress/tectonic setting (Henry et al., 1991; James and Henry, 1991) which can be divided into three periods. The first period (48-32 Ma) was a compressive regime thought, on the basis of trace element signatures and regional geology, to be related to eastward subduction of the Farallon plate below North America. This period is marked by the most voluminous and widespread magmatism, during which alkaline magmatism in the TPMP grades westward to the metaluminous Sierra Madre Occidental continental arc. This was followed by an incipient extensional regime (initial crustal thinning), absence of widespread normal faulting (31-28 Ma), and, after a hiatus, magmatism related to Basin and Range extension with accompanying abundant normal faults (24-17 Ma).

The 31-28 Ma period of magmatism associated with initial extension ($\sigma_{1:}$ vertical, $\sigma_{3:}$ E-NE, Henry et al., 1991) is spatially limited to the southern TPMP, in and north of Big Bend National Park. On the whole, igneous activity was less voluminous and more alkaline than the previous, compressive stage, and is dominantly bimodal: it is composed of silicic alkaline caldera-related eruptions and shallow intrusions, and mafic to intermediate alkaline sills (Henry et al., 1986 and James and Henry, 1991). There are approximately ten such sills emplaced in and around the Big Bend Area during this period, with bulk compositions ranging from basanite to benmoreite (syenogabbro to syenodiorite) (Carman, 1975). The 28.6 ± 0.4 Ma RMS, located near the western border of Big Bend National Park, is the best preserved, exposed, and studied of these occurrences (Carman et al., 1975, and Carman, 1994).

Overview of this study

This work examines melting and phase equilibria at pressures that correspond to depths in the lower crust and upper mantle (8-20 kb – proportional to ~26-66 km depth) for the monzonitic (benmoritic) Rattlesnake Mountain sill (RMS).

I undertook this study to investigate the high pressure phase relations of intermediate alkaline magmas generally and to evaluate the plausibility of deep fractionation in the petrogenesis of TPMP evolved mafic to intermediate magmas. I use RMS monzonite to pursue this.

Additionally, this work investigates the nature of melt chemistries during high pressure differentiation to see if there are possible links between silica-saturated and unsaturated, peralkaline, peraluminous, and metaluminous compositions.

As mentioned in the section above, the crystallization of silica-poor, alkali-rich amphibole has been shown, at least theoretically, to drive melt composition from silica-unsaturated to -saturated. Nekvasil et al. (2004) demonstrated the presence of Ti-rich biotite with kaersutite in experiments where fractionation led from silica-undersaturated to saturated compositions. However, to the knowledge of the author, it has not been previously documented that fractionation of biotite alone or biotite with only minor amphibole may accomplish this. Whether this mechanism (biotite-controlled changes in silica saturation) functions in the geologic environment is unresolved.

Multiple parental magmas and/or the incorporation of crustal components undoubtedly play a role in the evolution of some TPMP magma series; however, in light of the TPMP compositions and field relations, the possibility that fractionation at depth contributes to the magmatic diversity warrants investigation.

Analytical methods

Whole rock and trace element chemical analyses of the RMS field samples were conducted by XRF and ICP-MS at the Washington State University's Geoanalytical laboratory.

Experimental capsules were mounted in epoxy, ground to expose the sample, and polished for electron microprobe analysis on the University of Georgia's JEOL 8600 Superprobe. Analyses were calibrated with standard mineral and synthetic standards. Mineral analyses were performed with a 5 nA current and 15 kV accelerating voltage. Feldspars were analyzed with a 5 μm beam diameter when possible, but other mineral phases were analyzed with a focused beam that result in a <1 μm spot. Glasses were analyzed using 3 nA current and a x25000 scanning magnification. Corrections were made after Bence and Albee (1968).

Constraints on RMS magma origin and evolution

Table 2-1 includes RMS and other alkaline igneous whole rock and trace element geochemistry. Rattlesnake Mountain sill has trace element signatures characteristic of TPMP magmas from the initial extensional period (James and Henry, 1991). The border zone and chill margin rocks are analcime monzonites and the intruding melt composition is benmoritic and plots near the benmoreite-mugearite-phonotephrite corner in total alkali-silica space (after Le Bas et al., 1986). Figure 2-2a shows trace element distribution diagrams normalized to MORB after Pearce (1983). The lack of Nb depletion dispels arc magmatism as a source, since in subduction zone magmas Nb is depleted relative to LILE and some HFSE (LREE and Zr) which are compatible in slab-derived fluid. Figure 2-2b shows chondrite-normalized REE patterns. Low Y and HREE seen in Figure 2-2, characteristic of an intraplate or OIB-type source, result from deep melting in the garnet-lherzolite stability zone, where these elements remain in residual garnet (Davidson and Wolff, 1989; Pearce, 1979 and 1983).

Table 2-1A. Whole rock compositions of Rattlesnake Mountain Sill rocks. Sample RM02-17 is the starting material for piston-cylinder experiments. Lithology abbreviations: BZ = border zone, CZ = central zone, monz = monzonite, sy = syenite.

Lithology	Starting material	u. chill zone	l. chill zone	BZ monz	BZ monz	CZ monz	CZ sy
Sample	RM02-17	RM02-3	RM02-18A	RM02-8	RM02-8b	RM02-16	RM02-5
SiO_2	52.4	58.85	54.12	54.56	54.92	52.04	62.95
TiO_2	2.03	1.18	1.98	1.67	1.64	2.04	0.69
Al_2O_3	16.93	17.09	16.71	17.1	16.97	16.98	18.35
FeO	8.67	5.68	7.69	7.87	7.36	8.22	3.24
MnO	0.18	0.09	0.19	0.15	0.13	0.19	0.08
MgO	3.00	1.43	2.67	2.37	2.39	3.19	0.57
CaO	3.98	2.75	3.33	4.01	4.08	4.68	1.23
Na_2O	5.80	6.11	5.64	5.13	5.16	5.57	6.01
K_2O	3.25	4.07	3.47	3.75	3.82	3.02	6.77
P_2O_5	1.04	0.79	1.29	1.07	1.05	1.08	0.11
total	97.28	98.04	97.09	97.68	97.52	97.01	100.00
			major elements normalized to volatile-free 100%				
SiO_2	53.87	60.03	55.74	55.85	56.32	53.65	62.95
TiO_2	2.08	1.21	2.04	1.71	1.68	2.10	0.69
Al_2O_3	17.40	17.43	17.21	17.50	17.40	17.50	18.35
FeO	8.91	5.79	7.92	8.06	7.55	8.47	3.24
MnO	0.18	0.09	0.20	0.16	0.14	0.19	0.08
MgO	3.08	1.46	2.75	2.43	2.45	3.29	0.57
CaO	4.09	2.80	3.43	4.10	4.18	4.82	1.23
Na_2O	5.96	6.23	5.81	5.25	5.29	5.74	6.01
K_2O	3.34	4.15	3.57	3.84	3.92	3.11	6.77
P_2O_5	1.06	0.80	1.33	1.10	1.07	1.11	0.11
total	100	100	100	100	100	100	100
***Mg'*[1]**	38	31	38	35	37	41	24
Mg/Fe	0.62	0.45	0.62	0.54	0.58	0.69	0.31
PI[2]	0.77	0.85	0.78	0.73	0.74	0.73	0.94
ASI[3]	0.83	0.88	0.88	0.86	0.85	0.81	0.94
			CIPW norms (Fe^{2+}/Fe^{3+} adjusted after Irvine and Barager, 1971)				
%AN	19.4	12.2	14.5	22.4	21.4	22.2	5.8
Q		1.3					
or	19.7	24.5	21.1	22.6	23.1	18.3	39.9
ab	45.1	52.6	49.0	44.3	44.6	44.7	49.8
an	10.8	7.3	8.3	12.8	12.1	12.8	3.1
ne	2.8					2.0	0.5
C			0.7				
di	2.0	1.1		0.3	1.3	3.1	1.8
hy		5.2	7.2	8.0	7.9		
ol	8.0		1.8	1.6	0.7	7.3	0.4
mt	5.2	3.9	5.1	4.6	4.6	5.2	2.4
il	4.0	2.3	3.9	3.2	3.2	4.0	1.3
hem							0.6
ap	2.5	1.9	3.1	2.5	2.5	2.6	0.3

Table 2-1A. Whole rock compositions of Rattlesnake Mountain Sill rocks.

Lithology	Starting material	u. chill zone	l. chill zone	BZ monz	BZ monz	CZ monz	CZ sy
Sample	RM02-17	RM02-3	RM02-18A	RM02-8	RM02-8b	RM02-16	RM02-5
			trace elements				
Ni	3	4	4		3	2	2
Cr	4		1	1		4	
V	78	29	57	47	43	72	14
Ga	17	20	17	18	18	19	21
Cu	5	1	5	2	5	3	1
Zn	97	81	92	86	89	98	53
La	60.1	58.9	93.2	65.2	64.9	63.1	43.5
Ce	116.3	111.7	162.7	125.9	124.3	122.6	92.2
Pr	13.5	12.5	19.0	14.5	14.4	14.2	10.0
Nd	56.1	49.5	76.5	58.8	58.1	58.6	37.7
Sm	11.8	9.9	15.5	12.0	12.0	12.3	8.0
Eu	3.7	3.0	4.9	3.8	3.7	3.7	1.2
Gd	9.8	7.9	12.7	10.0	9.7	10.1	6.5
Tb	1.38	1.12	1.80	1.36	1.37	1.43	1.07
Dy	7.6	6.3	9.75	7.58	7.58	7.72	6.58
Ho	1.42	1.17	1.86	1.41	1.36	1.44	1.28
Er	3.49	3.01	4.78	3.53	3.46	3.57	3.65
Tm	0.48	0.44	0.64	0.48	0.48	0.49	0.56
Yb	2.84	2.66	3.83	2.9	2.88	2.9	3.6
Lu	0.44	0.42	0.61	0.45	0.44	0.46	0.58
Ba	1145	779	1495	1643	1763	1053	589
Th	5.5	6.85	7.34	6.02	6.13	5.76	11.28
Nb	86.28	94.72	98.06	89.21	89.08	84.75	131.88
Y	36.78	31.17	52.43	37.04	36.76	37.65	30.05
Hf	8.56	10.15	10.69	9.02	9.11	8.77	18.27
Ta	5.56	6.08	6.53	5.7	5.69	5.49	8.86
U	1.46	2.35	2.22	1.66	1.73	1.52	2.56
Pb	4.32	4.45	7.88	2.76	2.96	5.55	6.62
Rb	59.0	73.5	76.4	69.8	69.0	55.2	134.4
Cs	3.61	0.46	0.70	0.44	0.59	1.26	0.72
Sr	804	322	583	819	747	923	209
Sc	9.5	5.9	8.7	7.4	7.3	8.8	4.7
Zr	366	446	443	393	394	376	811

[1]*Mg'* = molar 100*Mg/(Mg+Fe)
[2]PI = peralkalinity index = molar (Na+K)/Al
[3]ASI = alumina saturation index = molar Al/(Na+K+2Ca)

Table 2-1B. Whole rock compositions of Rattlesnake Mountain Sill and other comparable magmas. The RM02-17 starting material composition is shown in Table 21A and other compositions are taken from the literature. See Table 2-1A for definition of geochemical parameters.

Lithology	Starting material	Avg. RMS border rock[1]	Calculated RMS monz[1]	Leon Mtn.[2]	Peña Mtn.[2]	scoria (ne-mug)[3]
Sample	RM02-17	n=5		LM64	PN21	2102
			normalized to volatile-free 100%			
SiO_2	53.87	52.8	52.5	53.78	52.59	49.05
TiO_2	2.08	2.11	2.41	1.96	2.32	2.20
Al_2O_3	17.4	16.94	16.84	18.1	17.68	15.46
FeO	8.91	9.48	9.67	8.61	9.31	10.03
MnO	0.18	0.20	0.20		0.17	0.16
MgO	3.08	3.41	3.31	1.87	2.85	7.23
CaO	4.09	5.21	5.41	5.7	5.72	6.54
Na_2O	5.96	5.61	5.41	6.35	5.33	5.76
K_2O	3.34	3.21	3.31	2.87	3.03	2.88
P_2O_5	1.06	1.00	0.90	0.76	0.75	0.68
total	100.00	100.00	100.00	100.00	100.00	100.00
Mg'	38	39	37	28	35	56
Mg/Fe	0.62	0.64	0.61	0.39	0.55	1.28
PI	0.77	0.75	0.74	0.75	0.68	0.81
ASI	0.83	0.76	0.75	0.76	0.79	0.63

[1] from Carman et al. (1975)
[2] compositions of other Big Bend differentiated sills from Carman (1994)
[3] Irving and Green's (2008) starting composition

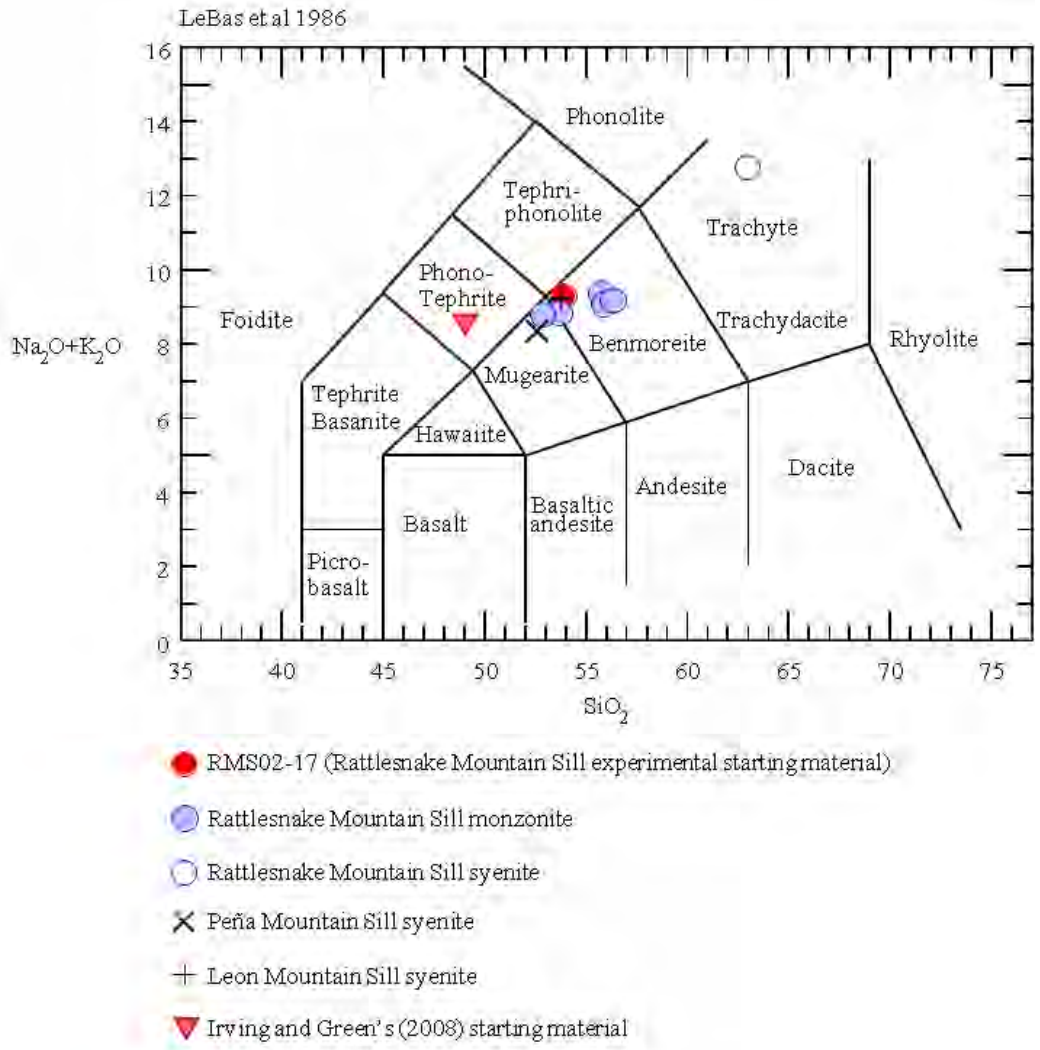

Figure 2-2. Total alkali-silica classification diagram for Big Bend differentiated sills and Irving and Green's (2008) starting composition. Diagram after LeBas et al. (1986).

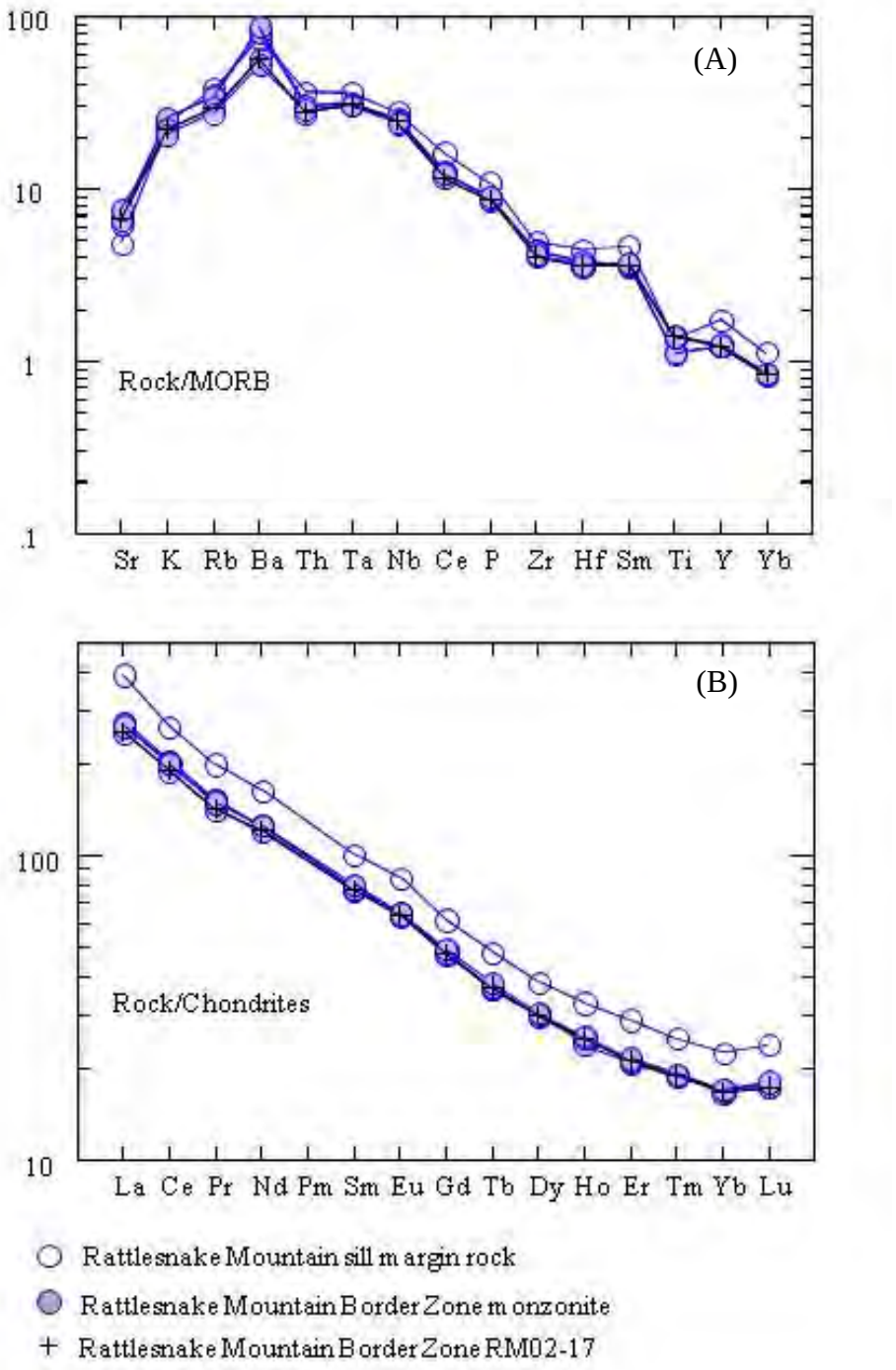

Figure 2-3. Trace element distribution diagrams for Rattlesnake Mountain Sill. A. MORB-normalized diagram after Pearce (1982). **B.** Chondrite-normalized REE diagram using values from Sun and McDonough (1989).

The mugearitic margin of Peña Mountain and the benmoritic margins of Rattlesnake Mountain and Leon Mountain sills (see Figure 2-1) contain plagioclase, olivine, Fe-Ti oxide, and apatite microphenocrysts (Carman, 1994); size measurements taken on plagioclase microphenocrysts in RMS margin rocks show a bimodal population, and Carman et al. (1975) interpreted these as one population that crystallized prior to intrusion and one that crystallized almost immediately afterwards. Examination of thin sections for this study confirms Carman's (1994) observations for RMS, though likely olivine grains were too serpentinized to definitively identify. Leon and Peña Mountain sills also contain clinopyroxene microphenocrysts. The Bone Springs sill tephritic margins contain olivine and Fe-Ti oxide that crystallized prior to intrusion and clinopyroxene, apatite, and nepheline that crystallized prior to or shortly after intrusion; there are also resorbed and unidentifiable mafic phenocrysts in the BSS lower margin (this study – see Chapter 3).

Rattlesnake Mountain sill (RMS) border zone samples have Ni contents of <5 ppm and *Mg'*s [100*MgO/(MgO+FeO)] of 23-28 (Table 2-1a), too low to have been in equilibrium with a mantle assemblage. Like other TPMP early extensional magmas, samples from the border zones of RMS do not have a negative Eu anomaly (Figure 2-3B; James and Henry, 1991). Thus, plagioclase fractionation is not an important part of their development and their source rock did not contain plagioclase. Plagioclase microphenocrysts in RMS probably do not represent extensive plagioclase fractionation.

Cameron et al. (1986) published isotopic data for RMS and other Big Bend rocks. RMS BZ syenodiorite has $^{87}Sr/^{86}Sr$ of 0.70383, $(^{87}Sr/^{86}Sr)_i$ of 0.70374, $^{143}Nd/^{144}Nd$ of 0.51272, and εNd of +2.0, which they (Cameron et al., 1986) interpreted as the signature of a magma relatively uncontaminated by continental crust. The RMS magma plots on $^{87}Sr/^{86}Sr$-εNd

diagrams near to the field of slightly depleted OIB or continental basalts (and rocks that are derived from them). These results match James and Henry's (1991) conclusions, based on trace element evidence and modeling, that the mafic and intermediate TPMP magmas from the extensional periods are relatively uncontaminated fractionated examples of mantle melts.

Trace elements indicate that the RMS parental magma arose from deep melting in the garnet stability field of the mantle. Because RMS is ne-normative, the parent magma would likely have been basanite, tephrite, or alkali basalt. The low Ni contents suggest olivine fractionation while the lack of a Eu anomaly suggests no significant fractionation of plagioclase.

Experiments

Starting material

The starting material for these experiments is an analcime-monzonite from Rattlesnake Mountain sill in Big Bend National Park, Texas (sample RM02-17). Comprehensive descriptions of petrography and composition of the intrusion can be found in Carman et al. (1975) and Carman (1994). In summary, it is composed of 65-70% feldspar zoned from Ca-plagioclase to anorthoclase, lesser augite, biotite, and amphibole (edenite with $\leq$ 3 wt.% Al_2O_3), with minor olivine. Analcime is found interstitially, pseduomorphed after nepheline, and in vugs and miarolitic cavities. Sample RM02-17 is from the RMS border zone which Carman et al. (1975) interpreted to closely represent the bulk composition of the sill. Samples collected from the 2 cm thick outermost glassy margin are devitrified, hydrothermally altered, and oxidized, and thus deemed poor candidates for experimentation. Sample RM02-17 is the freshest sample available that is also close enough to the outer margin to have experienced no apparent differentiation; i.e., no segregations of syenite were found in the vicinity of the sample.

The composition of RM02-17 is shown in Table 2-1a and in Table 2-1b it is listed along with calculated and average RMS compositions from Carman et al. (1975), other Big Bend sill compositions (Carman, 1994), and the experimental starting ne-mugearite composition of Irving and Green (2008). (Note: the Irving and Green [2008] sample is a ne-phonotephrite by IUGS nomenclature as documented in Le Maitre et al. [2002], but referred to in this study by Irving and Green's classification). There are slight differences between RMS compositions determined for this study and those from Carman et al. (1975), though all were determined by XRF. It is not known if these are due to sampling, to variation between labs, or to technology changes in the intervening ~30 years. The sample used here, RM02-17, is an analcime monzonite with the composition of a moderately hydrous benmoreite and is largely fresh besides scattered oxidation on the surface of mafic minerals. XRF analysis yields a 97.2 wt.% total, which reflects its modal% of analcime and lesser biotite and amphibole. It is slightly more evolved than Carman et al's (1975) RMS average and calculated compositions (Table 2-1b), having lower MgO, FeO, and CaO. However, it is representative of the RMS samples collected for this study (Table 2-1a) and of Big Bend intermediate shallow intrusions generally, as indicated by Leon and Peña Mountain sill compositions (Table 2-1b). The Mg/Fe of RM02-17 is lower than the other Big Bend compositions, due to having similar FeO(total) to Carman et al.'s (1975) RMS analyses and Carman's (1994) Peña and Leon samples, but higher MgO than Carman's (1994) Peña and Leon samples.

The ne-mugearite of Irving and Green (2008) is considerably more magnesian and alkaline than RM02-17 (Table 2-1b). These experiments on RMS extend those of Irving and Green (2008) from ne-mugearite to ne-benmoreite compositions.

Experimental method

Hand-crushed RM02-17 material was ground for >1 hour in a tungsten carbide shatter box. For each experiment 2 mg of crushed rock was loaded into Au capsules of 1 mm inner diameter and 0.2 mm thick walls with one end crimped and welded shut. Filled capsules were left open in an oven at 130° C for 24 hours to evaporate adsorbed moisture. For experiments with added H_2O, finely ground AgOH was then added as a delivery system for H_2O, after the method of Mirante (2003). Solid AgOH was dried in a desiccator for 48 hours prior to addition. Capsules were immediately crimped and sealed by spot welding while partially submerged in an acetone-saturated paper towel to wick heat and prevent devolatilization of the AgOH.

Heating during experiments liberates water from AgOH by the reaction:

$$2AgOH\ (s) \rightarrow 2Ag\ (m) + H_2O\ (v) + \tfrac{1}{2}O_2\ (v), \qquad (1)$$

yielding approximately 7% H_2O by weight. Mirante (2003) used the same furnace assembly and piston-cylinder apparatus as used in this study and he found Ag to behave inertly or to bond with the Au capsule (Mirante, personal communication). Mirante (2003) also found no discernable effect from liberated O_2 on the oxidation state of experimental products; this is expected because of the large mass of the furnace relative to the sample and because the furnace buffers fO_2 through the permeability of the Au capsule to both H and O (Patiño Douce and Beard, 1994).

Four capsules of crushed rock combined with AgOH, in proportions to yield 0, 2, 4, and 8 wt.% H_2O, were included in each experimental run. The starting material contains some water prior to the addition of AgOH; its 97.2 wt.% analytical total (Table 2-1a) demonstrates that it may contain up to 2.8 wt.% structurally bound H_2O.

For experiments performed below the melting curve of NaCl, capsules were encased in pressed NaCl and the plugs were inserted into 0.5 inch diameter NaCl-graphite cell assemblies.

For experimental conditions above the NaCl melting curve, capsules were encased in pressed fluorite + epoxy and a glass jacket separated the graphite inner cell from the NaCl outer jacket.

The starting material contains some water prior to the addition of AgOH; its 97.2 wt.% analytical total (Table 2-1a) demonstrates that it may contain up to 2.8 wt.% structurally bound H_2O.

Experiments were run in the University of Georgia's piston-cylinder apparatus with temperatures from 925-1165° C and pressures of 8-20 kb. Temperature was maintained and monitored by Pt-Re thermocouples and a Eurotherm 808 controller, which maintained temperature to ± 10° C in each experiment. Experiments were run by the "hot piston out" method: pressure was brought to within 2-3 kb of the target before heating the furnace to target temperature. Overpressure due to thermal expansion was then manually released. Pressure was maintained throughout the experiment to ±0.3 kb. Studies show that graphite cell assemblies such as those used here maintain log fO_2 between QFM and QFM-2 (e.g., Patiño Douce and Beard, 1996, and Patiño Douce, 2005). Most experiments were run for ~24 hours. See Table 2-2 for experimental conditions and results.

After quenching, capsules were liberated by dissolution in warm water for NaCl plugs and in HF^- for fluorite plugs. Capsules were inspected under a binocular microscope for tears and to check proximity of the thermocouple to the capsules. Unsuitable capsules were discarded.

Potential experimental and analytical problems

No attempt was made to reverse experiments. There is evidence for equilibrium in experimental runs above 1000° C in the form of mineral grains with euhedral crystal faces and consistent phase chemistry.

Table 2-2. Experimental run conditions and products. Phases in parentheses are partially or wholly relict. Minerals are listed by decreasing abundance but glass (gl) and vapor (v) are always listed last. Abbreviations are after Kretz (1983), except gl and v, and are listed in Appendix 4.

run	P (kb)	T(°C)	H2O added	Products
12	8	1085	2 wt.%	Cpx, Ap, gl
	8	1085	4 wt.%	Am, Bt, Ap, Ilm, gl, V
	8	1085	8 wt.%	Bt, Ap, Ilm, gl
1	9	975	0 wt.%	(Cpx, Fsp, Am, Fe-Ti ox, Bt, Ap), gl
	9	975	2 wt.%	(Cpx, Fsp, Am, Fe-Ti ox, Bt, Ap), gl
	9	975	4 wt.%	(Cpx, Fsp, Fe-Ti ox, Bt, Ap), gl
	9	975	8 wt.%	(Cpx, Fsp, Fe-Ti ox, Bt, Ap), gl
4	10	925	0 wt.%	
		925	2 wt.%	run #4 0, 2, & 4% H_2O had poor returns and
		925	4 wt.%	only apatites were analyzed
2	10	950	0 wt.%	(Cpx, Fsp, Am, Fe-Ti ox, Bt, Ap), gl
	10	950	2 wt.%	(Cpx, Fsp, Am, Fe-Ti ox, Bt, Ap), gl
	10	950	4 wt.%	(Cpx, Fsp, Am, Fe-Ti ox, Bt, Ap), gl
	10	950	8 wt.%	(Cpx, Fsp, Am, Fe-Ti ox, Bt, Ap), gl
13	12.5	1110	2 wt.%	gl
	12.5	1110	4 wt.%	gl
	12.5	1110	8 wt.%	Ilm, gl
8	15	1065	0 wt.%	Am, (Cpx), Gt, Ilm, Ap, gl
	15	1065	2 wt.%	Gt, Bt, Ap, Ilm, gl
	15	1065	4 wt.%	Bt, Ilm, Ap, gl
	15	1065	8 wt.%	Am, Bt, Ap, Ilm, gl, V
11	15	1125	0 wt.%	Gt, Am, Ap, Ilm, gl
	15	1125	2 wt.%	Am, Gt, Ap, Ilm, gl
	15	1125	4 wt.%	Ilm, gl
	15	1125	8 wt.%	Ap or Am?, gl, V
14	18	1165	0 wt.%	Am, Gt, Ap, Ilm, gl
	18	1165	2 wt.%	Am, Ap, Ilm, gl
	18	1165	4 wt.%	Am, Ap, Ilm, gl
	18	1165	8 wt.%	Cpx, Opx, Rt, gl
5	20	1125	0 wt.%	(Cpx), Gt, Am, Ab. Bt, Ilm, Ap, gl
	20	1125	2 wt.%	Gt, Am, Bt, (Cpx), Afs, Ilm, Ap, (Zrn), gl
	20	1125	4 wt.%	Am, Cpx, Ilm, Ap, gl
	20	1125	8 wt.%	Ilm, Am, Ap, gl

* All experiments ran for 24 +/1 hours except run 12, which ran for 7.5 hours.

Ratajeski and Sisson (1999) examined Fe-loss to Au capsules during melting experiments and found potentially significant mass changes to the sample, especially over long run times at low fO_2. Entirely molten samples present the worse scenario for Fe loss by diffusion (Ratajeski and Sisson, 1999). Capsules in this study were not analyzed for Fe, but glass analyses in superliquidus runs were compared to the starting material. Experimental runs at 12.5 kb, 1110°C, 2 and 4% added H_2O yielded superliquidus (all glass) run products and the 8% added H_2O run yielded a liquidus return with <1% ilmenite in glass. When normalized to 100% volatile-free totals and compared to the starting material, also normalized, these glass analyses show relative FeO losses of 22 to 31%.

Another complication arises from Na loss to migration and volatilization during electron microprobe analysis. This effect is most significant during analysis of hydrous glasses (Patiño Douce, 2005), despite attempts to minimize the effect by rastering the beam and using low beam currents with short count times. Comparing the experimental glass analyses from superliquidus runs to the starting material shows relative Na_2O losses of 19-22% (27-29% for unnormalized analyses). To compensate for this, reported Na contents were determined by mass balance when possible, as were Al contents. Mass balance calculations were determined using the least squares approach similar to the method Bryan et al. (1969) outlined for fractional crystallization analysis. In the case of Na and Al determination, phase compositions and modal proportions from the experiment were integrated to reach the starting bulk composition. Microprobe data for K, Ti, Si, and Ca in the experimental glass were used and Na and Al were solved for simultaneously.

Results

Phase equilibria

The experimental conditions and the resulting phase assemblages are summarized in Table 2-2. Abbreviations are after Kretz (1983), except for glass (gl) and vapor (v). See images of experimental run products in Figure 2-4. In some cases two phases of a mineral exist, such as biotite from runs 2-0, 2-8, and 5-2, and amphibole in runs 5-0, 14-0, and 12-4. These are discussed in more detail in the mineral sections, below. Figure 2-5 contains pressure-temperature phase diagrams from experiments. Figure 2-6 contains an isobaric phase diagram for 15 kilobars, and Figure 2-7 shows an isothermal phase diagram at 1125° C. Experiments run below <1000° C contain some phases I interpret as partially relict. These interpretations are based on texture or on phase chemistry, such as strong zonation or reaction rims. Some of these phases show resorption or extensive reaction rims. I have disregarded the few relict phases in making these diagrams.

When possible, I ground the experimental capsules so as to expose a vertical cross-section of the sample. This allows representative exposure unbiased by the effects of small-scale crystal settling or proximity to the thermocouple. I conducted modal analyses of the samples best exposed by this method using ImageJ software (Rasband, 1997-2007) and backscatter electron images. In some cases, mafic phases were not distinguished from one another due to similarity in average atomic number. These results are presented in Table 2-3.

Liquidus and near liquidus determination

The results of modal analyses in Table 2-3 provide some information on phase relations at or near the liquidus at experimental conditions. Runs at 12.5 kb, 1110° C, 2% (13-0) and 4% H_2O (13-4) yielded supersolidus run products (all glass), and at 8% H_2O (13-8) yield run products at or very near the liquidus with only trace ilmenite in glass. At 15 kb, 1125° C, and 4%

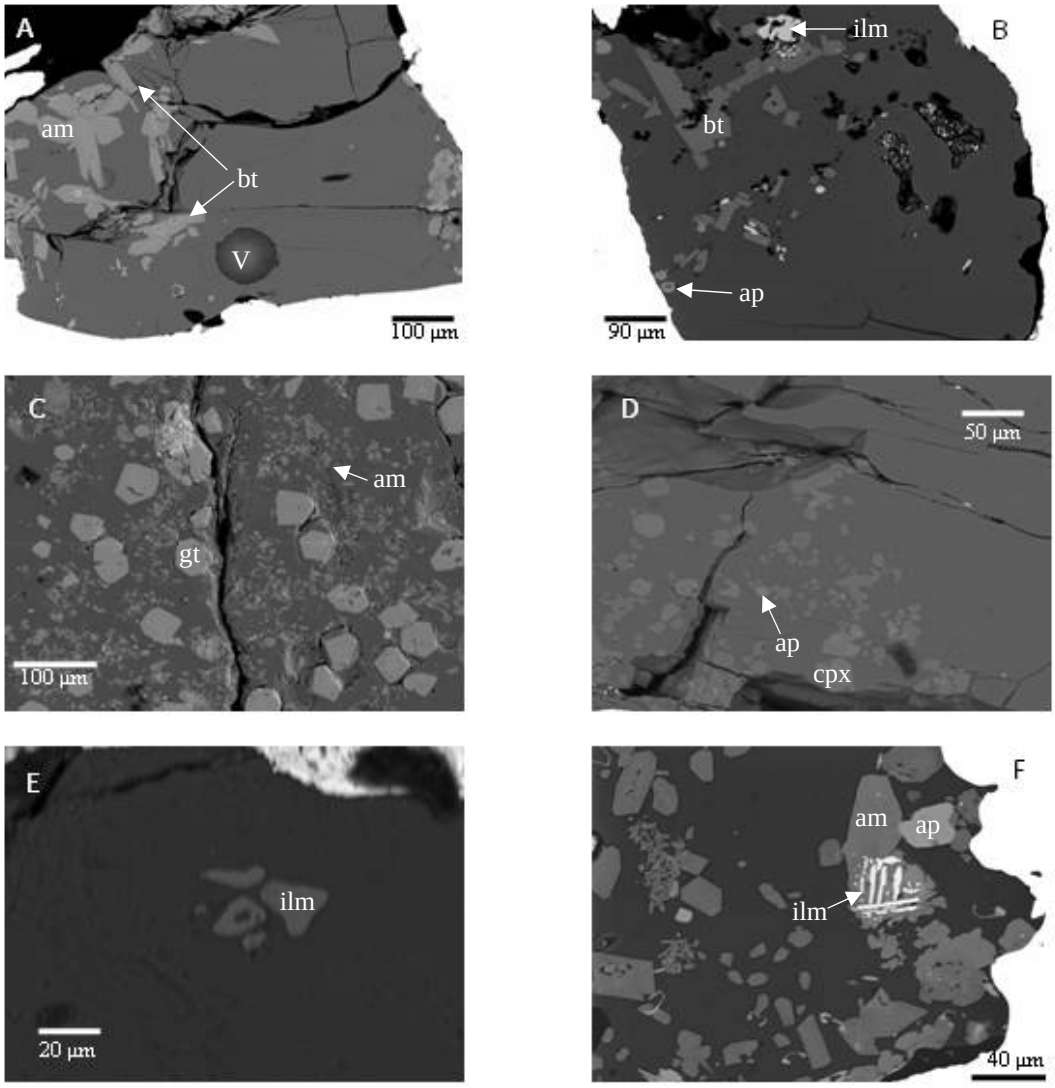

Figure 2-4. Backscatter electron images of experimental returns. A. Run 08-8: am, fine-grained bt laths, minor ap, trace ilm, with vapor-formed vesicle (V). **B.** Run 8-4: bt, ap, ilm. **C.** Run 5-2: gt with fine-grained am, bt, afs, ilm, ap. **D.** Run 12-0: cpx and ap. **E.** Run 13-8: liquidus ilm. **F.** Run 14-2: am, coarse ap, ilm.

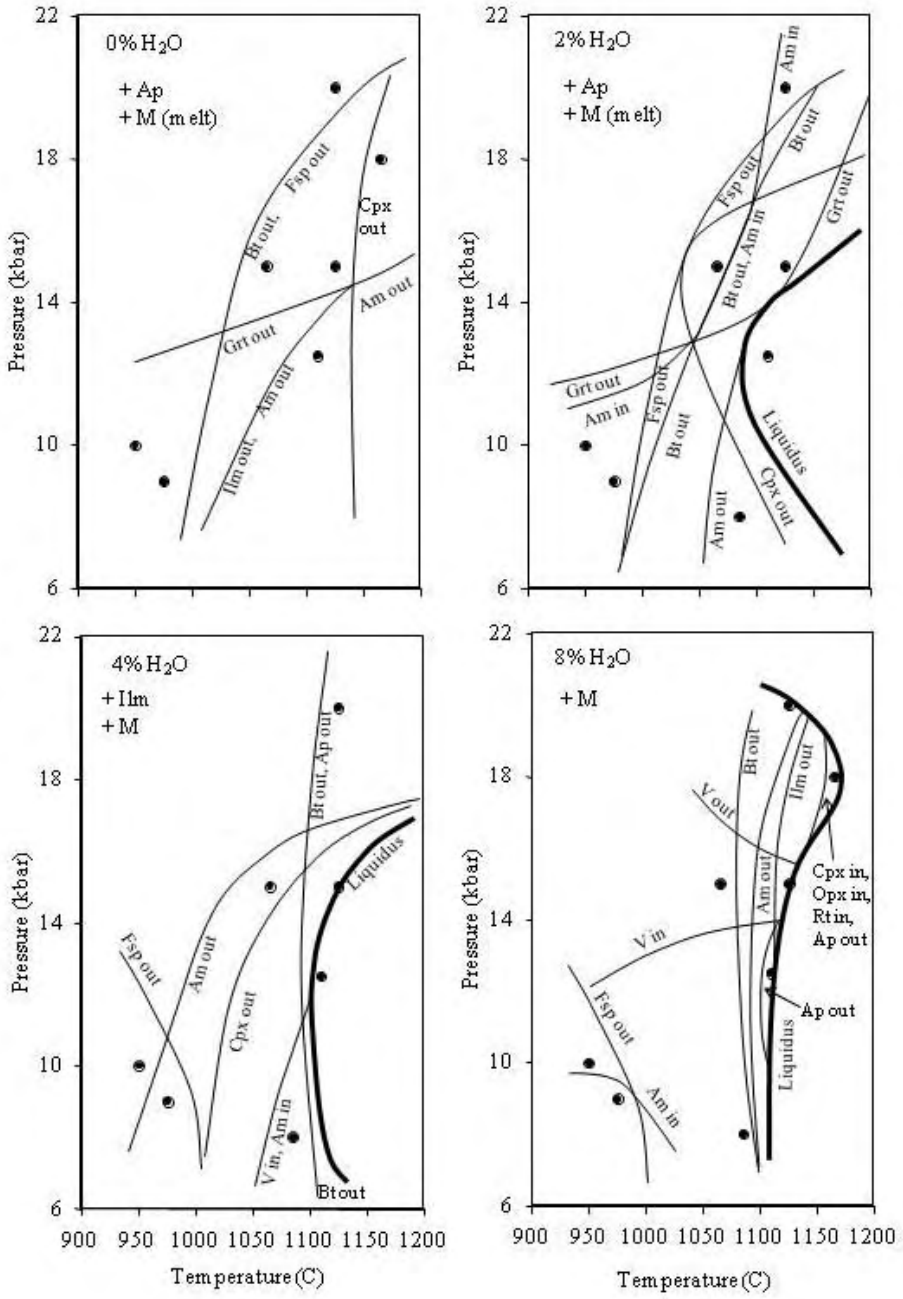

Figure 2-5. Pressure-temperature phase diagrams of RM02-17 at 0, 2, 4, and 8 wt.% added H_2O.

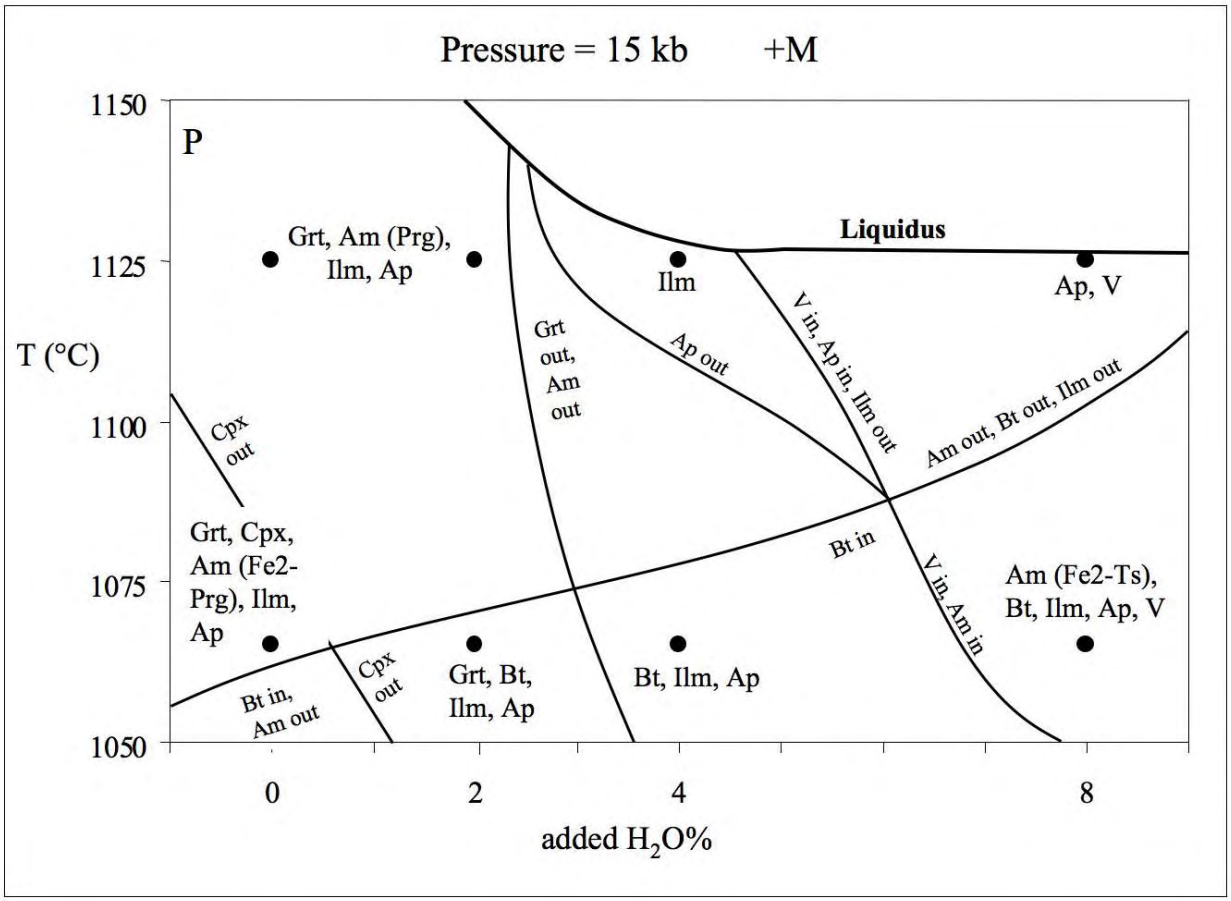

Figure 2-6. Isobaric temperature-H_2O phase diagram for RM02-17 at 15 kb. All experiments yielded melt (M).

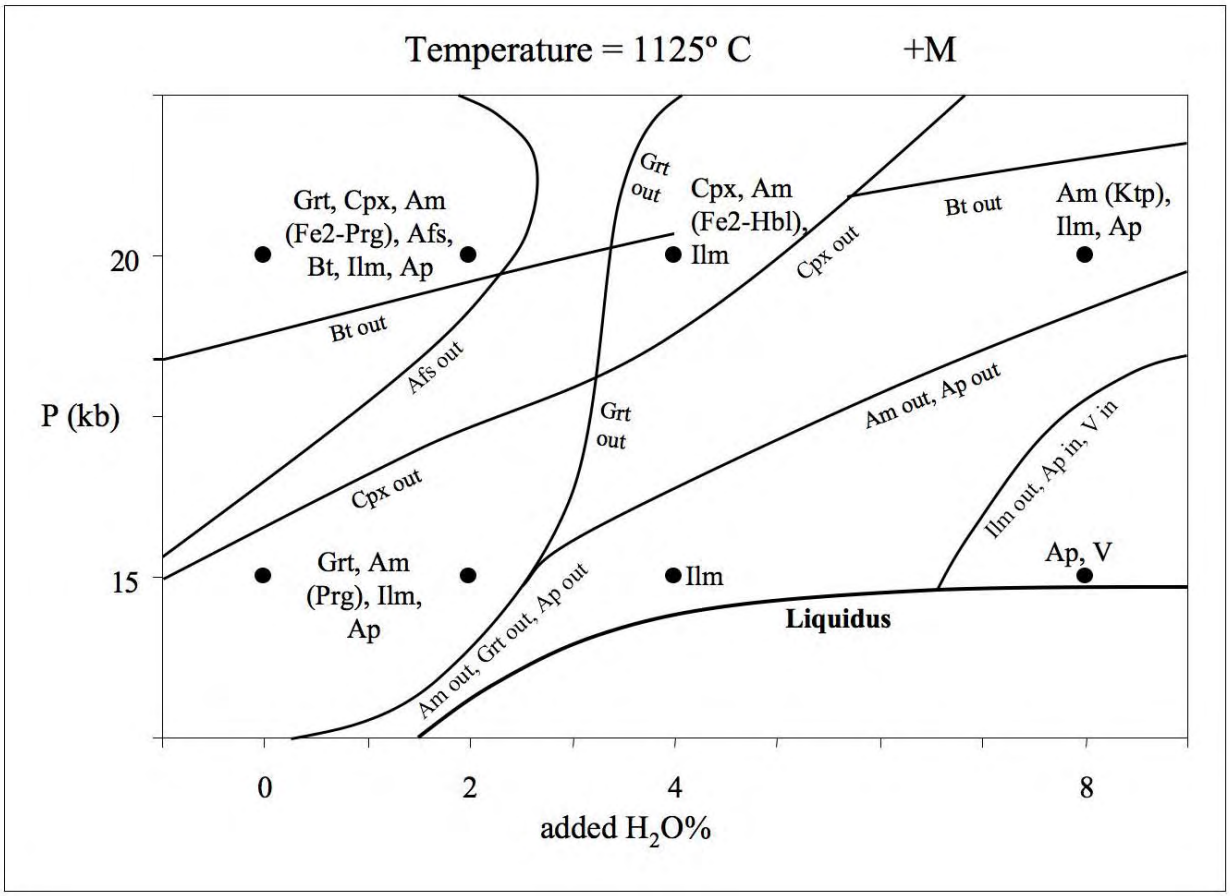

Figure 2-7. Isothermal pressure-H_2O phase diagram for RM02-17 at 1125° C. All experiments yielded melt (M).

Table 2-3. Modal% of phases in run products. Abundances are determined by image analysis or mass balance**.** For returns determined by both, results were a close match and mass balance results are reported. Runs are indicated by run number and added H_2O wt.%. (e.g., 12-4 is the 4% added H_2O experiment from run 12. See Table 2-2 for experimental conditions.

12	4	am+bt	17	12	8	bt	7
		ilm	2			ilm	2
		ap	1			ap	2
		vapor				glass	89
		glass	80				
8	0	am+bt+cpx	17	8	4	bt	16
		gt	3			ilm	1
		ilm	1			ap	3
		glass	79			glass	80
8	8	am	6				
		bt	5				
		ilm	1				
		ap	1				
		vapor					
		glass	87				
11	0	gt	13	11	2	gt	9
		am	10			am	2
		ap	1			ap	1
		ilm	trace			ilm	trace
		glass	77			glass	88
11	4	ilm	tr.	11	8	ap	trace
		gl	~99			vapor	
						glass	>95
14	0	gt	13	14	2	cpx	15
		am	6			am	8
		ap	1			ap	1
		glass	79			Ilm	1
						glass	75
14	4	am	17				
		ilm	1	14	8	cpx	~2
		ap	tr.			rut	tr
		cpx	tr			opx	tr
		gl	82			glass	~97
5	2	fsp	22	5	4	cpx	36
		gt	18			am	6
		bt	15			ilm	2
		ap	3			ap	1
		am	1			glass	55
		glass	41				

H_2O (11-4) ilmenite is a liquidus phase, and at 8% H_2O (11-8) apatite is a liquidus phase accompanied by a vapor phase (a vesicle). At 18 kb, 1165°, 8% H_2O (14-8), only trace amounts of clinopyroxene, rutile, and orthopyroxene were present, the latter two in one corner of the charge. This was the only appearance of either orthopyroxene or rutile in any experiment and it is possibly related to local disequilibrium or contamination.

At 20 kb, 1125° C, 8% H_2O (5-8), 95 modal% melt coexists with kataphoritic amphibole, ilmenite, and apatite. The sample from 15 kb, 1125° C, 2% H_2O (11-2) contains 95 modal% melt with 2.5% pargasitic amphibole, 1.8% apatite, and 0.5% garnet. The melt may have been multiply saturated at these conditions or some of these phases may crystallize just below liquidus temperatures. Modal results show that biotite is a likely near-liquidus phase, along with apatite and ilmenite at 8 kb, 1085° C, 8% H_2O (12-8) and at 15 kb, 1065° C, 4% H_2O (8-4).

The geological implications of the experimental phase relations are explored in the discussion section below, but several points are immediately apparent. The lack of olivine as a liquidus phase would indicate that the RMS magma is not a primary mantle melt, but other data, such as the low whole rock Ni contents, already suggest this. Across a range of pressures up to 30 kb, Irving and Green (2008) found that olivine was stable only within 25-100° C of the liquidus in the composition shown in Table 2-1b, which is slightly more mafic than RMS. Olivine was replaced by biotite or amphibole at sub-liquidus temperatures (Irving and Green, 2008); similar relations could be present in the RMS experiments where amphibole or biotite are near-liquidus phases, or amphibole or biotite could be in a peritectic relationship with olivine near the liquidus.

Clinopyroxene is not a liquidus or near-liquidus phase in any experiment. It generally disappears with increasing temperature and H_2O% and decreasing pressure, while amphibole

and/or biotite generally survive or replace clinopyroxene (Figures 2-5, 2-6, and 2-7). If clinopyroxene played a role in RMS pre-intrusion differentiation it requires lower pressures than those investigated here. Plagioclase also does not appear near the liquidus in any experiment. The plagioclase phenocrysts found in the RMS margins must have crystallized more shallowly than the ~24 km indicated by the lowest pressure (8 kb) experiments, possibly during ascent or synchronously with intrusion.

Vapor Exsolution

The exsolution of a fluid phase from a magma results in a significant volume expansion, shifts the solidus and liquidus of the melt (Wyllie and Tuttle, 1961), changes viscosity and other physical properties of the melt (Lange, 1994), raises the activity of silica in the melt (Kushiro, 1972), and may result in magma compositional changes due to partitioning of elements into the fluid phase (e.g., Kilinc and Burnham, 1972). The solubility of H_2O in silicate magma has been the subject of extensive investigation (e.g., Mysen and Cody, 2004, and references therein).

In piston cylinder experiments, vesicles that arise from exsolution during quenching are typically numerous and ≤1 μm in diameter and form frothy textures in glass, whereas vapor bubbles formed in equilibrium with melt at experimental conditions typically quench to vesicles >5 μm in diameter (e.g., Mysen and Cody, 2004). See Figure 2-4A for a backscatter image of a vesicle from exsolution at high pressure. Based on these textural criteria, three run products showed equilibrium vapor exsolution: at 8 kb, 4% added H_2O, 1085° C (12-8), and at 15 kb, 8% added H_2O, 1065° C (8-8) and 1125° C (11-8). At 8 kb, 1085° C, the exsolution of vapor between 2% and 4% added H_2O accompanies the appearance of amphibole, biotite, and ilmenite at the expense of clinopyroxene (Table 2-2 and Figure 2-5). The isobaric phase diagram for 15 kb is shown in Figure 2-6. At 1125°, apatite + vapor are stable on the liquidus at the expense of

ilmenite between 4 and 8% added H_2O; at 1065°, 16 modal% biotite at 4% added H_2O goes to vapor and approximately subequal biotite + amphibole at 8% added H_2O.

The dissolution of fluid also affects the solubility of apatite relative to melt SiO_2 and the halogen composition of apatite, discussed below.

Mineral compositions

In these experiments, discerning trends of phase composition with P and T is complicated by the nature of the method in that pressure and temperature were increased together. There were two experimental runs at 15 kb each at a different temperature and two at 1125° C each at a different pressure. Otherwise, there were no repeated pressures or temperatures.

Biotite

Table 2-4 shows average biotite compositions from the experimental runs. In several runs, (2-0, 2-2, 5-2) two compositions of biotite are present which differ primarily by Mg/Fe, probably from disequilibrium. The biotite phase relations with P-T-H_2O are shown in Figure 2-8. Biotite is absent at 12.5 kb, 1110° and at 18 kb, 1165° C. At 15 kb, biotite stability moves up-temperature with an increase from 0 to 2% added H_2O. At 20 kb, 1125°, biotite becomes unstable above 2% H_2O.

Biotite in these run products is highly enriched in Ti (TiO_2 = 2-7 wt.%). Ti-substitution mechanisms in biotite are incompletely understood, but the commonly invoked mechanisms are reviewed and described by Dymek (1983) and Abrecht and Hewitt (1988), among others. Some of the primary mechanisms are Ti-Tschermak's ($^{VI}Ti^{4+} + 2^{IV}Al^{3+} = 2^{IV}Si^{4+} + {}^{VI}[Fe,Mg]^{2+}$), Ti-oxy ($^{VI}Ti^{4+} + 2O^{2-} = {}^{VI}(Fe,Mg)^{2+} + 2[OH]^-$), and Ti-Al-oxy ($^{VI}Ti^{4+} + O^{2-} = {}^{VI}Al^{3+} + OH^-$). Biotite from run products are somewhat depleted in SiO_2 and Al_2O_3; calculated to 22 anions, all Al in all analyses resides in the tetrahedral site with Si and the tetrahedral sites remain unfilled (Table 2-

Table 2-4. Biotite compositions from run products. When multiple anlayses were gathered, mean compositions and *2σ* errors are presented. Mole fractions are calculated after Zhu and Sverjensky (1991).

Run	12		12		1	1	1	1	2
P (kb)	8		8		9	9	9	9	10
T (°C)	1085		1085		975	975	975	975	950
added H_2O%	4		8		0	2	4	8	0
number	n=5	*2 σ*	n=5	*2 σ*	n=1	n=1	n=1	n=1	n=1
SiO_2	36.08	*2.23*	37.01	*1.58*	33.85	35.73	35.11	37.57	33.81
Al_2O_3	16.86	*1.87*	15.95	*0.47*	17.61	15.81	16.93	16.34	15.37
TiO_2	4.54	*1.15*	4.46	*0.36*	7.06	4.1	6.33	5.28	3.79
MgO	10.57	*1.72*	12.66	*0.47*	11.91	13.59	10.86	13.53	5.94
FeO	16.77	*2.58*	14.24	*0.93*	16.07	16.67	17.38	13.23	28.36
MnO	0.11	*0.08*			0.13		0.37		
CaO	0.25	*0.62*	0.08	*0.09*	0.14	0.04	0.09	0.15	0.35
K_2O	8.03	*1.99*	8.04	*0.59*	8.59	8.01	8.55	7.43	8.01
Na_2O	0.72	*0.31*	0.73	*0.11*	0.77	0.66	0.94	0.76	0.51
BaO					1.23	1.13	1.05	0.86	0.89
F	0.14	*0.07*	0.17	*0.09*	0.21	0.42	0.54	0.19	0.29
Cl	0.07	*0.14*	0.04	*0.04*	0.03		0.04	0.08	0.02
Total'	94.15		93.44		97.6	96.22	98.18	95.49	97.46
-O=F	0.06		0.07		0.09	0.18	0.23	0.08	0.12
-O=Cl	0.02		0.01		0.01		0.01	0.02	0.00
Total	94.08		93.35		97.51	96.05	97.95	95.39	97.34
				ions per 22 O's					
T site									
Si	5.59		5.68		5.12	5.45	5.27	5.62	5.42
Al	0.83		0.81		1.26	0.74	1.12	0.93	0.72
M site									
Al									
O site									
Ti	1.96		1.84		2.00	1.81	1.91	1.84	1.85
Mg	2.44		2.90		2.68	3.09	2.43	3.02	1.42
Fe	2.17		1.83		2.03	2.13	2.18	1.66	3.80
Mn	0.02		0.01		0.02	0.01	0.05	0.01	0.02
X									
Ca	0.04		0.01		0.02	0.01	0.02	0.02	0.06
K	1.59		1.57		1.66	1.56	1.64	1.42	1.64
Na	0.22		0.22		0.23	0.20	0.27	0.22	0.16
Ba					0.07	0.07	0.06	0.05	0.06
OH site									
F	0.071		0.085		0.099	0.201	0.255	0.091	0.145
Cl	0.017		0.012		0.008		0.009	0.020	0.004
OH (ideal)	3.91		3.90		3.89	3.80	3.74	3.89	3.85
X_{Mg}	0.370		0.441		0.399	0.439	0.370	0.463	0.200
X_{Fe}	0.329		0.278		0.302	0.302	0.332	0.254	0.536
X_F	0.018		0.021		0.025	0.050	0.064	0.023	0.036
X_{Cl}	0.004		0.003		0.002		0.002	0.005	0.001
X_{OH}	0.978		0.976		0.973	0.950	0.934	0.972	0.963

Table 2-4, continued. Biotite compositions from run products.

Run	2	2		2		2	8	
P (kb)	10	10		10		10	15	
T (°C)	950	950		950		950	1065	
added H_2O%	0	4		8		8	2	
number	n=1	n=5	*2 σ*	n=2	*2 σ*	n=1	n=4	*2 σ*
SiO_2	37.19	37.3	*3.36*	37.29	*0.41*	34.09	36.19	*0.37*
Al_2O_3	14.8	15.03	*0.86*	15.43	*0.14*	15.53	15.89	*0.47*
TiO_2	2.26	4.43	*0.83*	2.84	*0.08*	2.75	6.05	*1.10*
MgO	9.23	8.22	*0.86*	15.93	*1.88*	8.86	12.69	*0.91*
FeO	21.82	21.98	*0.85*	15.74	*3.49*	25.39	14.19	*1.04*
MnO	0.30	0.29	*0.07*	0.50	*0.00*	0.77		*0.13*
CaO	0.15	0.34	*0.72*	0.06	*0.04*	1.26	0.33	*0.99*
K_2O	8.16	8.4	*0.76*	9.08	*0.88*	8.39	8.05	*0.35*
Na_2O	0.61	0.95	*0.69*	0.61	*0.09*	0.55	0.65	*0.16*
BaO	0.4	0.55	*0.30*	0.23	*0.01*	0.19		
F	0.16	0.37	*0.25*	0.39	*0.11*	0.47	0.21	*0.10*
Cl	0.04	0.04	*0.05*			0.02	0.03	*0.03*
Total'	95.11	97.91		98.08		98.27	94.4	
-O=F	0.07	0.16		0.16		0.2	0.09	
-O=Cl	0.01	0.01		0		0	0.01	
Total	95.03	97.75		97.92		98.06	94.31	
			ions per 22 O's					
T site								
Si	5.86	5.70		5.55		5.35	5.50	
Al	0.42	0.80		0.50		0.51	1.09	
M site								
Al								
O site								
Ti	1.76	1.73		1.73		1.83	1.82	
Mg	2.17	1.87		3.53		2.07	2.88	
Fe	2.88	2.81		1.96		3.33	1.80	
Mn	0.04	0.04		0.06		0.10	0.02	
X								
Ca	0.03	0.06		0.01		0.21	0.05	
K	1.64	1.64		1.72		1.68	1.56	
Na	0.19	0.28		0.18		0.17	0.19	
Ba	0.03	0.03		0.01		0.01		
OH site								
F	0.078	0.179		0.184		0.234	0.101	
Cl	0.010	0.011				0.004	0.007	
OH (ideal)	3.91	3.81		3.82		3.76	3.89	
X_{Mg}	0.317	0.291		0.485		0.282	0.442	
X_{Fe}	0.420	0.436		0.269		0.454	0.277	
X_F	0.020	0.045		0.046		0.059	0.025	
X_{Cl}	0.002	0.003				0.001	0.002	
X_{OH}	0.978	0.953		0.954		0.940	0.973	

Table 2-4, continued. Biotite compositions from run products.

Run	8		8		5	5		5
P (kb)	15		15		20	20		20
T (°C)	1065		1065		1125	1125		1125
added H_2O%	4		8		0	2		2
number	n=8	*2 σ*	n=4	*2 σ*	n=1	n=3	*2 σ*	n=1
SiO_2	35.32	*1.19*	35.39	*0.75*	44.52	37.79	*0.69*	39.09
Al_2O_3	16.75	*1.06*	17.13	*0.22*	17.58	17.19	*0.55*	20.41
TiO_2	4.72	*0.20*	4.57	*0.89*	2.83	4.78	*0.27*	4.06
MgO	13.07	*1.25*	11.5	*0.74*	6.5	12.31	*0.29*	9.39
FeO	15.28	*1.10*	16.95	*2.14*	15.67	13.29	*0.80*	14.23
MnO		*0.12*		*0.15*			*0.16*	
CaO	0.08	*0.06*	0.07	*0.10*	0.32	0.08	*0.08*	0.08
K_2O	8.04	*0.29*	8.27	*0.14*	6.69	7.63	*0.44*	8.05
Na_2O	0.79	*0.15*	0.61	*0.14*	3.62	5.42	*0.04*	5.45
BaO								
F	0.15	*0.07*	0.11	*0.00*		0.16	*0.10*	0.19
Cl	0.04	*0.02*	0.03	*0.03*	0.07	0.04	*0.04*	0.03
Total'	94.34		94.73		97.79	98.74		101.06
-O=F	0.06		0.05		0	0.07		0.08
-O=Cl	0.01		0.01		0.02	0.01		0.01
Total	94.26		94.67		97.77	98.66		100.97
				ions per 22 O's				
T site								
Si	5.43		5.47		6.47	5.54		5.61
Al	0.86		0.83		0.48	0.83		0.69
M site								
Al								
O site								
Ti	1.94		1.99		1.92	1.89		2.21
Mg	3.00		2.65		1.41	2.69		2.01
Fe	1.97		2.19		1.90	1.63		1.71
Mn	0.01		0.01		0.00	0.01		0.01
X								
Ca	0.01		0.01		0.05	0.01		0.01
K	1.58		1.63		1.24	1.43		1.48
Na	0.24		0.18		1.02	1.54		1.52
Ba								
OH site								
F	0.074		0.053			0.072		0.086
Cl	0.009		0.009		0.017	0.011		0.008
OH (ideal)	3.92		3.94		3.98	3.92		3.91
X_{Mg}	0.434		0.387		0.269	0.432		0.339
X_{Fe}	0.284		0.320		0.364	0.262		0.288
X_F	0.018		0.013			0.018		0.022
X_{Cl}	0.002		0.002		0.004	0.003		0.002
X_{OH}	0.979		0.985		0.996	0.979		0.976

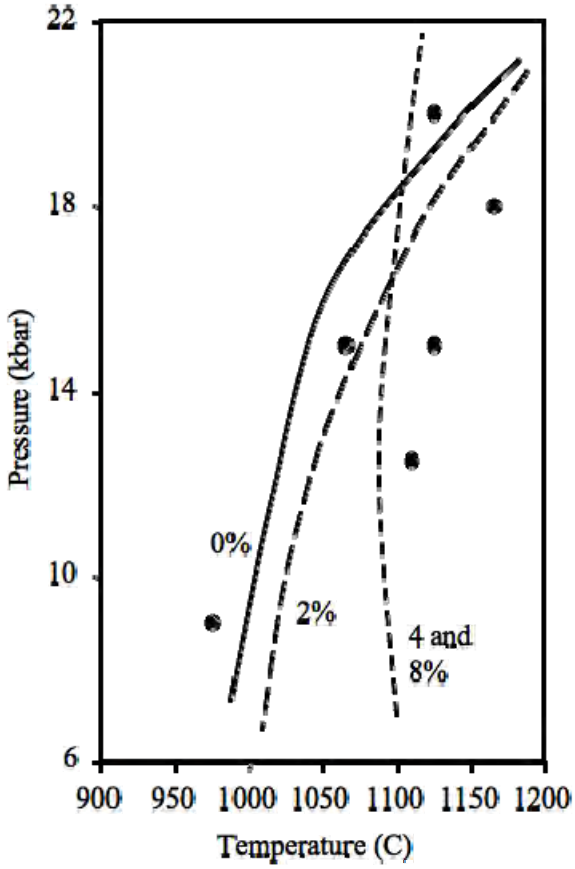

Figure 2-8. Biotite-out reaction lines from piston cylinder experiments. Reaction lines are compiled from Figure 2-5 and are labeled by the added H_2O%. Biotite disappears up-temperature of each line. At 15 kb, biotite stability moves up-temperature with an increase from 0 to 2% added H_2O. At 20 kb, 1125°, biotite becomes unstable with an increase in H_2O above 2%.

4). This suggests a role for Ti-Tschermak's. The significance of biotite disappearance with increasing H_2O at 20 kb suggests that an anhydrous Ti-oxy component may also play a role. Figure 2-9 shows plots of biotite cations that illustrate the functioning (or absence) of each of these mechanisms: (A) Ti-Al oxy: the lack of correlation between Al and Ti indicates that this mechanism is not a significant contributor; (B) Ti-oxy: the weak correlation (r = 0.58) of Mg + Fe and Ti shows that this mechanism may account for some Ti substitution; (C) Ti-Tschermak's: the moderately strong correlation (r = 0.84) of Ti + 2Al with 2Si +Mg + Fe illustrates that this mechanism probably accounts for the majority of Ti incorporation in biotite.

Biotite at 20 kb incorporates 3.6 and 5.4 wt.% Na_2O at 0% and 2% H_2O, respectively, while all other biotites contain 0.5-1.0 wt.% Na_2O. These high-Na biotites have molar K/Na < 1, which is very rare in natural biotites (Tischendorf et al., 2007). The Na-phlogopite endmember is aspidolite and is usually found in metamorphosed evaporites or other unusual bulk compositions (Banno et al., 2005, and references therein), though it has been found associated with chromite in layered intrusions and ophiolites and in gabbroic xenoliths from calc-alkaline rocks (Costa et al., 2001, and references therein). When present in igneous associations, aspidolite is thought to form by reactions between primitive magmas and aqueous fluids or mantle assemblages and aqueous fluids (see Peng et al., 1995). There is good evidence for the existence of a solvus between aspidolite (Na-phlogopite) and K-phlogopite at crustal pressures (Costa et al., 2001; Tischendorf et al., 2007), but no K-phlogopite grains were detected in Na-biotite-bearing run products from this study. No associations of aspidolite with alkaline rocks, including xenoliths, have been reported in the literature.

Biotites from RMS experiments have relatively low Cl of 0.03-0.08 wt.% and higher F of 0.11-0.54 wt.%. Biotites from runs of <1000° C have the highest F contents and all analyses with

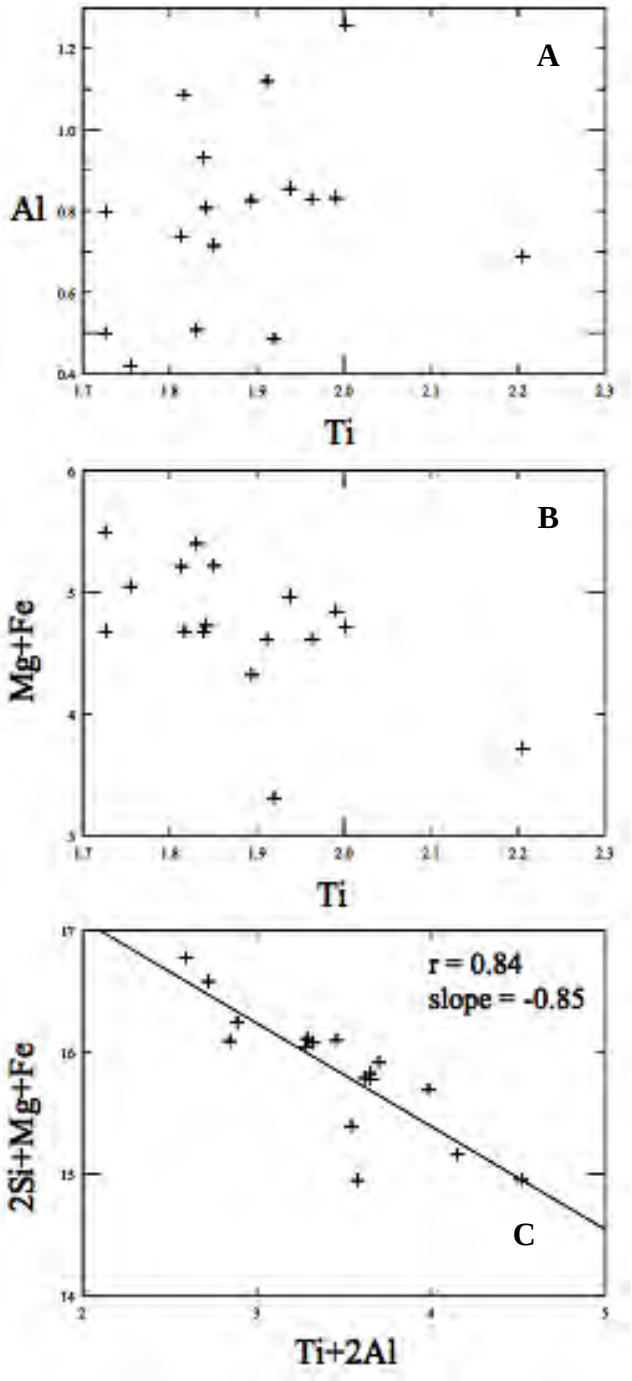

Figure 2-9. Biotite Ti-substitution mechanisms. All units are atoms per formula unit (apfu). Data are shown in Table 2-4. **(A)** shows the lack of the Ti-Al-oxy substitution ($^{VI}Ti^{4+} + O^{2-} = {}^{VI}Al^{3+} + OH^{-}$). **(B)** illustrates the possible function of the Ti-oxy substitution ($^{VI}Ti^{4+} + 2O^{2-} = {}^{VI}(Fe,Mg)^{2+} + 2[OH]$); the weak correlation shows this mechanism may account for some Ti substitution. **(C)** illustrates the function of the Ti-Tschermak substitution ($^{VI}Ti^{4+} + 2^{IV}Al^{3+} = 2^{IV}Si^{4+} + {}^{VI}(Fe,Mg)^{2+}$).

>0.22 wt.% F are from these runs. The relationship of Ti and F contents in experimental biotites are shown in Figure 2-10. There is no regular correlation between biotite Ti and F, but the highest F contents occur in <1000° experiments and all of the >1000° C runs contain biotite with <0.1 apfu F. Most high F in biotite is coupled with lower Ti contents. There is no apparent effect of added H_2O content. The Ti and F patterns in Figure 2-10, such as they are, may be due to avoidance effects on F of the octahedral Ti, similar to that of the Mg-Cl, Fe-F, and Al_{vi}-F avoidance documented by Munoz (1984) and Volfinger et al. (1985). Dooley and Patiño Douce (1996) found Ti-F avoidance in phlogopite in high Ti and F experimental systems.

Amphibole

Amphibole compositions and classifications after Leake et al. (1997) are shown in Table 2-5. Amphibole is a common phase in these experiments, but it is entirely absent at 8 kb, 1085° C (run 12) and at 12.5 kb, 1110° C (run 13); At 9 kb, 975° C (run 1), amphibole disappears above 2% added H_2O. At no conditions is amphibole shown definitively to be a liquidus phase, but at 15 kb, 1125° C, 2% H_2O (run 11-2), ~2.5% pargasite is present with less than 1% garnet, ilmenite, and apatite in melt, and at 20 kb, 1125° C, 8% H_2O (run 5-8), kataphorite, ilmenite, and apatite coexist with >95% melt. Amphibole is present with >75% melt, indicating it could be an important fractionating phase, across a range of other conditions (Table 2-3).

Amphiboles in the RMS intrusion are low-Al edenite ($\leq$ 3 wt.% Al_2O_3) in the monzonite and richterite in the syenite (Carman et al., 1975). None of the amphiboles in the experiments match the composition of those in the starting material, and those that approach or reach edenite compositions have higher Al_2O_3, with >6 wt.% (Table 2-5). The experimental runs with two amphibole phases (5-0, 14-0, and 12-4) do not, therefore, contain relict grains.

Table 2-5. Amphibole compositions from run products. Cations are allocated and ampiboles are classified after Leake et al. (1997) based on 23 O's and assuming 2 OH+F+Cl. When multiple analyses were gathered, a mean composition and 2σ error is shown.

Run	12		12		1		2	2		2	
P (kb)	8		8		9		10	10		10	
T (°C)	1085		1085		950		950	950		950	
added H_2O%	4		4		2		0	2		4	
number	n=2	*2 σ*	n=3	*2 σ*	n=3	*2 σ*	n=1	n=2	*2 σ*	n=6	*2 σ*
SiO_2	43.33	*2.83*	38.79	*0.76*	39.25	*0.78*	45.49	44.99	*2.73*	41.54	*2.24*
Al_2O_3	14.37	*4.13*	17.41	*1.01*	14.41	*0.99*	8.23	9.13	*3.05*	12.10	*2.26*
TiO_2	2.15	*0.33*	2.58	*0.52*	3.25	*0.27*	1.65	1.22	*1.20*	1.56	*0.69*
FeO	15.23	*2.62*	17.16		17.87	*0.13*	16.03	17.93	*3.32*	19.66	*3.07*
MgO	8.98	*4.13*	6.99	*1.36*	9.09	*1.48*	8.53	9.98	*4.70*	8.94	*1.97*
MnO	0.25	*0.07*	0.38	*1.25*	0.39	*0.62*	1.03	0.56	*0.11*	0.66	*0.26*
CaO	8.96	*1.60*	9.69	*0.39*	9.86	*0.40*	16.05	8.95	*2.62*	9.15	*2.47*
Na_2O	2.54	*0.25*	2.89	*0.13*	2.92	*1.11*	2.03	2.22	*0.15*	2.73	*0.23*
K_2O	1.45	*0.83*	1.55	*0.16*	1.52	*0.04*	0.36	1.65	*1.22*	1.15	*0.50*
F	0.14		0.08	*0.22*	0.13	*0.11*	0.20	0.52	*0.62*	0.20	*0.12*
Cl	0.03	*0.01*	0.06	*0.03*	0.03	*0.03*		0.03	*0.03*	0.03	*0.01*
Total	97.36		97.53		98.73		99.51	96.94		97.66	
Si	6.446		5.89		5.936		6.777	6.849		6.355	
Al IV	1.554		2.11		2.064		1.223	1.151		1.645	
Σ T	8		8		8		8	8		8	
Al VI	0.965		1.004		0.504		0.221	0.487		0.537	
Ti	0.24		0.295		0.37		0.185	0.14		0.179	
Fe2	1.89		2.18		2.26		2.00	2.28		2.52	
Mg	1.90		1.52		1.87		1.89	2.09		1.77	
Mn							0.13				
Σ C	5		5		5		4.43	5		5	
Fe2											
Mg	0.09		0.06		0.18			0.17		0.27	
Mn	0.03		0.05		0.05			0.07		0.09	
Ca	1.43		1.58		1.60		2.56	1.46		1.50	
Na	0.45		0.32		0.17			0.30		0.14	
Σ B	2		2		2		2.56	2		2	
Na	0.28		0.53		0.69		0.59	0.36		0.67	
K	0.28		0.30		0.29		0.07	0.32		0.22	
Σ A	0.56		0.83		0.99		0.65	0.68		0.89	
OH (calc.)	1.92		1.94		1.93		1.91	1.74		1.90	
F	0.067		0.040		0.062		0.092	0.251		0.094	
Cl	0.009		0.016		0.008			0.006		0.006	
Σ anion (ideal)	2		2		2		2	2		2	
classification	relict, zoned		Ferro-pargasite		Ferro-pargasite		Ferro-edenite	Edenite		Ferro-pargasite	

Table 2-5, continued. Amphibole compositions from run products.

Run	12	12	1	2	2	2
P (kb)	8	8	10	10	10	10
T (°C)	1085	1085	950	950	950	950
added H_2O%	4	4	2	0	2	4
number	n=2	n=3	n=3	n=1	n=2	n=6
X_F			0.031	0.046	0.125	0.047
X_{Cl}	0.004	0.008	0.004		0.003	0.003
X_{OH}	0.962	0.972	0.965	0.954	0.872	0.95
Si/(Na+K)	6.4	5.1	5.2	10.4	7.0	6.1
Mg'	51.3	42.1	47.6	48.7	49.8	44.8

Table 2-5, continued. Amphibole compositions from run products.

Run	2	8	8		11		11	14	14	
P (kb)	10	15	15		15		15	18	18	
T (°C)	950	1065	1065		1125		1125	1163	1163	
added H_2O%	8	0	8		0		2	0	0	
number	n=1	n=1	n=5	*2 σ*	n=3	*2 σ*	n=1	n=1	n=3	*2 σ*
SiO_2	46.91	41.57	38.67	*1.56*	40.64	*0.29*	41.77	50.08	39.29	*1.92*
Al_2O_3	6.51	14.62	17.42	*0.79*	14.49	*0.06*	13.74	16.44	17.16	*1.23*
TiO_2	4.07	3.01	2.73	*0.36*	4.41	*1.06*	4.11	2.79	4.02	*0.27*
FeO	14.32	13.85	17.26	*1.71*	13.38	*0.29*	10.83	11.96	15.28	*2.00*
MgO	5.67	9.11	7.60	*1.14*	9.86	*0.29*	13.21	7.94	8.62	*0.34*
MnO	0.13	0.11	0.34	*0.09*	0.17	*0.16*	0.20	0.31	0.18	*0.05*
CaO	9.41	8.79	9.84	*0.56*	9.83	*0.34*	10.35	7.47	9.02	*0.10*
Na_2O	7.36	2.97	2.94	*0.26*	3.06	*0.25*	2.94	2.57	3.06	*0.06*
K_2O	0.03	1.59	1.48	*0.18*	1.52	*0.23*	1.56	1.53	1.68	*0.12*
F	0.04		0.07	*0.11*			0.02			
Cl	0.00		0.07	*0.03*						
Total	94.44	95.62	98.37		97.42		98.74	101.24	98.37	
Si	7.23	6.287	5.827		6.067		6.085	6.895	5.85	
Al IV	0.77	1.713	2.173		1.933		1.915	1.105	2.15	
Σ T	8	8	8		8		8	8	8	
Al VI	0.413	0.893	0.921		0.616		0.444	1.563	0.862	
Ti	0.472	0.342	0.31		0.495		0.45	0.289	0.45	
Fe2	1.85	1.75	2.18		1.67		1.32	1.38	1.90	
Mg	1.30	2.01	1.59		2.20		2.79	1.63	1.79	
Mn	0.02				0.02			0.04		
Σ C	4.05	5	5		5		5	4.90	5	
Fe2										
Mg		0.04	0.11				0.08		0.13	
Mn		0.02	0.04				0.03		0.02	
Ca	1.55	1.42	1.59		1.57		1.62	1.10	1.44	
Na	0.45	0.52	0.26		0.42		0.28	0.69	0.41	
Σ B	2	2	2		2		2	1.80	2	
Na	1.75	0.35	0.60		0.46		0.56		0.48	
K	0.01	0.31	0.28		0.29		0.29	0.27	0.32	
Σ A	1.76	0.66	0.89		0.75		0.85	0.27	0.79	
OH (calc.)	1.98	2	1.95		2		1.99	2	2	
F	0.021		0.032				0.009			
Cl			0.017							
Σ anion (ideal)	2	2	2		2		2	2	2	
classification	Ferro-edenite	Magnesio-taramite	Ferro-pargasite		Pargasite		Pargasite	Barroisite	Magnesio-taramite	

Table 2-5, continued. Amphibole compositions from run products.

Run	2	8	8	11	11	14	14
P (kb)	10	15	15	15	15	18	18
T (°C)	950	1065	1065	1125	1125	1163	1163
added H_2O%	8	0	8	0	2	0	0
number	n=1	n=1	n=5	n=3	n=1	n=1	n=3
X_F					0.005		
X_{Cl}			0.008				
X_{OH}	1		0.976		0.996		
Si/(Na+K)	3.3	5.3	5.1	5.2	5.4	7.2	4.9
Mg'	41.4	54.0	44.0	56.8	68.5	54.2	50.1

Table 2-5, continued. Amphibole compositions from run products.

Run	14		5		5	5		5	5
P (kb)	18		20		20	20		20	20
T (°C)	1163		1125		1125	1125		1125	1125
added H_2O%	2		0		0	2		4	8
number	n=2	*2 σ*	n=3	*2 σ*	n=1	n=4	*2 σ*	n=1	n=1
SiO_2	41.38	*0.13*	53.05	*2.92*	59.49	40.08	*1.15*	51.77	46.66
Al_2O_3	13.66	*0.96*	11.50	*2.00*	16.89	17.90	*1.53*	6.34	11.25
TiO_2	4.95	*0.14*	0.40	*0.47*	0.23	0.90	*0.77*	0.85	4.24
FeO	14.56	*1.15*	11.45	*0.51*	6.98	15.59	*2.32*	13.85	12.74
MgO	9.57	*0.99*	5.68	*2.16*	2.85	8.87	*1.87*	7.64	3.77
MnO	0.19	*0.15*	0.53	*0.16*	0.18	0.52	*0.22*	0.31	0.31
CaO	8.95	*0.28*	11.71	*2.27*	6.90	8.57	*2.31*	12.14	6.68
Na_2O	3.59	*0.14*	3.57	*0.02*	3.40	3.64	*0.04*	8.37	8.38
K_2O	1.71	*0.28*	0.50	*0.45*	0.97	1.45	*0.35*	0.03	0.14
F	0.10					0.19	*0.13*	0.02	
Cl	0.02	*0.00*	0.02	*0.03*	0.02	0.03	*0.01*	0.01	
Total	98.72		98.40		97.92	97.65		101.32	94.18
Si	6.134		7.539		8.014	6.006		7.42	7.084
Al IV	1.866		0.461			1.994		0.58	0.916
Σ T	8		8		8.014	8			8
Al VI	0.521		1.466		2.681	1.167		0.491	1.097
Ti	0.552		0.042		0.024	0.101		0.091	0.484
Fe2	1.80		1.36		0.79	1.95		1.66	1.62
Mg	2.12		1.20		0.57	1.78		1.63	0.85
Mn	0.01		0.06		0.02			0.04	0.04
Σ C	5		4.14		4.09	5		3.91	5
Fe2									
Mg						0.20		0.00	0.00
Mn	0.02					0.07		0.00	0.04
Ca	1.42		1.78		1.00	1.38		1.86	1.09
Na	0.56		0.22		0.89	0.36		0.14	0.91
Σ B	2		2		1.88	2		2	2
Na	0.48		0.77		0.00	0.70		2.19	1.55
K	0.32		0.09		0.17	0.28		0.01	0.03
Σ A	0.80		0.86		0.17	0.98		2.20	1.58
OH (calc.)	1.95		2		2	1.90		1.99	2
F	0.046					0.090		0.000	
Cl	0.004		0.005		0.005	0.007		0.009	
Σ anion (ideal)	2		2		2	2		2	2
classification	Magnesio-taramite		Ferro-edenite		Ferro-winchite	Ferro-pargasite		Ferro-edenite	Kataphor-ite

Table 2-5, continued. Amphibole compositions from run products.

Run	14	5	5	5	5	5
P (kb)	18	20	20	20	20	20
T (°C)	1163	1125	1125	1125	1125	1125
added H_2O%	2	0	0	2	4	8
number	n=2	n=3	n=1	n=4	n=1	n=1
X_F	0.023			0.045		
X_{Cl}	0.002	0.002	0.002	0.004	0.004	
X_{OH}	0.975	0.998	0.998	0.952	0.996	1
Si/(Na+K)	4.5	7.0	7.6	4.5	3.2	2.8
Mg'	54.0	46.9	42.1	50.4	49.6	34.5

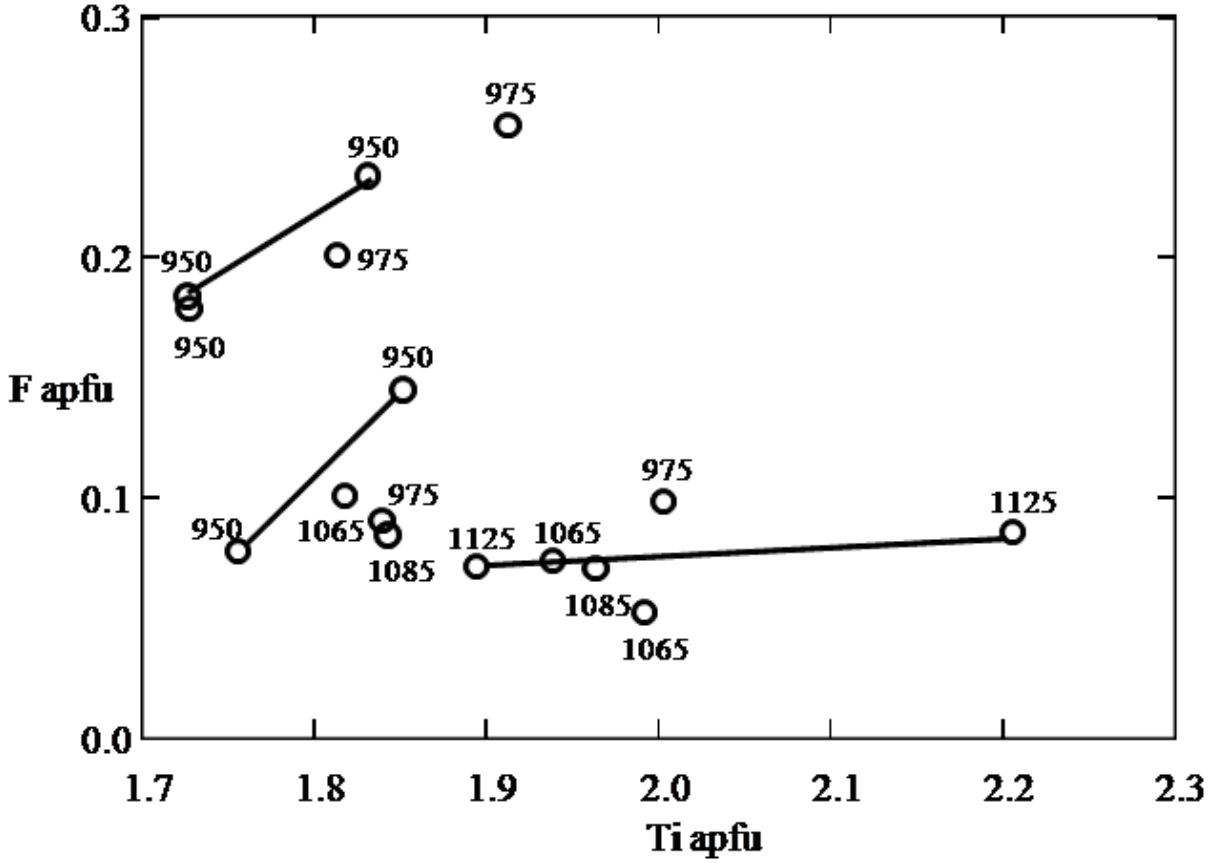

Figure 2-10. Biotite F-Ti compositions. Structural formulae determined on the basis of 22 O and OH. Data shown in Figure 2-4. Lines connect samples from the same experiment with different compositions. There is no correlation between F and Ti, but the highest F contents are from experimental runs of <1000° and most of the highest F contents are from biotite with the lower Ti contents.

Most amphiboles in these experiments are calcic (edenite, ferro-edenite, pargasite, or ferro-pargasite) but some are sodic-calcic (ferro-winchite, magnesio-taramite, barroisite, or kataphorite). Studies examining high-pressure fractionation in hydrous alkaline magmas commonly find titano-pargasite or kaersutite to be a common fractionating phases (e.g., Wilkinson and Hensel, 1991; Irving and Green, 2008). Among amphiboles that approach those compositions in this study, low Ti contents result in classification as (*sensu lato,* i.e., with or without *ferro-* prefixes) edenite or pargasite. All amphiboles with compositions of or approaching pargasite, including ferro-pargasite and magnesio-taramite, contain <42% SiO_2.

Experimental amphiboles with <42% SiO_2 show a slight reduction in Na with increasing pressure but the more striking patterns in amphibole composition are between Si/Na and added H_2O% and between Si/Na and pressure, shown in Figure 2-11A. Because Na is much more abundant in experimental amphiboles than K, Na dominates the pattern of alkali variation (compare Figure 2-10A to Figure 2-11B). One experiment was run at each pressure except for 15 kb, at which two were run (1065° and 1125°). Figure 2-11 shows:

(1) Amphibole Si/Na (and Si/(Na+K) decreases with increased H_2O in every experiment save one. Only in run 11 (15 kb, 1125°) is this relationship violated: the 2% H_2O amphiboles have slightly higher Si/Na than 0%; run 8 (15 kb, 1065°) amphiboles show the Si/Na-H_2O anticorrelation of other experiments.

(2) The pargasite, ferro-pargasite, and magnesio-taramite amphiboles (i.e., those with <42% SiO_2) have a negative correlation between Si/Na and pressure (r = -0.74, not shown on Figure 2-11).

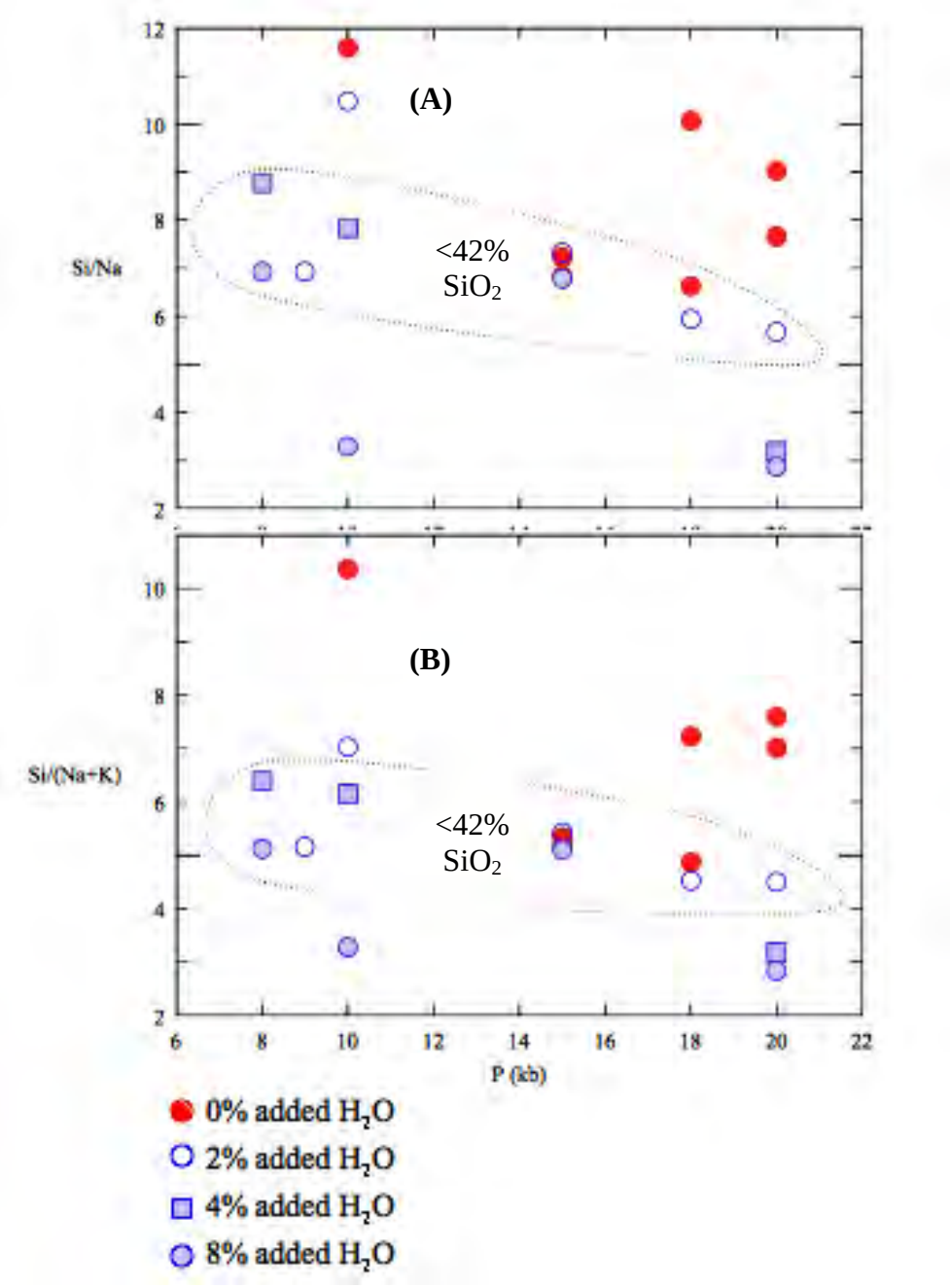

Figure 2-11. Amphibole Si/Na and Si/(Na+K) variations with pressure. Data are shown in Table 2-5. Alkali variation in experimental amphiboles is dominated by Na, but total alkali relation to SiO_2 is important in fractionation trends. Circled amphiboles with <42% SiO_2 are compositions of or approaching pargasite. **(A):** Si/Na in amphiboles plotted against pressure. At every pressure, the increase in added H_2O% correlates to an increase in Si/Na. For the circled *senso lato* pargasitic amphiboles, Si/Na has a slight inverse correlation with pressure. **(B):** Si/(Na+K) in amphiboles plotted against pressure. Similar to **(A)** but with less of an inverse correlation to pressure.

(3) The ferro-edenite from run 2, 8% H_2O, 10 kb, 950°, and the ferro-edenite and kataphorite from run 5, 4% and 8% H_2O, respectively, 20 kb, 1125°, have the lowest Si/Na compositions.

The above relationships hold for Si/(Na+K) as well as for Si/Na because K is a minor constituent in these amphiboles relative to Na. In these experiments, amphibole Si/alkalis is reduced by increasing H_2O, and, for those types of amphiboles commonly found in alkaline rocks (Evan and Nash, 1979; Barker, 1987), Si/alkalis is reduced by increasing pressure. One significant aspect of these data is that the lower the ratio of Si to alkalis in an amphibole the more efficiently its fractionation can raise the relative silica-enrichment of the melt (e.g., Giret et al., 1980). Fractionation of this RMS magma composition at varying depths and H_2O contents would result in varying liquid composition – possibly even silica-saturated and -unsaturated liquids.

For the two experiments conducted at 15 kilobars, *Mg'* and Ti in amphibole increase with temperature. For the two experiments conducted at 1125° C, *Mg'* and Ti decrease as pressure increases. These results agree with experiments by Irving and Green (2008) for a more mafic ne-mugearite starting material across a wider P-T range.

Ilmenite and rutile

The only oxide phase encountered was ilmenite, with the exception of a single rutile grain near the liquidus at 18 kb, 1165° C, 8% H_2O. This is reasonable given the relatively low oxidation state of the experiments, which apparently precludes the crystallization of titano-magnetite. Ilmenite is a liquidus phase in several runs – at 12.5 kb, 1110°, 8% H_2O and 15 kb, 1125°, 4% H_2O, and occurs with apatite near the liquidus at 15 kb, 1125°, 8% H_2O and 20 kb, 1125°, 8% water.

Garnet

Table 2-6 contains average garnet analyses. Garnet is present at 0% and 2% added H_2O at 15 and 20 kb runs and at 0% added H_2O at 18 kb. In no experimental run is garnet a definitive liquidus mineral, though 0.5% garnet persists with 95% melt at 15 kb, 1125° C, 2% H_2O (11-2) along with 2.5% pargasite and 1% each apatite and ilmenite.

Experimental garnets are consistently almandine-rich (Table 2-6). In any single experimental run (at set P and T) the *Mg'* of garnet increases as H_2O increases from 0 to 2 wt.%: from *Mg'* = 32 to 39 in run products 8-0 and 8-2 (15 kb, 1065°); from *Mg'* = 39 to 44 in run products 11-0 and 11-2 (15 kb, 1125°); from *Mg'* = 18 to 32 in run products 5-0 and 5-2 (20 kb, 1125°). Of the two 15 kilobar runs, *Mg'* is higher in the 1125° run than in the 1065° run. Of the two 1125° runs, *Mg'* is higher in the 15 kilobar run than in the 20 kilobar run. In summary, the limited results show that garnet *Mg'* increases with increasing H_2O wt.% and increasing temperature, and decreases as pressure increases.

Feldspars and feldspathoids

No feldspathoids were found in any run products. Feldspar is largely absent from run products above 1000° C, though alkali feldspar is found at 20 kb, 1125° C at 0 (albite) and 2% (anorthoclase) added H_2O. Feldspar analyses are found in Table 2-7.

Apatite

Apatite is a common phase in these experiments and occurs at or near the liquidus in several runs. It occurs in every subliquidus run with ≤ 2% added H_2O; at 4% added H_2O apatite occurs in all experiments ≤ 1085°; with 8% added H_2O, apatite is present in all experiments except on the liquidus at 1110°, 12.5 kb (13-8). Average apatite compositions are presented in Table 2-8. It is rich in the fluoroapatite component with ~1.5-3.5 wt.% F.

Table 2-6. Garnet compositions from run products. Cations are allocated on the basis of 12 O's. Mean compositions are presented with *2σ* errors.

Run	8		8		11		11		5		5	
P (kb)	15		15		15		15		20		20	
T (°C)	1065		1065		1125		1125		1125		1125	
added H_2O%	0		2		0		2		0		2	
number	n=3	*2σ*	n=5	*2σ*	n=5	*2σ*	n=4	*2σ*	n=4	*2σ*	n=8	*2σ*
SiO_2	37.84	*1.10*	37.01	*0.61*	37.49	*0.70*	37.64	*1.69*	36.59	*0.31*	36.83	*0.54*
Al_2O_3	21.39	*0.59*	21.13	*0.67*	21.03	*0.45*	21.37	*1.53*	20.75	*0.19*	20.89	*0.67*
TiO_2	1.06	*0.49*	1.47	*0.53*	1.72	*0.13*	1.10	*0.98*	0.77	*0.16*	1.44	*0.28*
MgO	6.29	*0.21*	8.20	*1.01*	8.32	*1.98*	10.24	*1.81*	3.44	*0.57*	6.30	*1.53*
FeO	24.04	*1.73*	23.71	*2.60*	21.83	*2.67*	22.73	*5.10*	27.21	*2.92*	24.67	*0.86*
MnO	1.56	*0.40*	1.00	*0.56*	1.00	*0.51*	0.83	*0.38*	1.90	*1.18*	0.85	*0.56*
CaO	7.52	*0.74*	6.49	*0.56*	7.70	*0.88*	5.32	*1.29*	8.31	*0.75*	8.78	*2.22*
Total	99.70	*0.70*	99.01	*1.59*	99.12	*1.00*	99.24	*1.17*	99.01	*1.42*	99.78	*0.84*
Si	2.95		2.90		2.91		2.91		2.94		2.89	
Al	1.96		1.95		1.92		1.94		1.96		1.95	
Ti	0.06		0.09		0.10		0.06		0.05		0.08	
Mg	0.73		0.97		0.94		1.18		0.41		0.76	
Fe	1.57		1.52		1.44		1.47		1.83		1.63	
Mn	0.10		0.07		0.07		0.05		0.13		0.05	
Ca	0.63		0.54		0.64		0.44		0.71		0.69	
sum	8.01		8.04		8.02		8.06		8.03		8.05	
Mg'	32		39		39		44		18		32	

Table 2-7. Feldspar compositions from run products. Cations are allocated based on 8 O's. When multiple analyses were gathered, a mean composition and *2σ* error is shown.

Run	1		1	1		2		2	2	
P (kb)	9		9	9		10		10	10	
T (°C)	975		975	975		950		950	950	
added H_2O%	0		0	2		0		0	2	
number	n=8	*2σ*		n=5	*2σ*	n=2	*2σ*		n=2	*2σ*
SiO_2	54.91	*1.73*	62.65	59.56	*2.17*	50.89	*1.58*	62.93	55.02	*3.45*
TiO_2	0.11	*0.12*		0.22	*0.58*				0.10	*0.12*
Al_2O_3	27.82	*1.83*	21.37	24.08	*1.11*	30.43	*0.13*	22.59	27.38	*1.85*
MgO	0.06	*0.07*		0.29	*1.11*					
FeO	0.56	*0.35*	0.57	0.80	*1.41*	0.55	*0.02*	0.43	0.63	*0.16*
CaO	9.63	*1.57*	2.91	4.86	*1.93*	13.23	*0.00*	3.59	9.48	*2.21*
K_2O	0.48	*0.44*	2.56	1.20	*1.20*	0.40	*0.04*	0.89	0.42	*0.16*
Na_2O	5.40	*0.83*	7.72	7.59	*1.02*	3.43	*0.58*	8.65	5.76	*1.61*
BaO	0.08	*0.15*	0.34	0.20	*0.29*	0.05	*0.13*	0.06	0.13	*0.17*
Total	99.09		98.46	98.87		99.08		99.34	98.97	
Si	2.501		2.843	2.698		2.341		2.810	2.511	
Ti	0.004			0.008					0.004	
Al	1.493		1.143	1.286		1.649		1.189	1.473	
Mg	0.004			0.020						
Fe	0.021		0.022	0.031		0.021		0.016	0.024	
Ca	0.470		0.141	0.236		0.652		0.172	0.464	
K	0.028		0.148	0.069		0.023		0.051	0.024	
Na	0.477		0.679	0.667		0.306		0.749	0.510	
Ba	0.001		0.006	0.004		0.001		0.001	0.002	
An%	48.2		14.6	24.3		66.5		17.7	46.5	
Ab%	48.9		70.1	68.6		31.1		77.1	51.1	
Or%	2.8		15.3	7.1		2.4		5.2	2.4	

Table 2-7, continued. Feldspar compositions from run products.

Run	2	2	2	2	5	5	5
P (kb)	10	10	10	10	20	20	20
T (°C)	950	950	950	950	1125	1125	1125
added H_2O%	4	4	4	4	0	0	2
number							
SiO_2	64.16	63.90	57.55	61.57	67.46	67.97	65.51
TiO_2							
Al_2O_3	22.04	23.24	26.66	24.53	21.04	21.09	21.55
MgO			0.06				
FeO	0.25	0.44	0.74	0.33	0.10	0.17	0.31
CaO	2.72	4.25	8.19	5.43	1.25	0.78	1.96
K_2O	0.96	0.99	0.48	0.80	0.68	0.11	1.77
Na_2O	9.07	8.02	6.42	7.69	10.57	11.14	9.09
BaO	0.02	0.08	0.06	0.10	0.02	0.03	0.09
Total	99.42	101.06	100.23	100.57	101.16	101.29	100.34
Si	2.851	2.803	2.581	2.725	2.929	2.938	2.887
Ti							
Al	1.154	1.201	1.409	1.279	1.076	1.074	1.119
Mg			0.004				
Fe	0.009	0.016	0.028	0.012	0.004	0.006	0.011
Ca	0.130	0.200	0.394	0.257	0.058	0.036	0.093
K	0.055	0.056	0.028	0.045	0.038	0.006	0.099
Na	0.781	0.682	0.558	0.660	0.890	0.933	0.777
Ba	0.000	0.001	0.001	0.002			0.002
An%	13.4	21.3	40.2	26.8	5.9	3.7	9.6
Ab%	80.9	72.8	57	68.6	90.3	95.7	80.2
Or%	5.6	5.9	2.8	4.7	3.8	0.6	10.3

Table 2-8. Apatite compositions from run products. When multiple anlayses were gathered, mean compositions and *2σ* errors are presented. Ions are allocated o nthe basis of 26 anions, and $OH^- + F^- + Cl^-$ is assumed to = 2 atoms per formula unit.

Run	12		12		4		4	4	11	
P (kb)	8		8		10		10	10	15	
T (°C)	1085		1085		925		925	925	1125	
added H_2O%	2		4		0		2	4	0	
number	n=4	*2σ*	n=4	*2σ*	n=2	*2σ*	n=1	n=1	n=3	*2σ*
P_2O_5	40.52	*1.13*	39.22	*0.83*	41.77	*0.34*	41.70	41.17	39.48	*3.57*
CaO	55.18	*0.93*	54.43	*1.82*	53.90	*2.63*	53.20	54.82	54.51	*3.46*
SiO_2	0.59	*0.54*	0.53	*0.46*	1.03	*1.05*	1.30	0.62	0.26	*0.24*
Al_2O_3	0.11	*0.09*			0.28	*0.33*	0.40	0.11		
FeO	0.41	*0.12*	0.54	*0.05*	0.40	*0.04*	0.60	0.30	0.41	*0.20*
MgO	0.16	*0.06*	0.28	*0.27*	0.12	*0.02*	0.20	0.08	0.25	*0.10*
Na_2O	0.08	*0.12*	0.07	*0.05*	0.12	*0.11*	0.20			
SrO	0.33	*0.05*	0.26	*0.12*	0.28	*0.04*	0.34	0.27	0.33	*0.11*
F	1.99	*0.08*	2.36	*0.14*	1.68	*0.77*	1.61	1.26	2.33	*0.78*
Cl	0.30	*0.12*	0.21	*0.06*	0.08	*0.05*	0.17	0.27	0.16	*0.06*
Total*	99.38		97.86		99.43		99.28	98.85	97.4	
ions based on 26 anions										
P	5.91		5.83		6.03		6.01	6.02	5.88	
Ca	10.18		10.23		9.84		9.70	10.15	10.29	
Si	0.10		0.09		0.18		0.23	0.11	0.05	
Al	0.02				0.06		0.07	0.02		
Fe	0.06		0.08		0.06		0.08	0.04	0.06	
Mg	0.04		0.07		0.03		0.04	0.02	0.07	
Na	0.03		0.03		0.04		0.06			
Sr	0.03		0.03		0.03		0.03	0.03	0.03	
F	1.08		1.31		0.90		0.87	0.69	1.29	
Cl	0.09		0.06		0.02		0.05	0.08	0.05	
OH (ideal)	0.83		0.63		1.08		1.08	1.23	0.66	
Total	18.37		18.36		18.27		18.22	18.39	18.38	
X_F	0.54		0.66		0.45		0.43	0.34	0.65	
X_{Cl}	0.04		0.03		0.01		0.02	0.04	0.02	
X_{OH}	0.41		0.31		0.54		0.54	0.62	0.33	

*Totals are calculated after accounting for F and Cl.

Table 2-8, continued. Apatite compositions from run products.

Run	13		11		14		5	
P (kb)	12.5		15		18		20	
T (°C)	1110		1125		1163		1125	
added H_2O%	0		2		0		0	
number	n=4	*2σ*	n=3	*2σ*	n=4	*2σ*	n=2	*2σ*
P_2O_5	42.94	*3.75*	38.13	*3.88*	38.69	*2.38*	37.64	*2.67*
CaO	52.22	*2.11*	51.22	*5.60*	55.18	*1.64*	52.23	*6.46*
SiO_2	0.88	*1.85*	3.87	*6.22*	0.41	*0.20*	1.32	*2.90*
Al_2O_3	0.22	*0.71*	1.35	*2.33*			1.73	*3.18*
FeO	0.24	*0.04*	1.03	*0.39*	0.49	*0.23*	0.36	*0.27*
MgO	0.19	*0.17*	0.76	*0.17*	0.19	*0.06*	0.11	*0.15*
Na_2O	0.15	*0.20*	0.28	*0.17*			0.10	*0.17*
SrO	0.59	*0.63*	0.38	*0.11*	0.28	*0.08*	0.25	*0.12*
F	2.42	*0.42*	1.39	*0.04*	2.33	*0.66*	2.37	*2.79*
Cl	0.02	*0.02*	0.08	*0.00*	0.16	*0.07*	0.23	*0.22*
Total*	99.36		98.49		97.43		96.08	
P	6.13		5.57		5.79		5.65	
Ca	9.44		9.46		10.45		9.92	
Si	0.15		0.66		0.07		0.24	
Al	0.05		0.27				0.37	
Fe	0.03		0.15		0.07		0.05	
Mg	0.05		0.19		0.05		0.03	
Na	0.05		0.09				0.04	
Sr	0.06		0.04		0.03		0.03	
F	1.29		0.76		1.30		1.32	
Cl	0.00		0.02		0.05		0.07	
OH (ideal)	0.70		1.22		0.65		0.61	
Total	17.95		18.43		18.46		18.33	
X_F	0.65		0.38		0.65		0.66	
X_{Cl}	0.00		0.01		0.02		0.03	
X_{OH}	0.35		0.61		0.33		0.30	

*Totals are calculated after accounting for F and Cl.

The variation of apatite X_F with pressure and added H_2O are shown in Figure 2-12. Of the five average compositions with $X_F > 0.6$, four are from experiments with 0% added H_2O and from pressures >12 kb. The one experiment with 0% added H_2O that contains apatite with X_F <0.6 is from the 925° C, 10 kb (4-0). The apatite data do not allow much comparison between compositions at constant P or T, but of the ones that do: at 15 kb, 11-0 has higher X_F than 11-2; at 10 kb, X_F in run 4-0 > 4-2 > 4-4; only in run 12, at 8 kb, does the higher added H_2O sample have higher X_F and that is the only analyzed sample with an exsolved vapor phase.

No run products contained apatite with La_2O_3, Y_2O_3, Ce_2O_3, or SO_3 above detection limit.

Glass composition

All experimental conditions are supersolidus and yield some quenched melt as glass. The amount of melt varies from ~30% to 100%.

As indicated above, analysis of alkali-rich hydrous glass in experimental charges is problematic and often leads to low Na results due to elemental migration and/or volatilization (e.g., Patiño Douce, 2005). A comparison of Na_2O wt.% from analysis of supersolidus run products (experiments 13-2 and 13-4) to the starting composition show a relative change of -19 to -22% for normalized and -27 to -29% for unnormalized results. To constrain Na contents in experimental glasses, I performed mass balance equations when possible using phase modes and compositions after the method of Bryan et al. (1969). In performing these calculations I determined that analytical results for Al in glass were slightly high and adjusted them accordingly.

Of the 16 sub-liquidus experiments for which I obtained glass analyses, there are only 7 for which I have phase composition and accompanying modal data sufficient to perform

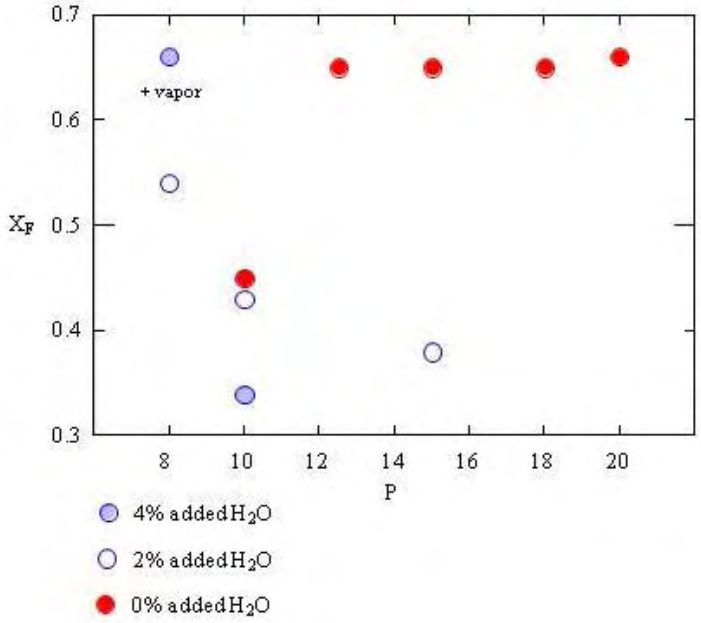

Figure 2-12. Apatite mole fraction F plotted against P (kb). Apatite X_F is higher in samples with the least added H_2O, or, in the case of the 8 kb sample 12-4, when a vapor phase is exsolved.

satisfactory mass balance calculations. Results of the glass analyses with calculated Na contents are shown in Table 2-9, along with CIPW norms. The range of Na correction by mass balance was 25-43 relative%, and no correlations are evident between degree of Na correction and phase assemblage, modal proportions of minerals or glass, experimental pressure, experimental temperature, added H_2O, or analytic totals.

For the 9 remaining glass analyses, mass balance corrections were not possible and I adjusted the results by the average mass balance calculations for samples in Table 2-9: Na_2O by +35 relative% and Al_2O_3 by -4 relative%. Raw and corrected analyses are shown in Table 2-10 – these include CIPW norms for both raw and corrected analyses for comparison.

Of all of the glass compositions with Na and Al calculated by mass balance or adjusted by fixed percentages in Tables 2-9 and Table 2-10, 6 are Q-normative (silica-oversaturated) and 10 are ne-normative (silica-undersaturated). The glasses from only two samples approach peralkalinity: P.I. = 0.99 for sample 11-0 and P.I. = 1.00 for sample 5-2. The glasses from several samples are corundum (C)-normative: C = 0.7% and A.S.I. = 1.13 for sample 1-2; C = 1.4% and A.S.I. = 0.99 for sample 14-2; and C = 4.5% and A.S.I. = 1.35 for sample 5-8. Although there are peraluminous rocks in the TPMP, they are typically high-silica rhyolites (White and Urbanczyck, 2001; Rubin et al., 1989) and not the mildly peraluminous ne-phonolite (14-2) or Q-trachyte (5-8) found in these experiments.

Phase equilibrium control of glass silica-saturation

Figure 2-13 shows the degree of silica saturation by plotting normative Q-ne against the Thornton-Tuttle (1960) differentiation index (D.I. = normative Q + ab + or + ne + NMS [sodium metasilicate]). Because Q and ne appear in both the x-axis and y-axis some covariance along one of two trends is expected (either with increasing Q or increasing ne, since their occurrences are

Table 2-9. Glass analyses from run products with Na and Al determined by mass balance. For these analyses there were sufficient phase modal and compositional data to calculate Na and Al by least squares mass balance. Geochemical parameters are described in Table 2-1A.

Run	8		8		11		11		14		14		5	
P (kb)	15		15		15		15		18		18		20	
T (°C)	1065		1065		1125		1125		1165		1165		1125	
added H_2O%	4		8		0		2		0		2		2	
number	n=3	2σ	n=5	2σ	n=6	2σ	n=5	2σ	n=4	2σ	n=4	2σ	n=5	2σ
SiO_2	58.50	*0.55*	48.49	*6.04*	55.58	*0.84*	52.20	*1.70*	59.10	*1.22*	51.45	*1.57*	64.39	*1.93*
TiO_2	0.46	*0.01*	0.93	*0.27*	0.98	*0.16*	1.29	*0.15*	1.40	*0.59*	0.92	*0.29*	0.21	*0.17*
Al_2O_3	*17.8*	*	*15.0*	*	*16.3*	*	*15.9*	*	*17.5*	*	*19.1*	*	*16.3*	*
FeO	3.93	*1.42*	5.46	*0.73*	3.50	*1.38*	4.70	*1.15*	4.87	*0.69*	3.27	*1.03*	1.24	*0.51*
MgO	0.74	*0.11*	1.72	*0.17*	1.07	*0.20*	2.02	*0.64*	1.60	*0.53*	0.70	*0.22*	0.20	*0.11*
CaO	2.76	*0.26*	3.67	*0.66*	2.23	*0.36*	3.36	*1.04*	3.09	*0.78*	0.98	*0.33*	0.71	*0.24*
Na_2O	*7.1*	*	*5.7*	*	*7.0*	*	*6.2*	*	*7.3*	*	*6.6*	*	*7.4*	*
K_2O	3.22	*0.34*	2.65	*0.73*	4.25	*0.78*	3.68	*0.61*	4.03	*0.45*	6.12	*0.36*	3.76	*0.78*
P_2O_5	0.32	*0.47*	0.58	*0.45*	0.57	*0.31*	0.81	*0.68*	0.75	*0.45*	0.58	*0.13*	0.23	*0.12*
Cl	0.09	*0.07*	0.08	*0.03*			0.07	*0.03*	0.06	*0.03*	0.13	*0.06*	0.07	*0.06*
Total	94.93		84.28		91.50		90.23		99.71		89.85		94.47	
normalized to volatile-free 100%														
SiO_2	61.68		57.59		60.74		57.90		59.31		57.35		68.20	
TiO_2	0.48		1.10		1.07		1.44		1.41		1.03		0.22	
Al_2O_3	*18.8*		*17.8*		*17.8*		*17.6*		*17.6*		*21.3*		*17.2*	
FeO	4.15		6.49		3.82		5.21		4.89		3.64		1.31	
MgO	0.78		2.04		1.17		2.24		1.61		0.78		0.21	
CaO	2.91		4.36		2.44		3.72		3.10		1.09		0.76	
Na_2O	*7.5*		*6.8*		*7.7*		*6.9*		*7.3*		*7.4*		*7.9*	
K_2O	3.40		3.15		4.64		4.08		4.04		6.82		3.98	
P_2O_5	0.33		0.68		0.62		0.90		0.75		0.65		0.25	
total	100		100		100		100		100		100		100	
Mg'	25.2		35.9		35.4		43.4		37		27.6		22.5	
PI	0.85		0.82		0.99		0.89		0.94		0.92		1.00	
ASI	0.88		0.79		0.80		0.78		0.8		0.99		0.93	
CIPW norms (calculated with all Fe as Fe^{2+})														
AN%	11.3		15.6		0.6		10.2		5.8		3.6			
Q													5.6	
or	20.1		18.6		27.4		24.1		23.9		40.3		23.5	
ab	59.4		48.2		51.0		45.8		50.6		32.2		66.4	
an	7.6		8.9		0.3		5.2		3.1		1.2			
ne	2.1		4.9		7.7		6.7		6.2		16.3			
C											1.4			
di	4.0		7.0		6.5		6.2		6.2				1.8	
hy													1.6	
ol	5.1		8.7		3.6		7.2		5.6		5.2			
il	0.9		2.1		2.0		2.7		2.7		2.0		0.4	
ap	0.8		1.6		1.4		2.1		1.7		1.5		0.6	
D.I.[1]	81.6		71.7		86.1		76.6		80.7		88.8		95.5	

[1]D.I. = Thornton and Tuttle's (1960) differentiation index = normative Q+or+ab+ne

Table 2-10. Glass analyses with Na and Al corrected. There were insufficient data for these run products to calculate Na and Al by mass balance, so average changes from calculations for other glasses (Table 2-9) of +35 relative% Na and -4 relative% Al were applied. Raw analyses with 2σ errors, compositions with raw and corrected Na_2O and Al_2O_3 normalized to 100% volatile-free totals, and CIPW norms for both raw and corrected compositions are all shown.

Sample	1-2		1-8		13-8		8-2		11-4	
P (kb)	9		9		12.5		15		15	
T (°C)	975		975		1110		1065		1125	
H_2O% added	2		8		8		2		4	
	n=4	2σ	n=5	2σ	n=6	2σ	n=5	2σ	n=6	2σ
SiO_2	64.35	*3.44*	59.72	*3.11*	49.20	*1.90*	58.49	*2.14*	50.83	*2.66*
TiO_2	0.46	*0.26*	0.70	*0.18*	1.66	*0.14*	0.72	*0.26*	1.88	*0.22*
Al_2O_3	19.45	*1.71*	18.68	*0.87*	15.96	*0.53*	17.15	*0.87*	16.72	*1.09*
FeO	2.85	*0.26*	2.75	*0.57*	6.08	*1.09*	3.13	*2.47*	7.50	*1.61*
MgO	0.46	*0.20*	0.81	*0.24*	2.61	*0.14*	0.81	*0.06*	2.84	*0.29*
CaO	2.15	*0.35*	2.82	*0.19*	4.00	*0.46*	2.47	*0.36*	4.42	*0.44*
Na_2O	4.84	*2.53*	4.98	*1.35*	4.24	*1.82*	4.49	*1.65*	4.68	*0.30*
K_2O	3.42	*1.86*	3.22	*0.47*	3.10	*0.87*	3.22	*0.20*	3.16	*0.33*
P_2O_5	0.16	*0.06*	0.29	*0.09*	1.04	*0.24*	0.37	*0.24*	0.88	*0.80*
Cl	0.08	*0.08*	0.22	*0.06*	0.45	*0.14*	0.08	*0.01*	0.08	*0.07*
Total	99.15		95.17		89.20		91.83		93.96	
100% volatile free	1-2 raw	1-2 Na, Al calc'd	1-8 raw	1-8 Na, Al calc'd	13-8 raw	13-8 Na, Al calc'd	8-2 raw	8-2 Na, Al calc'd	11-4 raw	11-4 Na, Al calc'd
SiO_2	64.92	64.95	62.89	62.89	55.44	55.45	63.75	63.76	54.17	54.15
TiO_2	0.47	0.47	0.73	0.73	1.87	1.87	0.78	0.78	2.01	2.01
Al_2O_3	19.62	18.85	19.67	18.88	17.98	17.26	18.69	17.95	17.81	17.10
FeO	2.87	2.88	2.90	2.90	6.85	6.85	3.41	3.41	7.99	7.99
MgO	0.46	0.46	0.85	0.85	2.94	2.94	0.88	0.88	3.03	3.03
CaO	2.17	2.17	2.97	2.97	4.50	4.50	2.70	2.70	4.71	4.71
Na_2O	5.87	6.60	6.29	7.08	5.73	6.45	5.87	6.60	5.98	6.72
K_2O	3.45	3.45	3.39	3.39	3.50	3.50	3.51	3.51	3.37	3.37
P_2O_5	0.16	0.16	0.31	0.31	1.18	1.18	0.41	0.41	0.94	0.94
total	100	100	100	100	100	100	100	100	100	100
Mg'	22.3	22.3	34.3	34.3	43.3	43.3	31.6	31.6	40.3	40.3
PI	0.60	0.68	0.62	0.71	0.65	0.73	0.63	0.72	0.66	0.76
ASI	1.25	1.13	1.11	1.01	0.91	0.84	1.12	1.02	0.87	0.81

Table 2-10, continued. Glass analyses with Na and Al corrected.

Sample	11-8		14-8		5-4		5-8	
P (kb)	15		18		20		20	
T (°C)	1125		1165		1125		1125	
H_2O% added	8		8		4		8	
	n=6	2σ	n=5	2σ	n=3	2σ	n=5	2σ
SiO_2	51.61	*1.91*	54.28	*0.81*	66.72	*2.05*	59.85	*3.02*
TiO_2	1.92	*0.35*	2.02	*0.31*	0.06	*0.10*	0.32	*0.16*
Al_2O_3	17.02	*0.56*	16.86	*0.44*	15.68	*1.11*	20.10	*1.52*
FeO	8.00	*1.25*	5.40	*0.76*	0.93	*0.28*	1.15	*0.20*
MgO	3.01	*0.51*	3.04	*0.44*	0.24	*0.05*	0.37	*0.13*
CaO	4.46	*0.44*	3.91	*0.27*	0.77	*0.30*	0.91	*0.04*
Na_2O	3.96	*0.76*	5.05	*0.39*	4.96	*0.54*	4.44	*0.37*
K_2O	3.25	*0.47*	3.65	*0.65*	3.05	*0.37*	4.13	*0.54*
P_2O_5	0.92	*0.46*	0.96	*0.18*	0.22	*0.13*	0.35	*0.20*
Cl	0.12	*0.07*	0.07		0.10	*0.09*	0.14	*0.15*
Total	94.99		96.33		93.83		92.52	
100% volatile free	11-8 raw	11-8 Na, Al calc'd	14-8 raw	14-8 Na, Al calc'd	5-4 raw	5-4 Na, Al calc'd	5-8 raw	5-8 Na, Al calc'd
SiO_2	54.36	54.41	56.44	56.39	71.27	71.18	64.69	64.79
TiO_2	2.02	2.02	2.10	2.09	0.06	0.06	0.35	0.35
Al_2O_3	17.92	17.22	17.53	16.82	16.75	16.06	21.73	20.89
FeO	8.43	8.44	5.62	5.61	1.00	1.00	1.24	1.24
MgO	3.17	3.17	3.16	3.15	0.25	0.25	0.40	0.40
CaO	4.69	4.70	4.07	4.06	0.82	0.82	0.99	0.99
Na_2O	5.01	5.64	6.30	7.08	6.36	7.14	5.76	6.49
K_2O	3.43	3.43	3.79	3.79	3.26	3.25	4.47	4.47
P_2O_5	0.96	0.96	1.00	1.00	0.24	0.24	0.38	0.38
total	100	100	100	100	100	100	100	100
Mg'	40.1	40.1	50.0	50.0	31.0	31.0	36.3	36.3
PI	0.59	0.67	0.73	0.83	0.73	0.84	0.59	0.66
ASI	0.94	0.88	0.87	0.80	1.22	1.08	1.50	1.35

Table 2-10, continued. Glass analyses with Na and Al corrected.

Sample	1-2 raw	1-2 Na, Al calc'd	1-8 raw	1-8 Na, Al calc'd	13-8 raw	13-8 Na, Al calc'd	8-2 raw	8-2 Na, Al calc'd	11-4 raw	11-4 Na, Al calc'd
P (kb)	9		9		12.5		15		15	
T (°C)	975		975		1110		1065		1125	
H_2O% added	2		8		8		2		4	
CIPW norms										
AN%	19.0	14.8	22.3	14.0	26.6	15.5	20.6	13.8	27.9	14.9
Q	16.5	6.4	10.9	0.8			13.8	4.1		
or	20.6	20.4	20.2	20.0	20.9	20.7	20.9	20.7	20.1	19.9
ab	41.8	55.9	44.8	59.9	40.8	42.8	41.8	55.9	42.6	37.3
an	9.8	9.7	12.8	9.8	14.8	7.8	10.8	9.0	16.5	6.5
ne						6.4				10.6
C	4.3	0.7	2.8		1.0		3.0			
di				2.5		5.7		1.5	0.8	9.0
hy	5.7	5.7	6.3	5.0	14.0		7.2	6.4	0.4	
ol					2.2	10.4			13.6	10.7
il	0.9	0.9	1.4	1.4	3.6	3.5	1.5	1.5	3.9	3.8
ap	0.4	0.4	0.7	0.7	2.8	2.7	1.0	0.9	2.2	2.2
D.I.	79	83	76	81	62	70	77	81	63	68

Table 2-10, continued. Glass analyses with Na and Al corrected.

Sample	11-8 raw	11-8 Na, Al calc'd	14-8 raw	14-8 Na, Al calc'd	5-4 raw	5-4 Na, Al calc'd	5-8 raw	5-8 Na, Al calc'd
P (kb)	15		18		20		20	
T (°C)	1125		1165		1125		1125	
H_2O% added	8		8		4		8	
CIPW norms								
AN%	32.5	22.3	22.7	6.4	5.4	3.4	5.6	4.2
Q					26.0	15.0	17.4	7.5
or	20.4	20.3	22.7	22.4	19.5	19.2	26.7	26.4
ab	35.6	40.3	44.9	42.6	45.3	60.4	41.0	54.9
an	17.1	11.5	13.2	2.9	2.6	2.1	2.4	2.4
ne		4.0		9.4				
C	1.1				3.6		8.2	4.5
di	0.0	4.6	0.5	8.8		0.3		
hy	17.7		6.3		2.4	2.2	2.7	2.7
ol	1.9	13.2	6.1	7.6				
il	3.9	3.8	4.0	4.0	0.1	0.1	0.7	0.7
ap	2.3	2.2	2.3	2.3	0.6	0.5	0.9	0.9
D.I.	56	65	68	74	91	95	85	89

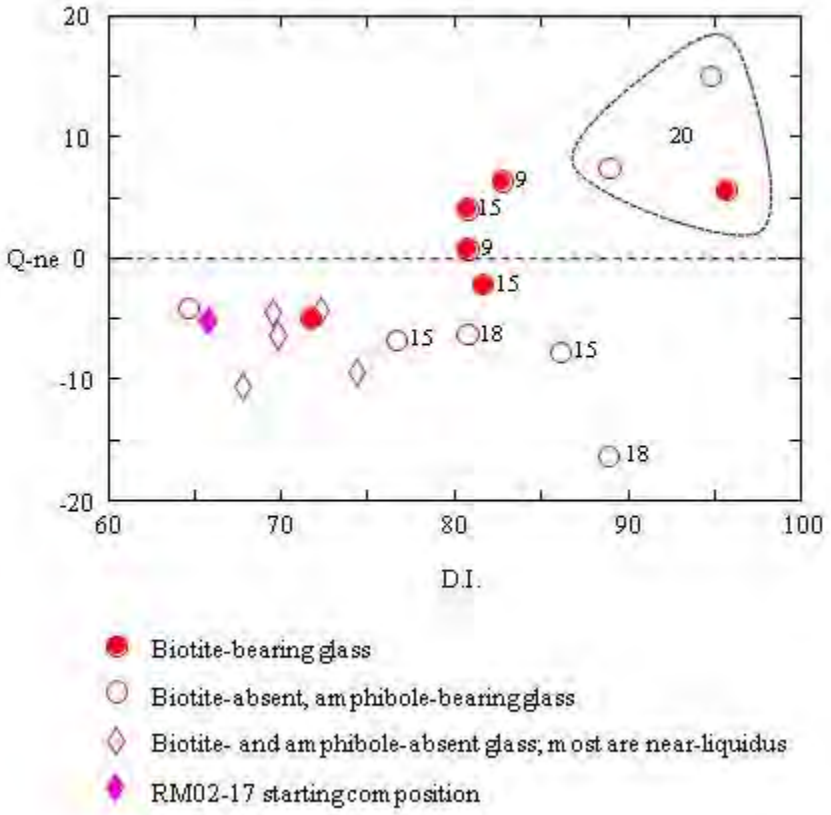

Figure 2-13. Thornton-Tuttle (1960) differentiation index versus normative Q-ne for all experimental glass compositions. D.I. = normative Q + ab + or + ne + NMS. Pressures are indicated for D.I. > 75.

mutually exclusive). Four of the 6 Q-normative compositions are from biotite-bearing run products and only 2 are from amphibole-bearing run products. Five of the 7 amphibole-bearing run products are ne-normative.

The Si/alkalis in these phases exerts an important, if not controlling, role in the silica-saturation of these melts. The starting material, RM02-17, has molar Si/(K+Na) = 3.40; fractionation of a phase with Si/(K+Na) > 3.40 will increase the melt Si/(K+Na) while fractionation of a phase with Si/(K+Na) < 3.40 will decrease the melt Si/(K+Na). Most biotite in these experiments has Si/(K+Na) of 2.7-3.5, while the Na-rich biotite from the 20 kb runs 5-0 and 5-2 have Si/(K+Na) < 2. Amphibole Si/(K+Na) varies from 4 to 10 in most of these experiments, though Na-rich amphiboles in the 10 kb run 2-8 and the 20 kb runs 5-4 and 5-8 have Si/(Na+K) of 2.8-3.2 (see Figure 2-11 for amphibole Si/Na and Si/[Na+K]). The 3.40 Si/(K+Na) of the starting material is lower than all amphiboles except those from the 20 kb run and higher than all but one biotite composition (run 1-8).

Figure 2-13 shows that most biotite-bearing run products and the 20 kb run products with high-Na amphiboles are Q-normative. The Si/(K+Na) of the biotite and amphibole in the run product relative to the Si/(K+Na) of the starting material corresponds well with melt silica saturation. Of course, other phases are present in most of these run products, including the essentially alkali-free silicates such as clinopyroxene and garnet. The effect of the biotite or amphibole crystallization on silica-saturation will be tempered or countered by these phases and others. Unfortunately, the modal data are not sufficient to test this relationship more rigorously.

Giret et al. (1980) invoked fractionation of alkali-rich, silica-poor amphibole (kaersutite or Ti-pargasite) in shifting silica-saturation of melts. This mechanism involving pargasitic amphibole would not work in the RMS composition at the investigated conditions because the

Si/(K+Na) of these amphiboles are not sufficiently low (i.e., not less than the Si/(K+Na) = 3.4 of the RMS material). However, fractionation of ferro-edenite or kataphorite amphibole at 20 kb, 4 and 8% added H_2O, respectively, could potentially fulfill Giret et al.'s (1980) proposal, as could biotite fractionation across a range of pressures.

Melt compositions and lithologic equivalents

Glass compositions and the RM02-17 starting material are plotted on a total alkali-silica diagram in Figure 2-14. Apart from the two 20 kb samples 5-4 and 5-8 and the 18 kb sample 14-2, the biotite-absent samples define a trend culminating in the ne-trachyte composition of the 15 kb sample 11-0. Biotite-bearing samples follow a less well-defined trend of higher silica:alkalis than the biotite-absent samples that continues to the high-silica trachytic composition of sample 5-2. The high-Al, high alkali sample 14-2 is amphibole-bearing but does not fall on either trend. As in Figure 2-13, the biotite-absent, amphibole-bearing 20 kb samples 5-8 and 5-4 plot with the biotite-bearing run products probably, as discussed above, due to their high Si/(K+Na) amphiboles. Glass from sample 5-8 is a peraluminous (A.S.I. = 1.35) Q-trachyte and sample 5-4 contains the most differentiated melt, a weakly peraluminous (A.S.I. = 1.08) rhyolite.

Temperature-composition relations

Glass SiO_2 generally decreases as temperature increases and with increased H_2O at a fixed temperature (Figure 2-15), which inversely correlates with increasing melt fraction as glass compositions approach that of the starting material (see Table 2-3). Glass SiO_2 increases significantly with increasing pressure at constant T from 15 to 20 kb. Glass SiO_2 also anticorrelates with melt fraction , as the 20 kb samples contain the least melt of any experiments (see samples 5-2 and 5-4 in Table 3). Unlike other experiments shown in Table 2-13, the 20 kb glasses do not show increasing SiO_2 with increased H_2O; sample 5-4 (20 kb, 4% H_2O) contains a

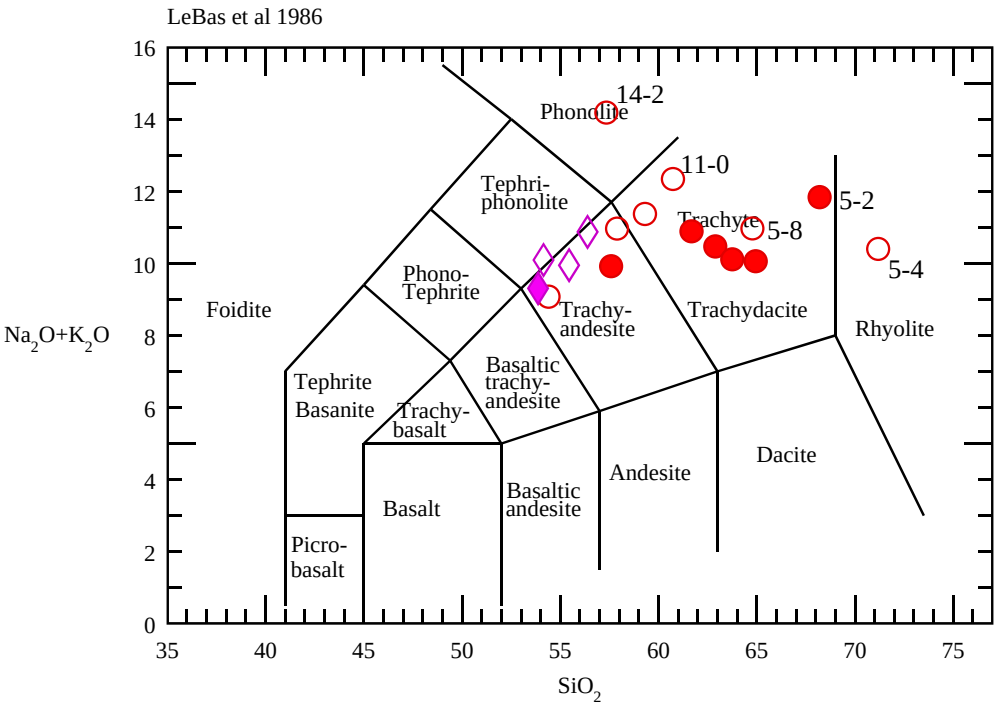

Figure 2-14. Total alkali-silica classification diagram for experimental glasses. Diagram after LeBas et al. (1986). Compositions are normalized to a volatile-free 100%. The symbols are: RM02-17 starting material – filled diamond; biotite-bearing samples – filled circles; biotite-absent, amphibole-bearing samples – open circles; biotite- and amphibole-absent samples – open diamonds. Glasses from selected samples, mentioned in the text, are labeled, including the 20 kb samples 5-2, 5-4, and 5-8, the 15 kb sample 11-0, and the 18 kb sample 14-2.

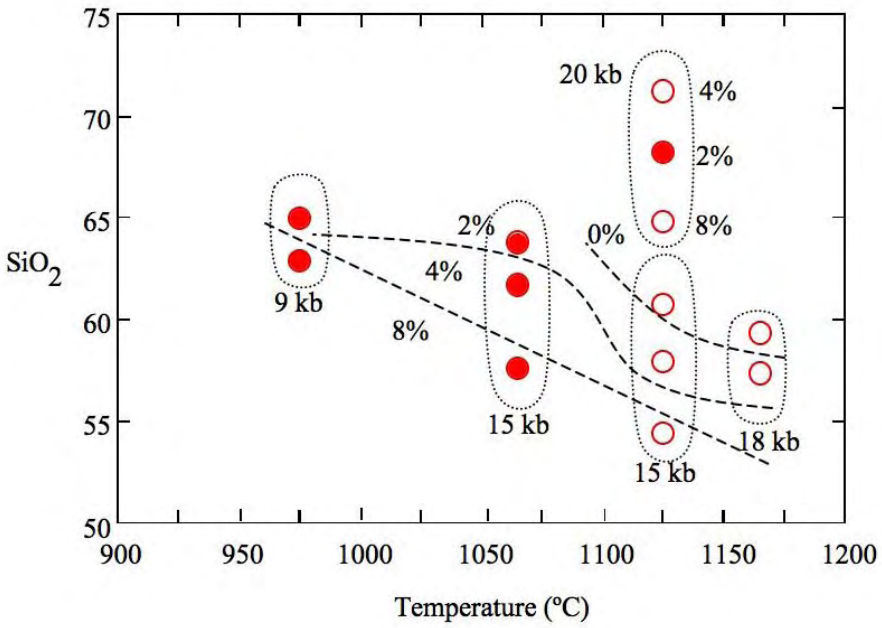

Figure 2-15. SiO_2 contents of glasses from experimental run products. Compositions are normalized to a volatile-free 100%. Filled circles represent samples containing biotite ± amphibole while open circles contain amphibole and no biotite. Pressures are indicated for circled groups from each experiment. Contours for added H_2O are drawn for the <20 kb experiments, and H_2O is indicated for each 20 kb return.

higher melt fraction than 5-2 (2% H_2O) (Table 2-3), but contains >70% SiO_2 while 5-2 contains ~68% SiO_2. This difference is attributable to the suppression of the crystallization of Si-rich alkali feldspar with increasing H_2O content between 5-2 and 5-4 (Figure 2-7). Glass from 5-2 has the composition of Q-normative trachyte (Table 2-9) while glass from 5-4 is rhyolitic (Table 2-10).

Figure 2-16 shows trends of K_2O, CaO, and TiO_2 variation with SiO_2 for experimental glasses and the RM02-17 starting material. Biotite-bearing glasses show a good correlation in SiO_2-K_2O space. The 20 kb and one 18 kb (14-2) glasses are all depleted in CaO as a result of the crystallization of the Ca-rich assemblages including calcic amphibole + apatite ± garnet ± clinopyroxene. Both biotite-bearing and biotite-absent trends show inverse correlations between SiO_2 and CaO, and the 20 kb samples also have among the lowest melt fractions. The SiO_2-TiO_2 trend is of a general inverse correlation with some scatter due to varying amount of ilmenite and biotite crystallization.

Apatite saturation

The solubility of P_2O_5 in a silicate melt increases with temperature, decreases with SiO_2 content (Watson 1979 and 1980; Harrison and Watson, 1984), and decreases with F content (Tollari et al., 2008). Perhaps counterintuitively, Tollari et al. (2006) also found phosphate solubility to increase with increasing CaO. Figure 2-17 shows SiO_2, CaO, and P_2O_5 contents of experimental glasses relative to apatite saturation. What may appear at first to be the suppression of apatite crystallization by high CaO (2-16a) or low SiO_2 (2-16b) is attributable to melting relations; the apatite-absent samples shown are all liquidus runs: runs 11-4 and 13-8 contained only trace ilmenite (Table 2-2) and run 14-8 contained trace orthopyroxene, clinopyroxene, and rutile, all three of which were found in one corner of the capsule and may represent

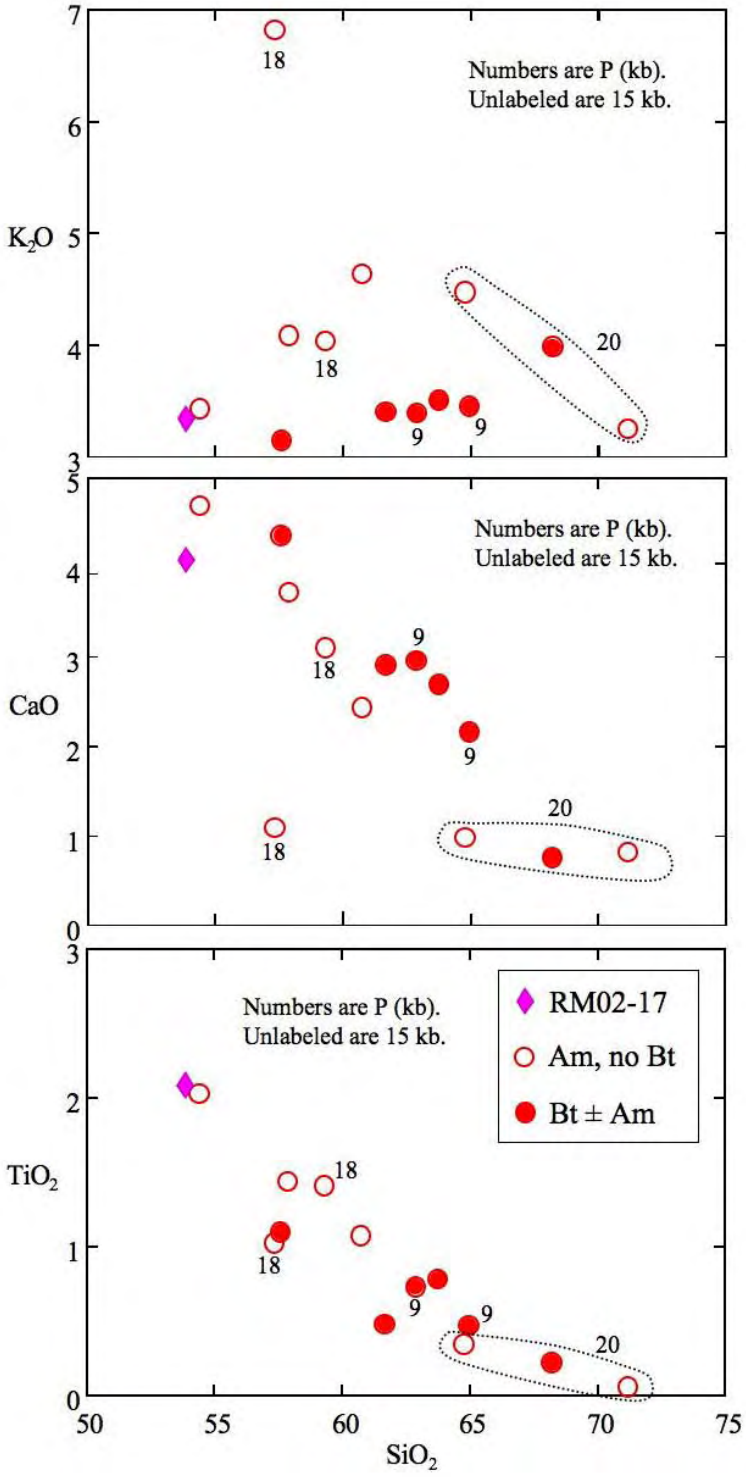

Figure 2-16. K_2O-, CaO-, and TiO_2-SiO_2 diagrams for experimental glasses. Compositions are normalized to a volatile-free 100%.

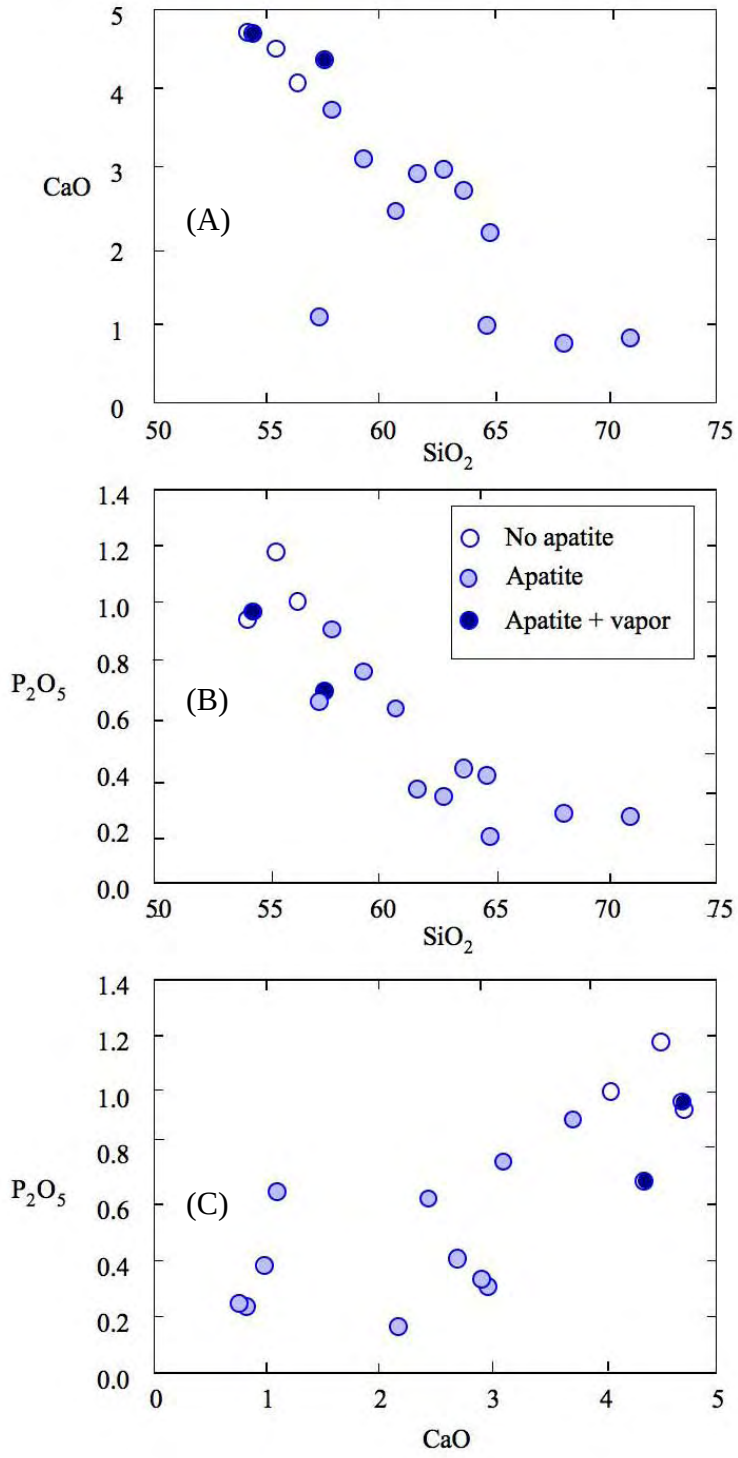

Figure 2-17. The variance of apatite and vapor saturation with CaO, P_2O_5, and SiO_2 in the experimental glass (melt). The apatite-absent experiments represent liquidus conditions.

disequilibrium. In the two samples containing apatite in melt above 3.7 wt.% CaO, the apatite coexists with a vapor phase (runs 11-8 and 8-8). At 15 kb, 1125°, apatite is absent in the 11-4 experiment and reappears in the 11-8 experiment concurrent with vapor exsolution. This suggests that either (1) the decrease of X_{H2O} in the melt by vapor exsolution lowers the solubility of apatite, (2) the increase of X_F in the melt by the absence of water lowers the solubility of the melt, as qualitatively described by Tollari et al. (2008), or (3) the solubility of apatite is decreased in the presence of a free fluid phase.

Element distribution between phases

Partitioning of F between mineral phases is shown in Figure 2-18. For coexisting amphibole and biotite, biotite F > amphibole F except for the Na-rich biotite-ferro-pargasite pair in experiment 5-2, which has a K_d slightly > 1. Apatite is strongly enriched in F relative to amphibole at 1085°, 8 kb (12-4) and biotite at 1165°, 18 kb. Fluorine contents in glass were consistently below the detection limit of ~0.4 wt.%; because apatite F varies from 1.6-2.4 wt.% this suggests minimum $K_d^{ap\text{-}gl}$ for F of 4-6, though the data are insufficient to substantiate this. This is higher than the published value of ~3.4 (Mathez and Webster, 2005).

Figure 2-19 shows partitioning of Cl between mineral and glass phases. In all experiments with sufficient data to evaluate glass-mineral partitioning, both amphibole and biotite are depleted in Cl relative to coexisting glass. In mafic compositions, $K_d^{ap\text{-}gl}$ has been measured at unity or slightly <1 (Mathez and Webster, 2005), but I could find no measured values for alkaline intermediate rocks. As shown in Figure 2-19A, the $K_d^{ap\text{-}gl}$ is 2.4 at 1125°, 15 kb, 2% H_2O (run 11-2) and 0.9 at 1165°, 18 kb, 2% H_2O (14-2). The glass composition in 11-0 is ne-normative trachyte and the glass in 14-2 is ne-normative phonolite (Figure 2-14).

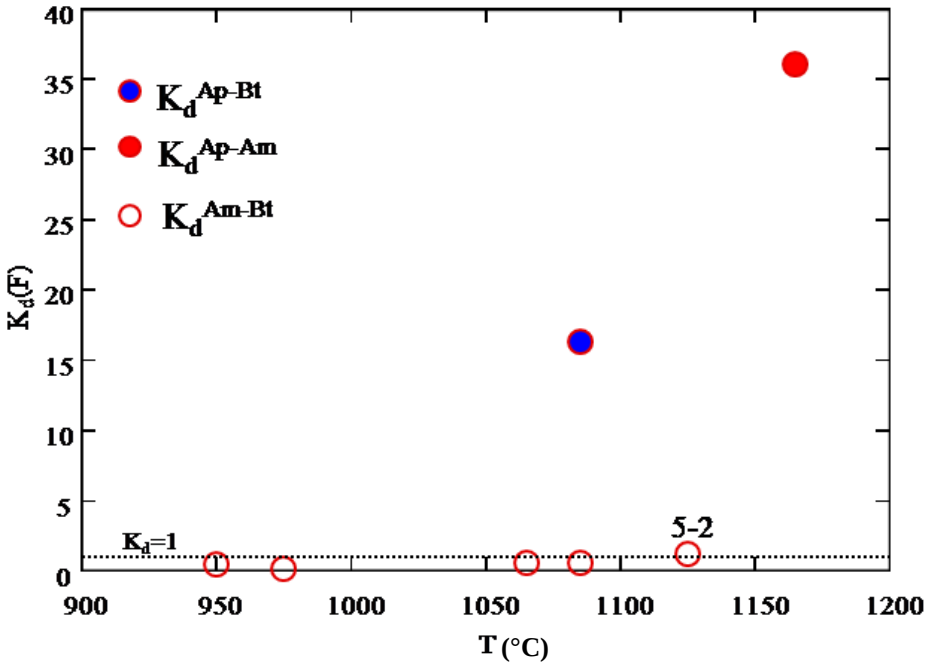

Figure 2-18. F partitioning between amphibole, biotite, and apatite. K_d = concentration in phase A/concentration in phase B. The K_d for amphibole-biotite in sample 5-2 is slightly >1.

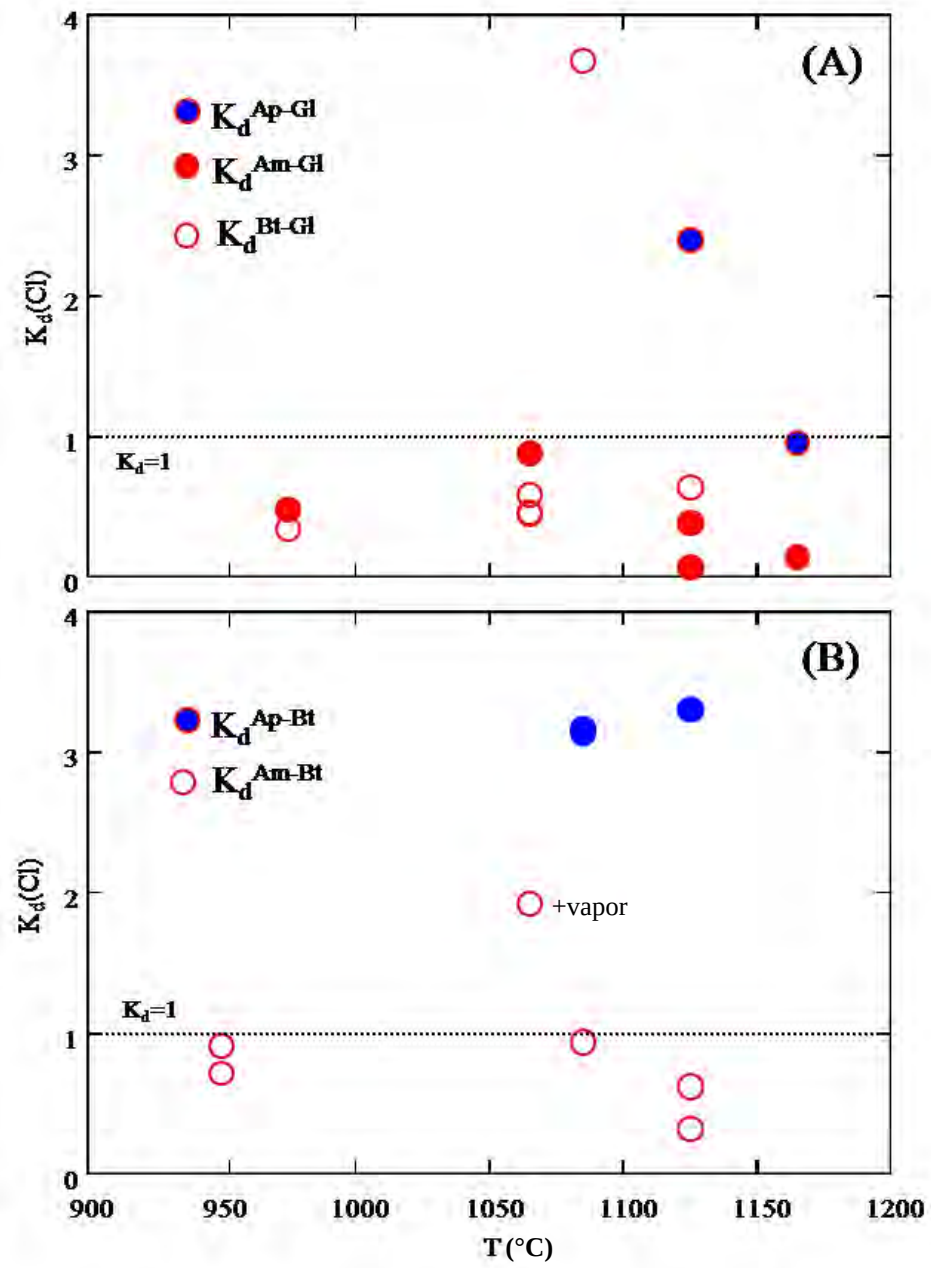

Figure 2-19. Cl partitioning between amphibole, biotite, apatite, and glass. (A): Mineral-melt partition coefficients for Cl plotted against temperature. **(B):** Mineral-mineral partition coefficients for Cl plotted against temperature. The 1065° sample from run 8-8 is the only plotted sample that contained an exsolved vapor phase and the only sample for which the Cl K_d^{Am-Bt} is >1.

Figure 2-19B shows mineral-mineral Cl partitioning. Biotite is enriched in Cl relative to coexisting amphibole except in the case of experiment 8-8 (1065 °, 15 kb), in which they coexist with an evolved vapor phase and amphibole contains more Cl than biotite. The composition of the biotite and amphibole (ferro-pargasite) are unremarkable in that experiment, so this suggests that X_{H2O} in the melt may affect Cl partitioning between biotite and amphibole; the mechanism for this is unclear, as the partitioning between two solid phases should be unaffected by melt composition (Zhu and Sverjensky, 1991).

Figure 2-20A shows TiO_2 partitioning. In all cases, both amphibole and biotite are enriched in TiO_2 relative to glass. The highest mineral-glass K_d for TiO_2 is 21 for the biotite-Q-trachyte pair in the 20 kb experiment 5-2. In all experiments with coexisting biotite and amphibole, biotite is enriched in TiO_2 relative to the amphibole ($K_d^{am\text{-}bt}$ <1) regardless of the type of amphibole. The $K_d^{am\text{-}bt}$ for TiO_2 is at its lowest (< 0.2) at 20. Figure 2-20B shows Mg/Fe partitioning for the same phases. Again, the highest mineral-glass K_d for Mg/Fe is for the biotite-Q-trachyte pair in the 20 kb experiment 5-2. Both biotite and amphibole have higher Mg/Fe than the glass in all cases except for the magnesio-taramite-ne-phonolite pair in experiment 14-2 (1165°, 18 kb). The $K_d^{am\text{-}bt}$ for Mg/Fe. is <1 at most conditions, though it is 1.1 and 1.2 at 950°, 10 kb with 2 and 4% added H_2O, respectively.

Discussion

Comparison to Irving and Green (2008) results

Despite the compositional differences between the RMS and Irving and Green's (2008) ne-mugearite compositions (Table 2-1b) the experimentally-derived phase diagrams are similar where conditions overlap. Figure 2-21 shows the portion of the 2% added H_2O phase diagram from Irving and Green (2008, their Figure 1) and the 2% added H_2O diagram for RM02-17 first

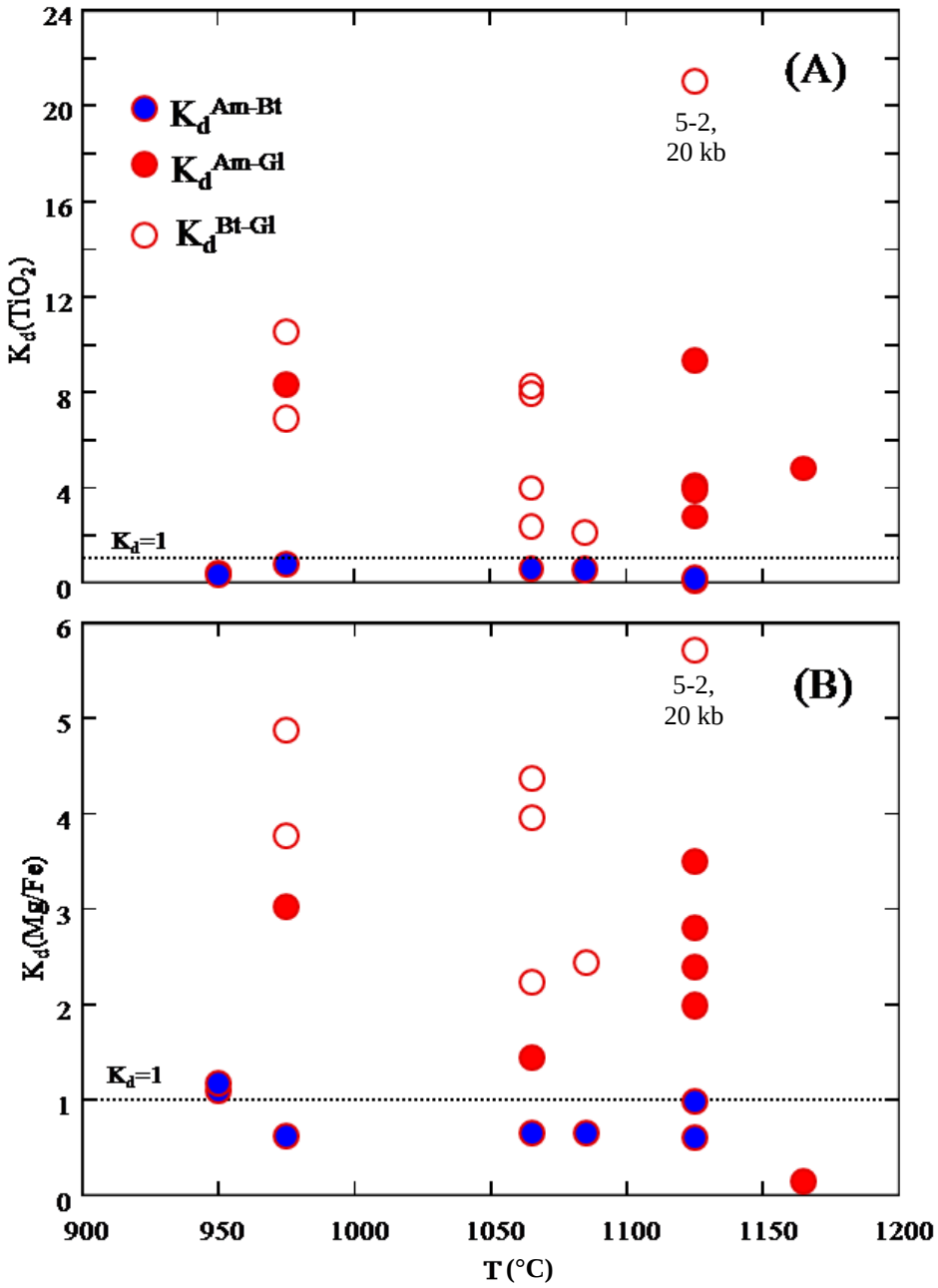

Figure 2-20. Partitioning of Mg/Fe and TiO_2 between amphibole, biotite, and glass. (A): Partition coefficients for TiO_2 plotted against temperature. In all cases, biotite and amphibole are enriched in TiO_2 relative to melt (glass), and biotite is enriched relative to amphibole. **(B):** Partition coefficients for Mg/Fe plotted against temperature. Of the biotite, the Na-rich biotite from experiment 5-2 is the most enriched in both TiO_2 and Mg/Fe relative to glass.

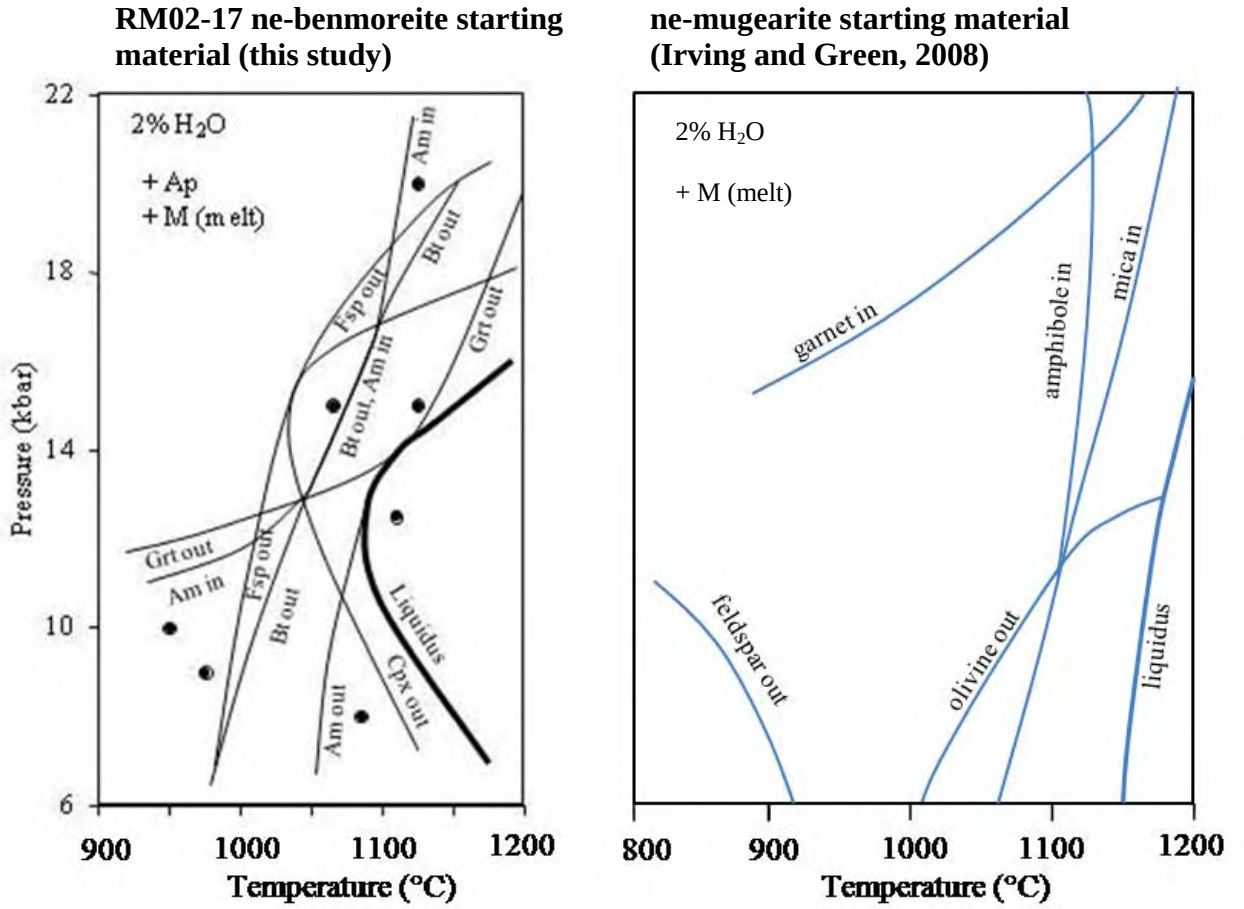

Figure 2-21. Comparison of phase relations of ne-benmoreite and ne-mugearite + 2% H_2O. The phase relations for the benmoreite RM02-17 starting material are from this study (left) and the ne-mugearite phase relations are from from Irving and Green's (2008) Figure 2. The diagram from Irving and Green (2008) is shown to a 100° C lower temperature to demonstrate the feldspar phase relations. The compositions of both materials are shown in Table 2-1b. RM02-17 contains more initial H_2O than the ne-mugearite. The reaction lines for RM02-17 are based on fewer data than those for the ne-mugearite, and most RM02-17 reaction lines could be shifted to be relatively close to those of Irving and Green (2008). However, compared to the Irving and Green (2008) phase diagram, the RM02-17 garnet stability field occurs at lower P, especially at higher T; feldspar occurs at higher P (20 kb) and T conditions in RM02-17 (where it is Na-rich); clinopyroxene occurs in lieu of olivine in RM02-17; the liquidus is at lower T, especially between ~10-15 kb.

shown in Figure 2-5 of this paper. These are the only conditions where the two studies overlap exactly. The Irving and Green (2008) dataset is much more extensive and their reaction lines in Figure 2-21 are better constrained than those from this study. The phase relations are similar despite the ne-mugearite being more significantly more mafic (e.g., 7.23 wt.% MgO vs. 3.08 wt.% for RMS02-17). The data from this study would allow for the amphibole and biotite reaction lines to almost overlap with those for the ne-mugearite, but the garnet field from this study extends to lower pressures at high temperature. Also, feldspar in this study reappears at high pressure (20 kb) where it is missing in the ne-mugearite composition, and perhaps most significantly, olivine occurs below ~12 kb in the ne-mugearite while clinopyroxene is present in lieu of olivine and at higher pressures in the RM02-17 composition.

No olivine was encountered in my experiments at any conditions, but Irving and Green (2008) found that olivine was only stable within 25-100° of the liquidus and was replaced at lower temperatures by clinopyroxene or by mica or amphibole ± vapor, depending on the conditions. At lower pressures of 3-8 kb, olivine is stable within 150° of the liquidus (Irving and Green, 2008). Olivine occurs as a sparse phenocryst in the RMS margins, indicating that olivine is stable near the liquidus in the RMS magma at pressures lower than are investigated here.

Irving and Green (2008) concluded that it was possible to reach the ne-mugearite composition by differentiation from a ne-basanite parent at a pressure of 14 kb with a fractionating assemblage of olivine, clinopyroxene, amphibole, mica, apatite, and Fe-Ti oxide. The RMS experiment 11-2 (15 kb and 1125° C, and 2% H_2O) containing 95 modal% melt with 2.5% pargasitic amphibole, 1.8% apatite, and 0.5% garnet is the closest match to the conditions Irving and Green (2008) determined for the likely conditions of fractionation (14 kb, 1090° C, 3.5% added H_2O). The low proportion of garnet in my experiment indicates that it would

probably disappear before encountering the liquidus, as it does it in their projections (Irving and Green, 2008, their Figure 1). The composition of pargasitic amphibole in experiment 11-2 is similar to their kaersutite (see Table 2-11), though the pargasite in 11-2 contains slightly less SiO_2, more TiO_2, and has a significantly lower *Mg'* of 68.5 than the 79.5 found in the Irving and Green (2008) kaersutite.

The RMS magma cannot be convincingly tied to differentiation from a mantle melt at depths implied for the more mafic ne-mugearite investigated by Irving and Green (2008). However, the possibility is open to near-liquidus or liquidus olivine in the RMS phase relations not found in these experiments.

Proposed TPMP magma trends

None of the experimental results, with the exception of the near-liquidus clinopyroxene at 18 kb, 1165°, 8% H_2O (14-8), supports the fractionation of clinopyroxene + olivine invoked (Carman et al., 1975) to connect the various Big Bend shallow intrusions. Neither do they support feldspar fractionation at ≥8 kb (~24 km depth). This suggests that if feldspar or clinopyroxene + olivine-controlled fractionation at Big Bend, RMS must have fractionated at lower pressure than investigated here, or under different fluid conditions.

The possibility is open as to the fractionation of near-liquidus kataphoritic (8% added H_2O) or pargasitic amphibole (up to 4% H_2O) across of range of investigated conditions. Apatite and ilmenite are found near the liquidus at most conditions of this study. At 1125° C, 15 kb, ilmenite is the sole liquidus phase at 4% H_2O and only apatite + vapor are present at 8% H_2O (run 11).

The kaersutite gabbro-olivine gabbro-quartz microsyenite complex at Slickrock Mountain lies several kilometers north of the RM intrusion. In terms of the Si, Al, Ti, and Ca contents, the

Table 2-11. Kaersutite compositions from Trans-Pecos alkaline rocks and from Irving and Green (2008) experiments.

source	1	2	3
type	megacryst	margin	experiment
location	Slickrock Mtn.	Diablo Plateau	experiment
sample	M2,1c	AS-10	from 2102
P (kb)	-		14
T (°C)	-		1090
H2O%	-		3.5
SiO_2	39.4	39.8	43.4
Al_2O_3	14.4	12.6	12.1
TiO_2	5.3	6.19	3.3
FeO	11.4	12.2	8.6
MgO	11.4	12.1	15.2
MnO	0.1	0.39	
CaO	9.3	10.6	9.9
Na_2O	2.3	2.67	2.9
K_20	1.0	1.6	1.5
F		0.08	
Cl			
Total	94.6	98.18	96.9
Mg'	64.1	63.9	75.9

Sources

1 = Hill and Barnes (1987)

2 = Barker and Hodge (1977)

3 = Irving and Green (2008)

composition of the pargasite from experiment 11-2 is quite similar to that of the megacrysts in the Slickrock kaersutite gabbro (Table 2-5 and Table 2-11) as are a number of amphiboles from 15 kb runs (11-0, 8-0), 9 and 10 kb runs (1-2, 2-4), and one from 18 kb (14-2). Other amphiboles with approximately the same Si contents tend towards higher Al (5-2, 14-0, 12-8, 8-8). Most, however, have significantly lower *Mg'* than the ~64 of the Slickrock Mountain samples. The closest sample is the pargasite from 11-2, with a *Mg'* of 68.5. It is problematic to use Mg/Fe to dismiss a synthetic phase as analogous to one in a natural rock because of the effects of Fe loss during experimentation. This is particularly true if the experimental phase has a higher Mg/Fe than the natural one. As to the lower Mg/Fe of most experimental amphiboles, it raises the possibility of the RMS and the Slickrock magmas having similar parents that underwent similar differentiation, but which were derived at different degrees of fractionation. This also might explain the lack of olivine in the RMS experiments. If RMS and the Slickrock magmas had similar parental magmas and underwent similar differentiation, the lower Mg/Fe of amphibole and the lack of olivine in RMS indicate Slickrock was the less differentiated of the two.

The experimental melt compositions preclude simple ties to the Slickrock quartz syenite. The experimental melts found here that are silica-saturated or approach silica-saturation have $Na_2O/K_2O > 1$, while the Slickrock quartz syenite has $Na_2O/K_2O < 1$ (Hill and Brown, 1987). The experimental melts also have higher Al_2O_3 than the 15-16 wt.% of the quartz syenites. Any possible relationship requires further crystal fractionation or crystal accumulation in the Slicrock quartz syenite.

Melt compositions

Most of the silica-undersaturated melt compositions from experiments are mildly ne-normative trachytes. There are many analogs in the TPMP, particularly near western Big Bend

National Park and the town of Terlingua, Texas, near RMS (Barker, 1987; Carman et al., 1975; Cameron et al., 1986). These compositions can probably be reached by a number of avenues that involve deep or shallow fractionation, assimilation, and magma mixing.

More interesting are the silica-saturated melts produced from the RMS ne-normative starting compositions. This study finds that Q-normative compositions can be reached by high-pressure fractionation of mildly ne-normative compositions, and that these melts are a mildly peralkaline Q-trachyte (5-2), metaluminous Q-trachytes (5-8, 8-2, 1-8, 1-2) and weakly peraluminous rhyolite (5-8). Quartz trachytes and quartz syenites, both peralkaline and metaluminous, are among the most common rocks encountered in the TPMP (Barker, 1987; White et al., 2006). Metaluminous rhyolites occur with quartz trachytes at the Levya Volcano in Big Bend Ranch State Park (White et al., 2001). A number of the Q-normative rocks have isotopic ratios compatible with petrogeneses by fractional crystallization without significant crustal input (Cameron et al., 1986).

Having shown this is possible, the more important question is: are there natural analogs in which these processes operate? It has not been demonstrated that alkaline felsic melts are generated at depths of 60 km (~20 kb equivalent) and increasing buoyancy with differentiation might preclude their prolonged residency at depth. There is a good case that some intermediate to felsic alkaline magmas could form by fractionation at 14-18 kb (Irving and Green, 2008), and if so, it is possible that further fractionation at those depths could derive melts such as the ones found in run 8-2 (Q-trachyte), or the ne-trachytes from the 11-0, 11-2, and 11-4 experiments. The 9 kb runs that yield Q-trachyte compositions in runs 1-2 and 1-8 represent lower crustal depths. They may be better analogs for partial fusion of previously emplaced ne-normative rocks; heat

sources in the form of intruding basaltic magma would be plentiful in the TPMP or other provinces.

In short, while this study raises interesting possibilities with regard to generating a variety of melt compositions by high-pressure fractionation, the simpler explanation for TPMP rocks is that posed by Barker (1977) and others – that both Q-normative and ne-normative mantle melts led to distinct magma series. This case is bolstered by the presence of Q-normative basalts within the TPMP, both in the western metaluminous belt and, more rarely, in the eastern alkalic belt (Barker, 1977; 1987).

Conclusions

(1) Olivine is not found in run products from any of these experiments. RM02-17 is too evolved to crystallize olivine at high pressure (≥8 kb) and crystallizes clinopyroxene, amphibole, or biotite instead. It is unlikely that RMS was in equilibrium with a lower crustal or mantle assemblage during fractionation.

(2) The very high Ti in experimental biotites results primarily from Ti-Tschermak's substitution ($^{VI}Ti^{4+} + 2^{IV}Al^{3+} = 2^{IV}Si^{4+} + {}^{VI}[Fe,Mg]^{2+}$), while the Ti-oxy substitution ($^{VI}Ti^{4+} + 2O^{2-} = {}^{VI}(Fe,Mg)^{2+} + 2[OH]^{-}$) probably plays a lesser role.

(3) These experiments yield amphiboles similar to those found in the margins of TPMP intrusions and the early rocks of intrusive suites. This provides a possible link to less-differentiated RMS-type magmas.

(4) The composition of the RMS magma is saturated with apatite up to high temperatures and pressures, and it is likely that apatite played a role in its fractionation. Other likely fractionating phases prior to magma emplacement are Ti-biotite and (*sensu latu*)

pargasitic or edenitic amphibole, and/or with clinopyroxene, depending on H_2O saturation.

(5) It is possible for silica-saturation to be achieved from undersaturated compositions with biotite rather than amphibole fractionation as the primary agent. In the melts generated at 20 kb in this study, a combination of Na-rich biotite and Na-rich ferro-edenitc or kataphoritic amphibole fractionation generated the most felsic and most silica-saturated melts.

CHAPTER 3

BONE SPRINGS SILL, TRANS-PECOS MAGMATIC PROVINCE, PART 1: DIFFERENTIATION OF A MONZOGABBRO-MONZOSYENITE SILL

Abstract

Bone Springs Sill (BSS) in northern Big Bend National Park crystallized from tephritic magma, a composition which is thought to represent the parent magma to many rocks in the Eastern Alkalic Belt of the Trans-Pecos magmatic province (TPMP). The intruding magma represented by BSS margin compositions shows little variation and trace element and fractional crystallization models do not indicate contamination by country rock, signifying that it is a good example of closed system fractional crystallization. The magma differentiated to a monzosyenitic residual liquid, some of which segregated into sheets and other small bodies within the sill. Though differentiation occurred on a relatively small scale in BSS, similar bimodal differentiates occur in the TPMP at the scale of small sills up to large volcanic complexes. The processes documented in BSS have ramifications for the petrogenesis of felsic alkaline rocks in the TPMP and elsewhere.

Bones Springs Sill differentiated at low pressure from hydrous tephritic magma to a bimodal monzogabbro-monzosyenite suite. Monzosyenite liquid was generated by ~50% crystallization of subequal amounts of clinopyroxene + plagioclase, lesser Fe-Ti oxide + olivine, and minor biotite + apatite + nepheline. Most of the monzosyenite liquid crystallized in the

interstices of the monzogabbro, but, after rupturing of the crystalline framework probably coincident with vapor exsolution, some liquid segregated into discrete monzosyenite bodies in the upper third of the sill. The most felsic monzosyenites in BSS were generated by an additional ~8% fractionation of alkali feldspar, amphibole, and nepheline (or analcime) with minor apatite and titanohematite.

Some analcime in BSS replaces early-crystallizing nepheline. Late-stage interstitial analcime, common in Trans-Pecos alkaline rocks, may have formed by late, wet magmatic crystallization, or it may have replaced residual crystallization of nepheline + alkali feldspar.

Purpose of study

This study characterizes the geochemistry, mineralogy, and field relations of the Bone Springs Sill (BSS) in Trans-Pecos Magmatic Province (TPMP). These data are used in conjunction with mineral-liquid equilibria and differentiation models to assess the intrusion's crystallization history. Though the sill is bimodal, the primary hypothesis tested is that the felsic portions are products of post-intrusion differentiation of the BSS magma. This is tested through fractional crystallization models and mineral equilibria – particularly olivine-liquid and clinopyroxene-liquid Mg/Fe partitioning. A second hypothesis is that the BSS intrusion contains all of the differentiation products and the compositions can thus be re-integrated to match the composition of the intruding magma, i.e., that the sill did not feed any volcanism of the resultant felsic magma.

Other than a general description and geochemical analyses of the mafic rocks in BSS published by Carmen et al. (1975) and Carman (1994), the sill has not been studied. The particular significance of this work is that the BSS magma represents a plausible parent magma to many of the alkaline rocks in the TPMP (Potter, 1996), including other less mafic

differentiated sills, and that the bimodal nature of BSS is mirrored in the TPMP not only in other sills but up to the scale of large volcanic complexes (e.g., Barker, 1987). Thus, processes of differentiation in BSS are relevant to many of the TPMP rocks, as well as on other alkaline rocks worldwide (for a review, see Carman, 1994).

Geologic setting

The Trans-Pecos Magmatic Province (TPMP) is an alkaline volcanic and intrusive belt delineated to the south and west by the Rio Grande River, to the east by the Pecos River, and to the north by a line 12 km north of the Texas-New Mexico border (Barker, 1977). (See Figure 3-1 for location map.) The borders of the TPMP are arbitrary to the south and southeast, as alkaline rocks continue into Mexico for at least 200 km (Barker, 1977). To the west, partially contemporaneous igneous rocks grade to a calc-alkaline composition, including the Sierra Madre Occidental continental arc and beyond to the western coast of Mexico (James and Henry, 1991) . The eastern border of the TPMP at the Pecos River marks the easternmost extent of exposed igneous rocks. Barker (1974) recognized a belt of broadly contemporaneous alkaline rocks stretching along the eastern border of the Cordillera from Canada into Mexico, of which the TPMP, at least spatially if not genetically, is a part.

The timing of magmatism in the TPMP spans from 48 to 17 Ma (Henry and McDowell, 1986). Despite its similarities to intraplate, rift-related magmatic provinces like that of Kenya, geophysical surveys have discerned no gravity or magnetic anomalies indicative of continental rifting (Barker, 1977 and 1987). Rather, studies such as Henry and others (1991) and James and Henry (1991) on the temporal relation of stress regimes to magma compositions indicate that magmatism in the TPMP spans three tectonic regimes. The first was a compressive regime, interpreted as related to eastward subduction of the Farallon plate below North America (48-32

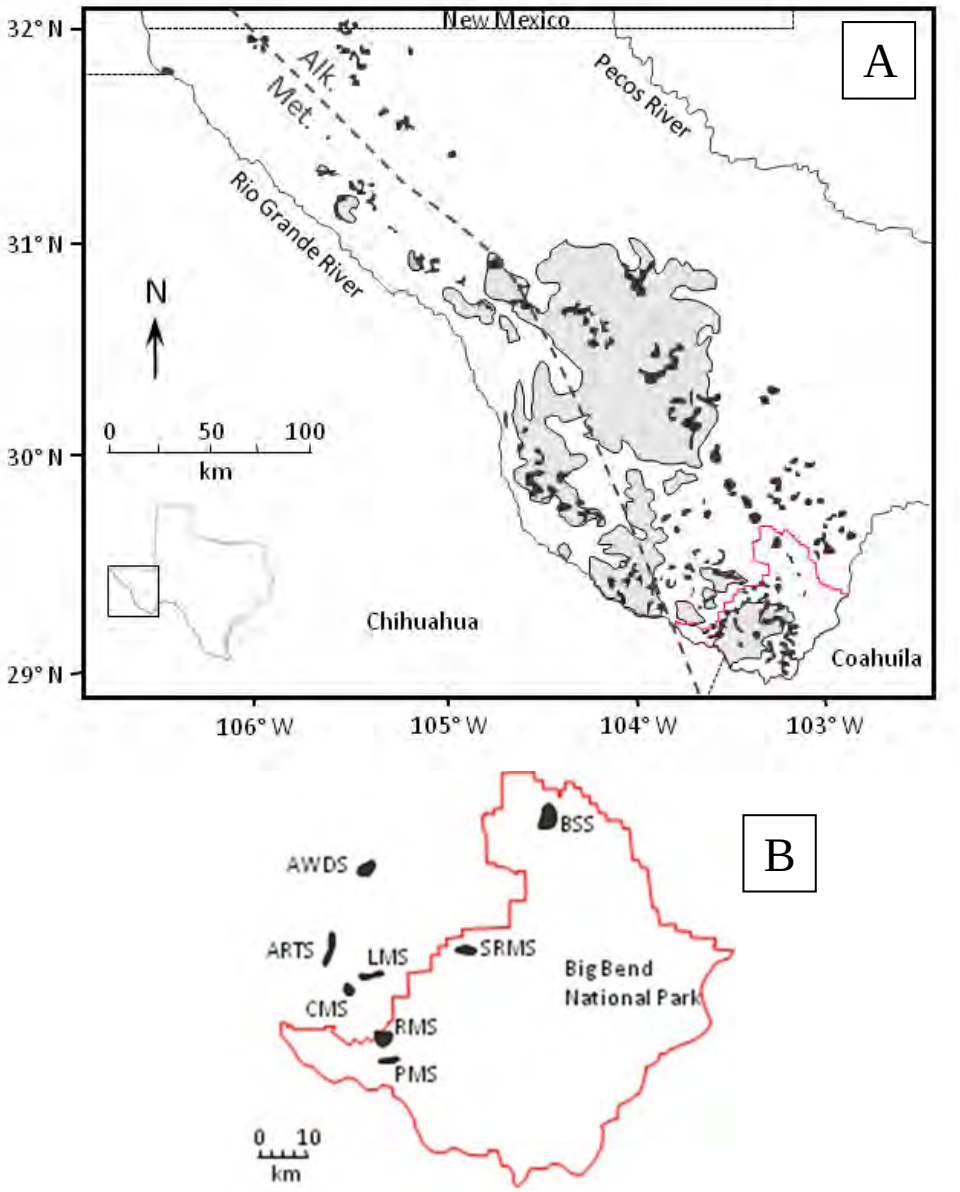

Figure 3-1. Tertiary igneous rocks of the Trans-Pecos Magmatic Province. (A): Distribution of Cenozoic volcanic (gray) and intrusive (black) rocks with locations adapted from Barker (1977) and White (2006); the green bold dashed line separates the western dominantly metaluminous subalkaline rocks from the Eastern Alkalic Belt (location after Barker [1977]); the boundary of Big Bend National Park is shown in red. **(B):** Inset of Big Bend National Park and selected early extensional internally differentiated sills: ARTS = Al Reed Trail Sill, AWDS = Adobe Walls Draw Sill, BSS = Bone Springs Sill (BSS), CMS = Cigar Mountain sill, LMS = Leon Mountain Sill, PMS = Peña Mountain Sill, RMS = Rattlesnake Mountain Sill, and SRMS = Slickrock Mountain Sill. Locations after Carman et al. (1975).

Ma), during which alkaline magmatism in the TPMP was accompanied to the west by the metaluminous Sierra Madre Occidental continental arc. This was followed by an incipient extensional regime absent of normal faulting (31-27 Ma), and, after a hiatus, magmatism related to Basin and Range extension with accompanying normal faults (24-17 Ma). The focus of Chapter 2 of this study, Rattlesnake Mountain Sill (RMS), with an age of 28.6 ± 0.4 Ma (Henry and McDowell, 1986) is the best exposed and studied of about ten syenodiorite to syenogabbro sills found in the Big Bend area (Carman, 1994) which are characteristic of the initial extensional regime. The subject of this chapter, Bone Springs Sill (BSS), is the most mafic of these early extensional sills.

The earlier igneous rocks of the TPMP (48-32 Ma) are differentiation-related suites, with examples of quartz-saturated and nepheline-normative series, ranging from basaltic to rhyolitic and trachytic compositions (James and Henry, 1991; Henry and McDowell, 1986). They occur within a compressional stress regime, as determined by structural measurements of folds, fractures and dike orientations (Henry et al., 1991; James and Henry, 1991), likely related to eastward subduction of the Farallon plate beneath western North America. The TPMP rocks of this period are contemporaneous with arc-related rocks to the west, and share trace element signatures with them, such as relative depletion in Ta and Nb, and high Ba/Nb, Y/Nb and Zr/Nb, which are consistent with an origin in a continental arc (Barker, 1987; James and Henry, 1991). During this period, the gradation of metaluminous rocks in Mexico to predominantly alkaline rocks in Texas is attributed by James and Henry (1991) to increasing W-E distance from the subduction trench, and a likely corresponding reduction in partial melt fractions. This period of magmatism is further divided into an early stage (48-38 Ma) and a main stage (38-32 Ma), characterized by a greater abundance of magmatism in the main stage rather than by any

compositional differences (Henry et al., 1991; James and Henry, 1991). Magmatism was widespread and varied during the main stage, and included the voluminous caldera-related Gomez tuff and Buckshot ignimbrite (Henry and McDowell, 1986), the Paisano Volcano (), the differentiation suites of intrusions in the Diablo Plateau in the north of the province (Barker et al., 1977), and the Pine Canyon Caldera in the Chisos Mountains (White et al., 2006).

The period of magmatism associated with initial extension spans from 31 to 28 Ma (Henry et al., 1991), and is spatially limited to the southern TPMP, in and north of the Big Bend area. On the whole, igneous activity was less voluminous and more alkaline than the previous, compressive stage, and is dominantly bimodal: it is comprised of silicic alkaline caldera-related eruptions and shallow intrusions, and by mafic alkaline sills (Henry et al., 1986; James and Henry, 1991). There are approximately ten alkaline mafic sills emplaced in and around the Big Bend Area during this period, with bulk compositions ranging from tephrite to mugearite (syenogabbro to syenodiorite) (Carman, 1994). Rattlesnake Mountain Sill, on the western border of Big Bend National Park, is the best preserved, exposed, and studied of these occurrences (Carman et al., 1975; Carman, 1994). Trace element signatures of these magmas are distinct from the earlier, compression-related phase, having lower Ba/Nb, Y/Nb and Zr/Nb; however, they partially overlap with later, Basin and Range magmas. This signature suggests a relation to oceanic island basalts (OIB) or continental rifting, rather than to arc magmatism (James and Henry, 1991).

There was little or no magmatism in the TPMP during the period 27-25 Ma (Henry et al., 1986). From 24-17 Ma, normal faulting began, marking the period of true Basin and Range extension (Henry et al., 1991). Magmatism during this period was dominated by alkali basalt

with trace element signatures similar to early extension-related magmatism but with even lower Zr/Nb, suggestive of OIB or continental rift-related magmatism.

The TPMP is divided into the dominantly metaluminous western belt and the eastern alkalic belt (Barker, 1977). The eastern alkalic belt has rocks differentiated to phonolite and nepheline trachyte (Potter, 1996). The likely parental magma to this series is a tephrite of which Bone Springs Sill is probably the best-exposed intrusive example (Potter, 1996).

Samples and analytical method

I conducted fieldwork in the Bone Springs area from 2004 to 2006, including field mapping, sample collection, and the measurement of a stratigraphic section on the southeast side of the intrusion.

Whole rock and trace element analyses were performed at the Washington State University's GeoAnalytical Lab. Ten major and minor elements and eighteen trace elements were determined using a ThermoARL AdvantXP sequential X-Ray fluorescence (XRF) spectrometer. Samples for XRF analysis were ground and fused with a di-lithium tetraborate flux, reground, re-fused, and polished for analysis after the method of Johnson et al. (1999). Twenty-seven trace elements were determined using an Agilent 4500 inductively coupled plasma mass spectrometer (ICP-MS). Samples for ICP-MS analysis were ground and fused with a di-lithium tetraborate flux, and the bead was then reground and dissolved in HF for analysis. Twenty-seven trace elements were determined using an Agilent 4500 inductively coupled plasma mass spectrometer (ICP-MS). Because of the greater accuracy and precision at low abundances, values from ICP-MS are presented for those elements determined by both methods. Trace elements reported from XRF analysis are V, Ni, Cr, Ga, Cu, Zn, and Pb, and the others are from ICP-MS.

Modal analyses were determined for 14 thin sections using transmitted and reflected light petrography. Three hundred points were counted for each thin section on a grid system.

Back-scatter electron images (BSI) and quantitative mineral analyses were collected with the JEOL 8600 Superprobe at the University of Georgia. The instrument was calibrated with standard mineral and synthetic standards and analyses were performed with a 15 nA current and 15 kV accelerating voltage. Most phases were analyzed with a <1 μm spot; when possible, feldspars were analyzed with a 5 μm beam diameter and analcime and thomsonite were analyzed using a rastered beam at x10,000 magnification. Corrections were made after Bence and Albee (1968).

Field relations of Bone Springs Sill

The Bone Springs Sill lies 1 km west of Highway 385 near the northern entrance to Big Bend National Park, Texas. Figure 3-2 is a geologic map of the sill, and Figure 3-3 shows a schematic cross section of BSS, including sample numbers in their approximate stratigraphic locations. Figure 3-4 (A) shows the sill as it appears from the Highway. Its aerial exposure is approximately 4.5 km^2 but scant outcrops extend its E-W length by as much as 1 km and its maximum possible length and width could define a >10 km^2 intusion. It is intruded into the limey sandstones and shales of the Cretaceous Aguja Formation. Several normal faults cut the sill and bring the down-dip portion to the surface, extending the aerial exposure. Sedimentary beds east of the sill generally dip ~20° to the southwest but beds steepen at the contact to 40-60°S. The lower intrusive contact is largely concordant to these beds but this relationship is locally obscured by faulting. Sedimentary beds on top of the sill are more flat-lying. Accurate measurement of the sill's thickness is complicated by normal faulting and the lack of marker units within the sill – aside from broad horizontal or sub-horizontal zones within the sill

Figure 3-2 (next page). Geologic map of Bone Springs Sill.

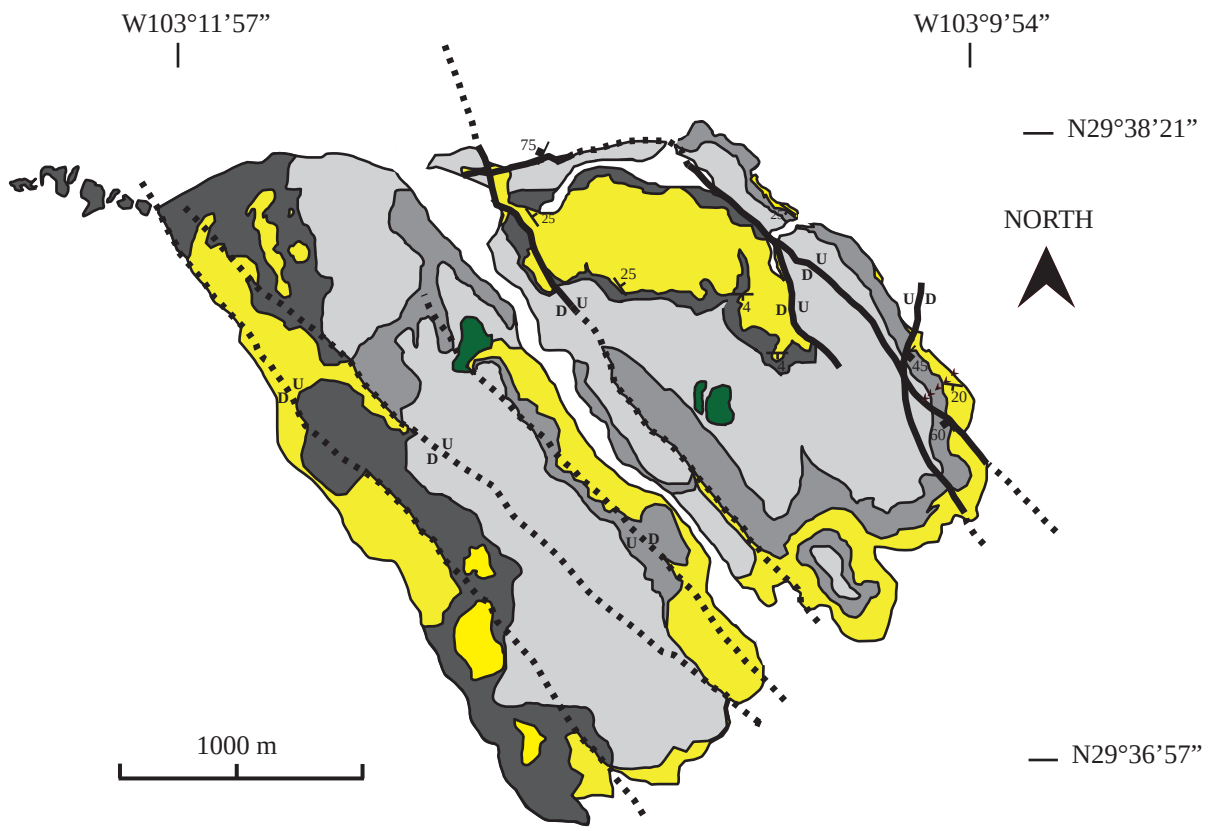

	Qal	*Recent alluvium: unconsolidated stream and flood deposits*
	Tte	*Tertiary tephrite: gray to gray-blue fine-grained analcime tephrite; preserved in local erosional lows*
	UBZ	*Upper border zone of Bone Springs sill: fine-grained, gray to black analcime micromonzogabbro or tephrite; pyroxene phenocrysts, analcime-filled miarolitic cavities, locally vesicular with calcite-filled ring structures*
	CZ	*Central zone of Bone Springs sill: medium-grained gray analcime monzogabbro that hosts segregations of locally pegmatitic gray to tan analcime monzosyenite*
	LBZ	*Lower border zone of Bone Springs sill: fine- to medium-grained gray to black analcime monzogabbro*
	Kag	*Aguja formation: Yellowish-gray to brown, medium-grained limey sandstone with interbedded brown and maroon clay- and siltstones*

45 Strike and dip of fault plane

20 Strike and dip of bedding or contact

U / D Fault trace with upthrown and downdropped sides indicated, dashed where inferred

Measured section

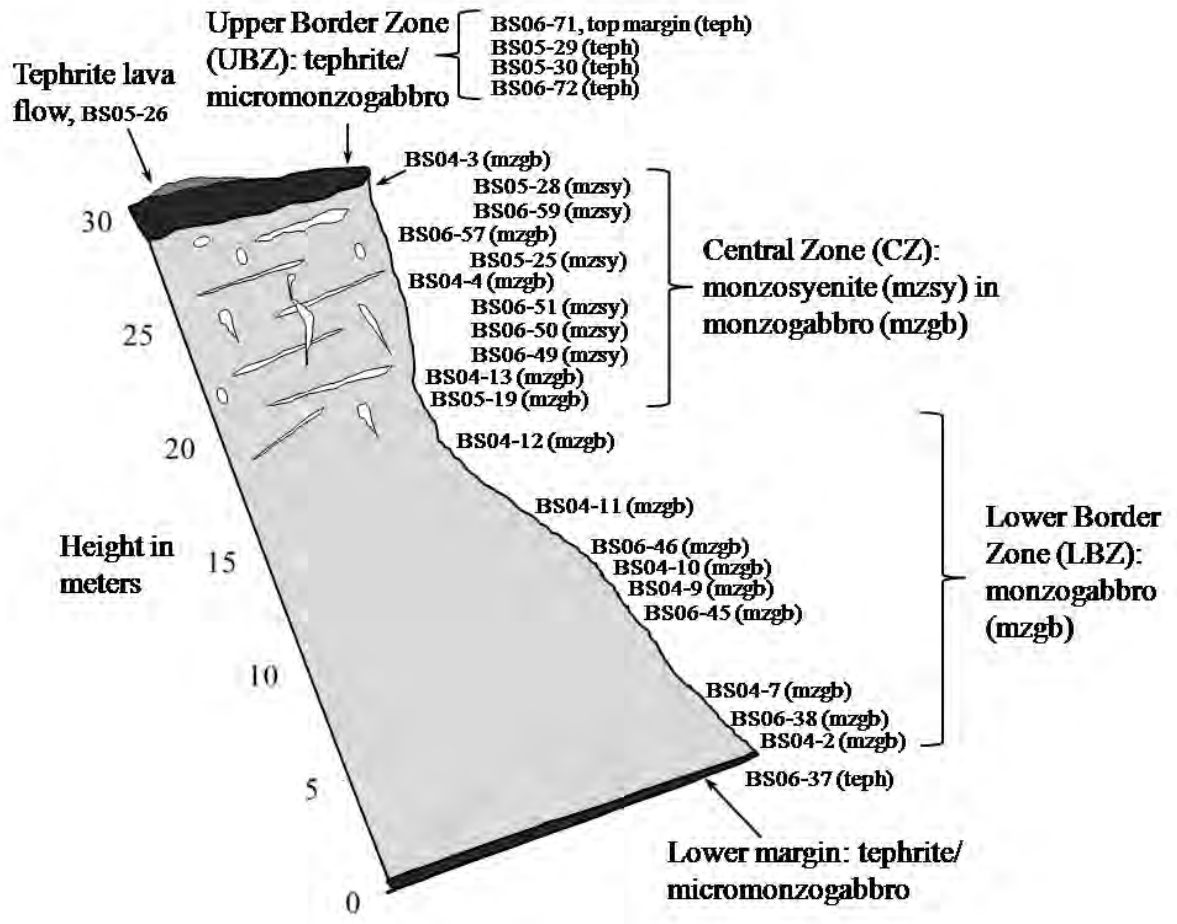

Figure 3-3. Schematic cross section of eastern Bone Springs Sill. All sample numbers are shown at their approximate stratigraphic height. Not all samples were taken from the measured section, so placements are not rigorously precise. Structural complications are ignored.

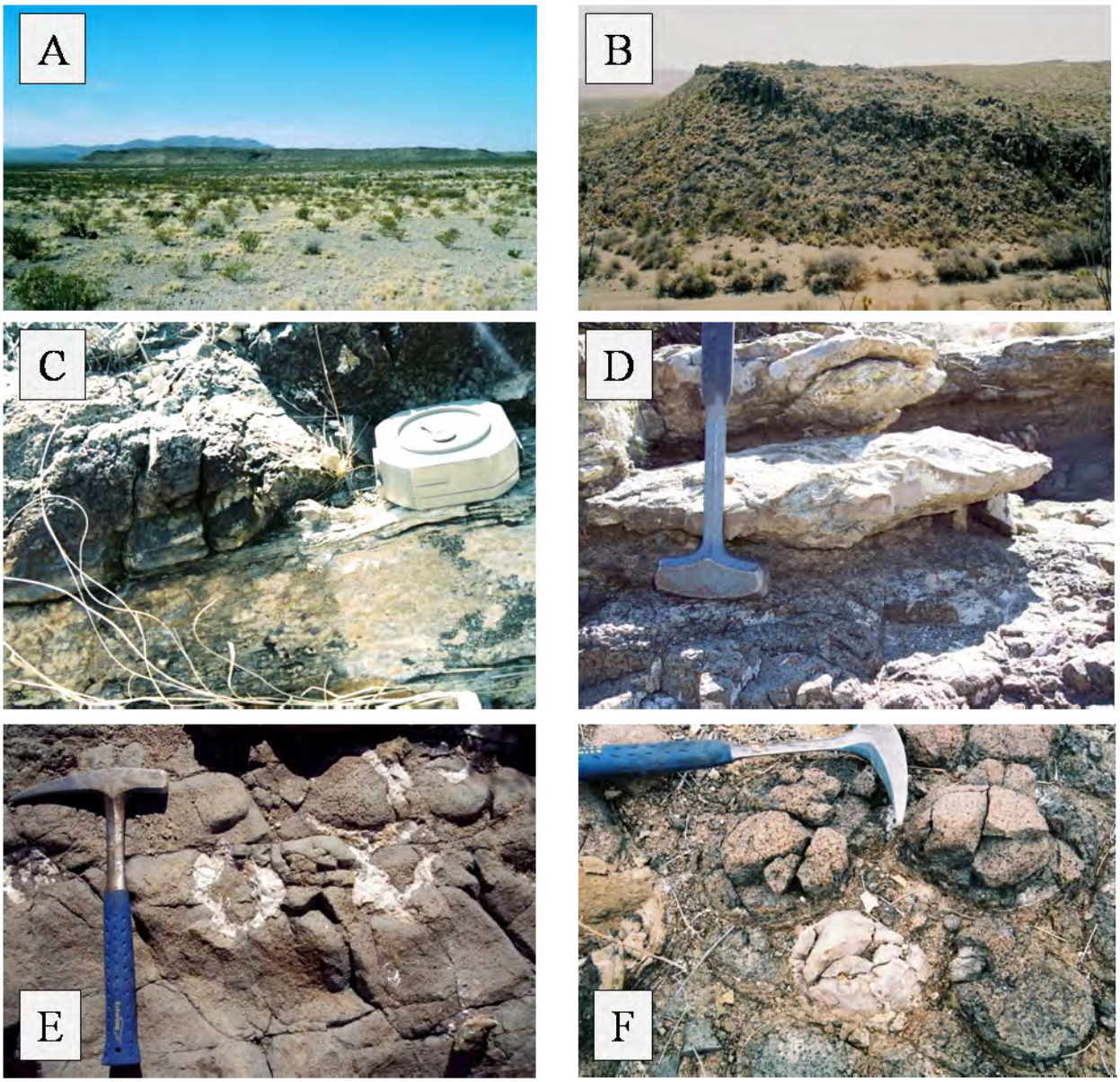

Figure 3-4. Photographs of Bone Springs Sill outcrops. A: Sill approached from the east. **B:** Looking across a gully to the south. Note the blocky layer dipping to the right – this is the base of the central zone. **C:** Lower contact KAg sedimentary rock. Not the 1-2 cm glassy chill zone on which the transit rests. **D:** Upper contact with KAg. **E** and **F:** Calcite-filled cylindroidal vugs in the fine grained UBZ rocks immediately below upper contact. **G** and **H:** Large scale and detail of monzosyenite segregations in monzogabbro. $\mathbf{H_1}$ marks the analcime monzogabbro with cm-scale ocelli of analcime-monzosyenite; $\mathbf{H_2}$ marks light gray pegmatitic analcime monzosyenite. **I:** Central zone – light gray equigranular monzosyenite with cm-scale analcime-filled miarolitic vugs. **J:** Central zone – subhorizontal layers of monzosyenite in monzogabbro; $\mathbf{J_1}$ is medium-grained monzogabbro; $\mathbf{J_2}$ is pegmatitic monzosyenite; $\mathbf{J_3}$ is equigranular monzosyenite. **K:** Central zone – rare vertical cylindrical pipe of monzosyenite in monzogabbro.

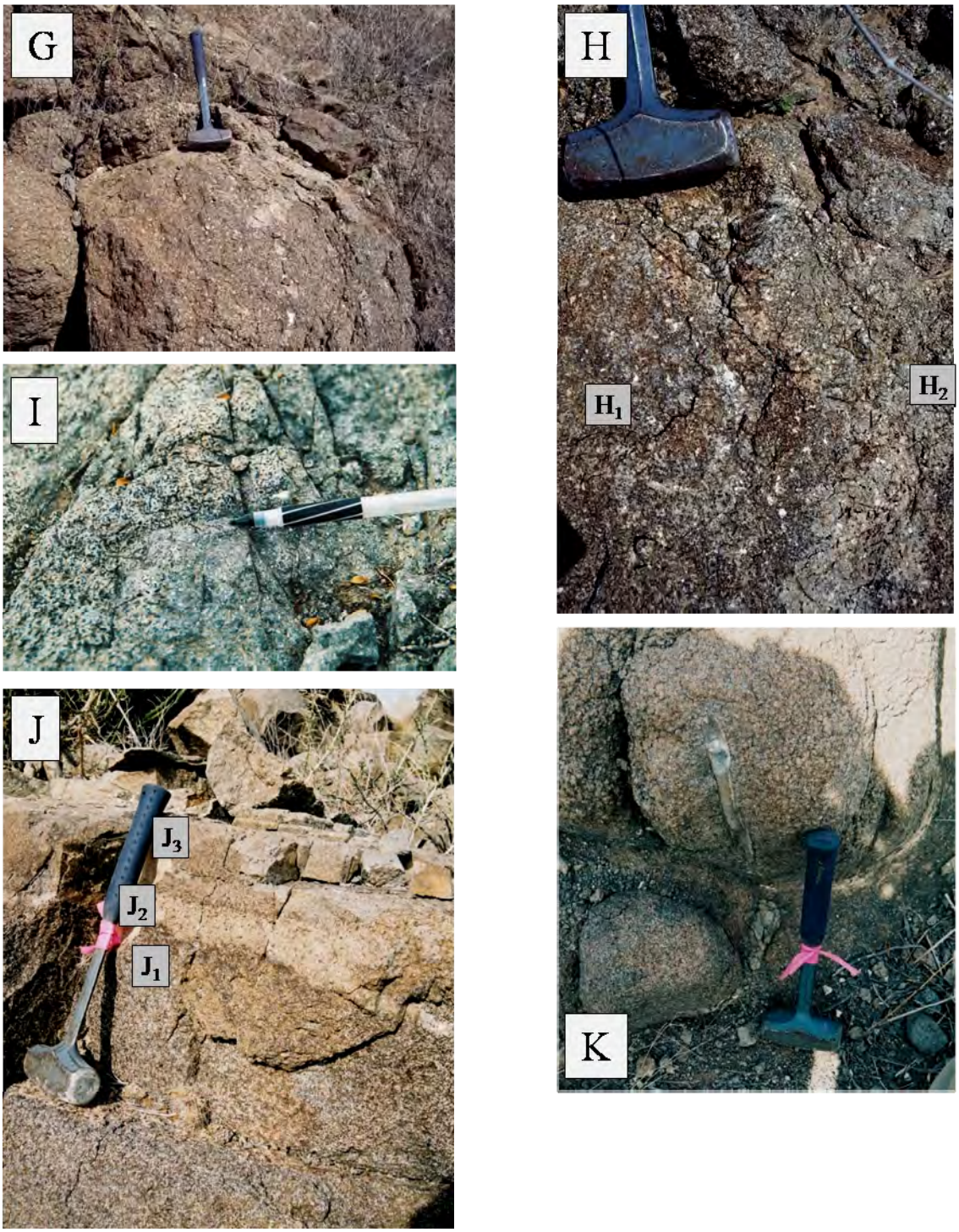

Figure 3-4, continued. Photographs of Bone Springs Sill outcrops.

(described below), there are no continuous layers or subzones. On its eastern edge, where the section was measured (see Figure 3-2), the sill is about 30 m thick.

Modes for melanocratic minerals (M: [Le Maitre et al., 2002]) – olivine, biotite, clinopyroxene, Fe-Ti oxides, apatite, and amphibole – determined by point counting under a petrographic microscope are shown in Table 3-1 and shown graphically in Figure 3-5. There is a thin zone (<1 m) of lightly baked sediments near the lower contact marked by an increase in grain size due to recrystallization. The sedimentary rock overlaying the sill experienced more significant thermal effects: it is distinctly lighter in color and more indurated than Aguja Formation rock below the sill or distant to it. The lower margin of the sill is chilled and is represented by sample BS06-37 (Figure 3-4, C). The sill coarsens upwards to a medium-grained plutonic texture within 0.5 m. From 0 to ~18.5 m in stratigraphic height the sill is variably gray to black analcime monzogabbro rich in melanocratic minerals (M = %olivine + %clinopyroxene + %Ti-magnetite + %biotite + %apatite ± %ilmenite ± %amphibole = 38 to 52; see Table 3-1). This section is mapped as the lower border zone (LBZ). It contains only a trace of felsic differentiated material locally present as dikelets and stringers to a thickness of 1 cm. Igneous layering is mostly absent, but structural fabrics are developed over 3-4 meters of thickness around normally oriented partially brittle shears and brittle faults. It is possible that the measured thickness of this layer is complicated by structural repeats.

Near the top of the LBZ a blocky layer 2-3 m thick marks the transition to the central zone (CZ) of the sill (Figure 3-4, B). The CZ, from about 19 to 28 m in stratigraphic height, comprises two lithologies: a gray analcime monzogabbro and a white/gray to tan analcime monzosyenite. The CZ analcime monzogabbro can be discerned from the LBZ rock in hand sample by its lower contents of melanocratic minerals (M = 27 to 39; see Table 3-1) and

Table 3-1. Mafic mineral modes for Bone Springs Sill rocks determined by point counting. Counts were made under transmitted light on a grid system with 300 points per thin section. Lithology abbreviations: mzgb = monzogabbro, mzsy = monzosyenite, teph = tephrite.

Lower Border Zone								
lith	mzgb	mzgb	mzgb	mzgb	mzgb	mzgb	mzgb	
sample	BS04-2	BS06-38	BS04-7	BS06-45	BS04-9	BS04-10	BS06-46	average
strat. height	0.8	2.3	3.8	8.0	9.5	10.2	11.0	
Bt	1.3	2.7	1.0	11.0	3.7	4.0	6.0	4.2
Am	0.3	0.7					0.7	
FeTi ox	8.0	10.0	11.0	8.7	8.3	8.3	9.7	9.1
Ap	4.0	1.0	4.0	3.3	3.0	4.0	2.0	3.0
Ol	7.0	10.0	3.3	10.0	7.3	12.3	9.3	8.5
Cpx	18.0	16.7	19.0	12.7	16.0	18.3	24.3	17.9
*M	38.7	41.0	38.3	45.7	38.3	47.0	52.0	43.0
Central Zone								
lith	mzgb	mzgb	mzgb	mzsy	mzsy			
sample	BS05-19	BS04-13	BS04-4	BS06-50	BS06-59			
strat. height	18.6	19.0	22.8	20.9	25.4			
Bt	0.0	0.3	1.0					
Am	0.0	5.7	0.7	8.0	3.0			
FeTi ox	5.7	6.3	8.3	1.7	4.7			
Ap	2.7	4.3	3.3	0.3				
Cb		2.0		1.7	4.0			
Ol	3.0	0.7	0.3	0.0	0.3			
Cpx	17.3	19.3	13.0	2.0	5.7			
*M	28.6	38.6	26.7	13.7	17.7			
Margins/chill zones								
lith	teph	teph						
sample	BS06-37	BS06-71						
strat. height	0.0	30.0						
FeTi ox	4.3	9.7						
Ap		0.7						
Ol	5.7	5.7						
Cpx	4.7	7.0						
**altr'd mafic	1.3	14.3						

* M = total melanocratic minerals in the plutonic rocks, after LeMaitre et al. (2002).
**Altered unknown mafic mineral, now finie-grained Fe±Ti oxide + chlorite.

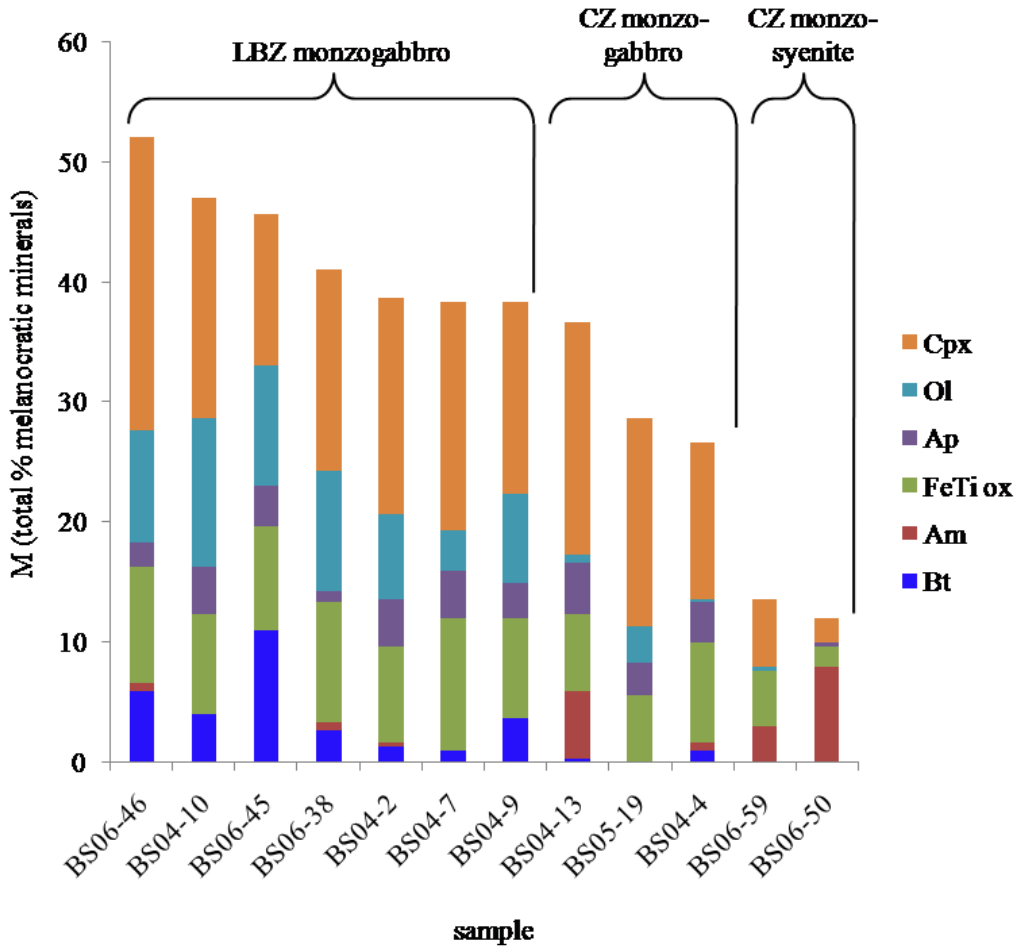

Figure 3-5. Proportions of melanocratic minerals in Bone Springs Sill rocks. Numerical data are shown in Table 3-1.

consistently coarser texture. The mineral assemblages of the CZ and the LBZ monzogabbroic rocks are the same, though proportions differ. The CZ monzosyenite occurs as sub-horizontal sheets and sub-vertical anastomizing dikes 10's of cm thick (see Figure 3-4, J), as rare vertical columns to 4 cm diameter (see Figure 3-4, K), and as irregular masses approaching the shape of ocelli (see Figure 3-4, G and H). Some thin stringers of monzosyenite cut into the monzogabbro on a cm scale. Thin reaction zones, when present, are marked by mm to cm scale zones rich in Fe-Ti oxide.

Monzosyenite is leucocratic (M < 18; see Table 3-1). Textures locally approach pegmatitic, with pyroxene or amphibole of very high aspect ratio (up to 15 cm long and 0.1 to 0.2 cm wide) set in a sugary matrix of feldspar and analcime. Other samples are closer to equigranular and contain miarolitic cavities to 0.5 cm filled with analcime ± thomsonite (see Figure 3-4, I). These textures indicate crystallization in the presence of a fluid phase at low pressure (< 1km depth [Barker, 1987]).

The upper 1-2 m of the sill is a dark gray to black aphanitic, locally vesicular rock that grades over 1-2 cm into the CZ rocks (see Figure 3-4, D). This is marked as the upper border zone (UBZ) on the map and throughout this paper. At the top, where the UBZ contacts the overlying Kag sedimentary rocks, vugs or cavities filled with calcite, up to 20 cm wide occur as columns and rings (see Figure 3-4, E and F). The textures indicate the presence of a free fluid during quenching of the liquid. Some of these cavities have an inverted teardrop shape indicating that they rose from depth, but whether the fluid was from the devolatilizing magma or derived from the sedimentary rocks and convected during early cooling is unclear.

At several sites in the sill patches of later analcime tephrite lava are preserved. It is fresher than other surface rocks, having only a thin orange-brown weathered rind; fresh surfaces

are gray-blue and aphanitic-porphyritic with clinopyroxene, plagioclase, and rare olivine phenocrysts. It appears to lie unconformably on the sill in slight erosional lows and is thus younger (post-BSS intrusion and uplift). Its field relations, however, are not fully established and are open to interpretation.

Lithologies

In hand sample and thin section, the total proportion of melanocratic minerals differentiates the LBZ rocks from the CZ mafic rocks. The LBZ rocks contain M of 38-52 with a mean of 39, while the CZ mafic rocks have M of 27-39 with a mean of 31. Specifically, the LBZ rocks have more olivine than do the CZ mafic rocks (mean 8.5 vol.% vs. mean 1.3 vol.%), more biotite (mean 4.2 vol.% vs. mean 0.4 vol.%), and more Fe-Ti oxide (mean 9.2 vol.% vs. mean 6.8 vol.%). Central zone mafic rocks have more amphibole, with a mean 2 vol.% while the LBZ gabbros contain only traces.

Modes for the felsic minerals are deemed too unreliable by this method to report as modal%, because analcime, which fills the interstices and is intergrown with fine-grained feldspar and thomsonite, and which partially replaces feldspar, obscures the proportions. However, ratios between plagioclase feldspar, alkali feldspar, and analcime from hand sample and thin section consistently place the LBZ rocks and the CZ mafic rocks into the field of (analcime) monzogabbro (plagioclase >An50) and the CZ felsic rocks into the field of (analcime) monzosyenite on the undersaturated portion of the QAPF classification diagram (Le Maitre et al., 2002). For the sake of brevity, in this document the rocks are referred to as LBZ, CZ mafic, and CZ felsic rocks, or monzogabbro and monzosyenite, when appropriate.

The margin and UBZ rocks are too fine-grained too name by the QAPF diagram. Figure 3-6 shows a total alkali-silica diagram after Le Bas et al. (1986) with all of the BSS rocks

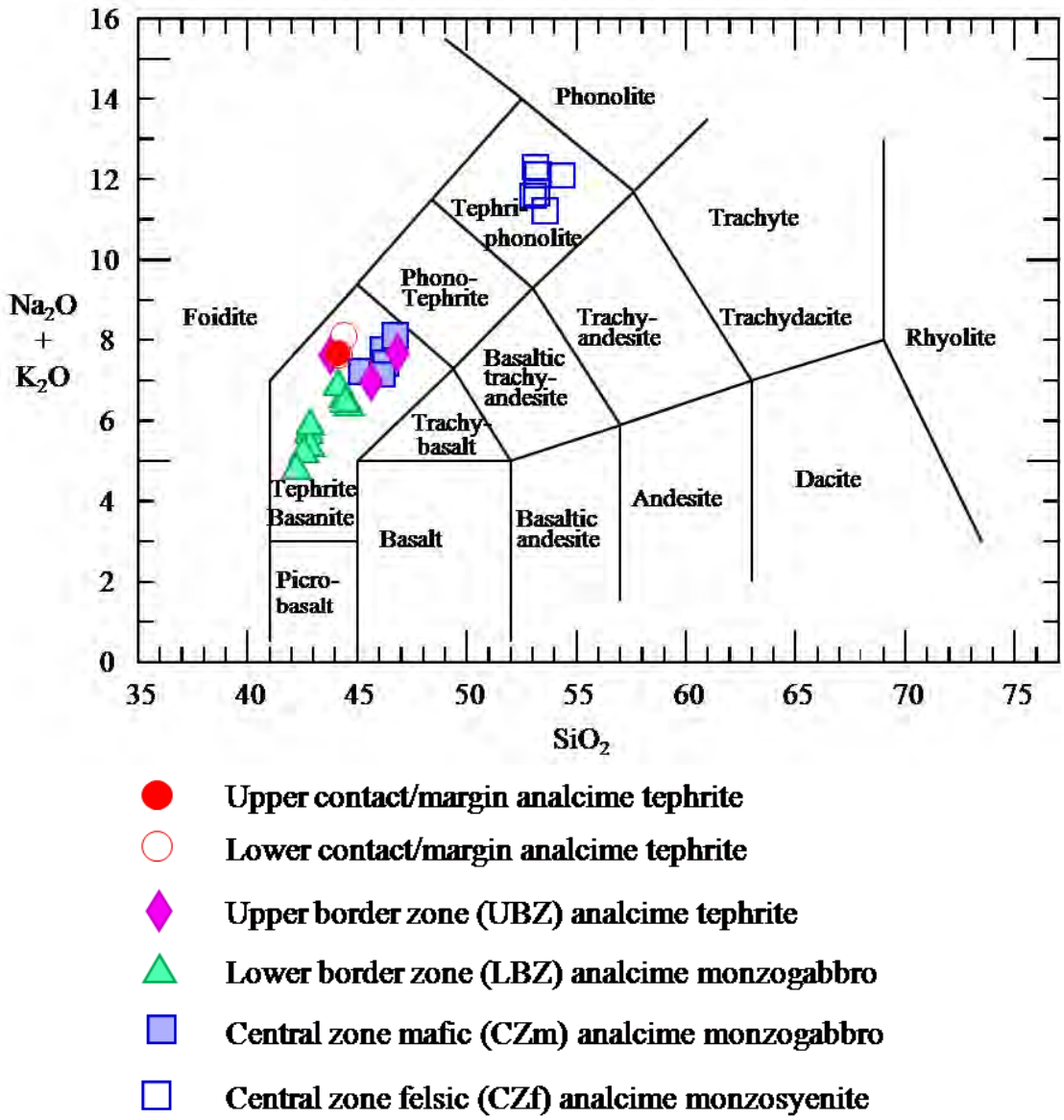

Figure 3-6. Total alkali-silica diagram for Bone Springs Sill rocks. The diagram is after Le Bas et al. (1986). Most BSS rocks are partially cumulate and do not represent liquid compositions, but the margin/contact rocks, the UBZ rocks, and the monzosyenites approach liquid compositions. These symbols are used through the rest of this paper.

plotted. Only the margin and UBZ rocks and possibly the CZ felsic rocks are reasonable candidates to be liquid compositions, but others are shown for comparison. By this diagram, all fine-grained mafic samples plot in the tephrite/basanite field and all but one are tephrites (normative ol <10%). The other, BS06-29, is a basanite. By the criteria of Le Bas et al. (1989), all would be basanites (>5% normative ab and <20% normative ne). Here, I refer to them as UBZ and contact rocks, or as tephrites, *sensu latu*. Because they approach liquid compositions, it is worth noting that the analcime monzosyenites have the composition of tephri-phonolite (Figure 3-6). Hence, I will refer to the UBZ and lower margin sample as micromonzogabbros, the LBZ and CZ mafic rocks as monzogabbros, and he CZ felsic rocks as monzosyenites

As discussed below, experimental evidence suggests that analcime in BSS rocks is unlikely to be a primary igneous phase and probably forms by a late reaction between nepheline, feldspar, and fluid. However, in hewing to the IUGS philosophy that rock names reflect what they are and not what they were or may have been (Le Maitre et al., 2002), a detailed classification would name these rocks as analcime micromonzogabbro, analcime monzogabbro, and analcime monzosyenite. Thin section microphotographs of BSS rocks are shown in Figure 3-7.

Minerals

Olivine

Olivine occurs in all BSS lithologies except the CZ monzosyenites, though it is often partially or wholly replaced by mixtures of serpentine, Fe-oxides/hydroxides, and minor chlorite. Most olivine is normally zoned and composition varies from Fo_{38} in thin, late rims in the CZ to Fo_{78} in clumps of grains that may have been carried in with the magma in the LBZ and UBZ.

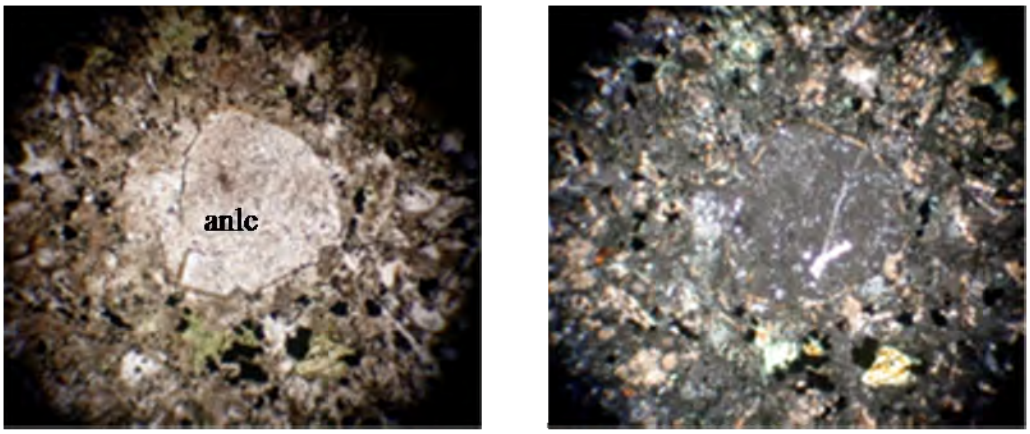

A: BS06-37: Lower contact, f.o.v. ~1.3 mm

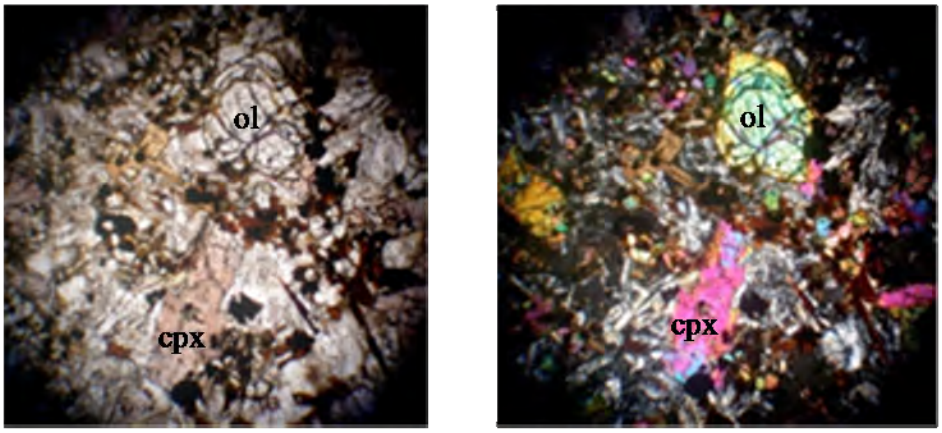

B: BS06-38: Lower border zone, f.o.v. ~3.6 mm

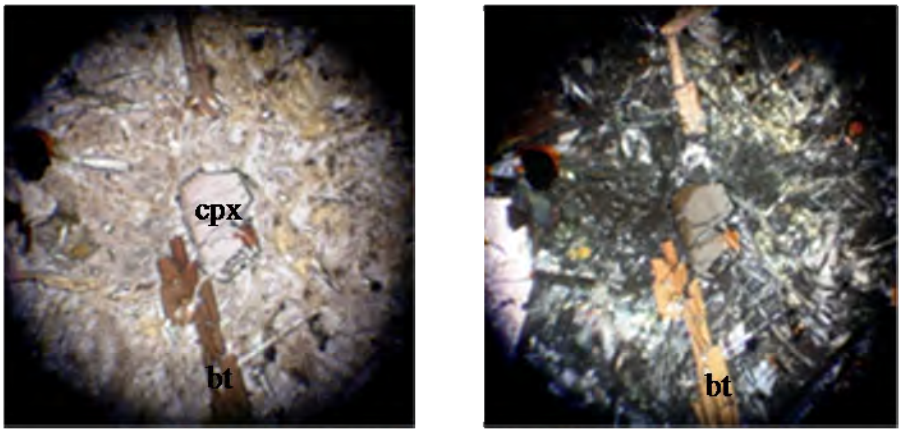

C: BS04-09: Lower border zone, f.o.v. ~1.3 mm

Figure 3-7. Images of Bones Spring Sill thin sections. Each image is part of a coupled PPL-XPL pair. Field of view = f.o.v. **A:** Analcime phenocryst, probably replacing nepheline, with microphenocrysts of sub- to euhedral olivine and early Fe-Ti oxide in analcime groundmass. **B:** Olivine with included apatite and Fe-Ti oxide, biotite and feldspar with late interstitial analcime and Fe-stained late biotite. **C:** Biotite, clinopyroxene, and abundant elongate apatite in analcime. **D:** Clinopyroxene with included apatite and Fe-Ti oxide with fresh feldspar and interstitial analcime. **E:** Kaersutitic amphibole with altered k-feldspar in analcime.

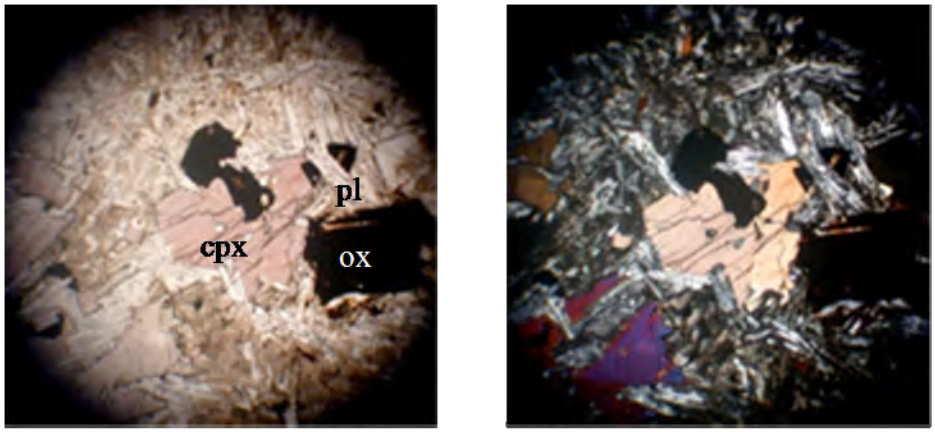

D: BS04-4 Central zone mafic, f.o.v. ~1.3 mm

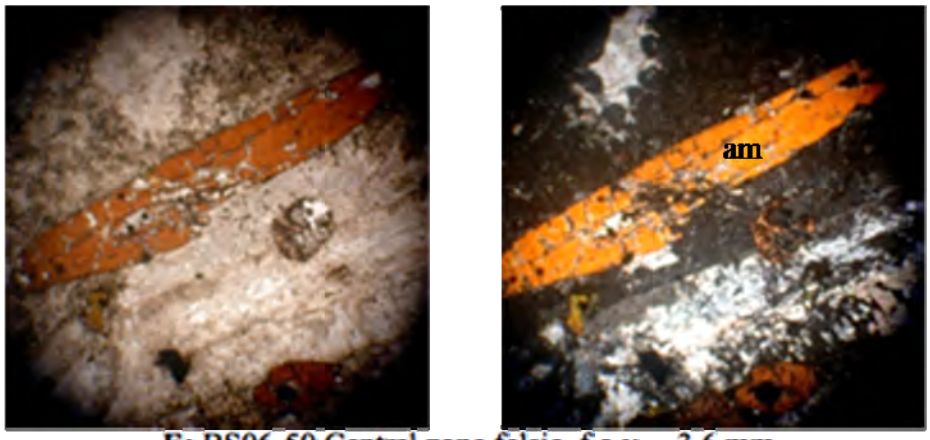

E: BS06-50 Central zone felsic, f.o.v. ~3.6 mm

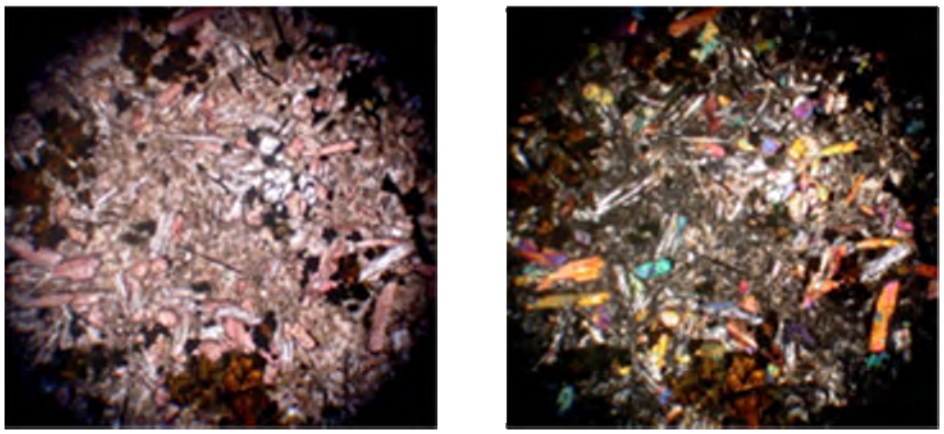

F: BS06-72 Upper border zone, f.o.v. ~3.6 mm

(**Figure 3-7, continued) F:** Olivine, clinopyroxene, feldspar and Fe-Ti oxide with interstitial analcime.

Table 3-2 shows olivine chemistry, and Figure 3-8 shows comparative summaries of olivine composition data by lithology.

Both the upper and lower margin contain 5-6 modal% clumps of serpentinized olivine grains of 500-700 μm with included and interstitial Ti-magnetite grains. The olivine is too altered for analysis. These appear to be phenocrysts or autoliths that intruded with the magma, but they do not contain a measurable chromite content. The Ti content of the oxide grains indicate that they are at least partly fresh and not products of serpentinization. The composition of the oxide inclusions is further discussed in the section on oxide minerals, below. Similar olivine-oxide clumps occur throughout the LBZ and are less altered.

The fine-grained UBZ rocks contain a population of 100-200 μm sub- to euhedral olivine grains and rare 400-500 μm grains with serpentinized cores. Upper border zone olivines have cores of Fo_{65-76} and rims of Fo_{60-66}.

Lower border zone samples contain from 3-12 modal% olivine. Within any sample between 10 and 90% of the olivine is altered to serpentine and iddingsite (chlorite, serpentine, Fe-oxide). Most grains are from 250 μm to 2 mm. Olivine is commonly rimmed by biotite but never by clinopyroxene. Occasional olivine grains truncate against earlier clinopyroxene, but most relationships indicate that olivine either crystallized in isolation and settled or ceased crystallizing before most other minerals. Some grains have serpentinized cores that may represent early, or even pre-intrusion, crystallization. The whole range of rims to cores in LBZ olivines is Fo_{58-78}. Most cores are Fo_{65-70} but there is a population usually found in clumps of 2-4 grains with cores of Fo_{78}. Most LBZ olivine rims are Fo_{60-65}. The most Mg-rich olivines in the LBZ and UBZ are interpreted to be pre-intrusion and carried in with the magma. Most of these contain inclusions of up to 100 μm Ti-magnetite, as in the UBZ (see above). Many of the less

Table 3-2. Bone Spring Sill olivine analyses. Sill zone abbreviations: CZ = central zone, LBZ = lower border zone, UBZ = upper border zone. Lithology abbreviations: mzgb = monzogabbro (micro- for UBZ), mzsy = monzosyenite, mix = intermingled mzgb and mzsy rocks in CZ. For description (desc.), "int" = intermediate between core and rim. These abbreviations are used throughout this document. Complete table of analyses are in the appendices. Blank entries are below detection limit (bdl). NiO is bdl in all analyses.

lithology	CZ mix	CZ mix	CZ mix	CZ mix	CZ mix	CZ mix	CZ mix	CZ mix	CZ mix
sample	BS05-18	BS05-18	BS05-18	BS05-20	BS05-20	BS05-20	BS05-20	BS05-18	BS05-20
desc.	core	core	core	core	core	core	core	core	core
analysis	35	34	38	51	49	45	48	41	50
SiO_2	37.61	37.71	37.32	35.78	35.81	35.87	35.68	34.93	34.86
TiO_2									
FeO	27.84	27.65	28.28	38.99	39.83	40.47	40.32	42.03	42.91
MgO	34.30	34.09	32.60	24.13	23.40	23.28	23.02	20.78	20.63
MnO	0.42	0.38	0.46	0.82	0.79	0.86	0.85	0.98	0.99
CaO	0.40	0.46	0.45	0.49	0.48	0.55	0.43	0.49	0.50
Total	100.74	100.45	99.31	100.27	100.42	101.09	100.40	99.29	100.14
				atoms per formula unit based on 4 O's					
Si	0.999	1.005	1.012	1.016	1.021	1.017	1.020	1.022	1.015
Ti									
Fe	0.618	0.616	0.641	0.926	0.949	0.960	0.964	1.029	1.044
Mg	1.358	1.354	1.318	1.022	0.994	0.984	0.981	0.907	0.895
Mn	0.009	0.008	0.011	0.020	0.019	0.021	0.021	0.024	0.024
Ca	0.011	0.013	0.013	0.015	0.015	0.017	0.013	0.015	0.016
total	2.996	2.996	2.995	2.999	2.998	2.999	2.998	2.998	2.994
Fo%	68.0	68.0	66.5	51.5	50.3	49.7	49.6	45.9	45.2

lithology	CZ mix	CZ mix	CZ mix	CZ mix	CZ mzgb	CZ mzgb	CZ mzgb	CZ mzgb	CZ mzgb
sample	BS05-18	BS05-20	BS05-18	BS05-18	BS04-4	BS04-4	BS04-4	BS04-4	BS05-19
desc.	core	rim	rim	rim	core	core	core	core	core
analysis	42	46	39	36	97	100	91	94	30
SiO_2	34.99	35.14	33.81	33.74	37.47	37.23	36.86	36.33	36.85
TiO_2		0.10							
FeO	43.85	42.25	47.31	49.22	27.41	28.74	31.89	33.41	33.92
MgO	19.56	21.46	17.13	16.17	34.19	33.39	31.13	30.34	28.00
MnO	1.30	1.04	1.21	1.65	0.63	0.64	0.64	0.64	0.70
CaO	0.46	0.48	0.56	0.55	0.39	0.45	0.43	0.43	0.50
Total	100.24	100.48	100.20	101.36	100.27	100.68	101.06	101.31	100.02
				atoms per formula unit based on 4 O's					
Si	1.024	1.014	1.007	1.002	0.999	0.994	0.995	0.977	1.022
Ti		0.002							
Fe	1.073	1.020	1.179	1.222	0.611	0.641	0.720	0.752	0.787
Mg	0.854	0.923	0.761	0.716	1.360	1.329	1.252	1.217	1.158
Mn	0.032	0.025	0.031	0.041	0.014	0.014	0.015	0.015	0.017
Ca	0.014	0.015	0.018	0.017	0.011	0.013	0.012	0.012	0.015
total	2.998	3.000	2.995	2.999	2.996	2.991	2.993	2.972	2.999
Fo%	43.3	46.6	38.3	35.8	68.1	66.5	62.7	61.0	58.6

Table 3-2, continued. Bone Spring Sill olivine analyses.

lithology	CZ mzgb	CZ mzgb	CZ mzgb	CZ mzgb	CZ mzgb	CZ mzgb	CZ mzgb	CZ mzgb	CZ mzgb
sample	BS05-19	BS05-19	BS04-4	BS04-4	BS04-4	BS05-19	BS05-19	BS04-4	BS05-19
desc.	int	int	rim	rim	rim	rim	rim	rim	
analysis	28	27	98	101	95	25	31	92	24
SiO_2	37.16	36.75	36.77	36.99	35.22	35.31	35.06	34.00	36.31
TiO_2									0.10
FeO	32.08	34.35	28.78	29.32	41.05	42.07	42.04	46.46	35.24
MgO	30.00	28.64	32.66	32.65	22.92	22.23	21.26	19.50	27.71
MnO	0.70	0.57	0.67	0.39	0.85	0.91	1.01	0.94	0.55
CaO	0.42	0.49	0.46	0.41	0.48	0.53	0.55	0.50	0.44
Total	100.49	100.81	99.43	99.88	100.69	101.16	99.98	101.60	100.43
			atoms per formula unit based on 4 O's						
Si	1.015	1.010	0.996	0.999	1.005	1.008	1.017	0.980	1.007
Ti									0.002
Fe	0.733	0.789	0.652	0.662	0.980	1.005	1.020	1.119	0.817
Mg	1.221	1.173	1.319	1.315	0.975	0.946	0.920	0.838	1.146
Mn	0.016	0.013	0.015	0.009	0.021	0.022	0.025	0.023	0.013
Ca	0.012	0.014	0.013	0.012	0.015	0.016	0.017	0.015	0.013
total	2.997	3.000	2.995	2.997	2.996	2.997	2.998	2.975	2.998
Fo%	61.6	59.0	66.0	65.8	49.0	47.6	46.4	42.0	57.6

lithology	LBZ mzgb	LBZ mzgb	LBZ mzgb	LBZ mzgb	LBZ mzgb	LBZ mzgb	LBZ mzgb	LBZ mzgb	LBZ mzgb
sample	BS04-9	BS04-9	BS04-9	BS04-9	BS04-9	BS04-9	BS06-46	BS06-46	BS06-46
desc.	core	core	core	core	core	core	core	core	core
analysis	88	83	80	85	74	71	117	112	107
SiO_2	39.13	38.61	38.68	38.79	37.67	37.30	36.78	36.72	36.51
TiO_2					0.09	0.09			
FeO	19.69	19.76	20.48	20.53	27.46	27.36	27.39	27.28	26.90
MgO	41.39	41.22	41.14	41.03	35.98	35.32	34.02	33.59	30.90
MnO	0.36	0.31	0.22	0.24	0.37	0.41	0.46	0.49	0.47
CaO	0.23	0.22	0.21	0.26	0.41	0.44	0.42	0.38	0.40
Total	101.00	100.31	100.88	101.16	101.35	100.45	99.32	98.61	95.27
				atoms per formula unit based on 4 O's					
Si	0.992	0.982	0.979	0.982	0.980	0.982	0.985	0.995	1.034
Ti					0.002	0.002			
Fe	0.417	0.420	0.433	0.434	0.578	0.585	0.613	0.618	0.637
Mg	1.564	1.563	1.552	1.548	1.396	1.386	1.359	1.358	1.304
Mn	0.008	0.007	0.005	0.005	0.008	0.009	0.010	0.011	0.011
Ca	0.006	0.006	0.006	0.007	0.011	0.012	0.012	0.011	0.012
total	2.987	2.977	2.974	2.976	2.976	2.977	2.980	2.993	2.998
Fo%	78.4	78.3	77.8	77.6	70.0	69.6	68.1	67.9	66.4

Table 3-2, continued. Bone Spring Sill olivine analyses.

lithology	LBZ mzgb	LBZ mzgb	LBZ mzgb	LBZ mzgb	LBZ mzgb	LBZ mzgb	LBZ mzgb	LBZ mzgb	LBZ mzgb
sample	BS04-9	BS06-46	BS06-46	BS04-9	BS04-9	BS04-9	BS04-9	BS06-46	BS06-46
desc.	core	core	core	core	core	core	core/int	int	int
analysis	68	103	108	78	76	73	70	118	113
SiO_2	36.75	37.15	35.96	36.76	36.70	35.65	37.78	36.95	36.77
TiO_2	0.09	0.09							
FeO	30.99	29.80	29.82	30.76	30.77	37.16	25.33	27.39	27.96
MgO	33.16	32.95	32.83	32.35	32.27	29.03	36.36	33.41	33.44
MnO	0.50	0.49	0.45	0.65	0.65	0.68	0.30	0.45	0.43
CaO	0.43	0.38	0.37	0.43	0.43	0.48	0.47	0.42	0.42
Total	100.90	101.00	99.76	101.23	101.01	101.49	100.20	98.76	99.20
				atoms per formula unit based on 4 O's					
Si	0.974	0.991	0.959	0.978	0.979	0.960	0.993	1.002	0.992
Ti	0.002	0.002							
Fe	0.660	0.665	0.665	0.685	0.686	0.794	0.551	0.621	0.631
Mg	1.311	1.311	1.305	1.284	1.283	1.166	1.425	1.351	1.345
Mn	0.011	0.011	0.010	0.015	0.015	0.015	0.007	0.010	0.010
Ca	0.012	0.011	0.011	0.012	0.012	0.014	0.013	0.012	0.012
total	2.971	2.990	2.950	2.973	2.975	2.949	2.990	2.997	2.989
Fo%	65.7	65.6	65.6	64.3	64.3	58.6	71.4	67.7	67.3

lithology	LBZ mzgb	LBZ mzgb	LBZ mzgb	LBZ mzgb	LBZ mzgb	LBZ mzgb	LBZ mzgb	LBZ mzgb	LBZ mzgb
sample	BS06-46	BS06-46	BS04-9	BS04-9	BS06-46	BS06-46	BS04-9	BS06-46	BS04-9
desc.	int	int	rim	rim	rim	rim	rim	rim	rim
analysis	109	104	72	89	110	119	86	115	69
SiO_2	36.27	36.80	37.03	37.52	35.78	36.20	37.17	36.10	36.31
TiO_2	0.12					0.23		0.09	0.09
FeO	28.64	30.06	29.37	28.92	29.62	30.63	30.75	30.40	30.95
MgO	33.50	32.50	35.86	33.59	32.66	32.15	32.43	31.28	31.15
MnO	0.47	0.48	0.42	0.47	0.65	0.52	0.64	0.50	0.61
CaO	0.38	0.41	0.39	0.41	0.35	0.36	0.40	0.39	0.41
Total	99.64	100.37	101.34	101.06	99.50	100.25	101.54	98.83	99.43
				atoms per formula unit based on 4 O's					
Si	0.968	0.987	0.957	0.998	0.957	0.971	0.989	0.989	0.992
Ti	0.002					0.005		0.002	0.002
Fe	0.639	0.674	0.588	0.643	0.663	0.687	0.684	0.697	0.702
Mg	1.332	1.300	1.381	1.332	1.303	1.286	1.287	1.278	1.269
Mn	0.011	0.011	0.009	0.010	0.015	0.012	0.015	0.011	0.014
Ca	0.011	0.012	0.011	0.012	0.010	0.010	0.011	0.012	0.012
total	2.962	2.984	2.946	2.996	2.947	2.970	2.987	2.989	2.991
Fo%	66.9	65.1	69.4	66.7	65.5	64.4	64.4	64.0	63.6

Table 3-2, continued. Bone Spring Sill olivine analyses.

lithology	LBZ mzgb	LBZ mzgb	LBZ mzgb	UBZ mzgb	UBZ mzgb	UBZ mzgb	UBZ mzgb	UBZ mzgb	UBZ mzgb
sample	BS04-9	BS06-46	BS06-46	BS05-30	BS05-30	BS05-30	BS05-30	BS05-30	BS05-30
desc.	rim	rim	rim	core	core	core	core	core	int
analysis	81	105	114	63	58	53	61	56	64
SiO_2	36.61	35.81	35.71	38.31	37.36	37.60	37.47	36.44	37.91
TiO_2			0.09				0.10	0.11	
FeO	30.97	32.39	33.09	21.69	25.95	24.58	26.51	31.70	21.98
MgO	31.24	29.05	28.29	38.82	38.05	37.29	37.50	32.26	38.88
MnO	0.64	0.75	0.55	0.37	0.37	0.47	0.36	0.48	0.29
CaO	0.43	0.32	0.32	0.30	0.39	0.39	0.52	0.43	0.29
Total	100.02	98.59	98.08	99.55	100.55	99.75	101.04	100.50	99.08
			atoms per formula unit based on 4 O's						
Si	0.995	1.000	1.006	0.999	0.959	0.983	0.963	0.975	0.989
Ti			0.002				0.002	0.002	
Fe	0.704	0.756	0.780	0.473	0.514	0.521	0.531	0.683	0.469
Mg	1.266	1.210	1.189	1.510	1.456	1.454	1.437	1.287	1.513
Mn	0.015	0.018	0.013	0.008	0.008	0.010	0.008	0.011	0.006
Ca	0.013	0.009	0.010	0.008	0.011	0.011	0.014	0.012	0.008
total	2.993	2.994	2.999	2.998	2.949	2.980	2.955	2.970	2.986
Fo%	63.4	60.7	59.7	75.5	73.2	72.8	72.2	64.6	75.8

lithology	UBZ mzgb	UBZ mzgb	UBZ mzgb
sample	BS05-30	BS05-30	BS05-30
desc.	rim	rim	rim
analysis	54	65	59
SiO_2	37.22	36.56	36.18
TiO_2	0.10		0.25
FeO	25.92	30.08	33.24
MgO	37.21	32.93	29.15
MnO	0.33	0.56	0.54
CaO	0.42	0.39	0.46
Total	100.08	99.75	99.85
atoms per formula unit based on 4 O's			
Si	0.967	0.981	0.999
Ti	0.002		0.005
Fe	0.529	0.654	0.768
Mg	1.441	1.318	1.200
Mn	0.007	0.013	0.013
Ca	0.012	0.011	0.014
total	2.958	2.978	2.999
Fo%	72.4	66.0	60.2

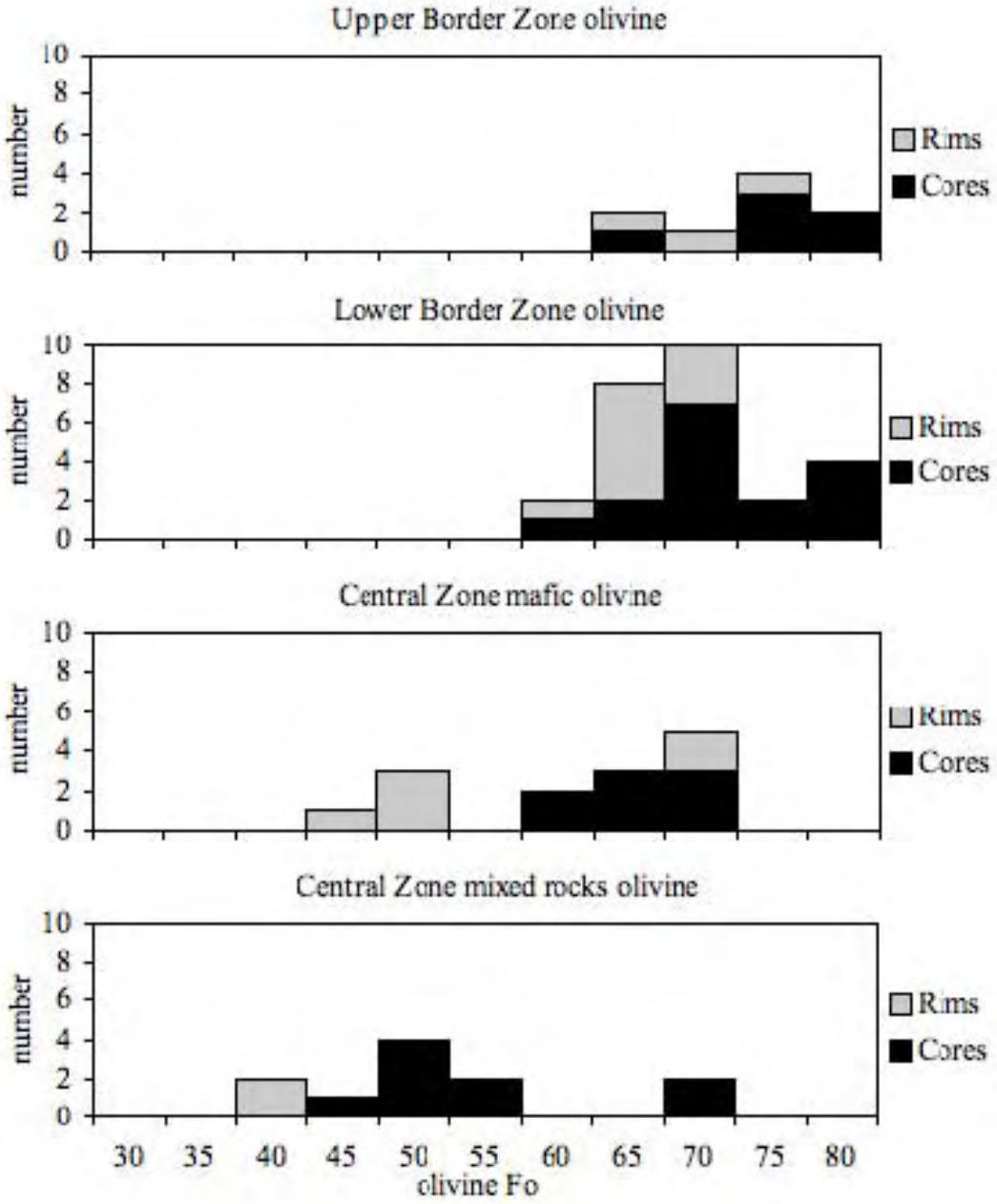

Figure 3-8. Bone Springs Sill olivine compositions. The most magnesian olivine cores in the UBZ and LBZ rocks are interpreted to have been carried in with the intruding magma. The most Fe-rich rims in the CZ mixed rocks are interpreted to have been in equilibrium with the most evolved monzosyenite liquid.

magnesian olivines contain apatite grains. That the most magnesian olivines predate intrusion is supported by their Mg/Fe ratios relative to whole rock Mg/Fe ratios, as explored in the section on mineral-liquid equilibrium, below.

Central zone mafic rocks contain <3 modal% olivine. Most grains are from 100-400 μm and are variably iddingsitized but less so than in the most altered LBZ samples. Some olivines crystallized later in the sequence than in the LBZ rocks and include plagioclase and apatite as well as Ti-magnetite. Cores in CZ olivines have compositions as magnesian as Fo_{68} and rims as ferroan as Fo_{42}. Two samples from the sill preserve mixed rocks in which thin segregations of monzosyenitic liquid infiltrates CZ monzodiorite. These samples contain olivines with cores similar to other CZ mafic rocks but also another less magnesian population with cores as low as Fo_{43}. Some of both types of olivine in these mixed rocks have thin, late rims of Fo_{36-38}.

Figure 3-8 shows that UBZ olivines are similar or identical to the more magnesian olivine in the LBZ. Olivines become less magnesian in the sequence LBZ to CZ mafic rocks to CZ mixed rocks. There is overlap in olivine composition between lithologies but the cores of olivines from later in the sequence tend to align with rims from the less evolved samples. Although no olivines were found and analyzed in the monzosyenite samples, the most Fe-rich rims in the CZ mixed rocks may have been in equilibrium with the felsic liquids. Based on olivine composition and whole rock chemistry, the most magnesian olivines in the sill are interpreted to have formed pre-intrusion; this is discussed at some length in the section *Mineral-liquid equilibrium and Mg/Fe*, below.

Clinopyroxene

Clinopyroxene is found in every BSS sample in proportions from 18 modal% in the LBZ to 4 modal% in the CZ monzosyenites. Only one intact grain was found in the fine-grained

contact rocks but clinopyroxene grains altered to chlorite, serpentine, and carbonate represent about 5 modal% of the chilled margins. Pyroxene grains are of diopsidic composition except for some of the latest rims and mantles, which are aegerine-augite.

In the LBZ, clinopyroxene varies from about 150 μm to about 3 mm and most exhibit one or more developed crystal faces, though few are euhedral. Some samples have pyroxene grains from 200-300 μm while two samples contain grains mostly of 600-800 μm. Clinopyroxene in the LBZ frequently includes grains of Ti-magnetite and euhedral apatite, and in some samples included and deeply embayed plagioclase grains result in sub-ophitic textures. Clinopyroxene rarely includes serpentinized olivine grains but does not exhibit rimming relationships with olivine. Clinopyroxene in the mafic CZ rocks are typically 200-400 μm and display relationships to plagioclase, apatite, and Fe-Ti oxides similar to LBZ pyroxenes. Clinopyroxenes in the CZ monzosyenites are 15-250 μm and are commonly cores to amphibole grains. Some cores of CZ felsic clinopyroxenes are diopsidic and similar to grains in less evolved lithologies, but rims are more Fe-rich and the latest rims of some grains are aegirine-augite.

Table 3-3 summarizes clinopyroxene chemistry. Analyses are recast into FeO and Fe_2O_3 after the method of Droop (1987). This is justified (1) by the presence of Ti-magnetite with clinopyroxene, indicating an oxidization state during clinopyroxene crystallization where Fe^{3+} was present, and (2) because cation totals prior to recasting consistently exceeded 4.00 per formula unit by 0.01-.07, suggesting some Fe^{3+} in the crystal.

Clinopyroxene crystal zoning and compositions

Most BSS clinopyroxene grains have minor normal zoning superimposed on sector zoning. Clinopyroxene compositions are used in later sections of this paper to constrain pre- and post-intrusion differentiation models, and this requires a thorough documentation of crystal

Table 3-3. Bone Springs Sill clinopyroxene compositions. Compositions for the lower border zone (LBZ) and central zone (CZ) monzogabbro and the upper border zone UBZ micromonzogabbro samples are presented as average, minimum, and maximum values for each oxide from multiple analyses of high-Z and low-Z domains of sector zoned pyroxenes (see text for explanation). Compositions for crystals without sector zoning – CZ monzosyenite and the lower margin micromonzogabbro samples – are single analyses of cores, a rim, and a mantle and are presented at the end of the table.

lithology	LBZ mzgb				LBZ mzgb				LBZ mzgb				LBZ mzgb			
Sample	BS04-10				BS04-10				BS04-2				BS04-2			
sector	low-Z				high-Z				low-Z				high-Z			
number	n=4				n=3				n=9				n=14			
	mean	*2σ*	Min	Max	mean	*2σ*	Min	Max	mean	*2σ*	Min	Max	mean	*2s*	Min	Max
SiO_2	48.10	*1.22*	47.32	48.78	45.20	*2.30*	44.01	46.31	47.83	*2.64*	44.44	48.82	43.60	*2.19*	41.60	45.92
Al_2O_3	5.06	*0.94*	4.48	5.63	7.55	*1.68*	6.67	8.34	5.12	*2.20*	4.24	7.94	8.49	*1.58*	7.16	10.20
TiO_2	2.64	*0.47*	2.32	2.86	4.00	*1.53*	3.15	4.63	2.93	*1.44*	2.39	4.75	5.06	*1.25*	3.72	5.90
***FeOt**	6.90	*0.52*	6.62	7.24	7.38	*0.46*	7.21	7.64	8.40	*2.87*	7.00	10.35	8.26	*1.32*	7.59	10.28
***(FeO)**	*4.72*	*0.45*	*4.41*	*4.90*	*5.14*	*1.04*	*4.84*	*5.74*	*6.32*	*2.32*	*5.30*	*8.72*	*5.55*	*1.02*	*4.54*	*6.68*
***(Fe_2O_3)**	*2.43*	*0.69*	*2.13*	*2.80*	*2.48*	*0.66*	*2.11*	*2.73*	*2.31*	*1.49*	*1.48*	*3.78*	*3.01*	*0.87*	*2.27*	*4.00*
MgO	13.65	*0.38*	13.50	13.92	12.15	*0.74*	11.83	12.55	12.41	*2.70*	10.68	13.68	11.18	*1.01*	10.12	12.07
MnO				0.19				0.18	0.17	*0.18*		0.27	0.15	*0.15*		0.30
CaO	23.10	*0.68*	22.73	23.50	22.84	*0.56*	22.54	23.09	22.58	*0.83*	21.99	23.25	22.92	*0.97*	22.14	23.75
Na_2O	0.47	*0.09*	0.43	0.54	0.53	*0.09*	0.50	0.59	0.65	*0.52*	0.42	1.13	0.66	*0.23*	0.52	0.98
Total	100.06	*0.84*	99.66	100.54	99.83	*0.49*	99.55	100.01	100.12	*1.27*	99.41	101.52	100.38	*1.09*	99.44	101.10
***(Total)**	*100.30*	*0.90*	*99.87*	*100.81*	*100.08*	*0.47*	*99.81*	*100.22*	*100.36*	*1.38*	*99.61*	*101.90*	*100.68*	*1.14*	*99.66*	*101.44*
cations allocated assuming 6 O's																
Si	1.798	*0.05*	1.769	1.824	1.704	*0.08*	1.662	1.746	1.798	*0.09*	1.684	1.828	1.647	*0.07*	1.584	1.719
Al	0.223	*0.04*	0.197	0.248	0.335	*0.08*	0.296	0.371	0.227	*0.10*	0.187	0.355	0.378	*0.07*	0.316	0.458
Ti	0.074	*0.01*	0.065	0.081	0.113	*0.04*	0.089	0.131	0.083	*0.04*	0.068	0.135	0.144	*0.04*	0.105	0.168
***Fe*t**	0.216	*0.02*	0.207	0.226	0.233	*0.01*	0.227	0.240	0.264	*0.09*	0.218	0.326	0.261	*0.04*	0.239	0.326
***(Fe2)**	*0.209*	*0.01*	*0.202*	*0.218*	*0.225*	*0.02*	*0.219*	*0.234*	*0.256*	*0.09*	*0.215*	*0.320*	*0.250*	*0.04*	*0.227*	*0.308*
***(Fe3)**	*0.097*	*0.04*	*0.082*	*0.119*	*0.099*	*0.04*	*0.077*	*0.112*	*0.086*	*0.07*	*0.051*	*0.151*	*0.123*	*0.05*	*0.085*	*0.166*
Mg	0.760	*0.02*	0.752	0.776	0.682	*0.04*	0.666	0.705	0.695	*0.14*	0.606	0.761	0.630	*0.05*	0.573	0.678
Mn				0.006				0.006	0.005	*0.01*		0.009	0.005	*0.00*		0.010
Ca	0.925	*0.03*	0.911	0.941	0.922	*0.03*	0.908	0.934	0.909	*0.03*	0.891	0.934	0.928	*0.03*	0.905	0.955
Na	0.034	*0.01*	0.032	0.039	0.039	*0.01*	0.037	0.043	0.047	*0.04*	0.031	0.082	0.048	*0.02*	0.038	0.072
sum	4.029	*0.01*	3.933	4.140	4.029	*0.01*	3.885	4.178	4.029	*0.02*	3.685	4.432	4.041	*0.02*	3.760	4.388

* FeOt was measured on the microprobe as FeO. Italicized values in parentheses are from Droop's (1987) allocation.

Table 3-3, continued. Bone Springs Sill clinopyroxene compositions.

lithology	LBZ mzgb				LBZ mzgb				LBZ mzgb				LBZ mzgb			
Sample	BS04-7				BS04-7				BS04-9				BS04-9			
sector	low-Z				high-Z				low-Z				high-Z			
number	n=4				n=4				n=5				n=3			
	mean	*2σ*	Min	Max	mean	*2σ*	Min	Max	mean	*2s*	Min	Max	mean	*2σ*	Min	Max
SiO_2	47.93	*0.83*	47.48	48.49	43.41	*3.52*	40.89	44.86	48.78	*0.99*	48.41	49.64	44.47	*2.52*	43.02	45.32
Al_2O_3	4.55	*0.17*	4.43	4.61	8.64	*2.91*	7.55	10.74	4.14	*0.14*	4.06	4.25	7.68	*2.18*	6.87	8.92
TiO_2	2.72	*0.13*	2.66	2.81	4.90	*1.76*	4.11	6.14	2.25	*0.27*	2.12	2.48	3.95	*1.41*	3.52	4.76
***FeOt**	7.75	*0.44*	7.46	7.97	7.98	*0.49*	7.72	8.30	7.33	*0.85*	6.80	7.82	7.82	*0.41*	7.69	8.06
***(FeO)**	*5.52*	*0.74*	*5.00*	*5.82*	*5.28*	*0.44*	*5.05*	*5.57*	*5.34*	*1.24*	*4.65*	*6.08*	*5.03*	*0.70*	*4.71*	*5.41*
***(Fe_2O_3)**	*2.48*	*0.53*	*2.11*	*2.73*	*3.00*	*0.66*	*2.57*	*3.36*	*2.22*	*1.53*	*1.01*	*2.80*	*3.11*	*0.41*	*2.95*	*3.34*
MgO	13.46	*0.49*	13.23	13.70	11.32	*1.03*	10.56	11.68	13.77	*0.56*	13.35	13.99	12.08	*1.15*	11.58	12.71
MnO	0.15	*0.12*		0.21					0.19	*0.04*	0.16	0.22				0.19
CaO	22.66	*0.99*	21.98	23.16	23.01	*0.27*	22.89	23.20	22.70	*0.79*	22.26	23.17	22.72	*0.42*	22.48	22.87
Na_2O	0.44	*0.11*	0.38	0.50	0.58	*0.10*	0.54	0.63	0.45	*0.05*	0.41	0.47	0.55	*0.08*	0.51	0.59
Total	99.69	*1.14*	99.09	100.40	99.96	*0.63*	99.62	100.29	99.70	*1.93*	98.36	100.80	99.44	*0.06*	99.42	99.47
***(Total)**	*99.94*	*1.11*	*99.34*	*100.61*	*100.26*	*0.69*	*99.87*	*100.63*	*99.92*	*2.02*	*98.46*	*100.99*	*99.75*	*0.10*	*99.72*	*99.81*
	cations allocated assuming 6 O's															
Si	1.804	*0.01*	1.798	1.811	1.645	*0.13*	1.553	1.699	1.830	*0.03*	1.813	1.845	1.688	*0.09*	1.637	1.721
Al	0.202	*0.01*	0.197	0.206	0.386	*0.13*	0.337	0.481	0.183	*0.01*	0.179	0.187	0.344	*0.10*	0.308	0.400
Ti	0.077	*0.00*	0.075	0.080	0.140	*0.05*	0.117	0.175	0.063	*0.01*	0.060	0.070	0.113	*0.04*	0.100	0.136
***Fe*t**	0.244	*0.01*	0.235	0.252	0.253	*0.02*	0.245	0.264	0.230	*0.02*	0.215	0.242	0.248	*0.01*	0.244	0.256
***(Fe2)**	*0.236*	*0.02*	*0.226*	*0.244*	*0.242*	*0.01*	*0.235*	*0.251*	*0.223*	*0.02*	*0.212*	*0.237*	*0.237*	*0.01*	*0.232*	*0.246*
***(Fe3)**	*0.096*	*0.03*	*0.077*	*0.111*	*0.125*	*0.04*	*0.100*	*0.144*	*0.087*	*0.07*	*0.033*	*0.113*	*0.133*	*0.03*	*0.121*	*0.148*
Mg	0.755	*0.03*	0.737	0.770	0.640	*0.06*	0.598	0.660	0.770	*0.02*	0.754	0.780	0.684	*0.06*	0.657	0.718
Mn	0.005	*0.00*		0.007					0.006	*0.00*	0.005	0.007				0.006
Ca	0.913	*0.03*	0.892	0.927	0.934	*0.01*	0.929	0.940	0.912	*0.04*	0.884	0.935	0.924	*0.02*	0.912	0.931
Na	0.032	*0.01*	0.028	0.037	0.043	*0.01*	0.039	0.046	0.033	*0.00*	0.030	0.034	0.040	*0.01*	0.037	0.043
sum	4.032	*0.01*	3.962	4.090	4.040	*0.01*	3.818	4.265	4.027	*0.03*	3.941	4.101	4.041	*0.01*	3.895	4.211

* FeOt was measured on the microprobe as FeO. Italicized values in parentheses are from Droop's (1987) allocation.

Table 3-3, continued. Bone Springs Sill clinopyroxene compositions.

lithology	LBZ mzgb				LBZ mzgb				CZ mzgb				CZ mzgb			
Sample	BSS-12				BSS-12				BS05-19				BS05-19			
sector	low-Z				high-Z				low-Z				high-Z			
number	n=3				n=5				n=3				n=3			
	mean	*2s*	Min	Max	mean	*2s*	Min	Max	mean	*2σ*	Min	Max	mean	*2s*	Min	Max
SiO_2	49.10	*2.36*	48.27	50.45	45.88	*0.96*	45.22	46.47	49.03	*1.33*	48.36	49.69	45.24	*5.26*	43.10	48.18
Al_2O_3	3.79	*0.92*	3.33	4.25	6.96	*0.95*	6.48	7.58	4.48	*1.07*	3.88	4.90	7.33	*4.23*	4.94	8.97
TiO_2	1.84	*0.45*	1.58	1.97	3.63	*0.53*	3.28	3.88	2.32	*0.74*	1.91	2.62	4.02	*3.02*	2.36	5.30
***FeOt**	8.17	*1.07*	7.85	8.79	7.46	*0.88*	6.95	8.07	7.31	*0.59*	6.97	7.51	7.93	*0.65*	7.74	8.31
***(FeO)**	*5.55*	*1.89*	*4.67*	*6.55*	*5.08*	*1.40*	*4.07*	*5.89*	*5.23*	*0.20*	*5.12*	*5.31*	*5.45*	*1.45*	*4.77*	*6.22*
***(Fe_2O_3)**	*2.91*	*2.55*	*1.44*	*3.74*	*2.65*	*0.66*	*2.41*	*3.20*	*2.31*	*0.46*	*2.06*	*2.51*	*2.76*	*1.85*	*1.69*	*3.31*
MgO	13.03	*0.89*	12.71	13.54	12.39	*0.55*	11.97	12.64	13.73	*0.54*	13.42	13.94	11.71	*1.01*	11.21	12.22
MnO	0.20	*0.24*		0.34	0.15	*0.06*		0.19	0.15	*0.24*		0.27	0.19	*0.14*		0.27
CaO	23.35	*1.35*	22.57	23.74	23.14	*1.06*	22.64	23.85	22.94	*1.10*	22.49	23.55	23.37	*1.08*	22.77	23.82
Na_2O	0.65	*0.25*	0.51	0.75	0.51	*0.13*	0.42	0.59	0.50	*0.06*	0.49	0.54	0.56	*0.11*	0.50	0.60
Total	100.14	*1.63*	99.53	101.06	100.18	*0.98*	99.59	100.77	100.50	*0.59*	100.21	100.80	100.41	*2.30*	99.09	101.18
***(Total)**	*100.43*	*1.82*	*99.67*	*101.44*	*100.45*	*1.04*	*99.84*	*101.09*	*100.73*	*0.61*	*100.44*	*101.05*	*100.69*	*2.48*	*99.26*	*101.50*
cations allocated assuming 6 O's																
Si	1.844	*0.08*	1.818	1.893	1.724	*0.05*	1.691	1.750	1.824	*0.04*	1.804	1.847	1.703	*0.21*	1.621	1.823
Al	0.168	*0.04*	0.147	0.187	0.308	*0.04*	0.288	0.334	0.197	*0.05*	0.170	0.215	0.325	*0.19*	0.220	0.398
Ti	0.052	*0.01*	0.045	0.056	0.103	*0.01*	0.093	0.109	0.065	*0.02*	0.053	0.074	0.114	*0.08*	0.067	0.150
***Fe*t**	0.257	*0.03*	0.246	0.275	0.235	*0.03*	0.217	0.255	0.227	*0.02*	0.216	0.233	0.250	*0.02*	0.244	0.260
***(Fe2)**	*0.246*	*0.03*	*0.235*	*0.260*	*0.226*	*0.03*	*0.207*	*0.247*	*0.221*	*0.02*	*0.211*	*0.226*	*0.240*	*0.02*	*0.232*	*0.249*
***(Fe3)**	*0.123*	*0.13*	*0.048*	*0.161*	*0.108*	*0.05*	*0.092*	*0.146*	*0.088*	*0.02*	*0.076*	*0.097*	*0.113*	*0.09*	*0.059*	*0.145*
Mg	0.730	*0.06*	0.709	0.762	0.694	*0.03*	0.675	0.705	0.761	*0.03*	0.744	0.771	0.657	*0.06*	0.629	0.689
Mn	0.006	*0.01*		0.011	0.005	*0.00*		0.006	0.005	*0.01*		0.009	0.006	*0.00*		0.009
Ca	0.939	*0.06*	0.907	0.959	0.931	*0.04*	0.916	0.955	0.914	*0.04*	0.899	0.938	0.942	*0.04*	0.923	0.960
Na	0.047	*0.02*	0.038	0.055	0.038	*0.01*	0.030	0.043	0.036	*0.00*	0.035	0.039	0.041	*0.01*	0.036	0.044
sum	4.044	*0.05*	3.910	4.198	4.036	*0.02*	3.909	4.158	4.030	*0.01*	3.922	4.126	4.038	*0.03*	3.740	4.333

* FeOt was measured on the microprobe as FeO. Italicized values in parentheses are from Droop's (1987) allocation.

Table 3-3, continued. Bone Springs Sill clinopyroxene compositions.

lithology	CZ mzgb				CZ mzgb				CZ mzgb				CZ mzgb			
Sample	BS05-13				BS05-13				BS04-4				BS04-4			
sector	low-Z				high-Z				low-Z				high-Z			
number	n=8				n=8				n=2				n=2			
	mean	*2σ*	Min	Max	mean	*2σ*	Min	Max	mean	*2σ*	Min	Max	mean	*2σ*	Min	Max
SiO_2	48.74	*0.81*	48.16	49.20	45.15	*4.42*	41.70	48.92	49.43	*0.01*	49.42	49.43	46.60	*0.95*	46.26	46.93
Al_2O_3	4.50	*0.43*	4.22	4.83	7.49	*3.19*	4.95	9.94	3.48	*0.14*	3.43	3.53	6.59	*0.98*	6.24	6.93
TiO_2	2.57	*0.56*	2.14	2.82	4.21	*2.29*	2.41	5.91	1.82	*0.08*	1.80	1.85	3.41	*0.51*	3.23	3.59
***FeOt**	7.53	*0.54*	7.22	7.95	7.97	*1.05*	7.27	9.00	8.36	*1.15*	7.96	8.77	7.81	*1.03*	7.45	8.18
***(FeO)**	*5.87*	*1.16*	*4.99*	*6.60*	*5.96*	*1.44*	*5.37*	*7.68*	*6.24*	*1.13*	*5.84*	*6.64*	*5.94*	*0.23*	*5.86*	*6.02*
***(Fe_2O_3)**	*1.85*	*1.08*	*0.93*	*2.48*	*2.24*	*0.93*	*1.47*	*2.81*	*2.36*	*0.02*	*2.35*	*2.37*	*2.08*	*1.41*	*1.59*	*2.58*
MgO	13.44	*0.37*	13.15	13.69	11.69	*1.39*	10.48	12.82	13.08	*0.65*	12.85	13.31	12.26	*0.24*	12.17	12.34
MnO	0.15	*0.14*		0.26	0.16	*0.15*		0.28	0.24	*0.08*	0.22	0.27				0.15
CaO	22.68	*0.64*	22.30	23.07	22.59	*0.54*	22.23	23.00	23.04	*0.11*	23.00	23.08	22.73	*0.52*	22.54	22.91
Na_2O	0.45	*0.11*	0.38	0.52	0.56	*0.14*	0.44	0.65	0.47	*0.05*	0.45	0.49	0.52	*0.11*	0.48	0.56
Total	100.06	*0.45*	99.81	100.42	99.85	*1.40*	98.87	100.72	99.93	*0.25*	99.84	100.01	100.05	*1.39*	99.56	100.55
***(Total)**	*100.25*	*0.53*	*99.97*	*100.67*	*100.07*	*1.41*	*99.08*	*100.87*	*100.16*	*0.25*	*100.07*	*100.25*	*100.26*	*1.53*	*99.72*	*100.80*
cations allocated assuming 6 O's																
Si	1.822	*0.03*	1.797	1.841	1.705	*0.15*	1.595	1.828	1.858	*0.00*	1.857	1.860	1.750	*0.02*	1.742	1.758
Al	0.198	*0.02*	0.186	0.212	0.334	*0.15*	0.218	0.448	0.154	*0.01*	0.152	0.156	0.292	*0.05*	0.275	0.308
Ti	0.072	*0.02*	0.060	0.079	0.120	*0.07*	0.068	0.170	0.052	*0.00*	0.051	0.052	0.096	*0.02*	0.091	0.102
***Fe*t**	0.235	*0.02*	0.225	0.249	0.252	*0.03*	0.231	0.281	0.263	*0.04*	0.250	0.276	0.245	*0.03*	0.235	0.256
***(Fe2)**	*0.230*	*0.02*	*0.218*	*0.243*	*0.245*	*0.03*	*0.225*	*0.277*	*0.255*	*0.04*	*0.243*	*0.268*	*0.239*	*0.02*	*0.230*	*0.248*
***(Fe3)**	*0.067*	*0.05*	*0.029*	*0.097*	*0.084*	*0.04*	*0.048*	*0.111*	*0.087*	*0.00*	*0.086*	*0.088*	*0.076*	*0.06*	*0.055*	*0.098*
Mg	0.749	*0.02*	0.734	0.761	0.658	*0.07*	0.598	0.722	0.733	*0.03*	0.721	0.745	0.686	*0.01*	0.683	0.689
Mn	0.005	*0.00*		0.008	0.005	*0.00*		0.009	0.008	*0.00*	0.007	0.009				0.005
Ca	0.908	*0.02*	0.894	0.923	0.914	*0.02*	0.904	0.932	0.928	*0.01*	0.926	0.930	0.914	*0.01*	0.909	0.919
Na	0.032	*0.01*	0.028	0.038	0.041	*0.01*	0.032	0.048	0.034	*0.00*	0.033	0.035	0.038	*0.01*	0.035	0.041
sum	4.022	*0.02*	3.924	4.112	4.028	*0.02*	3.645	4.437	4.030	*0.00*	3.996	4.064	4.022	*0.02*	3.971	4.077

* FeOt was measured on the microprobe as FeO. Italicized values in parentheses are from Droop's (1987) allocation.

Table 3-3, continued. Bone Springs Sill clinopyroxene compositions.

lithology	UBZ micro-mzgb				UBZ micro-mzgb				L. margin, micro-mzgb			CZ mzsy		CZ mzsy
Sample	BS06-71				BS06-71				BS06-37			BS06-50		BS06-59
sector	low-Z				high-Z				core	rim	mantle	rim	mantle	core
number	n=3				n=3									
	mean	*2σ*	Min	Max	mean	*2σ*	Min	Max						
SiO_2	48.12	*0.79*	47.67	48.37	44.29	*2.06*	43.12	45.08	47.87	47.87	48.45	48.92	50.08	48.99
Al_2O_3	4.81	*0.21*	4.71	4.92	8.17	*1.99*	7.43	9.30	5.40	5.05	3.43	3.54	0.59	2.99
TiO_2	2.62	*0.24*	2.51	2.76	4.31	*1.12*	3.90	4.95	2.75	2.55	2.48	1.84	0.93	1.34
***FeOt**	6.93	*0.66*	6.57	7.22	7.59	*0.65*	7.22	7.83	6.86	6.90	10.76	11.76	23.49	9.58
***(FeO)**	*5.55*	*1.24*	*4.92*	*6.16*	*5.14*	*0.72*	*4.80*	*5.52*	*5.34*	*4.63*	*9.23*	*9.31*	*16.50*	*7.17*
***(Fe_2O_3)**	*1.53*	*1.93*	*0.46*	*2.31*	*2.72*	*0.36*	*2.57*	*2.92*	*1.69*	*2.52*	*1.70*	*2.72*	*7.77*	*2.68*
MgO	13.50	*0.58*	13.24	13.81	11.54	*0.70*	11.14	11.79	13.81	13.23	10.24	10.28	3.06	12.38
MnO	0.21	*0.11*	0.15	0.25	0.15	*0.13*		0.20			0.17	0.39	0.45	0.27
CaO	22.28	*1.22*	21.90	22.98	23.13	*1.06*	22.53	23.55	21.83	23.56	20.91	22.45	14.40	22.56
Na_2O	0.43	*0.12*	0.37	0.48	0.55	*0.05*	0.52	0.57	0.45	0.49	1.28	0.87	4.94	0.48
Total	98.91	*2.66*	98.09	100.44	99.76	*0.27*	99.67	99.92	99.11	99.67	97.74	100.05	98.00	98.63
***(Total)**	*99.06*	*2.79*	*98.23*	*100.67*	*100.03*	*0.27*	*99.93*	*100.19*	*99.28*	*99.92*	*97.91*	*100.32*	*98.78*	*98.90*
cations allocated assuming 6 O's														
Si	1.815	*0.03*	1.800	1.830	1.676	*0.07*	1.636	1.701	1.799	1.798	1.878	1.867	2.038	1.876
Al	0.214	*0.01*	0.210	0.216	0.364	*0.09*	0.330	0.416	0.239	0.224	0.157	0.159	0.028	0.135
Ti	0.074	*0.01*	0.072	0.077	0.123	*0.03*	0.111	0.141	0.078	0.072	0.072	0.053	0.028	0.038
***Fe*t**	0.219	*0.02*	0.208	0.230	0.240	*0.02*	0.228	0.248	0.215	0.217	0.349	0.375	0.799	0.307
***(Fe2)**	*0.214*	*0.02*	*0.207*	*0.225*	*0.231*	*0.02*	*0.219*	*0.240*	*0.211*	*0.209*	*0.342*	*0.363*	*0.718*	*0.297*
***(Fe3)**	*0.057*	*0.08*	*0.014*	*0.089*	*0.111*	*0.02*	*0.100*	*0.121*	*0.060*	*0.103*	*0.057*	*0.096*	*0.304*	*0.100*
Mg	0.759	*0.01*	0.752	0.766	0.651	*0.04*	0.630	0.663	0.774	0.741	0.592	0.585	0.186	0.707
Mn	0.007	*0.00*	0.005	0.008	0.005	*0.00*		0.006			0.005	0.013	0.015	0.009
Ca	0.900	*0.03*	0.888	0.916	0.938	*0.04*	0.916	0.952	0.879	0.948	0.868	0.918	0.628	0.926
Na	0.032	*0.01*	0.027	0.036	0.040	*0.00*	0.038	0.042	0.033	0.035	0.096	0.064	0.390	0.035
sum	4.019	*0.03*	3.962	4.079	4.038	*0.01*	3.889	4.170	4.017	4.035	4.017	4.034	4.116	4.033

* FeOt was measured on the microprobe as FeO. Italicized values in parentheses are from Droop's (1987) allocation.

zonation patterns. It would be meaningless, for example, to compare Mg-depleted domains of sector-zoned crystals from one rock to Mg-enriched sector domains in another. Ti and Al are enriched and Si and Mg depleted in the (100) and (010) sectors relative to the (001) sectors. Fe is often slightly enriched in the (100) and (010) sectors as well, but Ca is not partitioned between sectors. It is difficult to differentiate (100) and (010) in backscatter images of grains that are often subhedral or are crystal fragments. However, the high average Z (atomic number) of (100) and (010) makes these sectors easily differentiated from low average Z (001) sectors in all cases when they are present, and so sector zones are differentiated in this study as high-Z sectors and low-Z sectors only. Table 3-4 shows the partition coefficient for high-Z/low-Z sectors (likely [100 and 010]/001), for clinopyroxenes from the BSS. Ti and Al are strongly partitioned into the high-Z sector (D_{Al}=1.5-1.9; D_{Ti}=1.5-2.0) while Na is less so (D_{Na}=0.8-1.3, though all but one sample have $D_{Na}\geq1$), and Si and Mg are partitioned into the low-Z sectors (D_{Si}=0.9; $D_{Mg}\approx0.9$). When treated as Fe*t*, Fe appears to be variably partitioned, though, when allocated to Fe^{2+} and Fe^{3+} after Droop (1987), Fe^{3+} is more commonly partitioned into the high-Z sector with Al and Si.

Most data shown in Table 3-3 are averages of pyroxene sector compositions by sample, with a low-Z and high-Z mean composition with standard deviation and minimum and maximum values for each measured oxide. Because they include analyses of cores and rims and of relatively early and late crystals, information on zonation within individual grains is obscured. To assess this, several core-to-rim transects of clinopyroxene grains were made across high-Z and low-Z sectors. These data are shown in Figure 3-9. In general, there is a slight decrease in Al and Ti pfu and increase in Si pfu from core to rim. Some outermost rims show a marked decrease in Mg pfu. With the exception of these Mg-poor rims, core-to-rim zoning is minimal.

Table 3-4. Partition coefficients for high-Z/low-Z domains in sector-zoned Bone Springs Sill clinopyroxenes. The number of analyses, integrated compositions and 2σ errors are shown in Table 3-3.

lithology	LBZ mzgb	LBZ mzgb	LBZ mzgb	LBZ mzgb	LBZ mzgb	CZ mzgb	CZ mzgb	CZ mzgb	U. margin, mzgb
sample	BS04-10 **D (high-Z/low-Z)**	BS04-2 **D (high-Z/low-Z)**	BS04-7 **D (high-Z/low-Z)**	BS04-9 **D (high-Z/low-Z)**	BSS-12 **D (high-Z/low-Z)**	BS05-19 **D (high-Z/low-Z)**	BS05-13 **D (high-Z/low-Z)**	BS04-4 **D (high-Z/low-Z)**	BS06-71 **D (high-Z/low-Z)**
measured									
SiO_2	0.94	0.91	0.91	0.91	0.93	0.92	0.93	0.94	0.92
Al_2O_3	1.49	1.66	1.90	1.85	1.84	1.63	1.67	1.89	1.70
TiO_2	1.52	1.73	1.80	1.75	1.98	1.73	1.64	1.87	1.64
FeOt	1.07	0.98	1.03	1.07	0.91	1.09	1.06	0.93	1.10
***(FeO)**	*1.09*	*0.88*	*0.96*	*0.94*	*0.91*	*1.04*	*1.02*	*0.95*	*0.93*
***(Fe_2O_3)**	*1.02*	*1.30*	*1.21*	*1.40*	*0.91*	*1.19*	*1.21*	*0.88*	*1.77*
MgO	0.89	0.90	0.84	0.88	0.95	0.85	0.87	0.94	0.86
CaO	0.99	1.01	1.02	1.00	0.99	1.02	1.00	0.99	1.04
Na_2O	1.14	1.01	1.34	1.22	0.79	1.11	1.25	1.12	1.26

*Fe^{2+}/Fe^{3+} partitioned after Droop (1987)

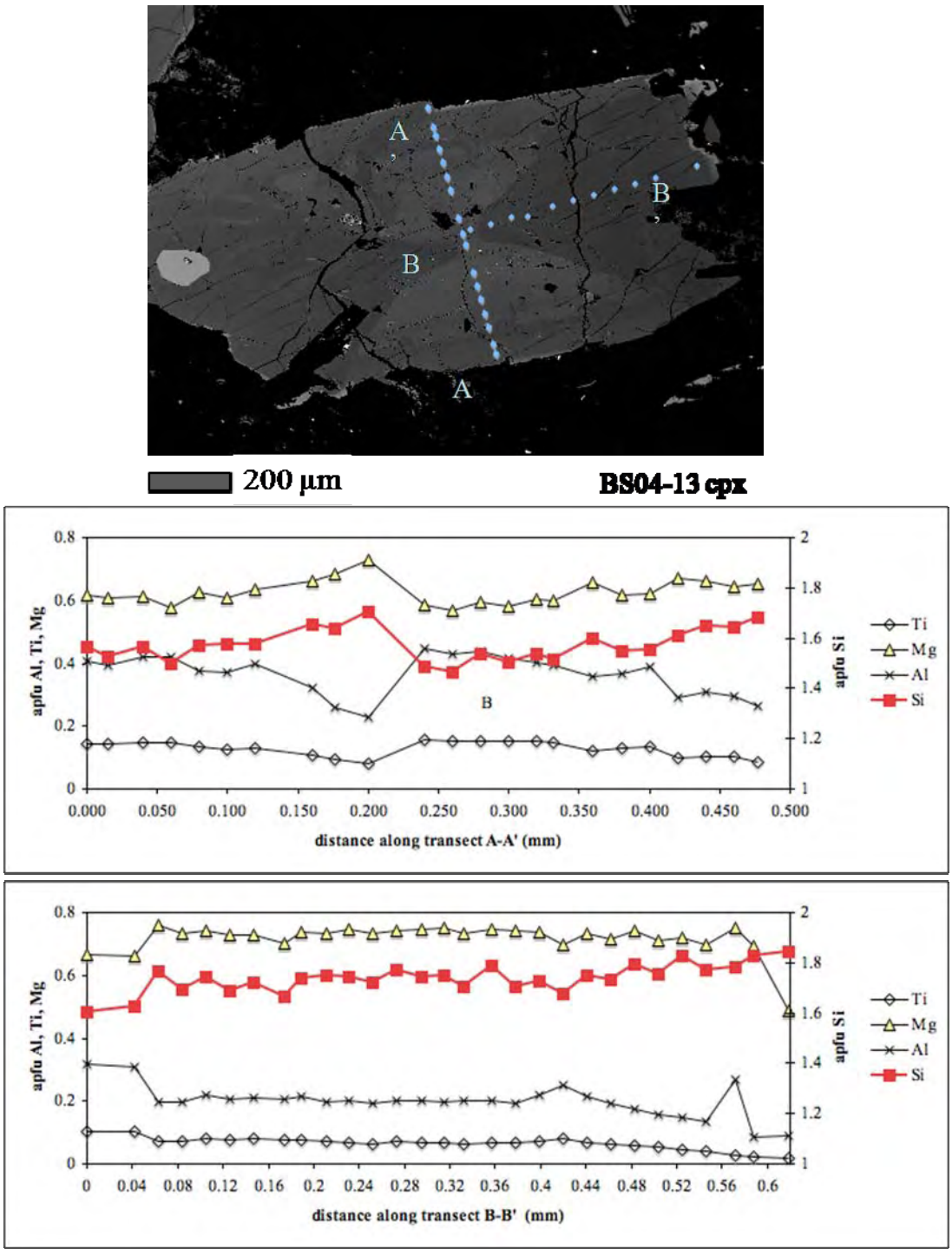

Figure 3-9. Compositional transects of Bone Springs Sill clinopyroxenes. 3-9A: Central zone monzogabbro BS04-13. [100] sections are higher-z (lighter color) and [001] sections are lower-z (darker in color).

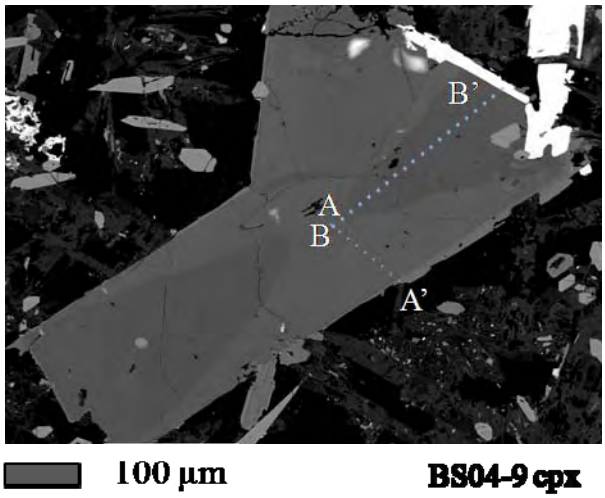

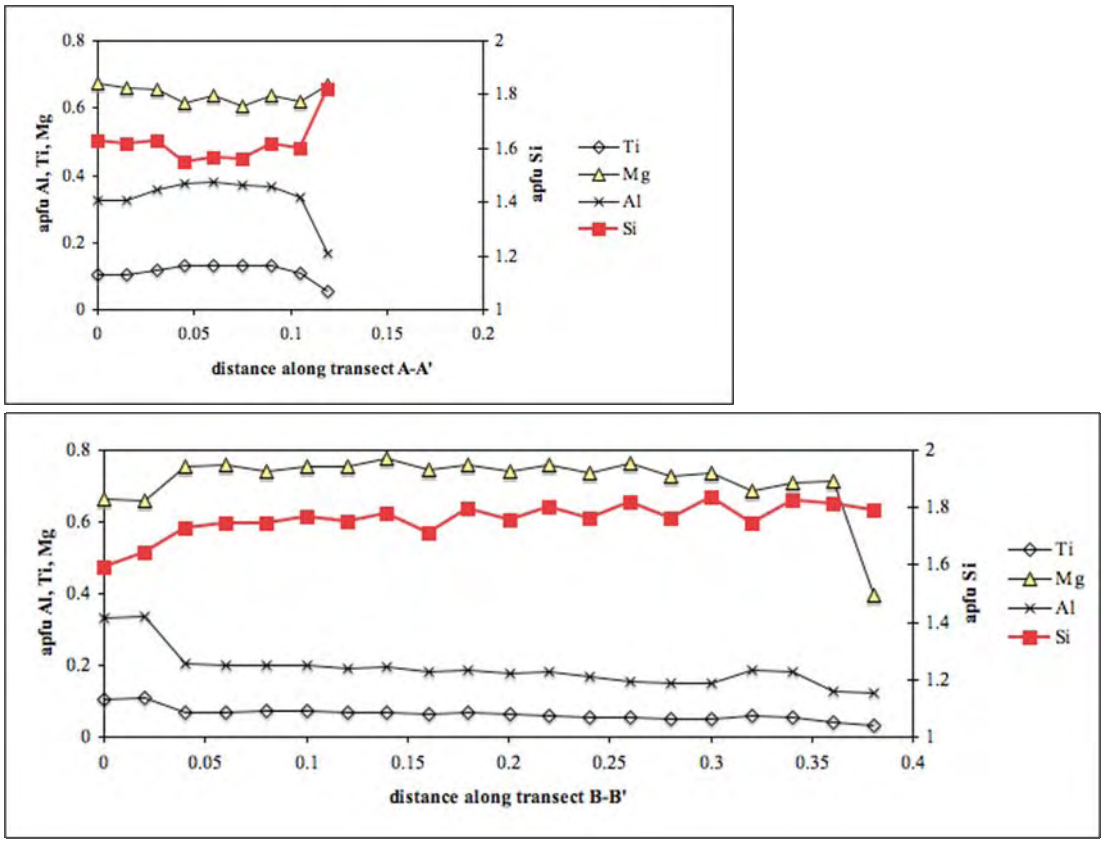

Figure 3-9, continued. Compositional transects of Bone Springs Sill clinopyroxenes. 3-9B: Lower border zone monzogabbro BS04-9.

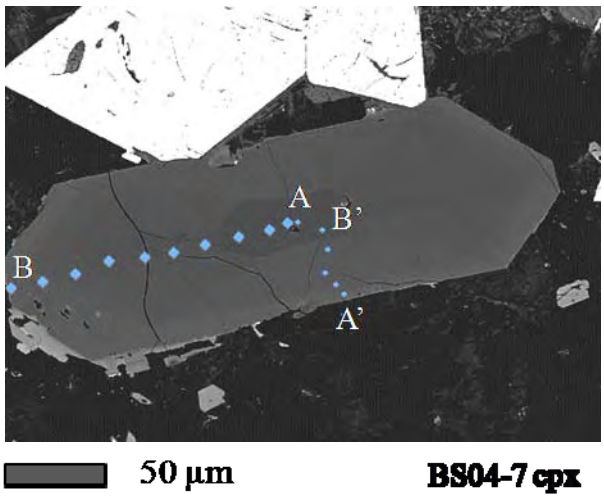

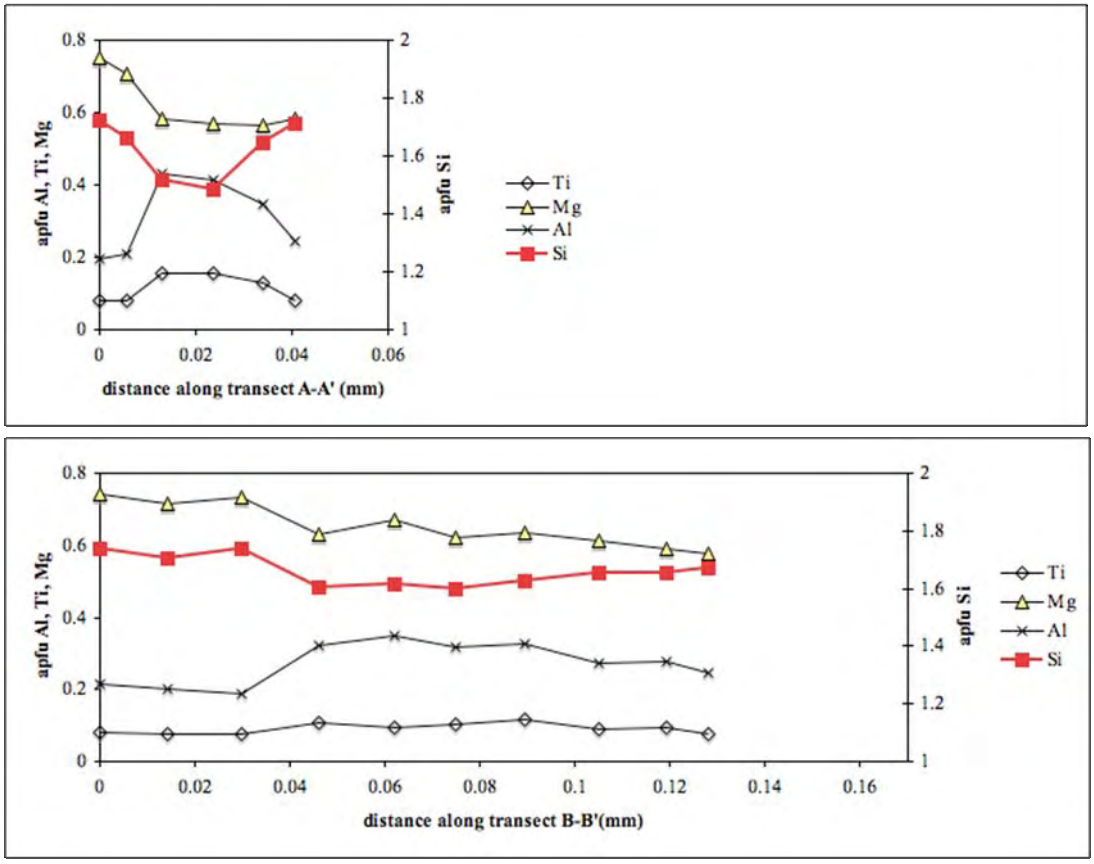

Figure 3-9, continued. Compositional transects of Bone Springs Sill clinopyroxenes. 3-9C: Lower border zone monzogabbro BS04-7.

In addition to sector-zoned pyroxenes from the LBZ, CZ, and UBZ, Table 3-3 contains data from an unzoned pyroxene grain in the lower chill zone and cores and rims from monzosyenite pyroxenes. Phenocryst clinopyroxenes in the lower chill margin have no perceptible sector zonation but those in the upper border zone and chill margin do. Figure 3-10a shows that all BSS pyroxenes cluster in the diopside field except for one Fe-rich rim in one monzosyenite sample. Figure 3-10b shows that all are quadrilateral pyroxenes with a minor jadeite and acmite components, except for the aegirine-augite rim.

The core from the lower chill zone is the most magnesian clinopyroxene in BSS (*Mg'* = 100*molar Mg/(Mg +Fe) = 78) and may represent a crystal carried in with the intruding magma. The lower margin clinopyroxene core and the integrated compositions from LBZ and CZ mafic samples span *Mg'* 78-72, the monzosyenite core analysis has an *Mg'* of 70, while the rims in the monzosyenite and the mantle in the lower chill zone have *Mg'* of 62 and 63, respectively. The aegirine-augite mantle in the monzosyenite sample has an *Mg'* of 21. Figures 3-11a and 3-11b show the variation in Na and Ti atoms per formula unit (apfu) with *Mg'* by lithology. The LBZ and CZ mafic pyroxenes show considerable overlap for both Na and Ti, but there is a trend of Na-enrichment anticorrelated with *Mg'* while Ti shows less regular variation. The most magnesian pyroxene is not the most Al- and Ti-rich. Figure 3-12 shows the strong correlation of Al and Ti.

Biotite

Biotite is a present in at least trace amounts in each BSS lithology. Lower border zone samples contain from 1-4 modal% biotite while CZ mafic rocks contain <1.5 modal% biotite. The UBZ, the margins, and the monzosyenite contain trace biotite. In LBZ rocks biotite occurs as early grains that postdate olivine crystallization and commonly include plagioclase and

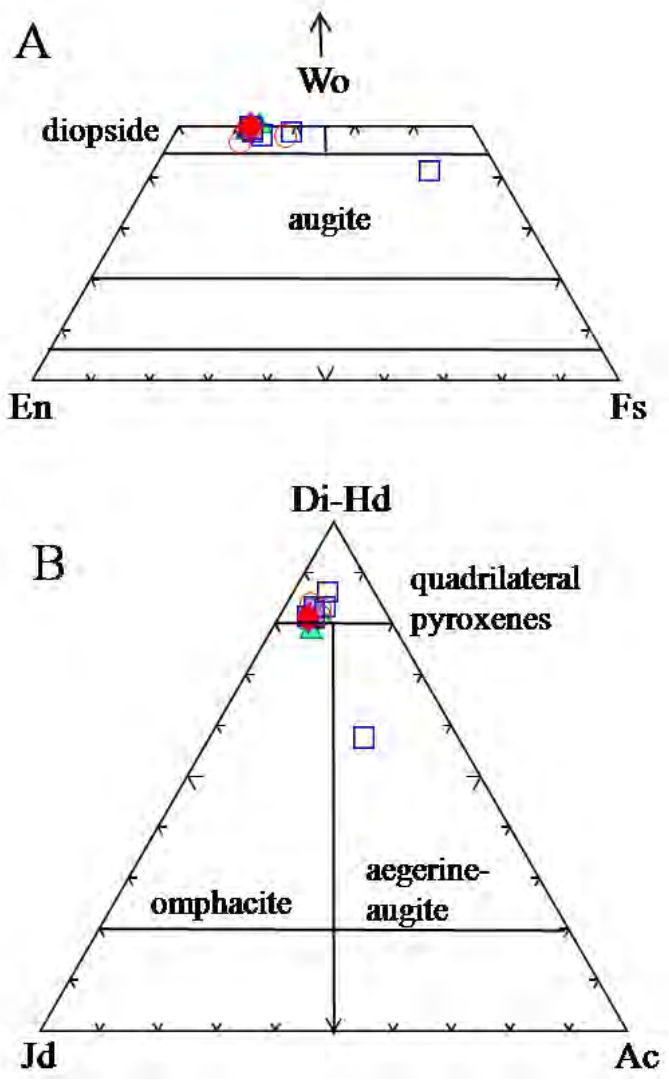

Figure 3-10. Bone Springs Sill clinopyroxenes. Pyroxenes are diopsidic except for one late-stage rim of aegirine-augite composition. Classification diagrams after Morimoto et al. (1988).

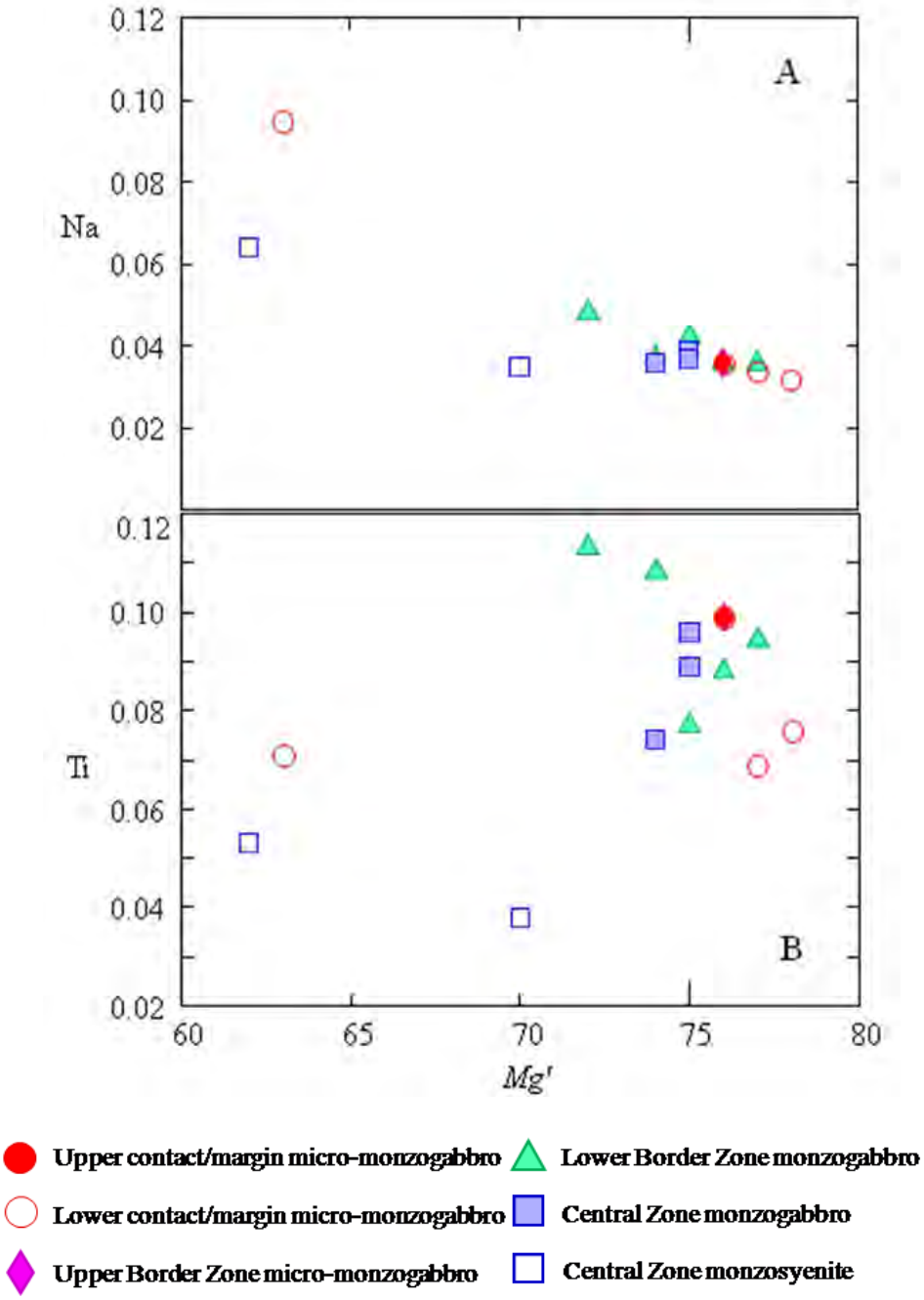

Figure 3-11. Bone Springs Sill clinopyroxene compositions: *Mg'* vs. atoms per formula (apfu) for (A) Na and (B) Ti.

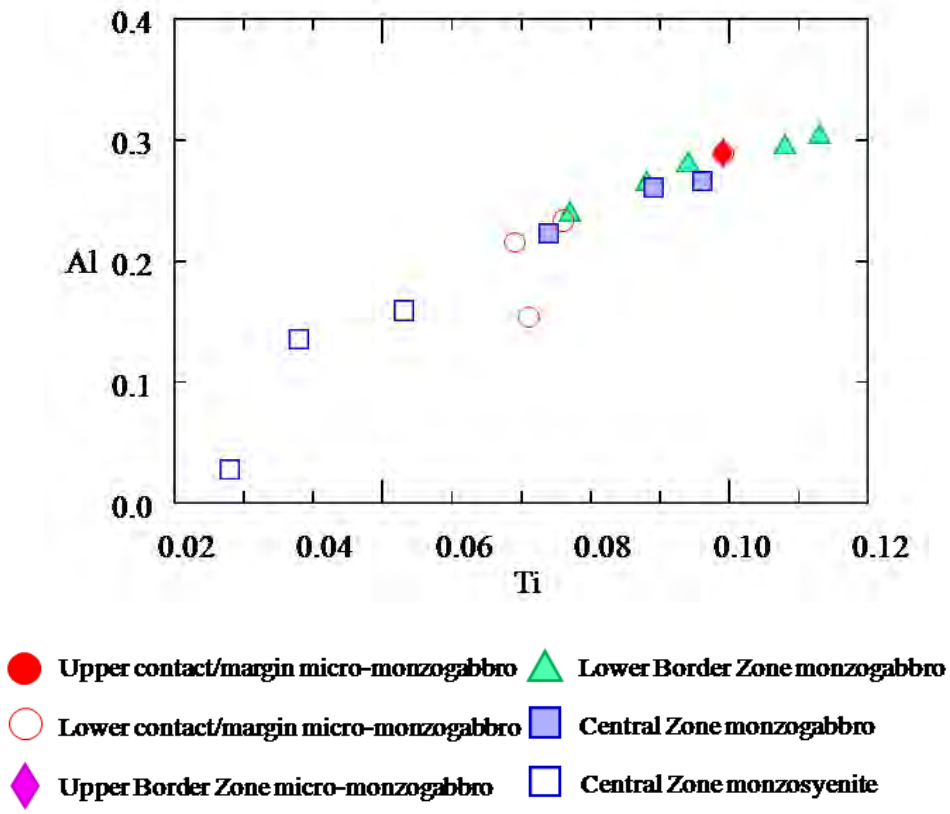

Figure 3-12. Bone Springs Sill clinopyroxene Al vs. Ti. Units are in atoms per formula unit. Although almost all BSS pyroxenes plot closely together on classification diagrams such as Figure 3-11, the Al-Ti diagram shows spread between the cumulate monzogabbros and the late-forming monzosyenites. The pyroxenes in the lower margin have intermediate values, demonstrating and increase in Al and Ti in the early LBZ cumulate pyroxenes followed by a decrease in pyroxene Al and Ti with further crystallization.

apatite. In some samples these early grains reach 1.5 mm in length. Other LBZ biotites are scattered and interstitial and are <300 μm. Biotite occurs in CZ rocks as <250 μm interstitial grains. In both LBZ and CZ rocks, biotite rims some olivine, pyroxene, and Fe-Ti oxide grains. Rarely, a reddish fine-grained biotite rims mafic minerals and this is interpreted to be from a late magmatic/hydrothermal episode.

Table 3-5 contains analyses of BSS biotite and mole fractions of Mg, Fe, F, and Cl calculated after Zhu and Sverjensky (1992). Bone Springs biotites are Ti-rich, containing TiO_2 up to 10 wt.%. In the lower margin and the UBZ, the few biotites analyzed have X_{Mg} 0.41-0.51, and the total range in the sill is ~0.2-0.7. Fluorine wt.% is as high as 2.7% in a few CZ mafic rocks, but the greatest number of biotites have F contents an order of magnitude lower. Bone Springs Sill biotite Cl is < 0.1 wt.%. Figure 3-13 shows the distributions of X_{Mg}, Ti wt.%, and X_F by lithology. The CZ mafic rocks and the LBZ have populations centered around similar X_{Mg} and TiO_2 wt%, though in both cases the LBZ biotites show considerably more spread. The CZ biotites have markedly higher X_F. Chapter 4 contains more detailed discussion of biotite occurrence and composition in BSS, especially with regards to halogen contents.

Plagioclase

Plagioclase occurs as a primary mineral in all Bone Springs sill lithologies. Feldspar analyses are shown in Table 3-6 and are plotted on ternary classification diagrams in Figure 3-14.

Plagioclase occurs in the margin rocks as 100-150 μm altered microphenocrysts. Although their cores appear intact in thin section they yield low totals under microprobe analysis. The UBZ samples contain plagioclase feldspars up to 300 μm. While most plagioclase grains are partially altered to analcime, some are included in, and armored by, clinopyroxene

Table 3-5. Bone Springs Sill biotite compositions. After the first 6 analyses from 4 samples, compositions are presented as averages by sample. Two of the BS04-13 analyses are presented apart from their sample average because they represent a distinct, late stage (hydrothermal?) population. Complete BSS biotite analyses can be found in Appendix 1.

lithology	UBZ mzgb	L. Marg. mzgb	LBZ mzgb	LBZ mzgb	CZ mzgb	CZ mzgb
sample:	BS05-29	BS06-37	BS06-45	BS06-45	BS04-13	BS04-13
number	-	-	-	-	-	-
desc.					v. late	v. late
SiO_2	31.44	33.58	35.32	36.36	32.99	32.55
Al_2O_3	15.31	14.29	14.02	13.51	26.03	27.05
TiO_2	5.94	7.48	8.07	6.87	0.73	0.87
MgO	11.52	9.22	12.86	14.83	0.66	0.73
FeO	21.22	19.32	16.16	13.16	25.14	23.66
MnO						0.27
CaO	0.33	0.10		0.05	0.27	0.16
K_2O	5.90	9.39	10.13	8.91	10.06	10.37
Na_2O	0.24	0.39	0.64	0.47	0.07	
BaO	0.40					
F	0.14	0.17	1.87	1.87		
Cl	0.014	0.059	0.060	0.085		
Total	92.40	93.91	98.33	95.31	95.95	95.65
atoms based on 22 anions						
Si	5.018	5.299	5.498	5.707	5.116	5.039
Al (iv)	2.880	2.657	2.502	2.293	2.884	2.961
Al (vi)			0.035	0.103	0.936	0.987
Ti	0.713	0.888	0.945	0.811	0.085	0.101
Mg	2.741	2.169	2.985	3.470	0.153	0.168
Fe	2.832	2.549	2.104	1.727	3.260	3.063
Mn						0.035
Ca	0.057	0.017	0.000	0.008	0.045	0.026
K	1.201	1.890	2.012	1.784	1.990	2.048
Na	0.075	0.119	0.194	0.142	0.021	
Ba	0.025					
total cat.	15.542	15.588	16.274	16.045	14.490	14.429
F	0.070	0.083	0.920	0.930		
Cl	0.004	0.016	0.016	0.023		
OH*	3.926	3.901	3.065	3.047	4.000	4.000
			****mole fractions**			
X_{Fe}	0.508	0.540	0.417	0.345	0.965	0.960
X_{Mg}	0.492	0.460	0.589	0.674	0.251	0.274
X_F	0.018	0.021	0.230	0.233		
X_{Cl}	0.001	0.004	0.004	0.006		
X_{OH}	0.982	0.975	0.766	0.762	1.000	1.000

* OH = 4-F-Cl

Table 3-5, continued. Bone Springs Sill biotite compositions.

lithology	LBZ mzgb	*2σ*	LBZ mzgb	*2σ*	CZ mzgb	*2σ*	CZ mzgb	*2σ*
sample:	BS04-9		BS06-38		BS05-19		BS04-4	
number	n=13		n=3		10		6	
desc.								
SiO_2	35.45	*2.24*	36.47	*1.00*	35.57	*1.49*	35.93	*0.72*
Al_2O_3	14.06	*0.83*	14.14	*0.61*	13.08	*1.17*	14.04	*0.56*
TiO_2	7.91	*2.56*	7.30	*2.02*	7.71	*2.24*	8.49	*0.46*
MgO	11.82	*3.10*	13.69	*0.35*	11.19	*2.39*	9.47	*1.91*
FeO	17.20	*2.34*	14.82	*3.16*	18.83	*3.70*	20.53	*2.22*
MnO	0.25	*0.21*	0.23	*0.00*	0.25	*0.11*	0.23	*0.10*
CaO	0.25	*0.43*	0.09	*0.00*	0.31	*0.78*	0.09	*0.00*
K_2O	8.56	*1.00*	9.64	*0.50*	9.12	*1.07*	8.98	*0.87*
Na_2O	0.58	*0.20*	0.66	*0.59*	0.57	*0.17*	0.59	*0.19*
BaO	1.17	*1.99*			0.15	*0.05*		
F	0.35	*0.24*	1.50	*0.03*	2.14	*0.61*	1.10	*0.20*
Cl	0.028	*0.02*	0.044	*0.05*	0.031	*0.03*	0.040	*0.00*
Total	96.70	*1.51*	97.73	*1.91*	97.82	*2.80*	98.81	*1.03*
atoms based on 22 anions								
Si	5.377	*0.270*	5.579	*0.118*	5.659	*0.208*	5.502	*0.063*
Al (iv)	2.499	*0.184*	2.421	*0.118*	2.329	*0.195*	2.488	*0.062*
Al (vi)	0.007	*0.052*	0.064	*0.022*	0.061	*0.107*	0.022	*0.038*
Ti	0.903	*0.296*	0.840	*0.237*	0.921	*0.262*	0.978	*0.059*
Mg	2.670	*0.666*	3.123	*0.049*	2.652	*0.521*	2.162	*0.409*
Fe	2.183	*0.321*	1.896	*0.392*	2.507	*0.548*	2.629	*0.317*
Mn	0.008	*0.031*	0.010		0.024	*0.035*	0.015	*0.034*
Ca	0.034	*0.071*	0.005	*0.017*	0.047	*0.128*	0.002	*0.012*
K	1.656	*0.202*	1.882	*0.101*	1.849	*0.200*	1.754	*0.173*
Na	0.172	*0.057*	0.195	*0.176*	0.177	*0.051*	0.176	*0.055*
Ba	0.038	*0.112*			0.003	*0.009*		
total cat.	15.545		16.016		16.229		15.730	
F	0.167	*0.115*	0.725	*0.021*	1.075	*0.305*	0.532	*0.102*
Cl	0.007	*0.005*	0.011	*0.013*	0.007	*0.010*	0.002	*0.009*
OH*	3.825	*0.118*	3.264	*0.024*	2.918	*0.310*	3.466	*0.102*
				****mole fractions**				
X_{Fe}	0.452	*0.088*	0.385	*0.045*	0.492	*0.095*	0.551	*0.076*
X_{Mg}	0.549	*0.093*	0.628	*0.047*	0.520	*0.104*	0.454	*0.071*
X_F	0.042	*0.029*	0.181	*0.005*	0.269	*0.076*	0.133	*0.026*
X_{Cl}	0.002	*0.001*	0.003	*0.003*	0.002	*0.003*	0.000	*0.002*
X_{OH}	0.956	*0.029*	0.816	*0.006*	0.729	*0.077*	0.866	*0.026*

* OH = 4-F-Cl

** mole fractions calculated after Zhu and Sverjensky (1991)

Table 3-5, continued. Bone Springs Sill biotite compositions.

lithology	LBZ mzgb	*2σ*	LBZ mzgb	*2σ*	LBZ mzgb	*2σ*	LBZ mzgb	*2σ*
sample:	BS04-10		BS04-12		BS04-2		BS04-7	
number	n=10		n=4		n=10		n=9	
desc.								
SiO_2	35.60	*1.61*	35.76	*0.53*	35.06	*1.41*	34.71	*1.85*
Al_2O_3	14.73	*0.46*	13.44	*0.57*	13.84	*0.71*	13.72	*1.48*
TiO_2	8.37	*2.23*	8.54	*2.22*	7.66	*1.61*	7.86	*2.01*
MgO	12.66	*1.70*	10.22	*3.62*	9.16	*1.68*	8.36	*3.59*
FeO	15.65	*2.12*	19.28	*3.85*	20.62	*3.66*	22.04	*5.87*
MnO					0.27	*0.11*	0.29	*0.14*
CaO	0.18	*0.36*	0.18	*0.28*	0.23	*0.16*	0.23	*0.26*
K_2O	8.81	*0.64*	9.35	*0.66*	8.47	*0.91*	8.92	*1.12*
Na_2O	0.61	*0.29*	0.68	*0.15*	0.58	*0.20*	0.49	*0.26*
BaO	1.06	*0.77*			0.36	*0.48*	0.59	*1.64*
F	0.27	*0.16*	1.03	*0.47*	0.47	*0.27*	0.36	*0.20*
Cl	0.019	*0.02*	0.07	*0.19*	0.025	*0.02*	0.020	*0.01*
Total	97.27	*2.07*	98.10	*1.02*	96.22	*2.78*	96.99	*1.83*
atoms based on 22 anions								
Si	5.311	*0.175*	5.506	*0.112*	5.424	*0.145*	5.382	*0.142*
Al (iv)	2.588	*0.118*	2.422	*0.098*	2.514	*0.088*	2.499	*0.250*
Al (vi)	0.001	*0.006*	0.009	*0.030*	0.005	*0.019*	0.004	*0.027*
Ti	0.939	*0.246*	0.989	*0.251*	0.890	*0.161*	0.915	*0.222*
Mg	2.814	*0.351*	2.347	*0.844*	2.111	*0.331*	1.928	*0.780*
Fe	1.953	*0.294*	2.481	*0.480*	2.671	*0.543*	2.861	*0.830*
Mn					0.032	*0.026*	0.025	*0.041*
Ca	0.023	*0.057*	0.023	*0.049*	0.034	*0.034*	0.038	*0.045*
K	1.676	*0.125*	1.836	*0.132*	1.671	*0.167*	1.765	*0.245*
Na	0.177	*0.082*	0.202	*0.046*	0.173	*0.055*	0.146	*0.076*
Ba	0.031	*0.069*			0.009	*0.027*	0.016	*0.072*
total cat.	15.512		15.813		15.533		15.581	
F	0.126	*0.072*	0.504	*0.233*	0.186	*0.231*	0.176	*0.099*
Cl	0.005	*0.005*	0.019	*0.049*	0.006	*0.006*	0.005	*0.003*
OH*	3.869	*0.074*	3.477	*0.266*	3.807	*0.229*	3.819	*0.097*
				****mole fractions**				
X_{Fe}	0.410	*0.062*	0.517	*0.132*	0.558	*0.086*	0.597	*0.160*
X_{Mg}	0.590	*0.063*	0.485	*0.138*	0.443	*0.087*	0.404	*0.157*
X_F	0.031	*0.018*	0.126	*0.058*	0.047	*0.058*	0.044	*0.025*
X_{Cl}	0.001	*0.001*	0.005	*0.012*	0.002	*0.001*	0.001	*0.001*
X_{OH}	0.967	*0.018*	0.869	*0.066*	0.952	*0.057*	0.955	*0.024*

* OH = 4-F-Cl

** mole fractions calculated after Zhu and Sverjensky (1991)

Tale 3-5, continued. Bone Springs Sill biotite compositions.

lithology	CZ mzgb	*2σ*	CZ mzgb	*2σ*
sample:	BS04-13		BS05-19	
number	4		10	
desc.				
SiO_2	35.99	*0.87*	35.57	*1.49*
Al_2O_3	14.00	*0.71*	13.08	*1.17*
TiO_2	8.99	*0.40*	7.71	*2.24*
MgO	10.42	*1.51*	11.19	*2.39*
FeO	17.78	*2.04*	18.83	*3.70*
MnO	0.23	*0.05*	0.25	*0.11*
CaO	0.09	*0.00*	0.31	*0.78*
K_2O	9.38	*0.61*	9.12	*1.07*
Na_2O	0.56	*0.29*	0.57	*0.17*
BaO			0.15	*0.05*
F	1.90	*0.74*	2.14	*0.61*
Cl	0.025	*0.00*	0.031	*0.03*
Total	98.44	*0.82*	97.82	*2.80*
atoms based on 22 anions				
Si	5.602	*0.159*	5.659	*0.208*
Al (iv)	2.398	*0.159*	2.329	*0.195*
Al (vi)	0.085	*0.048*	0.061	*0.107*
Ti	1.053	*0.052*	0.921	*0.262*
Mg	2.418	*0.361*	2.652	*0.521*
Fe	2.315	*0.254*	2.507	*0.548*
Mn	0.015	*0.036*	0.024	*0.035*
Ca	0.015	*0.014*	0.047	*0.128*
K	1.862	*0.114*	1.849	*0.200*
Na	0.170	*0.088*	0.177	*0.051*
Ba			0.003	*0.009*
total cat.	15.933		16.229	
F	0.934	*0.366*	1.075	*0.305*
Cl	0.007	*0.003*	0.007	*0.010*
OH*	3.059	*0.366*	2.918	*0.310*
	****mole fractions**			
X_{Fe}	0.498	*0.062*	0.492	*0.095*
X_{Mg}	0.519	*0.066*	0.520	*0.104*
X_F	0.234	*0.092*	0.269	*0.076*
X_{Cl}	0.002	*0.001*	0.002	*0.003*
X_{OH}	0.765	*0.091*	0.729	*0.077*

* OH = 4-F-Cl

** mole fractions calculated after Zhu and Sverjensky (1991)

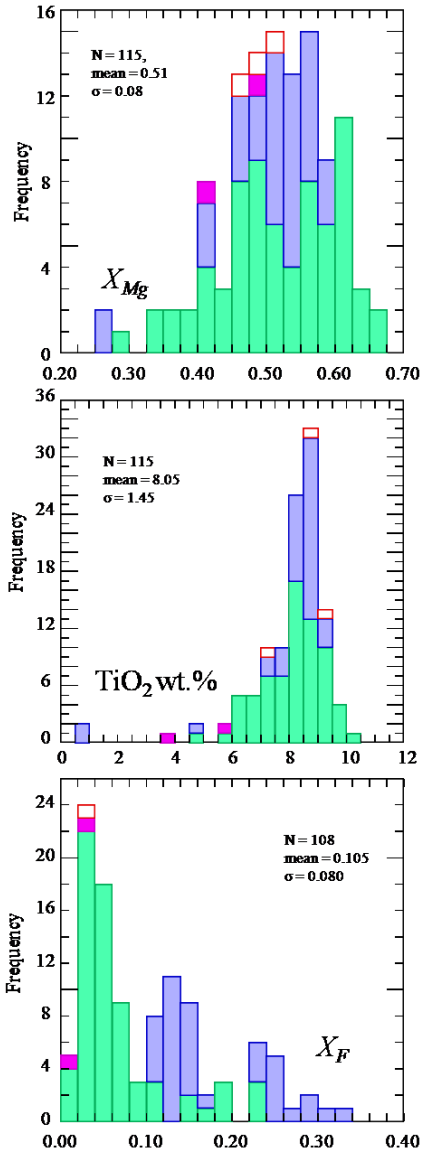

Figure 3-13. Histograms of X_{Mg}, TiO_2 wt.%, and X_F for Bone Springs Sill biotites. Purple = UBZ/margins micro-monzogabbro; green = LBZ monzogabbros; blue = CZ monzogabbro; red-bordered white = tertiary tephrite overlying Bone Springs Sill. The highest biotite X_{Mg} are in the LBZ; biotite TiO_2 contents are as high as ~10 wt.%; biotite X_F is highest in the more (slightly) evolved rocks of the CZ.

Table 3-6. Bone Springs Sill feldspar compositions. Determined by microprobe analysis. Compositional distributions are displayed in Figure 3-14. The abbreviation anlc = analcime.

Lithology	UBZ mzgb	UBZ mzgb	UBZ mzgb	UBZ mzgb	UBZ mzgb	UBZ mzgb	UBZ mzgb	UBZ mzgb	UBZ mzgb	UBZ mzgb	UBZ mzgb
Sample	BS06-29	BS06-29	BS06-29	BS06-29	BS06-30	BS06-30	BS06-30	BS06-72	BS06-72	BS06-72	BS06-72
desc.	core										with anlc
analysis	68	72	71	74	86	85	82	31	27	12	20
SiO_2	60.09	64.28	64.31	63.98	47.58	54.46	65.85	48.40	52.98	64.51	62.96
Al_2O_3	24.38	19.48	19.03	18.98	31.90	27.69	19.31	31.86	28.79	18.66	18.66
FeO	0.39	0.32	0.42	0.62	0.48	0.27		0.58	0.95	0.52	1.06
CaO	5.42	0.43	0.23	0.44	15.72	10.06	0.36	16.49	12.28	0.28	0.44
K_2O	0.79	10.06	11.19	11.28	0.15	0.57	11.74	0.04	0.17	12.18	12.95
Na_2O	7.42	4.02	3.45	3.07	2.25	4.97	2.75	2.49	4.59	3.60	1.79
BaO	0.36	0.23	0.21	0.21	0.16	0.30	0.23				0.95
SrO								0.56	0.45	0.31	0.68
Total	98.85	98.82	98.84	98.58	98.24	98.32	100.24	100.42	100.21	100.06	99.49
atoms per formula unit, based on 8 O's											
Si	2.710	2.950	2.964	2.958	2.220	2.498	2.982	2.222	2.406	2.961	2.905
Al	1.296	1.054	1.034	1.034	1.754	1.497	1.031	1.724	1.541	1.009	1.015
Fe	0.015	0.012	0.016	0.024	0.019	0.010		0.022	0.036	0.020	0.041
Ca	0.262	0.021	0.011	0.022	0.786	0.494	0.017	0.811	0.597	0.014	0.022
K	0.046	0.589	0.658	0.665	0.009	0.033	0.678	0.002	0.010	0.713	0.762
Na	0.649	0.358	0.308	0.275	0.203	0.442	0.241	0.222	0.404	0.320	0.160
Ba	0.006	0.004	0.004	0.004	0.003	0.005	0.004				0.017
Sr								0.015	0.012	0.008	0.018
sum	4.984	4.988	4.995	4.982	4.994	4.979	4.953	5.018	5.006	5.045	4.940
Mole Fractions											
An	0.27	0.02	0.01	0.02	0.79	0.51	0.02	0.78	0.59	0.01	0.02
Ab	0.68	0.37	0.32	0.29	0.20	0.46	0.26	0.21	0.40	0.31	0.17
Or	0.05	0.61	0.67	0.69	0.01	0.03	0.72	0.00	0.01	0.68	0.81

Table 3-6, continued. Bone Springs Sill feldspar compositions.

Lithology	LBZ mzgb	LBZ mzgb	LBZ mzgb	LBZ mzgb	LBZ mzgb	LBZ mzgb	LBZ mzgb	LBZ mzgb	LBZ mzgb	CZ mzgb	CZ mzgb
Sample	BS04-10	BS04-10	BS04-10	BS04-12	BS04-2	BS04-2	BS04-7	BS04-7	BS04-9	BS04-3	BS04-4
desc.	rim	core	in anlc	in anlc	core		rim	core	rim	in anlc	encased in cpx
analysis	54B	53B	52C	61	10	9	33	32	95	15	45
SiO_2	65.81	66.43	65.80	64.23	65.98	65.40	50.09	49.66	64.85	64.81	51.41
Al_2O_3	19.50	19.52	19.64	18.45	18.33	18.49	30.52	31.25	19.40	17.96	30.60
FeO	0.28			0.20	0.47	0.20	0.88	0.57	0.22		0.57
CaO	0.66	0.58	0.07	0.04	0.11	0.09	14.30	14.68	0.54		13.76
K_2O	8.86	9.04	14.65	15.11	10.96	12.99	0.12	0.13	10.17	15.67	0.18
Na_2O	4.87	4.30	0.07	0.15	3.45	2.21	3.35	2.78	3.95	0.15	3.88
BaO				0.54					0.25		
SrO			0.70								0.45
Total	99.98	99.87	100.93	98.72	99.30	99.38	99.26	99.07	99.38	98.59	100.85
atoms per formula unit, based on 8 O's											
Si	2.961	2.983	2.985	3.000	3.010	3.002	2.301	2.285	2.955	3.023	2.327
Al	1.034	1.033	1.050	1.016	0.985	1.000	1.653	1.694	1.042	0.987	1.632
Fe	0.010			0.008	0.018	0.008	0.034	0.022	0.008		0.022
Ca	0.032	0.028	0.003	0.002	0.005	0.005	0.704	0.723	0.026		0.667
K	0.508	0.518	0.848	0.900	0.638	0.761	0.007	0.008	0.591	0.932	0.011
Na	0.425	0.374	0.006	0.014	0.305	0.197	0.298	0.248	0.349	0.013	0.340
Ba				0.010					0.004		
Sr			0.018								0.012
sum	4.970	4.936	4.910	4.950	4.961	4.973	4.997	4.980	4.975	4.955	5.011
Mole Fractions											
An	0.03	0.03			0.01		0.70	0.74	0.03		0.66
Ab	0.44	0.41	0.01	0.01	0.32	0.20	0.30	0.25	0.36	0.01	0.33
Or	0.53	0.56	0.99	0.98	0.67	0.79	0.01	0.01	0.61	0.99	0.01

Table 3-6, continued. Bone Springs Sill feldspar compositions.

Lithology	CZ mzgb	CZ mzgb	CZ mzgb	CZ mzgb	CZ mzsy	CZ mzsy	CZ mzsy	CZ mzsy	CZ mzsy	CZ mzsy
Sample	BS04-4	BS04-4	BS04-4	BS04-4	BS05-28	BS05-28	BS06-51	BS06-51	BS06-59	BS06-59
desc.				in anlc	rim	core	in anlc	core, euhedral	rim	core
analysis	49	52B	53	24	31B	51	5	25	41	42
SiO_2	66.78	65.03	64.64	64.93	64.97	65.74	64.78	65.10	66.16	64.84
Al_2O_3	20.28	19.94	19.35	18.75	19.53	19.01	18.51	19.07	19.33	18.44
FeO				0.32			0.21			
CaO	0.62	0.77	0.31	0.07	0.29	0.23	0.10	0.11	0.25	0.10
K_2O	4.41	9.99	11.18	14.49	9.49	10.39	15.41	14.49	10.72	12.40
Na_2O	8.35	4.80	3.53	1.02	4.36	3.83	0.92	0.29	4.71	2.64
BaO			0.20				0.47	1.31		
SrO	0.61	0.34	0.78				0.33	0.43	0.29	0.33
Total	101.05	100.87	99.99	99.58	98.64	99.20	100.73	100.80	101.46	98.75
atoms per formula unit, based on 8 O's										
Si	2.940	2.930	2.953	2.990	2.964	2.990	2.984	2.986	2.964	2.994
Al	1.052	1.059	1.042	1.017	1.050	1.019	1.005	1.031	1.021	1.003
Fe				0.012			0.008			
Ca	0.029	0.037	0.015	0.004	0.014	0.011	0.005	0.005	0.012	0.005
K	0.248	0.574	0.652	0.851	0.552	0.603	0.905	0.848	0.613	0.730
Na	0.713	0.419	0.313	0.091	0.386	0.338	0.082	0.026	0.409	0.237
Ba			0.004				0.008	0.024		
Sr	0.016	0.009	0.021				0.009	0.011	0.008	0.009
sum	4.998	5.028	5.000	4.965	4.966	4.961	5.006	4.931	5.027	4.978
Mole Fractions										
An	0.03	0.04	0.02	0.00	0.01	0.01	0.00	0.01	0.01	0.01
Ab	0.72	0.41	0.32	0.10	0.41	0.35	0.08	0.03	0.40	0.24
Or	0.25	0.56	0.67	0.90	0.58	0.63	0.91	0.96	0.59	0.75

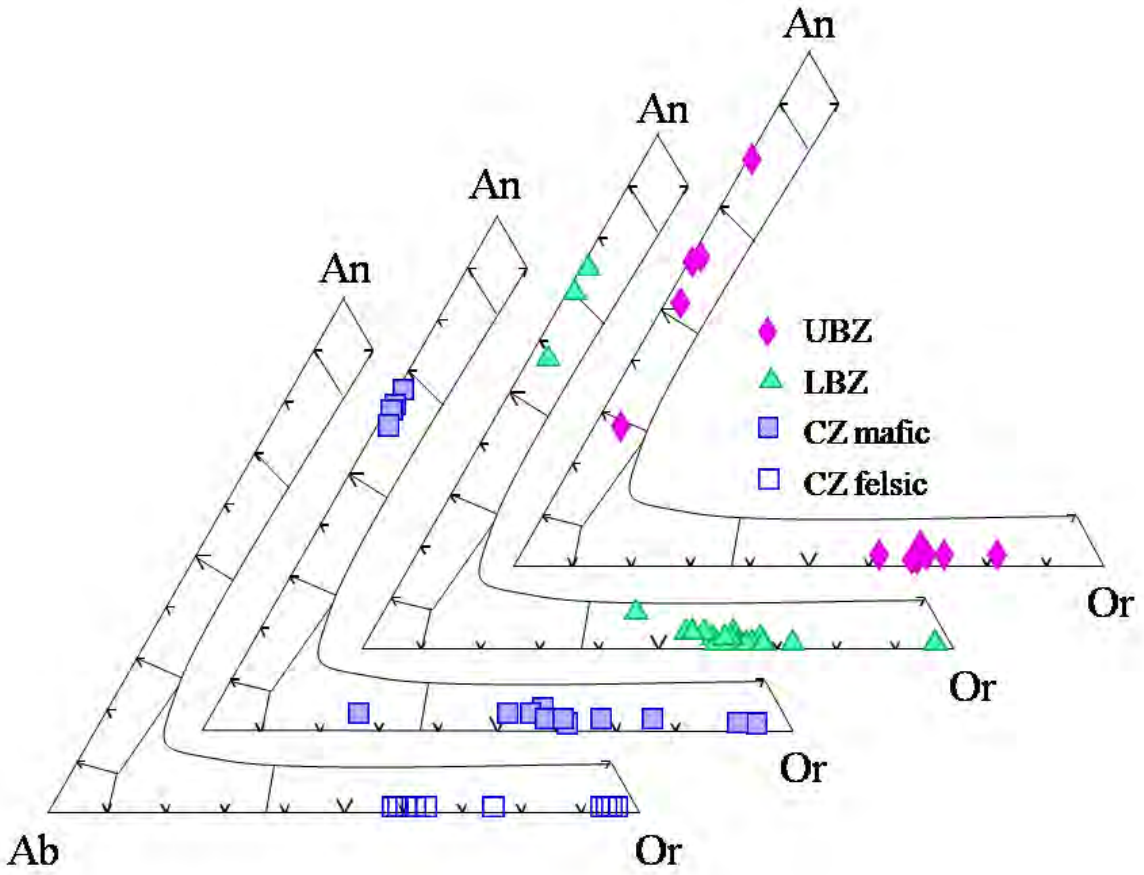

Figure 3-14. Bone Springs Sill feldspar compositions. All but one plagioclase analysis is >An_{50} and all but one is <An_{80}. All analyses of >Or_{90} are from fine-grained feldspar intimately associated with analcime.

grains. Plagioclase grains show no cross-cutting or inclusion relationships with olivine. Armored and rare unaltered, unarmored grains are as calcic as An_{79}. Others are normally zoned from An_{60} to An_{56} with one analyzed rim of An_{27}.

Lower border zone and central zone plagioclase occur as 500 μm to 1 mm grains that often include clinopyroxene. Petrography indicates that plagioclase continued nucleating after the inception of clinopyroxene crystallization and that the two phases grew concurrently. Plagioclase also occurs interstitially as fine 50-250 μm grains. Lower border zone plagioclase has cores as calcic as An_{74} and rims as sodic as An_{57}. Central zone plagioclase has core to rim relationships bracketed by An_{66} to An_{59}. Plagioclase is rare in the monzosyenites and is usually analcimized.

Alkali feldspar

Primary alkali feldspar is found in all lithologies except the lower chill zone and uppermost contact – in the latter samples, alkali feldspar is present but it is unclear whether it is primary or a product of the late analcime-forming event (see below). Primary alkali feldspar in other samples occurs as subhedral to euhedral blocky grains to up to 300 μm. Anorthoclase is uncommon and most grains are from $Or_{50\text{-}80}$. Zonation is only weakly developed, but some grains in the CZ mafic rocks show core to rim relationships of $Or_{50}Ab_{47}$ to $Or_{54}Ab_{43}$. Most primary alkali feldspar grains have a calcic component of $An_{1\text{-}4}$. Alkali feldspar also occurs in all lithologies as anhedral clumps or radiating masses from 5-50 μm. These are interstitial and associated with analcime. In some cases, hexagonal grains of early forming minerals are replaced by a mixture of analcime + K-feldspar ± thomsonite. This late alkali feldspar is usually $>Or_{90}$ and commonly approaches endmember K-feldspar. Some interstitial alkali feldspar in UBZ samples is intermixed with analcime and is $\sim Or_{80}$. It is likely that K-rich feldspar associated with

analcime is a reaction product of the breakdown of nepheline to analcime + feldspar. This is discussed under the section on analcime, below

Apatite

Apatite is found in all BSS rocks and is among the earliest-forming minerals. It comprises 0.5-1 modal% of the UBZ rocks and up to 4 modal% of the LBZ and CZ mafic rocks. The monzosyenitic rocks contain the least apatite (<0.5 modal%). The chill zone and margin rocks have needle-like and skeletal apatite up to 100 µm in length and these quench textures indicate that the liquid was saturated with apatite upon intrusion. Upper border zone rocks contain some skeletal apatite and some fine (20-50 µm) but well-developed grains. In LBZ and CZ rocks, apatite is commonly included in olivine. The largest apatite grains are >2 mm and found at the top of the LBZ.

Apatite chemistry is shown in Table 3-7. Bone Springs apatite is fluoroapatite and contains up to 4 wt.% F. Some of the most F-rich apatites are from the CZ mafic rocks and the least F-rich are from the UBZ samples, but all lithologies show a range of F contents in apatite (see Figure 3-15 for F contents in apatite). Chlorine is present as <0.5 wt.%.

Some BSS apatites, particularly in the fine-grained UBZ, are very enriched in SiO_2 (most are <10 wt.% and but several contain 39-40 wt.%) and Al_2O_3 (up to 14 wt.%) which are strongly correlated as shown in Figure 3-16a. Si + Al also inversely correlates with P + Ca, indicating a coupled substitution of $Si^{4+}+Al^{3+} = P^{5+}+Ca^{2+}$ (Figure 3-16b). To the knowledge of the author, this substitution has not been documented in alkaline igneous rocks or elsewhere. The substitution documented by Rønsbo (1989) of $Si^{4+}+REE^{3+} = P^{5+}+Ca^{2+}$ in Ilímaussaq syenites may function in a similar manner, as evident from the $Si^{4+}+La^{3+}$ correlation with $P^{5+}+Ca^{2+}$ in BSS rocks (see Figure 3-16c) but the inverse correlation may be spurious as Si itself is strongly

Table 3-7. Average apatite compositions for Bone Springs Sill lithologies. See text and Figures 3-16a-d for discussions of elemental distributions and substitution. Appendix 2 contains complete apatite analyses.

lithology	LBZ mzgb AVG.	*2σ*	CZ mzgb AVG.	*2σ*	CZ mzsy AVG.	*2σ*	UBZ mzgb AVG.	*2σ*
number	n=43		n=55		n=7		n=6	
P_2O_5	39.50	*2.45*	38.75	*3.56*	36.92	*7.96*	30.47	*15.00*
CaO	55.00	*3.13*	54.13	*4.15*	52.97	*8.93*	40.36	*22.32*
SiO_2	0.97	*1.99*	0.88	*2.14*	2.69	*5.26*	12.77	*27.50*
Al_2O_3	0.10	*0.51*	0.18	*0.78*	1.14	*4.38*	4.72	*9.54*
FeO	0.47	*0.80*	0.93	*3.01*	1.02	*3.59*	2.83	*7.03*
MnO	0.04	*0.08*	0.04	*0.09*	0.04	*0.07*	0.02	*0.04*
MgO	0.16	*0.29*	0.13	*0.38*	0.31	*1.62*	0.65	*0.94*
Na_2O	0.07	*0.13*	0.05	*0.05*	0.09	*0.10*	1.61	*4.44*
SrO	0.31	*0.10*	0.30	*0.07*	0.28	*0.18*	0.41	*0.35*
F	2.46	*0.83*	2.70	*1.01*	2.90	*0.79*	2.29	*0.75*
Cl	0.16	*0.06*	0.20	*0.25*	0.04	*0.04*	0.08	*0.05*
Total'	99.78	*2.40*	98.82	*2.54*	99.53	*2.95*	97.01	*6.50*
-O=F	1.04		1.14		1.22		0.96	
-O=Cl	0.04		0.05		0.01		0.02	
Total	98.70	*2.39*	97.63	*2.46*	98.31	*3.22*	96.02	*6.44*
atoms per formula unit, based on 26 anions								
P	5.80	*0.28*	5.76	*0.43*	5.44	*1.10*	4.50	*2.47*
Ca	10.22	*0.61*	10.18	*0.76*	9.89	*1.56*	7.52	*4.51*
Si	0.17	*0.34*	0.15	*0.38*	0.47	*0.93*	2.10	*4.19*
Al	0.02	*0.11*	0.04	*0.16*	0.24	*0.91*	0.92	*1.71*
Fe	0.07	*0.12*	0.14	*0.45*	0.15	*0.53*	0.43	*1.09*
Mn	0.01	*0.01*	0.01	*0.01*	0.01	*0.01*	0.00	*0.01*
Mg	0.04	*0.08*	0.04	*0.10*	0.08	*0.43*	0.17	*0.25*
Na	0.02	*0.04*	0.02	*0.02*	0.03	*0.04*	0.53	*1.47*
Sr	0.03	*0.01*	0.03	*0.01*	0.03	*0.02*	0.04	*0.03*
F	1.35	*0.46*	1.50	*0.56*	1.60	*0.48*	1.25	*0.46*
Cl	0.05	*0.02*	0.06	*0.07*	0.01	*0.01*	0.02	*0.02*
***OH (ideal)**	0.60	*0.46*	0.44	*0.53*	0.39	*0.47*	0.72	*0.47*
Total	18.41	*0.29*	18.40	*0.29*	18.41	*0.20*	18.27	*1.72*
mole fractions								
X_F	0.68	*0.23*	0.75	*0.28*	0.80	*0.24*	0.63	*0.23*
X_{Cl}	0.02	*0.01*	0.03	*0.04*	0.01	*0.01*	0.01	*0.01*
X_{OH}	0.30	*0.23*	0.22	*0.26*	0.19	*0.23*	0.36	*0.24*

* OH = 2-F-Cl

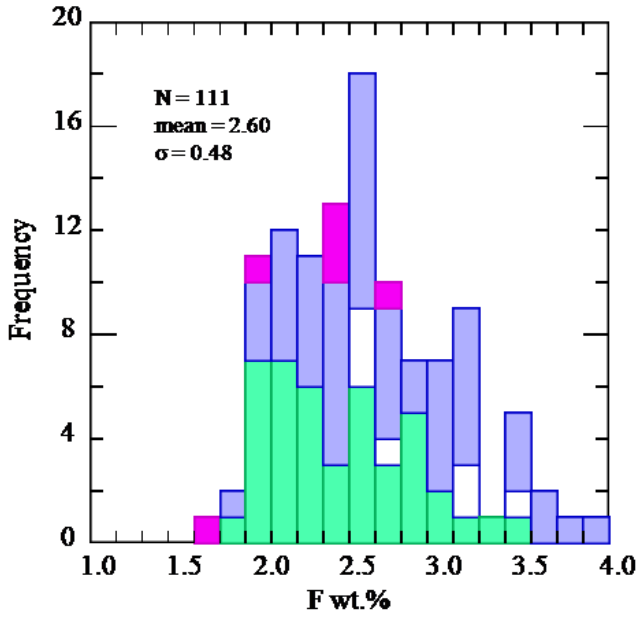

Figure 3-15. Histogram of F wt.% in Bone Springs Sill apatites. Pink = UBZ/margins micro-monzogabbro; green = LBZ monzogabbros; blue = CZ monzogabbro; blue-bordered white = CZ monzosyenites. All lithologies show a spread in their apatite F contents, but those with the highest F are in CZ monzogabbro**.**

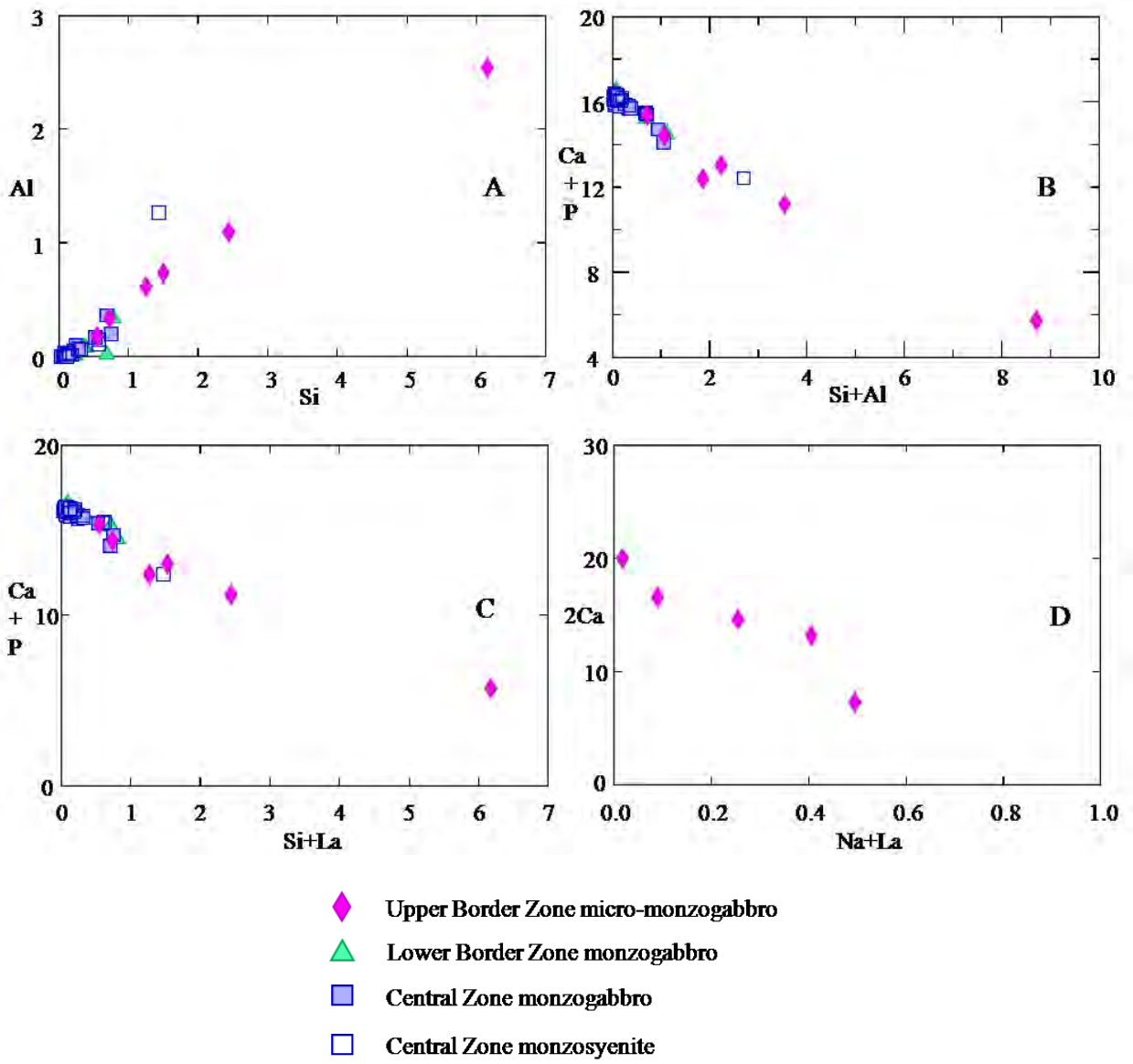

Figure 3-16. Cation substitutions in Bone Springs Sill apatite. Atoms per formula unit calculated on the basis of 26 oxygens + OH, F, Cl per formula unit. The correlation of Si and Al (**A**) and the inverse correlation of Si+Al to Ca+P (**B**) indicate that $Si^{4+}+Al^{3+} = Ca^{2+}+P^{5+}$ is an important substitution in some Bones Spring Sill apatite. A correlation of Ca+P with Si+La (**C**) suggests the substitution documented by Rønsbo (1989) of $REE^{3+}+Si^{4+} = Ca^{2+}+P^{5+}$ is possible, but the abundance of Si so outweighs La that the latter might be irrelevant. There is some correlation in UBZ apatites between $2Ca^{2+}$ and $Na^{+}+La^{3+}$ (**D**).

inversely correlated with P + Ca and La is a relatively minor component. The substitution $Na^{+}+La^{3+} = 2Ca^{2+}$ suggested by Harlov et al. (2002) also seems to operate in the UBZ rocks (see Figure 3-16d).

Apatite occurrence and chemistry, including substitution mechanisms, are discussed in more detail in Chapter 4, especially with regard to halogen composition.

Analcime and thomsonite

Analcime occurs in all BSS rocks as late interstitial anhedral masses and as a replacement to plagioclase feldspar. It occurs in CZ felsic rocks filling 0.2-1 cm vugs or ocelli. It is always associated with anhedral crystals or radiating aggregates of K-feldspar and it is usually associated with the zeolite Ca-thomsonite, (ideally $NaCa_2Al_5Si_5O_2[6H_2O]$) which was identified by microprobe analysis; in a few cases small blebs of quartz were found in the analcime. Mineral chemistry of the zeolites is shown in Table 3-8. Analcime is always dominant, but the relative amounts of K-feldspar and Ca-thomsonite vary. Analcime replacing plagioclase contains more Ca-thomsonite than interstitial analcime and interstitial analcime in the monzosyenites contains less Ca-thomsonite than in the monzogabbro. In some samples there occurs an early-crystallizing, euhedral hexagonal or rounded mineral that is now replaced by or broken down to analcime + thomsonite + K-feldspar. I interpret these grains to have been nepheline. A rounded grain like this occurs as one of the earliest crystallizing phenocrysts in the margin rocks and is shown in Figure 3-7a. For one such grain (see Figure 3-17) in a CZ monzogabbro, I analyzed the constituent phases and reintegrated the composition based on proportions derived by image analysis; the integration yields a moderately Ca-rich and potassic (3.25 wt.% CaO and 1.61 wt.% K_2O) analcime composition. Most BSS analcime contains <0.3 wt.% CaO, but a few analyses of

Table 3-8. Average compositions of analcime and thomsonite from Bone Springs Sill rocks.

Mineral	analcime		analcime		analcime		analcime	
Label	LBZ mzgb		CZ mzgb		CZ mzsy		UBZ mzgb	
number	n = 4		n = 5		n = 6		n = 11	
	mean	*2σ*	mean	*2σ*	mean	*2σ*	mean	*2σ*
SiO_2	55.71	*1.86*	55.01	*5.22*	52.75	*4.56*	54.87	*4.52*
Al_2O_3	23.10	*0.72*	24.49	*2.22*	25.31	*4.33*	25.31	*4.33*
FeO	0.10	*0.16*	0.05	*0.14*	0.14	*0.22*	0.14	*0.24*
CaO	0.10	*0.08*	0.13	*0.14*	0.35	*0.52*	0.59	*1.82*
K_2O	0.17	*0.22*	0.43	*1.22*	0.30	*0.58*	0.09	*0.24*
Na_2O	12.99	*0.80*	11.43	*6.86*	11.55	*1.36*	11.69	*2.84*
Total	92.25	*2.18*	91.67	*3.18*	90.40	*3.00*	92.20	*3.72*
atoms per formula unit based on 6 O								
Si	2.02	*0.02*	2.00	*0.09*	1.95	*0.12*	1.99	*0.08*
Al	0.99	*0.02*	1.05	*0.07*	1.10	*0.18*	1.05	*0.11*
Fe	0.00	*0.00*	0.00	*0.00*	0.00	*0.00*	0.00	*0.01*
Ca	0.00	*0.00*	0.01	*0.00*	0.01	*0.02*	0.02	*0.07*
K	0.01	*0.01*	0.02	*0.05*	0.01	*0.02*	0.00	*0.01*
Na	0.92	*0.07*	0.81	*0.50*	0.83	*0.10*	0.82	*0.20*
total	3.94		3.89		3.90		3.89	
Si/Al	2.05		1.91		1.78		1.89	

Mineral	thomsonite		thomsonite		thomsonite	
Label	LBZ mzgb		CZ mzgb		UBZ mzgb	
number	n = 4		n = 7		n =6	
	mean	*2σ*	mean	*2σ*	mean	*2σ*
SiO_2	38.95	*0.88*	38.71	*2.44*	41.03	*2.78*
Al_2O_3	29.84	*1.24*	30.22	*1.14*	30.56	*1.96*
FeO	0.13	*0.08*	0.13	*0.30*	0.22	*0.78*
CaO	12.09	*0.94*	12.87	*0.86*	12.01	*0.54*
K_2O	0.03	*0.02*	0.02	*0.06*	0.01	*0.02*
Na_2O	4.23	*0.62*	3.96	*0.64*	3.42	*3.32*
Total	85.29	*1.24*	86.17	*3.96*	88.06	*3.32*
atoms per formula unit based on 6 O						
Si	1.581	*0.03*	1.561	*0.04*	1.607	*0.06*
Al	1.427	*0.05*	1.437	*0.04*	1.411	*0.06*
Fe	0.004	*0.00*	0.004	*0.01*	0.007	*0.03*
Ca	0.526	*0.05*	0.556	*0.05*	0.504	*0.03*
K	0.001	*0.00*	0.001	*0.00*	0	*0*
Na	0.332	*0.04*	0.31	*0.04*	0.261	*0.25*
total	3.87		3.87		3.79	
Si/Al	1.11		1.09		1.14	

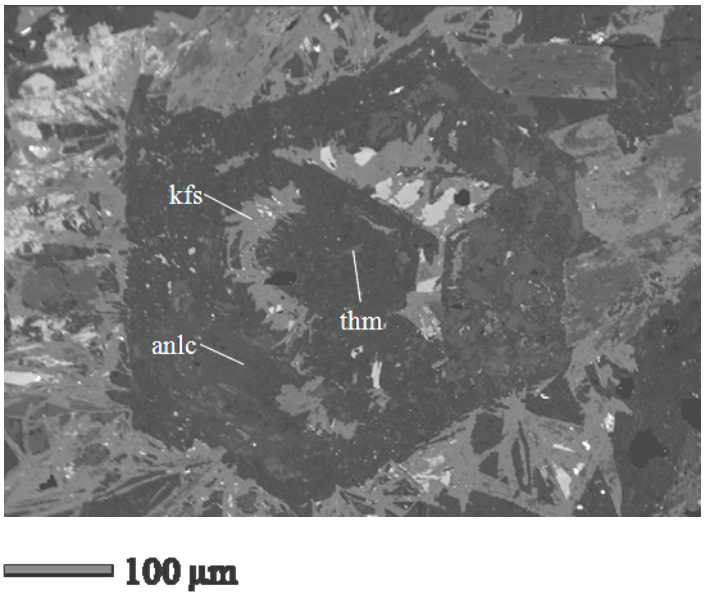

Figure 3-17. Backscatter electron image of a pseudomorph after nepheline. From Central Zone monzogabbro sample BS05-19. The minerals are intergrown analcime (anlc), thomsonite (thm) and K-feldspar (kfs).

analcime partially replacing plagioclase grains have 1.6-3.0 wt.% CaO (Table 3-8). Most analcime has <0.3 wt.% K_2O and all, even the reintegrated composition, have <1.7 wt.% K_2O.

Primary or secondary analcime?

Experimental evidence from the silica-undersaturated residua system, albite-orthoclase-nepheline-kalsilite (Bowen, 1915; Thornton and Tuttle, 1960) in the presence of H_2O indicates that analcime is only stable in the presence of melt from 5-13 kilobars and 600-640º C (Roux and Hamilton, 1976). Although K-solid solution in analcime may somewhat extend the thermal stability (Peters et al., 1966), these results seemingly preclude a primary origin for most analcime found in igneous rocks and particularly for the shallowly emplaced TPMP sills.

Analcime and leucite have similar open framework structures and analcime will quickly replace leucite by K^+-Na^+ cation exchange in the presence of a NaCl brine (Gupta and Fyfe, 1975; Putnis et al., 2007), which can result in analcime pseudomorphs of leucite that appear primary. At the extreme, this mechanism has been invoked to explain the almost wholesale conversion of ultrapotassic protolith rocks to apparently sodic igneous rocks – see Prelevic et al. (2004) for a possible example from Serbia. This mechanism is unlikely for BSS rocks as there is compelling evidence that they originated from sodic magmas: they contain Rb of <50 ppm in the interpreted intruding magma to ~80 ppm in the monzosyenites – contents likely too low for potassic rocks; although they contain primary biotite, the pyroxenes follow a trend of Na-enrichment (Figure 3-11A); and though some TPMP rocks have intact nepheline and/or sodalite (e.g., Barker, 1987), to the author's knowledge none have been reported to bear leucite.

Analcime can also form by the breakdown of albite + nepheline in the presence of H_2O: $NaAlSi_3O_8$ (ab) + $NaAlSiO_4$ (ne) + H_2O = $2NaAlSi_2O_6(H_2O)$ (anlc) at 400-500º C and <1 kilobar (Manghani, 1970; Liou, 1971). If sufficient H_2O is present and the analcime is Si-rich, a second

reaction can occur below 200º C and the analcime may break down further to analcime + quartz (Liou, 1971); this second step is possible because analcime is capable of incorporating Si beyond its stoichiometric composition to that of a hydrated albite ($NaAlSi_3O_8[1.5H_2O]$) (Wilkinson and Hensel, 1994), and this excess Si is not stable in the mineral at low temperatures (<200º C). Very small blebs of apparently amorphous silica are found in some interstitial analcime in BSS. Analcime may vary in solid solution from a hydrated albite composition mentioned above to natrolite ($NaAlSi_{1.5}O_5[0.75H_2O]$). Although stoichiometric analcime has Si/Al of 2, actual analcime Si/Al can vary from ~1.4, approaching nepheline compositions, to 3, at the albite composition (Saha, 1961). Bone Springs Sill analcimes have Si/Al between 1.55 and 2.09, and the average Si/Al by lithology ranges from 1.78 ± 0.21 (CZ monzosyenites) to 2.05 ± 0.03 (LBZ), almost overlapping within error (Table 3-8). The preponderance of analyses with Si/Al <2 suggests that a precursor feldspathoid was involved in the analcime-forming reaction. The variation in analcime Si/Al likely reflects changes in the proportions of albite:nepheline reacted or changes in fluid temperature or composition, either spatially or temporally, in the cooling regime.

The contents of Ca and K in the analcime and thomsonite raise the possibility that there was some replacement of sodalite series minerals in BSS as well as a reaction of nepheline + feldspar. Sodalite occurs with nepheline in some intrusions in the Diablo Plateau in the northern TPMP (Barker and Hodges, 1977), although the Diablo Plateau intrusions are considerably more differentiated than BSS (Barker et al., 1977). However, the Si/Al of sodalite minerals is ~1 (Deer et al., 1996) and the Si/Al of analcime and the reintegrated composition of replaced minerals is consistently > 1.5, even in the most differentiated monzosyenites.

The evidence suggests that some of the analcime in Bone Springs Sill is secondary and formed by the replacement of nepheline and the albite component of feldspars. This is true for the hexagonal and rounded early grains (Figure 3-7a and Figure 3-17). The kalsilite component of nepheline and the orthoclase component of feldspar was partially incorporated into analcime and otherwise crystallized as secondary K-feldspar. Calcium from the anorthite component of feldspar was largely incorporated into subordinate thomsonite. Petrography indicates that nepheline was in some cases early-formed euhedral crystals. Some analcime partially replaces plagioclase and may be from a reaction of plagioclase + late interstitial melt.

However, a secondary genesis is less well-supported for the ubiquitous, structureless, clear to white analcime in the mesostasis of BSS rocks. No distinct replaced grains are apparent – if the analcime formed by replacement of alkali or ternary feldspar and nepheline from the residual melt then these precursor minerals were probably intimately intergrown from cotectic crystallization.

Many other TPMP rocks contain analcime. In the nepheline- and quartz-bearing syenites, trachytes, and phonolites of the Diablo plateau, which comprise some of the most differentiated TPMP rocks, all lithologies contain Ca-poor analcime and natrolite (Barker and Hodges, 1977). Analcime is found replacing nepheline and lining cavities while natrolite is present interstitially and is interpreted by Barker and Hodges (1977) to be a product of deuteric alteration of alkali feldspar in the groundmass. In the Diablo plateau, Ca-bearing zeolites in the thomsonite series are limited to one unit of nepheline syenite (Barker and Hodges, 1977). In the internally differentiated monzonite-syenite Rattlesnake Mountain Sill (RMS), Carman et al. (1975) report analcime but not thomsonite or natrolite. Analcime in RMS monzonite is relatively Ca-rich, containing 1.34 wt.% CaO from a single analysis, while analcime from an analysis in the syenite

contains 0.02 wt.% CaO (Carman et al., 1975, Table 3). At RMS, much analcime occurs interstitially in a fashion similar to the mesostasis of BSS. This mode of occurrence is common in TPMP rocks (Befus et al., 2009; Henry et al., 1989), and the lack of obvious replacement textures for this analcime led Henry et al. (1989) to propose a late magmatic origin rather than a subsolidus replacement. As discussed above, experimental evidence would seem to preclude a magmatic origin – even a late-stage magmatic replacement (e.g., Roux and Hamilton, 1976; Liou, 1971) – in these shallow intrusions. Analcime is probably common in TPMP rocks because most intruding magmas were hydrous and the exposed dikes, sills, stocks, and laccoliths were all emplaced under low pressure at shallow depths (Barker, 1987) – conditions that are ideal for the reaction of nepheline to analcime.

Perhaps the most compelling evidence that BSS analcime formed by subsolidus isochemical processes, as opposed to by externally-derived hydrothermally mobilized elements (i.e., the manner of leucite replacement after Prelevic et al., 2004), is that the whole rock composition of the differentiated rocks plot near the thermal minimum in the undersaturated portion of the residual system $NaAlSiO_4$-SiO_2-$KAlSiO_4$-H_2O from Hamilton and MacKenzie (1965) (Figure 3-18). It is unlikely that reactions involving mass exchange (beyond water) with the country rocks or with externally imposed hydrothermal fluid would preserve the K/Na ratio and mimic the approach to the eutectic composition.

Amphibole

Amphibole occurs from 3-8 modal% in Bone Springs monzosyenites. Its occurrence in other rocks is variable: one CZ monzogabbro sample contains almost 6 modal%, about half of the other examined LBZ and CZ samples contain 0.3-0.6 modal%, and the others contain none. Some CZ monzosyenite samples have textures approaching pegmatitic and contain elongate

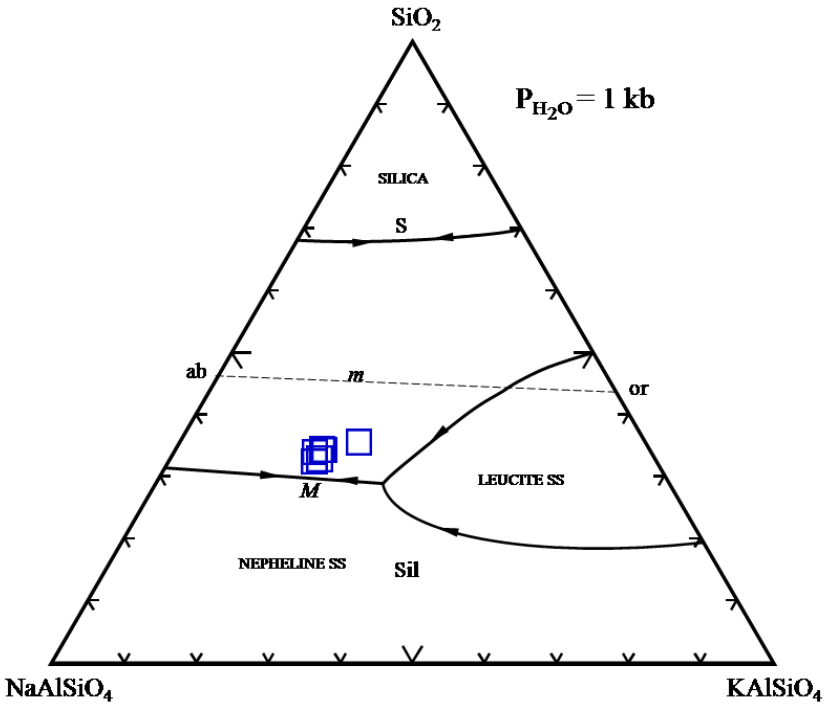

Figure 3-18. Bone Springs Sill monzosyenites plotted in the $NaAlSiO_4$-SiO_2-$KAlSiO_4$-H_2O system. Fields are from Hamilton and Mackenzie (1965) for P_{H2O} = 1kb. These evolved rocks plot near the thermal minimum for silica-undersaturated liquids at *M* (750±7° C) and in the low-T trough that runs from *M* to the feldspar thermal minimum at *m*.

kaersutitic amphiboles up to several centimeters in length. Others are euhedral and 2-3 mm in length. Amphibole chemical analyses are shown in Table 3-9.

Amphiboles in CZ monzosyenites have edenite or kaersutite cores as magnesian as *Mg'* = 69 and ferro-kaersutite or kaersutite rims with *Mg'* as low as 48. Petrographically, edenite is generally finer-grained than kaersutite and appears to be the earlier phase. Kaersutite contains ~6-8 TiO_2 wt.%.

Fe-Ti oxide

Fe-Ti oxide minerals are particularly abundant in Bone Springs Sill rocks. The lower chill zone contains over 4 modal% Fe-Ti oxide. Most LBZ and UBZ rocks contain 8-10 modal% Fe-Ti oxide. Central zone mafic and felsic rocks contain 5-7%. Almost all Fe-Ti oxides show extensive exsolution, though some unexsolved grains are present, usually included in other minerals. Compositions of oxide minerals are shown in Table 3-10, which includes both homogeneous grains and compositions of exsolved grains reintegrated from host and lamellae analyses and proportions obtained from image analysis. Fe^{2+}/Fe^{3+} ratios were determined by charge balance after Carmichael (1967) – a method that yields the same results as the Droop (1987) routine used for clinopyroxenes. Mole fractions were determined after Andersen and Lindsley (1988). BSS rocks contain two Fe-Ti oxides: titanohematite-ilmenite and magnetite-ulvöspinel. The most consistently Ti-rich oxides are found in the lower chilled margin, with minerals of X_{ilm} to 0.96 and X_{usp} to 0.87. Ulvöspinel from the chilled margin and those found as <10 μm inclusions in high-Mg olivine clumps (possibly carried in with the magma – see entries 24 an 26 in Table 3-10) have the highest spinel components, with MgO to 4.1 and Al_2O_3 to 5.8 wt.%. Interestingly, the oxides associated with and included in the earliest olivines are not Cr-rich, and in fact Cr_2O_3 is below detection limit. BSS monzogabbros have oxides with 0.36-0.98

Table 3-9. Amphibole compositions from Bone Springs Sill. Classification and cation allocation after Leake et al. (1997). Krs = kaersutite, Ed = edenite, Fe2 = ferro-.

sample	BS04-10	BS05-28	BS05-28	BS05-28	BS05-28	BS05-28	BS05-28	BS06-50	BS06-50	BS06-59
analysis#	10	20	21	22	23	25	26	50	51	35
lith	LBZ mzgb	CZ mzsy	CZ mzsy	CZ mzsy	CZ mzsy	CZ mzsy	CZ mzsy	CZ mzsy	CZ mzsy	CZ mzsy
label		amph-1	amph-2	rim amph-3	core amph-3	rim amph-4	core amph-4	core amph-5	rim amph-5	
SiO_2	47.89	38.76	39.96	40.37	38.38	50.04	47.07	38.89	39.80	49.20
Al_2O_3	3.64	12.16	11.18	10.93	12.79	2.60	3.00	13.02	11.08	2.23
TiO_2	2.15	7.12	6.21	5.83	8.10	0.88	6.00	8.00	6.27	0.94
FeO	12.62	14.71	14.97	14.95	12.77	13.01	8.86	12.58	16.77	10.25
MgO	9.46	9.43	9.55	9.72	10.68	9.85	11.01	10.99	8.53	11.12
MnO	0.18	0.23	0.37	0.07	0.21	0.30	0.19	0.16	0.19	0.18
CaO	22.44	12.14	12.21	11.82	12.48	22.92	23.27	12.31	12.00	21.86
Na_2O	1.23	2.80	2.75	2.82	2.76	1.02	0.60	2.35	2.74	0.50
K_2O	0.03	1.36	1.58	1.66	1.26	0.03	0.01	1.21	1.59	0.00
BaO	0.03	0.20	0.12	0.13	0.14		0.01	0.03	0.01	
F	0.10	0.25	0.36	0.76	0.36		0.10	0.02	0.24	
Cl		0.02	0.01	0.01	0.01				0.07	0.07
Total'	99.68	99.18	99.28	99.08	99.94	100.64	100.02	99.57	99.29	96.36
O=F	0.002	0.105	0.152	0.321	0.151		0.002	0.006	0.103	0.000
O=Cl		0.004	0.002	0.002	0.003				0.016	0.017
Total	99.66	99.07	99.13	98.75	99.78	100.64	100.00	99.56	99.17	96.34
Si	7.082	5.829	6.011	6.093	5.687	7.313	6.853	5.729	6.021	7.398
Al iv	0.634	2.155	1.982	1.907	2.233	0.448	0.515	2.261	1.975	0.396
Σ T	7.716	7.984	7.993	8.000	7.920	7.761	7.368	7.990	7.996	7.793
Al vi				0.037						
Ti	0.240	0.805	0.703	0.662	0.903	0.096	0.657	0.886	0.713	0.107
Fe2	1.561	1.850	1.883	1.887	1.582	1.590	1.079	1.550	2.121	1.289
Mg	2.086	2.114	2.142	2.187	2.359	2.146	2.390	2.414	1.924	2.493
Mn	0.022	0.029	0.048	0.009	0.026	0.037	0.023	0.020	0.024	0.023
Σ C	3.908	4.798	4.775	4.782	4.870	3.869	4.149	4.870	4.782	3.911
Ca	3.555	1.956	1.968	1.911	1.981	3.589	3.630	1.943	1.945	3.521
Ba	0.002	0.012	0.007	0.008	0.008		0.001	0.002	0.001	
Na		0.033	0.025	0.081	0.011			0.055	0.054	
Σ B	3.557	2.000	2.000	2.000	2.000	3.589	3.630	2.000	2.000	3.521
Na	0.353	0.784	0.778	0.744	0.782	0.290	0.169	0.616	0.748	0.145
K	0.006	0.262	0.304	0.320	0.238	0.005	0.002	0.228	0.306	0.000
Σ A	0.360	1.046	1.082	1.064	1.020	0.295	0.171	0.844	1.054	0.145
OH	1.998	1.869	1.821	1.628	1.823	2.000	1.999	1.998	1.882	2.000
F	0.002	0.012	0.007	0.008	0.008		0.001	0.002	0.001	
Cl		0.119	0.172	0.364	0.168				0.117	
Mg'	57	53	53	54	60	57	69	61	48	66
Class.	Ed	Krs	Krs	Krs	Krs	Ed	Ed	Krs	Fe2-krs	Ed

Table 3-10. Compositions of Fe-Ti oxides from Bone Springs Sill. This table contains homogeneous grains ("homog.") and integrated compositions ("integ."). The latter are proceeded by average compositions of the host and lamellae along with a fraction of each determined by image analysis. Mole fractions were calculated after Lindsley and Spencer (1982). For entries 27 and 28 from sample BS04-10, a temperature and fO_2 calculated after Andersen and Lindsley (1985) is shown.

	lower margin mzgb, BS06-37					LBZ mzgb, BS04-9	
data point	19	20	21	22	23	24	26
mineral	usp	hm-ilm	usp	ilm	usp	usp	usp
desc.						inclusions in high-Mg ol	
	n=3	n=2		homog.	homog.	homog.	homog.
fraction	0.64	0.36	integ.				
SiO_2	0.26	0.31	0.28			0.63	0.16
TiO_2	23.17	40.22	29.31	51.1	21.23	21.75	22.11
Al_2O_3	2.59	1.29	2.12		2.51	5.8	4.92
FeOt	68.14	50.45	61.77	43.97	69.88	64.13	65.04
FeO	*48.4*	*28.6*	*52.9*	*40.2*	*47.2*	*46*	*46*
Fe_2O_3	*21.9*	*24.3*	*9.9*	*4.2*	*25.2*	*20.1*	*21.1*
MnO	0.77	0.69	0.74	0.89	0.63	0.57	0.62
MgO	2.71	4.09	3.2	2.74	1.97	4.02	3.65
Cr_2O_3	0.1				0.14		
Total	97.75	97.04	97.43	98.69	96.37	96.9	96.5
Total w/Fe^{3+}	*99.94*	*99.48*	*98.42*	*99.12*	*98.9*	*98.92*	*98.62*
cations based on 3 O's (ilm) or 4 O's (usp)							
Si	0.010	0.008	0.010			0.023	0.006
Ti	0.634	0.747	0.808	0.960	0.592	0.585	0.602
Al	0.111	0.038	0.092		0.110	0.244	0.210
Fe2	*1.473*	*0.590*	*1.620*	*0.840*	*1.463*	*1.376*	*1.392*
Fe3	*0.599*	*0.452*	*0.272*	*0.079*	*0.702*	*0.541*	*0.576*
Mn	0.024	0.015	0.023	0.019	0.020	0.017	0.019
Mg	0.147	0.150	0.175	0.102	0.109	0.214	0.197
Cr	0.003				0.004		
	3.001	2.000	3.000	2.000	3.000	3.000	3.002
	X_{usp}	X_{ilm}	X_{usp}	X_{ilm}	X_{usp}	X_{usp}	X_{usp}
	0.692	0.774	0.876	0.960	0.641	0.646	0.653

Table 3-10, continued. Compositions of Fe-Ti oxides from Bone Springs Sill.

	LBZ mzgb, BS06-38			LBZ mzgb, BS04-10		CZ mzgb, BS04-4		
data point	4	5	6	27	28	7	8	9
mineral	hm-ilm	ilm	hm-ilm	usp	ilm	usp	ilm	hm-ilm
desc.		skeletal						
	n=2	n=1		homog.	homog.	n=3	n=4	
fraction	0.83	0.17	integ.			0.48	0.52	integ.
SiO_2	0.2	0.12	0.19	0.07	0.08	0.13		
TiO_2	11.71	48.74	18.01	25.53	51.95	23.33	53.37	38.96
Al_2O_3	0.4		0.34	2.2	0.05	2.01		0.96
FeOt	79.02	45.3	73.29	65.11	42.26	69.13	44.5	56.32
FeO	*10*	*40.9*	*15.2*	*50*	*40.1*	*50.4*	*43.5*	*31.3*
Fe_2O_3	*76.8*	*4.9*	*64.6*	*16.8*	*2.4*	*20.8*	*1.2*	*27.8*
MnO	0.63	1.17	0.72	0.69	0.71	0.96	0.99	0.96
MgO		0.99	0.18	2.44	3.34	0.92	1.99	1.55
Cr_2O_3	0.13		0.12					
Total	92.23	96.45	92.98	96.04	98.4	96.48	100.85	98.76
Total w/Fe^{3+}	*99.93*	*96.95*	*99.45*	*97.72*	*98.64*	*98.56*	*101*	*101.5*
cations based on 3 O's (ilm) or 4 O's (usp)								
Si	0.005	0.003	0.005	0.001	0.001	0.005		
Ti	0.231	0.949	0.354	0.716	0.976	0.658	0.989	0.727
Al	0.012		0.011	0.097	0.002	0.089		0.028
Fe2	*0.218*	*0.884*	*0.332*	*1.559*	*0.837*	*1.581*	*0.896*	*0.649*
Fe3	*1.513*	*0.096*	*1.270*	*0.471*	*0.046*	*0.586*	*0.021*	*0.519*
Mn	0.014	0.026	0.016	0.022	0.002	0.031	0.021	0.020
Mg		0.038	0.007	0.135	0.124	0.051	0.073	0.057
Cr	0.003		0.002					
	1.996	1.996	1.997	3.001	1.988	3.001	2.000	2.000
	X_{ilm}	X_{ilm}	X_{ilm}	X_{ilm}	X_{ilm}	X_{usp}	X_{ilm}	X_{ilm}
	0.242	0.952	0.364	0.770	0.978	0.711	0.989	0.741
T				755° C				
log(fO_2)				-18.2				

Table 3-10, continued. Compositions of Fe-Ti oxides from Bone Springs Sill.

	CZ mzgb, BS04-4			CZ mzsy, BS06-50		
data point	16	17	18	1	2	3
mineral	usp	ilm	usp	hm-ilm	usp	hm-ilm
desc.						
	n=2	n=3		homog.	homog.	homog.
fraction	0.94	0.06	integ.			
SiO_2		0.09		2.38	0.26	3.62
TiO_2	25.95	53.36	27.59	8.12	18.78	6.14
Al_2O_3	3.04	0.09	2.86	0.48	0.56	0.77
FeOt	68.37	43.33	66.86	78.2	71.77	80.34
FeO	*52.8*	*41.8*	*54.1*	*8.1*	*15.9*	*8.1*
Fe_2O_3	*17.3*	*1.7*	*14.2*	*77.9*	*62.1*	*80.3*
MnO	0.81	0.82	0.81	1.12	1.09	0.58
MgO	1.64	3.05	1.73			
Cr_2O_3						
Total	99.81	100.74	99.86	91.07	92.71	92.48
Total w/Fe^{3+}	*101.54*	*100.91*	*101.28*	*98.87*	*98.94*	*100.52*
cations based on 3 O's (ilm) or 4 O's (usp)						
Si		0.002		0.062	0.007	0.093
Ti	0.702	0.981	0.747	0.160	0.371	0.119
Al	0.129	0.003	0.121	0.015	0.017	0.023
Fe2	*1.589*	*0.855*	*1.630*	*0.179*	*0.349*	*0.173*
Fe3	*0.467*	*0.031*	*0.384*	*1.539*	*1.227*	*1.553*
Mn	0.025	0.017	0.025	0.025	0.024	0.013
Mg	0.088	0.111	0.093			
Cr						
	3.000	2.000	3.000	1.980	1.995	1.974
	X_{usp}	X_{ilm}	X_{usp}	X_{ilm}	X_{usp}	X_{ilm}
	0.782	0.984	0.827	0.231	0.387	0.224

X_{ilm} and 0.65-0.77 X_{usp}. Monzosyenites contain titano-hematite with 0.23-0.39 X_{ilm}. Ilmenite grains are exsolved into hematite-rich lamellae in ilmenite-rich hosts, while spinels typically show ulvöspinel lamellae in Ti-magnetite hosts. Figure 3-19 is a ternary diagram of homogeneous and reintegrated oxide compositions; it shows that all compositions fall essentially on the titanohematite-ilmenite and magnetite-ulvöspinel compositional lines.

Figure 3-20 shows back-scatter electron images of Fe-Ti oxides. As mentioned above, some oxides crystallized early and are included in olivine and clinopyroxene (Figure 3-20C). Many of the Ti-magnetite grains that are not associated with the earliest olivine aggregates have inclusions of apatite. Others are truncated against plagioclase grains. These spinel series minerals must have begun crystallizing very early and continued until late in the sequence. Some of the ilmenite-hematite series minerals are elongate and resemble quench textures (see Figure 3-20E and F; and entries 4-6 in Table 3-10).

Temperature and fO_2 ilmenite-ulvöspinel equilibrium

Only one analyzed ilmenite-ulvöspinel pair is in apparent equilibrium as determined by Mg/Mn partitioning (Bacon and Hirschmann, 1988). These are two homogeneous minerals were included in a large biotite from the LBZ monzogabbro sample BS04-10, shown as entries 27 and 28 in Table 3-10. Application of the Andersen and Lindsley (1988) geothermometer and oxygen barometer yields a temperature of 755° C and log(fO_2) of -18.2, which is ~2 log units below the quartz-fayalite-magnetite buffer. This temperature falls at the thermal minimum for the 1 kb P^{H2O} residual system ($NaAlSiO_4$-$KAlSiO_4$-SiO_2-H_2O) of 750 ± 7° C determined by Hamilton and MacKenzie (1965). This T-fO_2 point is unlikely to represent conditions at crystallization. These measured ilmenite and ulvöspinel are two of the only non-exsolved oxides encountered,

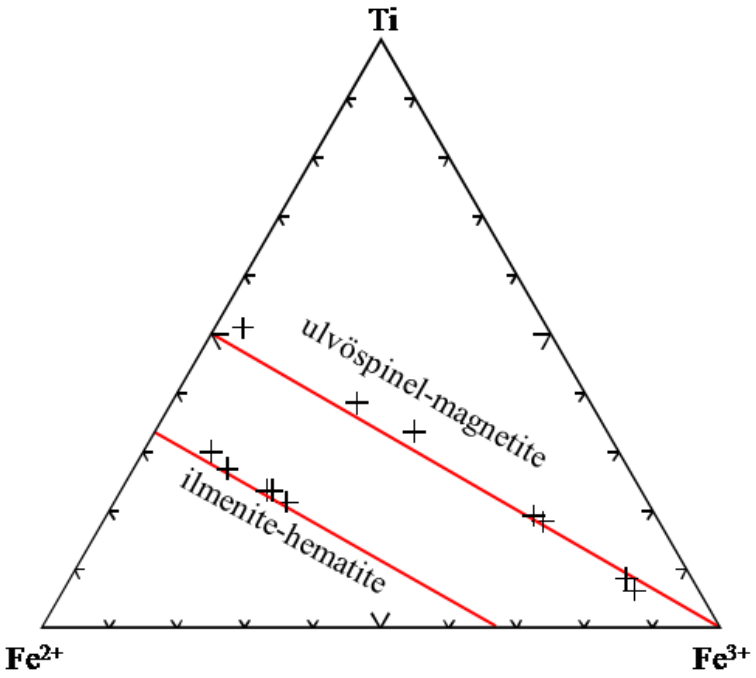

Figure 3-19. Compositions of Fe-Ti oxides from Bone Springs Sill. Plotted data are from homogeneous grains and exsolved grains reintegrated using image analysis and from host and lamellae microprobe data. Mole fractions were allocated, including ascribing Fe to Fe^{2+} and Fe^{3+}, after Lindsley and Spencer (1982). Prior to exsolution, BSS contained two oxides, ulvöspinel-magnetite series and ilmenite-hematite series. Depending on its original composition, each oxide mineral exsolved into a host of one mineral with lamellae of the other. Analyses and fractions are shown in Table 3-10.

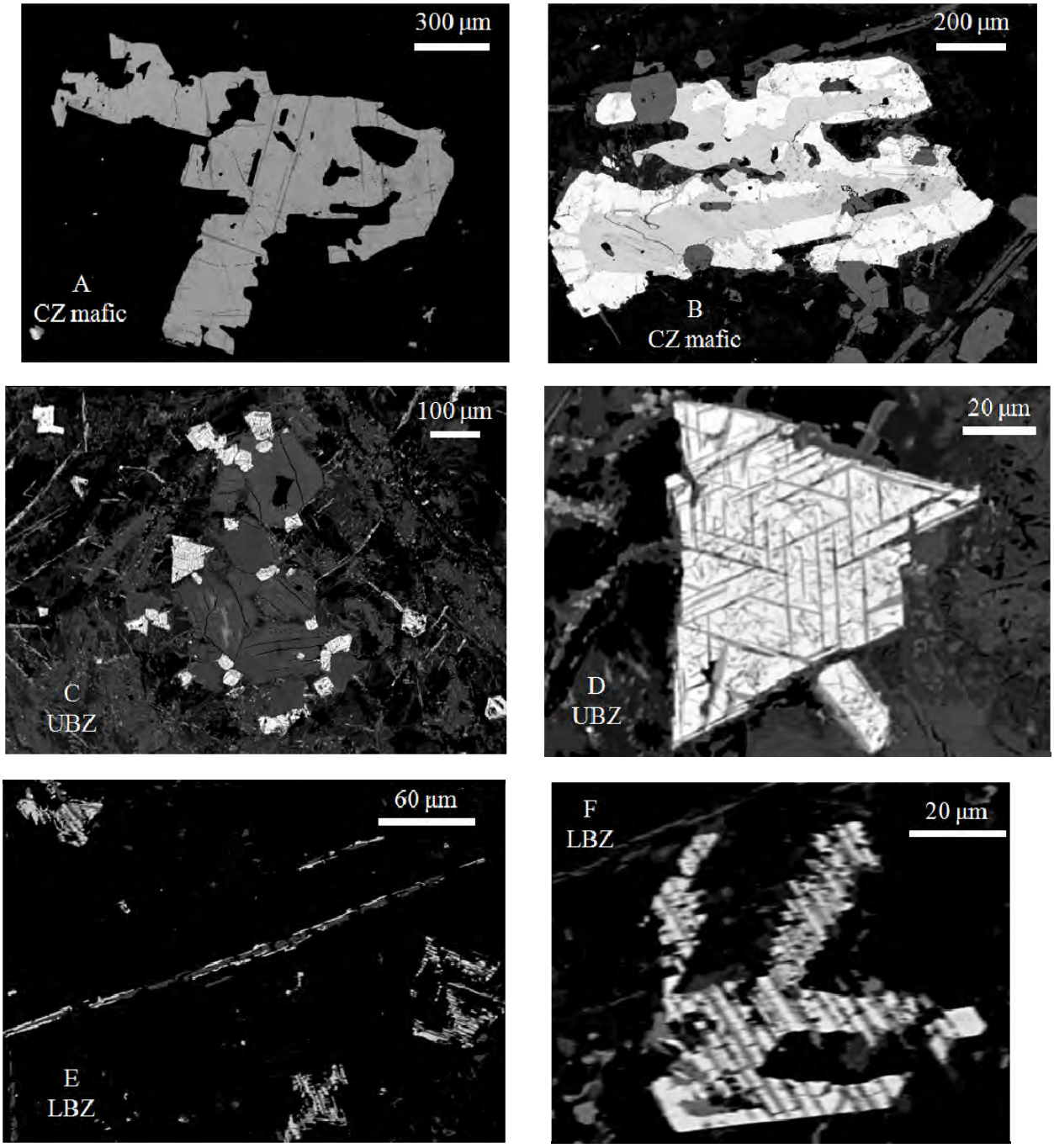

Figure 3-20. Backscatter electron images of Fe-Ti oxides in Bone Springs Sill. Central zone monzogabbro: **A** shows ilmenite lamellae in an ulvöspinel-rich host and **B** is an ilmenite core in an ulvöspinel host. Upper border zone: **C** show a cluster of partially serpentinized pre-intrusion olivine and associated ulvöspinel, now exsolved to an ulvöspinel/Ti-magnetite host with ilmenite lamellae. **D** is a close-up of the left central grain in **C**. Lower border zone: **E** shows long rod-like oxides with a ilmenite-hematite phase and exsolved T-magnetite, locally common in UBZ and some LBZ rocks, and exsolved ulvöspinel and ilmenite crystals found throughout the sill. **F** is a close-up of such a spinel series mineral crystal from the same thin section.

presumably because they were protected by the biotite crystal. This T-fO_2 point demonstrates moderately reducing conditions at the waning stages of crystallization history.

Other minerals

Zircon is rarely found in the CZ felsic rocks. Most mafic and felsic samples contain trace chalcopyrite, and some contain pyrite and/or sphalerite. A carbonate mineral, probably calcite, is found in many BSS rocks in trace amounts, and the mafic and felsic CZ rocks contain up to 4 modal% carbonate. There is no definitive evidence, textural or otherwise, that any carbonate is a primary igneous mineral – most or all of it is probably from secondary alteration.

Whole rock geochemistry

Geochemical data and CIPW norms for 26 samples of Bone Springs Sill rocks are shown in Table 3-11. All of the rocks have high alkalis and are nepheline-normative (7 to >20% normative ne) but not leucite-normative, which is typical of silica-undersaturated rocks of the TPMP (Barker, 1987, e.g.). Rocks from the margins, UBZ, and monzosyenites are interpreted to approach liquid compositions. None of the BSS rocks is peralkaline, although both peralkaline and metaluminous compositions are represented within TPMP ne-normative rocks. The margin and UBZ rocks have D.I.'s ≥ 63 (differentiation index, after Thornton and Tuttle [1960]), Ni contents of 26-43 ppm, and *Mg'* of 38-43. The relatively high D.I.'s and relatively low Ni contents and *Mg's* indicate that these are not primary mantle melts and have fractionated olivine and possibly other phases.

Table 3-11 contains loss on ignition (LOI) values for all but eight of the samples. The lowest measured LOI is 2.4 wt.% in LBZ sample BS06-38. The highest LOI values are from the lower margin and upper margin samples, BS06-37 and BS06-71, respectively, and another UBZ

Table 3-11. Whole rock (XRF) and trace element (ICP-MS) geochemistry and CIPW norms for Bone Springs Sill rocks. Whole rock data are presented unnormalized, some with loss on ignition (LOI) first, and then normalized with trace elements, so that %oxides + ppms or ppbs trace elements = 100% volatile-free.

lith	L.Margin	LBZ mzgb	LBZ mzgb	LBZ mzgb	LBZ mzgb	LBZ mzgb	LBZ mzgb
sample	BS06-37	BS04-2	BS04-7	BS04-9	BS04-10	BS04-11	BS06-38
strat (m)	0.1	0.8	3.8	9.5	10.2	13.3	2.3
SiO_2	40.61	43.14	42.82	43.39	41.16	41.67	41.46
TiO_2	3.93	3.83	3.73	3.78	3.98	4.34	3.93
Al_2O_3	16.47	15.86	15.74	16.01	15.20	15.57	14.40
FeO	11.45	12.13	12.16	12.52	13.51	13.01	13.85
MnO	0.11	0.17	0.18	0.18	0.18	0.17	0.19
MgO	4.47	6.74	6.24	6.36	7.53	6.56	8.65
CaO	5.74	7.39	7.97	8.14	8.08	9.76	7.58
Na_2O	4.98	3.84	4.15	4.31	3.39	3.29	3.67
K_2O	2.47	2.29	2.16	2.43	2.05	1.90	2.00
P_2O_5	0.97	0.92	0.89	0.85	0.78	0.74	0.71
LOI	8.01						2.38
Total	99.20	96.32	96.03	97.98	95.88	97.00	98.82
SiO_2	44.35	44.63	44.43	44.14	42.79	42.82	42.86
TiO_2	4.29	3.96	3.87	3.85	4.14	4.46	4.06
Al_2O_3	17.99	16.41	16.33	16.29	15.81	16	14.89
FeO	12.51	12.55	12.62	12.74	14.04	13.37	14.32
MnO	0.12	0.18	0.19	0.18	0.19	0.18	0.2
MgO	4.88	6.98	6.48	6.47	7.83	6.74	8.94
CaO	6.27	7.65	8.27	8.28	8.4	10.03	7.84
Na_2O	5.43	3.97	4.31	4.38	3.53	3.38	3.79
K_2O	2.69	2.37	2.24	2.47	2.13	1.95	2.07
P_2O_5	1.06	0.95	0.93	0.87	0.81	0.76	0.73
Total *	99.59	99.65	99.67	99.67	99.67	99.69	99.7
Mg' **	41	49.8	47.8	47.5	49.9	47.3	52.7
Ni	43.4	38.8	42.6	45.1	59.4	40.6	85.8
Cr	27.2	29.6	28.0	34.5	49.1	31.3	66.5
V	243	216	216	225	273	288	295
Ba	958	680	642	504	440	397	394
Ga	23.5	24.3	22.07	21.62	21.03	21.7	21.29
Cu	43.1	39.78	37.53	33.89	32.94	30.29	32.66
Zn	121.7	107.0	104.0	103.1	111.3	100.4	108.4
Pb	43.13	39.78	37.53	33.89	32.94	30.29	32.66
La	56.68	49.18	47.71	45.22	40.81	38.00	38.92
Ce	119.5	98.7	95.7	90.3	82.2	77.4	82.5
Pr	15.12	11.83	11.42	10.74	9.87	9.50	10.48
Nd	61.09	50.09	48.35	45.56	42.24	40.93	42.47
Sm	12.78	11.38	10.93	10.22	9.61	9.68	9.12

Table 3-11, continued. Whole rock (XRF) and trace element (ICP-MS) geochemistry and CIPW norms for Bone Springs Sill rocks.

lith	LBZ mzgb	LBZ mzgb	LBZ mzgb	CZ mzgb	CZ mzgb	CZ mzgb	CZ mzgb
sample	BS06-45	BS06-46	BS04-12	BS04-13	BS05-19	BS04-3	BS06-57
strat (m)	8	11	17.1	19	18.6	25.8	25
SiO_2	40.51	39.95	43.55	44.16	45.04	44.94	44.11
TiO_2	4.10	4.41	4.47	4.10	3.72	3.99	3.69
Al_2O_3	14.18	14.09	15.78	16.96	16.60	17.64	16.85
FeO	13.95	13.71	11.70	10.20	10.15	8.89	9.31
MnO	0.19	0.18	0.17	0.16	0.16	0.13	0.15
MgO	8.63	8.17	5.04	3.97	3.57	4.25	3.83
CaO	7.72	8.66	9.81	9.63	9.03	9.14	9.55
Na_2O	3.23	2.98	3.91	4.46	4.87	4.52	4.53
K_2O	1.71	1.53	2.38	2.59	2.70	2.69	2.31
P_2O_5	0.69	0.63	0.80	1.17	1.29	0.52	0.94
LOI	4.40	4.69			3.76		3.87
Total	99.31	98.99	97.61	97.40	100.90	96.73	99.12
SiO_2	42.54	42.23	44.47	45.18	46.2	46.3	46.15
TiO_2	4.31	4.66	4.57	4.19	3.82	4.11	3.86
Al_2O_3	14.89	14.89	16.11	17.36	17.03	18.17	17.62
FeO	14.65	14.49	11.95	10.44	10.42	9.16	9.74
MnO	0.2	0.19	0.17	0.16	0.16	0.14	0.15
MgO	9.06	8.64	5.15	4.07	3.66	4.38	4
CaO	8.11	9.15	10.02	9.85	9.26	9.42	9.99
Na_2O	3.39	3.15	3.99	4.56	5	4.66	4.74
K_2O	1.79	1.62	2.43	2.65	2.77	2.77	2.41
P_2O_5	0.73	0.67	0.82	1.2	1.32	0.53	0.99
Total *	99.67	99.69	99.68	99.66	99.64	99.64	99.65
Mg' **	52.4	51.5	43.4	41	38.5	46	42.3
Ni	84.1	71.7	19.9	9.8	7.1	19.6	10.3
Cr	66.7	53.8	8.1	1.9	1.1	0.0	0.6
V	325	364	228	169	153	177	181
Ba	395	373	457	529	579	581	499
Ga	21	19.66	21.6	18.97	22.39	21.5	21.97
Cu	32.24	30.23	37.31	37.9	48.49	27.82	37.56
Zn	113.0	108.0	94.4	86.9	95.6	74.5	81.9
Pb	32.24	30.23	37.31	37.90	48.49	27.82	37.56
La	37.62	34.95	44.75	50.27	58.29	41.89	50.00
Ce	80.3	75.6	91.1	102.3	118.1	82.7	107.1
Pr	10.24	9.80	11.08	12.40	14.22	9.80	13.71
Nd	42.18	40.97	47.33	53.28	61.14	41.22	56.56
Sm	9.08	9.01	11.08	12.36	13.85	9.49	12.28

Table 3-11, continued. Whole rock (XRF) and trace element (ICP-MS) geochemistry and CIPW norms for Bone Springs Sill rocks.

lith	CZ mzgb	CZ mix	CZ mix	CZ mzsy	CZ mzsy	CZ mzsy	CZ mzsy
sample	BS04-4	BS05-20	BS05-25	BS06-49	BS06-50	BS06-51	BS06-59
strat (m)	22.8		23.1	19.7	20.9	20.9	25.4
SiO_2	45.89	48.23	52.08	50.94	50.45	50.67	52.30
TiO_2	3.27	2.95	1.59	1.72	1.58	1.58	1.10
Al_2O_3	17.66	17.45	17.90	19.11	18.92	19.32	19.61
FeO	9.22	9.78	7.01	6.20	5.76	5.91	6.31
MnO	0.15	0.16	0.12	0.12	0.10	0.11	0.13
MgO	3.37	2.56	1.83	1.52	1.51	1.39	0.97
CaO	9.04	7.10	5.01	4.12	4.15	3.85	3.39
Na_2O	5.17	5.87	5.89	6.89	7.15	7.44	7.25
K_2O	2.79	2.77	5.01	4.28	4.32	4.29	4.39
P_2O_5	1.25	0.82	0.47	0.45	0.47	0.41	0.30
LOI		2.71	4.54	4.47	5.57	5.38	4.62
Total	97.82	100.41	101.45	99.81	99.99	100.36	100.37
SiO_2	46.75	49.13	53.55	53.2	53.23	53.13	54.36
TiO_2	3.33	3.01	1.64	1.8	1.67	1.66	1.14
Al_2O_3	17.99	17.78	18.4	19.96	19.97	20.26	20.38
FeO	9.39	9.96	7.21	6.47	6.08	6.2	6.56
MnO	0.15	0.16	0.12	0.12	0.1	0.11	0.14
MgO	3.44	2.61	1.89	1.58	1.6	1.46	1.01
CaO	9.2	7.23	5.15	4.3	4.38	4.03	3.53
Na_2O	5.26	5.98	6.06	7.2	7.55	7.8	7.53
K_2O	2.85	2.82	5.15	4.47	4.56	4.5	4.57
P_2O_5	1.28	0.83	0.48	0.47	0.5	0.43	0.31
Total *	99.64	99.51	99.65	99.57	99.64	99.58	99.53
Mg' **	39.5	31.8	31.8	30.3	31.9	29.6	21.5
Ni	4.9	3.9	2.6	3.3	4.1	2.1	2.3
Cr	1.9	0.6	0.4	2.0	1.5	0.7	0.8
V	122	50	26	29	37	27	7
Ba	629	1010	860	981	902	1004	1076
Ga	22.17	22.04	18.09	19.21	19.1	20.45	23.08
Cu	40.64	25.78	27.46	19.01	17.62	18.77	16.42
Zn	86.4	98.6	83.4	73.9	66.7	73.7	82.4
Pb	40.64	25.78	27.46	19.01	17.62	18.77	16.42
La	56.56	77.54	63.01	70.47	68.40	69.48	65.70
Ce	113.4	154.0	118.6	141.0	136.1	140.2	127.3
Pr	13.56	17.99	13.11	16.59	15.84	16.54	14.53
Nd	57.92	74.34	50.96	61.81	58.37	61.79	52.21
Sm	13.12	16.23	10.96	12.29	11.49	12.44	10.20

Table 3-11, continued. Whole rock (XRF) and trace element (ICP-MS) geochemistry and CIPW norms for Bone Springs sill rocks.

lith sample	CZ mzsy BS05-28	UBZ teph BS05-29	UBZ teph BS06-72	UBZ teph BS05-30	U. Margin BS06-71	Teph BS05-26
strat (m)	26.6	29.5	29	28.5	30	
SiO_2	51.21	41.47	44.72	44.51	39.67	44.73
TiO_2	1.73	3.99	3.47	3.72	3.82	3.77
Al_2O_3	19.00	16.99	16.51	16.29	16.42	16.08
FeO	6.76	13.67	10.34	11.69	11.36	11.94
MnO	0.12	0.09	0.16	0.17	0.09	0.18
MgO	1.54	4.68	4.25	4.76	4.76	5.41
CaO	4.16	5.39	7.47	8.25	5.63	8.44
Na_2O	7.14	5.03	4.67	4.39	4.80	4.37
K_2O	4.06	2.19	2.67	2.41	2.10	2.15
P_2O_5	0.48	0.96	0.88	0.94	0.94	0.93
LOI	5.40	8.73	4.19	3.51	8.80	2.37
Total	101.60	103.19	99.33	100.65	98.39	100.35
SiO_2	53.02	43.77	46.83	45.66	44.13	45.49
TiO_2	1.79	4.21	3.64	3.82	4.25	3.83
Al_2O_3	19.67	17.92	17.29	16.71	18.26	16.35
FeO	7	14.43	10.82	11.99	12.64	12.14
MnO	0.12	0.1	0.17	0.18	0.1	0.18
MgO	1.6	4.94	4.45	4.88	5.29	5.5
CaO	4.31	5.69	7.82	8.46	6.26	8.58
Na_2O	7.39	5.31	4.89	4.5	5.34	4.44
K_2O	4.2	2.31	2.79	2.48	2.33	2.18
P_2O_5	0.5	1.01	0.93	0.96	1.05	0.94
Total *	99.6	99.69	99.63	99.64	99.65	99.63
Mg' **	28.9	37.9	42.3	42	42.7	44.7
Ni	3.4	34.9	25.6	27.3	39.9	34.9
Cr	0.7	27.8	18.1	18.4	27.8	24.0
V	29	230	186	200	233	207
Ba	1048	647	649	607	618	561
Ga	22.84	23.53	20.52	22.5	24.58	20.08
Cu	17.41	46.05	37.38	40.4	45.83	41.24
Zn	78.8	123.2	95.9	98.5	112.2	101.9
Pb	17.41	46.05	37.38	40.40	45.83	41.24
La	64.95	52.52	50.92	50.07	57.40	50.11
Ce	122.4	106.0	106.5	100.6	121.4	100.7
Pr	13.56	12.68	13.31	12.02	15.37	12.00
Nd	52.68	54.49	53.26	51.31	62.01	50.84
Sm	11.28	12.56	11.33	11.56	12.98	11.57

Table 3-11, continued. Whole rock (XRF) and trace element (ICP-MS) geochemistry and CIPW norms for Bone Springs sill rocks.

lith	L.Margin	LBZ mzgb	LBZ mzgb	LBZ mzgb	LBZ mzgb	LBZ mzgb	LBZ mzgb
sample	BS06-37	BS04-2	BS04-7	BS04-9	BS04-10	BS04-11	BS06-38
Eu	4.08	3.62	3.47	3.35	3.13	3.14	2.98
Gd	10.82	9.92	9.71	9.18	8.68	8.73	7.93
Tb	1.54	1.41	1.36	1.31	1.22	1.23	1.13
Dy	8.34	7.49	7.25	6.83	6.44	6.40	6.02
Ho	1.48	1.34	1.31	1.22	1.16	1.15	1.08
Er	3.62	3.21	3.13	3.01	2.83	2.70	2.58
Tm	0.47	0.42	0.41	0.39	0.36	0.35	0.34
Yb	2.73	2.38	2.34	2.23	2.02	2.02	1.97
Lu	0.40	0.35	0.35	0.33	0.30	0.30	0.29
Ba	983.0	663.1	613.4	495.8	424.4	390.4	382.6
Th	5.35	4.62	4.63	4.32	3.83	3.46	3.85
Nb	53.26	48.88	49.12	45.94	41.66	39.17	37.64
Y	35.82	35.26	34.11	32.23	29.93	29.97	26.8
Hf	9.28	7.96	7.92	7.43	6.89	7.19	6.81
Ta	3.57	3.26	3.27	3.04	2.8	2.69	2.55
U	1.72	1.45	1.47	1.41	1.21	1.09	1.24
Pb	5.33	4.07	4.3	3.8	3.45	3.15	3.42
Rb	40.48	34.39	32.57	36.07	30.05	26.3	32.42
Cs	4.46	3.25	3.41	1.45	1.16	0.63	0.77
Sr	857.0	961.7	972.1	1182.3	1172.7	1179.7	1159.0
Sc	26.22	22.72	22.45	21.86	24.12	32.37	22.54
Zr	396.5	352.4	348.5	325.4	297.5	293.8	292.6
CIPW norms***							
%AN	43.8	49.1	50.2	53.1	59.0	62.7	55.0
or	15.9	14.0	13.2	14.6	12.6	11.5	12.2
ab	21.4	20.6	18.4	15.4	14.6	13.5	14.3
an	16.7	19.9	18.6	17.5	21.0	22.7	17.5
ne	13.2	7.0	9.7	11.7	8.2	8.2	9.6
di	5.8	9.3	13.0	14.2	12.2	17.4	13.2
ol	7.9	11.6	9.8	9.6	13.6	8.0	15.8
mt	8.4	7.9	7.8	7.7	8.2	8.6	8.0
il	8.1	7.5	7.3	7.3	7.8	8.4	7.7
ap	2.5	2.2	2.2	2.0	1.9	1.8	1.7
hem	0	0	0	0	0	0	0

* Normalized to volatile-free (100% - trace elements)
** Molar 100*Mg/(Mg+Fe)
*** FeO/Fe_2O_3 allocated after Irvine and Baragar (1971)

Table 3-11, continued. Whole rock (XRF) and trace element (ICP-MS) geochemistry and CIPW norms for Bone Springs sill rocks.

lith	LBZ mzgb	LBZ mzgb	LBZ mzgb	CZ mzgb	CZ mzgb	CZ mzgb	CZ mzgb
sample	BS06-45	BS06-46	BS04-12	BS04-13	BS05-19	BS04-3	BS06-57
Eu	3.00	3.00	3.50	3.95	4.27	3.20	4.00
Gd	7.94	7.99	10.17	10.95	12.13	8.51	10.88
Tb	1.12	1.13	1.44	1.52	1.72	1.24	1.53
Dy	5.99	6.12	7.53	8.04	9.07	6.73	8.18
Ho	1.07	1.07	1.38	1.43	1.62	1.20	1.44
Er	2.51	2.55	3.26	3.38	3.81	2.93	3.44
Tm	0.33	0.33	0.44	0.43	0.49	0.40	0.45
Yb	1.92	1.87	2.47	2.46	2.84	2.30	2.61
Lu	0.28	0.29	0.37	0.36	0.40	0.33	0.38
Ba	391.3	366.9	466.3	521.1	547.9	572.5	491.7
Th	3.61	3.24	4.39	4.51	5.41	4.5	4.75
Nb	36.51	33.8	48.55	49.84	55.65	49.15	47.74
Y	26.32	26.49	34.71	37.23	41.41	31.7	36.37
Hf	6.64	6.87	8.75	8.1	8.92	8.61	8.92
Ta	2.49	2.33	3.34	3.38	3.76	3.36	3.2
U	1.17	1.04	1.38	1.43	1.71	1.44	1.52
Pb	3.3	3.12	4.08	3.88	4.87	3.67	4.29
Rb	28.78	26.4	36.82	35.11	46.89	36.84	41.27
Cs	1.19	1.16	0.48	0.63	0.66	0.88	0.73
Sr	1178.6	1118.0	1070.8	1298.8	1160.1	1311.9	1316.4
Sc	25.33	33.89	33.07	24.32	19.68	30.17	29.95
Zr	279.4	273.1	360.1	349.1	398.9	367.6	378.5
CIPW norms***							
%AN	55.5	58.9	54.6	52.8	43.6	56.7	51.0
or	10.6	9.5	14.3	15.6	16.3	16.3	14.2
ab	16.1	15.1	15.6	17.0	20.4	15.6	18.9
an	20.1	21.6	18.8	19.0	15.8	20.4	19.6
ne	6.8	6.2	9.8	11.6	11.8	12.9	11.5
di	12.2	15.3	19.8	17.1	16.7	17.7	18.2
ol	16.1	13.0	2.5	1.5	1.0	1.9	1.1
mt	8.4	8.9	8.2	5.5	7.6	1.8	5.1
il	8.2	8.8	8.7	7.9	7.2	7.8	7.3
ap	1.7	1.5	1.9	2.8	3.1	1.2	2.3
hem	0	0	0.4	1.9	0.1	4.4	1.8

* Normalized to volatile-free (100% - trace elements)
** Molar 100*Mg/(Mg+Fe)
*** FeO/Fe_2O_3 allocated after Irvine and Baragar (1971)

Table 3-11, continued. Whole rock (XRF) and trace element (ICP-MS) geochemistry and CIPW norms for Bone Springs sill rocks.

lith	CZ mzgb	CZ mix	CZ mix	CZ mzsy	CZ mzsy	CZ mzsy	CZ mzsy
sample	BS04-4	BS05-20	BS05-25	BS06-49	BS06-50	BS06-51	BS06-59
Eu	4.16	5.38	3.34	3.74	3.35	3.67	3.44
Gd	11.40	13.58	9.20	10.07	9.52	10.35	8.37
Tb	1.61	2.02	1.43	1.58	1.50	1.60	1.30
Dy	8.53	10.98	8.01	8.88	8.54	9.14	7.59
Ho	1.50	1.96	1.51	1.64	1.59	1.70	1.46
Er	3.59	4.73	3.95	4.13	4.06	4.36	3.76
Tm	0.47	0.61	0.54	0.59	0.57	0.61	0.55
Yb	2.68	3.47	3.28	3.47	3.44	3.61	3.23
Lu	0.39	0.51	0.50	0.53	0.51	0.54	0.49
Ba	610.3	975.5	807.2	994.9	908.6	1017.7	1102.0
Th	5.18	5.86	8.98	8.99	9.59	9.18	9.43
Nb	52.06	66.45	76.57	84.13	85.1	94.43	84.38
Y	39.46	49.86	39.26	41.74	40.08	42.94	36.82
Hf	8.48	10.01	11.41	11.7	11.84	11.97	11.18
Ta	3.54	4.36	5.03	5.26	5.26	5.69	5.26
U	1.6	1.82	2.84	2.94	3.16	2.93	3.02
Pb	4.58	4.57	8.16	7.25	7.55	7.83	8.28
Rb	44.07	49.39	80.21	72.14	68.49	72.76	72.87
Cs	0.83	0.9	0.78	1.69	1.64	1.81	1.46
Sr	1294.1	1577.6	550.8	1077.1	593.4	790.0	1259.1
Sc	18.08	7.56	7.15	4.61	5.08	4.78	2.43
Zr	373.8	445.5	565.7	579.6	590.2	599.3	580.0
CIPW norms***							
%AN	46.1	32.1	23.1	22.8	20.1	19.6	20.6
or	16.8	16.7	30.4	26.4	27.0	26.6	27.1
ab	19.9	28.2	26.0	30.3	28.4	28.7	32.2
an	17.0	13.3	7.8	9.0	7.1	7.0	8.3
ne	13.3	12.1	13.7	16.6	19.2	20.2	17.2
di	15.7	13.7	11.9	7.4	9.0	8.2	6.0
ol	0.9	1.7	1.4	1.0	0.3	0.6	2.5
mt	7.0	6.5	4.6	4.8	4.6	4.6	3.8
il	6.3	5.7	3.1	3.4	3.2	3.2	2.2
ap	3.0	1.9	1.1	1.1	1.2	1.0	0.7
hem	0	0	0	0	0	0	0

* Normalized to volatile-free (100% - trace elements)
** Molar 100*Mg/(Mg+Fe)
*** FeO/Fe_2O_3 allocated after Irvine and Baragar (1971)

Table 3-11, continued. Whole rock (XRF) and trace element (ICP-MS) geochemistry and CIPW norms for Bone Springs sill rocks.

lith	CZ mzsy	UBZ teph	UBZ teph	UBZ teph	U. Margin	Teph
sample	BS05-28	BS05-29	BS06-72	BS05-30	BS06-71	BS05-26
Eu	3.57	4.13	3.64	3.72	4.21	3.74
Gd	9.55	11.25	9.78	10.19	11.26	10.04
Tb	1.47	1.58	1.39	1.45	1.61	1.45
Dy	8.11	8.30	7.50	7.81	8.64	7.81
Ho	1.53	1.50	1.36	1.40	1.55	1.38
Er	3.93	3.65	3.30	3.34	3.71	3.33
Tm	0.55	0.46	0.43	0.43	0.49	0.42
Yb	3.18	2.57	2.54	2.43	2.81	2.43
Lu	0.48	0.38	0.37	0.36	0.42	0.37
Ba	997.2	591.4	649.0	572.8	632.6	550.3
Th	8.28	4.96	5.37	4.8	5.57	4.77
Nb	79.68	51.55	53.91	49.61	54.7	49.86
Y	39.75	38.61	34.06	35.46	38.61	35.64
Hf	10.94	8.61	8.61	8.09	9.34	8.21
Ta	4.92	3.53	3.52	3.35	3.66	3.37
U	2.69	1.56	1.74	1.52	1.79	1.5
Pb	6.43	3.86	4.91	4.21	5	4.3
Rb	67.5	32.69	45.57	38.93	34.76	24.04
Cs	1.25	4.74	2.93	2.65	4.69	2.21
Sr	792.8	624.9	1249.6	1151.8	785.6	1286.1
Sc	4.78	22.75	19.74	21.61	25.01	21.26
Zr	527.8	371.0	393.5	358.4	411.1	359.9
CIPW norms***						
%AN	20.7	43.8	42.4	46.2	45.2	45.6
or	24.8	13.6	16.5	14.6	13.7	12.9
ab	31.1	23.3	23.1	21.0	23.0	21.7
an	8.1	18.2	17.0	18.0	18.9	18.2
ne	17.1	11.7	9.9	9.2	12.0	8.6
di	8.1	2.7	12.4	14.0	4.1	14.4
ol	1.5	11.9	4.7	6.0	9.5	7.1
mt	4.8	8.3	7.4	7.7	8.3	7.7
il	3.4	8.0	6.9	7.2	8.1	7.3
ap	1.2	2.3	2.2	2.2	2.4	2.2
hem	0	0	0	0	0	0

* Normalized to volatile-free (100% - trace elements)
** Molar 100*Mg/(Mg+Fe)
*** FeO/Fe_2O_3 allocated after Irvine and Baragar (1971)

sample, BS05-29, found within 10-20 cm of the upper margin – all have LOI of 8-9 wt.%. Other samples have LOI from 2.7-5.6 wt.%. All BSS rocks, even the earliest to crystallize, contain biotite and/or amphibole, but other than the water contained in those phases the volatiles are probably attributable to late stage magmatic or meteoric fluid. All samples contain analcime with 7-9 wt.% H_2O and some thomsonite with 12-15 wt.% H_2O, and some margin rocks and monzosyenites contain calcite; these phases probably host most of the remaining volatiles.

Figure 3-21 shows oxide variation with SiO_2 in Harker diagrams. For the most part, BSS rocks follow expected trends: Al_2O_3, Na_2O, and K_2O increase with SiO_2 and TiO_2, FeO, MnO, MgO, and CaO decrease with SiO_2; P_2O_5 behaves compatibly in the UBZ samples, increases with SiO_2 in the LBZ samples and some of the CZ mafic samples, but decreases suddenly in the middle of the CZ mafic trend. The margin and UBZ rocks were nearly saturated with apatite upon intrusion, indicated by the quench-textured apatite they contain, all LBZ rocks contain apatite as a cumulus phase and interstitially, and so the interstitial liquid was apparently largely depleted in P_2O_5 during crystallization of the CZ rocks.

There is some scatter along the trends in all Figure 3-21 charts, but the two margin samples (BS06-37 and BS06-71) and one UBZ sample (BS06-29) are anomalous. They plot together and slightly apart from the trends, most notably in the SiO_2-Al_2O_3, -MnO, -CaO, and -Na_2O charts. The remaining UBZ samples (BS05-30 and BS06-72) are on trend with other BSS rocks. Of the UBZ and margin samples – which represent quenched or quickly cooled intruding magma(s) – it is BS06-30 and BS06-72 that are most likely to be parental to the plutonic rocks in BSS. Figure 3-22 shows the trends of cumulate compositions and a liquid line of descent marking the separation of mafic minerals from a parental UBZ magma. The petrography of UBZ and margin rocks indicate that olivine and Fe-Ti oxide began crystallizing before magma

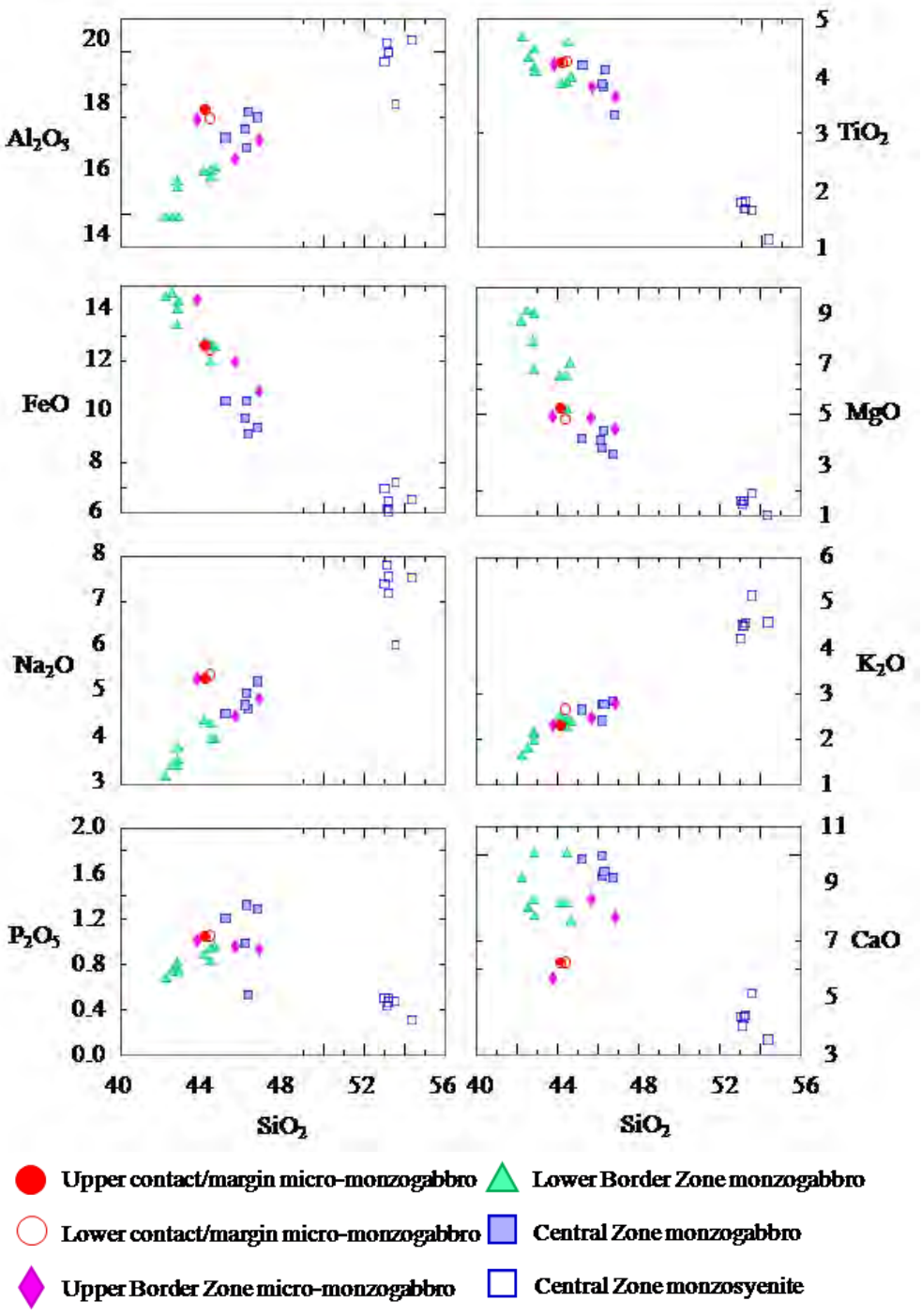

Figure 3-21. Harker diagrams of major elements vs. SiO_2 in Bone Springs Sill rocks. Symbols are the same as those used in Figure 3-6.

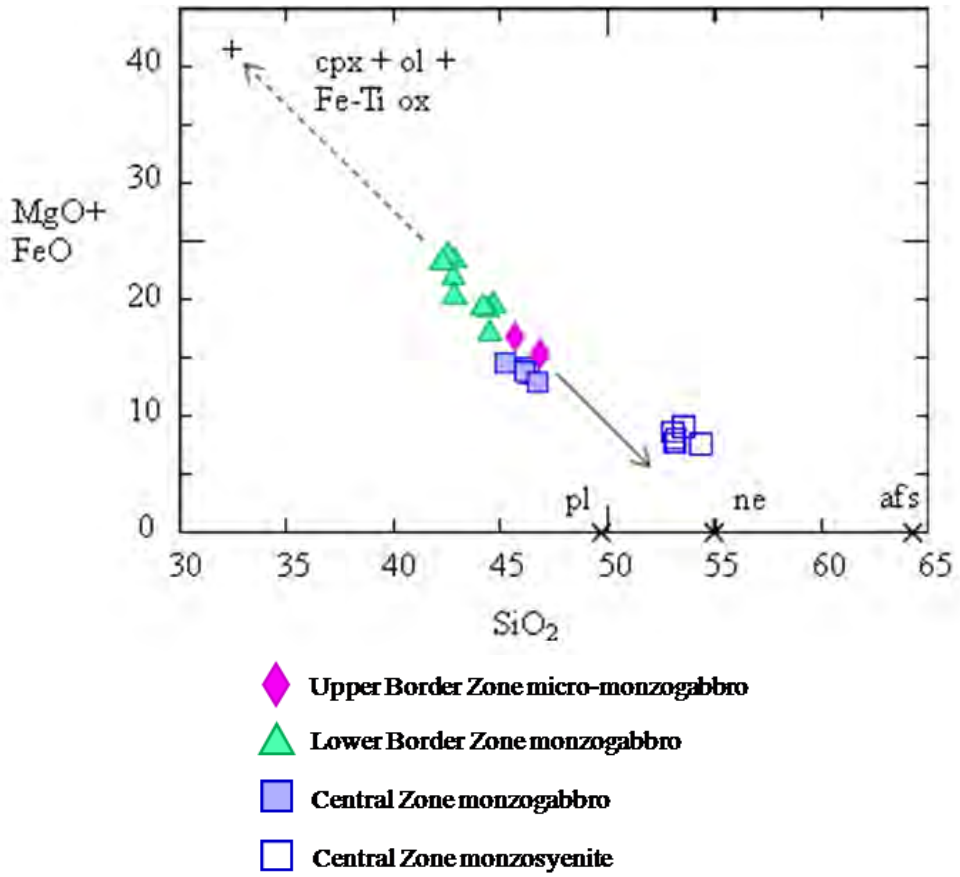

Figure 3-22. SiO_2 vs. MgO+FeO for Bone Springs Sill rock and mineral compositions. The cross at the upper left is the average composition of LBZ mafic cumulate minerals integrated by molar proportion. Feldspar and feldspathoid compositions are marked along the SiO_2-axis. The arrows originate between the two UBZ samples (BS05-30 and BS06-72) which are interpreted to be parental liquids to the BSS plutonic rocks; the dashed arrow points in the direction of cumulate minerals and the solid arrow points in the direction of liquid descent from extracting cumulate minerals. LBZ compositions fall on or near the cumulate trend. Offsets from either of these trends are interpreted as being due to: (1) the presence of apatite and some plagioclase and nepheline in the cumulate assemblage; (2) crystallization of plagioclase, nepheline, and alkali feldspar in the cumulus interstitial liquid; or (3) evolving plagioclase composition; and/or (4) changing modal proportions in the cumulate assemblage between LBZ and CZ mafic rocks.

intrusion and that apatite, nepheline, clinopyroxene, and plagioclase startied crystallizing shortly after intrusion. The bulk compositions of the LBZ rocks are largely controlled by the accumulation of olivine, clinopyroxene, and Fe-Ti oxide.

Determination of felsic mineral proportions from mass balance equations

The modal abundances of mafic minerals in BSS are fairly well constrained by point-counting in thin section (Table 3-1) though there are some complications from localized serpentinization of olivine and oxidation of some Fe-Ti oxides. Visual assessment of the abundances of the feldspars and analcime is problematic because they are intergrown and fine-grained. It is difficult to determine how much original feldspathoid was present and how much crystallized late at the expense of feldspar. For this reason, I calculated mineral abundances for the LBZ rocks by mass balance (after the method of Bryan et al., 1969) based on whole rock chemistry and mineral chemistries determined by electron microprobe. The calculated abundances of the melanocratic minerals can be checked by comparison to the point-counting data, and the proportions of leucocratic minerals can be used (1) to check lithological classification and (2) to assess fractional crystallization models, presented in sections below. The result is analogous to calculating a normative composition but using constraints on mineral compositions from analytical data.

Table 3-12 contains the mineral abundances from calculations and the sum of the squares of the residuals ($\sum r^2$) to assess the results. Mineral compositions from the samples themselves were used when possible, though averages for the lithology were used in some cases. The first portion of Table 3-12 contains modes calculated with analcime, while the second portion contains modes calculated using a nepheline composition based on literature compositions

Table 3-12. Modes for Bones Spring Sill LBZ monzogabbros determined by mass balance. Mafic mineral modes are well-constrained but felsic mineral proportions are difficult to determine due to the nature of the fine-grained interstitial material, intergrowth of feldspars, and analcimization. Modes are determined for an assemblage with analcime and with a model nepheline composition.

sample	BS04-9	BS04-7	BS04-2	BS04-12	BS-38	BS04-10	BS04-11	BS-45	BS-46	Avg. LBZ %
cpx	0.147	0.138	0.117	0.238	0.142	0.121	0.183	0.143	0.183	15.7
ol core	0.096	0.104	0.118	0.027	0.168	0.149	0.101	0.171	0.141	11.9
bt	0.077	0.042	0.065	0.077	0.079	0.060	0.045	0.068	0.068	6.5
ap	0.030	0.029	0.026	0.026	0.024	0.026	0.025	0.021	0.019	2.5
pl	0.201	0.211	0.219	0.193	0.196	0.263	0.285	0.223	0.237	22.5
afs	0.125	0.138	0.146	0.132	0.094	0.116	0.111	0.088	0.073	11.4
Ti-mt	0.111	0.115	0.105	0.117	0.105	0.115	0.124	0.109	0.114	11.3
anlc	0.217	0.206	0.187	0.189	0.179	0.128	0.110	0.146	0.128	16.6
total	1.004	0.983	0.985	0.999	0.986	0.976	0.985	0.969	0.962	98.3
resid	0.118	0.097	0.043	0.086	0.275	0.292	0.313	0.146	0.119	
∑ res^2	1.003	0.589	0.145	0.495	0.411	0.457	0.518	0.138	0.097	

sample	BS04-9	BS04-7	BS04-2	BS04-12	BS-38	BS04-10	BS04-11	BS-45	BS-46	Avg. LBZ %
cpx	0.197	0.149	0.116	0.270	0.155	0.138	0.188	0.152	0.190	17.3
ol core	0.070	0.112	0.134	0.012	0.179	0.139	0.102	0.180	0.149	12.0
bt	0.060	0.091	0.005	0.051	0.036	0.050	0.000	0.032	0.037	4.0
ap	0.021	0.027	0.025	0.020	0.020	0.023	0.024	0.018	0.016	2.2
pl	0.174	0.209	0.237	0.179	0.200	0.252	0.289	0.230	0.243	22.4
afs	0.109	0.088	0.169	0.131	0.088	0.103	0.117	0.086	0.071	10.7
Ti-mt	0.122	0.090	0.118	0.129	0.109	0.119	0.137	0.113	0.117	11.7
neph	0.239	0.214	0.165	0.196	0.186	0.144	0.117	0.148	0.129	17.1
total	0.992	0.979	0.969	0.988	0.973	0.968	0.975	0.958	0.952	97.3
resid	-0.464	-1.309	-0.058	-0.323	0.033	-0.278	0.127	-0.010	-0.017	
∑ res^2	1.166	2.255	0.026	0.558	0.067	0.276	0.340	0.004	0.002	

(Wilkinson and Hensel, 1994; Deer et al, 1996) and adjusted based on Na:K in reintegrated analcime compositions.

Overall, the abundances calculated for most samples show reasonably low $\sum r^2$, though some are >1 (Table 3-12). The abundances of mafic minerals calculated using nepheline better match the modal results from point-counting than those using analcime. For both sets of calculations, calculated olivine (12%) is higher on average than optical data (8.5%). This probably reflects that serpentinized olivine in the early-crystallizing clumps is not sufficiently assessed by point-counting. The calculated alkali feldspar is 7-17%, plagioclase is 17-29%, and analcime/nepheline is 11-24%. These felsic mineral abundances support the classification of these rocks as analcime monzogabbros and suggest that they may have been nepheline monzogabbros had they not experienced analcimization of nepheline.

Mineral-liquid equilibrium and Mg/Fe

The partitioning of Mg and Fe between mafic silicates and liquid is a principal concern in petrology. The $K_D^{Mg/Fe}$ for olivine-liquid and for clinopyroxene-liquid is known, and so the Mg/Fe contents of these minerals constrain the Mg/Fe of the liquids from which they crystallize. In the case of BSS, the compositions of olivine and clinopyroxene are here used to investigate whether these minerals (1) crystallized from liquids more magnesian than their host rocks, in which case they may be phenocrysts or xenocrysts transported with the liquid, (2) crystallized from liquids less magnesian than their host rocks, in which case the rocks may be cumulates from gravitational settling, liquid extraction, etc., or (3) are in equilibrium with their host rocks, in which case the host rocks may represent liquid compositions *or* the apparent equilibrium may be fortuitous, due to some combination of cumulate minerals and trapped liquid that migrated

from lower in the section. By applying these criteria to the margins, monzogabbros, and monzosyenites of BSS, a plausible crystallization history can be deduced.

Olivine Mg/Fe systematics

Bowen and Schairer (1935) were among the first to experimentally investigate the MgO-FeO-SiO_2 system and to construct the olivine X_{Fo}-T phase diagram. Roeder and Emslie (1970) showed that the $K_D{}_{ol-l}^{Mg/Fe}$ of 0.30 ± 0.03 was remarkably constant in multicomponent systems across a range of P, T, and liquid compositions. This K_D has since been widely used to evaluate equilibrium in experiments and natural systems. As experimental data in the literature accumulated, Mysen (1975) argued that Roeder and Emslie's (1970) published K_D was not valid for all conditions – specifically, it increased with pressure and with fayalite-rich compositions. Toplis (2005) supported Mysen's (1975) findings, documented additional effects from the activities of SiO_2 and alkalis in the melt, and quantified them with a thermodynamic treatment.

The histograms of olivine compositions in Figure 3-8 show the changes with lithology in the sill. Figure 3-23 shows Bone Springs Sill olivine molar Mg/Fe plotted against whole rock molar Mg/Fe. The K_D for Mg/Fe olivine/liquid of 0.30 ± 0.03 from Roeder and Emslie (19750), is plotted, with error, for reference. Of the changes in $K_D{}_{ol-l}^{Mg/Fe}$ documented by Toplis (2005), the possibly low a_{SiO2} and the high alkalis would move the 1σ envelope to the right and down on the diagram, and the K_D line for the most Fe- rich olivines would steepen in the lower left of the diagram.

Two groups of olivine plot above and left of the Roeder and Emslie (1970) partition field (Figure 3-23) and are too magnesian to have crystallized from a liquid of their host rock compositions; thus, they likely crystallized during magma ascent or in a deeper chamber and were carried in during intrusion. The first group includes olivine cores with $Fo_{>76}$ from the

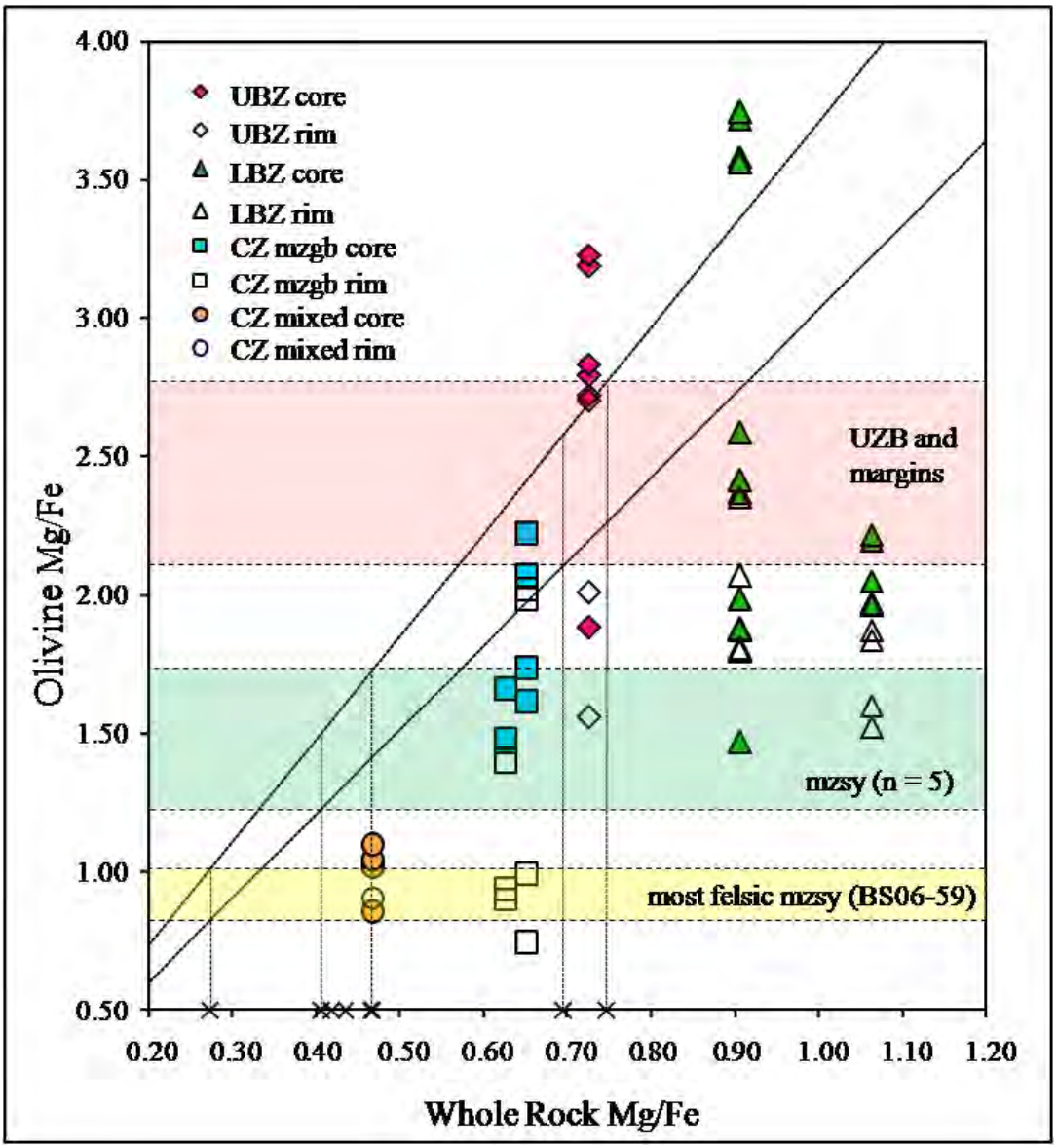

Figure 3-23. Bone Springs Sill olivine Mg/Fe vs. whole rock Mg/Fe. The diagonal lines delineate the field of $K_D{}_{ol-l}^{Mg/Fe}$ = 0.30 ± 0.03 from Roeder and Emslie (1970). Olivine compositions that plot within the K_D field are potentially in equilibrium with their host rocks, while olivines that plot above/left of the field are potentially phenocrystal and those that plot below/right of the field are potentially cumulate. The X's along the whole rock Mg/Fe axis mark the compositions of the Bone Springs samples interpreted to represent liquid compositions; their intersections with the K_D field define three shaded horizontal fields in which olivine compositions are in equilibrium with those liquids. As labeled, the yellow shaded field marks olivine equilibrium with the most felsic monzosyenite sample (BS06-59), the green shaded field marks olivine equilibrium with the other five analyzed monzosyenite samples, and the red shaded field marks olivine equilibrium with and is bounded by the upper and lower margin compositions (and all Upper Border Zone compositions fall between them)..

clusters of olivine + Fe-Ti oxide grains (a partially serpentinized example is shown in Figure 3-20c) from LBZ sample BS04-9 (whole rock Mg/Fe = ~0.91). These olivine compositions were in equilibrium with a melt of Mg/Fe = ~1.1, which is higher than rock sampled in BSS, and are thus interpreted to have been carried in with the intruding magma. The other group includes olivine cores and one rim of $Fo_{>73}$ from the UBZ sample BS05-30, an aphanitic-porphyritic sample. They are more magnesian than the margin sample that contains them and are interpreted to have crystallized shortly before intrusion and quenching of the margin but after the crystallization of the olivine + Fe-Ti oxide clusters.

All other LBZ and UBZ olivines fall to the right and below the Roeder and Emslie (1970) olivine-liquid Mg/Fe partition field on Figure 3-23. Some olivine cores and rims from BS04-9 (whole rock Mg/Fe = ~0.91) have Mg/Fe values of ~2.2-2.6, but all other cores and rims from UBZ and LBZ olivines are in the range of 1.4-2.2 Mg/Fe. All of these crystallized from liquids of a restricted compositional range that were less magnesian than their whole rock compositions. Thus, these olivines are cumulate. (By "cumulate" I mean an accumulation of minerals not proportional in abundance to their crystallizing assemblage. These are not necessarily only accumulations from crystal settling but more likely represent part of a residual assemblage after the removal of liquid pressed out of a crystalline framework).

All CZ mafic olivine cores and some rims have Mg/Fe of 1.4-2.2, similar to the LBZ and UBZ olivine cores and rims. Some of them (from sample BS04-4) plot in apparent equilibrium with their whole rock Mg/Fe values. This is likely fortuitous, as evidenced by the mantles on some of these BS04-4 olivines that are among the most Fe-rich in the sill (Mg/Fe < 1). It is more likely that this sample represents cumulate mafic minerals with enough felsic interstitial liquid to appear in equilibrium. These Fe-rich mantles are in the compositional range of one olivine core

and two rims from the mixed CZ samples that contain cm-scale segregations of monzosyenitic liquid. Other cores from mixed CZ samples are slightly more magnesian. The reasons I interpret the apparent olivine-melt CZ equilibrium compositions to be fortuitous are because of the Fe-rich rim compositions and because of the overrepresentation of felsic liquid in the CZ.

Also shown on the horizontal axis in Figure 3-23 are the whole rock Mg/Fe compositions of the BSS samples interpreted to represent liquids: the upper and lower contact rocks (BS06-71 and BS06-37, respectively), the most felsic monzosyenite sample (BS06-59), and the other five monzosyenite samples. Each sample or group of samples intersects with the $K_D{}_{ol-l}^{Mg/Fe}$ field to yield shaded horizontal fields delineating the range of olivine composition in equilibrium with these liquids. Their compositions constrain the likely Mg/Fe of the intruding (mafic) and residual (felsic) liquids in the sill. Of the olivines interpreted to have crystallized post-intrusion, some of those with the highest Mg/Fe cores plot in equilibrium with liquids bracketed by the margin compositions. Some LBZ and CZ olivine cores and rims are in equilibrium with the five monzosyenite samples, and no LBZ or UBZ olivines were in equilibrium with liquids more evolved than those five monzosyenites. I interpret this range of liquid to represent the interstitial liquid composition of the LBZ cumulates. While the LBZ rocks were cooling below their liquidus or a portion of their interstitial liquid was expelled, some CZ olivine grains were still nucleating. Both CZ monzogabbro samples represented contain olivine rims that were in equilibrium with the most felsic monzosyenite sample, as did some olivine from mixed samples. I interpret this most felsic monzosyenite liquid to represent most of the interstitial liquid in the CZ rocks. Only one CZ olivine rim is more Fe-rich than this liquid would produce.

Clinopyroxene Mg/Fe systematics

A diagram for clinopyroxene analogous to that for olivine is shown in Figure 3-24. The $K_D{}^{Mg/Fe}_{cpx-l}$ of 0.275 ± 0.067 that defines the field in Figure 3-24 is from Putirka et al. (2003) and is based on >440 experiments from 850-1875° C and from 1 bar to >100 kb, with silica-saturated and unsaturated liquid compositions up to 71 wt.% SiO_2, and with volatiles up to 12.7%. Exact H_2O-CO_2 compositions were not determined but some experiments contained up to 2.7% CO_2 (Putirka et al., 2003). The relative error for the $K_D{}^{Mg/Fe}_{cpx-l}$ is higher than that for $K_D{}^{Mg/Fe}_{ol-l}$ and so Figure 3-24 does not constrain the mineral-liquid relationships for clinopyroxene as well as Figure 3-23 does for olivine. The plotted clinopyroxene compositions from the LBZ and CZ mafic samples are integrations of high- and low-z (atomic number) sectors within pyroxenes and some normal zoning. The margin and monzosyenite clinopyroxene analyses are from grains without sector zonation and represent cores, rims, and mantles.

Clinopyroxene from LBZ and CZ mafic rocks have Mg/Fe = 2.6-3.3 and the core of a clinopyroxene from the most felsic monzosyenite sample (BS06-59) has Mg/Fe = 2.4. All of these compositions were potentially in equilibrium with a liquid of composition equal to the lower or upper contact margins. Most of these mineral compositions are integrated in such a way that obscures the normal zonation, but Figure 3-9 shows that the rims of these clinopyroxenes are more Fe-rich than the integrated compositions. Some of their rims, especially those from high Mg/Fe LBZ host rocks, probably equilibrated with liquids less magnesian than their whole rock compositions.

The lower margin clinopyroxene rim and core are slightly more magnesian with Mg/Fe of 3.4 and 3.6, respectively. The clinopyroxene core from the lower margin could be in equilibrium with the upper contact sample and the rim could be in equilibrium with either

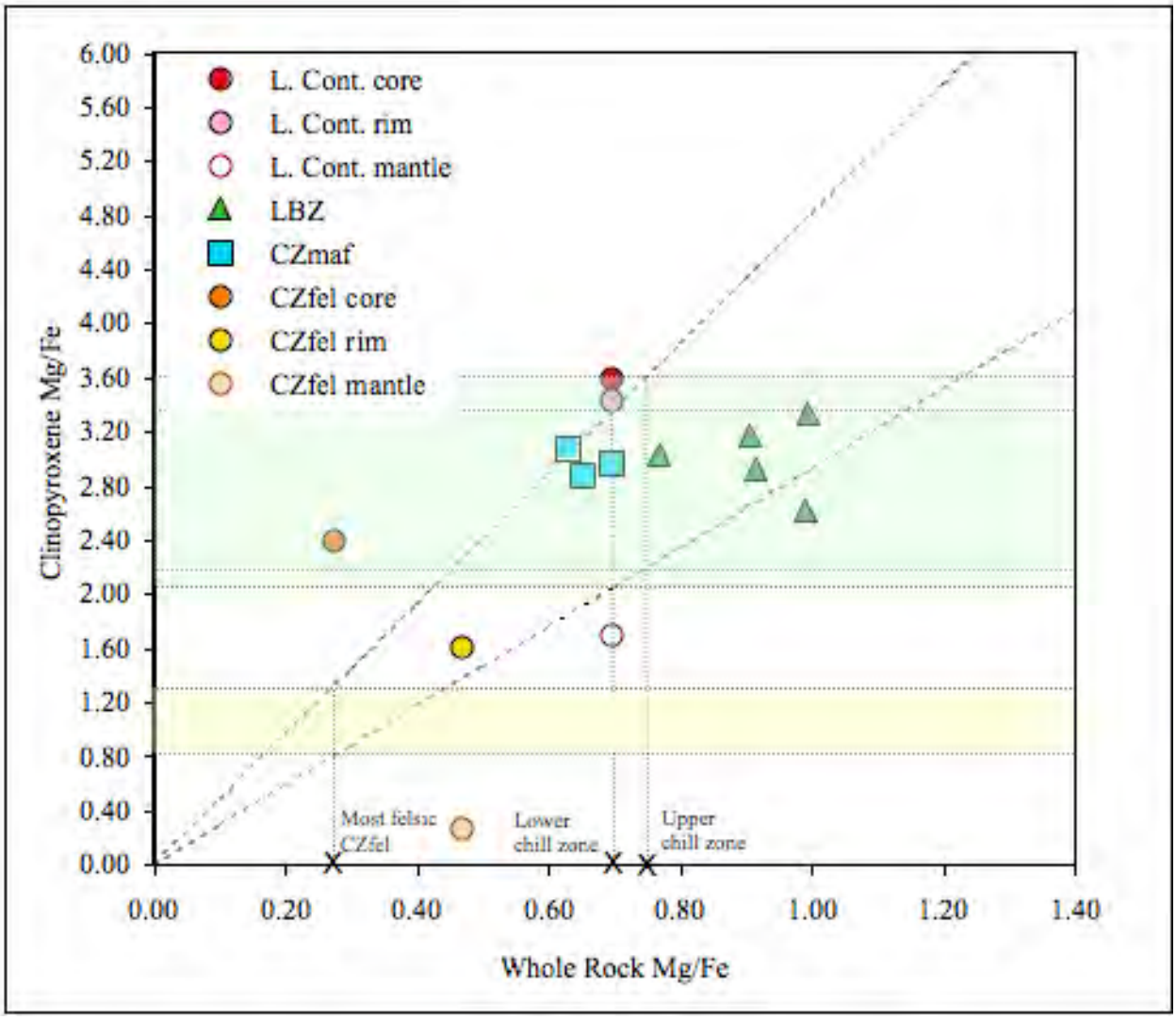

Figure 3-24. Bone Springs Sill clinopyroxene Mg/Fe vs. whole rock Mg/Fe. The field bounded by the dashed lines diverging from the origin is the $K_{D\,cpx-l}^{Mg/Fe}$ of 0.275 ± 0.067 from Putirka et al. (2003). Most rocks in BSS are partially cumulate, but the likely liquid compositions of the margin rocks and the monzosyenite are plotted on the x-axis and their fields of equilibrium clinopyroxene shown in horizontal green and yellow shaded fields. See text for discussion.

margin's composition. In both cases, they represent the high Mg/Fe end of the envelope and it is possible they crystallized from a liquid slightly more magnesian than the quenched margins and were carried in with the intruding magma.

A clinopyroxene rim from the CZ felsic sample (BS06-51) and the mantle from the lower margin clinopyroxene have similar Mg/Fe of ~1.6. In the case of the margin sample this is problematic; it is from a fine grained rock interpreted to have quenched upon intrusion, and this poses difficulties for any model that invokes a late stage fluid. It represents a single thin mantle on a single grain, and it may have resulted from a trace amount of evolved interstitial liquid that might not have been in contact with sill-wide monzosyenitic liquid. It could also have formed under hydrothermal conditions. The most Fe-rich mantle has a Mg/Fe of 0.26, and occurs on a monzosyenite sample. This would be in equilibrium with a liquid more felsic than anything present as a rock sampled at BSS.

The Mg/Fe data, in conjunction with field relations and petrography, indicate the following:

The BSS liquid was saturated in olivine and Fe-Ti oxide before intrusion. Olivine with Fo_{72-78} crystallized prior to intrusion in a magma chamber or during ascent and these grains are preserved in fine-grained UBZ rocks and in some of the LBZ cumulate rocks. Some of these olivines contain inclusions of Fe-Ti oxide.

The BSS liquid may have been saturated with clinopyroxene prior to intrusion, but the evidence is lacking. The most magnesian clinopyroxenes are found in the quenched rocks of the lower contact margin.

During post-intrusion crystallization of the BSS magma, Fo_{58-71} olivine crystallized and accumulated in the LBZ and CZ. The most Fe-rich of these compositions are late-forming cores

and rims on more magnesian grains. Olivine composition and petrographic data indicate that the LBZ and mafic CZ rocks contain up to 10 modal% cumulate olivine, and thus the whole rock compositions are more magnesian than any liquid present would have been.

The olivine phenocryst compositions from the UBZ show that these rocks are imperfect liquid compositions even though the phenocrysts represent only a few modal% of the rocks.

Most clinopyroxene compositions from LBZ and most CZ rocks are in approximate equilibrium with the intruding liquid and their whole rock compositions. Only one LBZ grain is definitively cumulate, though documented normal zoning suggests other grains were in late contact with relatively Mg-poor liquids.

Olivine cores (Fo_{51-52}) from the hybrid CZ rocks are in equilibrium with liquids slightly more magnesian than the most felsic monzosyenite (BS06-59). Olivine compositions of Fo_{36-50} are found in one core and several rims from mixed rocks and some olivine rims in CZ mafic rocks are in equilibrium with the BS06-59 monzosyenite sample.

The felsic liquid of most monzosyenite samples has the same Mg/Fe as the interstitial liquid in LBZ rocks and the most felsic monzosyenite sample has the same Mg/Fe as the interstitial liquid in CZ rocks. This is good evidence that the monzosyenite segregations are locally derived and not separately intruding liquids.

Some olivine grains my have accumulated by gravitational settling. The most likely candidates are those in multi-grain clusters with Fe-Ti oxide because of their relatively high density and size. Many, if not most, probably formed in the solidification fronts advancing from the roof and floor of the sill. Evolved liquid was removed – probably by buoyant ascent after rifting of the crystalline framework. This is likely the case for the clinopyroxenes as well, where only the rim compositions convincingly indicate contact with a more evolved liquid.

Determination of interstitial liquid fraction using Mg/Fe

As indicated by the Mg/Fe systematics, LBZ rocks have mineral abundances and compositions from which liquid is missing. Though some CZ mafic rocks have compositions that are permissibly in equilibrium with the mafic minerals they contain (Figures 3-23 and 3-24), petrography and mineral zonation indicates they are not equilibrium assemblages. In addition to olivine and clinopyroxene, petrography and modal proportions (Figure 3-1) indicate Fe-Ti oxides are also over-represented in these rocks. In an attempt to model the proportions of cumulate minerals to interstitial liquid, I used the techniques of Meurer and Boudreau (1998a) to assess the crystallized liquid fraction (CLF) in the LBZ and CZ mafic rocks.

Equations 1 to 3 calculate the amount of trapped liquid necessary to offset the abundance and *Mg's* (100*MgO/[MgO + FeO]) of the cumulate assemblage to the equilibrium composition.

$$MgO^{shift} = \left(\frac{\%Ol}{(100+CLF)}\right)\left(\frac{MgO^{ol}}{40.31}\right) + \left(\frac{\%Cpx}{(100+CLF)}\right)\left(\frac{MgO^{cpx}}{40.31}\right) + \left(\frac{CLF}{100}\right)\left(\frac{MgO^{liq}}{40.31}\right) \quad (1)$$

$$FeO^{shift} = \left(\frac{\%Ol}{(100+CLF)}\right)\left(\frac{FeO^{ol}}{71.85}\right) + \left(\frac{\%Cpx}{(100+CLF)}\right)\left(\frac{FeO^{cpx}}{71.85}\right) + \left(\frac{CLF}{100}\right)\left(\frac{FeO^{liq}}{71.85}\right) \quad (2)$$

$$Mg'^{shift} = \frac{MgO^{shift}}{MgO^{shift} + FeO^{shift}} \quad (3)$$

MgO and FeO are in wt.%. The CLF is found iteratively by adjustment in equations 1 and 2 until the Mg'^{shift} determined by equation 3 becomes equal to the *Mg'* of the starting liquid composition.

As described above and shown in Figures 3-21 and 3-22, two UBZ tephrite samples plot along a line between the LBZ cumulates and the monzosyenites. Of those, I chose sample BS05-30 as the parental liquid composition because it has the lower SiO_2., I used the compositions of

the olivine and clinopyroxene grains that are permissibly in equilibrium with the liquid according to the K_D's of Roeder and Emslie (1970) and Putirka et al. (2003). The Mg/Fe of BS05-30 falls between the margin samples shown on Figures 3-23 and 3-24. Thus, I used the most magnesian grains in each sample excluding those interpreted to have crystallized pre-intrusion. Both the clinopyroxene and olivine grains are normally zoned; for clinopyroxene, all but the most Fe-rich rims are in equilibrium with a liquid the composition of BS05-30; for olivine, the magnesian grains in equilibrium with the liquid composition were used. Most of the Ti-magnetite grains are interpreted to be cumulate in all LBZ and CZ mafic rocks, but the compositions are poorly constrained due to extensive exsolution. Because of the very low Mg/Fe in the Ti-magnetite, the Mg'^{shift} is very sensitive to small changes in their modal%. For this reason, I subtracted the FeO and MgO wt.% attributed to the oxide minerals from the starting liquid composition. This method is used by Meurer and Boudreau (1998) for FeO in plagioclase in the Stillwater complex because the equations are much less sensitive to starting liquid compositions – e.g., changes in 2 and 4 wt.% FeO in the starting compositions result in only 10-12 and 20-25 relative% change in the CLF (Meurer and Boudreau, 1998) – than to cumulate phase compositions.

The results of the CLF equations are shown in Table 3-13. Rocks from the LBZ have calculated CLFs from 15-37%, a similar range but a higher average (25%) than determined for the Stillwater section (Meurer and Boudreau, 1998a). The three CZ mafic samples tested have calculated CLFs of 50, 56, and 80%.

Petrography, trends in whole rock and mineral chemistry, mineral-liquid equilibria, and ratios of cumulate minerals to crystallized liquids (CLF) in Bone Springs Sill rocks depict the intrusion of a tephritic magma, represented by UBZ samples BS05-30 and/or BS06-72, and its progressive fractional crystallization. This results in lower SiO_2, high Mg/Fe cumulates (LBZ

Table 3-13. Results of the crystal liquid fraction (CLF) calculations for Bones Springs Sill monzogabbros. Equations used are from Meurer and Boudreau (1998a) and are shown as equations 1-3 in text. The CLF is the calculated % of trapped liquid in a cumulate sample. In the case of Bone Springs Sill, the CLF is a measurement of the amount of interstitial liquid remaining after segregation of the mozosyenite liquid. Mineral compositions and abundances of early-crystallizing minerals are balanced against the composition of the interpreted parent liquid, represented by sample BS05-30.

adjusted to BS05-30	LBZ	LBZ	LBZ	LBZ	LBZ	LBZ	LBZ	CZ	CZ	CZ
Sample	BS06-38	BS06-45	BS06-7	BS06-46	BS04-2	BS04-9	BS04-10	BS04-4	BS04-13	BS05-19
whole rock MgO	9.0	9.1	6.5	8.7	7.0	6.5	7.9	3.5	4.1	3.7
whole rock FeO	14.4	14.7	12.7	14.5	12.6	12.8	14.1	9.4	10.5	10.5
whole rock Mg'	53	52	48	52	50	48	50	40	41	39
%Fe-Ti ox	10	10	9	10	8	8	8	5	6	6
MgO Fe-Ti ox	3.0	3.0	3.0	3.0	3.0	3.0	3.0	3.0	3.0	3.0
FeO Fe-Ti ox	62.0	62.0	62.0	62.0	62.0	62.0	62.0	62.0	62.0	62.0
Mg'	8	8	8	8	8	8	8	8	8	0
whole rock MgO (-FeTi oxide)	8.7	8.8	6.2	8.4	6.8	6.3	7.6	3.3	3.9	3.5
whole rock FeO (-FeTi oxide)	8.2	8.7	7.3	8.6	7.8	7.8	9.1	6.3	6.5	6.9
whole rock Mg' (-FeTi oxide)	65	64	60	64	61	59	60	48	51	47
%Ol	10	10	3	9	7	7	12	0.3	1	0
MgO Ol	33.6	33.6	36.3	33.6	36.3	36.4	34.0	34.2	34.2	28.0
FeO Ol	27.2	27.2	25.3	27.2	26.4	25.3	27.4	27.4	27.4	33.9
Ol Mg'	69	69	72	69	71	72	69	69	69	60
%Cpx	17	13	19	24	18	16	18	13	19	17
MgO Cpx	12.9	12.9	12.4	12.9	11.8	12.9	12.9	12.7	12.6	12.6
FeO Cpx	7.1	7.1	7.9	7.1	8.3	7.6	7.1	8.1	7.8	7.6
Cpx Mg'	76	76	74	76	72	75	76	74	74	75
MgO shift	13.9	12.8	10.1	15.7	12.5	13.3	16.7	10.2	11.0	13.6
FeO shift	7.3	7.1	6.6	9.0	8.1	9.3	11.2	11.0	10.3	15.2
Mg' shift	65	64	61	64	61	59	60	48	51	47
CLF (%)	15	15	22	24	25	35	37	56	50	80

monzogabbros), higher SiO_2, low Mg/Fe residual liquids that separate to crystallize as CZ monzosyenites, and a mixture of cumulate minerals in a higher proportion of residual liquid represented by the CZ monzogabbros. The CZ mafic minerals spent a longer time in contact with a more evolved liquid than did the LBZ cumulate minerals, as evidenced by relatively Fe-rich clinopyroxene and olivine rims and feldspar compositions in CZ mafic rocks.

Differentiation of the sill

No samples I collected at BSS represent liquids intermediate between the margins/UBZ and the CZ felsic rocks because all liquid differentiated within the sill to the composition of the monzosyenite. The mafic rocks, aside from the fine-grained margins, are partially cumulate. Explicitly, my hypothesis, supported thus far by field relations and mineral and whole rock compositions, is as follows: the tephritic margins (including the UBZ) and the monzosyenites of BSS represent the mafic intruding magma and the felsic residual magma, respectively; the monzogabbros of the LBZ and CZ represent cumulate rocks with variable amount of crystallized monzosyenitic interstitial liquid. The monzosyenite segregations represent a fairly narrow range of SiO_2 and alkali contents but can be separated into more and less differentiated liquids based on their Mg/Fe contents. This differentiation can be tested by fractional crystallization models.

Of course, if the sill had crystallized without migration and segregation of interstitial fluid there would be no monzosyenite, only monzogabbro or perhaps monzodiorite with normally zoned crystals and felsic mesostasis, or perhaps some compositional layering if physical conditions permitted crystal settling. An essential second step in proving this hypothesis is a reintegration of the bimodal compositions to the original tephrite composition.

Choice of compositions for fractional crystallization modeling

As described above, two UBZ tephrite samples plot along a line between the LBZ cumulates and the monzosyenites (Figure 3-22). Of those, I chose sample BS05-30 as the parental liquid composition because it has the lower SiO_2. I use the composition of monzosyenite BS06-49 for the felsic composition as it is, by a very small margin, the least fractionated of the monzosyenite samples (i.e., higher FeO and lower alkalis) that plot in line with BSS cumulates and tephrites.

Because no liquids intermediate between the UBZ and the monzosyenites are found in BSS, I used an intermediate model composition to calculate multiple steps of fractional crystallization (FC). Most BSS rocks compositions line up well on Harker diagrams (Figure 3-21), so the liquid line of descent is fairly well-constrained and a liquid composition along that line is likely to have been present during the differentiation of the sill magma. I chose the distance along the line of descent such that the model composition has Mg/Fe ≈ 0.56 and would thus be in equilibrium with the most Fe-rich LBZ monzogabbro olivine cores (see Figure 3-23 for the liquid-olivine Mg/Fe equilibrium line). This model composition is equivalent to a mixture of 30% BS05-30 and 70% BS06-49 and falls on the phonotephrite-tephriphonolite join on a total alkali-silica diagram (Le Bas et al., 1986; not shown).

Furthermore, monzosyenite sample BS06-49 has Mg/Fe = 0.44 – in approximate equilibrium with the LBZ olivine rims and most of the CZ monzogabbro olivine cores as shown in Figure 3-23, and should represent the liquid extracted from the LBZ rocks. Finally, as a last step, I modeled differentiation between BS06-49 and the most evolved monzosyenite, BS06-59, which has Mg/Fe = 0.27 and would represent approximate equilibrium with the most Fe-rich

olivine compositions present as rims on CZ monzogabbro olivines and as rims and cores of CZ mixed rocks (Figure 3-23).

Results of major element fractional crystallization modeling

The model composition is shown along with results of least squares FC models after the methods of Bryan et al. (1969) in Table 3-14. Step 1 is a model of fractionation of the BSS magma from intrusion until LBZ cumulate olivine cores had crystallized (liquid Mg/Fe ≈ 0.56). The fractionating phases modeled, in descending abundance, are pl (An_{72}) + cpx + Ti-mt + ol (Fo_{67}) + ne+ ap + bt. Most of these phases appear to be early-crystallizing phases in LBZ rocks. Biotite is common in LBZ samples and often euhedral, but it is rarely included in other minerals. The presence of early nepheline is only constrained by analcime pseudomorphs after rounded and hexagonal minerals in the margin rocks. This stage proceeds through crystallization of 40 wt.% (F = 0.60) of the magma, at which point the LBZ early minerals are envisioned to have crystallized into a loose crystal-liquid mush below the upward-progressing solidification front. The $\sum r^2$ for this step is 0.288, which is reasonable considering the constraints (40% crystallization of solid-solution minerals and using a modeled nepheline composition). It is certainly possible that some amphibole or some alkali feldspar crystallized during this stage, but the petrography does not require either.

Step 2 models the period of differentiation between LBZ olivine core crystallization and the development of the least evolved monzosyenitic composition. The final liquid for this stage (represented by BS06-49, Mg/Fe = 0.44) was present interstitially to the LBZ cumulates and CZ mafic cumulates, as evidenced by olivine rim compositions and core compositions, respectively. The fractionating assemblage modeled is pl (An_{62}) + cpx + Ti-mt + ol (Fo_{60}) + bt + ap + ne, after which a total of 49 wt.% (F = 0.51) of the magma would have crystallized. Most of the

Table 3-14. Results of least-squares fractional crystallization models for Bone Springs Sill. The method is after Bryan et al. (1969).

Step 1: BS06-30 to model phonotephrite/tephriphonolite liquid

	Parent	BS04-10 cpx	Avg. BS06-46 ol core	Avg. LBZ ap	LBZ early pl	BS06-37 ox-4	Avg. BS06-38 bt		Daughter	calculated parent		
lith	UBZ	LBZ	LBZ	LBZ	LBZ	LM	LBZ	model	model			
	BS06-30	cpx	Fo67 ol	ap	An72 pl	Ti-mt	bt	neph	liquid		r	r^2
SiO_2	45.82	46.65	36.62	0.97	49.88	0.28	36.33	55.00	51.15	45.41	0.419	0.175
TiO_2	3.83	3.32	0.05	0.00	0.18	29.31	7.21	0.03	2.42	3.99	-0.155	0.024
Al_2O_3	16.77	6.30	0.04	0.10	30.89	2.12	14.16	29.00	19.06	16.75	0.015	0.000
FeOt	12.03	7.14	28.24	0.47	0.73	61.77	15.41	0.38	8.16	11.83	0.207	0.043
MnO	0.18	0.12	0.47	0.04	0.03	0.74	0.23	0.01	0.14	0.18	-0.003	0.000
MgO	4.90	12.90	32.86	0.16	0.13	3.20	13.18	0.02	2.58	5.06	-0.163	0.027
CaO	8.49	22.97	0.39	55.00	14.49	0.03	0.09	0.12	5.57	8.47	0.021	0.000
Na_2O	4.52	0.50	0.00	0.07	3.07	0.65	0.65	13.90	6.41	4.63	-0.108	0.012
K_2O	2.49	0.01	0.00	0.00	0.12	0.00	9.71	1.00	3.89	2.43	0.058	0.003
P_2O_5	0.97	0.00	0.00	39.50	0.00	0.00	0.00	0.00	0.62	0.91	0.060	0.004
Total	100.00	99.91	98.67	96.31	99.51	98.10	96.97	99.46	100.00		$\sum r^2$:	0.288
fraction:		0.113	0.053	0.014	0.121	0.072	0.004	0.020	0.604			
									F = 0.60			

Table 3-14, continued. Results of least-squares fractional crystallization models for Bone Springs Sill.

Step 2: Model liquid to monzosyenite BS06-49

sample	Parent	BS06-59 cpx core	Avg. BS05-19 ol core	Avg CZm ap	Avg. CZm plag	BS06-37 ox-4	AVG CZm bt		Daughter	calculated parent		
lith		CZf	CZm	CZm	CZm	LM	CZm	model	CZf			
	Model	cpx	Fo60 ol	ap	An62 pl	Ti-mt	bt	neph	BS06-49		r	r^2
SiO2	51.15	48.99	36.92	0.88	52.27	0.28	35.56	55.00	53.43	51.09	0.058	0.003
TiO2	2.42	1.34	0.02	0.00	0.18	29.31	8.43	0.03	1.81	2.39	0.030	0.001
Al2O3	19.06	2.99	0.00	0.18	30.14	2.12	13.88	29.00	20.04	19.03	0.028	0.001
FeOt	8.16	9.58	33.45	0.93	0.47	61.77	18.07	0.38	6.50	8.17	-0.006	0.000
MnO	0.14	0.27	0.66	0.04	0.04	0.74	0.23	0.01	0.13	0.15	-0.009	0.000
MgO	2.58	12.38	28.88	0.13	0.02	3.20	10.69	0.02	1.59	2.56	0.025	0.001
CaO	5.57	22.56	0.47	54.13	13.01	0.03	0.27	0.12	4.32	5.56	0.006	0.000
Na2O	6.41	0.48	0.00	0.05	4.20	0.65	0.58	13.90	7.23	6.40	0.012	0.000
K2O	3.89	0.00	0.00	0.00	0.22	0.00	8.96	1.00	4.49	3.90	-0.010	0.000
P2O5	0.62	0.00	0.00	38.75	0.00	0.00	0.00	0.00	0.47	0.62	0.002	0.000
Total	100.00	98.58	100.40	95.09	100.55	98.10	96.67	99.46	100.00		$\sum r^2$:	0.006
fraction:		0.038	0.018	0.006	0.058	0.024	0.014	0.005	0.837			

F = 0.837

F from BS06-30 = 0.51

Table 3-14, continued. Results of least-squares fractional crystallization models for Bone Springs Sill.

Step 3: Monzosyenite BS06-49 to monzosyenite BS06-59

sample	Parent	Avg CZm ap	Avg. CZf primary afs	BS06-50 ox-4	Avg. BS06-50 am core		Daughter	calculated parent		
lith	CZf	CZm	CZf	CZf	CZf	model	CZf			
	BS06-49	ap	Or63 afs	ilm-hm	kaer	neph	BS-59		r	r^2
SiO2	53.43	0.88	65.33	0.26	38.77	55.00	54.62	53.41	0.014	0.000
TiO2	1.81	0.00	0.07	18.78	7.95	0.03	1.15	1.61	0.194	0.037
Al2O3	20.04	0.18	19.07	0.56	12.84	29.00	20.48	20.00	0.043	0.002
FeOt	6.50	0.93	0.15	71.77	12.05	0.38	6.59	6.55	-0.046	0.002
MnO	0.13	0.04	0.04	1.09	0.16	0.01	0.14	0.13	-0.006	0.000
MgO	1.59	0.13	0.00	0.00	11.04	0.02	1.01	1.70	-0.106	0.011
CaO	4.32	54.13	0.22	0.04	12.41	0.12	3.54	4.27	0.047	0.002
Na2O	7.23	0.05	3.99	0.65	2.43	13.90	7.57	7.21	0.021	0.000
K2O	4.49	0.00	10.61	0.00	1.35	1.00	4.59	4.42	0.070	0.005
P2O5	0.47	39.50	0.00	0.00	0.00	0.00	0.31	0.53	-0.059	0.003
Total	100.00	95.84	99.48	93.16	98.99	99.46	100.00		$\sum r^2$:	0.064
fraction:		0.007	0.048	0.002	0.078	0.044	0.821			

F = 0.821

F from BS06-30 = 0.42

monzosyenite sampled is similar to this liquid composition, and it is likely that it represents the interstitial liquid trapped in the LBZ. The $\sum r^2$ for this step is 0.006, which is a good fit by any measure and supports the plausibility of this model.

Step 3 models the differentiation from the least to the most evolved monzosyenite. The fractionating assemblage is krs (amphibole) + afs ($Or_{63}Ab_{36}An_1$) + ne + ap + ilm-hm solid solution. Kaersutitic amphibole is present as a late phase in CZ, and rarely LBZ, monzogabbros, alkali feldspar is present in all rocks but may be a late forming magmatic mineral in all but the segregations of monzosyenite, ilmenite-hematite occurs throughout the sill but often as elongate, quench-textured interstitial sets of grains. All of these occur as the primary phases in the monzosyenites, along with lesser clinopyroxene that would have been in equilibrium with liquids from previous stages, and some edenitic amphibole. The model estimates 9 wt.% fractionation for this stage resulting in a total 58% (F = 0.42) crystallization of the parental magma. The $\sum r^2$ of 0.064 for this step demonstrates the model is a good fit.

Mass balance of cumulate minerals and interstitial liquid

Fractional crystallization modeling (Table 3-14) demonstrates a path of differentiation from BSS tephrite to monzosyenite using mineral compositions found in the sill. The cumulate minerals that compose the bulk of the BSS monzogabbros crystallized and the composition of monzosyenite liquid was reached by the end of step 2 in the model, when F = 0.51 (51% monzosyenite liquid remaining). This 51% represents a combination of the slightly less and more evolved monzosyenites reached in steps 2 and 3, and it should be present as both the interstitial liquid in the cumulate rocks and as the monzosyenite segregations. In order to further validate this model I estimated proportions of monzogabbro and monzosyenite rock in the sill based on field observations. With these field-based estimates I determined how much of the 51%

monzosyenite liquid can be accounted for by the mapped monzosyenite segregations and thus how much needs to have crystallized as the interstitial liquid in the monzogabbro. I then compared this value to the calculated crystallized liquid fraction (CLF) in the monzogabbros (see Table 3-13) and to more rigorous mass balance calculations, described below. This is done to corroborate the fractional crystallization model. In this section I am only concerned with the fractions of material in the LBZ and CZ because they contain the differentiated products in the sill; I exclude the very thin lower margin and the UBZ from calculations.

The early crystallizing phases that are integrated with the monzosyenite compositions do not include analcime or nepheline. To account for the post-magmatic incorporation of H_2O into analcime, whole rock compositions are normalized to a volatile-free 100%.

Field-based proportions and the fractionation model

In the field, structural complications and time constraints prevented reliable quantitative estimates of proportions of lithologies in the sill but, stratigraphically, the LBZ comprises about $2/3^{rd}$ (0.67) of the plutonic-textured (i.e., non-UBZ) rock (18 to 19 m of 28 m stratigraphic height) and the CZ about $1/3^{rd}$ (or 0.66; 9 to 10 m of 28 m stratigraphic height). All of the LBZ is monzogabbro and, based on field observations, I estimate about $1/4^{th}$ (0.25) of the CZ is made up of segregations of monzosyenite rock (sills, dikes, pods, ocelli, stringers, etc.), with the remaining $3/4^{th}$'s (0.75) of the CZ being monzogabbro.

The total fraction of monzogabbro is then: 0.67 LBZ (all monzogabbro) + 0.33 CZ * 0.75 monzogabbro in CZ = 0.92, and the remainder, 0.08, is the total fraction of monzosyenite rock (all found in the CZ).

No densities were measured for BSS rocks, but even if the values were as low as 2.7 g/cm^3 for average monzosyenites and as high as 3.0 g/cm^3 for average monzogabbros the

difference would be a relative ~10%. Other factors, such as variation within monzogabbro densities and errors in the estimates of percentages from field work, probably result in an equal or greater relative error, and so I have not converted these volume fractions to match the fractionation models calculated in wt.%.

The fraction of monzosyenitic liquid produced according to the fractional crystallization model is 0.51. If the field observations account for only a 0.08 fraction of monzosyenite rock, then the remaining fraction of 0.43, or 43%, must be present as the interstitial material in the BSS monzogabbros.

Mass balance determination of monzogabbro interstitial liquid

I performed a mass balance calculation again using the technique of Bryan et al. (1969) to integrate the cumulate mineral compositions with the compositions of the monzosyenite interstitial liquid to match the whole rock compositions of the monzogabbros. This technique yields fractions of cumulate minerals (which can be compared to modal data from point counting), fractions of monzosyenite liquid, and $\sum r^2$ values by which to evaluate the model. Table 3-15 contains the results of these mass balance calculations. For both LBZ and CZ monzogabbros the assemblage cpx + ol + pl + Ti-mt + bt is used as the cumulate assemblage, though LBZ compositions were integrated with and without biotite for comparison. Compositions for minerals except Fe-Ti oxide and plagioclase were varied according to the zone. The monzosyenite BS06-49 is used as the interstitial liquid composition for both LBZ and CZ rocks, even though data based on Mg/Fe equilibrium indicate the presence of some more evolved liquid represented by BS06-59 – the actual compositions of those two samples are similar enough that differences in mass balance modeling are overshadowed by changes in phase composition and analytical error. Also, even if the more evolved monzosyenite was present in

Table 3-15. Mass balance of cumulate minerals and interstitial liquid integrated to monzogabbro compositions. Representative cumulate mineral compositions, shown on top, are integrated with monzosyenite sample BS06-49, which is representative of the interstitial liquid in monzogabbros. LBZ compositions are integrated with and without biotite. Monzogabbro whole rock compositions are shown in Table 3-11.

	Phases used in mass balance for LBZ samples						Liquid comp.
label	BS04-10 cpx	BS04-9 Fo70	Avg. CZm plag	BS06-37 ox-4	Avg. LBZ ap	Avg. LBZ bt	BS06-49
lith	LBZ	LBZ	CZm	LM	LBZ	LBZ	mzsy
	cpx	Fo70 ol	An62 pl	Ti-mt	ap	bt	BS06-49
SiO2	46.65	37.67	52.27	0.28	0.97	35.41	53.43
TiO2	3.32	0.09	0.18	29.31	0.00	8.13	1.81
Al2O3	6.30	0.06	30.14	2.12	0.10	14.03	20.04
FeOt	7.14	26.56	0.47	61.77	0.47	18.14	6.50
MnO	0.12	0.37	0.04	0.74	0.04	0.26	0.13
MgO	12.90	35.98	0.02	3.20	0.16	10.98	1.59
CaO	22.97	0.41	13.01	0.03	55.00	0.19	4.32
Na2O	0.50	0.00	4.20	0.00	0.07	0.60	7.23
K2O	0.01	0.00	0.22	0.00	0.00	8.81	4.49
P2O5	0.00	0.00	0.00	0.00	39.50	0.00	0.47
Total	99.91	101.14	100.55	97.45	96.31	96.55	100.00

Results of mass balance

LBZ sample	fract. cpx	fract. ol	fract. pl	fract. Ti-mt	fract. ap		fract. liquid	$\sum r^2$
BS04-2	0.086	0.134	0.215	0.089	0.017		0.460	0.241
BS04-10	0.101	0.156	0.261	0.110	0.020		0.353	0.331
BS06-38	0.104	0.184	0.212	0.101	0.017		0.382	0.233
BS06-45	0.115	0.185	0.241	0.109	0.015		0.334	0.108
BS04-12	0.203	0.040	0.186	0.105	0.017		0.448	0.180
BS04-11	0.169	0.102	0.278	0.117	0.019		0.313	0.330
BS06-46	0.161	0.158	0.262	0.118	0.014		0.287	0.137
average	0.134	0.137	0.236	0.107	0.017		0.368	

LBZ sample	fract. cpx	fract. ol	fract. pl	fract. Ti-mt	fract. ap	fract. bt	fract. liquid	$\sum r^2$
BS04-2	0.092	0.119	0.209	0.080	0.017	0.053	0.430	0.061
BS04-10	0.107	0.141	0.255	0.101	0.020	0.053	0.325	0.139
BS06-38	0.108	0.175	0.208	0.095	0.017	0.032	0.364	0.104
BS06-45	0.119	0.176	0.237	0.103	0.015	0.035	0.315	0.006
BS04-12	0.208	0.028	0.181	0.097	0.018	0.044	0.424	0.075
BS04-11	0.175	0.090	0.274	0.110	0.020	0.047	0.289	0.202
BS06-46	0.166	0.147	0.257	0.111	0.014	0.040	0.265	0.009
average	0.139	0.125	0.232	0.100	0.017	0.043	0.345	

Table 3-15, continued. Mass balance of cumulate minerals and interstitial liquid integrated to monzogabbro compositions.

	Phases used in mass balance for CZ samples						Liquid comp.
label	Avg. CZ mzgb cpx	BS04-19 ol core	Avg. CZm plag	BS06-37 ox-4	Avg. LBZ ap	Avg.CZ mzgb bt	BS06-49
lith	LBZ	LBZ	CZm An62	LM	LBZ	LBZ	mzsy
	cpx	Fo60 ol	pl	Ti-mt	ap	bt	BS06-49
SiO2	46.65	37.67	52.27	0.28	0.97	35.41	53.43
TiO2	3.32	0.09	0.18	29.31	0.00	8.13	1.81
Al2O3	6.30	0.06	30.14	2.12	0.10	14.03	20.04
FeOt	7.14	26.56	0.47	61.77	0.47	18.14	6.50
MnO	0.12	0.37	0.04	0.74	0.04	0.26	0.13
MgO	12.90	35.98	0.02	3.20	0.16	10.98	1.59
CaO	22.97	0.41	13.01	0.03	55.00	0.19	4.32
Na2O	0.50	0.00	4.20	0.00	0.07	0.60	7.23
K2O	0.01	0.00	0.22	0.00	0.00	8.81	4.49
P2O5	0.00	0.00	0.00	0.00	39.50	0.00	0.47
Total	99.91	101.14	100.55	97.45	96.31	96.55	100.00

	Results of mass balance							
CZ mzgb sample	fract. cpx	fract. ol	fract. pl	fract. Ti-mt	fract. ap	fract. bt	fract. liquid	$\sum r^2$
BS04-13	0.160	0.010	0.211	0.077	0.027	0.063	0.454	0.134
BS05-19	0.145	0.017	0.143	0.076	0.028	0.011	0.580	0.033
BS06-57	0.172	0.012	0.222	0.071	0.021	0.032	0.470	0.196
BS04-4	0.118	0.019	0.184	0.061	0.029	0.018	0.571	0.174
average	0.149	0.015	0.190	0.071	0.026	0.031	0.519	

the CZ in some proportion, the sampling and the fractional crystallization modeling suggest that it was subordinate to the less evolved monzosyenite composition.

Lower border zone samples integrated with biotite as a crystallizing mineral have lower $\sum r^2$ than those without it, and biotite is calculated at 3-5% when included (Table 3-15). The results for melanocratic minerals are not dissimilar to LBZ modes calculated by mass balance (Table 3-12) or to the point counting data presented in Table 3-1 except that they overestimate olivine at the expense of clinopyroxene. This could be partly due to an underestimation on my part of fine-grained or serpentinized/iddingsitized olivine in thin sections. It could also be that reintegration of sector-zoned clinopyroxene compositions underestimates MgO, or that my integrated Fe-Ti oxide values overestimate FeOt content.

The fractions of crystallized monzosyenitic liquid in LBZ monzogabbros estimated by this method is 0.27-0.43, average 0.35, with biotite as a cumulate mineral and 0.29-0.46, average .037, without it. The percentages estimated in CZ monzogabbroic rocks is 0.45-0.58, average 0.52. When combined with the field proportions, these numbers yield: 0.67 LBZ (all monzogabbro) * 0.35 LBZ interstitial monzosyenite (Table 3-15) + 0.33 CZ * 0.75 monzogabbro in CZ * 0.52 CZ monzogabbro interstitial monzosyenite (Table 3-15) = 0.36, or 36%. Considering the possible sources of error (e.g., field estimates, averaging the mass balance results for LBZ and for CZ into one value, etc.), this 36% calculated by mass balance is reasonably close to the 43% estimated by the fractionation model.

Comparison to CLF

The calculated CLF for LBZ monzogabbros were 0.17-0.37 with an average of 0.25, and the calculated CLF's for CZ monzogabbros were 0.50, 0.56, and 0.80, for an average of 0.62. When combined with the field proportions, the total BSS monzogabbro CLF is: 0.67 LBZ (all

monzogabbro) * 0.25 LBZ CLF + 0.33 CZ * 0.75 monzogabbro in CZ * 0.62 CZ monzogabbro CLF = 0.32, or 32%. This is lower than the 36% value obtained by mass balance which is in turn lower than the 43% interstitial liquid in monzogabbro estimated by the fractionation model. However, the range of values from CLF calculations and mass balance calculations overlap for both LBZ and for CZ monzogabbros. The CLF equations only use Mg/Fe composition and modal% of mafic silicates. Though they successfully elucidate patterns in the BSS system, they are better suited to systems with cumulate-intercumulate relations more clear-cut than in BSS.

Trace element chemistry

Table 3-11 contains abundances of 27 trace elements for BSS rocks. Many studies of TPMP igneous rocks use the incompatible element Nb as an index of differentiation (e.g., White and Urbanczyk, 2001; White et al., 2006), and Figure 3-25 shows Nb plotted against SiO_2 and against normative ab+or+ne. These normative minerals comprise those components in "Petrogeny's Residua System" (Bowen, 1937) present in BSS norms and their sum is thus equivalent to the Thornton-Tuttle differentiation index (D.I.) (Thornton and Tuttle, 1960). Both charts show a strong correlation with Nb, indicating that it is a reasonable proxy for degree of differentiation in these samples.

Figure 3-26 show the variation of 8 trace elements with Nb: high field strength elements (HFSE) Th, Ta, U; the large ion lithophile element (LILE) Rb and other low field strength elements Ba and Sr; and the transition metal Ni. The elements Ba, Th, Rb, U, and especially Ta, behave incompatibly and increase steadily with Nb, i.e., as crystallization of the sill proceeded they were concentrated in the monzosyenite liquid and are less abundant in the cumulate rocks composed of early-crystallizing minerals. Nickel is very compatible – it is concentrated in the LBZ rocks and is almost completely depleted in the monzosyenite liquid. The CZ monzogabbros

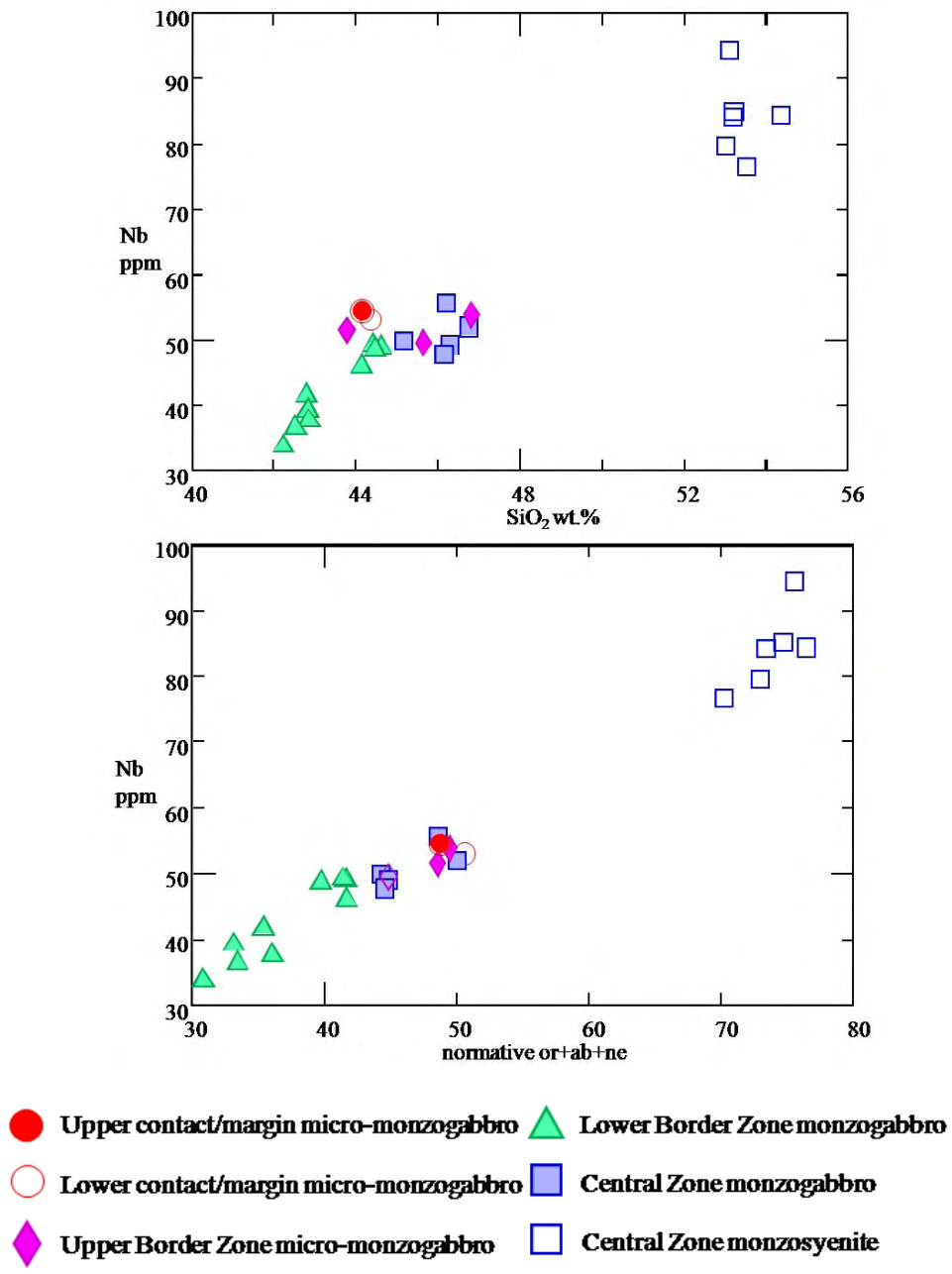

Figure 3-25. SiO_2 wt.% and normative or+ab+ne plotted against Nb (ppm). Normative or+ab+ne is equivalent to Thornton and Tuttle's (1960) differentiation index (D.I.) in BSS rocks. Both charts show a strong correlation, demonstrating that Nb is a good proxy for differentiation in these samples.

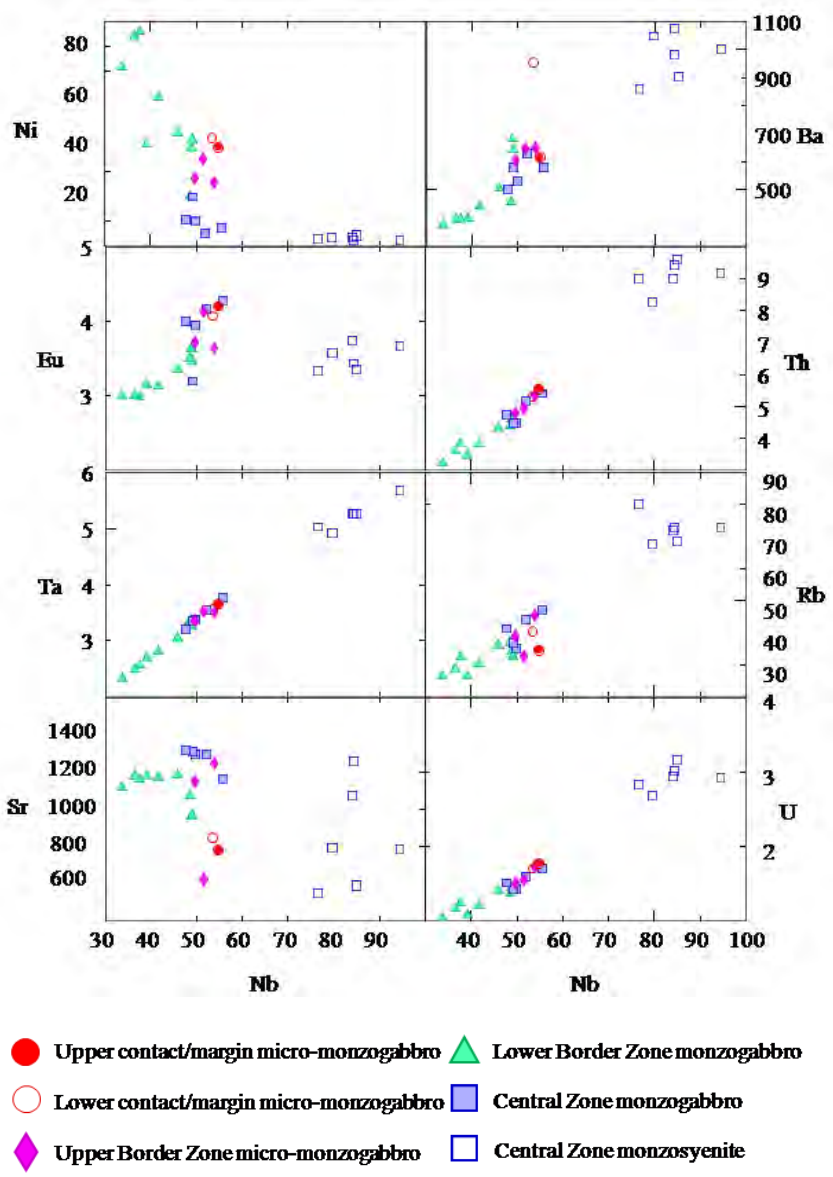

Figure 3-26. Bone Springs Sill trace elements plotted against Nb. All values in ppm. See text for discussion.

follow a trend of depletion in Ni as (1) the later mafic minerals crystallized from an increasingly depleted liquid and (2) CZ mafic rocks incorporate larger amounts of almost completely depleted monzosyenite liquid than do LBZ rocks.

Strontium behavior in BSS is more complex. Strontium behaves most like Ca in igneous systems, and the Harker diagrams (Figure 3-21) show that CaO has less regular behavior than other oxides in BSS, though it is depleted in the felsic rocks relative to the parental UBZ rocks so its behavior is compatible when taken in total. Strontium, however, shows a flat trend when plotted against Nb (Figure 3-26) in the LBZ and CZ monzogabbros until the most evolved samples of those rocks, which show the beginning of Sr depletion. The monzosyenites have Sr abundances approximately equal to or slightly lower than the intruding magma. Though Sr substitutes for Ca in and is thus compatible in plagioclase and less so in apatite (Matsui et al., 1977; Watson and Green, 1981), it is incompatible in clinopyroxene (Adam And Green, 2006), and is almost as compatible in alkali feldspar as in plagioclase (Larsen, 1979). Thus, Sr is neither very compatible nor incompatible and the monzosyenites show a range in Sr values as large as the rest of the BSS rocks. Bone Springs Sill monzosyenites contain carbonate, and sample BS06-59, which has the most Sr of the monzosyenites (>1200 ppm, Table 3-11), contains 4 modal% carbonate (Table 3-1). The range of Sr abundances in the felsic rocks may be due in large part to secondary carbonation.

Because the LBZ and CZ mafic rocks incorporate late stage liquid as interstitial material, the latest (highest Nb) of them must incorporate some of this range of monzosyenite liquid. Europium is discussed in the context of the rare earth element (REE) group below, but Figure 3-26 shows that it peaks in abundance in the CZ mafic rocks. Lemarchand et al. (1987) showed that Eu is more strongly partitioned into clinopyroxene, magnetite, and amphibole in the

presence of trachytic magma (K_d >2.4 for all) than in a basinitic or mugearitic magma (K_d's ≤ 1). The rims and late cores of cumulate minerals in the CZ monzogabbros were in equilibrium with more felsic liquid, and thus may have incorporated more Eu.

REE and trace element distribution

Multielement plots for all Bone Springs Sill rocks are shown in Figure 3-27. Figure 3-27A is a chondrite-normalized REE plot using values from Sun and McDonough (1989). All BSS rocks show the light REE (LREE)-enrichment common in alkaline igneous rocks and typical of TPMP rocks (e.g., Barker, 1987). This pattern is typical of ocean island basalts (OIB) and many other alkaline igneous rocks that show: (1) relative enrichment in all REE, as expected if alkaline parental magmas form by small degrees of mantle melting (Edgar, 1987) and if REEs are incompatible in mantle assemblages (Hanson, 1980); and (2) LREE-enrichment due to alkaline melts having their source in the mantle at pressures high enough to stabilize garnet and where garnets preferentially retain heavy REE (HREE). None of the BSS samples show a pronounced negative Eu anomaly that would result from significant pre-intrusion plagioclase fractionation or the convex downward pattern which can result from pre-intrusion amphibole fractionation (amphiboles themselves have a humped pattern due to preferential retainment of middle REE [MREE]) (Hanson, 1980). Figure 3-27B shows a multielement, MORB-normalized diagram after Pearce (1983). The pattern is similar to typical OIBs. The marked depletion in P and Ti in the monzosyenites is apparent in the Harker diagrams as well (Figure 3-21) and is due to the early crystallization and accumulation of apatite and Ti-magnetite in BSS.

The subtleties of BSS chondrite-normalized REE patterns are more easily discerned in Figure 3-28, on which only selected samples are plotted. Figure 3-28A shows the LBZ cumulate monzogabbro sample with the least amount of interstitial liquid – BS06-46 (see Table 3-15 for

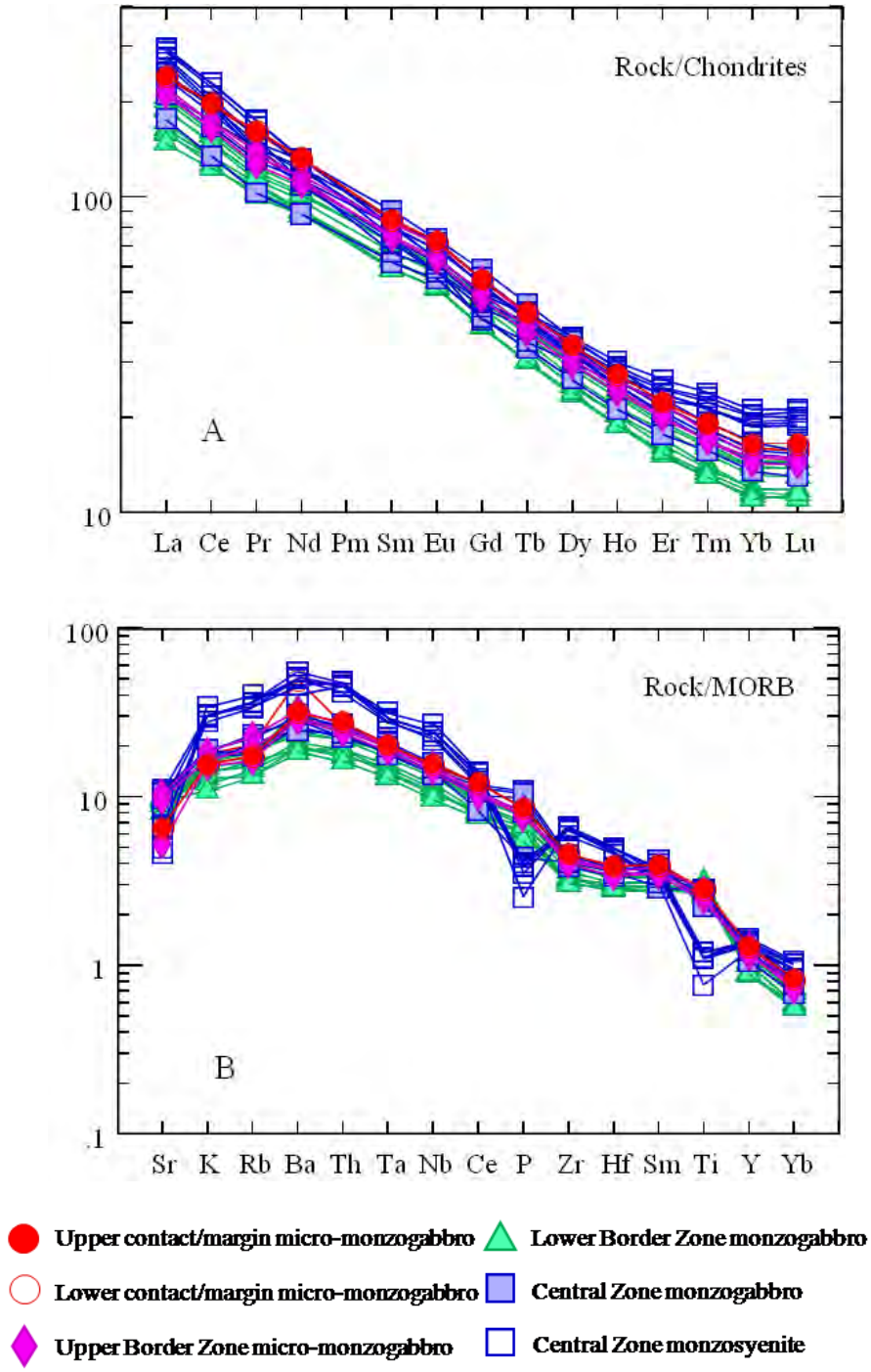

Figure 3-27. Chondrite-normalized rare earth element and MORB-normalized element plot for Bone Springs Sill rocks. (A) Chondrite values are from Sun and McDonough (1989). **(B)** Values and plot after Pearce (1983).

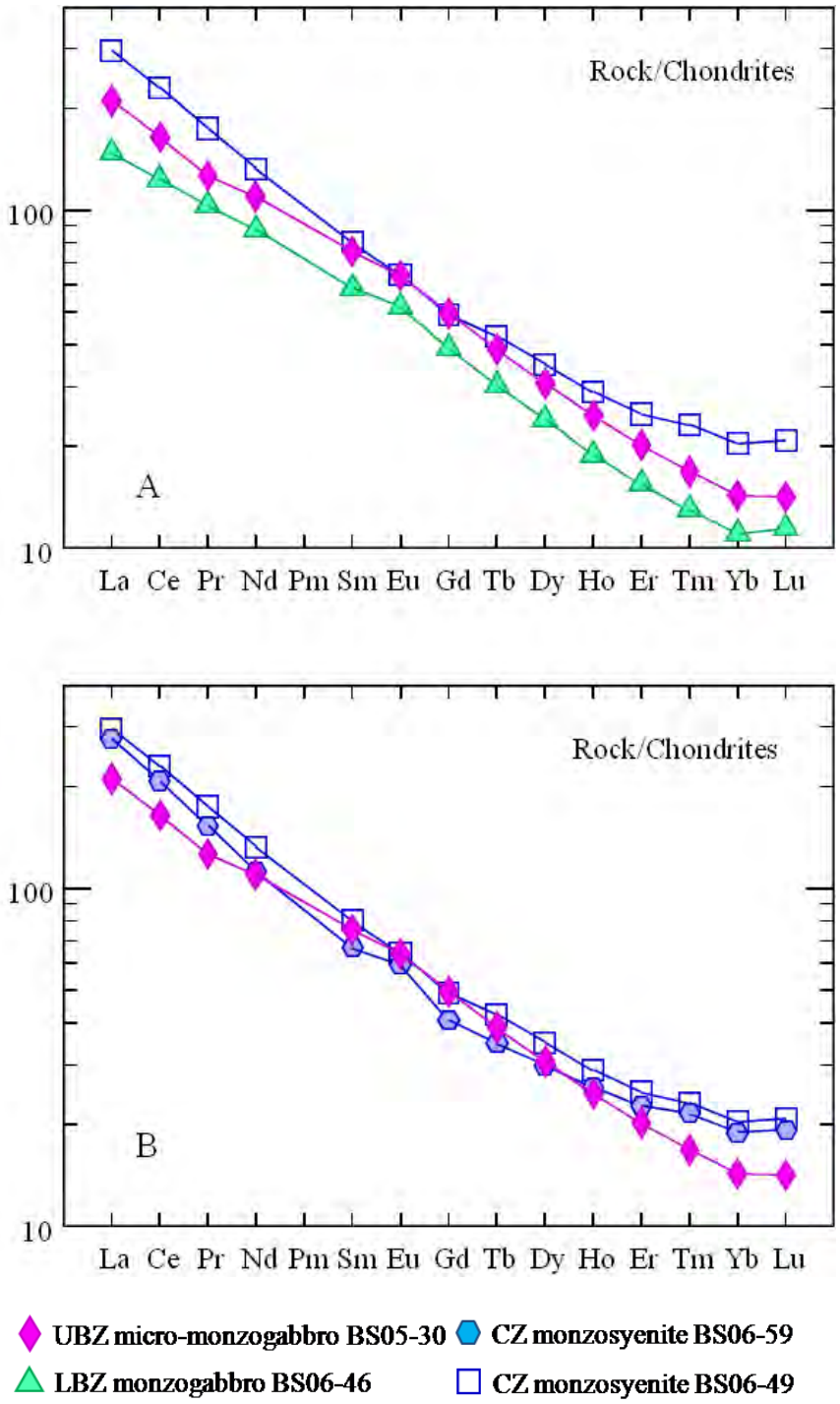

Figure 3-28. Chondrite-normalized REE diagrams for select Bone Springs Sill rocks. All values are normalized after Sun and McDonough (1989). Figure **3-28(A):** LBZ cumulate sample BS06-46, possible parental magma UBZ sample BS05-30, and CZ monzosyenite sample BS06-49. Figure **3-28(B):** Possible parental magma UBZ sample BS05-30, CZ monzosyenite sample BS06-49, and the most differentiated monzosyenite sample, BS06-59.

proportions of cumulate minerals to monzosyenitic liquid), the UBZ sample used as the parental magma in FC models – BS05-30, and the less evolved monzosyenite used in models for FC and for mixing with cumulate minerals – BS06-49 (see Table 3-14 and 3-15). The LBZ and the monzosyenite samples show conjugate patterns reflected across BS05-30, except that the LBZ sample is only slightly convex upward while the monzosyenite is significantly convex downward. The convex pattern of BS06-49 is interpreted to be due to the fractionation of kaersutitic amphibole, which preferentially incorporates MREE (Hanson, 1980). Figure 3-28B shows the BS05-30 and BS06-49 samples but also includes the more evolved monzosyenite sample used in FC models – BS06-59. Sample BS06-59 has fractionated enough amphibole, and thus MREE, that it contains less Sm, Eu, Gd, and Tb than the intruding magma while still being relatively enriched in LREE and HREE. Sample BS06-59 also shows a slight positive Eu anomaly superimposed on the convex downward hump because amphibole incorporates Eu preferentially over the other MREE (Hanson, 1980). Figure 3-29 shows the same samples as 3-28, including the end-member cumulate sample BS06-46, normalized this time to the parental magma represented by BS05-30.

Trace element modeling of fractional crystallization

I tested the results of the major element FC models by incorporating the resulting calculated phase abundances (Table 3-14) into trace element models. Partition coefficients ($K_d = C^{solid}/C^{liquid}$) for trace elements were taken from published values and were carefully chosen to match as closely as possible the liquid compositions in the three modeled steps of the major element models (tephrite, phonotephrite, and tephriphonolite). Table 3-16 contains all partition coefficients used for each step of modeling, their source in the literature, the composition from which they were derived, and the bulk partition coefficients ($D = \sum XK_d$, where X is the fraction

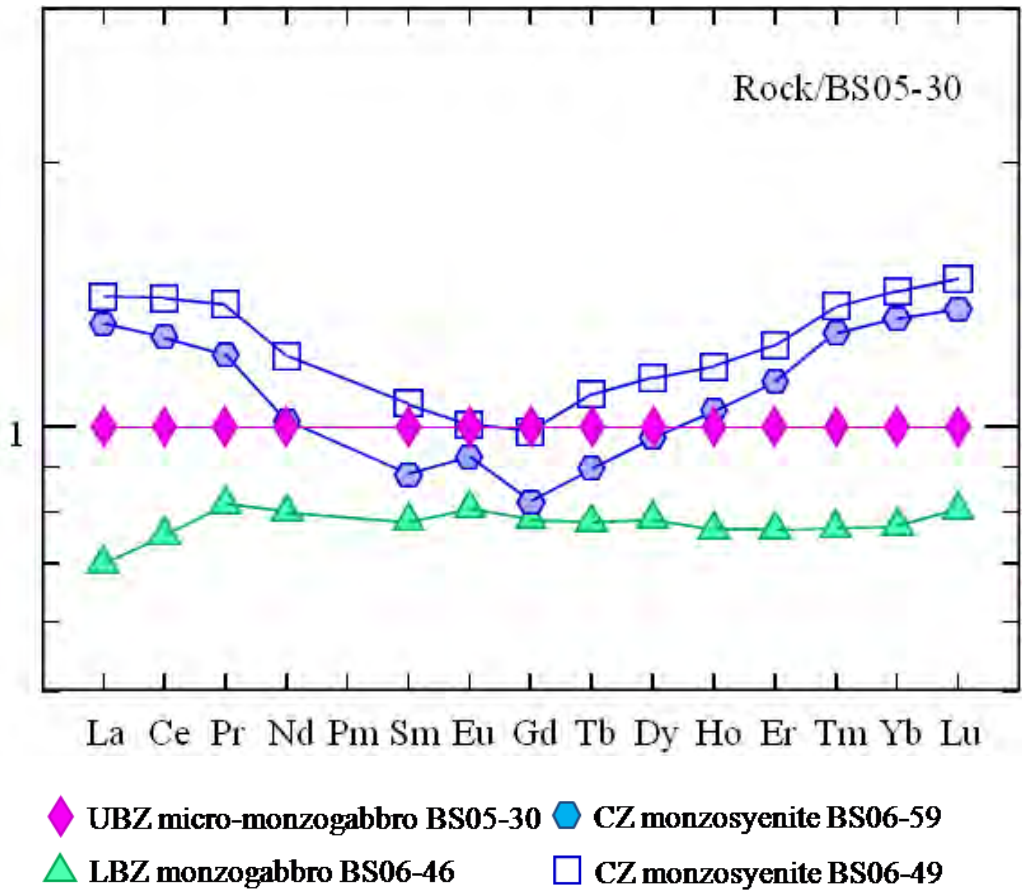

Figure 3-29. REE plot of select Bone Springs rocks normalized to UBZ sample BS05-30. Samples plotted are: LBZ cumulate sample BS06-46, CZ monzosyenite sample BS06-49, and CZ monzosyenite sample BS06-59 (blue hexagons), all normalized to the composition of probable parental sample UBZ sample BS05-30.

Table 3-16. Partition coefficients used in trace element fractional crystallization modeling. Modeling was performed in the same three steps used in major element fractional crystallization models (see Table 3-14). Phases and proportions determined by major element models were used in trace element modeling. Entries for each mineral and element include the mineral-melt partition coefficient (K_d), the reference number in parentheses, and the lithology from the literature for which each K_d was measured. The top row of each step's table includes elements used and the bulk mineral-melt distribution coefficient (D) determined by mass balance proportions and K_d's. References are shown below the tables.

Step 1: BS05-30 to phonotephrite	Sr, D = 1.10	Rb, D = 0.237	Ta, D = 0.143	Zr, D = 0.273	Th, D = 0.126	Sc, D = 1.21
clinopyroxene	0.109 (1) basanite	0.03 (8) basanite-hawaiite	0.08 (8) basanite-hawaiite	0.3 (8) basanite-hawaiite	0.06 (8) basanite-hawaiite	2.8 (8) basanite-hawaiite
olivine	0.02 (2) alkali basalt	0.02 (8) basanite-hawaiite	0.02 (8) basanite-hawaiite	0.07 (8) basanite-hawaiite	0.02 (8) basanite-hawaiite	0.15 (8) basanite-hawaiite
apatite	1.3 (3) basanite	.003 (9) pantellerite	0.0005 (12) pantell.-trachyte	0.636 (14) pantell.-trachyte	1.6 (12) pantell.-trachyte	0.45 (15) trachyandesite
plagioclase	2.94 (4) alkali basalt	0.39 (8) basanite-hawaiite	0.03 (8) basanite-hawaiite	0.09 (8) basanite-hawaiite	0.05 (8) basanite-hawaiite	0.02 (8) basanite-hawaiite
Ti-magnetite	0.7 (5) low-SiO_2 rhyolite	0.32 (8) basanite-hawaiite	0.56 (8) basanite-hawaiite	0.71 (8) basanite-hawaiite	0.19 (8) basanite-hawaiite	1.59 (8) basanite-hawaiite
biotite	0.7 (2) alkali basalt	2.48 (10) basanite	0.56 (2) alkali basalt	0.017 (10) basanite	0.12 (2) alkali basalt	8.3 (2) alkali basalt
nepheline	0.24 (6) peralkaline trachyte	0.01 (estimate - none available)	0.01 (estimate - none available)	0.005 (6) peralk. trach.	0.014 (6) peralk. trach.	0.01 (estimate - none available)

Step 2: Phonotephrite to BS06-49	Sr, D = 1.278	Rb, D = 0.210	Ta, D = 0.457	Zr, D = 0.304	Th, D = 0.151	Sc, D = 5.370
clinopyroxene	0.109 (1) basanite	0.03 (8) mugearite	0.23 (8) mugearite	0.44 (8) mugearite	0.15 (8) mugearite	2.5 (2) alkali basalt
olivine	0.02 (2) alkali basalt	0.02 (8) mugearite	0.02 (8) mugearite	0.07 (8) mugearite	0.03 (8) mugearite	15.5 (16) basalt
apatite	1.3 (3) basanite	0.003 (9) pantellerite	0.0005 (12) pantellerite - trachyte	0.636 (14) pantellerite - trachyte	1.6 (12) pantellerite - trachyte	0.01 (estimate - none available)
plagioclase	2.94 (4) alkali basalt	0.39 (8) mugearite	2.17 (8) mugearite	0.04 (8) mugearite	0.03 (8) mugearite	0.45 (2) alkali basalt
Ti-magnetite	0.7 (5) low-silica rhyolite	0.32 (8) mugearite	0.03 (8) mugearite	0.94 (8) mugearite	0.25 (8) mugearite	19 (17) basalt
biotite	0.7 (2) alkali basalt	1.46 (11) trachyte	0.88 (11) trachyte	0.22 (11) basanite	0.1 (11) trachyte	1.3 (2) alkali basalt
nepheline	0.24 (6) peralkaline trachyte	0.01 (estimate - none available)	0.01 (estimate - none available)	0.005 (6) peralkaline trachyte	0.014 (6) peralkaline trachyte	0.01 (estimate - none available)

Table 3-16, continued. Partition coefficients used in trace element fractional crystallization modeling.

Step 3: BS06-49 to BS06-59	Sr, D = 0.985	Rb, D = 0.213	Ta, D = 0.498	Zr, D = 0.390	Th, D = 0.111	Sc, D = 6.750
apatite	1.3 (3) basanite	0.003 (9) pantellerite	0.0005 (12) pantellerite-trachyte	0.636 (14) pantellerite trachyte	1.6 (12) pantellerite - trachyte	0.3 (12) pantellerite-trachyte
alkali feldspar	2.3 (6) peralkaline trachyte	0.16 (8) benmoreite-trachyte	0.05 (8) benmoreite-trachyte	0.17 (8) ben.-trachyte	0.06 (8) benmoreite-trachyte	0.08 (8) benmoreite-trachyte
ilmenite	0.74 (5) peralkaline rhyolite	0.14 (8) benmoreite-trachyte	2.7 (13) basalt-andestite	0.29 (18) alkali basalt	0.00055 (18) alkali basalt	0.58 (18) alkali basalt
amphibole	0.58 (7) basalt-trachyte	0.14 (8) benmoreite-trachyte	1.02 (8) benmoreite-trachyte	0.72 (8) benmoreite-trachyte	0.07 (8) benmoreite-trachyte	15.3 (8) benmoreite-trachyte
nepheline	0.24 (6) peralkaline trachyte	0.44 (6) peralkaline trachyte	0.01 (estimate - none available)	0.005 (6) peralkaline trachyte	0.014 (6) peralkaline trachyte	0.01 (estimate - none available)

Reference numbers refer to numbers in parentheses in table entries.

1 Adam & Green (2006)

2 Villemant et al. (1981)

3 Watson & Green (1981)

4 Matsui et al. (1977)

5 Ewart & Griffin (1994)

6 Larsen (1979)

7 Nagasawa (1973)

8 Lemarchand et al. (1987)

9 Klemme (2003)

10 Latourette et al. (1995)

11 Villemant (1988)

12 Mahood & Stimac (1990)

13 Green & Pearson (1987)

14 Fujimaki (1986)

15 Luhr et al. (1984)

16 Mysen (1978)

17 Nielsen (1992)

18 Zack & Brumm (1998)

of each contributing phase) for each element in each step. The equation for Rayleigh fractionation was used for modeling:

$$C_L = (F^{(D-1)})*C_0 \quad (4)$$

where C_L is the concentration of the element in question in the liquid at the end of the fractionation step, C_0 is the initial concentration of the element in the liquid, F is fraction of melt remaining at the end of the step, and $D = \sum XK_d$, as described above. All of the inputs for the model except contained in Tables 3-14 and 3-16, except for the C_0 for step 1, for which data from Table 3-11 are taken. Models and equations for *in situ* crystallization (Langmuir, 1989) could have been used instead of the Rayleigh model, but were not for the following reasons: (1) there is evidence in BSS for some gravitational sorting of crystals, from the high abundances of olivine and Fe-Ti-oxide in the LBZ relative to the CZ (Table 3-1) and from the relatively more magnesian olivine in the LBZ (Figure 3-23); (2) the monzosyenite segregations are clear field evidence that liquid separated from the crystalline framework in BSS; and (3) models that assess proportions of early-forming minerals to interstitial liquid, such as the CLF (Table 3-13) or the least squares mass balance (Table 3-15), suggest that these proportions differ between samples and between zones.

Table 3-17 summarizes the numerical results of the trace element modeling and Figure 3-30 shows the plotted modeled results and actual data for the points that correspond to samples (all but the model composition at the end of the step 1). Results are plotted against the SiO_2 of the compositions used in the major element FC modeling (Table 3-14). The model results are quite close in most cases. Where there is a discrepancy it lies between the two monzosyenite compositions (before and after step 3), and the largest discrepancy by far is at that point for Sr. As Figure 3-26 shows, the monzosyenite samples show a large spread in Sr data that does not

Table 3.17. Results of trace element fractional crystallization modeling. The trace element values for the starting sample are from geochemical analysis, but the others are calculated based on modal proportions from major element fractional crystallization modeling as described in the text and recounted in Table 3-14. Partition coefficients used are shown in Table 3-16. Degree of melt remaining (F) refers to the end of each step.

	Lithology	Sample	Sr	Rb	Ta	Zr	Th	Sc	
Step 1: F=0.60	tephrite	BS05-30 *	1152	39	3.4	358	4.8	21.6	parent
	phono-tephrite	model	1102	57	5.2	517	7.0	19.4	daughter
Step 2: F=0.51	phono-tephrite	model	1102	57	5.2	517	7.0	19.4	parent
	monzosyenite (tephriphonolite)	BS06-49	1049	68	5.7	585	8.7	8.9	daughter
Step 3: F=0.42	monzosyenite (tephriphonolite)	BS06-49	1049	68	5.7	585	8.7	8.9	parent
	monzosyenite (tephriphonolite)	BS06-59	1053	77	6.3	660	10.3	2.9	daughter

* Trace element data for the starting sample (BS05-30) can be found in Table 3-11. All other data are calculated from the trace element model.

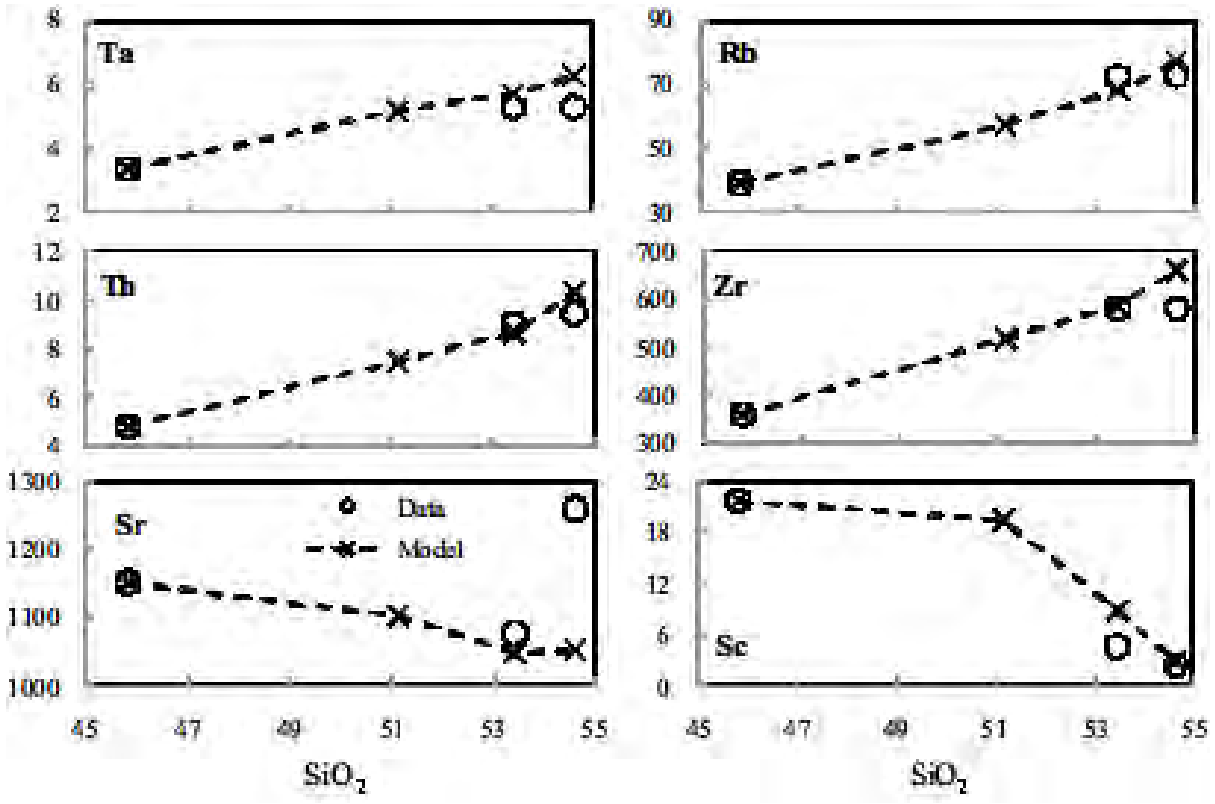

Figure 3-30. Results of the trace element fractional crystallization calculations. Compositions correspond to the range from BSS mafic margin composition to the most felsic monzosyenite sample. Corresponding numerical data are found in Table 3-17. Partition coefficients are shown in Table 3-16. Phase proportions are from the major element fractional crystallization model summarized in Table 3-14. The SiO_2 compositions are from the geochemical data and the model composition for the end of step 1 (see text for explanation). Model element abundances are calculated and shown in comparison to geochemical data.

correlate with Nb, which itself does not correlate well with SiO_2 in these samples. The trace element model here uses a K_d for Sr in alkali feldspar of 2.3 from the data of Larsen (1979) in peralkaline trachyte compositions, which contributes largely to a bulk partition coefficient (D) of 0.985 (Table 3-16). This $D \approx 1$ explains why the model Sr value is almost unchanged in this third step, and if the K_d for alkali feldspar is too high then this explains some of the underestimation of Sr. Additionally, sample BS06-59, the most evolved monzosyenite used as the final product of the model, contains 4 modal% carbonate (Table 3-1) – for BSS, a relatively high amount of a phase not included in the FC modeling and one that would be expected to sequester Sr.

The incompatible element models, especially for Th, Rb, and Zr, support the major element FC models and the degree of crystallization (1-F) they predict. With the exception of Sr, the accuracy of the model even when passing through a model composition at the end of step 1/beginning of step 2 supports the fractionating assemblage and proportions.

Formation of the bimodal rock suite in Bone Springs Sill

Many Trans-Pecos intrusions and thick lava flows contain felsic segregations in intermediate to mafic hosts (Barker, 1987), including dikes (Barker, 2000), thick flows (Maxwell et al., 1967), and sills (Carman, 1994). Similar segregations occur in alkaline rocks throughout the world – Canada (Philpotts and Hodgson, 1968), Montana (Nash, 1982), NSW, Australia (Mackenzie and White, 1970), and Transbaikalia, Russia (Litvinovsky et al., 2002), to name a few. Liquid immiscibility has been invoked for some of these occurrences (Philpotts and Hodgeson, 1968; Kendrick and Edmond, 1981). In the case of the Shonkin Sag laccolith in Montana, this hypothesis has been controversial, with Nash (1982) arguing for fractional crystallization. Analogous differentiates also occur in subalkaline basalt sills (Marsh, 2002).

A very convincing case for the formation of these felsic segregations by fractional crystallization and subsequent liberation and migration of evolved interstitial residual liquid has been made in the general case (Marsh, 2002) and for RMS and other Big Bend sills in particular (Carman, 1994). From the perspective of physical processes, the work of Carman et al. (1975) and Carman (1994) on Rattlesnake Mountain Sill (RMS) make up arguably the most comprehensive work on segregated alkaline intrusions. These studies document that RMS is broadly symmetric: the upper and lower portions (the upper and lower border zones) of RMS are composed of a monzodiorite that crystallized with strong mineral zonation and minor amounts of syenite segregations, while the central zone is composed of a similar but more mafic monzodiorite and abundant syenite segregations. The RMS felsic rocks exhibit a bimodal distribution of plagioclase-rich syenites and less abundant plagioclase-poor syenites. The similarities to BSS are obvious (enough that I borrowed the nomenclature for BSS map units from Carman et al. [1975]) and Carman (1994) includes some characteristics of BSS in his review of differentiated Big Bend sills. However, there are significant differences between BSS and RMS beyond the more mafic nature of the former. The more mafic monzodiorite in RMS, i.e., that from which more liquid has been extracted, is in the center and hosts the majority of the syenite bodies; in BSS the more mafic monzogabbro is the LBZ in the lower portion of the sill and the extracted liquid has migrated upwards, such that the less mafic monzogabbro (named the CZ only because it is overlain by the quenched rock of the narrow UBZ) hosts virtually all of the monzosyenite. The plagioclase-rich and plagioclase-poor syenites of RMS are probably analogous to the less and more evolved monzosyenites in BSS, but there are not enough analyzed samples of BSS monzosyenite to delineate a bimodal population. Also, mineral zoning is much more pronounced at RMS than BSS; in the former all feldspar is zoned from plagioclase to

anorthoclase and Carman et al. (1975) found no evidence of co-precipitation of plagioclase and alkali feldspar.

Marsh describes the general case for felsic segregations in mafic rocks pertaining to subalkaline or alkaline rocks (1996 and 2002), which entails the development of a rigid crystalline framework by the symmetric advance of the solidification front that follows the geotherms from the upper and lower borders of a sill during cooling. Marsh (1996) downplays crystal settling and suggests that most layering in intrusions is due to subsequent pulses of magma differentiating at depth. Marsh (1996) suggested that gravitational instabilities develop in the upper solidification front of some sills, and that these can lead to rifting and tearing of the crystalline framework. These tears can then be filled with relatively buoyant differentiated interstitial liquid. Carman (1994) applies earlier Marsh models to RMS and similar sills and envisions the development of a semi-rigid crystalline framework in which differentiation of the interstitial liquid proceeds by strong mineral zonation; an eventual rupturing of this framework due to contraction during cooling or expansion during second boiling leads to liberation of the interstitial liquid into the various forms of syenite bodies.

These models can be applied to BSS, albeit with some modification. Bones Springs Sill underwent differentiation by fractional crystallization and the segregation of interstitial liquid, but BSS lacks the symmetry expected from Marsh's (1996 and 2002) models that is observed in RMS. Bone Springs Sill experienced gravitational settling or convective sorting of the densest early crystals. This density sorting in BSS is evidenced by the higher modal abundances of olivine and Fe-Ti oxides in the LBZ (Table 3-1). The Mg/Fe compositional trends in olivine (Figures 3-8 and 3-23) suggest but do not require gravitational settling: the trends include olivines with higher Mg/Fe occurring in the margins and the LBZ and more Fe-rich rims found

in CZ monzogabbros, but this may be due to liquid extraction from rocks lower in the sill. This differentiated liquid would be in contact longer with CZ rocks and would continue to differentiate, thus promoting more Fe-rich olivine rims. A substantial portion of olivine occurs in the LBZ as clumps of three or more grains with included and interstitial Fe-Ti oxides, and the increased size of these particles caused by amalgamation would have increased their settling velocity and their efficient accumulation. Clinopyroxene in the CZ monzogabbro is equal to or greater in abundance than in the LBZ. The cores of most clinopyroxenes in BSS have similar compositions, a product of equilibrium crystallization prior to liquid removal from the LBZ. Some CZ clinopyroxenes have more Fe-rich rims that formed during their extended interaction with the liquid (see Figure 3-24). For example, the CZ monzogabbros contain more interstitial liquid than the LBZ monzogabbros when calculated by mass balance (Table 3-15) or by CLF equations (Table 3-13) and the CZ monzogabbros host the monzosyenite segregations. A substantial portion of the interstitial liquid was removed from the LBZ and migrated up to the CZ.

Tearing and infilling of the crystalline framework can occur by gravitational instability alone (Marsh, 1996, 2002) or it can be aided by the mechanical effects of vapor exsolution, like volume expansion and the disruption of moving bubbles. Vapor exsolution also enables efficient removal of interstitial melt by filter pressing (Propach, 1976). An event of “second boiling” is common during magma crystallization, and it would be expected in the BSS magma, which contained enough H_2O to stabilize biotite early and to generate pegmatitic textures in the late monzosyenites. Chapter 4 documents strong evidence for such an event in the F and Cl systematics of apatite and biotite in BSS.

Conclusions

Bones Springs Sill provides an excellent natural laboratory for the study of low pressure differentiation from a mafic to felsic alkaline magma. The BSS parental magma is as SiO_2-poor as any in the TPMP and represents an endmember composition of differentiated suites in the region, including the nepheline syenites and phonolites of the eastern alkalic belt (Potter, 1996). Though most other differentiated Big Bend sills fractionate from hawaiite to benmoreite or transitional phonotephrite/benmoreite (Carman, 1975), only BSS and the more silicic Adobe Walls Sill (Cameron et al., 1986) are of the tephrite to phonotephrite series. The BSS differentiation demonstrates the mechanisms by which a bimodal alkaline magma association can be produced and expands the research on bimodal sill differentiation (Marsh, 2002; Carman, 1994) to more mafic and alkaline compositions.

Though differentiation occurred on a relatively small scale in BSS, similar bimodal differentiates occur in the TPMP on a large scale, such as the plutonic suite in the Diablo Plateau (Barker et al., 1977) or the Paisano mugearite-trachyte volcanic complexes (Parker, 1983). Monzosyenite liquid at BSS was produced with only 50 wt.% crystallization, and more efficient liquid segregation could yield a substantial amount of felsic magma for eruption or higher level intrusion. The processes documented here have ramifications for the petrogenesis of felsic alkaline rocks in the TPMP and in general.

CHAPTER 4

BONE SPRINGS SILL, TRANS-PECOS MAGMATIC PROVINCE, PART 2: BIOTITE AND APATITE F AND CL

Abstract

Fluorine-rich apatite began crystallizing in Bone Springs Sill magma either before or coincident with intrusion. Early apatites in the fine-grained margins contain 1.7-2.7 wt.% F and show extensive $Si^{4+}+Al^{3+} = Ca^{2+}+P^{5+}$ substitution. Calculated phosphate saturation temperatures indicate that margin samples have whole rock compositions that should preclude phosphate crystallization. However, high H_2O and F contents in the magma probably stabilized apatite and contributed to the unusual compositions. Apatite crystallized throughout the differentiation history of the sill, though in reduced abundance in the residual monzosyenite liquid. Fluorine behaves incompatibly and increases in apatite and biotite with differentiation.

Mineral compositions record Cl loss concurrent with the separation and segregation of the differentiated monzosyenite liquid. This is probably related to the exsolution of a volatile phase during which fluid volume expansion ruptured the crystalline framework and allowed migration of the differentiated interstitial liquid. Devolatilization caused an attendant loss of Cl by its partitioning into the vapor phase. The upper $1/3^{rd}$ of the sill hosts much of the late monzosyenite as segregations and as crystallized interstitial liquid and its apatite and biotite have the highest F/Cl in the sill as a result of F increase with differentiation and Cl loss to vapor exsolution. An apatite-biotite mineral pair included in Ti-magnetite from the upper $1/3^{rd}$ of Bone Springs Sill records the highest calculated temperature of 1093° ± 103° C. These minerals have

high F and low Cl, suggesting that their inclusion postdates devolatilization and segregation of the residual liquid.

Bone Springs and Rattlesnake Mountain Sills have F-enriched and high F/Cl minerals common in the Trans-Pecos Magmatic Province (TPMP). Apatites in alkaline intrusions have much higher F/Cl and a more limited range in F/Cl than mafic layered complexes. The data presented here show that fine-scale differences in Cl contents, on the order of hundredths of atoms of Cl pfu, can differentiate between otherwise similar alkaline intrusions within the TPMP and between alkaline provinces.

Introduction

Volatile budgets have important effects on magmatic and magmatic-hydrothermal processes. Water and F act as fluxes to lower liquidus and solidus temperatures and affect liquidus mineral assemblages (Wyllie and Tuttle, 1961). Chlorine is a primary complexing agent in transporting metals in aqueous phases (Williams et al., 1995; Boudreau and McCallum, 1996; Yang and Scott, 2002) and F complexes can mobilize elements normally immobile under hydrothermal conditions (e.g., Zr) (Humphris and Thompson, 1978). Water and F alter the densities and viscosities of magmas (Lange, 1994). Because Cl preferentially partitions into vapor while F partitions into the melt (Carroll and Webster, 1994), careful documentation of their relative behavior can lend insight into magmatic-hydrothermal behavior (Zhu and Sverjensky, 1992).

Apatite is a ubiquitous mineral in igneous rocks on Earth and other planetary bodies. As the chief, and often the only, carrier of halogens in igneous and metamorphic rocks, its importance in aiding understanding of halogen abundances and behavior in these systems belies its occurrence as a trace mineral. Apatite has been investigated as a probe into F-Cl-OH

systematics in terrestrial planetary systems (Patiño Douce and Roden, 2006), mantle xenoliths (Wass and Roger, 1980; O'Reilly and Griffin, 2000), mid-ocean ridge cumulates (Meurer and Natland, 2001), layered mafic intrusions – specifically the Stillwater Complex (Boudreau and McCallum, 1989), the Great Dyke in Zimbabwe (Boudreau et al., 1995), and the Bushveld Complex (Willmore et al., 2000), to name a few – felsic igneous rocks (Piccoli and Candela, 1994), hydrothermal systems (Zhu and Sverjensky, 1991), and alkaline igneous rocks (Nash, 1972) and carbonatites (Seifert et al., 2000).

Biotite halogen contents have been investigated in magmatic-hydrothermal systems to unravel fluid conditions (Munoz, 1984 and 1992; Zhu and Sverjensky, 1991; Ayati et al., 2008), in silica-saturated felsic igneous rocks (Sallet, 2000; Dooley and Patiño Douce, 1996), and in potassic and ultrapotassic rocks (Edgar and Arima, 1985; Foley, 1989).

The contents of octahedral sites in biotite exert a significant effect on halogen contents – the so-called "Mg-Cl" and "Fe-F avoidance effects" (Munoz, 1984; Volfinger et al., 1985), whereas apatite exhibits no such crystal control on F-Cl-OH contents and the mixing of these elements can be treated as ideal at high temperatures (Tacker and Stormer, 1989). With appropriate mixing models, the halogen contents of coexisting biotite and apatite are used as a geothermometer (Stormer and Carmichael, 1971; Zhu and Sverjensky, 1992).

It is generally accepted that alkaline magmas are enriched in halogens, especially F, relative to sub- or nonalkaline magmas (Bailey, 1977; Caroll and Webster, 1994; Sallet, 2000). This enrichment is owing to (1) the association of F and Cl with Na and K by magmatic and fluid complexing (Caroll and Webster, 1994); (2) the incompatible behavior of F and Cl coupled with the enrichment of alkaline rocks in incompatible elements (Edgar, 1987; Caroll and Webster, 1994); and possibly (3) the presence of halogens in mantle source regions in phases such as

phlogopite (Edgar and Arima, 1985; Edgar, 1987), apatite, and/or amphibole (Wass and Rogers, 1980). The last argument is particularly compelling for potassic and ultrapotassic rocks.

Geologic setting

Bone Springs Sill (BSS) is a ~30 meter thick alkaline intrusion located in northern Big Bend National Park in the southern Trans-Pecos Magmatic Province (TPMP). The intruding analcime tephrite magma differentiated to cumulate-dominated analcime monzogabbro and liquid-dominated analcime monzosyenite. The analcime is interpreted to be a product of late stage magmatic or subsolidus reaction of nepheline + albite + H_2O. The petrology, field relations, and crystallization history are covered in detail in a companion paper in this document (Chapter 3). In summary: the ~2 m thick upper border zone (UBZ) of the sill is fine-grained tephrite/micro-monzogabbro compositionally representative of the intruding magma; the 15-20 m thick lower border zone (LBZ) is cumulate monzogabbro with a locally variable amount (~30-40%) of crystallized interstitial liquid; sandwiched between is the ~10 m thick central zone (CZ) composed of monzogabbro with 40-60% crystallized liquid and segregations of monzosyenite liquid in the form of dikes, sills, pods, tubes, and ocelli.

Biotite, apatite, and amphibole are the halogen-bearing phases in BSS. Apatite is among the earliest-forming minerals: it occurs in all BSS rocks, it exhibits both euhedral and quench textures in the fine-grained margin rocks, and it cross-cuts some of the earliest olivine grains. Biotite started crystallizing shortly after magma emplacement and occurs in the sill margins. Apatite is less abundant in the residual monzosyenites due to P_2O_5-depletion, and amphibole crystallizes at the expense of biotite, though small amounts of late stage, possibly hydrothermal, biotite can be found throughout the intrusion.

An analcime tephrite lava flow that is compositionally very similar to the BSS magma is locally preserved on top of the sill. It was apparently erupted after uplift and erosion of the sill and preserved in topographic lows. It also contains biotite and apatite and the analyses from one sample of this rock are presented here.

In addition to BSS, apatites from Rattlesnake Mountain Sill, also a Big Bend intrusion were analyzed. Rattlesnake Mountain is a monzodiorite-syenite differentiated sill that is the subject of Chapter 2 of this document. Descriptions of the sill can be found in Cameron et al. (1975), Cameron (1994), and Chapter 2. Whole rock compositions can be found in Table 3-1.

Whole rock compositions of BSS and the tephrite lava flow can be found in Table 3-11, Chapter 3.

Analytical methods and analytical errors

Back-scatter electron images (BSI) and quantitative mineral analyses were collected with the JEOL 8600 Superprobe at the University of Georgia. The instrument was calibrated with standard mineral and synthetic standards: Durango and Wilburforce apatites and synthetic fluorophlogopite were used for F standards and halite and scapolite were used for Cl standards. Analyses were performed with a 15 nA current and 15 kV accelerating voltage. Chlorine and F were counted first for 30 seconds to minimize effects from migration, while other elements were counted for 60 seconds. A layered W-Si crystal (LDE1) was used for F detection. Biotites were analyzed with a <1μm diameter beam. For apatites, Fialin and Chopin (2006) recommend using a 30 μm diameter beam, but the grain size of apatite in the Bones Springs Sill samples is frequently <30 μm in the shortest dimension and so a more realistic beam diameter of 5 μm was employed. Detection limits for F were <0.29 wt.% for apatite and <0.16% for biotite; for Cl, detection limits were <0.032 wt.% for apatite and either ~0.0305 wt.% or 0.0104 wt.% for

biotite, depending on the analytical routine. No data are presented that are below the detection limits. Analytical error for F is 6-15% for apatite and 5-20% in biotite; for Cl, analytical errors are 2-13% for apatite and from 3-90% for biotite depending on the Cl contents.

Assessment of error for apatite F and Cl data

There are well-documented problems in analyzing halogens by electron microprobe that are especially pronounced in the measurement of F in phosphate minerals (Stormer et al., 1993; Ottolini et el., 2000; Fialin and Chopin, 2006). Interaction with the electron beam during microanalysis of apatite causes F to migrate in the near-surface crystal matrix, which can yield inaccurately high results; this effect is anisotropic and is strongest when the c-axis of the crystal is perpendicular to the electron beam (Stormer et al., 1993). The analytical routine for apatites used in this study was based in part on Ottolini et al.'s (2000) recommended settings and counting times and the W-Si crystal was used after Stormer et al.'s (1993) recommendation. The routine is similar to that employed by Boudreau and Simon (2007) (in terms of instrument settings, counting halogens first, and the use of the W-Si crystal), who found that it minimized the halogen migration documented by Stormer et al. (1993) sufficiently such that the effects were below detection limits.

To assess the effects of halogen migration during my apatite analytical routine, I analyzed a standard set of fluorapatite and chlorapatite grains before, and in some cases after, analysis of BSS samples from Bones Spring Sill. For this standard set I acquired three oriented sections of Durango fluorapatite and 20 randomly oriented grains of chlorapatite from Ödergården, Norway. The Durango apatite is a USGS microprobe standard and was described by Young et al. (1969) as having 3.53 wt.% F; however, the samples used here were not issued by the USGS and there is some question as to the chemical consistency between Durango apatite samples (Stormer et al,

1993). The Durango samples were mounted with the c-axes oriented so as to be parallel to, perpendicular to, and of intermediate angle to the microscope stage. There is no accepted standard composition for the chlorapatite from Ödergården. For these reasons, my results bear on precision more than accuracy.

Table 4-1 contains a summary of analytical results for F and Cl in Durango and Ödergården apatites. Analyses of the C-perpendicular Durango apatite report F over 0.50 wt.% higher on average than analyses of C-parallel and C-intermediate grains, as expected from the work of Stormer et al. (1993). They also have a higher standard deviation and resultant relative% error. The Cl analyses for the C-perpendicular analyses are lower on average than analyses of C-parallel and C-intermediate grains by 0.05 wt.%. This was not expected based on previous work, which predicted Cl behavior to mimic patterns of F migration but to a lesser degree. The average of all Durango analyses gives a relative error based on 1σ spread of 14.3% for F and 11.6% for Cl. This represents the case of 24% (14 of 59) apatite grains in a sample set being oriented perpendicular to the plane of the thin section, which is a high but not unreasonable proportion and yields a conservative error. The routines used in this paper for thermometry and element portioning use mole fractions of volatiles rather than elemental or oxide abundances. The deviations and relative errors for X_F, X_{Cl}, and X_{OH} are also shown in Table 4-1. The relative errors for all Durango apatite analyses are 9.4% for X_F, 75.0% for X_{Cl}, and 72.7% X_{OH}. The relatively low error of 11.6 wt.% Cl translates into a high error for X_{Cl} and X_{OH}.

The results of analyses of Ödergården apatites (Table 4-1) show high relative errors for F of 21% and low relative errors for Cl at 5%. Fluorine was consistently near the detection limit of 0.14 and for 28 of the 64 analyses it was below it. Chlorine was found to be high in the Ödergården apatites at 5.90 wt.% average. These results are only tangentially relevant to the

Table 4-1. Summary statistics for F and Cl analysis of Durango and Ödergärden apatite standards. Durango apatite grains were mounted with the c-axis perpendicular to, parallel to, and of intermediate angle to the microprobe stages. These are not known to be the same Durango apatite grains used in the lab as a USGS microprobe calibration standard. The Ödergärden apatite standard comprised 20 randomly oriented grains. Complete analyses can be found in Appendix 5.

Durango apatite	n	F wt.%	1σ	% error	n	Cl wt.%	1σ	% error
C perp. to stage	14	3.70	0.51	13.8	9	0.39	0.05	12.8
C par. to stage	13	3.12	0.35	11.2	8	0.44	0.05	11.4
C int. to stage	32	3.17	0.39	12.3	22	0.44	0.05	11.4
Total	59	3.29	0.47	14.3	39	0.43	0.05	11.6
Ödergården apatite	36	0.19	0.04	21.1	64	5.90	0.30	5.1

Durango apatite	n	X_F	1σ	% error	X_{Cl}	1σ	% error	X_{OH}	1σ	% error
C perp. to stage	14	0.91	0.05	5.5	0.03	0.03	100.0	0.05	0.06	120.0
C par. to stage	13	0.83	0.08	9.6	0.04	0.03	75.0	0.13	0.09	69.2
C int. to stage	32	0.84	0.08	9.5	0.04	0.03	75.0	0.12	0.08	66.7
Total	59	0.85	0.08	9.4	0.04	0.03	75.0	0.11	0.08	72.7
Ödergården apatite	66	0.03	0.03	100.0	0.83	0.16	19.3	0.14	0.15	107.1

analysis of the F-rich apatites in TPMP rocks, but they demonstrate that this analytical routine is precise with regards to analyzing Cl in chlorapatite.

The resulting 1σ errors for Durango apatite mole fractions (Table 4-1) are used to propagate errors in temperatures determined by apatite-biotite thermometry described below. A secondary purpose of this error assessment is to document actual performance of this routine with regard to both fluoroapatite and chlorapatite analysis, so that readers and other researchers can make a fully informed evaluation of data in this paper.

Halogen-bearing minerals in the Bone Springs Sill

Biotite

Compositions of selected biotite analyses from BSS and from the tephrite lava are shown in Table 4-2 (the complete set of 124 analyses can be found in the Appendix) along with mole fractions calculated after Zhu and Sverjensky (1992) based on 22 anions: X_{Fe} = (Fe+Al_{VI})/(Fe+Al_{IV}+Mg), and X_{Mg} = (1-X_{Fe}); OH was calculated by difference as 4-(F+Cl), X_F = F/(F+Cl+OH), X_{Cl} = Cl/(F+Cl+OH), and X_{OH} = OH/(F+Cl+OH).

Bone Springs biotites are Ti-rich (up to 10% TiO_2) and depleted in Si and Al such that they are insufficient to fill the tetrahedral site. Barker (1987, Table 2 in that paper) summarizes Mg' (molar 100*Mg/Mg+Fe) and TiO_2 biotite compositions for TPMP mafic rocks: 6.9-9 wt.% TiO_2 and 43-61 Mg'; BSS biotites have some higher and lower values in both categories (Table 4-2) but match Barker's (1987) summary well. Biotite contains up to 3 wt.% F and most of the higher values occur in CZ monzogabbro samples. Biotite F varies within each sample of Bone Springs rock and there is often no visible difference (in mode of occurrence, color, etc.) between grains with different F wt.%. Though there is within-sample spread and overlap between samples, some patterns are evident on the scale of the intrusion. Figure 4-1 shows histograms of

Table 4-2. Selected biotite analyses from Bone Springs Sill rocks.

sample	BS06-37	BS06-37	BS04-10	BS04-10	BS04-10	BS04-10	BS04-12	BS04-2	BS04-2	BS04-7	BS04-7
strat.	0	0	10.2	10.2	10.2	10.2	17.1	0.8	0.8	3.8	3.8
lith.	L. chill zone	L. chill zone	LBZ mzgb	LBZ mzgb	LBZ mzgb	LBZ mzgb	LBZ mzgb	LBZ mzgb	LBZ mzgb	LBZ mzgb	LBZ mzgb
pt.#	30	33	6	7	11	8b	29	38	15a	12a	15b
SiO_2	34.10	33.58	34.76	35.40	35.28	35.15	35.79	35.25	34.90	34.40	34.94
Al_2O_3	14.50	14.29	14.24	14.20	14.99	14.86	13.53	13.69	13.66	13.74	13.73
TiO_2	8.70	7.48	8.58	8.84	6.69	6.49	8.47	7.67	7.02	7.94	8.32
MgO	9.63	9.22	12.10	11.38	12.69	12.44	10.10	8.89	8.49	7.75	8.62
FeO	18.26	19.32	16.63	16.52	16.87	16.85	19.18	20.77	21.88	23.60	20.45
MnO	0.21		0.22					0.24	0.36	0.24	
CaO		0.10	0.15	0.13	0.33	0.59	0.35	0.32	0.23	0.16	0.22
K_2O	8.78	9.39	9.32	9.64	9.00	8.48	8.99	8.79	8.52	9.22	9.12
Na_2O	1.01	0.39	0.51	0.55	0.36	0.48	0.61	0.58	0.48	0.46	0.58
BaO			0.25	0.15							0.28
F		0.166	0.240	0.200	0.217	0.159	1.216	0.584	0.598	0.323	0.513
Cl	0.024	0.059			0.016	0.021	0.026	0.023	0.024	0.026	0.016
Total'	95.21	93.99	97.00	97.00	96.44	95.52	98.25	96.82	96.15	97.86	96.78
-O=F	0.00	0.07	0.10	0.08	0.09	0.07	0.51	0.25	0.25	0.14	0.22
-O=Cl	0.01	0.01	0.00	0.00	0.00	0.00	0.01	0.01	0.01	0.01	0.00
Total	95.21	93.91	96.90	96.92	96.35	95.45	97.74	96.56	95.90	97.72	96.56
atoms based on 22 anions											
Si	5.24	5.30	5.25	5.33	5.32	5.34	5.54	5.47	5.49	5.33	5.43
Al (iv)	2.62	2.66	2.53	2.52	2.66	2.66	2.46	2.50	2.51	2.51	2.51
Al (vi)	0.00	0.00	0.00	0.00	0.00	0.00	0.00	0.00	0.01	0.00	0.00
Ti	1.00	0.89	0.97	1.00	0.76	0.74	0.99	0.90	0.83	0.93	0.97
Mg	2.20	2.17	2.72	2.55	2.85	2.82	2.33	2.06	1.99	1.79	2.00
Fe	2.34	2.55	2.10	2.08	2.13	2.14	2.48	2.70	2.88	3.06	2.66
Mn	0.03	0.00	0.03	0.00	0.00	0.00	0.00	0.03	0.05	0.03	0.00
Ca	0.00	0.02	0.02	0.02	0.05	0.10	0.06	0.05	0.04	0.03	0.04
K	1.72	1.89	1.80	1.85	1.73	1.64	1.77	1.74	1.71	1.82	1.81
Na	0.30	0.12	0.15	0.16	0.11	0.14	0.18	0.18	0.15	0.14	0.17
Ba			0.01	0.01							0.02
F		0.08	0.11	0.10	0.10	0.08	0.59	0.29	0.30	0.16	0.25
Cl	0.01	0.02			0.00	0.01	0.01	0.01	0.01	0.01	0.00
OH	3.99	3.90	3.89	3.90	3.89	3.92	3.40	3.71	3.70	3.83	3.74
Total	19.46	19.59	19.59	19.51	19.61	19.57	19.82	19.63	19.64	19.63	19.59
Mg'	48	46	56	55	57	57	48	43	41	37	43
X_{Fe}	0.515	0.540	0.435	0.449	0.427	0.432	0.516	0.567	0.592	0.631	0.571
X_{Mg}	0.485	0.460	0.565	0.551	0.573	0.568	0.485	0.433	0.410	0.369	0.429
X_F		0.021	0.029	0.024	0.026	0.019	0.149	0.072	0.074	0.040	0.063
X_{Cl}	0.002	0.004			0.001	0.001	0.002	0.001	0.002	0.002	0.001
X_{OH}	0.998	0.975	0.971	0.976	0.973	0.980	0.850	0.927	0.924	0.959	0.936

Table 4-2, continued. Selected biotite analyses from Bone Springs Sill rocks.

sample	BS04-7	BS04-9	BS04-9	BS04-9	BS04-9	BS06-38	BS06-45	BS04-3	BS04-3	BS05-19	BS05-19
strat.	3.8	9.5	9.5	9.5	9.5	2.3	8	25.8	25.8	18.6	18.6
lith.	LBZ mzgb	LBZ mzgb	LBZ mzgb	LBZ mzgb	LBZ mzgb	LBZ mzgb	LBZ mzgb	CZ mzgb	CZ mzgb	CZ mzgb	CZ mzgb
pt.#	17b	20	22	25	23a	20a	4b	36	7c	13	10c
SiO_2	33.59	33.79	35.58	34.91	33.71	36.80	36.36	36.15	35.52	35.07	35.83
Al_2O_3	12.62	14.29	14.08	13.91	14.69	13.99	13.51	14.00	13.82	13.78	13.99
TiO_2	6.87	9.17	8.21	7.32	9.32	7.02	6.87	8.78	8.62	8.28	8.04
MgO	7.20	9.89	11.11	10.28	10.53	13.87	14.83	9.69	10.08	12.33	12.38
FeO	24.75	17.66	17.81	18.66	17.94	15.71	13.16	17.65	17.68	15.86	17.82
MnO	0.36	0.20									0.20
CaO	0.32	0.17	0.54	0.64	0.17	0.09	0.05	0.34	0.38	0.75	0.28
K_2O	9.29	8.25	9.24	9.54	8.11	9.58	8.91	8.74	8.75	9.00	9.35
Na_2O	0.40	0.59	0.56	0.42	0.59	0.52	0.47	0.60	0.51	0.80	0.53
BaO	0.14	2.18	0.52	0.39	2.34				0.36		
F	0.368	0.270	0.268	0.307	0.157	1.490	1.874	1.050	0.859	2.344	1.916
Cl	0.020	0.010	0.021	0.024	0.025	0.024	0.085	0.011	0.014	0.075	0.021
Total'	95.93	96.46	97.94	96.40	97.57	99.09	96.11	97.01	96.59	98.29	100.36
-O=F	0.15	0.11	0.11	0.13	0.07	0.63	0.79	0.44	0.36	0.99	0.81
-O=Cl	0.00	0.00	0.00	0.01	0.01	0.01	0.02	0.00	0.00	0.02	0.00
Total	95.77	96.35	97.82	96.27	97.50	98.46	95.31	96.56	96.23	97.29	99.55
atoms based on 22 anions											
Si	5.39	5.22	5.35	5.38	5.14	5.60	5.71	5.58	5.50	5.58	5.52
Al (iv)	2.39	2.60	2.50	2.53	2.64	2.40	2.29	2.42	2.50	2.42	2.48
Al (vi)	0.00	0.00	0.00	0.00	0.00	0.05	0.10	0.06	0.01	0.08	0.03
Ti	0.83	1.07	0.93	0.85	1.07	0.80	0.81	1.02	1.00	0.99	0.93
Mg	1.72	2.28	2.49	2.36	2.39	3.14	3.47	2.23	2.33	2.92	2.85
Fe	3.32	2.28	2.24	2.41	2.29	2.00	1.73	2.28	2.29	2.11	2.30
Mn	0.05	0.03	0.00	0.00	0.00	0.00	0.00	0.00	0.00	0.00	0.03
Ca	0.06	0.03	0.09	0.11	0.03	0.01	0.01	0.06	0.06	0.13	0.05
K	1.90	1.63	1.77	1.88	1.58	1.86	1.78	1.72	1.73	1.83	1.84
Na	0.13	0.18	0.16	0.13	0.17	0.15	0.14	0.18	0.15	0.25	0.16
Ba	0.01	0.13	0.03	0.02	0.14				0.02		
F	0.19	0.13	0.13	0.15	0.08	0.72	0.93	0.51	0.42	1.18	0.93
Cl	0.01	0.00	0.01	0.01	0.01	0.01	0.02	0.00	0.00	0.02	0.01
OH	3.81	3.87	3.87	3.84	3.92	3.28	3.05	3.48	3.58	2.80	3.06
Total	19.79	19.44	19.57	19.66	19.43	20.02	20.05	19.54	19.59	20.30	20.18
Mg'	34	50	53	50	51	61	67	49	50	58	55
X_{Fe}	0.658	0.500	0.473	0.504	0.489	0.395	0.345	0.512	0.497	0.428	0.450
X_{Mg}	0.342	0.500	0.527	0.496	0.511	0.615	0.674	0.501	0.505	0.587	0.556
X_F	0.047	0.033	0.032	0.037	0.019	0.179	0.233	0.128	0.105	0.295	0.234
X_{Cl}	0.001	0.001	0.001	0.002	0.002	0.002	0.006	0.001	0.001	0.005	0.001
X_{OH}	0.952	0.966	0.967	0.961	0.980	0.819	0.762	0.871	0.894	0.700	0.765

Table 4-2, continued. Selected biotite analyses from Bone Springs Sill rocks.

sample	BS05-19	BS05-29	BS05-26	BS05-26	BS05-26
strat.	18.6	29.5			
lith.	CZ mzgb	UBZ teph	Teph	Teph	Teph
pt.#	12b	23d	14a	16b	19e
SiO_2	36.09	31.44	35.88	36.16	38.32
Al_2O_3	12.46	15.31	13.27	13.76	13.92
TiO_2	7.00	5.94	9.19	9.27	6.03
MgO	11.01	11.52	12.46	12.77	15.21
FeO	19.28	21.22	15.41	15.24	12.45
MnO	0.34			0.29	
CaO	0.18	0.33	0.08	0.15	1.41
K_2O	9.39	5.90	9.20	9.07	9.08
Na_2O	0.58	0.24	0.69	0.62	0.44
BaO		0.40	0.34	0.27	
F	2.623	0.139	0.405	0.330	0.200
Cl	0.030	0.014	0.031	0.046	0.028
Total'	98.98	92.46	96.95	97.97	97.09
-O=F	1.10	0.06	0.17	0.14	0.08
-O=Cl	0.01	0.00	0.01	0.01	0.01
Total	97.87	92.40	96.77	97.82	97.00
atoms based on 22 anions					
Si	5.84	5.02	5.41	5.37	5.60
Al (iv)	2.16	2.88	2.36	2.41	2.40
Al (vi)	0.11	0.00	0.00	0.00	0.00
Ti	0.85	0.71	1.04	1.04	0.66
Mg	2.66	2.74	2.80	2.83	3.32
Fe	2.61	2.83	1.94	1.89	1.52
Mn	0.05	0.00	0.00	0.04	0.00
Ca	0.03	0.06	0.01	0.02	0.22
K	1.94	1.20	1.77	1.72	1.69
Na	0.18	0.08	0.20	0.18	0.13
Ba		0.03	0.02	0.02	0.00
F	1.34	0.07	0.19	0.16	0.09
Cl	0.01	0.00	0.01	0.01	0.01
OH	2.65	3.93	3.80	3.83	3.90
Total	20.42	19.54	19.56	19.51	19.54
Mg'	50	49	59	60	69
X_{Fe}	0.506	0.508	0.410	0.401	0.315
X_{Mg}	0.514	0.492	0.590	0.599	0.685
X_F	0.336	0.018	0.048	0.039	0.023
X_{Cl}	0.002	0.001	0.002	0.003	0.002
X_{OH}	0.662	0.982	0.950	0.958	0.975

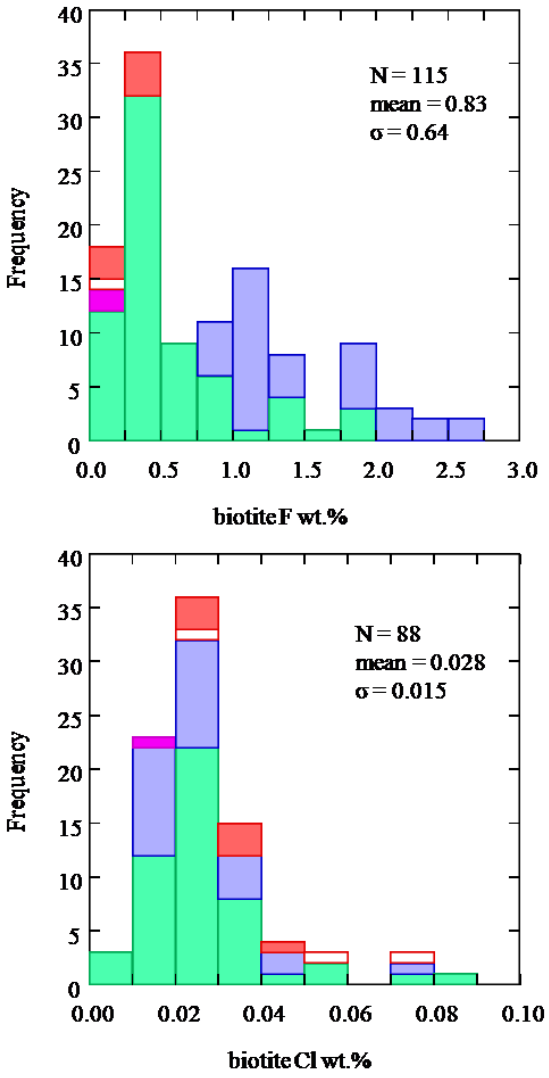

Figure 4-1. Histograms of Bones Spring Sill biotite F and Cl wt.%. Unfilled with red border = lower chill margin micro-monzogabbro, green = LBZ monzogabbro, blue = CZ monzogabbro, purple = UBZ micro-monzogabbro, and red = tephrite lava flow.

biotite F and Cl wt.%. The lower chill zone and the UBZ contain some biotites with measurable but low 0.1-0.3 wt.% F. Biotites from LBZ samples have up to 1.3 wt.%. The CZ monzogabbro samples contain igneous biotite with up to 2.7 wt.% F, the highest in the sill. BSS biotite Cl contents are generally <0.1 wt.%. Biotites in the tephrite lava flow contain 0.21-0.41 wt.% F and 0.029-0.046 Cl wt.% (Table 4-2).

Apatite

Table 4-3 contains selected analyses of apatites from BSS and the tephrite lava flow (a complete set of the 116 analyses can be found in Appendix). Here, OH is calculated by difference [2-(F+Cl)] based on 26 anions. X_F in apatite is F/(F+Cl+OH), X_{Cl} by Cl/(F+Cl+OH), and X_{OH} is OH/(F+Cl+OH). Figure 4-2 shows a histogram of apatite F and Cl wt.%. Apatite F contents show considerable overlap between lithologies, but the CZ monzogabbros and monzosyenites have the highest F with up to 4 wt.%. The UBZ samples contain apatite with the lowest F wt.% (~1.6%). The lowermost LBZ sample (BS04-2) has F contents almost as high as CZ rocks. Apatite Cl contents in the LBZ rocks are <0.2 wt.% except for two outliers, and all but one CZ monzogabbro samples (BS04-4, discussed below) have lower apatite Cl with <0.16 wt.%. The CZ monzosyenites have lower Cl still, all <0.07 wt.%. The UBZ samples have 0.05-0.12 wt.% Cl. The tephrite lava flow apatites have 1.8-3.8 wt.% F and 0.21-0.30 wt.% Cl (4-3).

Early crystallizing phosphate minerals and magma volatile chemistry

The phosphate minerals from the least differentiated magmas in the BSS area – the BSS lower margin and UBZ tephrites and the tephrite lava flow – are unusually Si- and Al-enriched at the expense of Ca and P. These minerals exhibit a wide range of SiO_2 contents from 1.6 to 39.65 wt.% and Al_2O_3 up to 13.9 wt.% see Table 4-3. There is a strong correlation in these minerals between Si+Al and Ca+P (r = 0.98) shown in Figure 4-3. If this were the only functioning

Table 4-3. Selected apatite analyses from Bone Springs Sill.

sample	BS04-10	BS04-10	BS04-10	BS04-2	BS04-2	BS04-7	BS04-7	BS04-7	BS04-9	BS04-9
strat.	10.2	10.2	10.2	0.8	0.8	3.8	3.8	3.8	9.5	9.5
lith.	LBZ mzgb	LBZ mzgb	LBZ mzgb	LBZ mzgb	LBZ mzgb	LBZ mzgb	LBZ mzgb	LBZ mzgb	LBZ mzgb	LBZ mzgb
pt.#	4	9	5	15	20	16a	23a	18b	29	31
P_2O_5	39.97	39.32	36.77	35.37	39.81	39.99	37.62	39.72	40.89	40.99
CaO	56.71	56.13	57.25	48.66	55.65	55.25	54.13	55.69	55.03	55.37
SiO_2	0.34	0.42	0.39	4.44	0.74	0.58	2.01	1.34	0.28	0.39
Al_2O_3		0.03	0.03	1.62		0.04	0.43	0.11	0.02	0.01
FeO	0.22	0.26	0.34	2.33	0.53	0.47	1.92	0.47	0.20	0.37
MnO			0.02	0.05	0.08	0.03		0.08		0.16
MgO	0.18	0.08	0.16	0.92	0.17	0.14	0.47	0.15	0.13	0.09
Na_2O	0.02	0.03	0.05	0.06	0.03	0.04	0.08	0.32	0.04	0.07
La_2O_3	0.36		0.30	0.37	0.06	0.36		0.12	0.06	
Ce_2O_3	0.14	0.18		0.57	0.44	0.18		0.45	0.27	
SrO	0.37	0.30	0.38	0.23	0.29	0.25	0.39	0.35	0.32	0.31
Y_2O_3		0.04		0.07	0.07	0.10	0.04	0.02	0.02	0.12
SO_3	0.02				0.03	0.02	0.07		0.01	
F	2.601	2.607	2.582	2.816	3.360	2.057	2.492	2.688	1.956	2.110
Cl	0.134	0.194	0.157	0.118	0.180	0.160	0.148	0.189	0.140	0.146
Total'	101.06	99.59	98.43	97.61	101.44	99.68	99.81	101.69	99.37	100.15
-O=F	1.10	1.10	1.09	1.19	1.41	0.87	1.05	1.13	0.82	0.89
-O=Cl	0.03	0.04	0.04	0.03	0.04	0.04	0.03	0.04	0.03	0.03
Total	99.93	98.45	97.31	96.40	99.99	98.78	98.73	100.52	98.51	99.23
atoms based on 26 anions										
P	5.66	5.64	5.42	5.12	5.56	5.75	5.40	5.57	5.87	5.83
Ca	10.16	10.19	10.67	8.92	9.83	10.05	9.83	9.88	10.00	9.97
Si	0.06	0.07	0.07	0.76	0.12	0.10	0.34	0.22	0.05	0.07
Al		0.01	0.01	0.33		0.01	0.09	0.02	0.00	0.00
Fe	0.03	0.04	0.05	0.33	0.07	0.07	0.27	0.07	0.03	0.05
Mn			0.00	0.01	0.01	0.00		0.01		0.02
Mg	0.04	0.02	0.04	0.23	0.04	0.03	0.12	0.04	0.03	0.02
Na	0.01	0.01	0.02	0.02	0.01	0.01	0.03	0.10	0.01	0.02
La	0.02		0.02	0.02	0.00	0.02		0.01	0.00	
Ce	0.01	0.01		0.04	0.03	0.01		0.03	0.02	
Sr	0.04	0.03	0.04	0.02	0.03	0.02	0.04	0.03	0.03	0.03
Y		0.00		0.01	0.01	0.01	0.00	0.00	0.00	0.01
S	0.00				0.00	0.00	0.01		0.00	
F	1.38	1.40	1.42	1.52	1.75	1.10	1.34	1.41	1.05	1.12
Cl	0.04	0.06	0.05	0.03	0.05	0.05	0.04	0.05	0.04	0.04
OH	0.59	0.55	0.53	0.44	0.20	0.85	0.62	0.54	0.91	0.84
Total	18.03	18.01	18.33	17.81	17.72	18.10	18.13	17.98	18.05	18.03
X_F	0.688	0.698	0.710	0.762	0.876	0.552	0.668	0.704	0.524	0.561
X_{Cl}	0.019	0.028	0.023	0.017	0.025	0.023	0.021	0.026	0.020	0.021
X_{OH}	0.293	0.274	0.266	0.221	0.099	0.425	0.311	0.269	0.455	0.419

Table 4-3, continued. Selected apatite analyses from Bone Springs Sill.

sample	BS04-9	BS04-3	BS04-3	BS04-3	BS05-13	BS05-13	BS05-19	BS05-19	BS05-19	BS05-19
strat.	9.5	25.8	25.8	25.8	19.0	19.0	18.6	18.6	18.6	18.6
lith.	LBZ mzgb	CZ mzgb	CZ mzgb	CZ mzgb	CZ mzgb	CZ mzgb	CZ mzgb	CZ mzgb	CZ mzgb	CZ mzgb
pt.#	35	1b	12b	4a	15d	9a	4b	7d	9b	3b
P_2O_5	39.66	38.86	39.35	38.80	40.87	41.48	37.72	36.61	37.23	36.73
CaO	56.87	53.89	54.88	54.58	54.59	55.41	56.44	53.67	54.36	55.89
SiO_2	0.29	0.19	0.48	0.28	0.32	0.19	0.38	3.03	0.50	0.29
Al_2O_3		0.02	0.17			0.01	0.01	0.82	0.02	
FeO	0.62	0.21	0.57	0.22	0.17	0.26	0.77	0.96	0.86	0.79
MnO	0.06		0.02	0.05			0.02			
MgO	0.10	0.02	0.06	0.01	0.16	0.13	0.02	0.22	0.08	0.00
Na_2O	0.06	0.03	0.03	0.08	0.04	0.07	0.03	0.06	0.05	0.03
La_2O_3			0.25	0.19	0.19			0.06	0.19	
Ce_2O_3	0.23		0.27	0.50		0.05	0.22	0.44		0.18
SrO	0.40	0.26	0.28	0.34	0.31	0.27	0.27	0.31	0.27	0.37
Y_2O_3	0.25	0.15	0.04	0.04	0.02		0.04		0.04	
SO_3	0.09			0.02	0.01	0.03		0.01	0.01	0.04
F	2.604	3.080	3.220	3.610	2.176	2.516	3.030	3.210	3.170	3.770
Cl	0.144	0.117	0.109	0.087	0.151	0.134	0.113	0.044	0.137	0.096
Total'	101.36	96.82	99.74	98.81	99.01	100.55	99.05	99.45	96.92	98.19
-O=F	1.10	1.30	1.36	1.52	0.92	1.06	1.28	1.35	1.33	1.59
-O=Cl	0.03	0.03	0.02	0.02	0.03	0.03	0.03	0.01	0.03	0.02
Total	100.24	95.50	98.36	97.27	98.06	99.46	97.75	98.09	95.55	96.58
atoms based on 26 anions										
P	5.62	5.67	5.60	5.56	5.86	5.84	5.47	5.22	5.48	5.34
Ca	10.19	9.95	9.88	9.89	9.91	9.86	10.35	9.68	10.13	10.28
Si	0.05	0.03	0.08	0.05	0.05	0.03	0.06	0.51	0.09	0.05
Al		0.00	0.03			0.00	0.00	0.16	0.00	
Fe	0.09	0.03	0.08	0.03	0.02	0.04	0.11	0.14	0.13	0.11
Mn	0.01		0.00	0.01			0.00			
Mg	0.02	0.00	0.02	0.00	0.04	0.03	0.00	0.06	0.02	0.00
Na	0.02	0.01	0.01	0.03	0.01	0.02	0.01	0.02	0.02	0.01
La			0.02	0.01	0.01			0.00	0.01	
Ce	0.01		0.02	0.03		0.00	0.01	0.03		0.01
Sr	0.04	0.03	0.03	0.03	0.03	0.03	0.03	0.03	0.03	0.04
Y	0.02	0.01	0.00	0.00	0.00		0.00		0.00	
S	0.01			0.00	0.00	0.00		0.00	0.00	0.01
F	1.38	1.68	1.71	1.93	1.17	1.32	1.64	1.71	1.74	2.05
Cl	0.04	0.03	0.03	0.02	0.04	0.04	0.03	0.01	0.04	0.03
OH	0.58	0.29	0.26	0.04	0.79	0.64	0.33	0.28	0.22	
Total	18.08	17.74	17.76	17.65	17.94	17.86	18.06	17.85	17.90	17.93
X_F	0.689	0.839	0.855	0.966	0.583	0.661	0.820	0.855	0.872	0.986
X_{Cl}	0.020	0.017	0.016	0.012	0.022	0.019	0.016	0.006	0.020	0.014
X_{OH}	0.291	0.143	0.129	0.022	0.396	0.320	0.163	0.139	0.108	

Table 4-3, continued. Selected apatite analyses from Bone Springs Sill.

sample	BS06-50	BS06-59	BS05-28	BS05-28	BS05-29	BS05-29	BS05-26	BS05-26	BS05-26
strat.	20.9	25.4	26.6	26.6	29.5	29.5			
lith.	CZ mzsy	CZ mzsy	CZ mzsy	CZ mzsy	UBZ teph	UBZ teph	Teph	Teph	Teph
pt.#	30	31	24a	26a	29a	31a	13e	15f	14c
P_2O_5	33.11	37.04	38.91	28.31	32.55	31.68	36.54	36.94	36.35
CaO	53.20	53.34	54.71	43.08	36.82	36.04	55.11	53.39	52.83
SiO_2	5.88	0.79	1.60	8.11	6.74	14.28	1.62	1.62	3.44
Al_2O_3	1.77	0.10	0.32	6.07	2.83	5.44	0.14	0.15	0.61
FeO	0.13	0.29	0.44	5.07	9.66	1.21	0.65	0.61	0.52
MnO		0.05	0.05	0.05	0.04		0.13	0.11	
MgO				2.14	0.76	0.72	0.30	0.22	0.28
Na_2O	0.17	0.34	0.08	0.14	0.68	1.22	0.11	0.09	0.14
La_2O_3	0.06	0.12	0.46	0.49	0.18		0.56	0.06	
Ce_2O_3	1.05	1.61	0.61	0.40	0.13	0.44	0.84	0.58	0.58
SrO	0.09	0.28	0.29	0.22	0.32	0.33	0.29	0.31	0.28
Y_2O_3	0.08	0.06	0.12	0.06	0.04	0.02	0.16	0.23	0.23
SO_3	0.02		0.01		0.03	0.06	0.04		
F	3.770	4.690	2.746	3.530	2.017	2.668	1.792	2.410	3.410
Cl	0.101	0.032	0.047	0.027	0.099	0.071	0.219	0.237	0.299
Total'	99.43	98.74	100.40	97.70	92.90	94.19	98.51	96.96	98.98
-O=F	1.59	1.97	1.16	1.49	0.85	1.12	0.75	1.01	1.44
-O=Cl	0.02	0.01	0.01	0.01	0.02	0.02	0.05	0.05	0.07
Total	97.82	96.76	99.23	96.21	92.03	93.05	97.71	95.89	97.47
atoms based on 26 anions									
P	4.70	5.30	5.53	4.09	4.98	4.46	5.42	5.47	5.18
Ca	9.55	9.65	9.84	7.87	7.14	6.42	10.35	10.01	9.53
Si	0.99	0.13	0.27	1.38	1.22	2.38	0.28	0.28	0.58
Al	0.35	0.02	0.06	1.22	0.60	1.07	0.03	0.03	0.12
Fe	0.02	0.04	0.06	0.72	1.46	0.17	0.10	0.09	0.07
Mn		0.01	0.01	0.01	0.01		0.02	0.02	
Mg				0.54	0.21	0.18	0.08	0.06	0.07
Na	0.06	0.11	0.03	0.05	0.24	0.39	0.04	0.03	0.04
La	0.00	0.01	0.03	0.03	0.01		0.04	0.00	
Ce	0.06	0.10	0.04	0.02	0.01	0.03	0.05	0.04	0.04
Sr	0.01	0.03	0.03	0.02	0.03	0.03	0.03	0.03	0.03
Y	0.01	0.01	0.01	0.01	0.00	0.00	0.01	0.02	0.02
S	0.00		0.00		0.00	0.01	0.01		
F	2.00	2.50	1.46	1.90	1.15	1.40	0.99	1.33	1.82
Cl	0.03	0.01	0.01	0.01	0.03	0.02	0.07	0.07	0.09
OH			0.53	0.09	0.82	0.58	0.94	0.60	0.10
Total	17.78	17.91	17.90	17.96	17.92	17.14	18.46	18.08	17.68
X_F	0.986	0.996	0.729	0.951	0.577	0.702	0.497	0.667	0.908
X_{Cl}	0.014	0.004	0.007	0.004	0.015	0.010	0.033	0.035	0.043
X_{OH}			0.264	0.045	0.408	0.288	0.471	0.298	0.050

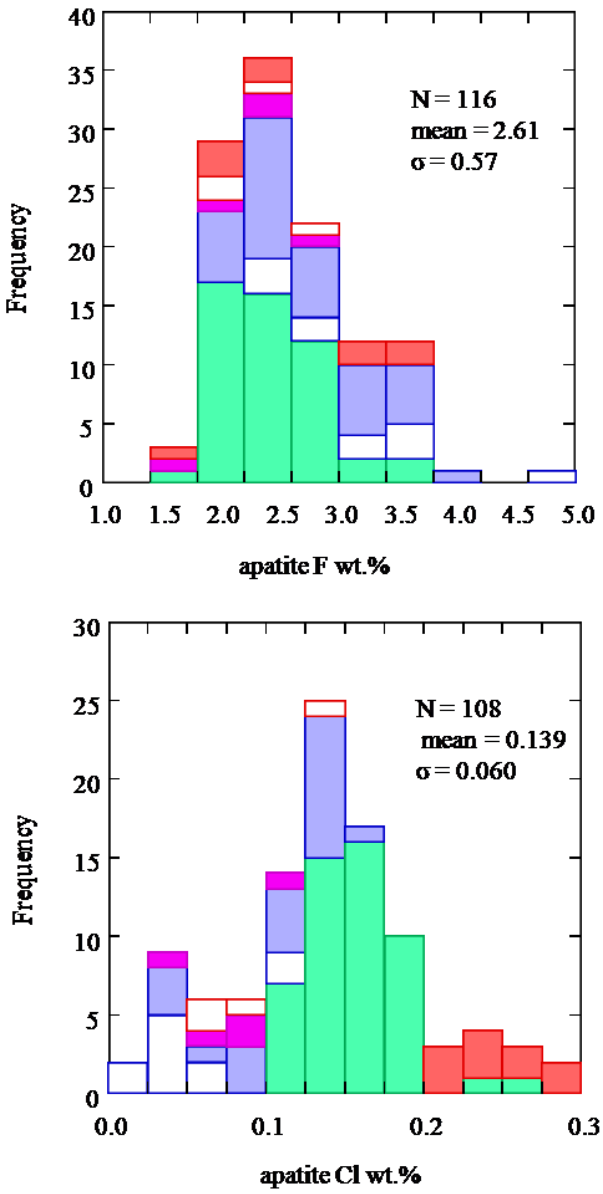

Figure 4-2. Histograms of Bone Springs Sill apatite F and Cl wt.%. Unfilled with red border = lower chill margin tephrite, green = LBZ monzogabbro, blue = CZ monzogabbro, unfilled with blue border = CZ monzosyenite, purple = UBZ tephrite, and red = tephrite lava flow. The lava flow samples have the most consistently high Cl wt.% and the monzosyenites have the consistently lowest Cl wt.%.

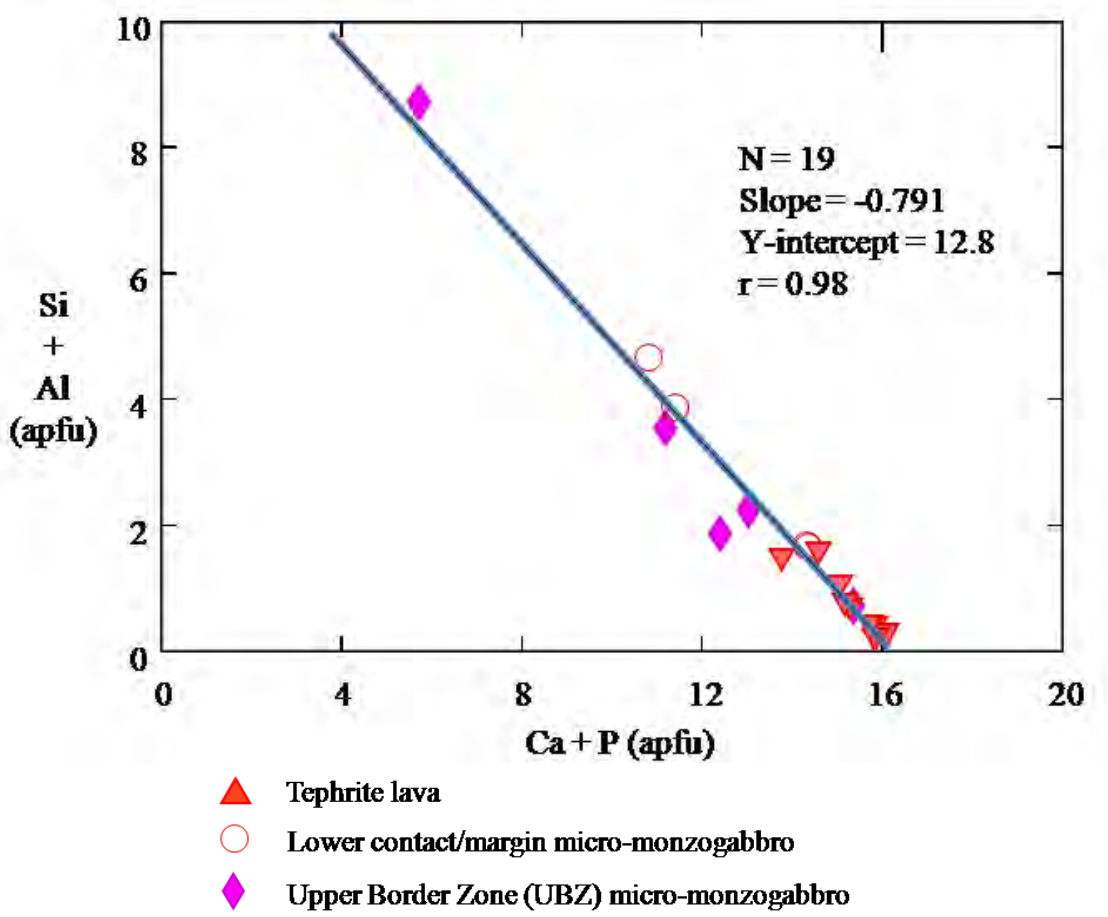

Figure 4-3. Correlation of apatite Si + Al with Ca + P (atoms per formula unit) in Bone Springs Sill mafic magmas. The inverse correlation of Si + Al to Ca + P indicates that $Si^{4+}+Al^{3+} = Ca^{2+}+P^{5+}$ is an important substitution in some early-crystallizing Bones Spring Sill apatite.

substitution the slope of the correlation line would be -1, but it is actually -0.79, indicating other substitutions for Ca and P such as $Na^{+}+REE^{3+} = 2Ca^{2+}$ (Harlov et al., 2002). Though Si is commonly mentioned, and Al less commonly, as a possible substituting cation in apatite (Pan and Fleet, 2002), this apparent $Si^{4+}+Al^{3+} = Ca^{2+}+P^{5+}$ substitution has not, to the author's knowledge, been explicitly documented as occurring in alkaline rocks and is not easily found in the review literature (Pan and Fleet, 2002; Piccoli and Candela, 2002). The most likely analog might be the substitution $REE^{3+} + Si^{4+} = Ca^{2+} + P^{5+}$ (Rønsbo, 1989), or, taken to extreme, solid solution with minerals of the britholite series $(Ce,Y)_6Ca_4(SiO_4)_6(OH)_2$ (Oberti et al., 2001), REE-rich members of which were documented in the evolved members of the Shonkin Sag laccolith (Nash, 1972). In that case, the britholite solid solution occurred as rare grains in the residual system (soda syenite) when REE contents were high and P_2O_5 was probably too low to stabilize pure REE-phosphate minerals (Nash, 1972). This substitution found here is analogous to britholite solid solution but not equivalent because of the substitution of Al^{3+} instead of REE^{3+} or the equivalent Ce^{3+} or Y^{3+} – Bone Springs UBZ, margin, and the tephrite lava apatites are no more REE-enriched than other BSS apatites.

Phosphate saturation is not usually achieved in basalts until considerable fractionation occurs and the melt reaches 3-4 wt.% P_2O_5 (Watson 1979 and 1980), although the addition of alkalis decreases the solubility of phosphate in the melt (e.g., Sha, 2000). The temperature of crystallization is not known for the BSS UBZ rocks, margins, and tephrite lava but it can be assumed to have been >1000° and probably closer to 1200° C. According to the experimentally derived apatite saturation data from Watson (1979), at 1000° C, ~2 wt.% P_2O_5 would need to be present at the BSS magma SiO_2 abundances (44.1-46.8 wt.%) to stabilize apatite and; at 1100° C apatite crystallization would require 4-5 wt.% P_2O_5 – much higher than the mafic BSS P_2O_5

contents of 0.93-1.06 wt.%. Based on the anhydrous phosphate saturation equations of Tollari et al. (2006), temperatures would have to be <700° C before apatite (or whitlockite) would crystallize in the BSS compositions. Tollari et al. (2008) found that F lowered the solubility of apatite, though those experiments contained ≥5 wt.% P_2O_5 so there is no quantitative application to the BSS rocks. The nucleation and growth of ferromagnesian crystals in a magma may result in the local saturation of the melt in apatite (Bacon, 1989); this can lead to the crystallization of apatite earlier than would be predicted by saturation indices such as Watson's (1979) or Tollari et al.'s (2008). This would explain those BSS apatites associated with and included in olivine and pyroxene particularly well (Bacon, 1989).

Apatite is found in some mantle xenoliths that have been infiltrated (i.e., metasomatized) by incompatible-element bearing melts or fluids (e.g., Wass and Rogers, 1980). Apatite also occurs early in the crystallization of volatile-enriched potassic series (Nash, 1972; Carmichael, 1967b). Bones Spring Sill would seem to be analogous in that early forming phosphate minerals crystallized under conditions of high volatile abundances. In the case of BSS, the earliest apatites contain an average of 2.52 wt.% F and so the melt or melt + fluid was F-rich. I hypothesize that apatites in the mafic BSS liquids crystallized because of the abundance of volatiles, especially F, in the melt, and that a F-phosphate mineral formed despite the relative paucity of Ca and P in the melt, incorporating available Si and Al instead. Though the substitution is clearly documented in early-forming BSS rocks (Figure 4-3), it is perhaps counterintuitive that Si^{4+} and Al^{3+} would be the substituting cations in a silica undersaturated alkaline melt. This is beyond the scope of this study but it warrants further investigation.

Amphibole

Amphibole and clinopyroxene are the dominant mafic phases in monzosyenites, and amphibole occurs as a late-forming mineral in some monzogabbros. Petrography indicates that amphibole crystallization began when biotite crystallization ended, though there is probably some overlap. Amphiboles are dominantly kaersutite or ferro-kaersutite with subordinate edenite, but ferro-eckermannite occurs in the most evolved samples. Amphiboles contain 0.24-0.76 wt.% F and <0.07 wt.% Cl.

Biotite-apatite equilibrium and thermometry

Stormer and Carmichael (1971) were the first to propose using F-OH exchange between apatite and biotite as a geothermometer, but the technique was hampered by the lack of consistent thermodynamic data for halogen-bearing endmember species and an incomplete understanding of biotite mixing. Luddington (1978) refined the Stormer and Carmichael (1971) geothermometer to account for biotite octahedral mixing. A major difficulty stems from the recognition that F-Cl-OH exchange between minerals or minerals and fluid is strongly dependent on the composition of the phases as well as *T*, and, to a lesser extent, *P* (Zhu and Sverjensky, 1991). It has been unambiguously shown that, all other conditions being equal, biotite octahedral Mg has a reciprocal effect on Cl that results in “Mg-Cl avoidance”; there is a similar “Fe-F avoidance effect”, and the degree of reciprocity is also T-dependent (Munoz, 1984; Volfinger et al., 1985; Zhu and Sverjensky, 1991 and 1992). Octahedral Al is included in the biotite mole fraction calculations of the Zhu and Sverjensky (1992) because Al has been empirically demonstrated to mimic Fe in its reciprocal effect on halogen incorporation (Munoz, 1984; Zhu and Sverjensky, 1992).

Octahedral Ti is ignored in this routine, under the justification that even if it had the same scale of effect as Al (for which there is no evidence) its dilute concentrations in biotite would result in changes in the partition calculations less than the error (Zhu and Sverjensky, 1992). However, Dooley and Patiño Douce (1996) found a negative correlation between F and Ti in experimental systems rich in Ti and F. This is consistent with the Ti-oxy substitution of $Ti^{4+} + O^{2-} = Mg^{2+} + OH^-$ (Abrecht and Hewitt, 1988) and the $F^- = OH^-$ substitution, where more F might limit the availability of OH for Ti-oxy substitution (Dooley and Patiño Douce, 1996). Bone Springs Sill biotites are more unusually Ti-rich (Table 4-2), but exhibit no positive or negative Ti-F correlation (Figure 4-4), so the routines of Zhu and Sverjensky (1992) excluding Ti were applied.

Unlike biotite, cation exchange in apatite causes little distortion of the hydroxyl site and it has been found that mixing of F-Cl-OH in apatite can be treated as ideal at geologic conditions (Tacker and Stormer, 1989; Candela, 1986). The mole fractions of F and OH are used in the geothermometer without any activity expressions.

Zhu and Sverjensky (1991) published standard state thermodynamic properties of Cl and F, Mg, and Fe endmembers of biotite internally consistent with the Berman (1988) database, and applied molten salt mixing models (Wood and Nicholls, 1978) first used for biotite mixing by Munoz (1984) to account for non-ideality of mixing in biotite. Zhu and Sverjensky (1992) revised the apatite-biotite geothermometer equation to:

$$T(°C) = \frac{8852 - 0.024P(bars) + 5000X_{Fe}^{bt}}{1.987 \ln K_{D,F}^{Ap/Bt} + 3.3666} - 273.15 \quad (4),$$

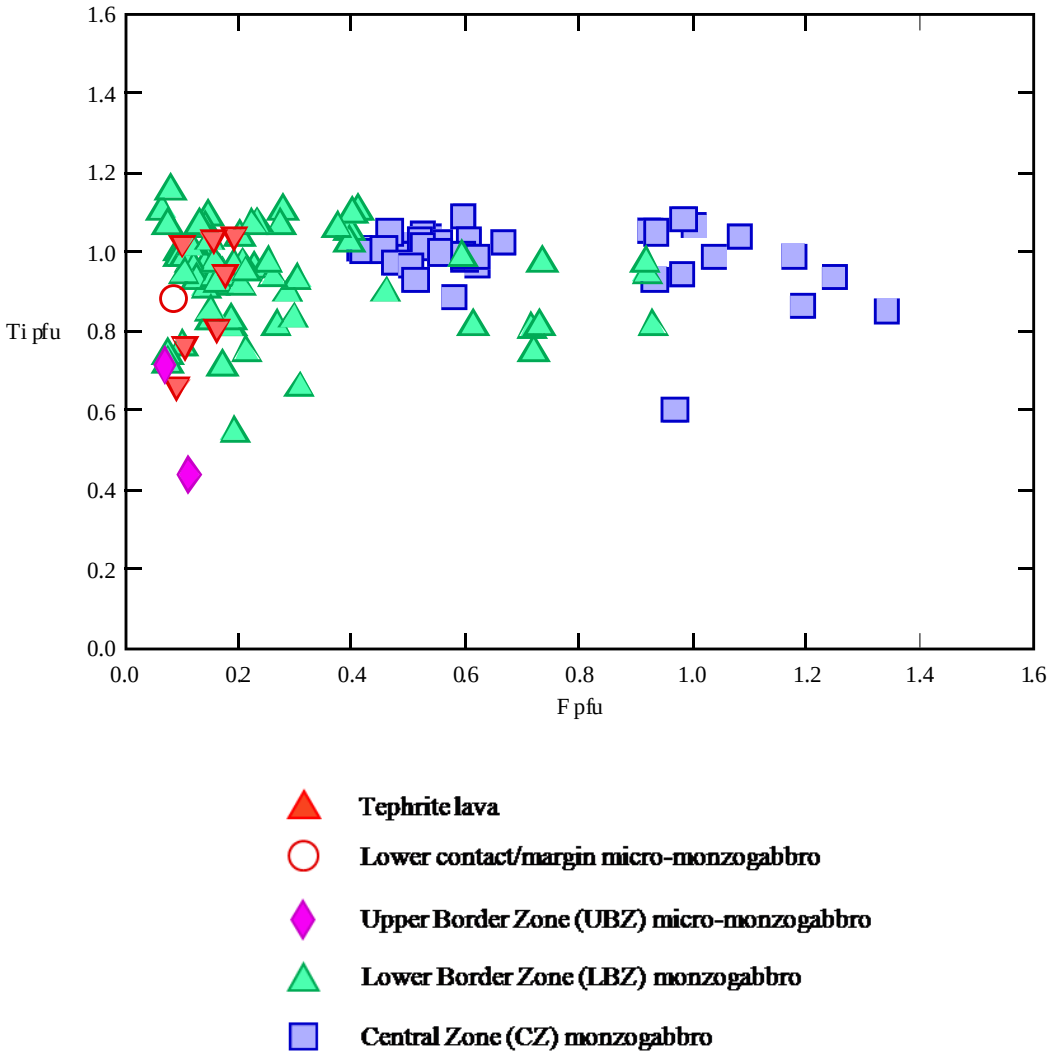

Figure 4-4. Biotite Ti apfu plotted against F apfu. These data show no correlation and thus no obvious Ti-F avoidance. However, the effects octahedral site contents anions in biotite are not always readily evident except within a population that experienced the same temperature and fluid history (Zhu and Sverjensky, 1992).

where $K_{D,F}^{Ap/Bt} = \dfrac{\left(\dfrac{X_F}{X_{OH}}\right)^{Ap}}{\left(\dfrac{X_F}{X_{OH}}\right)^{Bt}}$ (5).

and X_F and X_{OH} are calculated as described above. The X_{Fe} term is included on the top of equation (5) due to account for the above mentioned octahedral effect on biotite halogens.

Error propagation

The error for $\ln K_{D,F}^{Ap/Bt}$ from Zhu and Sverjensky (1992) is:

$$\sigma^2_{\ln K_{D,F}^{Ap,Bt}} = \left(\frac{\sigma_{X_F^{Bt}}(1-X_{Cl})}{X_F(1-X_F-X_{Cl})}\right)^2_{Bt} + \left(\frac{\sigma_{X_{Cl}^{Bt}}}{1-X_F-X_{Cl}}\right)^2_{Bt} + \left(\frac{\sigma_{X_F^{Ap}}(1-X_{Cl})}{X_F(1-X_F-X_{Cl})}\right)^2_{Ap}$$

$$+ \left(\frac{\sigma_{X_{Cl}^{Ap}}}{1-X_F-X_{Cl}}\right)^2_{Ap} \quad (6).$$

The error for temperature from the apatite-biotite thermometer of Zhu and Sverjensky (1992) is:

$$\sigma_T = \sigma_{\ln K_{D,F}^{Ap,Bt}} \left(\frac{1.987(8852 - 0.024P + 5000X_{Fe}^{Bt})}{(1.987\ln K_{D,F}^{Ap,Bt} + 3.3666)^2}\right) \quad (7).$$

Results of BSS apatite-biotite thermometry

Thermometry and routines for the determination of fluid chemistry require all phases to be in equilibrium. There are potential pitfalls in using apatite-biotite pairs, even if proximal, for these calculations; e.g., phases may reequilibrate with changes in melt or fluid compositions and the halogen contents in apatite and biotite show considerable spread within samples (Tables 4-2 and 4-3). For this reason I only used apatite-biotite pairs in contact and I analyzed the grains as

close to the points of contact as possible. Figure 4-5 contains images of some of the apatite-biotite pairs used for thermometry.

Table 4-4 contains temperature results calculated using the Zhu and Sverjensky (1992) calibration of the apatite-biotite thermometer and 1σ errors for T and $\ln K_D$. All temperatures were calculated at P = 300 bars. This pressure is justified by the presence of miarolitic cavities in BSS border and CZ rocks and calculations of stratigraphic overburden on TPMP early extensional intrusions into the Aguja formation, both of which indicate shallow intrusion of perhaps <1 km depth (Carman et al., 1975; Barker, 1987; Carman, 1994). The pressure selection is all but moot, however, because like most exchange reactions used for geothermometry, the $\Delta S/\Delta V$ is high and the reaction is relatively pressure-insensitive. For instance, changing the input pressure to 5 kilobars results in temperatures only ~10° C lower. To test the validity of excluding Ti from mole fraction calculations, I calculated several temperatures for the high-Ti BSS biotites including Ti in the denominator of the Zhu and Sverjensky (1992) X_{Fe} expression and found X_{Fe} reduced by 15-20% and temperatures increased by ~40° C on average, less than 1σ errors, as they report.

Calculated temperatures in Bones Spring Sill rocks range from 600 to 1093° C with 1σ errors from 43 to 103° C. The apatite-biotite pairs from CZ monzogabbro sample BS05-19 are inclusions trapped in an early cumulate Ti-magnetite; the highest is 1093 ± 103° and the other two of these overlap within 1σ error of a 901 ± 54° temperature from LBZ sample BS04-7. The lowest temperature calculated from sill rocks is 600 ± 45° from LBZ sample BS04-10, though a lower temperature of 450 ± 80° is obtained from the tephrite lava flow.

Petrography indicates that both apatite and biotite are early phases, that biotite crystallization persists at least until the time of the monzosyenite liquid separating from the

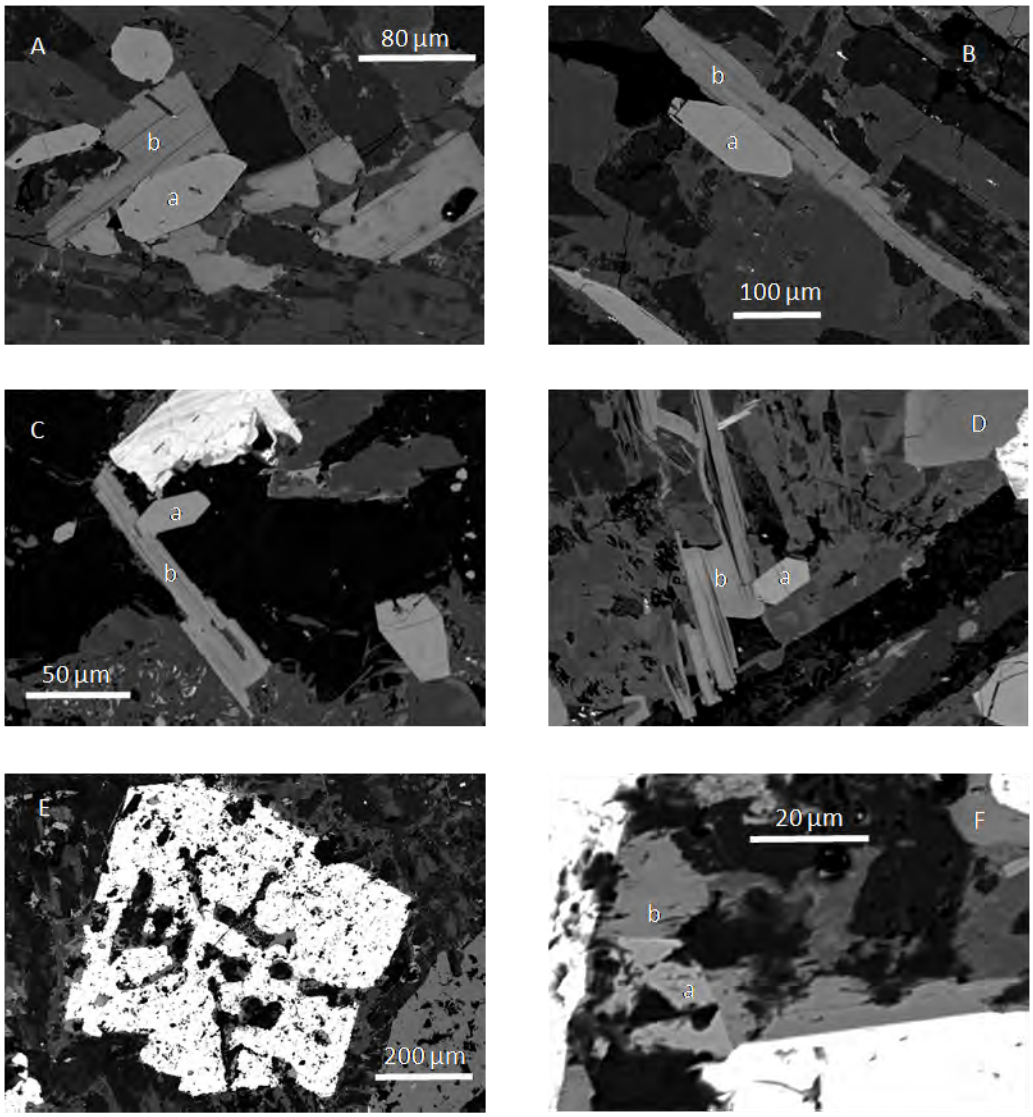

Figure 4-5. Backscatter electron images of apatite-biotite pairs used in geothermometry. Lower case "a" and "b" in each image except **E** mark the apatite and biotite, respectively, analyzed for thermometry. **A** and **B**: CZ monzogabbro sample BS04-3. **C**: LBZ monzogabbro sample BS04-2. **D**: LBZ monzogabbro sample BS04-10. **E**: Ti-magnetite with inclusions of apatite and biotite in CZ monzogabbro sample BS05-19. **F**: Close-up of upper left quadrant of the Ti-magnetite grain in image **E**.

Table 4-4. Results of apatite-biotite geothermometry of Bone Springs Sill rocks. Analysis numbers refer to data in Tables 4-2 and 4-3. Temperatures and errors were calculated using equations and calibrations from Zhu and Sverjensky (1992). Analytical errors used in error propagations were propagated from microprobe analytical errors to mole fractions. All temperatures were calculated at P = 300 bars.

Lithology	LBZ mzgb	LBZ mzgb	LBZ mzgb	LBZ mzgb	LBZ mzgb	LBZ mzgb	LBZ mzgb	LBZ mzgb
sample	BS04-10	BS04-10	BS04-10	BS04-10	BS04-2	BS04-2	BS04-7	BS04-7
Biotite								
analysis #	7	11	6	8b	15a	38	15b	17b
$\mathbf{X_{Fe}}$	0.449	0.427	0.435	0.432	0.592	0.567	0.571	0.658
$\mathbf{X_{F}}$	0.024	0.026	0.029	0.019	0.074	0.072	0.063	0.047
$\mathbf{X_{Cl}}$	0.000	0.001	0.000	0.001	0.002	0.001	0.001	0.001
$\mathbf{X_{OH}}$	0.976	0.973	0.971	0.980	0.924	0.927	0.936	0.952
T (°C)	600	610	640	653	655	797	827	842
σ (T)	45	43	43	57	77	54	44	46
$\boldsymbol{lnK_{D,F}^{Ap/Bt}}$	4.69	4.56	4.38	4.28	4.71	3.80	3.66	3.78
$\boldsymbol{\sigma(lnK_{D,F}^{Ap/Bt})}$	0.33	0.30	0.29	0.37	0.53	0.28	0.21	0.23
Apatite								
analysis #	5	9	4	10	20	15	18b	23
$\mathbf{X_{F}}$	0.710	0.698	0.688	0.562	0.876	0.762	0.704	0.668
$\mathbf{X_{Cl}}$	0.023	0.028	0.019	0.038	0.025	0.017	0.026	0.021
$\mathbf{X_{OH}}$	0.266	0.274	0.293	0.400	0.099	0.221	0.269	0.311

Lithology	LBZ mzgb	LBZ mzgb	LBZ mzgb	LBZ mzgb	LBZ mzgb	CZ mzgb	CZ mzgb
sample	BS04-7	BS04-9	BS04-9	BS04-9	BS04-9	BS04-3	BS04-3
Biotite							
analysis #	12a	23a	25	22	20	7c	36
$\mathbf{X_{Fe}}$	0.631	0.489	0.504	0.473	0.500	0.497	0.512
$\mathbf{X_{F}}$	0.040	0.019	0.037	0.032	0.033	0.105	0.128
$\mathbf{X_{Cl}}$	0.002	0.002	0.002	0.001	0.001	0.001	0.001
$\mathbf{X_{OH}}$	0.959	0.980	0.961	0.967	0.966	0.894	0.871
T (°C)	901	684	713	802	822	723	770
σ (T)	54	61	43	51	53	67	72
$\boldsymbol{lnK_{D,F}^{Ap/Bt}}$	3.45	4.24	4.11	3.55	3.52	4.03	3.81
$\boldsymbol{\sigma(lnK_{D,F}^{Ap/Bt})}$	0.23	0.38	0.25	0.25	0.25	0.38	0.38
Apatite							
analysis #	16a	31	35	29	29	12	12
$\mathbf{X_{F}}$	0.552	0.561	0.689	0.524	0.524	0.855	0.855
$\mathbf{X_{Cl}}$	0.023	0.021	0.020	0.020	0.020	0.016	0.016
$\mathbf{X_{OH}}$	0.425	0.419	0.291	0.455	0.455	0.129	0.129

Table 4-4, continued. Results of apatite-biotite geothermometry of Bone Springs sill rocks.

Lithology	CZ mzgb	CZ mzgb	CZ mzgb	teph	teph	teph
sample	BS05-19	BS05-19	BS05-19	BS05-26	BS05-26	BS05-26
Biotite						
analysis #	13	10c	12b	14a	19e	16b
$\mathbf{X_{Fe}}$	0.428	0.450	0.506	0.410	0.315	0.401
$\mathbf{X_{F}}$	0.295	0.234	0.336	0.048	0.023	0.039
$\mathbf{X_{Cl}}$	0.005	0.001	0.002	0.002	0.002	0.003
$\mathbf{X_{OH}}$	0.700	0.765	0.662	0.950	0.975	0.958
T (°C)	917	969	1093	450	682	684
σ (T)	95	72	103	80	55	74
$\boldsymbol{lnK_{D,F}^{Ap/Bt}}$	2.95	2.80	2.50	5.88	3.79	4.01
$\boldsymbol{\sigma(lnK_{D,F}^{Ap/Bt})}$	0.37	0.26	0.32	0.84	0.32	0.44
Apatite						
analysis #	9a	4b	7d	14c	13e	15f
$\mathbf{X_{F}}$	0.872	0.820	0.855	0.908	0.497	0.667
$\mathbf{X_{Cl}}$	0.020	0.016	0.006	0.043	0.033	0.035
$\mathbf{X_{OH}}$	0.108	0.163	0.139	0.050	0.471	0.298

cumulate crystal framework, and that minor apatite crystallized after that. None of the calculated temperatures are magmatic peak temperatures and there is a continuous distribution between ~1100° and 600° C. Seven of 18 calculated sill temperatures fall within 1σ error of the thermal minimum in the 1 kb P^{H2O} residual system ($NaAlSiO_4$-$KAlSiO_4$-SiO_2-H_2O) of 750 ± 7° C determined by Hamilton and MacKenzie (1965) and only 5 calculated temperatures fall below it.

If there was an H_2O-rich subsolidus analcimization event in BSS experimental evidence indicates it should have occurred at <500° C (Manghani, 1970; Liou, 1971), and no temperatures record it. Apatite-biotite thermometry can record temperatures of hydrothermal events <300° C (e.g., Ayati et al., 2008) and significant events can entirely reset the F-Cl systematics, including the apatite-biotite temperatures (Zhu and Sverjensky, 1992). Either analcimization occurred at higher, possibly even magmatic, temperatures, in BSS or the fluid present was insufficient to reset the F-Cl systematics.

For context, these data can be compared to apatite-biotite temperatures calculated using the routines of Zhu and Sverjensky (1992) on other relevant igneous systems. These BSS temperatures range higher than the 500-700° (average 564°) calculated for the Great Dyke in Zimbabwe (Boudreau et al., 1995) but match well temperatures calculated for the Bushveld complex, which are as low as 600°, exhibit a cluster of temperatures around 850°, and have one high temperature from the lower zone of ~1050° C (Willmore et al., 2000). Bone Springs Sill apatite-biotite temperatures are similar in pattern to those of the Bushveld complex (Willmore et al., 2000).

Fluorine and chlorine systematics in Bone Springs Sill apatite and biotite

Fluorine and Cl are not incorporated into common igneous minerals aside from apatite, mica, and amphibole. In all of these minerals, F is preferentially incorporated over Cl (Mathez

and Webster, 2005) and the F-endmember is stable at the highest temperature of the F-Cl-OH phases (Patiño Douce and Roden, 2006). In mafic compositions, F is partitioned into apatite over melt with a K_d (concentration in apatite/concentration in liquid) of >3 (Mathez and Webster, 2005) while the K_d for Cl is close to unity or slightly <1 (Mathez and Webster, 2005). Both F and Cl are preferentially partitioned into biotite over melt but measured K_d's vary widely (e.g., Larourrette et al., 1995).

In BSS, both biotite and apatite crystallized early; biotite occurs as 1 to 6 modal% in most monzogabbros with one outlier sample that contains 11% biotite and apatite occurs at 1-4 modal% in monzogabbro (see Chapter 3, Table 3-1 for modal data). Both occur in trace amounts in BSS monzosyenites. Though both minerals occur in relatively high amounts in the BSS monzogabbros compared to other mafic rocks, they are still minor phases. Thus, their bulk partition coefficients (*D*'s) in BSS and most rocks are <1, and their contents in the melt increase with crystallization and down-temperature. The *D* for F is higher than for Cl, and so F/Cl will decrease with crystallization (e.g., Boudreau, 1995) unless in the presence of a vapor phase, into which Cl is strongly partitioned (Kilinc and Burnham, 1972; Carroll and Webster, 1994).

Fluorine and chlorine compositions and stratigraphy

Figure 4-6 shows the molar F and Cl contents of Bone Springs Sill apatite and biotite by stratigraphy. The fine-grained margins should approximate the halogen budget of the intruding magma and they serve as good yardsticks by which to measure halogen depletion and enrichment during crystallization. For both minerals, the F and Cl contents are essentially the same at the lower chill margin and the fine-grained UBZ samples. Only for biotite Cl is this relationship unclear, but only one UBZ biotite grain analyzed contained Cl above the detection limit.

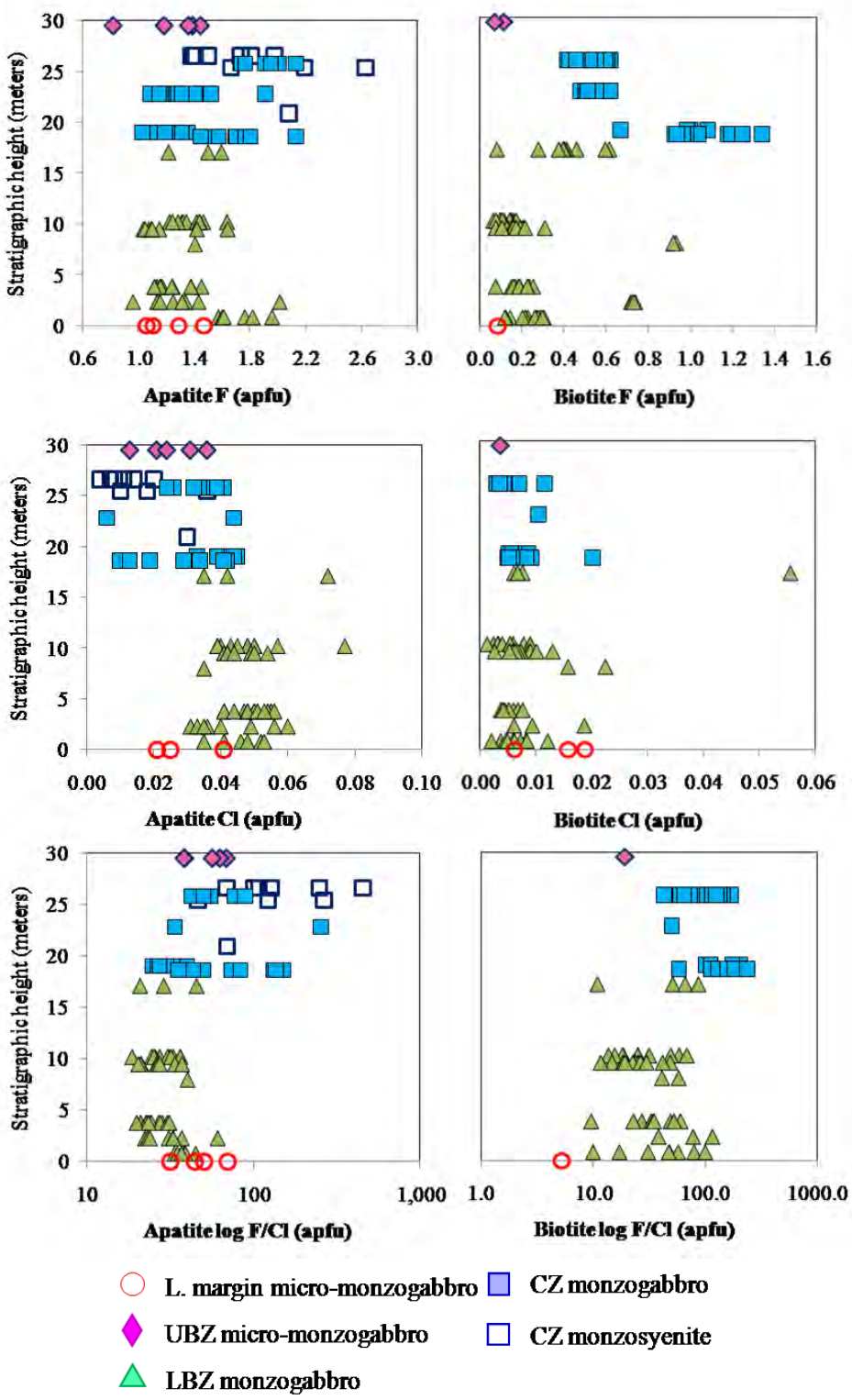

Figure 4-6. Apatite and biotite F, Cl, and log F/Cl (all apfu) in Bone Springs Sill by stratigraphy.

Each sample on Figure 4-6 was taken at one stratigraphic interval (the vertical spread in analyses), and most samples contain apatites and biotites that span a range of halogen contents (the horizontal spread in analyses). Apatites with a range of F/Cl are found in samples examined from most layered intrusions: the Stillwater complex (Boudreau and McCallum, 1989), the Great Dyke (Boudreau et al., 1995), Bushveld (Willmore et al., 2000), and oceanic cumulates (Meurer and Natland, 2001). There are several possible reasons for this: (1) analytical error, though this is <15 relative% on average for both F and Cl wt.% (Table 4-1), and would somewhat obscure but not obliterate patterns of change by height; (2) disequilibrium due to partial resetting of mineral compositions during thermal or fluid events – this is probably partially true, though apatite is less prone to subsolidus re-equilibration than biotite (Boudreau et al., 1995); (3) some version of the "trapped liquid shift" phenomenon named by Barnes (1986) to describe Mg/Fe systematics in the presence of trapped interstitial liquid, where some grains continue to grow, new grains crystallize, and some may partially re-equilibrate with the trapped liquid. The model assumes that if there is enough interstitial melt present and a sufficient thermal and chemical impetus, this process potentially goes to completion and is equivalent to equilibrium crystallization. Cawthorn (1994) applied the concept of the trapped liquid shift to the behavior of F/Cl in apatites in the Stillwater and Bushveld complexes to explain the presence of Cl-rich apatites low in the sections. Boudreau (1995) refuted Cawthorn's (1994) interpretation of wholesale change from F-rich to Cl-rich compositions but acknowledged the "relatively modest" effects that such reequilibration may have. Meurer and Meurer (2006) purported that the trapped liquid effect in the sense of closed system equilibration, which requires zero permeability, does not occur, but no one disputes the crystallization of and partial reequilibration with interstitial liquid and its "relatively modest" effects (Boudreau, 1995) in cumulate rocks. Proponents of this perspective

refer to the “crystallized liquid” instead of the “trapped liquid” to denote the open system behavior of cumulate systems (e.g., Meurer and Boudreau, 1998a; Meurer and Meurer, 2006). In BSS, significant zonation is not observed in apatite and biotite, but the range of F/Cl found in every sample suggests interaction with an evolving liquid.

Bone Springs Sill apatite F and Cl contents (Figure 4-6) show an excursion to higher values immediately above the base of the sill. Apatite F then reverts to the composition of the margins before both apatite F and Cl increase slightly until the CZ is reached. Fluorine is significantly higher and Cl significantly lower in the CZ than in the LBZ. The CZ monzosyenites have more pronounced F enrichment and Cl depletion on average than the CZ monzogabbros and show less overlap with the LBZ compositions. The apatite log (F/Cl) data show have a C-shaped curve with F/Cl decreasing from the lower contact through the LBZ, increasing in the CZ, and peaking in the uppermost CZ monzosyenites. The highest F/Cl of the CZ monzogabbro apatites are at the LBZ-CZ interface, represented by sample BS05-19: the highest F/Cl apatites in this sample are in polymineralic inclusions in Ti-magnetite (see Figure 4-5). The apatite and biotite in this inclusion yield the highest temperatures by apatite-biotite thermometry.

Like with apatite, BSS biotite F contents increase immediately above the lower margin (Figure 4-6). Biotite F remains essentially constant, with some high-F outliers, until the sample immediately below the LBZ-CZ, which have a higher range of values. The highest CZ biotite F compositions are found in the two samples within a meter of the interface, and the remaining CZ monzogabbro biotites contain less F but are still enriched relative to most LBZ analyses. Biotite Cl contents are low (most are less than 0.03 Cl apfu) and are mostly consistent throughout the stratigraphy. Biotite F/Cl within the sill is enriched relative to the margin compositions and the highest are, like the apatite, found in the CZ.

Discussion of mineral F/Cl distribution with stratigraphy

Bone Springs Sill is only ~30 m thick and was emplaced in the shallow crust so it should have cooled approximately symmetrically from the roof and floor (Marsh, 1996). Any primary asymmetry, i.e., any that occurred prior to late stage liquid migration, would be due to early density sorting by settling or convection or early venting of fluid through the roof, which could result in localized quenching near the top of the sill. Mineral Mg/Fe compositions provide evidence for some density sorting of the earliest olivine in BSS but none for clinopyroxene (see Chapter 3 for detailed descriptions). Thus cooling would advance from the roof and floor of the sill along a solidification front which would generate a rigid crystalline framework (see Marsh [1996] for a detailed description of this well-established model). Much apatite crystallized early and would have been incorporated in this framework. As discussed above, progressive crystallization of a magma should produce increasing Cl and decreasing F/Cl in halogen-bearing minerals. This is the basic pattern shown in apatite F/Cl compositions in Figure 4-6, with the exception of the monzosyenites and some of the lowest Cl and highest F/Cl compositions in CZ monzogabbros, which are discussed below. Crystallization resulted in increasing Cl inwards, though the resolution of the Cl data is imperfect and decreasing F/Cl which reaches a minimum near the center of the sill.

Superimposed on that concave-rightward pattern in apatite F/Cl composition (Figure 4-6) is the distribution of high F, low Cl monzosyenite. Furthermore, the highest F/Cl apatite analyses in CZ monzogabbros are in samples with the highest proportion of crystallized liquid:mafic minerals, i.e., the samples with the most differentiated liquid present (see sample BS05-19 in Tables 3-13 and 3-15 in Chapter 3 as an example). This material rose from deeper in the sill and concentrated in the upper third of the sill here called the CZ. As a late stage differentiate it is

possible that the high F of the segregated monzosyenite and interstitial liquid could be produced by fractionation alone, but this does not explain its low Cl and resultant high F/Cl. Those characteristics require Cl loss by a boiling event.

Coupled with field observations, these data suggest a vapor exsolution event that approximately coincided with the separation of the monzosyenite magma from the crystalline framework of the cooling sill. Many BSS monzosyenite samples contain miarolitic cavities and pegmatitic textures, both indications of crystallization in the presence of a vapor phase. Because Cl will partition strongly from a silicate melt into a vapor phase (Kilinc and Burnham, 1972) it would be partially depleted in the melt and mineral phases during a boiling event. For example, Boudreau and Simon (2007) documented apatite Cl depletion across a gabbronorite-pegmatite border in the Basement Sill, Antarctica.

When crystallization/solidification fronts in sills rupture and tear they fill with liberated buoyant interstitial melt (Marsh, 1996; Carman, 1994). Fluid exsolution aids this process by: (1) boiling events cause volume expansion which can trigger gravitational instabilities and rifting in the upper solidification front (Marsh, 1992), and (2) boiling events can lead to localized voids by the coalescence of bubbles, which may then fill with migrating liquid (Carman, 1994).

Biotite F and Cl compositions (Figure 4-6) support this interpretation, though the patterns are less clear. There are no biotite analyses from monzosyenite, but the highest F and F/Cl compositions are from the CZ monzogabbros and the very highest is from the lowermost CZ sample BS05-19 mentioned above as having the most crystallized interstitial liquid – reflecting F-enrichment from differentiation and Cl-depletion from boiling. Biotite is more prone to reequilibrate during later hydrothermal events than apatite (Boudreau et al., 1995) and biotite

halogen compositions are more dependent on temperature and composition than are those for apatite (Zhu and Sverjensky 1991 and 1992), potentially complicating patterns.

Biotite and fluid chemistry variation with temperature

Assuming apatite-biotite temperatures calculated in BSS are to be trusted (and it is possible that some may be faulty due to disequilibrium), they can provide insight into the halogen-temperature history of BSS. Calculated temperatures in BSS range from 1093 ± 103° C in the biotite-apatite pairs from multiple inclusions in Ti-magnetite in CZ monzogabbro sample BS05-19 to 600 ± 45° C in LBZ monzogabbro sample BS04-10 (Table 4-4). As discussed above, some of these temperatures may represent magmatic temperatures during cooling and some may record subsolidus hydrothermal activity. The underpinning of mineral thermometers is that they record temperatures at equilibrium, and in the case of the apatite-biotite thermometer of Zhu and Sverjensky (1992) the equilibrium is of volatile compositions of apatite and volatile and octahedral compositions of biotite. Biotite halogen composition is more temperature-dependent than apatite's, and apatite will reflect fluid composition better (Zhu and Sverjensky, 1991 and 1992).

Figure 4-7 shows apatite $\log(X_F/X_{OH})$, $\log(X_{Cl}/X_{OH})$, and $\log(X_F/X_{Cl})$ plotted against temperature. None of the plots shows a definitive correlation. The highest temperatures are from the inclusions in Ti-magnetite in sample BS05-19, though two of those overlap within error with other sample. The highest F/OH samples are the CZ monzogabbros and one anomalous LBZ sample from the bottom of the sill (see Figure 4-6). The relatively low F/Cl of all LBZ apatites suggests that devolatilization had not yet occurred when they equilibrated and cooled below the solidus of the interstitial melt.

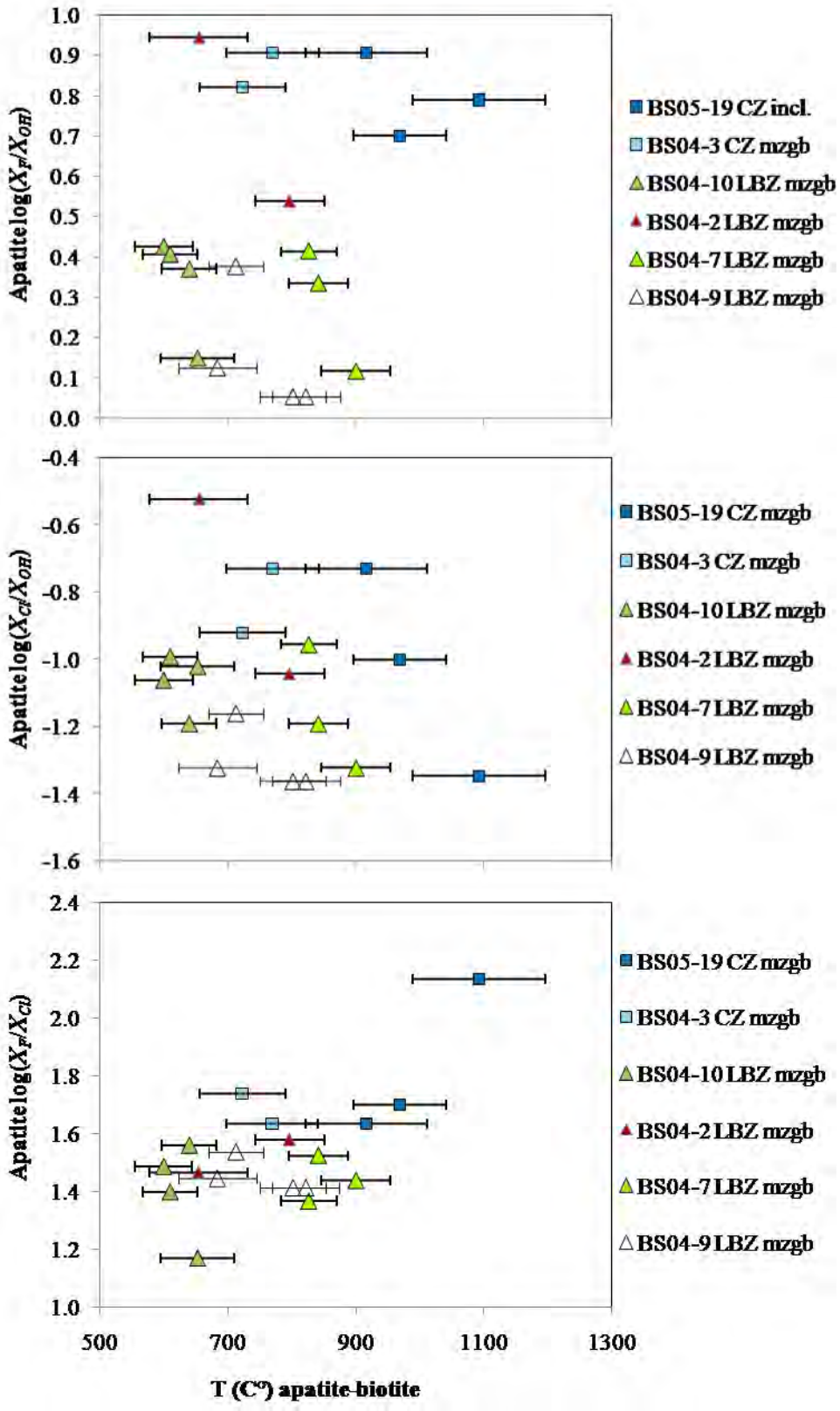

Figure 4-7. Bones Spring Sill apatite log(X_F/X_{OH}), log(X_{Cl}/X_{OH}), and log(X_F/X_{Cl}) plotted against temperatures calculated by apatite-biotite thermometry.

The halogen-temperature signatures of two individual apatites warrant mention (Figure 4-7). (1) One of the apatites from LBZ sample BS04-2 has the highest F/OH and the highest Cl/OH but its F/Cl plots with all other LBZ samples. This is from the lowest sample (aside from the thin margin) in the sill and records a near-solidus or subsolidus temperature, as do many others in the LBZ. Assuming the halogen compositions are not in error, this apatite may record an early dry (low OH) magma.

(2) The highest temperature apatite (from CS05-19) has high F/OH, among the lowest Cl/OH, and by far the highest F/Cl. This is the signature of high F from differentiation and low Cl from devolatilization, suggesting that the devolatilization event and the migration of monzosyenite occurred above 1093 ± 103° C. It is not clear why other apatites included in the same mineral equilibrated at higher Cl with signatures similar to CZ monzogabbro from BS04-3, which are not included in armoring grains. Perhaps the other inclusions were open to the surrounding magma longer during Ti-magnetite crystallization.

Figure 4-8 shows biotite halogen-temperature systematics. Because octahedral cation contents are influenced by temperature and in turn influence biotite halogen contents, comparing biotite F or Cl weight percents or mole fractions alone across temperature can be misleading. The parameters $\log(X_F/X_{OH})/X_{Fe}$, $\log(X_{Cl}/X_{OH})/X_{Mg}$, and $\log(X_F/X_{Cl})/X_{Fe}$ calculated after Zhu and Sverjensky (1992) account for the effects of biotite crystal chemistry and provide a measure of halogen enrichment unbiased by biotite octahedral compositional changes with differentiation.

As stated above, biotite halogen compositions are more strongly affected by temperature than are those of apatite, so some correlations between biotite F/OH and temperature are expected. Figure 4-8 shows that the biotites that record the highest temperatures (from the BS05-19 Ti-magnetite-hosted inclusions) have the highest $\log(X_F/X_{OH})/X_{Fe}$ and among the highest

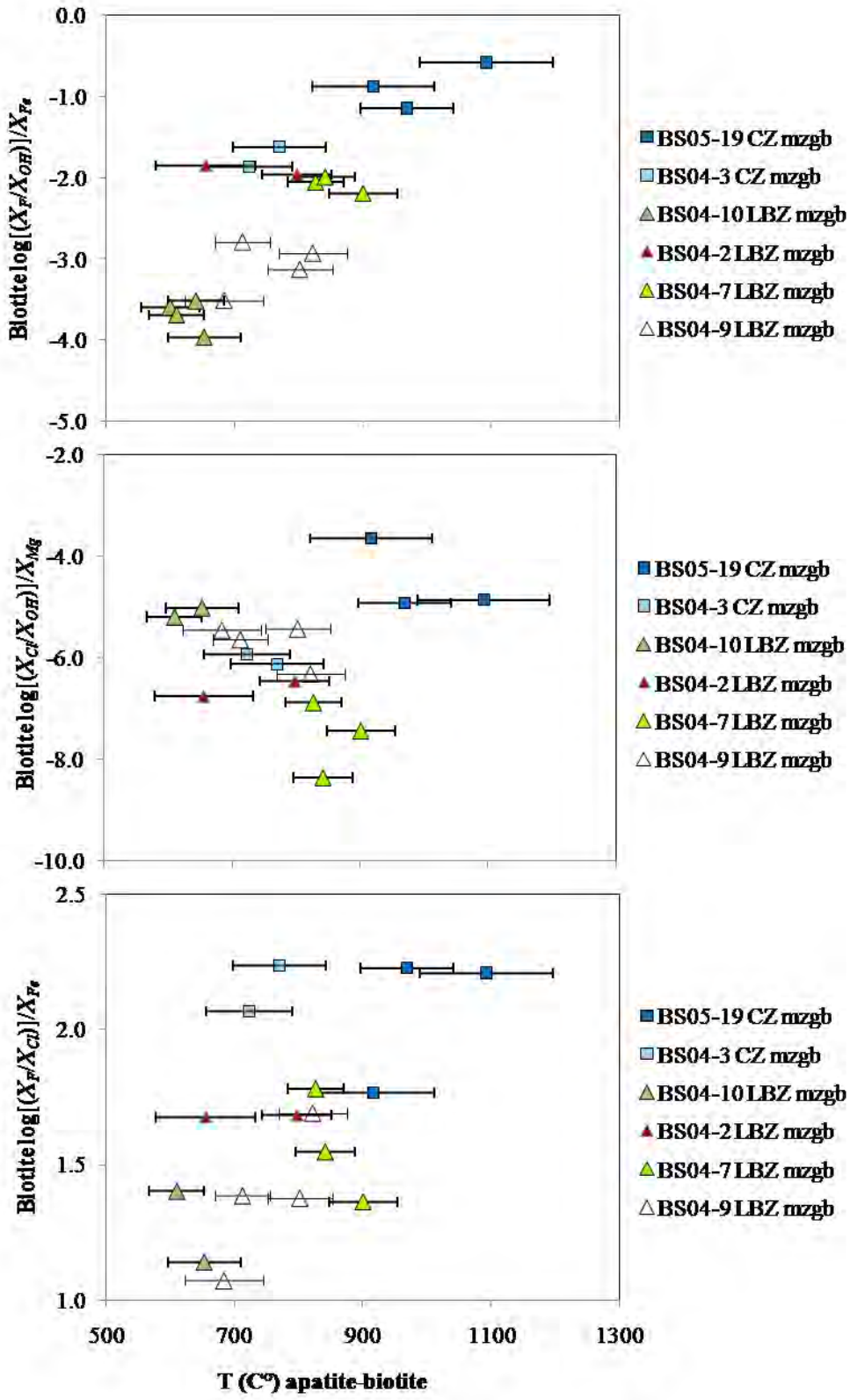

Figure 4-8. Bone Springs Sill biotite $\log(X_F/X_{OH})/X_{Fe}$, $\log(X_{Cl}/X_{OH})/X_{Mg}$, and $\log(X_F/X_{Cl})/X_{Fe}$ plotted against temperatures calculated by apatite-biotite thermometry.

$\log(X_{Cl}/X_{OH})/X_{Mg}$ and $\log(X_F/X_{Cl})/X_{Fe}$. The high $\log(X_{Cl}/X_{OH})/X_{Mg}$ of the grain that records the highest temperature is in contrast to the adjoining apatite with among the lowest Cl/OH (Figure 4-8). Both biotite and apatite are Cl-poor in BSS, but biotite X_{Cl} is 1-2 orders of magnitude lower than apatite X_{Cl}. The high-temperature biotite grains from the inclusions contain only X_{Cl} of 0.001-0.005 (Table 4-4), but their F contents are an order of magnitude higher than other BSS biotites measured for thermometry (Table 4-4), resulting in a corresponding drop in X_{OH}. Thus the anomaly is a result of high F. Aside from that, $\log(X_F/X_{OH})/X_{Fe}$ is positively correlated and $\log(X_{Cl}/X_{OH})/X_{Mg}$ is negatively correlated to temperature. This is largely an issue of covariance, as biotite incorporates more F at higher temperatures (e.g., Dooley and Patiño Douce, 1996). The anti-correlation of $\log(X_{Cl}/X_{OH})/X_{Mg}$ with temperature is again due to a reduction of X_{OH} with increasing X_F.

Bone Springs Sill apatite halogen contents in comparison to other intrusions

The importance of fluorine in the petrogenesis and differentiation of Trans-Pecos magmatic rocks has often been suggested. White et al. (2006) invoked fluorine-fluxed melting of lower crust in the generation of Pine Canyon magmas in Big Bend National Park. They based this on the presence of F-rich biotite and the decoupling of expected trace element patterns involving the F-complexed elements Rb and Zr. Zirconium in particular is considered to be immobile except in the presence of fluoride (Humphris and Thompson, 1978). Carman (1994) and Cameron et al. (1986) documented hydrothermal redistribution of Zr in TPMP alkaline mafic and felsic rocks, and noted that many of the microsyenites have associated fluorite deposits. Carman et al. (1975) and Carman (1994) noted the presence of early fluorapatite and F-rich biotite and late F-rich amphibole in most intermediate to mafic shallow intrusions in the southern

TPMP. (Bone Springs Sill is one of those examined.) The source of this F is probably the parental mafic alkaline magmas, as it is in the adjacent Rio Grande rift (Lueth et al., 2005).

Compared to large mafic nonalkaline layered intrusions like Stillwater, Montana, U.S.A., Bushveld, R.S.A., the Great Dyke, Zimbabwe, and Muni Muni, Australia, apatites from the Big Bend mafic alkaline sills are consistently F-rich and Cl-poor. Figure 4-9 shows data from these intrusions and from Bones Springs and Rattlesnake Mountain Sills (RMS). The Stillwater and Bushveld data plotted are from the lower zones that have resorbed exsolved Cl-rich fluids (Boudreau and McCallum, 1989; Willmore et al., 2000) and they represent only parts of those intrusions. The data from the Great Dyke and the Muni Muni complex contain F-rich apatite but also compositions that are 20 to >30 mole% chlorapatite. Apatites from TPMP rocks have so little Cl they plot almost on the F-OH line in Figure 4-9. These distributions are partially due to the F-rich nature of alkaline magmas, but the more striking characteristic of the TPMP rocks is their deficiency in Cl.

One possible contributing factor in to the low Cl in TPMP apatite may be Cl loss to devolatilization, and perhaps the size of the layered mafic complexes may be such that Cl resorbs elsewhere in the intrusion rather than escaping. However, at least some large alkaline layered intrusions like Ilímaussaq (>1700 m exposed thickness and >850 km^2 aerial extent) in Greenland also contain low Cl apatite. Figure 4-10 shows a plot of F-Cl apfu compositions of apatites from alkaline intrusions and the tephrite lava flow on BSS. The highest Cl contents are <0.13 apfu, and these would all plot together on a F-Cl-OH ternary diagram like that of Figure 4-9. Shonkin Sag, BSS, and RMS are all internally differentiated mafic to intermediate alkaline intrusions. The Ilímaussaq complex samples are highly differentiated agpaitic nepheline syenites which, other than augite syenite, fall under the somewhat cryptic taxonomy of the agapaitic rocks: pulaskite,

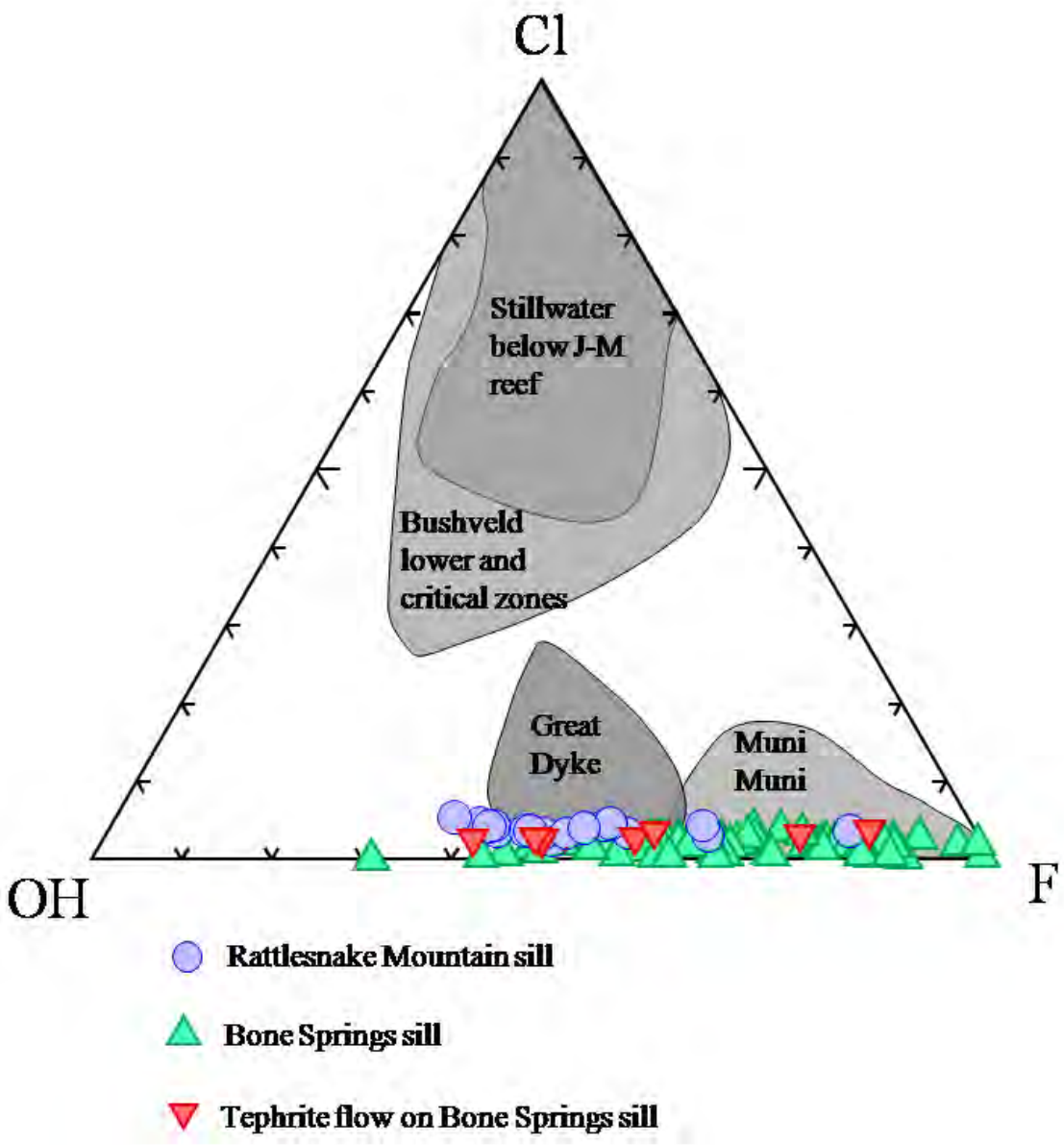

Figure 4-9 Ternary diagram of apatite F-Cl-OH components from Trans-Pecos rocks and layered mafic intrusions. Data for layered intrusions compiled by Boudσreau (1995). The Stillwater and Bushveld data only include apatites from lower levels of the intrusions that are interpreted to have resorbed exsolved Cl-rich fluids – other zones of both intrusions include more F-rich apatite. Apatites from TPMP rocks are markedly Cl-poor in comparison. Rattlesnake Mountain sill analyses can be found in the appendices.

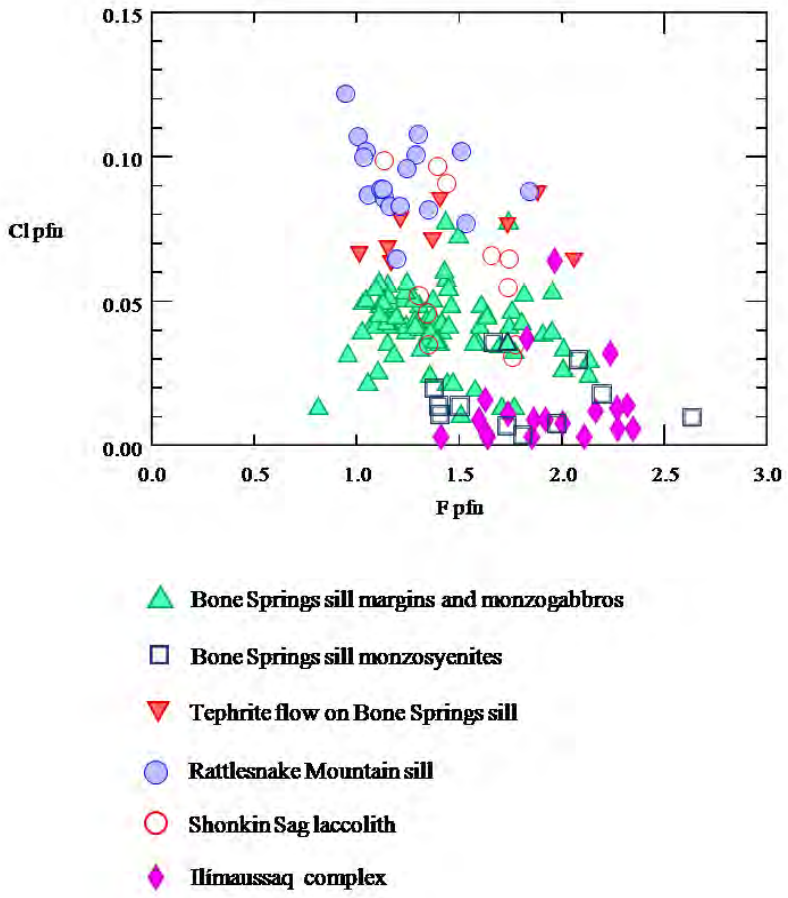

Figure 4-10. Apatite F and Cl (apfu) from Big Bend and other alkaline intrusions and flows. Atoms are calculated to 26 anions. Rattlesnake Mountain sill apatites shown span from the analcime mugearite chilled margin to analcime monzodiorites. Shonkin Sag analyses range from the shonkinite chilled margin to nepheline syenite segregations (Nash, 1972). Ilímaussaq analyses are from highly differentiated syenites (Rønsbo, 1989). Data from Bones Springs and Rattlesnake Mountain sills and the tephrite flow are from this study (see appendices for entire dataset.)

foyaite, sodalite foyaite, naujaite, kakortokite, and lujarvite (Rønsbo, 1989). The intruding magma of Shonkin Sag was shonkinitic (for which the intrusion is the type locality) and it differentiated to nepheline syenites, some pegmatitic (Nash, 1972). Apatites from the range of Shonkin Sag lithologies are presented in Figure 4-10 and they show about the same Cl variation as the BSS apatites do, displaced to slightly higher Cl values. Otherwise, there is surprisingly little overlap between RMS monzodiorites (of mugearitic/benmoritic composition), the tephrite flow on BSS, BSS monzogabbros, and the felsic rocks of BSS and Ilímaussaq, which plot together. The minute differences in apatite Cl that divide these sample groups raise the question as to whether these patterns are governed by the halogen budget of the intruding magmas or by concentration and/or loss during differentiation and vapor exsolution. What drives and preserves these signatures? The small but definitive differences between intrusions evident in Figure 4-10 also raise the possibility of using careful Cl analyses of apatite in provenance studies. It appears that a few quality apatite Cl analyses of a TPMP igneous rock could allow for identification of its source. If this were consistently true for volcanic deposits, for instance, it would be a useful tool in determining stratigraphy and in structural reconstructions. As more apatite analyses are gathered and published from TPMP and from elsewhere, this may prove possible.

Conclusions

Apatite and biotite halogen systematics in BSS constrain the behavior of F and Cl in the melt and hydrothermal fluids. The BSS magma was rich in F and H_2O upon intrusion, which is common for TPMP magmas (Carman, 1994) and for alkaline magmas from other provinces (Carroll and Webster, 1994). The F contents of apatite increase with differentiation and, coupled with Cl loss by vapor exsolution, the F/Cl increases by an order of magnitude between the chilled margin rocks and the most evolved monzosyenites. The same pattern is true for biotite

but is less pronounced. This correlation of differentiation with F/Cl in apatite is borne out by the compositions of apatites from the Ilímaussaq complex and from the Shonkin Sag laccolith, though compositions in apatites from the latter never reach the F/Cl of BSS monzosyenites or Ilímaussaq rocks.

The apatite-biotite thermometry complements the information gleaned from the halogen systematics, especially in conjunction with fractional crystallization modeling explained in Chapter 3. The discovery of the apatite-biotite pair enclosed in a Ti-magnetite grain in the BSS CZ was fortuitous. This inclusion is interpreted to record conditions at the calculated temperature of 1093° ± 103° C because it was isolated from later interaction with the melt or with hydrothermal fluid. The high F and high F/Cl of the apatite and biotite in this inclusion indicate that the inclusion was closed to the melt after differentiation and devolatilization, and thus the calculated temperature constrains the boiling event to have occurred >990° C.

CHAPTER 5

CONCLUSIONS

Rattlesnake Mountain Sill piston-cylinder experiments

Phase equilibria and RMS differentiation

The geochemistry of RMS samples provides some clues as to the magma's source and pre-intrusion differentiation. The chondrite-normalized REE pattern is depleted in HREE which is characteristic of melting in the garnet-lherzolite region of the mantle, and the isotopic data (Cameron et al., 1986) suggest an OIB-type mantle source with little or no contamination from continental crust. The low *Mg'* and Ni indicate that the RMS magma experienced olivine fractionation prior to emplacement, while the lack of a Eu anomaly relative to chondrite or mantle composition suggests that the magma did not fractionate significant amounts of plagioclase.

The RMS chill zone contains microphenocrysts of olivine and plagioclase (Carman et al., 1975). The presence of plagioclase coupled with the geochemical evidence discounting plagioclase fractionation indicates that it began crystallizing shortly before or during intrusion.

Phase equilibria determined by piston cylinder experiments do not include olivine, though several of the experiments overlap with the olivine-stability field found by Irving and Green's (2008) work for the more mafic ne-mugearite. It is possible that olivine would have appeared in my experiments had I been more successful in placing experiments directly on the liquidus, but it is more likely that RM02-17 is too evolved to crystallize olivine at high pressure

(>8 kb) and crystallizes clinopyroxene, amphibole, or biotite instead. Thus, it is unlikely that RMS was in equilibrium with a lower crustal or mantle assemblage during fractionation. It probably fractionated at mid-crustal depths or shallower. This concurs with the regional evidence from the TPMP, where most rocks have fractionated olivine (James and Henry, 1991) and few rocks contain mantle xenoliths (Barker, 1987, and 2000) – conditions that suggest a density and/or magma "plumbing" regime where melts are residing and differentiating in the crust.

Melt compositions

In addition to the expected ne-trachyte and one ne-phonolite compositions, this study finds that Q-normative compositions can be reached by high-pressure fractionation of mildly ne-normative compositions. These melts are mildly peralkaline or metaluminous Q-trachytes and a weakly peraluminous rhyolite. It has been demonstrated that the fractionation of silica-poor calcic amphibole can drive liquids across the thermal divide from silica-unsaturated to silica-saturated compositions (Giret et al., 1980; Martin, 2007), though it is controversial how often or even whether this occurs in natural rocks. My experiments show that it is possible to reach silica-saturation from under-saturated compositions with biotite rather than amphibole fractionation as the primary agent. The most felsic and silica-saturated melts are from 20 kb experiments that crystallize both Na-rich biotite and amphibole – both with a low Si/(Na+K). To the knowledge of the author, Na-rich biotite has not been reported in alkaline igneous rocks or high-pressure xenoliths, which suggests that this mechanism is not common. Though the melt compositions found in this study correspond to some of the range found in the TPMP, the simpler scenario relies on the presence of both Q-normative and ne-normative parental magmas in TPMP petrogenesis.

Mineral compositions

The following observations can be made concerning the experimental mineral compositions:

(1) The very high Ti in experimental biotites results primarily from Ti-Tschermak's substitution ($^{VI}Ti^{4+} + 2^{IV}Al^{3+} = 2^{IV}Si^{4+} + {}^{VI}[Fe,Mg]^{2+}$), while the Ti-oxy substitution ($^{VI}Ti^{4+} + 2O^{2-} = {}^{VI}(Fe,Mg)^{2+} + 2[OH]^{-}$) plays a lesser role.

(2) Amphibole Si/Na (and Si/[Na+K]) decreases with increased H_2O in every experiment save one at 15 kb, where all compositions have very similar Si/(Na+K). The pargasite, ferro-pargasite, and magnesio-taramite amphiboles (i.e., those with <42% SiO_2) have a negative correlation between Si/Na and pressure (r = -0.74).

(3) The exsolution of vapor stabilizes apatite in two 15 kb runs; both runs have higher melt CaO than any other apatite-bearing run products (attributable to large melt fraction and near liquidus conditions), and one has apatite + vapor where apatite is absent at the same pressure and temperature but with lower added H_2O.

(4) At all measured conditions, amphibole and biotite are depleted in Cl relative to the melt.

(5) In all experiments with coexisting biotite and amphibole, biotite is enriched in TiO_2 relative to the amphibole ($K_d^{am\text{-}bt}$ <1) regardless of the type of amphibole.

Bone Springs Sill

Crystallization and F-Cl systematics

Monzosyenite liquid in BSS was generated by ~50% crystallization of subequal clinopyroxene + plagioclase, lesser Fe-Ti oxide + olivine, and minor biotite + apatite + nepheline. Most of the monzosyenite liquid crystallized as the interstices of the monzogabbro, but, after rupturing of the crystalline framework probably coincident with vapor exsolution, some

liquid segregated into discrete monzosyenite bodies in the upper third of the sill. The most felsic monzosyenites in BSS were generated by an additional ~8% fractionation of alkali feldspar, amphibole, and nepheline (or analcime) with minor apatite and titanohematite. Calculations based on modes from fractional crystallization modeling, estimates of rock proportions in the field, and calculations of the crystallized liquid fractions based on Mg/Fe compositions suggest that all liquid in BSS is accounted for, i.e., there was no associated volcanism or further intrusion up-section.

Apatite and biotite F and Cl compositions in BSS show progressive crystallization from the margins of sill, indicated by increasing Cl and decreasing F/Cl. This pattern changes with the migration of monzosyenite with high F/Cl as a result of F increase with differentiation and Cl loss to vapor exsolution. The monzosyenite migrates to the top 1/3rd of the sill and segregates into discrete bodies. This is probably related to the exsolution of a volatile phase during which fluid volume expansion ruptured the crystalline framework and allowed migration of the differentiated interstitial liquid.

An apatite-biotite mineral pair included in Ti-magnetite from the upper 1/3rd of Bone Springs Sill records the highest calculated temperature of 1093° ± 103° C. These minerals have high F and low Cl, suggesting that their inclusion postdates devolatilization and segregation of the residual liquid. Thus, a minimum temperature of 990° C constrains the conditions of (1) 50% crystallization required for differentiation to monzosyenite, (2) devolatilization and (3) monzosyenite migration.

Chemical substitution in apatite

Apatites from the least differentiated magmas in the BSS – the lower margin and UBZ tephrites and the tephrite lava flow – are unusually Si- and Al-enriched at the expense of Ca and

P. This indicates a $Si^{4+}+Al^{3+} = Ca^{2+}+P^{5+}$ substitution. These phosphate minerals exhibit a wide range of SiO_2 contents from 1.6 to 39.65 wt.% and Al_2O_3 up to 13.9 wt.%. To the knowledge of the author, this is a substitution mechanism not previously reported in alkaline rocks.

Comparison of F and Cl between select igneous rocks

Compared to large mafic nonalkaline layered intrusions like Stillwater, Montana, U.S.A., Bushveld, R.S.A., the Great Dyke, Zimbabwe, and Muni Muni, Australia, apatites from the Big Bend mafic alkaline BSS and RMS are F-rich and Cl-deficient. The Ilímaussaq and Shonkin Sag alkaline intrusions have similar F and Cl contents to BSS and RMS. However, each of these alkaline igneous intrusions have a distinct range signatures in the Cl contents that overlap little with one another.

REFERENCES

Abrecht, J., and Hewitt, D.A., 1988, Experimental evidence on the substitution of Ti in biotite, *American Mineralogist,* v. 73, pp. 1275-1284.

Adam, J., and Green, T., 2006, Trace element portioning between mica- and amphibole-bearing garnet lherzolite and hydrous basinitic melt: 1. Experimental results and investigation of controls on partitioning behavior, *Contributions to Mineralogy and Petrology*, v. 152, pp. 1-17.

Andersen, D.J. and Lindsley, D.H., 1988, Internally consistent solution models for Fe-Mg-Mn-Ti oxides: Fe-Ti oxides, *American Mineralogist,* v. 73, pp. 714-726.

Ayati, F., Yavuz, F., Nogbreyan, M., Haroni, H.A., and Yavuz, R., 2008, Chemical characteristics and composition of hydrothermal biotite from the Dalli porphyry copper prospect, Arak, central province of Iran, *Mineralogy and Petrology*, v. 94, pp. 107-122.

Bacon, C.R., 1989, Crystallization of accessory phases in magmas by local saturation adjacent to phenocrysts, *Geochimica et Cosmochimica Acta*, v. 53, pp. 1055-1066.

Bacon, C.R. and Hirschmann, M.M., 1988, Mg/Mn partitioning as a test for eqilibrium between coexisting Fe-Ti oxides, *American Mineralogist*, v. 73, pp. 57-61.

Bailey, J.C., 1977, Fluorine in granitic rocks and melts: A review, *Chemical Geology*, v. 19, pp. 19-42.

Banno, Y., Miyawaki, R., Kogure, T., Matsubara, S., Kamiya, T., and Yamada, S., 2005, Aspidolite, the Na analogue of phlogopite, from Kasuga-mura, Gifu Prefecture, central Japan: description and structural data, *Mineralogical Magazine*, v. 69, no. 5, pp. 1047-1057.

Barker, D.S., 1976, Phase relationships in the system $NaAlSiO_4$—SiO_2—NaCl—H_2O at 400°-800° C and 1 kilobar, and petrologic implications, *Journal of Geology*, v. 84, pp. 97-106.

Barker, D.S., 1977, Northern Trans-Pecos magmatic province: Introduction and comparison with the Kenyan rift, *Geological Society of America Bulletin*, v. 88, pp. 1421-1427.

Barker, D.S., 1979, Cenozoic magmatism in the Trans-Pecos province: Relation to the Rio Grande rift, in Rio Grande Rift: Tectonics and Magmatism, ed. by R.E. Riecker, American Geophysical Institute, Washington, D.C., pp. 382-392.

Barker, D.S., 1987, Tertiary alkaline magmatism in Trans-Pecos Texas, in Alkaline Igneous Rocks, ed. by J.G. Fritton and B.G.J. Upton, Geological Society Special Publication, No. 30, pp. 415-431.

Barker, D.S., 2000, Emplacement of a xenoliths-rich sill, Lajitas, Texas, *Journal of Volcanology and Geothermal Research*, v. 104, pp. 153-168.

Barker, D.S. and Hodges, F.N., 1977, Mineralogy of intrusions in the Diablo Plateau, northern Trans-Pecos magmatic province, Texas and New Mexico, *Geological Society of America Bulletin*, v. 88, pp. 1437-1446.

Barker, D.S., Long, L.W., Hoops, G.K., and Hodges, F.N., 1977, Petrology and Rb-Sr isotope geochemistry of intrusions in the Diablo Plateau, northern Trans-Pecos magmatic province, Texas and New Mexico, *Geological Society of America Bulletin*, v. 88, pp. 1447-14461.

Barnes, S.-J., 1986, The effect of trapped liquid crystallization on cumus mineral compositions in layered intrusions, *Contributions to Mineralogy and Petrology*, v. 101, pp. 447-457.

Befus, K.S., Hanson, R.E., Miggins, D.P., Breyer, J.A., and Busbey, A.B., 2009, Nonexplosive and explosive magma/wet-sediment interaction during emplacement of Eocene intrusions into Cretaceous to Eocene strat, Trans-Pecos igneous province, West Texas, *Journal of Volcanology and Geothermal Research*, v. 181, pp. 155-172.

Bence, A.E. and Albee, A.L., 1968, Empirical correction factors for the electron microanalysis of silicates and oxides, *Journal of Geology*, v. 76, pp. 382-403.

Berman, R.G., 1988, Internally consistent thermodynamic data for minerals in the system Na_2O-CaO-MgO-FeO-Fe_2O_3-Al_2O_3-SiO_2-TiO_2-H_2O-CO_2: Representation, estimation and high temperature extrapolation, *Journal of Petrology*, v. 29, pp. 445-522.

Best, M.G., and Christiansen, E.H., 1991, Limited extension during peak Tertiary volcanism, Great Basin of Nevada and Utah, *Journal of Geophysical Research*, v. 96:B8, pp. 13,509-13,528.

Binns, R.A., Duggan, M.B., and Wilkinson, J.F.G., 1970, High pressure megacrysts in alkaline lavas from northeastern new South Wales, *American Journal of Science*, v. 269, pp. 132-168.

Boudreau, A.E., 1995, Formation of chlor- and fluor-apatite in layered intrusions: A comment, *Mineralogical Magazine*, v. 59, pp. 757-760.

Boudreau, A.E., and McCallum, I.S., 1989, Investigations of the Stillwater Complex: Part V. Apatites as indicators of evolving fluid compositions, *Contributions to Mineralogy and Petrology*, v. 102, pp. 138-153.

Boudreau, A.E., Love, C., and Prendergrast, M.D., 1995, Halogen geochemistry of the Great Dyke, Zimbabwe, *Contributions to Mineralogy and Petrology*, v. 122, pp. 289-300.

Boudreau, A., and Simon, A., 2007, Crystallization and degassing in the Basement Sill, McMurdo Dry Valleys, Antarctica, *Journal of Petrology*, v. 48, pp. 1369-1386.

Boudreau, A.E., Love, C., and Prendergast, M.D., 1995, Halogen Geochemistry of the Great Dyke, Zimbabwe, *Contributions to Mineralogy and Petrology*, v. 122, pp. 289-300.

Bowen, N.L., 1915, Crystallization differentiation in silicate liquids, *American Journal of Science*, v. 39, pp. 175-191.

Bowen, N.L., 1937, Recent high-temperature research on silicates and its significance in igneous petrology, *American Journal of Science*, v. 33, pp. 397-411.

Bowen, N.L. and Schairer, J.F., 1935, The system MgO-FeO-SiO_2, *American Journal of Science*, v. 29, pp. 151-217.

Boyce, Jeremy W., and Hervig, Richard L., 2008, Magmatic degassing histories from apatite volatile stratigraphy, *Geology*, v. 36, no. 1, pp. 63-66.

Brenan, James, 1994, Kinetics of fluorine, chlorine and hydroxyl exchange in fluoroapatite, *Chemical Geology*, v. 110, pp. 195-210.

Bryan, W.B., finger, L.W., and Chayes, F., 1969, Estimating proportions in petrographic mixing equations by least-squares approximation, *Science*, v. 168, no. 3870, pp. 926-927.

Candela, P.A., 1986, Toward a thermodynamic model for the halogens in magmatic systems: an application to melt-vapor-apatite equilibria, *Chemical Geology*, v. 57, pp. 289-301.

Cameron, M., Cameron, K.L. Carman, M.F., Jr., 1986, Alkaline rocks in the Terlingua-Big Bend area of Trans-Pecos Texas, Guidebook 23, Bureau of Economic Geology, University of Texas at Austin, pp. 123-142.

Carman, M.F., Jr., Cameron, M., Gunn, B., Cameron, K.L., and Butler, J.C., 1975, Petrology of The Rattlesnake Mountain Sill, Big Bend National Park, Texas, *Geological Society of America Bulletin*, v. 86, pp.177-193.

Carman, M.F., Jr., 1994, Mechanisms of differentiation in shallow mafic alkaline intrusions, as illustrated in the Big Bend area, western Texas, *Journal of Volcanology and Geothermal Research*, v. 61, pp. 1-44.

Carmichael, I.S.E., 1967a, The iron-titanium oxides of salic volcanic rocks and their associated ferromagnesian silicates, *Contributions to Mineralogy and Petrology*, v. 14, pp. 36-64.

Carmichael, I.S.E., 1967b, The mineralogy and petrology of the volcanic rocks from the Leucite Hills, Wyoming, *Contributions to Mineralogy and Petrology*, v. 15, pp. 24-66.

Carroll, M.R. and Webster, J.D., 1994, Solubilities of sulfur, noble gases, nitrogen, chlorine, and fluorine in magmas, in *Volatiles in Magmas, Reviews in Mineralogy, v. 30,* ed. by M.R. Carroll and J.R. Holloway, Mineralogical Society of America, Washington D.C., pp. 231-280.

Cawthorn, R.G., 1994, Formation of chlor- and fluor-apatite in layered intrusions, *Mineralogical Magazine*, v. 58, pp. 299-306.

Costa, F., Dungan, M.A., and Singer, B.S., 2001, Magmatic Na-rich phlogopite in a suite of gabbroic crustal xenoliths from Volcán San Pedro, Chilean Andes: Evidence for a solvus relation between phlogopite and aspidolite, *American Mineralogist*, v. 86, pp. 29-35.

Deer, W.A., Howie, R.A., and Zussman, J., 1996, An Introduction to the Rock-Forming Minerals, 2nd edition, Prentice Hall, 712 p.

Dooley, D.F., and Patiño Douce, A.E., 1996, Fluid-absent melting of F-rich phlogopite + rutile + quartz, *Amrican Mineralogist*, v. 81, pp. 202-212.

Dorais, M.J. and MacRae, N.D., 1994, Amphibole zoning in the Garland Peak syenite, Red Hill complex, New Hampshire: camptonitic parental magmas and differentiation to silica-oversaturated syenites, *Contributions to Mineralogy and Petrology*, v. 117, pp. 76-86.

Droop, G.T.R., 1987, A general equation for estimating Fe^{3+} in ferromagnesian silicates and oxides from microprobe analysis, using stoichiometric criteria, *Mineralogical Magazine*, v. 51, pp. 431-437.

Dymek, R.F., 1983, Titanium, aluminum and interlayer cation substitutions in biotite from high-grade gneisses, West Greenland, *American Mineralogist*, v. 68, pp. 880-899.

Edgar, A.D., 1974, Chapter V.1. Experimental Studies, in The Alkaline Rocks, ed. by H. Sørensen, John Wiley and Sons, Letchworth, U.K., pp. 355-388.

Edgar, A.D., 1987, The genesis of alkaline magmas with emphasis on their source regions: inferences from experimental studies, in Alkaline Igneous Rocks, ed. by J.G. Fritton and B.G.J. Upton, Geological Society Special Publication, No. 30, pp.29-52.

Edgar, A.D., and Arima, M., 1985, Fluorine and chlorine contents of phlogopites crystallized from ultrapotassic rock compositions in high pressure experiments: implications for halogen reservoirs in source regions, *American Mineralogist*, v. 70, pp. 529-536.

Evans, B.E., 2007, The synthesis and stability of some end-member amphiboles, *Reviews in Mineralogy and Geochemistry*, v. 67, pp. 261-286.

Evans, S.H., Jr., and Nash, W.P., 1979, Petrogenesis of xenolith-bearing basalts from southeastern Arizona, *American Mineralogist*, v. 64, pp. 249-267.

Ewart, A., and Griffin, W.L., 1994, Application of proton-microprobe data to trace-element partitioning in volcanic rocks, *Chemical Geology*, v. 117, pp. 251-284.

Fialin, M. and Chopin, C., 2006, Electron-beam (5-10 keV) damage in triplite-group phosphates: Consequences for electron-microprobe analysis of fluorine, *American Mineralogist*, v. 91, pp. 503-510.

Foley, S.F., 1989, Experimental constraints on phlogopite chemistry in lamproites: 1. The effect of water activity and oxygen fugacity, *European Journal of Mineralogy*, v. 1, p. 411-426.

Fujimaki, H., 1986, Partition-coefficients of Hf, Zr, and REE between zircon, apatite, and liquid, *Contributions to Mineralogy and Petrology*, v.94, no. 1, pp. 42-45.

Giret, A., Bonin, B., and Leger, J-M., 1980, Amphibole compositional trends in oversaturated and undersaturated alkaline plutonic ring complexes, *Canadian Mineralogist, v. 18, pp. 481-495.*

Green, T.H. and Pearson, N.J., 1987, An experimental study of Nb and Ta partitioning between Ti-rich minerals and silicate liquids at high pressure and temperature, *Geochimica et Cosmochimica Acta*, v. 51, pp. 55-62.

Griffin, W.L., Åmli, R., and Heier, K.S., 1972, Whitlockite and apatite from lunar rock 14310 and from Ödergården, Norway, *Earth and Planetary Science Letters*, v. 15, pp. 53-58.mm

Gupta, A.K. and Fype, W.S., 1975, Leucite survival: The alteration to analcime, *Canadian Mineralogist*, v. 13 pp. 361-363.

Hamilton, D.L. and Mackenzie, W.S., 1965, Phase-equilibrium studies in the system $NaAlSiO_4$ (nepheline)–$KalSiO_4$ (kalsilite)–SiO_2–H_2O, *Mineralogical Magazine*, v. 34, no. 268, pp. 214-231.

Hanson, G.K., 1980, Rare earth elements in petrogenetic studies of igneous systems, *Annual Review of Earth and Planetary Sciences*, v. 8, pp. 371-406.

Harkins, E., and Hollister, L.S., 1977, Sector zoning of clinopyroxenes from a weakly metamorphosed diabase, *American Mineralogist*, v. 62, p. 390-394.

Harlov, D.E., Förster, H.-J., and Nijland, T.G., 2002, Fluid-induced nucleation of (Y + REE)-phosphate minerals within apatite: Nature and experiment. Part I. Chlorapatite, *American Mineralogist*, v. 87, pp. 245-261.

Harrison, T.M. and Watson, E.B., 1984, The behavior of apatite during crustal anatexis: Equilibrium and kinetic considerations, *Geochiica et Cosmochimica Acta*, v. 48, pp. 1467-1477.

Henry, C.D., and McDowell, F.E., 1986, Geochronology of the mid-Tertiary volcanic field, Trans-Pecos Texas, Guidebook 23, Bureau of Economic Geology, University of Texas at Austin, pp. 99-122.

Henry, C.D., Price, J.G., and Miser, D.E., 1989, Geology and Tertiary igneous activity of the Hen Egg Mountain and Christmas Mountains Quadrangles, Big Bend region, Trans-Pecos Texas, Report of Investigations, v. 183, University of Texas at Austin, Bureau of Economic Geology, 105 p.

Henry, C.D., Price, J.G., and James, E.W., 1991, Mid-Cenozoic stress evolution and magmatism in the southern Cordillera, Texas and Mexico: Transition from continental arc to intraplate extension, *Journal of Geophysical Research*, v. 96:B8, pp. 13,545-13,560.

Hill E. and Barnes, C.G., 1987, Slickrock Mountain intrusive complex, Big Bend National Park, Texas, Geological Society of America Special Paper 215, 305-316.

Hollister, L.S., 1979, Origin, mechanism, and consequences of compositional sector-zoning in staurolite, *American Mineralogist*, v. 55, p. 742-766.

Hollister, L.S., and Garcanz, A.J., 1971, Compositional sector-zoning in clinopyroxene from the Narce area, Italy, *American Mineralogist*, v. 56, p. 959-979.

Humphris, S.E. and Thompson, G. 1978, Trace element variation mobility during hydrothermal alteration of oceanic basalts, *Geochimica et Cosmochimica Acta*, v. 42, pp. 127-136.

Irvine, T.N., and Baragar, W.R.A., 1971, A guide to the chemical classification of the common volcanic rocks, *Canadian Journal of Earth Sciences*, v. 8, pp. 523-548.

Irving, A.J., and Green, D.H., 2008, Phase Relationships of hydrous alkalic magmas at high pressures: production of mugearitic liquids by amphibole-dominated fractional crystallization within the lithospheric mantle, *Journal of Petrology*, v. 49, no. 4, 741-756.

Irving, A.J., and Price, R.C., 1981, Geochemistry and evolution of lherzolitic-bearing phonolitic lavas from Nigeria, Australia, East Germany and New Zealand, *Geochimica et Cosmochimica Acta*, v. 45, p. 1309-1320.

James, E.W., and Henry, C.D., 1991, Compositional changes in Trans-Pecos magmatism coincident with Cenozoic stress realignment, *Journal of Geophysical Research*, v. 96:B8, pp. 13,561-13,575.

James, E.W., and Henry, C.D., 1993a, Southeastern extent of the North American craton in Texas and northern Chihuahua as revealed by Pb isotopes, *Geological Society of America Bulletin*, v. 105, pp. 116-126.

James, E.W., and Henry, C.D., 1993b, Pb isotopes of ore deposits in Trans-Pecos Texas and northeastern Chihuahua, Mexico: Basement, igneous, and sedimentary sources of metals, *Economic Geology*, v. 88, pp.931-947.

Jenkins, D.M., 1983, Stability and composition relations of calcic amphiboles in ultramafic rocks, *Contributions to Mineralogy and Petrology*, v. 83, pp. 375-384.

Johnson, D.M., Hooper, P.R., and Conrey, R.M., 1999, XRF analysis of rocks and minerals for major and trace elements on a single low dilution Li-tetraborate fused bead, *Advances in X-ray Analysis*, v. 41, pp. 843-867.

Karlsson, R.H. and Clayton, R.N., 1991, Analcime phenocrysts in igneous rocks: Primary or secondary, *American Mineralogist*, v. 76, pp. 189-199.

Keith, S.B., 1978, Paleosubduction geometries inferred from Cretaceous and Tertiary magmatic patterns in southwestern north America, *Geology*, v. 6, no. 9, pp. 516-521.

Kendrick, G.C. and Edmond, C.L., 1981, Magma immiscibility in the Shonkin Sag and Square Butte Laccoliths, Geology, v. 9, pp. 615-619.

Kilinc, I.A. and Burnham, C.W., 1972, Partitioning of chloride between a silicate melt and coexisting vapor phase from 2 to 8 kb, *Economic Geology*, v. 67, pp. 231-235.

Klemme, S., 2003, Trace element partitioning between apatite and carbonatite melt, *American Mineralogist*, v. 88, pp. 639-646.

Knutson, J., and Green, T.H., 1975, Experimental duplication of a high-pressure megacryst/cumulate assemblage in a near-saturated hawaiite, *Contributions to Mineralogy and Petrology*, v. 52, pp. 121-132.

Kretz, R., 1983, Symbols for rock-forming minerals, *American Mineralogist*, v. 68, p. 277-279.

Kushiro, I., 1972, Effect of water on the composition of magmas formed at high pressures, *Journal of Petrology*, v. 13, pp. 311-334.

Lange, R.A., 1994, The effect of H_2O, CO_2, and F on the density and viscosity of silicate melts, in *Volatiles in Magmas*, *Reviews in Mineralogy*, *v. 30*, ed. by M.R. Carroll and J.R. Holloway, Mineralogical Society of America, Washington D.C., pp. 331-370.

Langmuir, C.H., 1989, Geochemical consequences of *in situ* crystallization, *Nature*, v. 340, pp. 199-205.

Larsen, L.M., 1979, Distribution of REE and other trace-elements between phenocrysts and peralkaline undersaturated magmas, exemplified by rocks from the Gardar igneous province, south Greenland, *Lithos*, v. 12, no. 4, pp. 303-315.

Latourrette, T., Hervig, R.L., and Holloway, J.R., 1995, Trace-element partitioning between amphibole, phlogopite, and basanite melt, *Earth and Planetary Science Letters*, v. 135, pp. 13-30.

Leake, B.E., Woolley, A.R., Arps, C.E.S, et al, 1997, Nomenclature of amphiboles: Report of the subcommittee on amphiboles of the International Mineralogical Association, Commission on New Minerals and Mineral Name, *Canadian Mineralogist*, v.35, p.219-246.

Le Bas, M.J., 1989, Nephelinitic and basanitic rocks, *Journal of Petrology*, v. 30, pp. 1299-1312.

Le Bas, M.J., Le Maitre, R.W., Streckeisen, A., and Zanettin, B., 1986, A chemical classification of volcanic rocks based on the total alkali-silica diagram, *Journal of Petrology*, v. 27, pp. 745-750.

Le Maitre. R.W., Streckeisen, A., Zanettin, B., Le Bas, M.J., Bonin, B., and Bateman, P., 2002, A Classification of Igneous Rocks and Glossary of Terms: Recommendations of the International Union of Geological Sciences Subcommission on the Systematics of Igneous Rocks, *ed.* by R.W. Le Maitre, Blackwell Scientific Publications, Oxford, U.K., 252 p.

Lemarchand, F., Villemant, B., and Calas, G., 1987, Trace element distribution in alkaline series, *Geochimica et Cosmoshimica Acta*, v. 51, pp. 1071-1081.

Li, Z., Tainosho, Y., Shiraishi, K., and Owada, M., 2003, Chemical characteristics of fluorine-bearing biotite of early Paleozoic plutonic rocks from he Sør Rondane mountains, East Antarctica, *Geochemical Journal*, v. 37, pp. 145-161.

Lindsley, D.H., and Spencer, K.J., 1982, Fe-Ti oxide geothermometry: Reducing analyses of coexisting Ti-magnetite (Mt) and ilmenite (Ilm), *Eos, Transactions of the American Geophysical Union*, v. 63, p. 471.

Liou, J.G., 1971, Analcime equilibria, *Lithos*, v. 4, pp. 389-402.

Lipman, P.W., and Glazner, A.F., 1991, Introduction to Middle Tertiary Cordilleran volcanism: magma sources and relations to regional tectonics, *Journal of Geophysical Research*, v. 96:B8, pp. 13,193-13,199.

Litvinosky, B.A., Jahn, B.-m., Zanvilevich, A.N., Shadaev, M.G., 2002, Crystal fractionation in the petrogenesis of an alkali monzodiorite-syenite series: The Oshurkovo plutonic sheeted complex, Transbaikalia, Russia, *Lithos*, v. 64, pp. 97-130.

Luddington, S., 1978, The biotite-apatite geothermometer revisited, *American Mineralogist*, v.63, pp. 511-553.

Lueth, V.W., Rye, R.O., and Peters, L., 2005, "Sour gas" hydrothermal jorosite: ancient to modern acid-sulfate mineralization in the southern Rio Grande Rift, *Chemical Geology*, v. 215, pp. 339-360.

Luhr, J.F., Carmichael, I.S.E. and Varekamp, J.C., 1984, The 1982 eruptions of El Chichon volcano, Chiapas, Mexico: Mineralogy and petrology of the anhydrite-bearing pumices, *Journal of Volcanology and Geothermal Research*, v. 23, pp. 69-108.

Mackenzie, D.E. and White, A.J.R., 1970, Phonolite globules in basanite from Kiandra, Australia, *Lithos*, v. 3, no. 4, pp. 309-317.

Mahood, G.A. and Stimac, J.A., 1990, Trace-element partitioning in pantellerites and trachytes, *Geochimica et Cosmochimica Acta*, v. 54, pp. 2257-2276.

Manghnani, M.H., 1970, Analcite-jadeite phase boundary, *Physics of Earth and Planetary Interiors*, v. 3, p. 456-461.

Marks, M. Halama, R., Wenzel, T., and Markl, G., 2004, Trace element variations in clinopyroxene and amphibole from alkaline to peralkaline syenites and granites: implications for mineral-melt trace-element partitioning, *Chemical Geology*, v. 211, pp. 185-215.

Marsh, B.D., 1996, Solidification fronts and magmatic evolution, *Mineralogical Magazine*, v. 60, pp. 5-40.

Marsh, B.D., 2002, On bimodal differentiation by solidification front instability in basaltic magmas, part 1: Basic mechanics, *Geochmica et Cosmochimica Acta*, v. 66, no. 12, pp. 2211-2229.

Martin, R.F., 2007, Amphiboles in the Igneous Environment, *Review in Mineralogy and Geochemistry*, v. 67, pp. 323-358.

Mathez, E.A., and Webster, J.D., 2005, Partitioning behavior of chlorine and fluorine in the system apatite-silicate melt-fluid, *Geochimica et Cosmochimica Acta*, v. 69, no. 5, pp. 1275-1286.

Matsui, Y., Onuma, N., Nagasawa, H., Higuchi, H. and Banno, S., 1977, Crystal structure control in trace element partitioning between crystal and magma, *Tectonics*, v. 100, pp. 315-324.

Maxwell, R.A., Lonsdale, J.T., Hazard, R.T., and Wilson, J.A., 1967, Geology of Big Bend National Park, Brewster County, Texas, University of Texas Bureau Economic Geology Publication 6711, 320 p.

McDonough, W.F., and Sun, S.S., 1995, The composition of the Earth, *Chemical Geology*, v. 120, pp. 223-253.

Meurer, W.P., and Natland, J.H., 2001, Apatite compositions from oceanic cumulates with implications for the evolution of mid-ocean ridge magmatic systems, *Journal of Volcanology and Geothermal Research*, v. 110, pp. 281-298.

Meurer, W.P. and Bodreau, A.E., 1998a, Compaction of igneous cumulates part I: Geochemical consequences for cumulates and liquid fractionation trends, *Journal of Geology*, v. 106, pp. 281-292.

Meurer, W.P. and Bodreau, A.E., 1998b, Compaction of igneous cumulates part II: Compaction and the development of igneous foliations, *Journal of Geology*, v. 106, pp. 293-304.

Meurer, W.P., and Meurer, M.E.S.. 2006, Using apatite to dispel the "trapped liquid" concept and to understand the loss of interstitial liquid by compaction in mafic cumulates: an example from the Stillwater Complex, Montana, *Contributions to Mineralogy and Petrology*, v. 151, pp. 187-201.

Mirante, D.C., 2003, AgOH as an H_2O delivery vector for vapor-fluxed melting experiments, *Geological Society of America, Abstracts with Programs*, v.35, n.6, p. 593.

Morimoto, N., Fabries, J., Ferguson, A.K., Ginzburg, I.V., Ross, M., Seifert, F.A., and Zussman, J., 1988, Nomenclature of pyroxenes, *Mineralogical Journal*, v. 14, no. 5, pp. 198-221.

Munoz, J.L. and Eugster, H.P., 1969, Experimental control of fluorine reactions in hydrothermal systems, *American Mineralogist*, v. 54, pp. 943-959.

Munoz, J.L., 1984, F-OH and Cl-OH exchange in micas with applications to hydrothermal ore deposits, In Mineralogical Society of America Reviews in Mineralogy, v. 13, pp. 469-493.

Munoz, J.L., 1992, Calculation of the HF and HCl fugacities from biotite compositions: revised equations, *Geological Society of America Abstracts with Programs*, v. 24, p. A221.

Mysen, B.O., 1975, Partitioning of iron and magnesium between crystals and partial melts in peridotite upper mantle, *Contributions to Mineralogy and Petrology*, v. 52, pp. 69-76.

Mysen, B.O., 1978, Experimental determination of nickel partition coefficients between liquid, pargasite and garnet peridotite minerals and concentration limits of behavior according to Henry's Law at high pressure and temperature, *American Journal of Science*, v. 278, pp. 217-224.

Mysen, B.O., 1987, Magmatic silicate melts: Relations between bulk composition, structure and properties, *in* Magmatic Processes: Physiochemical Principle, Special Publication No. 1 of the Geochemical Society, *ed.* by B.O. Mysen, 500 p.

Mysen, B.O., and Acton, M., 1999, Water in H_2O-saturated magma-fluid systems: Solubility behavior in K_2O-Al_2O_3-SiO_2-H_2O to 2.0 GPa and 1300° C, *Geochimica et Cosmochimica Acta*, v. 63, no. 22, pp. 3799-3815.

Mysen, B.O., and Cody, G.D., 2004, Solubility and solution mechanism of H_2O in alkali silicate melts and glasses at high pressure and temperature, *Geochimica et Cosmochimica Acta*, v. 68, no. 24, pp. 5113-5126.

Nagasawa, H., 1973, Rare-Earth distribution in alkali rocks from Oki-Dogo Island, Japan, *Contributions to Mineralogy and Petrology*, v. 39, p. 301-308.

Nakamura, Y., 1973, Origin of sector-zoning of igneous clinopyroxenes, *American Mineralogist*, v. 58, p. 986-999.

Nash, W.P., 1972, Apatite chemistry and phosphorous fugacity in a differentiated igneous intrusion, *American Mineralogist*, v. 57, pp. 877-886.

Nash, W.P., 1982, Magma immiscibility in the Shonkin Sag and Square Butte Laccoliths, Comment, *Geology*, b. 10, pp. 444-445.

Nekvasil, H., Dondolini, A., Horn, J., Filiberto, J., Long, H., and Lindsley, D.H., 2004, The origin and evolution of silica-saturated alkalic suites: An experimental study, *Journal of Petrology*, v. 45, pp. 693-721.

Nielsen, R.L., 1985, A method for the elimination of the compositional dependence of trace element distribution coefficients, *Geochimica et Cosmoshimica Acta*, v. 49, pp. 1775-1779.

Nielsen, R.L., 1992, BIGD: a FORTRAN program to calculate trace-element partition coefficients for natural mafic and intermediate composition magmas, *Computers and Geosciences*, v. 18, pp. 773-788.

Oberti, R., Ottolini, L., Ventura, D.G., and Parodi, G.C., 2001, On the symmetry and crystal chemistry of britholite: New structural and microanalytical data, *American Mineralogist*, v. 86, pp. 1066-1075.

O'Reilly, S.Y., and Griffin, W.L., 2000, Apatite in the mantle; implications of metasomatic processes and high heat production in Phanerozoic mantle, *Lithos*, v. 53, pp. 217-232.

Ottolini, L., Cámara, F., and Bigi, Simona, 2000, An investigation of matrix effects in the analysis of fluorine in humite-group minerals by EPMA, SIMS, and SREF, *American Mineralogist*, v. 85, pp. 89-102.

Pan, Y., and Fleet, M.F., 2002, Compositions of the apatite-group minerals: Substitution mechanisms and controlling factors, *Reviews in Mineralogy and Geochemistry*, v. 48, no. 1, pp. 13-48.

Parker, D.F., 1983, Origin of the trachyte-quartz trachyte-peralkalic rhyolite suite of the Oligocene Paisano volcano, Trans-Pecos Texas, *Geological Society of America Bulletin*, v. 94, no. 5, pp. 614-629.

Patiño Douce, A. E., 2005, Vapor-absent melting of tonalite at 15-32 kbar, *Journal of Petrology*, v. 46, p. 275-290.

Patiño Douce, A. E. and Johnston, A. D., 1991, Phase equilibria and melt productivity in the pelite system: implications for the origin of peraluminous granitoids and aluminous granulites, *Contributions to Mineralogy and Petrology*, v. 107, p. 202–218.

Patiño Douce, A. E. and Beard, J. S., 1994, H_2O loss from hydrous melts during fluid-absent piston cylinder experiments, *American Mineralogist*, v. 79, pp. 585-588.

Patiño Douce, A. E. and Beard, J. S., 1996, Effects of P, f(O_2) and Mg/Fe ratio on dehydration-melting of model metagreywackes, *Journal of Petrology*, v. 37, p. 999–1024.

Patiño Douce, A. E and Roden, M.F., 2006, Apatite as a probe of halogen and water fugacities in the terrestrial planets, *Geochimica et Cosmochimica Acta*, v. 70, pp. 477-492.

Pearce, J.A., and Norry, M.J., 1979, Petrogenetic implications of Ti, Zr, Y, and Nb variations in volcanic rocks, *Contributions to Mineralogy and Petrology*, v. 69, pp. 33-47.

Pearce, J.A., 1982, Trace element characteristics of lavas from destructive plate boundaries, in *Andesites*, ed. by R.S. Thorpe, Wiley, Chichester, pp. 525-548.

Pearce, J.A., 1983, Role of the sub-continental lithosphere in magma genesis at active continental margins. in: *Continental Basalts and Mantle Xenoliths*, ed. by C.J. Hawkesworth and M.J. Norry, Shiva, nantwich, pp. 230-249.

Peng, G., Lewis, J., Lipin, B., Bao, P., and Wang, X., 1995, Inclusions of phlogopite and phlogopite hydrates in chromite from the Hongguleleng ophiolite in Xinjiang, northwest China, *American Mineralogist*, v. 80, pp. 1307-1316.

Peters, T., Luth, W.C., and Tuttle, O.F., 1966, The melting of analcite solid solutions in the system $NaAlSi_3O_8$-$NaAlSiO_4$-H_2O, *American Mineralogist*, v. 51, pp. 736-763.

Philpotts, A.R. and Hodgson, C.J., 1968, Role of liquid immiscibility in alkaline rock genesis, Proceedings of the XXIII International Geochemical Conference, Prague, v. 2, pp. 175-188.

Piccolli, P. and Candela, P., 1994, Apatite in felsic rocks: a model for the estimation of initial halogen concentrations in the Bishop Tuff (Long Valley) intrusive suite (Sierra Nevada batholith) magmas, *American Journal of Science*, v. 294, pp. 92-135.

Piccolli, P., and Candela, P., 2002, Apatite in igneous systems, *Reviews in Mineralogy and Geochemistry*, v. 48, no. 1, pp. 255-292.

Potter, L.S., 1996, Chemical variation along strike in feldspathoidal rocks of the Eastern Alkalic Belt, Trans-Pecos Magmatic Province, Texas and New Mexico, *The Canadian Mineralogist*, v. 34, pp. 241-264.

Prelevic, D., Foley, S.F., Cvetkovic, V., and Romer, R.L., 2004, The analcime problem and its impact on the geochemistry of ultrapotassic rocks from Serbia, *Mineralogical Magazine*, v. 68, no. 4., pp. 633-648.

Price, R.C. and Wallace, R.C., 1976, The significance of corona textured inclusions from a high pressure fractionated alkalic lava, North Otago, New Zealand, *Lithos*, v. 9, pp. 319-329.

Propach, G., 1976, Models of filter differentiation, *Lithos*, v. 9, pp. 203-209.

Putirka, K.D., Mikaelian, H., Ryerson, F., and Shaw, H., 2003, New clinopyroxene-liquid thermobarometers for mafic, evolved, and volatile-bearing lava compositions, with applications to lavas from Tibet and the Snake River Plain, Idaho, *American Mineralogist*, v. 88, pp. 1542-1554.

Putnis, C.V., Geisler, T., Schmid-Beurmann, P., Stephan, T., and Giampaolo, C., 2007, An experimental study of the replacement of leucite by analcime, *American Mineralogist*, v. 92, pp. 19-26.

Rasband, W.S., ImageJ, U. S. National Institutes of Health, Bethesda, Maryland, USA, http://rsb.info.nih.gov/ij/, 1997-2007.

Ratajeski, K., and Sisson, T.W., 1999, Loss of iron to gold capsules in rock-melting experiments, *American Mineralogist*, v. 84, p. 1521-1527.

Roeder, P.L., and Emslie, R.F., 1970, Olivine-liquid equilibrium, *Contributions to Mineralogy and Petrology*, v. 29, no. 4, pp. 275-289.

Rønsbo, J.G., 1989, Coupled substitutions involving REEs and Na and Si in apatites in alkaline rocks from the Ilímaussaq intrusion, South Greenland, and the petrological implications, *American Mineralogist*, v. 74, pp. 896-901.

Rønsbo, J.G., 2008, Apatite in the Ilímaussaq alkaline complex: Occurrence, zonation and compositional variation, *Lithos*, v. 106, pp. 71-82.

Roux, J., and Hamilton, D.L., 1976, Primary igneous analcite – and experimental study, *Journal of Petrology*, v. 17, no. 2, pp. 244-257.

Rubin, J.N., Henry, C.D., and Price, J.G., 1989, Hydrothermal zircons and zircon overgrowths, Sierra Blanca Peaks, Texas, *American Mineralogist*, v. 74, pp. 865-869.

Saha, P., 1961, The system $NaAlSiO_4$ (nepheline)-$NaAlSi_3O_8$ (albite)-H_2O, *American Mineralogist*, v. 46, pp. 859-884.

Sallet, R., 2000, Fluorine as a tool in the petrogenesis of quartz-bearing magmatic associations: application of an improved F-OH biotite apatite thermometer grid, *Lithos*, v. 50, pp. 241-253

Schwandt, C.S., and McKay, 2006, Minor- and trace-element sector zoning in synthetic enstatite, *American Mineralogist*, v. 91, p. 1607-1615.

Seifert, W., Kämpf, H., and Wasternack, J., 2000, Compositional variation in apatite, phlogopite and other accessory minerals of the ultramafic Delitzsch complex, German: implication for cooling history of carbonatites, *Lithos*, v.53, pp. 81-100.

Sha, L., 2000, Whitlockite solubility in silicate melts: Some insights into lunar and planetary evolution, *Geochimica et Cosmochimica Acta*, v. 64, pp. 3217-3236.

Signorelli, S., and Carroll, M.T., 2000, Solubility and fluid-melt partitioning of Cl in hydrous phonolitic melts, *Geochimica et Cosmochimica Acta*, v. 64, no. 16, pp. 2851-2862.

Stormer, J.C., and Carmichael, I.S.E., 1971, Fluorine-hydroxyl exchange in apatite and biotite: A potential igneous geothermometer, *Contributions to Mineralogy and Petrology*, v. 31, pp. 121-131.

Stormer, J.C., Pierson, M.L., and Tacker, R.C., 1993, Variation of F and Cl X-ray intensity due to anisotropic diffusion in apatite during electron microprobe analysis, *American Mineralogst, v. 78, pp. 641-648.*

Sun, S.S., and McDounough, W.F., 1989, Chemical and isotopic systematics of oceanic basalts: Implications for mantle composition and processes, in: *Magmatism in Ocean Basins*, ed. by A.D. Saunders and M.J. Norry, Geological Society of London Special Publication 42, pp. 313-345.

Tacker, R.C., and Stormer, J.C., 1989, A thermodynamic model for apatite solid solutions, applicable to high-temperature geologic problems, *American Mineralogist*, v. 74, pp. 877-888.

Thornton and Tuttle, 1960, Chemistry of igneous rocks I: Differentiation Index, *American Journal of Science*, v. 258, p. 664-684.

Tischendorf, G., Förster, H.-J., Gottesmann, B., and Rieder, M., 2007, True and brittle micas: composition and solid-solution series, *Mineralogical Magazine*, v. 71, no. 3, pp. 285-320.

Tollari, N., Toplis, M.J., and Barnes, S.-J., 2006, Predicting phosphate saturation in silicate magmas: an experimental study of the effects of melt composition and temperature, *Geochimica et Cosmochimica Acta*, v. 70, no 6, pp. 1518-1536

Tollari, N., Baker, C.R., and Barnes, S.-J., 2008, Experimental effects of pressure and fluorine on apatite saturation in mafic magmas, with reference to layered intrusions and massif anorthosites, *Contributions to Mineralogy and Petrology*, v. 156, pp. 161-175.

Toplis, M.J., 2005, The thermodynamics of iron and magnesium partitioning between olivine and liquid: criteria for assessing and predicting equilibrium in natural and experimental systems, *Contributions to Mineralogy and Petrology*, v. 149, pp. 22-39.

Villemant, B., Jaffrezic, H., Joron, J.L. and Treuil, M., 1981, Distribution coefficients of major and trace-elements – fractional crystallization in the alkali basalt series of Chaine-Des-Puys (Massif Central, France), *Geochimica et Cosmochimica Acta*, v. 45, no. 11, pp. 1997-2016.

Villemant, B., 1988, Trace-element evolution in the Phlegrean Fields (Central-Italy) – Fractional Crystallization and Selective Enrichment, *Contributions to Mineralogy and Petrology*, v. 98, no. 2, pp. 169-183.

Volfinger, M., Robert, J.L., Vielzeuf, D., and Neiva, A.M.R., 1985, Structural control of the chlorine content of OH-bearing silicates (micas and amphiboles), *Geochimica et Cosmochimica Acta*, v. 49, p. 37-48.

Wass, S.Y. and Rogers, N.W., 1980, Mantle-metasomatism – precursor to continental alkaline volcanism, *Geochimica et Cosmochimica Acta*, v. 44, pp. 1811-1823.

Watson, E.B., 1979, Apatite saturation in basic to intermediate magmas, *Geophysical Research Letters*, v. 6, no. 12, pp. 937-940.

Watson, E.B., 1980, Apatite and phosphorous in mantle source regions: an experimental study of apatite/melt equilibria at pressures to 25 kbar, *Earth and Planetary Science Letters*, vol. 51, pp. 322-335.

Watson, E.B., and Green, T.H., 1981, Apatite/liquid partition coefficients for the rare earth elements and strontium, *Earth and Planetary Science Letters*, v. 56, pp. 405-421.

White, J.C., Benker, C.S., Ren, M., Urbanczyk, and Corrick, D.W., 2006, Petrogenesis and tectonic setting of the peralkaline Pine Canyon caldera, Trans-Pecos Texas, USA, *Lithos*, v. 91, pp. 76-94.

White, J.C. and Urbanczyk, K.M., 2001, Origin of a silica-oversaturated quartz trachyte-rhyolite suite through combined crustal melting, magma mixing, and fractional crystallization: the Leyva Canyon volcano, Trans-Pecos Magmatic Province, Texas, *Journal of Volcanology and Geothermal Research*, v. 111, pp. 155-182.

Wilkinson, J.F.G., and Hensel, H.D., 1991, An analcime mugearite-megacryst association from north-eastern New South Wales: implications for high pressure amphibole-dominated fractionation of alkaline magmas, *Contributions to Mineralogy and Petrology*, v. 109, p. 240-251.

Wilkinson, J.F.G., and Hensel, H.D., 1994, Nephelines and analcimes in some alkaline igneous rocks, *Contributions to Mineralogy and Petrology*, v. 118, pp. 79-91.

Williams, T.J., Candela, P.A., and Piccoli, P.M.,1995, The partitioning of copper between silicate melts and two-phase aqueous fluids: an experimental investigation at 1 kilobar, 800° C and ½ kilobar, 800°C, *Contributions to Mineralogy and Petrology*, v.121, pp. 388-399.

Willmore, C.C., Boudreau, A.E., and Kruger, F.J., 2000, The halogen geochemistry of the Bushveld Complex, Republic of South Africa: Implications for chalcophile element distribution in the lower and critical zones, *Journal of Petrology*, v. 41, no. 10, pp. 1517-1539.

Wood, B.J. and Nicholls, J., 1978, The thermodynamic properties of reciprocal salt solutions, *Contributions to Mineralogy and Petrology*, v. 66, pp. 389-400.

Woodhead, J., Eggins, S., and Gamble, J., 1993, High field strength and transition element systematics in island arc and back-arc basin basalts: evidence for multi-phase melt extraction and a depleted mantle wedge, *Earth and Planetary Science Letters*, v. 114, pp. 491-504.

Wright, J.B., 1966, Olivine nodules in a phonolite of the East Otago alkaline province, New Zealand, *Nature*, v. 210, pp. 519.

Wright, J.B., 1969, Olivine nodules and related inclusions in trachyte from the Jos Platwau, Nigeria, *Mineralogical Magazine*, v. 37, pp. 370-374.

Wyllie, P.J., and Tuttle, O.F., 1961, Experimental investigation of silicate systems containing two volatile components, *American Journal of Science*, v. 259, pp. 128-143.

Yang, K. and Scott, S.D., 2002, Magmatic degassing of volatiles and ore metals into a hydrothermal system on the modern sea floor of the eastern Manus back-arc basin, western Pacific, *Economic Geology*, v. 97, pp. 1079-1100.

Young, E.J., Myers, A.T., Munson, E.L., and Conklin, N.M., 1969, Mineralogy and geochemistry of fluoroapatite from Cerro de Mercado, Durango, Mexico, *U.S. Geological Survey Professional Paper 650-D*, pp. D84-D93.

Zack, T. and Brumm, R., 1998, Ilmenite/liquid partition coefficients of 26 trace elements determined through ilmenite/clinopyroxene partitioning in garnet pyroxene, *in: 7th International Kimberlite Conference*, ed. by J.J. Gurney, J.L. Gurney, M.D. Pascoe, and S.H. Richardson, Red Roof Design, Cape Town, pp. 986-988.

Zhu, C. and Sverjensky, D.A., 1991, Partitioning of F-Cl-OH between minerals and hydrothermal fluids, *Geochimica et Cosmochimica Acta*, v. 55, pp. 1837-1858

Zhu, C. and Sverjensky, D.A., 1992, F-Cl-OH partitioning between biotite and apatite, *Geochimica et Cosmochimica Acta*, v. 56, pp. 3435-3467.

APPENDIX 1:

BONE SPRINGS SILL BIOTITE ANALYSES

Appendix 1. Bone Springs Sill biotite analyses with atoms per formula unit allocated based on 22 O and OH.

sample	BS06-37	BS06-37	BS06-37	BS04-10	BS04-10	BS04-10	BS04-10	BS04-10	BS04-10	BS04-10	BS04-10	BS04-10
analysis	30	32	33	4	6	7	8	10	11	60	61	62
lithology	L. chill zone	L. chill zone	L. chill zone	LBZ mzgb	LBZ mzgb	LBZ mzgb	LBZ mzgb	LBZ mzgb	LBZ mzgb	LBZ mzgb	LBZ mzgb	LBZ mzgb
SiO_2	34.10	33.51	33.58	35.86	34.76	35.40	34.18	35.38	35.28	37.58	35.90	35.44
Al_2O_3	14.50	14.85	14.29	14.74	14.24	14.20	14.81	15.03	14.99	14.39	14.71	14.25
TiO_2	8.70	9.16	7.48	8.74	8.58	8.84	9.71	8.18	6.69	7.47	9.83	9.35
MgO	9.63	9.78	9.22	13.47	12.10	11.38	10.29	12.95	12.69	13.15	12.48	12.76
FeO	18.26	16.64	19.32	15.19	16.63	16.52	17.65	15.61	16.87	15.32	15.15	14.12
MnO	0.21				0.22							
CaO		0.09	0.10		0.15	0.13	0.05	0.07	0.33	0.17	0.07	0.06
K_2O	8.78	8.55	9.39	8.81	9.32	9.64	9.11	9.06	9.00	8.71	9.27	8.59
Na_2O	1.01	0.76	0.39	0.61	0.51	0.55	0.57	0.56	0.36	0.71	0.82	0.88
BaO				0.59	0.25	0.15	1.13	1.04				
F			0.17	0.31	0.24	0.20	0.13	0.34	0.22	0.33	0.31	0.30
Cl	0.024	0.072	0.059	0.010			0.013	0.013	0.016	0.024	0.032	0.036
Total	95.21	93.40	93.91	98.20	96.90	96.92	97.59	98.09	96.35	97.71	98.43	95.65
Si pfu	5.237	5.202	5.299	5.29	5.25	5.326	5.162	5.27	5.321	5.526	5.279	5.327
Al (iv) pfu	2.624	2.717	2.657	2.563	2.535	2.518	2.636	2.638	2.664	2.474	2.549	2.524
Al (vi) pfu	0	0	0	0	0	0	0	0	0	0.01	0	0
Ti pfu	1.005	1.07	0.888	0.97	0.975	1	1.103	0.916	0.759	0.826	1.087	1.057
Mg pfu	2.205	2.263	2.169	2.962	2.724	2.553	2.317	2.876	2.853	2.883	2.736	2.86
Fe pfu	2.345	2.16	2.549	1.874	2.1	2.078	2.229	1.944	2.127	1.884	1.863	1.775
Mn pfu	0.027	0	0	0	0.028	0	0	0	0	0	0	0
Ca pfu	0	0.015	0.017	0	0.025	0.021	0.008	0.011	0.053	0.027	0.011	0.01
K pfu	1.72	1.693	1.89	1.658	1.795	1.85	1.755	1.721	1.731	1.634	1.739	1.647
Na pfu	0.301	0.23	0.119	0.174	0.148	0.159	0.168	0.162	0.106	0.201	0.233	0.255
Ba pfu				0.034	0.015	0.009	0.067	0.061				
F pfu			0.083	0.147	0.114	0.095	0.064	0.161	0.103	0.152	0.146	0.142
Cl pfu	0.006	0.019	0.016	0.003			0.003	0.003	0.004	0.006	0.008	0.009
OH pfu	3.994	3.981	3.901	3.851	3.886	3.905	3.933	3.836	3.892	3.842	3.846	3.848
Mg'	48	51	46	61	56	55	51	60	57	60	59	62
X_{Fe}	0.515	0.488	0.54	0.387	0.435	0.449	0.49	0.403	0.427	0.396	0.405	0.383
X_{Mg}	0.485	0.512	0.46	0.613	0.565	0.551	0.51	0.597	0.573	0.606	0.595	0.617
X_F			0.021	0.037	0.029	0.024	0.016	0.04	0.026	0.038	0.036	0.036
X_{Cl}	0.002	0.005	0.004	0.001			0.001	0.001	0.001	0.002	0.002	0.002
X_{OH}	0.998	0.995	0.975	0.963	0.971	0.976	0.983	0.959	0.973	0.961	0.962	0.962

Appendix 1, continued. Bone Springs Sill biotite analyses with atoms per formula unit allocated based on 22 O and OH.

sample	BS04-10	BS04-10	BS04-10	BS04-10	BS04-10	BS04-10	BS04-12	BS04-12	BS04-12	BS04-12	BS04-12	BS04-12
analysis	65	66	11a	30a	6a	8b	5	9	12	15	16	28
	LBZ	LBZ	LBZ	LBZ	LBZ	LBZ	LBZ	LBZ	LBZ	LBZ	LBZ	LBZ
lithology	mzgb	mzgb	mzgb	mzgb	mzgb	mzgb	mzgb	mzgb	mzgb	mzgb	mzgb	mzgb
SiO_2	37.18	35.90	35.48	36.64	35.78	35.15	36.60	35.84	35.39	34.00	36.02	35.42
Al_2O_3	14.14	14.71	14.77	14.28	14.73	14.86	12.58	13.04	13.47	14.56	13.72	13.62
TiO_2	8.31	8.65	8.86	8.98	8.41	6.49	7.74	9.15	9.53	10.16	7.01	9.43
MgO	12.99	13.34	13.18	13.80	13.14	12.44	9.99	9.63	8.43	11.13	12.72	8.90
FeO	15.34	15.06	15.14	15.36	14.59	16.85	20.75	20.40	20.92	16.18	16.60	19.25
MnO				0.21							0.20	
CaO	0.05	0.07	0.08	0.05		0.59	0.57	0.11	0.09			0.10
K_2O	8.63	8.43	8.14	8.32	8.91	8.48	8.77	9.15	9.60	8.04	9.66	9.41
Na_2O	0.65	0.75	0.61	0.58	0.55	0.48	0.46	0.69	0.63	0.83	0.78	0.56
BaO			1.73		0.80					2.42		
F		0.30	0.20	0.23	0.37	0.16	0.94	0.82	0.85	0.17	1.26	0.82
Cl			0.006		0.022	0.021		0.030	0.024		0.212	
Total	97.29	97.08	98.11	98.35	97.14	95.45	98.01	98.51	98.57	97.41	97.60	97.17
Si pfu	5.444	5.318	5.253	5.345	5.341	5.335	5.631	5.48	5.441	5.141	5.564	5.467
Al (iv) pfu	2.44	2.568	2.577	2.455	2.591	2.658	2.281	2.35	2.44	2.595	2.436	2.478
Al (vi) pfu	0	0	0	0	0	0	0	0	0	0	0.031	0
Ti pfu	0.915	0.964	0.987	0.985	0.944	0.741	0.896	1.052	1.102	1.156	0.814	1.095
Mg pfu	2.836	2.946	2.909	3.001	2.924	2.815	2.291	2.195	1.932	2.509	2.929	2.048
Fe pfu	1.878	1.865	1.874	1.874	1.821	2.139	2.67	2.608	2.689	2.046	2.144	2.485
Mn pfu	0	0	0	0.026	0	0	0	0	0	0	0.026	0
Ca pfu	0.008	0.01	0.013	0.007	0	0.096	0.094	0.019	0.015	0	0	0.017
K pfu	1.612	1.593	1.537	1.548	1.697	1.642	1.721	1.785	1.883	1.551	1.903	1.853
Na pfu	0.185	0.215	0.174	0.163	0.16	0.141	0.137	0.204	0.189	0.243	0.233	0.168
Ba pfu			0.1		0.046					0.143		
F pfu		0.141	0.095	0.106	0.173	0.076	0.459	0.396	0.411	0.081	0.614	0.401
Cl pfu			0.001		0.005	0.006		0.008	0.006		0.055	
OH pfu	4	3.859	3.904	3.894	3.822	3.918	3.541	3.596	3.583	3.919	3.33	3.599
Mg'	60	61	61	62	62	57	46	46	42	55	58	45
X_{Fe}	0.398	0.388	0.392	0.384	0.384	0.432	0.538	0.543	0.582	0.449	0.426	0.548
X_{Mg}	0.602	0.612	0.608	0.616	0.616	0.568	0.462	0.457	0.418	0.551	0.58	0.452
X_F		0.035	0.024	0.027	0.043	0.019	0.115	0.099	0.103	0.02	0.154	0.1
X_{Cl}			0		0.001	0.001		0.002	0.002		0.014	
X_{OH}	1	0.965	0.976	0.973	0.956	0.98	0.885	0.899	0.896	0.98	0.833	0.9

Appendix 1, continued. Bone Springs Sill biotite analyses with atoms per formula unit allocated based on 22 O and OH.

sample	BS04-12	BS04-12	BS04-12	BS04-12	BS04-2	BS04-2	BS04-2	BS04-2	BS04-2	BS04-2	BS04-2	BS04-2
analysis	29	4a	6b	7a	14	17	38	39	40	41	46	47
lithology	LBZ mzgb	LBZ mzgb	LBZ mzgb	LBZ mzgb	LBZ mzgb	LBZ mzgb	LBZ mzgb	LBZ mzgb	LBZ mzgb	LBZ mzgb	LBZ mzgb	LBZ mzgb
SiO_2	35.79	36.00	35.01	35.55	35.11	35.68	35.25	35.27	34.81	33.79	35.54	35.82
Al_2O_3	13.53	13.09	14.07	13.63	14.28	14.54	13.69	13.95	13.72	13.29	13.97	13.91
TiO_2	8.47	8.87	9.58	9.23	7.92	8.42	7.67	7.94	6.85	6.16	9.25	8.51
MgO	10.10	9.84	9.97	9.77	9.69	10.92	8.89	9.46	8.93	8.44	9.35	9.98
FeO	19.18	18.89	17.56	19.38	20.51	16.88	20.77	18.54	20.62	23.39	18.92	20.31
MnO		0.28			0.20	0.34	0.24		0.22	0.28		0.24
CaO	0.35	0.18		0.06	0.33		0.32	0.20	0.21	0.19		0.11
K_2O	8.99	9.24	9.47	9.18	8.10	8.93	8.79	8.82	8.77	7.81	8.31	8.97
Na_2O	0.61	0.61	0.65	0.70	0.56	0.66	0.58	0.59	0.63	0.47	0.68	0.79
BaO				0.16	0.65	0.45		0.17				
F	1.22	0.81	0.57	0.78	0.30	0.48	0.58	0.62	0.54	0.42	0.57	0.26
Cl	0.026				0.032	0.029	0.023	0.014	0.017	0.008		0.048
Total	97.74	97.47	96.65	98.10	97.55	97.11	96.56	95.31	95.08	94.07	96.35	98.83
Si pfu	5.54	5.527	5.36	5.429	5.347	5.4	5.473	5.493	5.485	5.426	5.444	5.368
Al (iv) pfu	2.46	2.369	2.538	2.453	2.563	2.593	2.505	2.507	2.515	2.515	2.522	2.457
Al (vi) pfu	0.004	0	0	0	0	0	0	0.027	0.016	0	0	0
Ti pfu	0.986	1.024	1.103	1.06	0.907	0.958	0.896	0.93	0.812	0.744	1.066	0.959
Mg pfu	2.331	2.252	2.275	2.224	2.2	2.464	2.058	2.196	2.098	2.02	2.135	2.23
Fe pfu	2.482	2.425	2.248	2.475	2.612	2.136	2.697	2.414	2.717	3.141	2.424	2.545
Mn pfu	0	0.036	0	0	0.025	0.043	0.032	0	0.029	0.038	0	0.031
Ca pfu	0.057	0.03	0	0.01	0.054	0	0.053	0.034	0.035	0.033	0	0.017
K pfu	1.775	1.81	1.849	1.788	1.573	1.724	1.741	1.752	1.763	1.6	1.624	1.715
Na pfu	0.182	0.181	0.194	0.206	0.166	0.194	0.176	0.179	0.191	0.147	0.202	0.229
Ba pfu				0.009	0.039	0.027		0.01				
F pfu	0.595	0.395	0.278	0.374	0.143	0.228	0.287	0.303	0.267	0.215	0.275	0.123
Cl pfu	0.007				0.008	0.007	0.006	0.004	0.005	0.002		0.012
OH pfu	3.398	3.605	3.722	3.626	3.848	3.765	3.707	3.693	3.729	3.783	3.725	3.865
Mg'	48	48	50	47	46	54	43	48	44	39	47	47
X_{Fe}	0.516	0.518	0.497	0.527	0.543	0.464	0.567	0.526	0.566	0.609	0.532	0.533
X_{Mg}	0.485	0.482	0.503	0.473	0.457	0.536	0.433	0.479	0.438	0.391	0.468	0.467
X_F	0.149	0.099	0.069	0.094	0.036	0.057	0.072	0.076	0.067	0.054	0.069	0.031
X_{Cl}	0.002				0.002	0.002	0.001	0.001	0.001	0.001		0.003
X_{OH}	0.85	0.901	0.931	0.906	0.962	0.941	0.927	0.923	0.932	0.946	0.931	0.966

Appendix 1, continued. Bone Springs Sill biotite analyses with atoms per formula unit allocated based on 22 O and OH.

sample	BS04-2	BS04-2	BS04-2	BS04-2	BS04-2	BS04-2	BS04-7	BS04-7	BS04-7	BS04-7	BS04-7	BS04-7
analysis	48	49	50	10b	15a	17a	18	19	21	23	24	12a
	LBZ	LBZ	LBZ	LBZ	LBZ	LBZ	LBZ	LBZ	LBZ	LBZ	LBZ	LBZ
lithology	mzgb	mzgb	mzgb	mzgb	mzgb	mzgb	mzgb	mzgb	mzgb	mzgb	mzgb	mzgb
SiO_2	35.05	34.92	34.93	35.92	34.90	34.08	35.25	35.12	35.98	33.83	35.80	34.40
Al_2O_3	14.17	14.42	13.80	13.57	13.66	13.82	13.11	13.34	13.31	14.55	14.01	13.74
TiO_2	8.83	9.04	7.97	7.41	7.02	8.66	8.23	8.86	7.07	9.26	8.21	7.94
MgO	9.98	9.94	8.30	8.44	8.49	8.38	7.51	6.97	11.49	9.93	10.12	7.75
FeO	19.83	18.67	22.23	22.03	21.88	21.30	23.68	23.36	20.74	18.82	18.83	23.60
MnO		0.19	0.18	0.30	0.36	0.25	0.24	0.28		0.28	0.22	0.24
CaO	0.08	0.08	0.04	0.32	0.23	0.14	0.41	0.25	0.12	0.05	0.05	0.16
K_2O	7.19	8.52	8.06	8.08	8.52	7.88	9.08	8.96	7.64	8.61	9.52	9.22
Na_2O	0.65	0.62	0.53	0.46	0.48	0.56	0.46	0.59	0.43	0.77	0.48	0.46
BaO						0.16		0.13		0.89		
F	0.25	0.42	0.53		0.60		0.34	0.31	0.39	0.48	0.38	0.32
Cl				0.033	0.024	0.019	0.023	0.017	0.015		0.021	0.026
Total	95.92	96.65	96.35	96.55	95.90	95.24	98.19	98.05	97.01	97.26	97.47	97.72
Si pfu	5.34	5.323	5.435	5.484	5.485	5.284	5.43	5.406	5.469	5.197	5.429	5.331
Al (iv) pfu	2.544	2.591	2.531	2.441	2.515	2.525	2.38	2.42	2.384	2.634	2.504	2.51
Al (vi) pfu	0	0	0	0	0.008	0	0	0	0	0	0	0
Ti pfu	1.012	1.036	0.933	0.851	0.83	1.01	0.954	1.026	0.808	1.07	0.936	0.926
Mg pfu	2.267	2.259	1.925	1.921	1.989	1.937	1.725	1.6	2.604	2.274	2.288	1.791
Fe pfu	2.526	2.38	2.892	2.812	2.876	2.762	3.05	3.007	2.636	2.418	2.388	3.058
Mn pfu	0	0.025	0.024	0.038	0.047	0.032	0.032	0.036	0	0.036	0.028	0.032
Ca pfu	0.012	0.013	0.007	0.052	0.038	0.024	0.068	0.042	0.019	0.008	0.008	0.026
K pfu	1.397	1.657	1.6	1.573	1.708	1.559	1.784	1.759	1.481	1.687	1.841	1.823
Na pfu	0.192	0.184	0.16	0.135	0.146	0.169	0.138	0.177	0.126	0.229	0.141	0.138
Ba pfu						0.01		0.008		0.054		
F pfu	0.118	0.202	0.261		0.297		0.166	0.15	0.189	0.233	0.182	0.158
Cl pfu				0.008	0.006	0.005	0.006	0.005	0.004		0.005	0.007
OH pfu	3.882	3.798	3.739	3.992	3.697	3.995	3.827	3.845	3.807	3.767	3.813	3.835
Mg'	47	49	40	41	41	41	36	35	50	48	49	37
X_{Fe}	0.527	0.513	0.6	0.594	0.592	0.588	0.639	0.653	0.503	0.515	0.511	0.631
X_{Mg}	0.473	0.487	0.4	0.406	0.41	0.412	0.361	0.347	0.497	0.485	0.489	0.369
X_F	0.03	0.05	0.065		0.074		0.042	0.038	0.047	0.058	0.045	0.04
X_{Cl}				0.002	0.002	0.001	0.002	0.001	0.001		0.001	0.002
X_{OH}	0.97	0.95	0.935	0.998	0.924	0.999	0.957	0.961	0.952	0.942	0.953	0.959

Appendix 1, continued. Bone Springs Sill biotite analyses with atoms per formula unit allocated based on 22 O and OH.

sample	BS04-7	BS04-7	BS04-7	BS04-7	BS04-9	BS04-9	BS04-9	BS04-9	BS04-9	BS04-9	BS04-9	BS04-9
analysis	15b	16a	17b	19a	20	22	25	26	35	43	44	67
lithology	LBZ mzgb	LBZ mzgb	LBZ mzgb	LBZ mzgb	LBZ mzgb	LBZ mzgb	LBZ mzgb	LBZ mzgb	LBZ mzgb	LBZ mzgb	LBZ mzgb	LBZ mzgb
SiO_2	34.94	33.52	33.59	33.82	33.79	35.58	34.91	34.97	37.60	35.93	35.84	36.05
Al_2O_3	13.73	14.84	12.62	14.79	14.29	14.08	13.91	13.93	14.44	14.17	14.27	13.50
TiO_2	8.32	6.04	6.87	9.16	9.17	8.21	7.32	8.16	4.83	8.13	8.53	8.64
MgO	8.62	5.82	7.20	9.76	9.89	11.11	10.28	11.61	14.53	11.72	12.41	12.43
FeO	20.45	25.90	24.75	17.01	17.66	17.81	18.66	17.74	15.32	17.11	15.25	17.13
MnO		0.39	0.36		0.20							
CaO	0.22	0.40	0.32	0.10	0.17	0.54	0.64	0.24	0.07		0.06	
K_2O	9.12	8.95	9.29	8.48	8.25	9.24	9.54	8.80	7.96	8.43	8.58	9.15
Na_2O	0.58	0.27	0.40	0.72	0.59	0.56	0.42	0.55	0.53	0.70	0.81	0.54
BaO	0.28		0.14	1.82	2.18	0.52	0.39	0.32				
F	0.51	0.15	0.37	0.46	0.27	0.27	0.31	0.33	0.41	0.34	0.44	0.34
Cl	0.016	0.029	0.020	0.016	0.010	0.021	0.024	0.024	0.051	0.034	0.036	0.024
Total	96.56	96.23	95.77	95.93	96.35	97.82	96.27	96.54	95.56	96.41	96.04	97.65
Si pfu	5.425	5.309	5.391	5.248	5.224	5.354	5.383	5.327	5.637	5.421	5.405	5.393
Al (iv) pfu	2.512	2.691	2.387	2.705	2.603	2.497	2.528	2.501	2.363	2.519	2.536	2.38
Al (vi) pfu	0	0.04	0	0	0	0	0	0	0.094	0	0	0
Ti pfu	0.972	0.72	0.829	1.069	1.066	0.929	0.849	0.935	0.545	0.922	0.968	0.972
Mg pfu	1.995	1.374	1.723	2.258	2.279	2.493	2.363	2.637	3.248	2.636	2.79	2.772
Fe pfu	2.655	3.43	3.322	2.207	2.283	2.241	2.406	2.26	1.921	2.158	1.923	2.143
Mn pfu	0	0.052	0.049	0	0.026	0	0	0	0	0	0	0
Ca pfu	0.036	0.068	0.055	0.017	0.028	0.087	0.106	0.04	0.011	0	0.01	0
K pfu	1.806	1.808	1.902	1.678	1.627	1.774	1.876	1.71	1.522	1.622	1.65	1.746
Na pfu	0.173	0.083	0.126	0.215	0.177	0.162	0.126	0.163	0.155	0.204	0.238	0.156
Ba pfu	0.017		0.009	0.111	0.132	0.031	0.023	0.019				
F pfu	0.252	0.075	0.187	0.225	0.132	0.127	0.15	0.159	0.194	0.164	0.207	0.159
Cl pfu	0.004	0.008	0.005	0.004	0.003	0.005	0.006	0.006	0.013	0.009	0.009	0.006
OH pfu	3.744	3.917	3.808	3.771	3.865	3.867	3.844	3.834	3.793	3.828	3.783	3.835
Mg'	43	29	34	51	50	53	50	54	63	55	59	56
X_{Fe}	0.571	0.716	0.658	0.494	0.5	0.473	0.504	0.462	0.383	0.45	0.408	0.436
X_{Mg}	0.429	0.292	0.342	0.506	0.5	0.527	0.496	0.538	0.635	0.55	0.592	0.564
X_F	0.063	0.019	0.047	0.056	0.033	0.032	0.037	0.04	0.049	0.041	0.052	0.04
X_{Cl}	0.001	0.002	0.001	0.001	0.001	0.001	0.002	0.002	0.003	0.002	0.002	0.001
X_{OH}	0.936	0.979	0.952	0.943	0.966	0.967	0.961	0.959	0.948	0.957	0.946	0.959

Appendix 1, continued. Bone Springs Sill biotite analyses with atoms per formula unit allocated based on 22 O and OH.

sample	BS04-9	BS04-9	BS04-9	BS04-9	BS04-9	BS04-9	BS04-9	BS06-38	BS06-38	BS06-38	BS06-38	BS06-45
analysis	79	21b	23a	24a	47a	65a	66a	20a	22a	23b	24b	3
lithology	LBZ mzgb	LBZ mzgb	LBZ mzgb	LBZ mzgb	LBZ mzgb	LBZ mzgb	LBZ mzgb	LBZ mzgb	LBZ mzgb	LBZ mzgb	LBZ mzgb	LBZ mzgb
SiO_2	37.06	35.10	33.71	34.69	36.36	35.50	35.64	36.80	36.71	35.89	35.90	35.32
Al_2O_3	13.21	14.03	14.69	14.53	14.05	14.06	13.71	13.99	13.94	14.49	14.20	14.02
TiO_2	5.77	7.93	9.32	8.47	6.26	8.33	8.33	7.02	6.46	8.42	6.95	8.07
MgO	15.16	10.74	10.53	11.69	14.07	12.57	11.51	13.87	13.69	13.52	11.62	12.86
FeO	15.60	18.05	17.94	16.72	15.67	16.26	18.63	15.71	15.76	13.00	17.17	16.16
MnO		0.37					0.18		0.23			
CaO	0.07	0.50	0.17	0.17			0.06	0.09				
K_2O	8.11	8.62	8.11	8.40	8.59	8.50	8.03	9.58	9.92	9.43	9.90	10.13
Na_2O	0.51	0.51	0.59	0.59	0.52	0.79	0.68	0.52	0.46	1.00	0.61	0.64
BaO		0.29	2.34	2.19								
F	0.64	0.42	0.16	0.40	0.36	0.45	0.22	1.49	1.49	1.52	1.48	1.87
Cl	0.029	0.026	0.025	0.040			0.021	0.024	0.072	0.036		0.060
Total	95.89	96.41	97.50	97.72	95.73	96.27	96.92	98.46	98.09	96.65	97.21	98.33
Si pfu	5.605	5.377	5.136	5.268	5.483	5.368	5.368	5.596	5.628	5.513	5.591	5.498
Al (iv) pfu	2.355	2.533	2.637	2.6	2.497	2.506	2.434	2.404	2.372	2.487	2.409	2.502
Al (vi) pfu	0	0	0	0	0	0	0	0.052	0.073	0.068	0.099	0.035
Ti pfu	0.656	0.914	1.068	0.967	0.71	0.947	0.944	0.803	0.745	0.973	0.814	0.945
Mg pfu	3.418	2.453	2.392	2.647	3.163	2.834	2.585	3.145	3.129	3.096	2.698	2.985
Fe pfu	1.973	2.312	2.285	2.123	1.976	2.056	2.346	1.998	2.02	1.67	2.236	2.104
Mn pfu	0	0.048	0	0	0	0	0.023	0	0.03	0	0	0
Ca pfu	0.011	0.083	0.027	0.028	0	0	0.01	0.015	0	0	0	0
K pfu	1.565	1.684	1.576	1.627	1.652	1.64	1.543	1.858	1.94	1.848	1.967	2.012
Na pfu	0.151	0.151	0.174	0.174	0.151	0.231	0.199	0.153	0.136	0.296	0.184	0.194
Ba pfu		0.017	0.139	0.131								
F pfu	0.308	0.205	0.075	0.191	0.172	0.214	0.104	0.717	0.721	0.736	0.73	0.92
Cl pfu	0.007	0.007	0.006	0.01			0.005	0.006	0.019	0.009		0.016
OH pfu	3.685	3.788	3.918	3.799	3.828	3.786	3.891	3.277	3.26	3.254	3.27	3.065
Mg'	63	51	51	55	62	58	52	61	61	65	55	59
X_{Fe}	0.366	0.485	0.489	0.445	0.384	0.42	0.476	0.395	0.401	0.36	0.464	0.417
X_{Mg}	0.634	0.515	0.511	0.555	0.616	0.58	0.524	0.615	0.613	0.655	0.556	0.589
X_F	0.077	0.051	0.019	0.048	0.043	0.054	0.026	0.179	0.18	0.184	0.183	0.23
X_{Cl}	0.002	0.002	0.002	0.003			0.001	0.002	0.005	0.002		0.004
X_{OH}	0.921	0.947	0.98	0.95	0.957	0.946	0.973	0.819	0.815	0.814	0.817	0.766

Appendix 1, continued. Bone Springs Sill biotite analyses with atoms per formula unit allocated based on 22 O and OH.

sample	BS06-45	BS06-45	BS04-13	BS04-13	BS04-13	BS04-13	BS04-13	BS04-13	BS04-3	BS04-3	BS04-3	BS04-3
analysis	4b	5a	27	23c	25a	26a	7b	8a	31	34	36	37
lithology	LBZ mzgb	LBZ mzgb	CZ mzgb	CZ mzgb	CZ mzgb	CZ mzgb	CZ mzgb	CZ mzgb	CZ mzgb	CZ mzgb	CZ mzgb	CZ mzgb
SiO_2	36.36	35.83	32.55	36.31	35.35	32.99	36.21	36.08	35.30	35.35	36.15	35.21
Al_2O_3	13.51	14.23	27.05	14.11	14.45	26.03	13.70	13.72	13.73	15.06	14.00	14.38
TiO_2	6.87	8.37	0.87	8.87	8.78	0.73	9.09	9.22	9.32	7.63	8.78	8.98
MgO	14.83	13.93	0.73	10.63	9.34	0.66	11.11	10.59	11.10	10.51	9.69	11.43
FeO	13.16	14.13	23.66	17.81	19.19	25.14	16.84	17.29	16.07	18.24	17.65	15.96
MnO			0.27	0.22				0.25		0.19		
CaO	0.05		0.16	0.09	0.15	0.27	0.04	0.08	0.25	0.30	0.34	0.22
K_2O	8.91	9.65	10.37	9.07	9.78	10.06	9.41	9.24	8.94	8.85	8.74	8.72
Na_2O	0.47	0.64		0.66	0.35	0.07	0.64	0.60	0.61	0.46	0.60	0.72
BaO									0.17			0.79
F	1.87	1.88		2.20	1.36		2.04	1.99	1.21	1.19	1.05	1.10
Cl	0.085			0.020	0.025		0.022	0.033	0.014		0.011	
Total	95.31	97.87	95.65	99.05	98.19	95.95	98.24	98.26	96.20	97.28	96.56	97.05
Si pfu	5.707	5.52	5.039	5.651	5.484	5.116	5.643	5.631	5.483	5.456	5.576	5.415
Al (iv) pfu	2.293	2.48	2.961	2.349	2.516	2.884	2.357	2.369	2.513	2.544	2.424	2.585
Al (vi) pfu	0.103	0.051	0.987	0.12	0.063	0.936	0.08	0.078	0	0.098	0.06	0.011
Ti pfu	0.811	0.97	0.101	1.038	1.024	0.085	1.066	1.082	1.089	0.886	1.019	1.039
Mg pfu	3.47	3.199	0.168	2.466	2.16	0.153	2.581	2.464	2.57	2.418	2.228	2.621
Fe pfu	1.727	1.82	3.063	2.318	2.489	3.26	2.195	2.257	2.087	2.354	2.276	2.052
Mn pfu	0	0	0.035	0.029	0	0	0	0.033	0	0.025	0	0
Ca pfu	0.008	0	0.026	0.015	0.024	0.045	0.007	0.014	0.041	0.049	0.056	0.037
K pfu	1.784	1.896	2.048	1.801	1.935	1.99	1.871	1.84	1.771	1.742	1.72	1.711
Na pfu	0.142	0.191		0.199	0.105	0.021	0.195	0.183	0.185	0.138	0.179	0.215
Ba pfu									0.01			0.047
F pfu	0.93	0.917		1.082	0.667		1.003	0.984	0.597	0.579	0.512	0.536
Cl pfu	0.023			0.005	0.006		0.006	0.009	0.004		0.003	
OH pfu	3.047	3.083		2.912	3.327		2.991	3.007	3.4	3.421	3.485	3.464
Mg'	67	64	5	52	46	4	54	52	55	51	49	56
X_{Fe}	0.345	0.369	0.96	0.497	0.542	0.965	0.468	0.486	0.448	0.503	0.512	0.44
X_{Mg}	0.674	0.641	0.274	0.527	0.472	0.251	0.548	0.53	0.552	0.517	0.501	0.562
X_F	0.233	0.229		0.271	0.167		0.251	0.246	0.149	0.145	0.128	0.134
X_{Cl}	0.006			0.001	0.002		0.001	0.002	0.001		0.001	
X_{OH}	0.762	0.771	1	0.728	0.832	1	0.748	0.752	0.85	0.855	0.871	0.866

Appendix 1, continued. Bone Springs Sill biotite analyses with atoms per formula unit allocated based on 22 O and OH.

sample	BS04-3	BS04-3	BS04-3	BS04-3	BS04-3	BS04-3	BS04-3	BS04-3	BS04-3	BS04-3	BS04-3	BS04-3
analysis	15c	26b	27a	29a	30b	32a	33a	35a	4c	5b	6c	7c
lithology	CZ mzgb	CZ mzgb	CZ mzgb	CZ mzgb	CZ mzgb	CZ mzgb	CZ mzgb	CZ mzgb	CZ mzgb	CZ mzgb	CZ mzgb	CZ mzgb
SiO_2	34.51	34.54	36.14	35.60	35.56	34.56	35.05	35.35	35.59	35.78	34.86	35.52
Al_2O_3	14.74	14.41	14.42	14.17	14.25	14.65	14.73	14.51	13.72	14.04	13.72	13.82
TiO_2	8.56	8.94	8.42	8.57	8.92	8.42	8.59	8.89	8.82	8.78	8.88	8.62
MgO	10.73	10.44	11.89	11.07	11.03	11.05	11.76	11.44	10.73	11.01	10.80	10.08
FeO	17.27	17.24	15.93	16.29	17.09	16.97	15.74	16.30	16.37	16.84	15.97	17.68
MnO		0.18		0.19	0.20	0.24	0.19			0.20	0.19	
CaO			0.30	0.22	0.24	0.31	0.60	0.30	0.24	0.17	0.33	0.38
K_2O	8.94	9.06	9.02	9.23	9.06	8.29	8.24	8.60	8.72	8.97	8.11	8.75
Na_2O	0.61	0.49	0.55	0.54	0.51	0.68	0.65	0.69	0.54	0.50	0.60	0.51
BaO	1.71	1.54	0.24		0.31	1.76	1.92	1.01	0.41	0.47		0.36
F	1.01	1.07	1.29	1.03	1.25	1.22	1.23	1.14	1.06	0.86	0.94	0.86
Cl	0.044	0.021	0.019	0.013		0.022	0.017		0.027	0.027	0.027	0.014
Total	97.69	97.47	97.67	96.49	97.89	97.66	98.19	97.75	95.77	97.27	94.02	96.23
Si pfu	5.344	5.367	5.518	5.484	5.458	5.368	5.382	5.413	5.534	5.464	5.477	5.498
Al (iv) pfu	2.656	2.633	2.482	2.516	2.542	2.632	2.618	2.587	2.466	2.527	2.523	2.502
Al (vi) pfu	0.017	0.003	0.056	0.028	0.018	0.025	0.024	0.016	0.024	0	0.008	0.01
Ti pfu	0.997	1.045	0.967	0.993	1.03	0.984	0.992	1.024	1.031	1.008	1.049	1.004
Mg pfu	2.477	2.419	2.706	2.542	2.524	2.559	2.692	2.612	2.487	2.506	2.529	2.326
Fe pfu	2.236	2.24	2.034	2.098	2.193	2.204	2.021	2.087	2.128	2.15	2.098	2.288
Mn pfu	0	0.024	0	0.025	0.026	0.031	0.025	0	0	0.025	0.025	0
Ca pfu	0	0	0.05	0.036	0.04	0.052	0.098	0.049	0.04	0.027	0.055	0.063
K pfu	1.766	1.796	1.757	1.814	1.774	1.643	1.614	1.68	1.729	1.747	1.625	1.728
Na pfu	0.184	0.147	0.164	0.162	0.152	0.206	0.193	0.205	0.162	0.149	0.182	0.153
Ba pfu	0.104	0.094	0.014		0.018	0.107	0.115	0.061	0.025	0.028		0.022
F pfu	0.497	0.525	0.62	0.499	0.607	0.598	0.596	0.553	0.52	0.413	0.466	0.421
Cl pfu	0.012	0.005	0.005	0.003		0.006	0.004		0.007	0.007	0.007	0.004
OH pfu	3.492	3.469	3.375	3.497	3.393	3.396	3.399	3.447	3.473	3.58	3.527	3.576
Mg'	53	52	57	55	54	54	57	56	54	54	55	50
X_{Fe}	0.476	0.481	0.436	0.455	0.467	0.466	0.432	0.446	0.464	0.462	0.454	0.497
X_{Mg}	0.527	0.519	0.576	0.551	0.537	0.54	0.573	0.557	0.541	0.538	0.547	0.505
X_F	0.124	0.131	0.155	0.125	0.152	0.149	0.149	0.138	0.13	0.103	0.116	0.105
X_{Cl}	0.003	0.001	0.001	0.001		0.001	0.001		0.002	0.002	0.002	0.001
X_{OH}	0.873	0.867	0.844	0.874	0.848	0.849	0.85	0.862	0.868	0.895	0.882	0.894

Appendix 1, continued. Bone Springs Sill biotite analyses with atoms per formula unit allocated based on 22 O and OH.

sample	BS04-3	BS04-4	BS04-4	BS04-4	BS04-4	BS04-4	BS04-4	BS05-19	BS05-19	BS05-19	BS05-19	BS05-19
analysis	9a	51	52	53	54	55	56	1	2	13	10c	11b
lithology	CZ mzgb	CZ mzgb	CZ mzgb	CZ mzgb	CZ mzgb	CZ mzgb	CZ mzgb	CZ mzgb	CZ mzgb	CZ mzgb	CZ mzgb	CZ mzgb
SiO_2	35.43	36.11	35.92	35.69	35.72	35.59	36.56	35.42	35.03	35.07	35.83	36.45
Al_2O_3	14.26	14.07	13.85	14.40	14.09	13.60	14.22	12.72	13.04	13.78	13.99	13.05
TiO_2	8.74	8.83	8.42	8.70	8.46	8.35	8.20	8.21	7.85	8.28	8.04	7.33
MgO	10.42	9.29	8.65	9.49	8.28	10.47	10.66	10.62	10.64	12.33	12.38	12.24
FeO	18.30	19.99	21.91	20.00	21.97	19.49	19.81	18.74	19.33	15.86	17.82	18.08
MnO		0.29	0.21	0.19				0.26	0.32		0.20	0.24
CaO	0.29					0.09		0.05	0.05	0.75	0.28	1.17
K_2O	8.68	9.01	8.44	9.50	8.73	9.48	8.73	9.34	9.49	9.00	9.35	9.14
Na_2O	0.57	0.69	0.60	0.64	0.54	0.43	0.67	0.56	0.56	0.80	0.53	0.59
BaO	0.79								0.16			
F	0.94	1.09	0.98	1.15	1.27	1.03	1.07	2.05	1.94	2.34	1.92	2.41
Cl	0.014	0.040						0.026	0.032	0.075	0.021	0.035
Total	98.04	98.94	98.57	99.27	98.52	98.10	99.47	97.12	97.62	97.29	99.55	99.71
Si pfu	5.422	5.513	5.517	5.453	5.539	5.476	5.514	5.671	5.595	5.575	5.524	5.706
Al (iv) pfu	2.572	2.487	2.483	2.547	2.461	2.466	2.486	2.329	2.405	2.425	2.476	2.294
Al (vi) pfu	0	0.023	0.012	0.023	0.057	0	0.021	0.035	0.025	0.079	0.033	0.057
Ti pfu	1.006	1.014	0.973	1	0.987	0.966	0.93	0.989	0.943	0.99	0.932	0.863
Mg pfu	2.377	2.115	1.98	2.161	1.914	2.402	2.397	2.535	2.534	2.922	2.845	2.857
Fe pfu	2.342	2.552	2.814	2.555	2.849	2.508	2.498	2.509	2.582	2.108	2.297	2.367
Mn pfu	0	0.037	0.027	0.025	0	0	0	0.035	0.043	0	0.027	0.032
Ca pfu	0.048	0	0	0	0	0.014	0	0.008	0.008	0.128	0.047	0.196
K pfu	1.694	1.755	1.653	1.851	1.727	1.861	1.679	1.907	1.934	1.825	1.839	1.825
Na pfu	0.169	0.205	0.179	0.188	0.161	0.129	0.196	0.173	0.174	0.247	0.158	0.178
Ba pfu	0.047								0.01			
F pfu	0.456	0.526	0.476	0.555	0.622	0.503	0.512	1.039	0.981	1.178	0.934	1.193
Cl pfu	0.004	0.01						0.007	0.009	0.02	0.006	0.009
OH pfu	3.541	3.464	3.524	3.445	3.378	3.497	3.488	2.954	3.01	2.801	3.06	2.798
Mg'	50	45	41	46	40	49	49	50	50	58	55	55
X_{Fe}	0.496	0.549	0.588	0.544	0.603	0.511	0.512	0.501	0.507	0.428	0.45	0.459
X_{Mg}	0.504	0.456	0.415	0.461	0.409	0.489	0.492	0.506	0.498	0.587	0.556	0.552
X_F	0.114	0.131	0.119	0.139	0.156	0.126	0.128	0.26	0.245	0.295	0.234	0.298
X_{Cl}	0.001	0.003						0.002	0.002	0.005	0.001	0.002
X_{OH}	0.885	0.866	0.881	0.861	0.844	0.874	0.872	0.739	0.753	0.7	0.765	0.7

Appendix 1, continued. Bone Springs Sill biotite analyses with atoms per formula unit allocated based on 22 O and OH.

sample	BS05-19	BS05-19	BS05-19	BS05-19	BS05-19	BS05-29	BS05-29	BS05-26	BS05-26	BS05-26	BS05-26	BS05-26	BS05-26
analysis	12b	3a	6d	7d	9b	22b	23d	14a	15d	16b	17c	18a	20b
	CZ	CZ	CZ	CZ	CZ	UBZ	UBZ						
lithology	mzgb	mzgb	mzgb	mzgb	mzgb	diab.	diab.	Teph	Teph	Teph	Teph	Teph	Teph
SiO_2	36.09	35.19	34.34	35.46	36.85	31.13	31.44	35.88	36.18	36.16	34.58	35.38	36.25
Al_2O_3	12.46	13.64	12.17	12.78	13.14	16.41	15.31	13.27	13.34	13.76	13.60	13.29	14.30
TiO_2	7.00	4.93	8.65	8.82	7.94	3.58	5.94	9.19	9.09	9.27	6.98	8.35	6.83
MgO	11.01	11.38	9.11	9.69	12.53	8.96	11.52	12.46	12.39	12.77	15.18	15.01	13.96
FeO	19.28	20.27	22.12	20.21	16.55	24.89	21.22	15.41	15.59	15.24	11.61	12.41	14.82
MnO	0.34		0.19	0.20		0.28				0.29			
CaO	0.18	0.14		0.07	0.12	0.41	0.33	0.08	0.10	0.15	1.45	1.17	0.15
K_2O	9.39	7.71	8.94	9.59	9.22	6.65	5.90	9.20	9.17	9.07	9.53	9.34	10.04
Na_2O	0.58	0.53	0.51	0.53	0.56	0.25	0.24	0.69	0.62	0.62	0.29	0.34	0.32
BaO				0.12	0.15		0.40	0.34	0.25	0.27	0.28	0.38	0.13
F	2.62	1.89	1.81	1.87	2.51	0.22	0.14	0.41	0.21	0.33	0.33	0.37	0.22
Cl	0.030		0.021	0.019	0.020		0.014	0.031	0.036	0.046	0.029	0.037	0.030
Total	97.87	94.88	97.10	98.57	98.53	92.69	92.40	96.77	96.89	97.82	93.72	95.92	96.95
Si pfu	5.84	5.716	5.559	5.608	5.79	5.062	5.018	5.409	5.413	5.37	5.321	5.33	5.41
Al (iv) pfu	2.16	2.284	2.322	2.382	2.21	2.938	2.88	2.358	2.352	2.408	2.466	2.359	2.515
Al (vi) pfu	0.108	0.163	0	0	0.112	0.103	0	0	0	0	0	0	0
Ti pfu	0.852	0.602	1.053	1.049	0.938	0.438	0.713	1.042	1.023	1.035	0.808	0.946	0.767
Mg pfu	2.656	2.756	2.199	2.285	2.935	2.172	2.741	2.801	2.764	2.827	3.483	3.371	3.106
Fe pfu	2.609	2.753	2.994	2.673	2.174	3.384	2.832	1.943	1.95	1.892	1.494	1.563	1.849
Mn pfu	0.046	0	0.027	0.027	0	0.039	0	0	0	0.036	0	0	0
Ca pfu	0.031	0.024	0	0.012	0.02	0.072	0.057	0.013	0.017	0.024	0.24	0.189	0.024
K pfu	1.938	1.597	1.846	1.935	1.848	1.379	1.201	1.769	1.75	1.718	1.871	1.795	1.911
Na pfu	0.181	0.168	0.16	0.163	0.17	0.08	0.075	0.201	0.181	0.18	0.087	0.1	0.092
Ba pfu				0.007	0.009		0.025	0.02	0.015	0.015	0.017	0.023	0.008
F pfu	1.342	0.968	0.924	0.936	1.249	0.113	0.07	0.193	0.102	0.155	0.163	0.176	0.105
Cl pfu	0.008		0.006	0.005	0.005		0.004	0.008	0.009	0.012	0.008	0.009	0.008
OH pfu	2.649	3.032	3.07	3.059	2.745	3.887	3.926	3.799	3.889	3.833	3.83	3.815	3.887
Mg'	50	50	42	46	57	39	49	59	59	60	70	68	63
X_{Fe}	0.506	0.514	0.577	0.539	0.438	0.616	0.508	0.41	0.414	0.401	0.3	0.317	0.373
X_{Mg}	0.514	0.515	0.423	0.461	0.584	0.402	0.492	0.59	0.586	0.599	0.7	0.683	0.627
X_F	0.336	0.242	0.231	0.234	0.312	0.028	0.018	0.048	0.025	0.039	0.041	0.044	0.026
X_{Cl}	0.002		0.001	0.001	0.001		0.001	0.002	0.002	0.003	0.002	0.002	0.002
X_{OH}	0.662	0.758	0.767	0.765	0.686	0.972	0.982	0.95	0.972	0.958	0.957	0.954	0.972

APPENDIX 2:

BONE SPRINGS SILL APATITE ANALYSES

Appendix 2. Bone Springs Sill apatite analyses with atoms per formula unit allocated based on 26 O and OH.

sample	BS06-37	BS06-37	BS06-37	BS06-37	BS04-10	BS04-10	BS04-10	BS04-10	BS04-10	BS04-10	BS04-10	BS04-10	BS04-10
analysis	100	101	102	103	5	2	3	9	5b	6	7	4	9b
lithology	L. chill zone	L. chill zone	L. chill zone	L. chill zone	LBZ mzgb	LBZ mzgb	LBZ mzgb	LBZ mzgb	LBZ mzgb	LBZ mzgb	LBZ mzgb	LBZ mzgb	LBZ mzgb
P_2O_5	25.34	27.05	32.02	33.60	36.77	38.69	39.08	39.32	39.35	39.42	39.57	39.97	40.46
CaO	38.15	39.65	48.68	49.84	57.25	55.36	56.19	56.13	55.91	55.45	55.82	56.71	55.67
SiO_2	18.10	14.76	6.79	6.85	0.39	0.27	0.43	0.42	0.42	0.96	0.33	0.34	0.35
Al_2O_3	7.52	6.41	2.19	2.33	0.03	0.00	0.06	0.03	0.05	0.04	0.04		0.03
FeO	0.86	3.28	1.91	0.38	0.34	0.05	0.35	0.26	0.30	0.36	0.22	0.22	0.16
MnO	0.07	0.03	0.01	0.03	0.02		0.02			0.02	0.02		
MgO	0.23	0.67	0.43	0.02	0.16	0.12	0.07	0.08	0.16	0.14	0.04	0.18	0.09
Na_2O	1.02	1.14	0.27	1.07	0.05	0.00	0.06	0.03	0.02	0.01	0.05	0.02	0.04
La_2O_3	0.18		0.12		0.30	0.36					0.18	0.36	0.12
Ce_2O_3	0.38	0.61	0.52	0.57		0.05	0.50	0.18	0.32	0.77		0.14	0.32
SrO	0.38	0.35	0.33	0.27	0.38	0.29	0.38	0.30	0.29	0.34	0.37	0.37	0.33
Y_2O_3	0.26	0.20		0.10		0.02		0.04		0.10	0.04		0.14
F	2.02	1.92	2.26	2.66	2.58	2.33	2.97	2.61	2.32	2.22	2.60	2.60	2.42
Cl	0.0870	0.0700	0.1340	0.0710	0.1570	0.1610	0.1530	0.1940	0.1690	0.1710	0.2590	0.1340	0.1360
Total	94.25	95.79	95.27	97.30	97.96	97.27	99.73	99.12	98.89	99.60	99.08	100.59	99.89
P pfu	3.715	3.99	4.89	4.979	5.575	5.826	5.747	5.801	5.822	5.796	5.834	5.816	5.899
Ca pfu	7.079	7.401	9.409	9.347	10.985	10.55	10.457	10.48	10.468	10.317	10.415	10.444	10.272
Si pfu	3.135	2.572	1.225	1.199	0.07	0.048	0.075	0.073	0.074	0.166	0.057	0.059	0.06
Al pfu	1.535	1.316	0.466	0.48	0.006	0	0.013	0.005	0.011	0.007	0.008		0.006
Fe pfu	0.125	0.478	0.288	0.055	0.05	0.007	0.05	0.038	0.043	0.053	0.033	0.032	0.023
Mn pfu	0.011	0.004	0.001	0.004	0.004		0.004			0.003	0.003		
Mg pfu	0.06	0.174	0.117	0.005	0.042	0.031	0.018	0.022	0.041	0.036	0.009	0.046	0.023
Na pfu	0.344	0.384	0.095	0.362	0.018	0.001	0.019	0.009	0.007	0.004	0.017	0.007	0.014
La pfu	0.012		0.008		0.02	0.024					0.012	0.023	0.008
Ce pfu	0.024	0.039	0.034	0.037		0.003	0.032	0.012	0.02	0.049		0.009	0.02
Sr pfu	0.038	0.035	0.035	0.027	0.04	0.03	0.038	0.03	0.029	0.034	0.038	0.036	0.033
Y pfu	0.024	0.018		0.009		0.002		0.004		0.01	0.004		0.013
F pfu	1.105	1.055	1.288	1.471	1.462	1.308	1.632	1.437	1.281	1.22	1.434	1.414	1.319
Cl pfu	0.025	0.021	0.041	0.021	0.048	0.048	0.045	0.057	0.05	0.05	0.077	0.039	0.04
OH (ideal)	0.87	0.925	0.672	0.508	0.49	0.644	0.323	0.506	0.669	0.73	0.489	0.547	0.641
Total	18.101	18.412	18.568	18.505	18.809	18.521	18.453	18.473	18.516	18.474	18.431	18.474	18.378
X_F	0.552	0.527	0.644	0.735	0.731	0.654	0.816	0.718	0.641	0.61	0.717	0.707	0.66
X_{Cl}	0.013	0.01	0.02	0.01	0.024	0.024	0.022	0.029	0.025	0.025	0.038	0.019	0.02
X_{OH}	0.435	0.462	0.336	0.254	0.245	0.322	0.161	0.253	0.334	0.365	0.245	0.274	0.32

Appendix 2, continued. Bone Springs Sill apatite analyses with atoms per formula unit allocated based on 26 O and OH.

sample	BS04-10	BS04-10	BS04-12	BS04-12	BS04-12	BS04-2	BS04-2	BS04-2	BS04-2	BS04-2	BS04-2	BS04-7	BS04-7
analysis	10	11	12	13	14	15	16	17	18	19	20	23a	44
lithology	LBZ mzgb	LBZ mzgb	LBZ mzgb	LBZ mzgb	LBZ mzgb	LBZ mzgb	LBZ mzgb	LBZ mzgb	LBZ mzgb	LBZ mzgb	LBZ mzgb	LBZ mzgb	LBZ mzgb
P_2O_5	40.99	41.16	38.88	39.54	40.35	35.37	37.82	38.19	38.99	39.67	39.81	37.62	39.04
CaO	56.20	55.41	52.19	54.60	54.45	48.66	52.34	55.38	53.27	53.70	55.65	54.13	53.36
SiO_2	0.26	0.28	4.01	1.25	0.35	4.44	2.20	0.75	0.74	0.53	0.74	2.01	1.38
Al_2O_3	0.00		0.06	0.09		1.62	0.37	0.04	0.05	0.03		0.43	0.02
FeO	0.23	0.21	0.41	0.56	0.28	2.33	0.48	0.40	0.38	0.24	0.53	1.92	0.65
MnO		0.19	0.02	0.05	0.04	0.05	0.01	0.04	0.04	0.06	0.08		0.04
MgO	0.12	0.17	0.06	0.06	0.06	0.92	0.09	0.18	0.03	0.09	0.17	0.47	0.23
Na_2O		0.01	0.02	0.14	0.08	0.06	0.01	0.06	0.07	0.05	0.03	0.08	0.05
La_2O_3		0.42	0.36	0.24	0.12	0.37			0.19	0.25	0.06		0.42
Ce_2O_3	0.23	0.23	0.18	0.82	0.27	0.57	0.53	0.71	0.44	0.13	0.44		0.90
SrO	0.24	0.35	0.27	0.25	0.27	0.23	0.39	0.36	0.30	0.31	0.29	0.39	0.28
Y_2O_3	0.08		0.02	0.19	0.19	0.07	0.02	0.17	0.04	0.02	0.07	0.04	0.13
F	2.29	2.49	2.76	2.93	2.20	2.82	2.86	3.54	2.88	3.18	3.36	2.49	2.23
Cl	0.1350	0.1470	0.2500	0.1190	0.1410	0.1180	0.1370	0.1800	0.1620	0.1560	0.1800	0.1480	0.1780
Total	100.38	100.63	98.99	100.34	98.41	97.11	96.81	99.35	97.16	97.85	100.84	99.36	98.57
P pfu	5.938	5.949	5.636	5.755	5.961	5.282	5.662	5.646	5.835	5.876	5.758	5.547	5.792
Ca pfu	10.303	10.134	9.574	10.057	10.179	9.195	9.916	10.361	10.088	10.066	10.186	10.101	10.018
Si pfu	0.045	0.048	0.687	0.214	0.062	0.783	0.388	0.131	0.131	0.092	0.127	0.35	0.242
Al pfu	0.001		0.012	0.019		0.337	0.076	0.007	0.011	0.005		0.087	0.005
Fe pfu	0.033	0.031	0.058	0.08	0.041	0.344	0.071	0.058	0.056	0.035	0.076	0.28	0.095
Mn pfu		0.027	0.003	0.008	0.006	0.007	0.001	0.005	0.005	0.009	0.011		0.006
Mg pfu	0.032	0.043	0.015	0.015	0.015	0.241	0.024	0.046	0.009	0.025	0.043	0.123	0.06
Na pfu		0.003	0.007	0.046	0.026	0.02	0.004	0.02	0.023	0.018	0.009	0.027	0.017
La pfu		0.026	0.023	0.015	0.008	0.024			0.012	0.016	0.004		0.027
Ce pfu	0.014	0.014	0.011	0.052	0.017	0.037	0.035	0.045	0.029	0.009	0.028		0.058
Sr pfu	0.024	0.034	0.027	0.025	0.027	0.023	0.04	0.036	0.031	0.032	0.029	0.04	0.028
Y pfu	0.008		0.002	0.018	0.018	0.006	0.002	0.016	0.004	0.002	0.006	0.004	0.012
F pfu	1.241	1.342	1.496	1.592	1.213	1.571	1.599	1.955	1.608	1.759	1.815	1.372	1.237
Cl pfu	0.039	0.043	0.072	0.035	0.042	0.035	0.041	0.053	0.048	0.046	0.052	0.044	0.053
OH (ideal)	0.72	0.615	0.431	0.373	0.745	0.394	0.36		0.344	0.194	0.132	0.584	0.71
Total	18.397	18.312	18.055	18.307	18.36	18.299	18.227	18.372	18.247	18.184	18.281	18.569	18.368
X_F	0.621	0.671	0.748	0.796	0.607	0.785	0.799	0.977	0.804	0.88	0.908	0.686	0.619
X_{Cl}	0.02	0.021	0.036	0.017	0.021	0.018	0.02	0.027	0.024	0.023	0.026	0.022	0.026
X_{OH}	0.36	0.308	0.216	0.187	0.373	0.197	0.18	-0.004	0.172	0.097	0.066	0.292	0.355

Appendix 2, continued. Bone Springs Sill apatite analyses with atoms per formula unit allocated based on 26 O and OH.

sample	BS04-7	BS04-7	BS04-7	BS04-7	BS04-7	BS04-7	BS04-7	BS04-7	BS04-7	BS04-7	BS04-7	BS04-9	BS04-9
analysis	45	46	47	48	18b	50	51	52	53	54	55	56	57
lithology	LBZ mzgb	LBZ mzgb	LBZ mzgb	LBZ mzgb	LBZ mzgb	LBZ mzgb	LBZ mzgb	LBZ mzgb	LBZ mzgb	LBZ mzgb	LBZ mzgb	LBZ mzgb	LBZ mzgb
P_2O_5	39.21	39.30	39.33	39.39	39.72	39.80	39.99	39.99	40.02	40.13	40.47	38.41	38.77
CaO	56.00	55.27	55.25	56.06	55.69	55.69	55.25	56.03	54.32	54.38	54.67	55.11	57.55
SiO_2	0.71	0.78	0.49	1.15	1.34	1.14	0.58	0.82	1.12	1.22	0.79	0.51	0.36
Al_2O_3		0.01		0.36	0.11	0.14	0.04	0.02	0.16	0.03	0.07	0.01	0.01
FeO	0.28	0.49	0.57	0.44	0.47	0.34	0.47	0.42	0.65	0.71	0.29	0.41	0.35
MnO	0.01	0.04	0.01		0.08	0.07	0.03	0.04		0.09		0.02	0.01
MgO	0.13	0.14	0.10	0.12	0.15	0.27	0.14	0.09	0.20	0.19	0.12	0.15	0.14
Na_2O	0.05	0.07	0.05	0.18	0.32	0.26	0.04	0.06	0.17	0.09	0.12	0.06	0.02
La_2O_3		0.12		0.24	0.12		0.36	0.30	0.30	0.18	0.41		0.30
Ce_2O_3	0.05	0.18		0.32	0.45	0.18	0.18	0.36	0.41	0.18		0.14	0.09
SrO	0.35	0.30	0.37	0.23	0.35	0.31	0.25	0.28	0.32	0.30	0.40	0.31	0.24
Y_2O_3	0.02	0.19	0.06	0.08	0.02		0.10	0.02	0.19		0.10	0.02	0.06
F	2.01	2.04	2.08	2.12	2.69	2.29	2.06	2.54	2.13	2.03	2.14	1.83	2.99
Cl	0.1600	0.1680	0.1700	0.1870	0.1890	0.1390	0.1600	0.1720	0.1400	0.1910	0.1660	0.1620	0.1490
Total	98.65	98.82	98.10	100.51	101.21	100.28	99.31	100.68	99.79	99.36	99.38	96.81	100.51
P pfu	5.811	5.816	5.858	5.736	5.732	5.78	5.88	5.805	5.843	5.87	5.916	5.818	5.68
Ca pfu	10.503	10.35	10.414	10.332	10.17	10.235	10.281	10.293	10.037	10.066	10.114	10.563	10.67
Si pfu	0.125	0.137	0.087	0.197	0.228	0.196	0.101	0.141	0.193	0.211	0.136	0.091	0.063
Al pfu		0.002		0.074	0.021	0.027	0.008	0.003	0.033	0.007	0.015	0.002	0.001
Fe pfu	0.041	0.072	0.083	0.064	0.067	0.049	0.069	0.06	0.093	0.103	0.042	0.062	0.051
Mn pfu	0.001	0.006	0.002		0.012	0.011	0.005	0.005		0.014		0.003	0.002
Mg pfu	0.034	0.037	0.026	0.031	0.038	0.07	0.036	0.023	0.052	0.048	0.03	0.041	0.037
Na pfu	0.018	0.025	0.016	0.06	0.105	0.087	0.012	0.018	0.058	0.029	0.04	0.019	0.008
La pfu		0.008		0.015	0.008		0.023	0.019	0.019	0.011	0.026		0.019
Ce pfu	0.003	0.012		0.02	0.028	0.011	0.012	0.023	0.026	0.011		0.009	0.006
Sr pfu	0.036	0.031	0.037	0.023	0.035	0.031	0.026	0.028	0.032	0.03	0.04	0.032	0.024
Y pfu	0.002	0.017	0.006	0.008	0.002		0.01	0.002	0.017		0.01	0.002	0.006
F pfu	1.113	1.129	1.154	1.152	1.449	1.243	1.13	1.375	1.162	1.111	1.168	1.034	1.636
Cl pfu	0.048	0.05	0.051	0.055	0.054	0.041	0.047	0.05	0.041	0.056	0.048	0.049	0.044
OH (ideal)	0.839	0.822	0.795	0.793	0.497	0.717	0.823	0.575	0.797	0.833	0.783	0.917	0.32
Total	18.577	18.522	18.529	18.562	18.446	18.504	18.464	18.421	18.41	18.4	18.371	18.643	18.566
X_F	0.556	0.564	0.577	0.576	0.724	0.621	0.565	0.688	0.581	0.556	0.584	0.517	0.818
X_{Cl}	0.024	0.025	0.025	0.027	0.027	0.02	0.023	0.025	0.02	0.028	0.024	0.025	0.022
X_{OH}	0.42	0.411	0.397	0.397	0.248	0.358	0.412	0.287	0.399	0.416	0.392	0.459	0.16

Appendix 2, continued. Bone Springs Sill apatite analyses with atoms per formula unit allocated based on 26 O and OH.

sample	BS04-9	BS04-9	BS04-9	BS04-9	BS04-9	BS04-9	BS06-38	BS06-38	BS06-38	BS06-38	BS06-38	BS06-38	BS06-38
analysis	35	59	60	61	31	63	104	105	106	107	108	109	110
lithology	LBZ mzgb	LBZ mzgb	LBZ mzgb	LBZ mzgb	LBZ mzgb	LBZ mzgb	LBZ mzgb	LBZ mzgb	LBZ mzgb	LBZ mzgb	LBZ mzgb	LBZ mzgb	LBZ mzgb
P_2O_5	39.66	40.42	40.74	40.89	40.99	42.73	38.03	38.77	39.04	39.32	39.65	34.95	38.72
CaO	56.87	55.18	55.74	55.03	55.37	54.77	57.30	57.50	55.95	55.90	56.59	50.43	56.04
SiO_2	0.29	0.90	0.44	0.28	0.39	0.24	0.72	0.39	0.20	0.28	0.38	3.21	0.16
Al_2O_3		0.12	0.01	0.02	0.01	0.01	0.00		0.00	0.02	0.01	0.04	0.01
FeO	0.62	0.45	0.38	0.20	0.37	0.34	0.25	0.39	0.16	0.35	0.20	0.25	0.16
MnO	0.06	0.06	0.05		0.16		0.03	0.08	0.06	0.09	0.07		0.06
MgO	0.10	0.37	0.15	0.13	0.09	0.11		0.12	0.10	0.19	0.04	0.15	0.14
Na_2O	0.06	0.03	0.04	0.04	0.07	0.07	0.15	0.01	0.05	0.09	0.01	0.10	
La_2O_3		0.24		0.06		0.06		0.06	0.18		0.12	0.25	0.18
Ce_2O_3	0.23	0.41		0.27		0.32	0.76	0.46	0.14	0.29	0.19	0.14	0.46
SrO	0.40	0.25	0.30	0.32	0.31	0.34	0.12	0.25	0.34	0.27	0.32	0.25	0.24
Y_2O_3	0.25	0.12	0.04	0.02	0.12	0.08	0.06		0.10		0.07		
F	2.60	2.02	1.92	1.96	2.11	2.04	3.67	2.42	1.71	2.04	2.27	2.42	2.35
Cl	0.1440	0.1860	0.1700	0.1400	0.1460	0.1430	0.1110	0.1240	0.1040	0.1650	0.1900	0.1900	0.1340
Total	100.90	100.40	99.63	99.01	99.77	100.94	100.55	100.15	97.82	98.63	99.71	91.94	98.22
P pfu	5.773	5.867	5.945	5.996	5.964	6.105	5.575	5.712	5.862	5.843	5.826	5.52	5.797
Ca pfu	10.476	10.136	10.293	10.212	10.196	9.902	10.631	10.721	10.632	10.512	10.523	10.079	10.617
Si pfu	0.05	0.154	0.076	0.049	0.067	0.04	0.125	0.069	0.036	0.049	0.066	0.599	0.029
Al pfu		0.023	0.003	0.005	0.003	0.001	0.001		0	0.004	0.002	0.009	0.002
Fe pfu	0.089	0.064	0.054	0.03	0.053	0.048	0.036	0.056	0.024	0.051	0.029	0.039	0.024
Mn pfu	0.009	0.009	0.007		0.024		0.004	0.012	0.008	0.013	0.011		0.008
Mg pfu	0.025	0.095	0.037	0.033	0.024	0.027		0.031	0.026	0.051	0.011	0.041	0.036
Na pfu	0.019	0.01	0.015	0.012	0.022	0.024	0.052	0.004	0.016	0.03	0.003	0.036	
La pfu		0.015		0.004		0.004		0.004	0.012		0.008	0.017	0.012
Ce pfu	0.014	0.026		0.017		0.02	0.048	0.029	0.009	0.018	0.012	0.009	0.03
Sr pfu	0.04	0.025	0.03	0.032	0.031	0.034	0.012	0.025	0.035	0.028	0.032	0.027	0.024
Y pfu	0.023	0.011	0.004	0.002	0.011	0.007	0.005		0.009		0.007		
F pfu	1.416	1.095	1.046	1.071	1.147	1.09	2.01	1.334	0.959	1.131	1.246	1.429	1.311
Cl pfu	0.042	0.054	0.05	0.041	0.042	0.041	0.033	0.036	0.031	0.049	0.056	0.06	0.04
OH (ideal)	0.542	0.851	0.905	0.888	0.811	0.869		0.63	1.009	0.82	0.698	0.511	0.649
Total	18.529	18.436	18.463	18.392	18.396	18.219	18.49	18.663	18.669	18.6	18.531	18.377	18.579
X_F	0.708	0.547	0.523	0.536	0.573	0.545	0.984	0.667	0.48	0.566	0.623	0.715	0.656
X_{Cl}	0.021	0.027	0.025	0.021	0.021	0.02	0.016	0.018	0.016	0.025	0.028	0.03	0.02
X_{OH}	0.271	0.426	0.452	0.444	0.405	0.435		0.315	0.505	0.41	0.349	0.255	0.324

Appendix 2, continued. Bone Springs Sill apatite analyses with atoms per formula unit allocated based on 26 O and OH.

sample	BS06-38	BS06-45	BS04-3	BS04-3	BS04-3	BS04-3	BS04-3	BS04-3	BS04-3	BS04-4	BS04-4	BS04-4	BS04-4
analysis	111	112	4a	1b	23	12b	25	26	27	28	29	30e	31e
lithology	LBZ mzgb	LBZ mzgb	CZ mzgb	CZ mzgb	CZ mzgb	CZ mzgb	CZ mzgb	CZ mzgb	CZ mzgb	CZ mzgb	CZ mzgb	CZ mzgb	CZ mzgb
P_2O_5	39.01	38.84	38.80	38.86	38.93	39.35	40.46	40.57	40.95	35.27	37.85	38.04	39.07
CaO	56.26	57.96	54.58	53.89	56.26	54.88	54.18	55.07	55.26	46.69	53.16	53.53	55.64
SiO_2	0.74	0.26	0.28	0.19	0.23	0.48	0.32	0.34	0.33	3.93	1.18	1.35	0.36
Al_2O_3	0.09	0.01		0.02	0.03	0.17			0.01	1.74	0.23	0.47	0.01
FeO	0.30	0.24	0.22	0.21	0.33	0.57	0.34	0.27	0.24	7.31	0.84	2.81	0.38
MnO	0.05	0.08	0.05			0.02	0.08	0.13	0.04	0.17	0.02		0.02
MgO	0.03	0.14	0.01	0.02	0.05	0.06	0.02	0.07	0.04	0.44	0.06	0.40	0.15
Na_2O	0.14	0.04	0.08	0.03	0.06	0.03	0.04	0.05	0.06	0.06	0.11	0.06	0.03
La_2O_3	0.31		0.19		0.31	0.25	0.31	0.19	0.06	0.12	0.36		
Ce_2O_3	1.01	0.05	0.50		0.54	0.27	0.50	0.18	0.23	0.45	0.55	0.05	0.32
SrO	0.19	0.24	0.34	0.26	0.33	0.28	0.23	0.33	0.33	0.29	0.22	0.27	0.29
Y_2O_3	0.06	0.13	0.04	0.15	0.20	0.04				0.13	0.19	0.11	
F	2.09	2.56	3.61	3.08	3.17	3.22	3.93	3.61	3.55	2.66	2.70	2.32	2.37
Cl	0.1190	0.1180	0.0870	0.1170	0.1400	0.1090	0.0840	0.1350	0.1330	0.1460	0.0220	0.2160	0.3920
Total	100.02	100.21	98.16	96.27	100.01	99.16	99.80	100.29	100.59	98.94	97.00	99.22	98.61
P pfu	5.753	5.708	5.774	5.864	5.73	5.789	5.874	5.866	5.892	5.263	5.714	5.635	5.807
Ca pfu	10.501	10.78	10.279	10.292	10.48	10.217	9.955	10.076	10.063	8.817	10.156	10.036	10.466
Si pfu	0.129	0.046	0.049	0.033	0.04	0.083	0.055	0.058	0.056	0.693	0.211	0.236	0.064
Al pfu	0.019	0.003		0.004	0.006	0.034			0.002	0.362	0.048	0.096	0.003
Fe pfu	0.043	0.035	0.033	0.031	0.048	0.083	0.049	0.038	0.034	1.077	0.125	0.411	0.056
Mn pfu	0.007	0.012	0.007			0.003	0.012	0.019	0.005	0.026	0.002		0.003
Mg pfu	0.008	0.035	0.003	0.005	0.012	0.016	0.006	0.017	0.01	0.117	0.015	0.104	0.039
Na pfu	0.048	0.014	0.026	0.01	0.021	0.01	0.014	0.015	0.02	0.022	0.037	0.021	0.011
La pfu	0.02		0.012		0.02	0.016	0.02	0.012	0.004	0.008	0.023		
Ce pfu	0.064	0.003	0.032		0.035	0.017	0.031	0.011	0.014	0.029	0.036	0.003	0.021
Sr pfu	0.02	0.024	0.035	0.027	0.033	0.028	0.023	0.033	0.033	0.029	0.023	0.027	0.029
Y pfu	0.005	0.012	0.004	0.015	0.018	0.004				0.012	0.018	0.01	
S pfu			0.003									0.004	0.002
F pfu	1.152	1.403	2.007	1.736	1.743	1.769	2.131	1.95	1.908	1.48	1.521	1.284	1.314
Cl pfu	0.035	0.035	0.026	0.035	0.041	0.032	0.024	0.039	0.038	0.044	0.006	0.064	0.117
OH (ideal)	0.813	0.563		0.229	0.216	0.198		0.011	0.054	0.476	0.472	0.652	0.57
Total	18.617	18.672	18.257	18.28	18.443	18.302	18.038	18.145	18.133	18.456	18.41	18.584	18.5
X_F	0.576	0.701	1.003	0.868	0.871	0.885	1.066	0.975	0.954	0.74	0.761	0.642	0.657
X_{Cl}	0.018	0.017	0.013	0.018	0.021	0.016	0.012	0.02	0.019	0.022	0.003	0.032	0.058
X_{OH}	0.406	0.281	-0.016	0.114	0.108	0.099	-0.078	0.006	0.027	0.238	0.236	0.326	0.285

Appendix 2, continued. Bone Springs Sill apatite analyses with atoms per formula unit allocated based on 26 O and OH.

sample	BS04-4	BS04-4	BS04-4	BS04-4	BS04-4	BS04-4	BS04-4	BS04-4	BS04-4	BS04-4	BS04-4	BS05-13	BS05-13
analysis	32	33	34	35e	36	37	38	39	40	41	42	64	65
lithology	CZ mzgb	CZ mzgb	CZ mzgb	CZ mzgb	CZ mzgb	CZ mzgb	CZ mzgb	CZ mzgb	CZ mzgb	CZ mzgb	CZ mzgb	CZ mzgb	CZ mzgb
P_2O_5	39.07	39.24	39.31	39.40	39.41	39.44	39.68	39.84	40.19	40.63	41.04	39.25	39.40
CaO	55.64	53.72	53.91	55.17	55.44	55.47	52.14	54.68	55.73	54.93	52.80	53.94	52.92
SiO_2	0.36	0.50	0.76	0.36	0.24	0.26	0.65	0.45	0.34	0.47	0.96	0.14	0.24
Al_2O_3	0.01		0.09	0.03		0.02	0.10	0.01					
FeO	0.38	0.56	0.74	0.16	0.16	0.32	0.23	0.18	0.36	0.20	0.23	0.18	0.29
MnO	0.02		0.10	0.02	0.03	0.04	0.03		0.03	0.10			0.06
MgO	0.15				0.04	0.12	0.01	0.09	0.11	0.04	0.12	0.10	0.15
Na_2O	0.03	0.06	0.12	0.09	0.01	0.04	0.08	0.06	0.04	0.07	0.07	0.02	0.03
La_2O_3				0.54	0.30		0.36				0.18	0.32	0.32
Ce_2O_3	0.32	0.68	0.41	0.46			0.87	0.41	0.41	0.23		0.23	0.18
SrO	0.29	0.31	0.25	0.30	0.33	0.31	0.26	0.32	0.28	0.33	0.37	0.29	0.27
Y_2O_3		0.28	0.34	0.19		0.17	0.11		0.06	0.11	0.09		0.18
F	2.37	2.52	3.48	2.64	2.07	2.54	2.48	2.38	2.33	2.15	1.98	2.28	1.96
Cl	0.3920	0.2260	0.2530	0.4360	0.2900	0.3500	0.3570	0.3720	0.4100	0.2800	0.3420	0.1420	0.1490
Total	98.61	97.67	99.15	99.32	97.94	98.63	96.96	98.36	99.88	99.16	97.80	96.48	95.78
P pfu	5.807	5.869	5.775	5.822	5.886	5.841	5.946	5.899	5.879	5.953	6.04	5.93	5.985
Ca pfu	10.466	10.168	10.023	10.317	10.478	10.396	9.887	10.245	10.317	10.185	9.833	10.313	10.173
Si pfu	0.064	0.088	0.132	0.063	0.042	0.046	0.115	0.079	0.059	0.082	0.166	0.026	0.044
Al pfu	0.003		0.018	0.006		0.004	0.022	0.003					
Fe pfu	0.056	0.082	0.108	0.024	0.024	0.047	0.034	0.027	0.053	0.029	0.033	0.026	0.043
Mn pfu	0.003		0.015	0.003	0.004	0.007	0.005		0.005	0.015			0.009
Mg pfu	0.039				0.011	0.032	0.002	0.025	0.027	0.011	0.03	0.027	0.04
Na pfu	0.011	0.019	0.04	0.031	0.004	0.015	0.029	0.02	0.013	0.023	0.023	0.005	0.011
La pfu				0.035	0.019		0.023				0.011	0.021	0.021
Ce pfu	0.021	0.044	0.026	0.029			0.056	0.026	0.026	0.014		0.015	0.012
Sr pfu	0.029	0.032	0.025	0.03	0.034	0.032	0.027	0.033	0.028	0.033	0.037	0.03	0.028
Y pfu		0.026	0.032	0.018		0.016	0.01		0.006	0.01	0.008		0.017
F pfu	1.314	1.408	1.91	1.458	1.152	1.406	1.387	1.315	1.274	1.176	1.086	1.285	1.111
Cl pfu	0.117	0.068	0.075	0.129	0.087	0.104	0.107	0.11	0.12	0.082	0.101	0.043	0.045
OH (ideal)	0.57	0.525	0.016	0.413	0.761	0.491	0.506	0.575	0.606	0.742	0.813	0.672	0.844
Total	18.5	18.334	18.195	18.379	18.502	18.435	18.163	18.356	18.414	18.356	18.183	18.395	18.382
X_F	0.657	0.704	0.955	0.729	0.576	0.703	0.693	0.657	0.637	0.588	0.543	0.642	0.555
X_{Cl}	0.058	0.034	0.037	0.064	0.043	0.052	0.054	0.055	0.06	0.041	0.05	0.022	0.023
X_{OH}	0.285	0.262	0.008	0.206	0.38	0.245	0.253	0.288	0.303	0.371	0.407	0.336	0.422

Appendix 2, continued. Bone Springs Sill apatite analyses with atoms per formula unit allocated based on 26 O and OH.

sample	BS05-13	BS05-13	BS05-13	BS05-13	BS05-19	BS05-19	BS05-19	BS05-19	BS05-19	BS05-19	BS05-19	BS05-19	BS05-28
analysis	66	15d	68	9a	70	7d	3b	73	9b	75	4b	77	26a
lithology	CZ mzgb	CZ mzgb	CZ mzgb	CZ mzgb	CZ mzgb	CZ mzgb	CZ mzgb	CZ mzgb	CZ mzgb	CZ mzgb	CZ mzgb	CZ mzgb	CZ mzsy
P_2O_5	39.96	40.87	41.01	41.48	33.46	36.61	36.73	37.18	37.23	37.54	37.72	38.17	28.31
CaO	54.25	54.59	55.22	55.41	49.08	53.67	55.89	55.14	54.36	56.17	56.44	54.09	43.08
SiO_2	0.23	0.32	0.27	0.19	4.11	3.03	0.29	0.64	0.50	0.43	0.38	1.85	8.11
Al_2O_3				0.01	0.92	0.82		0.01	0.02	0.06	0.01	0.32	6.07
FeO	0.28	0.17	0.20	0.26	3.96	0.96	0.79	0.92	0.86	0.44	0.77	1.38	5.07
MnO	0.06							0.09		0.11	0.02	0.05	0.05
MgO	0.06	0.16	0.14	0.13	0.91	0.22	0.00	0.08	0.08	0.03	0.02	0.26	2.14
Na_2O	0.04	0.04	0.03	0.07	0.06	0.06	0.03	0.03	0.05	0.06	0.03	0.03	0.14
La_2O_3	0.25	0.19	0.13		0.06	0.06		0.25	0.19	0.19			0.49
Ce_2O_3			0.09	0.05	0.09	0.44	0.18	0.27		0.31	0.22	0.49	0.40
SrO	0.30	0.31	0.26	0.27	0.30	0.31	0.37	0.33	0.27	0.37	0.27	0.29	0.22
Y_2O_3	0.08	0.02	0.21						0.04	0.15	0.04	0.14	0.06
F	1.84	2.18	2.42	2.52	2.97	3.21	3.77	2.55	3.17	2.81	3.03	2.74	3.53
Cl	0.1290	0.1510	0.1140	0.1340	0.0420	0.0440	0.0960	0.1350	0.1370	0.0630	0.1130	0.0330	0.0270
Total	97.14	98.61	99.74	100.09	95.51	98.88	97.52	97.17	96.35	98.26	98.51	99.34	97.08
P pfu	5.985	6	5.961	5.992	5.146	5.398	5.562	5.656	5.675	5.647	5.649	5.619	4.242
Ca pfu	10.283	10.142	10.157	10.129	9.552	10.015	10.711	10.616	10.486	10.694	10.696	10.078	8.168
Si pfu	0.041	0.056	0.047	0.032	0.747	0.528	0.052	0.115	0.091	0.076	0.067	0.321	1.435
Al pfu				0.002	0.197	0.167		0.002	0.004	0.012	0.002	0.065	1.266
Fe pfu	0.041	0.025	0.028	0.037	0.602	0.14	0.118	0.139	0.13	0.066	0.114	0.201	0.75
Mn pfu	0.009							0.013		0.016	0.003	0.007	0.008
Mg pfu	0.016	0.042	0.035	0.033	0.245	0.058	0.001	0.021	0.021	0.009	0.005	0.068	0.566
Na pfu	0.013	0.013	0.011	0.023	0.02	0.022	0.01	0.011	0.017	0.022	0.01	0.009	0.048
La pfu	0.016	0.012	0.008		0.004	0.004		0.017	0.013	0.012			0.032
Ce pfu			0.006	0.003	0.006	0.028	0.012	0.018		0.02	0.014	0.031	0.026
Sr pfu	0.031	0.031	0.026	0.027	0.032	0.031	0.038	0.034	0.028	0.038	0.027	0.029	0.022
Y pfu	0.007	0.002	0.02						0.004	0.015	0.004	0.013	0.006
F pfu	1.028	1.193	1.312	1.358	1.707	1.768	2.133	1.449	1.805	1.577	1.695	1.509	1.976
Cl pfu	0.039	0.044	0.033	0.039	0.013	0.013	0.029	0.041	0.042	0.019	0.034	0.01	0.008
OH (ideal)	0.934	0.763	0.655	0.603	0.28	0.219		0.51	0.153	0.404	0.271	0.482	0.016
Total	18.442	18.323	18.309	18.282	18.56	18.393	18.511	18.643	18.469	18.631	18.591	18.441	18.569
X_F	0.514	0.596	0.656	0.679	0.854	0.884	1.066	0.724	0.902	0.789	0.847	0.754	0.988
X_{Cl}	0.019	0.022	0.017	0.019	0.006	0.006	0.015	0.021	0.021	0.01	0.017	0.005	0.004
X_{OH}	0.467	0.381	0.328	0.302	0.14	0.11	-0.081	0.255	0.077	0.202	0.136	0.241	0.008

Appendix 2, continued. Bone Springs Sill apatite analyses with atoms per formula unit allocated based on 26 O and OH.

sample	BS05-28	BS05-28	BS05-28	BS05-28	BS05-28	BS05-28	BS06-50	BS06-59	BS06-59	BS06-59	BS05-29	BS05-29	BS05-29
analysis	89	90	91	24a	93	94	30	114	115	31	95	31a	104
lithology	CZ mzsy	CZ mzsy	CZ mzsy	CZ mzsy	CZ mzsy	CZ mzsy	CZ mzsy	CZ mzsy	CZ mzsy	CZ mzsy	UBZ diab.	UBZ diab.	UBZ diab.
P_2O_5	35.90	38.05	38.61	38.91	39.08	39.59	33.11	30.41	34.54	37.04	15.52	31.68	32.25
CaO	53.19	53.96	55.70	54.71	54.29	55.88	53.20	40.98	50.98	53.34	22.13	36.04	44.49
SiO_2	3.23	3.33	1.09	1.60	0.65	0.84	5.88	11.34	1.60	0.79	39.65	14.28	8.66
Al_2O_3	0.53	0.76	0.07	0.32	0.08	0.13	1.77	6.23	0.11	0.10	13.90	5.44	3.60
FeO	0.15	0.53	0.18	0.44	0.22	0.57	0.13	0.48	0.12	0.29	0.55	1.21	3.35
MnO		0.10	0.06	0.05		0.04		0.09		0.05			0.02
MgO								0.02			0.32	0.72	1.49
Na_2O	0.13	0.01	0.02	0.08	0.10	0.13	0.17	0.19	0.13	0.34	1.57	1.22	0.19
La_2O_3	0.75	0.38	0.06	0.46	0.31	0.69	0.06		0.93	0.12	0.37		0.37
Ce_2O_3	0.98	0.90	0.13	0.61	0.40	0.54	1.05	0.28	1.57	1.61	0.09	0.44	0.62
SrO	0.15	0.27	0.41	0.29	0.24	0.36	0.09	0.27	0.08	0.28	0.77	0.33	0.34
Y_2O_3	0.28	0.34		0.12		0.02	0.08	0.14	0.13	0.06	0.09	0.02	0.20
F	3.23	2.59	2.53	2.75	3.12	2.53	3.77	2.99	3.70	4.69	1.66	2.67	2.47
Cl	0.0120	0.0470	0.0370	0.0470	0.0250	0.0690	0.1010	0.1210	0.0560	0.0320	0.0480	0.0710	0.0830
Total	97.96	100.79	98.45	99.91	97.96	100.98	98.76	93.06	93.28	97.91	96.85	93.72	97.70
P pfu	5.376	5.505	5.731	5.691	5.809	5.761	4.889	4.522	5.479	5.565	2.041	4.588	4.742
Ca pfu	10.079	9.88	10.462	10.127	10.213	10.29	9.942	7.712	10.233	10.141	3.682	6.605	8.278
Si pfu	0.571	0.569	0.19	0.277	0.113	0.144	1.026	1.992	0.3	0.14	6.158	2.443	1.504
Al pfu	0.111	0.152	0.014	0.066	0.016	0.027	0.364	1.29	0.025	0.02	2.544	1.097	0.737
Fe pfu	0.022	0.075	0.026	0.064	0.033	0.082	0.018	0.071	0.018	0.043	0.071	0.174	0.487
Mn pfu		0.015	0.009	0.007		0.006		0.013		0.008			0.003
Mg pfu								0.005			0.073	0.184	0.385
Na pfu	0.043	0.004	0.006	0.027	0.035	0.042	0.058	0.065	0.048	0.118	0.474	0.405	0.065
La pfu	0.049	0.024	0.004	0.029	0.02	0.044	0.004		0.064	0.008	0.021		0.024
Ce pfu	0.064	0.056	0.009	0.039	0.026	0.034	0.067	0.018	0.107	0.105	0.005	0.028	0.039
Sr pfu	0.015	0.027	0.042	0.029	0.024	0.036	0.009	0.027	0.009	0.028	0.069	0.033	0.035
Y pfu	0.026	0.03		0.011		0.002	0.007	0.013	0.013	0.005	0.008	0.002	0.019
F pfu	1.807	1.397	1.403	1.5	1.732	1.377	2.079	1.663	2.192	2.632	0.815	1.443	1.356
Cl pfu	0.004	0.014	0.011	0.014	0.007	0.02	0.03	0.036	0.018	0.01	0.013	0.021	0.024
OH (ideal)	0.19	0.589	0.586	0.486	0.26	0.603		0.301			1.173	0.536	0.62
Total	18.357	18.338	18.494	18.367	18.29	18.473	18.387	17.734	18.297	18.182	17.203	17.566	18.316
X_F	0.903	0.699	0.702	0.75	0.866	0.689	0.986	0.831	0.992	0.996	0.407	0.722	0.678
X_{Cl}	0.002	0.007	0.005	0.007	0.004	0.01	0.014	0.018	0.008	0.004	0.006	0.01	0.012
X_{OH}	0.095	0.295	0.293	0.243	0.13	0.301		0.151			0.586	0.268	0.31

Appendix 2, continued. Bone Springs Sill apatite analyses with atoms per formula unit allocated based on 26 O and OH.

sample	BS05-29	BS05-29	BS05-26	BS05-26	BS05-26	BS05-26	BS05-26	BS05-26	BS05-26	BS05-26	BS05-26	BS05-26
analysis	29a	99	78	79	80	81	82	14c	13e	15f	86	87
lithology	UBZ diab.	UBZ diab.	Teph	Teph	Teph	Teph	Teph	Teph	Teph	Teph	Teph	Teph
P_2O_5	32.55	35.42	32.26	33.73	35.00	35.57	36.03	36.35	36.54	36.94	37.41	38.10
CaO	36.82	52.19	45.39	51.67	53.59	50.50	51.76	52.83	55.11	53.39	53.22	55.40
SiO_2	6.74	3.04	6.03	4.59	2.00	3.43	4.36	3.44	1.62	1.62	2.54	1.16
Al_2O_3	2.83	0.86	1.96	3.94	0.34	0.82	1.62	0.61	0.14	0.15	0.05	0.24
FeO	9.66	1.80	2.88	0.66	0.89	2.15	0.27	0.52	0.65	0.61	0.65	0.81
MnO	0.04	0.04	0.08	0.03	0.05		0.03		0.13	0.11	0.03	0.06
MgO	0.76	0.44	2.65	0.04	0.40	0.62	0.01	0.28	0.30	0.22	0.40	0.00
Na_2O	0.68	0.04	0.11	0.30	0.08	0.12	0.36	0.14	0.11	0.09	0.03	0.11
La_2O_3	0.18	0.06	0.19	0.25	0.13	0.19	0.25		0.56	0.06	0.25	
Ce_2O_3	0.13	0.54	0.79	0.49	0.31	0.04	0.31	0.58	0.84	0.58	0.05	0.45
SrO	0.32	0.35	0.29	0.24	0.25	0.19	0.23	0.28	0.29	0.31	0.28	0.21
Y_2O_3	0.04	0.12	0.08	0.06	0.08			0.23	0.16	0.23	0.18	0.27
F	2.02	2.45	2.11	3.16	3.03	2.05	2.54	3.41	1.79	2.41	2.05	3.77
Cl	0.0990	0.1170	0.2570	0.2610	0.2490	0.2110	0.2890	0.2990	0.2190	0.2370	0.2300	0.2220
Total	92.54	97.07	94.70	98.86	95.86	95.59	97.59	98.36	98.18	96.52	97.02	100.16
P pfu	5.101	5.361	4.955	4.962	5.386	5.423	5.336	5.377	5.537	5.622	5.619	5.577
Ca pfu	7.302	9.997	8.822	9.619	10.436	9.743	9.702	9.89	10.568	10.283	10.117	10.262
Si pfu	1.248	0.544	1.094	0.798	0.364	0.618	0.763	0.601	0.29	0.291	0.451	0.2
Al pfu	0.618	0.181	0.419	0.807	0.074	0.173	0.334	0.126	0.031	0.032	0.01	0.05
Fe pfu	1.495	0.27	0.437	0.097	0.135	0.323	0.039	0.076	0.098	0.091	0.096	0.117
Mn pfu	0.006	0.006	0.013	0.005	0.007		0.004		0.019	0.017	0.005	0.009
Mg pfu	0.21	0.118	0.718	0.01	0.109	0.166	0.003	0.074	0.079	0.058	0.107	0
Na pfu	0.242	0.014	0.039	0.102	0.028	0.042	0.121	0.047	0.038	0.033	0.011	0.038
La pfu	0.013	0.004	0.013	0.016	0.008	0.013	0.016		0.037	0.004	0.016	
Ce pfu	0.009	0.035	0.053	0.031	0.021	0.003	0.02	0.037	0.055	0.038	0.003	0.028
Sr pfu	0.035	0.036	0.03	0.024	0.027	0.019	0.023	0.028	0.03	0.033	0.029	0.021
Y pfu	0.004	0.011	0.008	0.006	0.008			0.022	0.015	0.022	0.017	0.025
F pfu	1.181	1.386	1.212	1.736	1.742	1.167	1.407	1.884	1.014	1.37	1.152	2.061
Cl pfu	0.031	0.036	0.079	0.077	0.077	0.064	0.086	0.088	0.067	0.072	0.069	0.065
OH (ideal)	0.788	0.578	0.709	0.187	0.182	0.768	0.507	0.027	0.919	0.558	0.779	
Total	18.287	18.583	18.6	18.475	18.603	18.536	18.362	18.278	18.802	18.524	18.485	18.332
X_F	0.59	0.693	0.606	0.868	0.871	0.584	0.704	0.942	0.507	0.685	0.576	1.031
X_{Cl}	0.016	0.018	0.039	0.038	0.038	0.032	0.043	0.044	0.033	0.036	0.035	0.033
X_{OH}	0.394	0.289	0.355	0.093	0.091	0.384	0.254	0.014	0.46	0.279	0.39	-0.063

APPENDIX 3:

RATTLESNAKE MOUNTAIN SILL APATITE ANALYSES

Appendix 3. Rattlesnake Mountain Sill apatite analyses with atoms per formula unit allocated based on 26 O and OH.

sample	RM-18	RM-18	RM-18	RM-18	RM-18	RM-18	RM-8	RM-8	RM-8	RM-8	RM-8	RM-8	RM-8
analysis	26	27	29	30	28	31	7	12	9	8	6	11	10
lithology	l. chill zone	l. chill zone	l. chill zone	l. chill zone	l. chill zone	l. chill zone	BZ monz	BZ monz	BZ monz	BZ monz	BZ monz	BZ monz	BZ monz
P_2O_5	39.15	39.52	39.68	40.38	40.46	40.87	37.25	38.77	39.16	39.51	39.79	40.11	40.25
CaO	53.62	54.64	54.34	54.10	54.12	54.14	52.80	55.30	55.53	56.47	55.59	57.37	56.02
SiO_2	1.08	0.17	0.23	0.13	0.11	0.12	3.37	0.49	0.38	0.34	0.14	0.25	0.49
Al_2O_3	0.39	0.04	0.01	0.01		0.01	0.71	0.05	0.07	0.05	0.03	0.03	0.06
FeO	0.34	0.53	0.32	0.40	0.44	0.47	0.77	0.37	0.50	0.37	0.50	0.35	0.35
MnO	0.01	0.14	0.08	0.05	0.14	0.03	0.16	0.05	0.06	0.16	0.12	0.16	0.09
MgO	0.35	0.38	0.36	0.48	0.53	0.35	0.26	0.25	0.28	0.35	0.41	0.28	0.31
Na_2O	0.10	0.17	0.09	0.08	0.17	0.15	0.12	0.07	0.09	0.08	0.17	0.08	0.08
La_2O_3	0.06		0.24		0.24	0.18		0.37	0.43	0.31			
Ce_2O_3	0.22	0.13	0.44	0.22	0.31		0.49	0.09	0.44	0.35	0.09	0.13	0.09
SrO	0.34	0.28	0.32	0.34	0.31	0.33	0.24	0.31	0.33	0.29	0.29	0.30	0.34
Y_2O_3				0.10		0.20	0.06	0.04	0.04	0.06			0.14
F	2.06	1.85	2.08	1.93	1.74	1.92	2.21	2.23	2.10	2.54	1.96	2.94	2.19
Cl	0.3048	0.3661	0.3074	0.3522	0.4201	0.3470	0.2235	0.2853	0.2981	0.2900	0.3025	0.2765	0.2942
Total	97.14	97.53	97.73	97.72	98.17	98.33	97.73	97.66	98.80	100.11	98.61	100.98	99.86
P pfu	5.821	5.888	5.895	5.977	5.981	6.004	5.505	5.790	5.801	5.761	5.869	5.772	5.844
Ca pfu	10.089	10.301	10.217	10.135	10.125	10.064	9.875	10.451	10.410	10.420	10.376	10.448	10.293
Si pfu	0.189	0.029	0.040	0.022	0.019	0.021	0.588	0.086	0.066	0.058	0.025	0.042	0.084
Al pfu	0.080	0.007	0.002	0.003		0.002	0.146	0.011	0.014	0.011	0.006	0.005	0.012
Fe pfu	0.050	0.078	0.047	0.058	0.064	0.068	0.112	0.055	0.074	0.053	0.073	0.050	0.050
Mn pfu	0.002	0.020	0.011	0.008	0.021	0.004	0.024	0.007	0.009	0.023	0.017	0.024	0.014
Mg pfu	0.092	0.100	0.093	0.125	0.137	0.091	0.066	0.067	0.072	0.090	0.106	0.071	0.080
Na pfu	0.033	0.059	0.031	0.028	0.059	0.052	0.042	0.022	0.032	0.028	0.057	0.027	0.026
La pfu	0.004		0.016		0.016	0.012		0.024	0.028	0.019			
Ce pfu	0.014	0.009	0.028	0.014	0.020		0.031	0.006	0.028	0.022	0.006	0.008	0.006
Sr pfu	0.034	0.029	0.032	0.035	0.031	0.033	0.024	0.032	0.034	0.029	0.029	0.029	0.033
Y pfu				0.009		0.018	0.006	0.004	0.004	0.006			0.013
F pfu	1.144	1.029	1.155	1.065	0.963	1.053	1.221	1.243	1.160	1.386	1.078	1.578	1.189
Cl pfu	0.091	0.109	0.091	0.104	0.124	0.102	0.066	0.085	0.088	0.085	0.089	0.080	0.086
OH (ideal)	0.765	0.862	0.753	0.830	0.913	0.845	0.712	0.672	0.751	0.530	0.833	0.342	0.725
Total	18.409	18.520	18.412	18.414	18.473	18.369	18.419	18.554	18.571	18.520	18.564	18.477	18.454
X_F	0.572	0.514	0.578	0.533	0.481	0.527	0.611	0.621	0.580	0.693	0.539	0.789	0.594
X_{Cl}	0.045	0.055	0.046	0.052	0.062	0.051	0.033	0.043	0.044	0.042	0.045	0.040	0.043
X_{OH}	0.383	0.431	0.377	0.415	0.457	0.422	0.356	0.336	0.376	0.265	0.416	0.171	0.363

Appendix 3, continued. Rattlesnake Mountain Sill apatite analyses with atoms per formula unit allocated based on 26 O and OH.

sample	RM-16	RM-16	RM-16	RM-16	RM-16
analysis	24	23	25	22	21
	CZ	CZ	CZ	CZ	CZ
lithology	monz	monz	monz	monz	monz
P_2O_5	38.73	40.09	40.11	40.49	42.22
CaO	55.01	55.88	54.62	56.07	56.50
SiO_2	0.16	0.24	0.19	0.21	0.16
Al_2O_3	0.04	0.04	0.04	0.03	0.06
FeO	0.28	0.40	0.35	0.60	0.42
MnO	0.04		0.08	0.09	0.01
MgO	0.16	0.13	0.07	0.08	0.13
Na_2O	0.04	0.05	0.04	0.05	0.06
La_2O_3	0.12		0.06	0.37	
Ce_2O_3	0.44	0.44	0.22	0.26	
SrO	0.34	0.34	0.24	0.33	0.31
Y_2O_3		0.14		0.06	0.02
F	2.37	2.42	2.31	3.57	2.95
Cl	0.3702	0.3553	0.3330	0.3167	0.3713
Total	97.01	99.44	97.65	100.96	101.90
P pfu	5.823	5.861	5.939	5.805	5.952
Ca pfu	10.467	10.339	10.234	10.174	10.080
Si pfu	0.028	0.042	0.033	0.035	0.026
Al pfu	0.009	0.008	0.008	0.006	0.012
Fe pfu	0.042	0.058	0.051	0.085	0.058
Mn pfu	0.006		0.011	0.013	0.002
Mg pfu	0.041	0.034	0.018	0.019	0.032
Na pfu	0.012	0.017	0.015	0.017	0.018
La pfu	0.008		0.004	0.023	
Ce pfu	0.029	0.028	0.014	0.016	
Sr pfu	0.035	0.035	0.025	0.032	0.030
Y pfu		0.013		0.005	0.002
F pfu	1.333	1.324	1.278	1.912	1.555
Cl pfu	0.111	0.104	0.099	0.091	0.105
OH (ideal)	0.556	0.572	0.623	-0.003	0.340
Total	18.499	18.436	18.351	18.232	18.211
X_F	0.666	0.662	0.639	0.956	0.778
X_{Cl}	0.056	0.052	0.049	0.045	0.052
X_{OH}	0.278	0.286	0.312	-0.001	0.170

APPENDIX 4:

MINERAL ABBREVIATIONS

Most abbreviations used are from Kretz (1983).

Ab	Albite	Fsp	Feldspar
Aeg	Aegirine	F-ap	Fluorapatite
Afs	Alkali Feldspar	Hd	Hedenbergite
Am	Amphibole	Ilm	Ilmenite
An	Anorthite	Jd	Jadeite
Anl	Analcime	Ktp	Kataphorite
Ap	Apatite	Krs	Kaersutite
Brs	Barroisite	Kfs	K-feldspar
Cpx	Clinopyroxene	Mg-Tmt	Magnesio-taramite
Cl-ap	Chlorapatite	Mt	Magnetite
Di	Diopside	Ne	Nepheline
En	Enstatite	Ol	Olivine
Fe2-Ed	Ferro-edenite	Opx	Orthopyroxene
Fe2-krs	Ferro-kaersutite	Or	Orthoclase
Fe2-Prg	Ferro-pargasite	Phl	Phlogopite
Fe2-win	Ferro-winchite	Pl	Plagioclase
Fs	Ferrosilite	Rt	Rutile

Srp	Serpentine
Usp	Ulvöspinel
Zrn	Zircon

APPENDIX 5:

ANALYSES OF ORIENTED SECTIONS OF DURANGO APATITE

Appendix 5. Analyses of oriented sections of Durango apatite. Orientations: C-perp. = C-axis mounted perpendicular to stage, C-par. = C-axis mounted parallel to stage, and C-int. = C-axis mounted at an intermediate angle to stage.

orientation	C-perp.	C-perp.	C-perp.	C-perp.	C-perp.	C-perp.	C-perp.	C-perp.	C-perp.	C-perp.	C-perp.	C-perp.	C-perp.
label	p31	p33	p34	p34b	p10	p10b	p13	p18	p2	p20	p28	p6	p21
P_2O_5	36.27	36.03	39.49	36.13	38.45	36.82	37.42	39.25	38.58	38.60	41.14	38.02	38.20
CaO	55.23	55.96	55.39	56.21	58.40	55.35	55.68	53.96	57.49	53.84	55.32	57.44	55.93
SiO_2	0.36	0.39	0.35	0.40	0.38	0.42	0.34	0.31	0.41	0.35	0.40	0.35	0.37
Na_2O	0.28	0.22	0.21	0.21	0.23	0.33	0.25	0.30	0.33	0.25	0.25	0.19	0.22
La_2O_3	0.55	0.93					0.74	0.56				0.57	
Ce_2O_3				0.58	1.03			0.64	0.63			0.67	0.79
SrO			0.10	0.07					0.08		0.09		
Y_2O_3			0.18							0.20			0.18
SO_3	0.58	0.38	0.73	0.36	0.29	0.48	0.33	0.21	0.29	0.15	0.70	0.30	0.62
F	3.27	4.08	3.32	4.62	3.74	4.02	3.83	3.24	3.36	3.28	3.05	3.96	3.34
Cl		0.37		0.35	0.37	0.47	0.36	0.36	0.38	0.50		0.37	
Total'	96.54	98.36	99.78	98.94	102.89	97.90	98.95	98.82	101.54	97.17	100.95	101.88	99.66
-O=F	1.38	1.72	1.40	1.95	1.57	1.69	1.61	1.36	1.41	1.38	1.28	1.67	1.41
-O=Cl	0.00	0.08	0.00	0.08	0.08	0.11	0.08	0.08	0.09	0.11	0.00	0.08	0.00
Total	95.16	96.56	98.38	96.91	101.24	96.10	97.26	97.38	100.04	95.68	99.66	100.13	98.25
P	5.606	5.489	5.759	5.430	5.554	5.542	5.592	5.823	5.622	5.802	5.886	5.549	5.643
Ca	10.804	10.789	10.222	10.690	10.676	10.543	10.531	10.132	10.601	10.242	10.017	10.608	10.456
Si	0.066	0.071	0.061	0.072	0.065	0.075	0.060	0.055	0.070	0.061	0.067	0.060	0.065
Na	0.098	0.075	0.070	0.073	0.077	0.115	0.087	0.100	0.109	0.087	0.083	0.064	0.076
La	0.037	0.062					0.048	0.036				0.037	
Ce				0.038	0.064			0.041	0.040			0.042	0.050
Sr			0.010	0.007					0.008		0.008		
Y			0.016							0.019			0.017
S			0.095	0.047	0.037	0.064	0.043	0.028	0.037	0.020	0.089	0.038	0.081
F	1.888	2.322	1.808	2.593	2.018	2.260	2.138	1.796	1.829	1.842	1.630	2.159	1.843
Cl		0.112		0.105	0.108	0.142	0.108	0.107	0.112	0.150		0.109	
OH (ideal)	0.112		0.192					0.098	0.059	0.008	0.370		0.157
Total	18.611	18.486	18.234	18.358	18.474	18.340	18.361	18.215	18.487	18.232	18.151	18.399	18.390
X_F	0.944	1.161	0.904	1.297	1.009	1.130	1.069	0.898	0.914	0.921	0.815	1.079	0.922
X_{Cl}		0.056		0.052	0.054	0.071	0.054	0.053	0.056	0.075		0.054	
X_{OH}	0.056		0.096					0.049	0.030	0.004	0.185		0.078

Appendix 5, continued. Analyses of oriented sections of Durango apatite.

orientation	C-perp.	C-perp.	C-perp.	C-perp.	C-par.	C-par.	C-par.	C-par.	C-par.	C-par.	C-par.
label	p26	Avg.	1σ	n	pl-31	pl-37	pl-10	pl-13	pl-16	pl-18	pl-27
P_2O_5	39.20	38.11	1.41	14	34.77	40.06	38.32	37.66	37.63	39.07	38.27
CaO	55.59	55.84	1.22	14	55.51	56.42	55.06	54.83	55.68	54.54	55.26
SiO_2	0.33	0.37	0.03	14	0.39	0.37	0.39	0.41	0.38	0.41	0.44
Na_2O	0.22	0.25	0.04	14	0.21	0.26	0.25	0.27	0.30	0.34	0.24
La_2O_3	0.62	0.66	0.14	6	0.68			0.63	1.13	0.68	
Ce_2O_3	0.58	0.70	0.15	7		0.49		0.88	0.74	0.69	0.76
SrO	0.08	0.08	0.01	5		0.11		0.08	0.10	0.13	
Y_2O_3	0.20	0.19	0.01	4							
SO_3	0.55	0.43	0.18	14	0.33	0.24	0.40	0.37	0.30		0.49
F	4.73	3.70	0.51	14	3.16	3.15	3.00	3.40	3.17	2.95	2.72
Cl		0.39	0.05	9	0.44	0.47	0.52	0.37	0.37	0.41	
Total'	102.09	99.68	1.87	14	95.49	101.58	97.94	98.92	99.81	99.21	98.18
-O=F	1.99	1.56	0.21	14	1.33	1.33	1.26	1.43	1.33	1.24	1.15
-O=Cl	0.00	0.06	0.04	14	0.10	0.11	0.12	0.08	0.08	0.09	0.00
Total	100.10	98.06	1.85	14	94.06	100.15	96.56	97.40	98.39	97.88	97.03
P	5.640	5.639	0.128	14	5.446	5.783	5.730	5.641	5.617	5.806	5.725
Ca	10.123	10.460	0.254	14	11.003	10.307	10.420	10.393	10.519	10.258	10.462
Si	0.056	0.065	0.006	14	0.072	0.063	0.069	0.073	0.068	0.072	0.078
Na	0.072	0.085	0.015	14	0.076	0.086	0.086	0.094	0.102	0.116	0.082
La	0.039	0.043	0.009	6	0.047			0.041	0.074	0.044	
Ce	0.036	0.045	0.009	7		0.031		0.057	0.048	0.044	0.049
Sr	0.008	0.008	0.001	5		0.011		0.009	0.010	0.013	
Y	0.018	0.017	0.001	4							
S	0.070	0.054	0.024	12	0.046	0.031	0.053	0.050	0.040		0.064
F	2.542	2.048	0.285	14	1.849	1.698	1.673	1.902	1.768	1.637	1.521
Cl		0.117	0.016	9	0.137	0.136	0.156	0.112	0.111	0.121	
OH (id.)		0.142	0.108	7	0.014	0.166	0.171		0.122	0.243	0.479
Total	18.062	18.343	0.145	14	18.689	18.311	18.358	18.358	18.477	18.353	18.461
X_F	1.271	1.024	0.142	14	0.924	0.849	0.836	0.951	0.884	0.818	0.761
X_{Cl}		0.058	0.008	9	0.069	0.068	0.078	0.056	0.055	0.060	
X_{OH}		0.071	0.054	7	0.007	0.083	0.085		0.061	0.121	0.239

Appendix 5, continued. Analyses of oriented sections of Durango apatite

orientation	C-par.	C-par.	C-par.	C-par.	C-par.	C-par.	C-par.	C-par.	C-int.	C-int.	C-int.
label	pl-30	pl-6	pl-9	pl-21	pl-27	Avg.	1σ	n	i-22	i-23	i-20
P_2O_5	37.13	36.82	39.99	39.24	38.94	38.31	1.47	13	36.81	38.70	39.62
CaO	55.51	55.05	55.35	55.91	54.61	55.31	0.50	13	54.47	54.18	54.63
SiO_2	0.35	0.37	0.44	0.39	0.43	0.40	0.03	13	0.44	0.44	0.40
Na_2O	0.33	0.27	0.27	0.26	0.28	0.27	0.04	13	0.25	0.25	0.28
La_2O_3	0.61			0.49		0.70	0.20	6	0.74	0.99	0.62
Ce_2O_3	0.63	0.94	0.72	0.70		0.72	0.12	10			0.85
SrO	0.08	0.08	0.09	0.07	0.08	0.09	0.02	10			0.11
Y_2O_3		0.25	0.19			0.21	0.03	3			
SO_3	0.57	0.53	0.37	0.72	0.44	0.44	0.13	12	0.58	0.26	0.47
F	2.73	3.35	2.99	3.07	4.11	3.12	0.35	13	4.29	4.02	4.00
Cl		0.42	0.50			0.44	0.05	8			
Total'	97.94	98.09	100.91	100.86	98.89	99.09	1.58	13	97.59	98.84	100.96
-O=F	1.15	1.41	1.26	1.29	1.73	1.32	0.15	13	1.81	1.69	1.68
-O=Cl	0.00	0.10	0.11	0.00	0.00	0.06	0.05	13	0.00	0.00	0.00
Total	96.78	96.58	99.54	99.57	97.16	97.72	1.59	13	95.79	97.15	99.28
P	5.621	5.569	5.804	5.714	5.730	5.694	0.107	13	5.553	5.734	5.749
Ca	10.635	10.537	10.166	10.303	10.169	10.410	0.226	13	10.399	10.159	10.032
Si	0.063	0.066	0.075	0.067	0.075	0.070	0.004	13	0.079	0.078	0.068
Na	0.114	0.094	0.091	0.087	0.095	0.092	0.012	13	0.088	0.085	0.092
La	0.040			0.031		0.046	0.013	6	0.049	0.064	0.039
Ce	0.041	0.062	0.045	0.044		0.046	0.008	10			0.053
Sr	0.008	0.008	0.009	0.007	0.008	0.009	0.002	10			0.011
Y		0.024	0.017			0.020	0.003	3			
S	0.076	0.071	0.048	0.093	0.057	0.058	0.017	12	0.078	0.034	0.060
F	1.545	1.893	1.621	1.670	2.259	1.736	0.196	13	2.417	2.225	2.168
Cl		0.128	0.146			0.131	0.015	8			
OH (id.)	0.455		0.233	0.330		0.18	0.21	13			
Total	18.598	18.432	18.255	18.346	18.134	18.388	0.140	13	18.246	18.153	18.104
X_F	0.773	0.946	0.811	0.835	1.129	0.868	0.098	13	1.209	1.112	1.084
X_{Cl}		0.064	0.073			0.065	0.008	8			
X_{OH}	0.227		0.117	0.165		0.09	0.11	13			

Appendix 5, continued. Analyses of oriented sections of Durango apatite

orientation	C-int.	C-int.	C-int.	C-int.	C-int.	C-int.	C-int.	C-int.	C-int.	C-int.	C-int.
label	i-19	i-17	i-9	i-8	i-7	i-6	i-5	i-4	i-3	i-28	i-27
P_2O_5	38.23	39.64	37.61	38.64	36.57	39.28	38.84	39.72	38.32	37.84	39.74
CaO	55.18	54.99	54.77	55.52	55.35	56.60	55.90	56.30	56.64	55.57	55.49
SiO_2	0.43	0.42	0.36	0.36	0.44	0.36	0.36	0.36	0.33	0.37	0.37
Na_2O	0.26	0.30	0.17	0.33	0.28	0.29	0.24	0.21	0.21	0.24	0.20
La_2O_3	0.68	0.55		0.75		0.80		0.69	0.86	0.85	
Ce_2O_3	0.48	0.70	0.81	0.80	0.76	0.85	0.94	0.81		0.85	0.67
SrO		0.07	0.08	0.14	0.11			0.10		0.08	0.10
Y_2O_3										0.18	
SO_3	0.67	0.46		0.44	0.28	0.42	0.29		0.32	0.37	0.54
F	3.17	3.26	3.19	3.07	2.77	2.80	3.41	2.98	2.85	2.73	2.96
Cl			0.39	0.51	0.50	0.47	0.39	0.38	0.38		
Total'	99.10	100.39	97.38	100.57	97.06	101.88	100.38	101.55	99.92	99.08	100.07
-O=F	1.33	1.37	1.34	1.29	1.17	1.18	1.44	1.26	1.20	1.15	1.25
-O=Cl	0.00	0.00	0.09	0.12	0.11	0.11	0.09	0.08	0.09	0.00	0.00
Total	97.76	99.02	95.95	99.16	95.78	100.59	98.85	100.21	98.64	97.93	98.82
P	5.674	5.784	5.708	5.688	5.600	5.708	5.701	5.781	5.673	5.671	5.800
Ca	10.364	10.154	10.519	10.343	10.725	10.409	10.385	10.370	10.611	10.539	10.249
Si	0.076	0.072	0.065	0.063	0.079	0.062	0.063	0.062	0.058	0.066	0.063
Na	0.087	0.102	0.060	0.112	0.097	0.096	0.082	0.071	0.073	0.082	0.067
La	0.044	0.035		0.048		0.051		0.044	0.056	0.056	
Ce	0.031	0.044	0.053	0.051	0.050	0.053	0.060	0.051		0.055	0.042
Sr		0.007	0.008	0.015	0.012			0.010		0.008	0.010
Y										0.017	
S	0.088	0.059		0.058	0.038	0.055	0.038		0.043	0.050	0.070
F	1.757	1.777	1.808	1.688	1.584	1.518	1.870	1.622	1.575	1.526	1.613
Cl			0.118	0.151	0.153	0.136	0.115	0.110	0.112		
OH (id.)	0.243	0.223	0.074	0.161	0.264	0.345	0.015	0.269	0.312	0.474	0.387
Total	18.365	18.257	18.413	18.377	18.601	18.435	18.328	18.389	18.512	18.543	18.302
X_F	0.879	0.888	0.904	0.844	0.792	0.759	0.935	0.811	0.788	0.763	0.806
X_{Cl}			0.059	0.076	0.076	0.068	0.058	0.055	0.056		
X_{OH}	0.121	0.112	0.037	0.080	0.132	0.173	0.007	0.134	0.156	0.237	0.194

Appendix 5, continued. Analyses of oriented sections of Durango apatite

orientation	C-int.	C-int.	C-int.	C-int.	C-int.	C-int.	C-int.	C-int.	C-int.	C-int.	C-int.	C-int.
label	i-23	i-2	i-16b	i-15b	i-14b	i-13b	i-12	i-11	i-10	i-1	i-34	i-33
P_2O_5	37.44	39.62	39.32	39.43	39.91	36.55	36.54	38.34	37.87	38.45	41.93	39.22
CaO	52.78	56.37	52.86	53.71	54.40	54.85	54.48	54.43	55.44	56.39	54.51	55.31
SiO_2	0.42	0.37	0.42	0.40	0.42	0.38	0.43	0.42	0.47	0.39	0.40	0.36
Na_2O	0.24	0.32	0.31	0.22	0.23	0.33	0.29	0.27	0.21	0.23	0.27	0.26
La_2O_3	0.55			0.80		0.97						
Ce_2O_3	0.85	0.63	0.82	0.78	0.78	0.57	0.83			0.94	0.98	0.63
SrO		0.11		0.11	0.09	0.09	0.08				0.07	
Y_2O_3					0.18					0.19		
SO_3	0.42	0.32				0.34	0.29	0.41	0.34	0.32	0.36	0.32
F	3.94	2.94	2.92	3.08	2.93	3.22	2.99	3.17	3.03	2.99	2.99	3.18
Cl		0.42	0.50	0.43	0.41	0.50	0.49	0.46	0.44	0.37	0.45	0.38
Total'	96.64	101.10	97.16	98.96	99.35	97.78	96.42	97.51	97.79	100.27	101.98	99.65
-O=F	1.66	1.24	1.23	1.30	1.23	1.36	1.26	1.33	1.28	1.26	1.26	1.34
-O=Cl	0.00	0.09	0.11	0.10	0.09	0.11	0.11	0.10	0.10	0.08	0.10	0.09
Total	94.98	99.77	95.81	97.56	98.03	96.32	95.05	96.07	96.42	98.92	100.61	98.23
P	5.691	5.759	5.908	5.857	5.879	5.573	5.619	5.745	5.686	5.672	5.965	5.769
Ca	10.153	10.369	10.052	10.097	10.142	10.584	10.603	10.322	10.534	10.527	9.814	10.296
Si	0.075	0.064	0.075	0.070	0.074	0.068	0.079	0.074	0.083	0.068	0.068	0.062
Na	0.085	0.107	0.107	0.073	0.078	0.114	0.101	0.094	0.073	0.076	0.089	0.087
La	0.037			0.052		0.064						
Ce	0.056	0.039	0.053	0.050	0.050	0.038	0.055			0.060	0.060	0.040
Sr		0.011		0.011	0.009	0.010	0.009				0.007	
Y					0.017					0.017		
S	0.056	0.041				0.045	0.039	0.055	0.045	0.041	0.045	0.041
F	2.237	1.596	1.638	1.709	1.610	1.834	1.717	1.774	1.699	1.648	1.591	1.747
Cl		0.122	0.151	0.128	0.121	0.152	0.149	0.138	0.132	0.110	0.128	0.113
OH (id.)		0.282	0.211	0.163	0.269	0.014	0.134	0.087	0.169	0.241	0.281	0.140
Total	18.153	18.391	18.195	18.211	18.248	18.495	18.504	18.289	18.420	18.462	18.049	18.295
X_F	1.119	0.798	0.819	0.854	0.805	0.917	0.858	0.887	0.850	0.824	0.795	0.874
X_{Cl}		0.061	0.076	0.064	0.061	0.076	0.075	0.069	0.066	0.055	0.064	0.057
X_{OH}		0.141	0.106	0.081	0.135	0.007	0.067	0.044	0.085	0.121	0.141	0.070

Appendix 5, continued. Analyses of oriented sections of Durango apatite

orientation	C-int.	C-int.	C-int.	C-int.	C-int.	C-int.		all	all	all
label	i-31	i-30	i-29	Avg.	1σ	n		Avg.	1σ	n
P_2O_5	38.29	37.26	38.57	38.57	1.26	32		36.49	7.69	65
CaO	54.68	54.65	54.57	55.00	0.93	32		52.32	11.70	65
SiO_2	0.44	0.43	0.39	0.40	0.03	32		0.78	2.27	65
Na_2O	0.28	0.28	0.21	0.26	0.04	32		0.66	2.29	65
La_2O_3		0.56	0.56	0.71	0.15	17		0.97	1.25	35
Ce_2O_3	0.58			0.76	0.13	25		1.04	1.60	48
SrO	0.09			0.10	0.02	16		0.49	1.77	37
Y_2O_3	0.23			0.19	0.02	4		0.56	1.09	17
SO_3	0.27	0.34	0.32	0.39	0.11	26		0.84	2.31	58
F	3.10	3.36	3.31	3.17	0.39	32		3.52	1.90	65
Cl	0.40	0.49	0.51	0.44	0.05	22		0.77	1.67	45
Total'	98.36	97.37	98.44	99.07	1.61	32		93.58	22.12	65
-O=F	1.31	1.41	1.39	1.34	0.16	32		1.72	2.12	65
-O=Cl	0.09	0.11	0.11	0.07	0.05	32		0.48	2.32	65
Total	96.97	95.85	96.93	97.66	1.67	32		92.22	21.78	65
P	5.726	5.643	5.745	5.728	0.096	32		5.766	1.687	65
Ca	10.349	10.473	10.286	10.343	0.207	32		10.170	1.864	65
Si	0.078	0.077	0.068	0.070	0.007	32		0.480	2.321	65
Na	0.097	0.097	0.073	0.089	0.013	32		0.499	2.318	65
La		0.037	0.036	0.046	0.010	17		0.384	1.383	35
Ce	0.038			0.049	0.008	25		0.398	1.717	48
Sr	0.009			0.010	0.002	16		0.414	1.791	37
Y	0.022			0.018	0.002	4		0.426	1.136	17
S	0.036	0.046	0.043	0.051	0.014	26		0.479	2.217	56
F	1.732	1.901	1.841	1.763	0.226	32		2.137	2.061	65
Cl	0.118	0.149	0.151	0.131	0.016	22		0.494	1.730	45
OH (id.)	0.150		0.008	0.148	0.216	32		0.507	2.331	65
Total	18.355	18.373	18.251	18.341	0.131	32		17.642	3.232	65
X_F	0.866	0.950	0.921	0.881	0.113	32		1.276	2.188	65
X_{Cl}	0.059	0.074	0.075	0.065	0.008	22		0.436	1.742	45
X_{OH}	0.075		0.004	0.074	0.108	32		0.461	2.328	65